CRANFIELD UNIVERSITY

WILSON VESGA RIVERA

AN EVALUATION OF THE STRUCTURAL INTEGRITY OF HSLA STEELS EXPOSED IN SIMULATED FLUE-GASES UNDER DYNAMIC CONDITIONS FOR ANTHROPOGENIC CO_2 TRANSPORT.

SCHOOL OF ENERGY, ENVIRONMENT AND AGRIFOOD

PhD, Full time

PhD Thesis

Supervisor: Professor Feargal Brennan
December 2014

CRANFIELD UNIVERSITY

SCHOOL OF ENERGY, ENVIRONMENT AND AGRIFOOD
PhD, Full time

PhD THESIS

WILSON VESGA RIVERA

AN EVALUATION OF THE STRUCTURAL INTEGRITY OF HSLA STEELS EXPOSED IN SIMULATED FLUE-GASES UNDER DYNAMIC CONDITIONS FOR ANTHROPOGENIC CO_2 TRANSPORT.

Supervisor: Professor Feargal Brennan

December 2014

This thesis is submitted in partial fulfilment of the requirements for the degree of PhD.

Dedicated especially to;

My lovely and wonderful wife and mother, Luz Dary, her love, strength, sacrifice and support may the difference through these years and pushing me to keep going in hard times. You make the difference in my life.

To my princes Lina Gabriela, you are always my source of understanding why the life is worthy. Your smile, kindness, warming and endearing love are one of the most beautiful and precious gift that I have received in my life. You are so wonderful and gorgeous.

To my son Andres Felipe whose constant thirst for learning about everything that occurred around him has taught me to understand simple things and see how brilliant and unique you are. Trying to understand the way you see life has helped to change my perspective about the world.

Wilson

ABSTRACT

Carbon capture and storage (CCTS) is a transitional technology offering a near-term method of mitigating climate change. Pipelines are considered to be the most suitable systems for CCTS; however, structural integrity of pipeline has to be guaranteed in order for this technology to become a practical technical solution.

The investigation detailed here is based on a systematic experimental approach to investigate the structural integrity of API X100, X60 and X70 steels exposed in simulated flue-gas under dynamic conditions. A core of the structured experiments through some methods such as aging test, tensile properties, fracture toughness, residual stress and engineering critical assessment was accomplished in parent material and exposed samples on flue-gas.

The temperature range of evaluation for tensile test covers -70°C to 21°C while fracture toughness was over the range -196°C to 21°C. Tensile properties of virgin material show that steels meet standard specification while aging samples do not show significant scatter compared with parent steels. Ovalisation of the fracture surface and splitting phenomenon was observed which is related with steel anisotropy. Fracture toughness obtained from experiment was compared with that calculate by two existing correlations. However both correlations did not predict the level of fracture toughness expected indicating the methods used in this work has limited applicability under the test conditions used here.

Residual stress (RS) induced in API X100 steel by cold rolling method was characterised using two complementary techniques known as Neutron Diffraction (ND) and Incremental Hole Drilling (IHD). The RS distribution shows good agreement for both techniques used but reproducibility of them depends on their own inaccuracies. An Engineering Criticality Assessment (ECA) was performed based in Failure Assessment Diagram (FAD) approach using all the experimental data obtained by a leak-before-break method under three operational pressures. The results showed the effect on the integrity of material under the presence of a flaw length assessed.

Overall, the thesis presents a combined engineering critical assessment which involved the examination of materials used to transport flue-gas and established a methodology to determine fracture toughness alongside with the FAD to assess the integrity of pipelines.

Keywords: Supercritical CO_2 and impurities; fracture toughness; HSLA steel

ACKNOWLEDGEMENTS

I could not have completed this research without the contribution of many people who made significant contributions throughout the course of this work in time, advice and wisdom.

I am extremely grateful to my supervisor, Professor Feargal Brennan, for his guidance, support and his unique manner of teaching and motivating throughout this project; as well as providing me with various opportunities to interact with people across academia and industry. I am very grateful to Dr. Amir Chahardehi, for his assistance, advice and encouragement, particularly relating to residual stress analysis, cold rolling tests and neutron diffraction test.

The author would like to acknowledge the support and the technical guidance from Dr Harry Coulee during the performance of cold rolling tests and discussion about residual stress. Sincere thanks to the staff at The Welding Centre at Cranfield University. My thanks also go to Dr Athanasios Kolios and Eng Ravaal Sookoo for their help during the test at FRM II facilities. I would like to thank the staff at STRESS-SPEC at the FRM II facilities in Munich for allowing to perform the neutron diffraction experiments and processing the experimental data.

At Cranfield University, I would like to thank Sam Skears & Graham Lee for their support and guidance during the different stages of the project. I wish to give thanks to Dr David Ayre, Benn Hopper, Dr James Watson and his team, Barry Walker, Derek Brown, Kevin White, Ian Hancock, Lucy Kings and Sue Bennett for all their support and assistance. I would also like to thank Cranfield University, Roberto Rocca Education Program (RREP) and Colfuturo for providing the funding to complete this work.

To all the staff at Cranfield University that offered me generous help and advice assistance, with special mention to the staff of the Library (Kingston and MIRC), IT Department, Financial department and Housing Office.

I would like to express my thanks to all my dear friends and colleagues at Cranfield University with especial gratitude to Payam, Xiaojian Hung, Grema Alhaji, Mahadi Abd Murad, Eloy Perez, Sergio Contesse, Daniel Cozzolino, Adepipe, for their friendship, help and memories we have during our studies.

I would like to take this opportunity to express my deepest gratitude to Alan, Cathy, Rebecca, Michael and Richard Horgan for their unfailing support, help, friendship and love. To my friend Antonio Caraballo for his support, help and assistance. To Jacinto Carrasco for his friendship, support and the opportunity to build a great friendship.

Last, but no means, I would also like to thank Reynaldo, Luz Marina and Maria Carlina, my father, mother and sister-in-law, for their love and support to myself, my wife Luz Dary and my children Lina Gabriela and Andres Felipe. I would like to thank my father Eusebio (q.e.p.d), my mother Laura Maria, my sister Luz Stella and my brothers Henry, Daniel, Abelardo, Samuel and my aunt Maria Smith for their support and love. To all the people I have learnt from and the list does no stop growing.

To God because of his great love and mercy with me and my family.

TABLE OF CONTENTS

LIST OF FIGURES

LIST OF TABLES

LIST OF EQUATIONS

SYMBOLS

Symbol	Definition	Units
A_f	Elongation after fracture	%
CVN	Charpy V-notch energy	J
G_{Ic}	Plain strain Mode I toughness	N/m
J_{Ic}	Critical Mode I value of *J*-integral in plane strain	N/m
K	Stress intensity factor	MPa√m
K_{Ic}	Plane strain fracture toughness in Mode I	MPa√m
K_{Id}	Dynamic plane strain fracture toughness in Mode I	MPa√m
K_Q	Plain critical stress intensity factor obtained from specimens that do not conform to recommended standard	MPa√m
K_{Jc}	Material toughness derived from J-integral	MPa√m
K_{mat}	Material toughness measured by stress intensity factor	MPa√m
Y	Stress intensity correction factor	
T_{28J}	Temperature for energies of 28 J measured in a standard Charpy V specimen	°C
T_{40J}	Temperature for energies of 40 J measured in a standard Charpy V specimen	°C
{hkl}	Miller indices describing a family of crystalline planes	
d	Inter-planar spacing (d-spacing) -the perpendicular distance between adjacent parallel crystallographic planes.	Å
d_0	Strain free inter-planar spacing	Å
a	Crack length	mm
a_i	Notch length before crack initiation	mm
an, an+1	Current crack lengths measured at two successive steps n and n+1	mm
Δa	Change in crack length	mm
P_{max}	Maximum load	N
P_{min}	Minimum load	N
R	Ratio of minimum to maximum load or stress	-
K_{res}	Stress intensity due to residual stress	MPa√m
K_{max}	Maximum stress intensity	MPa√m
K_{norm}	Normalized stress intensity	MPa√m
ΔK	Stress intensity range	MPa√m
ΔKapp	Applied stress intensity range	MPa√m
ΔK_{eff}	Effective stress intensity range	MPa√m
ΔK_{cl}	$\Delta K_{app} - \Delta K_{eff}$, stress intensity reduction due to closure	MPa√m
K_r	Fracture ratio of applied elastic K value to K_{mat}	-
L_r	Ratio of applied load to yield load	-
M	Bulging correction factor	
P	Primary stress	MPa
Q	Secondary stress	MPa
P_m	Primary bending stress	MPa
Q_m	Secondary bending stress	MPa

GREEK SYMBOLS

Symbol	Definition	Units
E	Modulus of elasticity	GPa
ν	Poisson's ratio	
δ	Crack tip opening displacement (CTOD)	mm
δ_{mat}	Material toughness measured by CTOD	
ρ	Plasticity correction factor	
$\varepsilon_1, \varepsilon_2, \varepsilon_3,$	Principal strains acting in the principal directions	µs
ε_x	Strain measured in the in-plane X	µs
ε_y	Strain measured in the in-plane Y	µs
ε_z	Strain measured in the in-plane Z	µs
σ	Normal stress	MPa
σ_x	Stress acting in the X direction	MPa
σ_y	Stress acting in the Y direction	MPa
σ_z	Stress acting in the Z direction	MPa
$\sigma_1, \sigma_2, \sigma_3$	Principal stresses acting in the principal directions	MPa
$\sigma_{0,2}$/ $R_{p0.2}$	Yield strength (0.2% non-proportional extension)	MPa
$\sigma_{0,5}$/ $R_{p0.5}$	Yield strength (0.5% Extension-Under-Load))	MPa
σ_{UTS}/R_m	Ultimate tensile strength	MPa
σ_y	Lower yield strength	MPa
E_{hkl}	Modulus of elasticity in *h,k,l* directions	GPa

LIST OF ABBREVIATIONS

4PB	Four-point bending
ACC	Accelerated cooling process
AFAs	Abnormal fracture appearances
API	American Petroleum Institute
ASME	American Society of Mechanical Engineers
BCC	Body- Centred Cubic
BTCM	Battelle Two-Curve Model
CCS	Carbon Capture and Storage
CCT	Continuous Cooling Transformation Diagram
CCTS	Carbon Capture, Transport and Storage
CEN	Carbon equivalent
CDF	Crack driving force
CMOD	Crack Mouth Opening Displacement
CRs	Corrosion rates
CT	Compact tension
CTOA	Crack Tip Opening Angle Displacement
CTOD	Crack Tip Opening Displacement
CVN	Charpy-V notch
DBTT	Ductile-brittle transition temperature
DWTT	Drop Weight Tear Test
EBDS	Electron Backscatter Diffraction Analysis
EGIG	European Gas Pipeline Incident Data Group
EIS	Electrochemical Impedance Spectroscopy
EOR	Enhanced Oil Recovery
EPFM	Elastic-plastic fracture mechanics
FAD	Failure assessment diagram
FFS	Fitness-for-service
FITNET	European fitness for service network
FITT	Fracture initiation toughness temperature
FTTP	Fracture propagation transition temperature

GHGs	Greenhouse gases
HIC	Hydrogen Induced cracking
HLP	High Strength Line Pipe Committee in ISIJ
HSLA	High strength low carbon alloy
HTP	High Temperature Process
HTs	High temperatures
IEA	International Energy Agency
IGCC	Integrated gasification combined cycle
IPCC	Intergovernmental panel on climate change
LAGBs	Low angle grain boundaries
LEFM	Linear elastic fracture mechanics
MC	Master Curve
OM	Optical microscope
PCCVN	Precracked Charpy V-notch
Q & T	Quenched and tempered
RDF	Running ductile fracture
SC^3	Super Critical CO_2 Corrosion Rig
SCC	Stress corrosion cracking
SEM	Scanning electron microscope
SINTAP	Structural Integrity Assessment Procedures for European Industry
SOHIC	Stress Oriented Hydrogen Induced Cracking
SSC	Sulphide stress cracking
SZW	Stretch zone width
TMCP	Thermo-Mechanically Controlled Processed

1 STRUCTURAL INTEGRITY OF MATERIALS FOR CO_2 TRANSPORT

1.1 Introduction and background

The effort required to reduce emissions of large amounts of carbon dioxide (CO_2) and other greenhouse gases (GHGs) is a priority with immediate action required to keep CO_2 out of the atmosphere. The main sector with the highest emissions of CO_2 is the energy area, with approximately 77% of total GHGs originating from the burning of oil, coal and gas by power plants for electricity generation (Figure 1-1). Thus, burning fossil fuels at power stations requires technical solutions to be found for the capture, transport and storage of anthropogenic CO_2 [1,2].

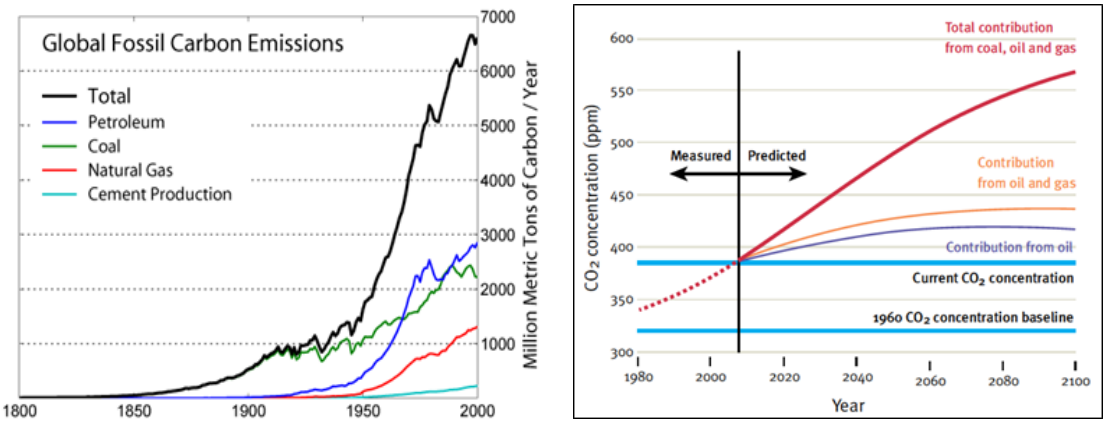

(a) Global CO_2 emissions [3] (b) CO_2 concentrations [4]

Figure 1-1 Global perception of CO_2 emissions

Within the energy sector five approaches have been proposed as alternatives to tackling climate change: energy efficiency, decreasing fuel use, renewable energy, nuclear power, and carbon capture and storage (CCS) (Figure 1.2). Renewable energy and nuclear energy could offer a clean technological solution for zero emissions and help to tackle climate change but there is not enough development into supplying the worldwide demand for delivering all of the GHGs' reductions [5].

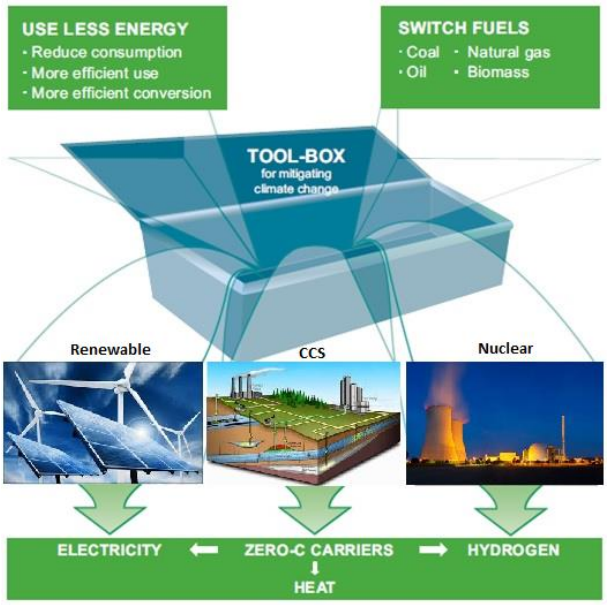

Figure 1-2 Technological keys to tackle climate change (After Kårstad[1])

In the short term, only CCS has the potential to reduce 20% of greenhouse emissions by 2050, using engineering methods [1,6]. Figure 1-3 shows the CCS scheme that comprises the capture of CO_2 from large sources such as power stations or industrial facilities, transportation of the CO_2 to a suitable storage point and injection underground either for storage or via enhanced oil recovery (EOR) [1,7].

The chain clearly involves transportation which undoubtedly has to be included as part of the system. Proposals to rename CCS as CCTS (Carbon Capture Transportation and Storage) have been raised as the former does not include transportation which it is one of the main parts of this technology. Hereafter the CCTS acronym will be used as it better describes this system.

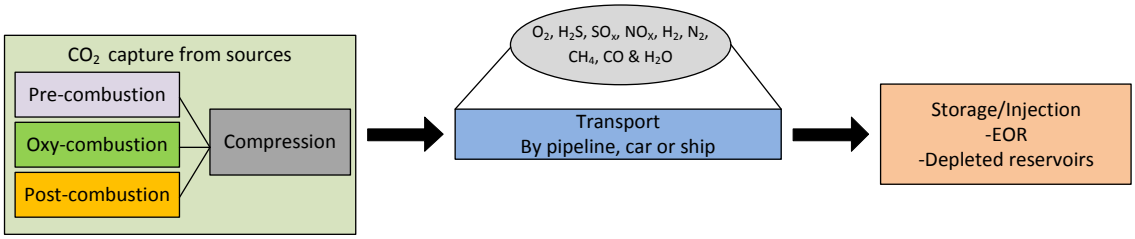

Figure 1-3 CCTS chain

[1] Original Illustration source: Kårstad, Freund. “Keeping the lights on”. Universitetsforlaget, 2007.

Even though on a commercial scale CO_2 can be transported via tankers or ships, transporting anthropogenic CO_2 from the energy or industry plants to a remote sequestration place may be an issue for CCTS systems due to the feasibility of applying this technology [8–11]. In this framework, pipelines – both onshore and offshore – are considered to be the most suitable solution to transport safely, efficiently and with least expense, supercritical or dense phase CO_2 over long distances [1,12,13].

Conveying CO_2 by pipeline is not a new concept in the world. There is a 40 years experiences transporting CO_2 from natural and anthropogenic sources for EOR application, mainly in the USA. However, with only approximately 7000 km of pipelines operating worldwide without environmental, health or safety issues this could be insufficient or inadequate for UK or European scenarios [9,14] as there are differences between the existing and new pipelines to transport anthropogenic CO_2 [15]. This dissimilarities are summarised in Table 1-1.

Table 1-1 Differences between current and new pipelines transporting CO_2

Parameters	**Existing CO_2 pipelines**	**New CO_2 pipelines**
Application	EOR	CCTS
Sources	Nearly pure CO_2	Impurities depending on capture method
Transited areas	Remote or unpopulated	Populated
Demand	‘Static’	Fluctuation due to load factors
Perception	Benign	Higher throughput

From a captured standpoint, CO_2 may contain impurities that could affect CCTS systems. Non-condensable components such as nitrogen (N_2), oxygen (O_2) and water (H_2O), but also air pollutants such as sulphur oxides (SO_x), nitrogen oxides (NO_x), hydrochloric acid (HCl), hydrogen fluoride (HF), mercury (Hg), Argon (Ar), hydrogen sulphide (H_2S), Methane (CH_4), hydrogen (H_2) and carbon

monoxide (CO) can also have negative impacts on the physical properties of CO_2 [16–21].

Normal operating conditions (recompression distance & hydraulic behaviour), material properties (corrosion, embrittlement) and design (fracture control & propagation) could be affected [22,23]. Likewise large variations in composition are anticipated in CCTS due to the inclusion of other CO_2 sources for this technology to be economically viable.

Thus, composition will depend mainly on fuel type, energy conversion process and capture process [24–30]. Also networks connecting multiple sources of anthropogenic CO_2 would be required for appropriate specification; however, a review of the codes and standards focused on the transport of fluids has revealed that suitable guidelines for anthropogenic CO_2 transportation are not available.

In this scenario, transportation of supercritical CO_2 with impurities in a CCTS framework is undoubtedly critical; however, it has not been well addressed. While little effort has been conveyed in filling the existing gap of knowledge in CO_2 transport in a safe, efficient and convenient manner, capture and storage have been receiving major attention. Therefore, while most of the know-how is already available for natural gas and pure CO_2 transportation systems, which could be used in CCTS, it cannot be applied directly to anthropogenic CO_2 transportation.

The lack of CCTS operational knowledge, combined with the uncertain long-term financial environment, the regulatory constraints and the acceptability and capacity of selected areas, will impact on the general development of anthropogenic CO_2 capture, transport and sequestration technologies, particularly in the UK and extending to Europe. Unless efforts to reduce this gap are made and help is given to decrease these barriers, the acceptability of CCTS as a potential key both to reduce GHGs and to achieve the 2020 targets agreed by the European Union in June 2009 will be at higher risk.

1.2 The need for this research

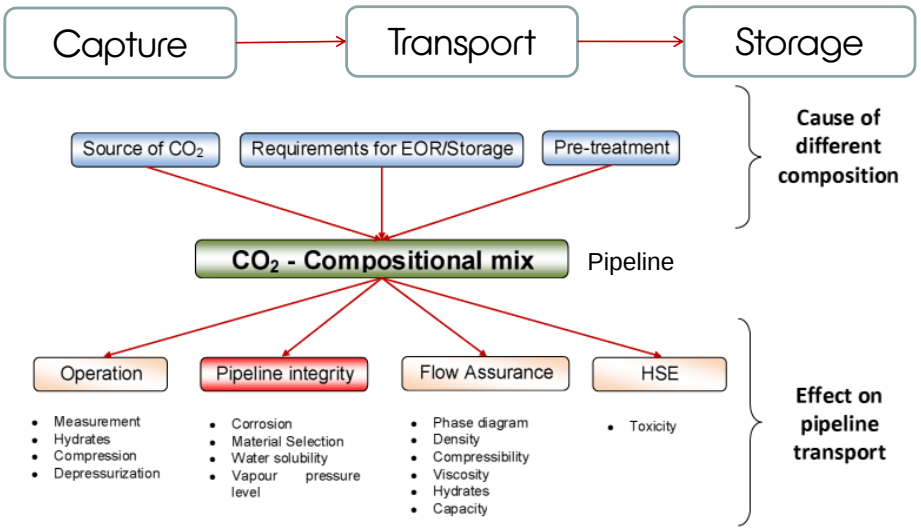

Figure 1-4 Challenges in CO_2 transportation

Technical challenges exits for transporting supercritical CO_2. Even though transport of natural gas by pipeline is well established, CO_2 transportation, particularly with impurities, is not well understood as there are significant differences in terms of physical properties and behaviour during pipeline transportation. The implicated issues with the process are summarised in Figure 1-4 [31]. From a structural integrity standpoint, the most significant differences between both these could be:

- Susceptibility to long-running ductile fracture propagation in natural gas pipelines operating at the same conditions and using similar grade of steels, as the CO_2 decompression curve is more severe than that of natural gas-CH_4 (Figure 1-5). As a result, the driving force is stronger and the crack arrest conditions could be reached only using steel with high toughness or using crack arrestors.
- The probability of lower temperatures during pipeline operation or an unlikely event of a leakage when there are sudden drops in temperature due to the Joule Thompson effect. This can have material implications such as embrittlement (local brittle behaviour & high local residual stress) and also promote the behaviour of material change from ductile to brittle.

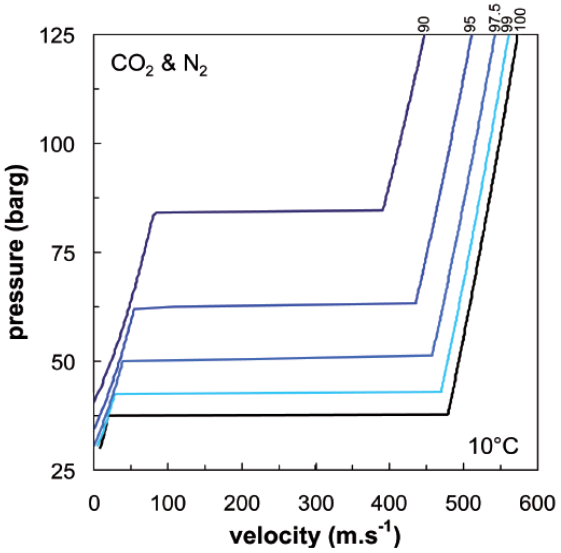

Figure 1-5 Experimental and theoretical decompression curves for pure CO_2 and CO_2 & N_2 [15]

- The presence of non-condensable and free water causes the formation of acid components and also promotes hydrate formation, which increases corrosion rates (CRs) and/or stress corrosion susceptibility as well as material embrittlement. Although, a high pressure dry CO_2 is essentially non-corrosive, the formation of a moisture environment could change its behaviour, affecting pipeline integrity.
- There is no international regulatory framework for specific design or fitness-for-service (FFS) procedure for CO_2 pipelines and a compositional specification for a CO_2 mixture to be transported by pipelines does not exist.

Data concerning the effects of impurities along CO_2 transport are non-existent; thus, this gap in knowledge will be addressed in order to generate reliable data for determining the ability to re-use existing or to develop new steel pipeline systems for transporting anthropogenic CO_2. Although, there is a consensus to transport CO_2 with small remaining impurities in order to make CCTS economically feasible and avoid energy penalties due to the extra purification process, it is necessary to establish acceptance levels [32], [33].

Pipelines are designed using defect-tolerant principles, where knowledge of defects or crack-like flaws can be used to predict or determine the remaining life of a component. Up to now, there has been little or no information or data about the effects of anthropogenic CO_2 on integrity in low carbon pipeline steels. Therefore, the mechanical and material behaviour of these pipelines cannot be accounted for by using the current gas concepts, but this knowledge could be a baseline for future developments in order to deliver a fail-safe structural integrity assessment.

1.2.1 Current approach

To evaluate or assess the remaining life of pipeline or structural components, one approach known as failure assessment diagram (FAD), is used (Figure 1-6).

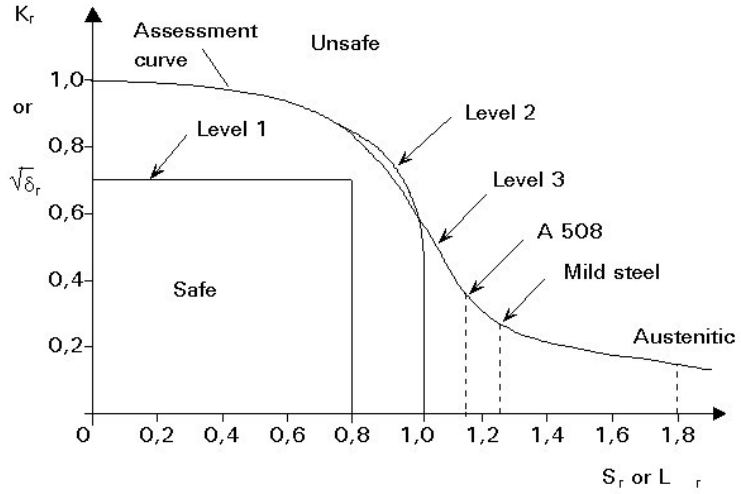

Figure 1-6 FAD levels, after [35]

This approach has been incorporated into international codes and other guidelines such as API 579 [34], BS 7910 [35], PD6493 [36], R-6 [37], PDAM [38], SINTAP [39], and FITNET-FFS [40] for FFS purposes.

FAD is classified into three different types depending on the information available and accuracy required. Increasing levels require more complex data but are less conservative. Levels 1 and 2 involve universal failure assessment curves independent of material properties.

Level 3 considers material-specific data such as strain, true strain, true stress and elastic modulus, obtained from the tensile curve, and fracture mechanics parameters from impact toughness or fracture toughness tests.

Fracture toughness evaluation could be performed by many approaches such as J-integral, Crack Tip Opening Displacement (CTOD), Crack Tip Opening Angle Displacement (CTOA) and Crack Mouth Opening Displacement (CMOD) where the stress intensity factor (K) and plane strain stress intensity factor (K_{Ic}) are determined [41–45]. These parameters are used to assess fracture control and propagation of fracture but issues in terms of size of specimen (thickness), costs and functionality restrict their use as quality control tools in industry [29]. Two experimental methods, called Drop Weight Tear Test (DWTT) and Charpy-V notch (CVN) test impacts, are generally used to prevent propagating fractures with higher acceptance of performance integrity assessment.

Both are cheaper and feasible to perform but these approaches, particularly CVN, evaluate the fracture resistance rather than fracture toughness which is not considered a suitable method for fracture toughness measurement [46–48]. Empirical correlations in order to estimate fracture toughness have been applied for years; however, these are not accurate and are restricted to particular materials strength, thickness and test temperature range in which the correlations were established [49], [50].

Likewise, as both are not suitable for evaluating toughness from pipes due to the small scale specimen and accuracy, then conservative predictions cannot be obtained from them. Battelle Memorial Institute introduced an approach, namely the Battelle Two-Curve Model (BTCM). It is being used as a tool to control the fracture initiation and prevent propagation in pipelines transporting gas, particularly, for lower and medium high strength steel pipelines rather than steel grades above API X65 grade. To overcome this, the application of a correction factor extrapolation of arrest energy from lower to higher grades of pipeline is suggested. However, it does highly question the data and issues emerging on steels above X90 as this correction factor is still not easy to be determined [51,52].

Furthermore, the CVN, DWTT and BTC approaches require a minimum toughness value which could be achieved if the energy values were on the upper scale of the ductile-brittle transition temperature curve [53]. Also, as presented in Figure 1-5, there is huge concern over crack propagation speed when the material exposed to flue gases of CO_2 is decompressed.

Avoidance of brittle fracture and arresting running ductile fracture (RDF) might be considered to hold fracture resistance demands. Using BTC and its variant, known as the HLP approach (High Strength Line Pipe Committee), could predict the final crack length of a RDF. Nevertheless, as explained above, many drawbacks exist with the application of these methods due to the lack of knowledge on how anthropogenic CO_2 will affect brittle or ductile mechanisms.

Higuchi et al. [54] have proposed an alternative method as well as the modification of DWTT specimens using pre-cracked samples to give a new concept of crack arrestability. Even though DWTT and Charpy energy correspondence is not linear, the method proposed is to convert the Charpy absorbed energy to pre-crack DWTT. New parameters are introduced to compensate for the size effect on fracture velocity in the model. Even if the model can predict arrestability in higher grade steels, it is only applicable in natural gas transportation at a higher pressure by pipeline.

To overcome fracture toughness concerns originating from Charpy energies correlations, Wallin [55] developed a new methodology to characterise the fracture toughness in the lower transition region. It is named the “Master Curve” (MC) and has proved that valid MCs can be determined with small Charpy size specimens on ferritic steels [56], [57] .

Even though the MC was developed mainly to be applied to nuclear surveillance, the methodology has demonstrated that estimated fracture toughness on ferritic steels covering quenched and tempered (Q&T) martensitic and bainitic steels rely on the same tendency to form transition curves of the same shape. Also a step-by-step procedure has been developed which allows a reliable assessment with quantified probability and confidence levels [58].

Due to some constraints with MC, Schindler and Kalkhof [59] developed a mathematical model in order to fill the gap when lower-bound fracture toughness values are required which MC and American Society of Mechanical Engineers (ASME) lower-bound are unable to offer.

1.2.2 Problem statement

One of the biggest problems facing the development of large pipe diameters with small thickness to save weight and reduce costs is the manufacturing limitations (Transporting CO_2 will be at high pressures, >>120 bar). The complexity behind developing high strength steels and optimisation of mechanical properties such as toughness and corrosion resistance depends on many factors such as:

- The technological feasibility of manufacturing steel that achieves high levels of toughness and mechanical strength due to the opposite effect of both. Corrosion resistance is the other issue in high strength low carbon alloy (HSLA) steels.
- Lack of experimental data about the decompression of anthropogenic CO_2 from supercritical conditions that can provide a suitable explanation of driving forces during the ductile fracture propagation event; this is not available in the literature.
- Limitations of traditional fracture parameters to correctly describe the resistance to crack propagation; this leads to the difficulty of designing and evaluating appropriate materials as well as failing to predict arrest/propagation cracks.
- Lack of knowledge predicting structural crack arrest behaviour using small-scale material characterisation tests.

1.3 Aim and objectives of the present work

This research is specifically aimed at defining the toughness requirements, material compatibility and behaviour of high strength low alloy (HSLA) steels exposed to flue gases containing supercritical CO_2 as well as providing empirical data to establish failure criteria. This overall aim will be achieved by:

a) Evaluating and developing test methods which will:
    - Determine the modes of fracture failure in HSLA pipeline steels immersed in a CO_2 environment with impurities.
    - Generate toughness, yield and ductility date to quantify the fracture behaviour of HSLA pipeline steels exposed to a CO_2 environment with impurities.
b) Quantitatively measuring the impurities and establishing their role on failure mechanisms, and their contribution to material damage properties of HSLA steels.
c) Providing guidance on performing failure assessment defects for axial external/internal surface flaws in HSLA steels immersed in an anthropogenic CO_2 environment.

The framework of the present investigation is presented in Figure 1-7. Within it are clearly defined the main aspects to study, which cover different topics to explain the possible mechanical behaviour of material and the environmental effect on the integrity of steels used to transport CO_2.

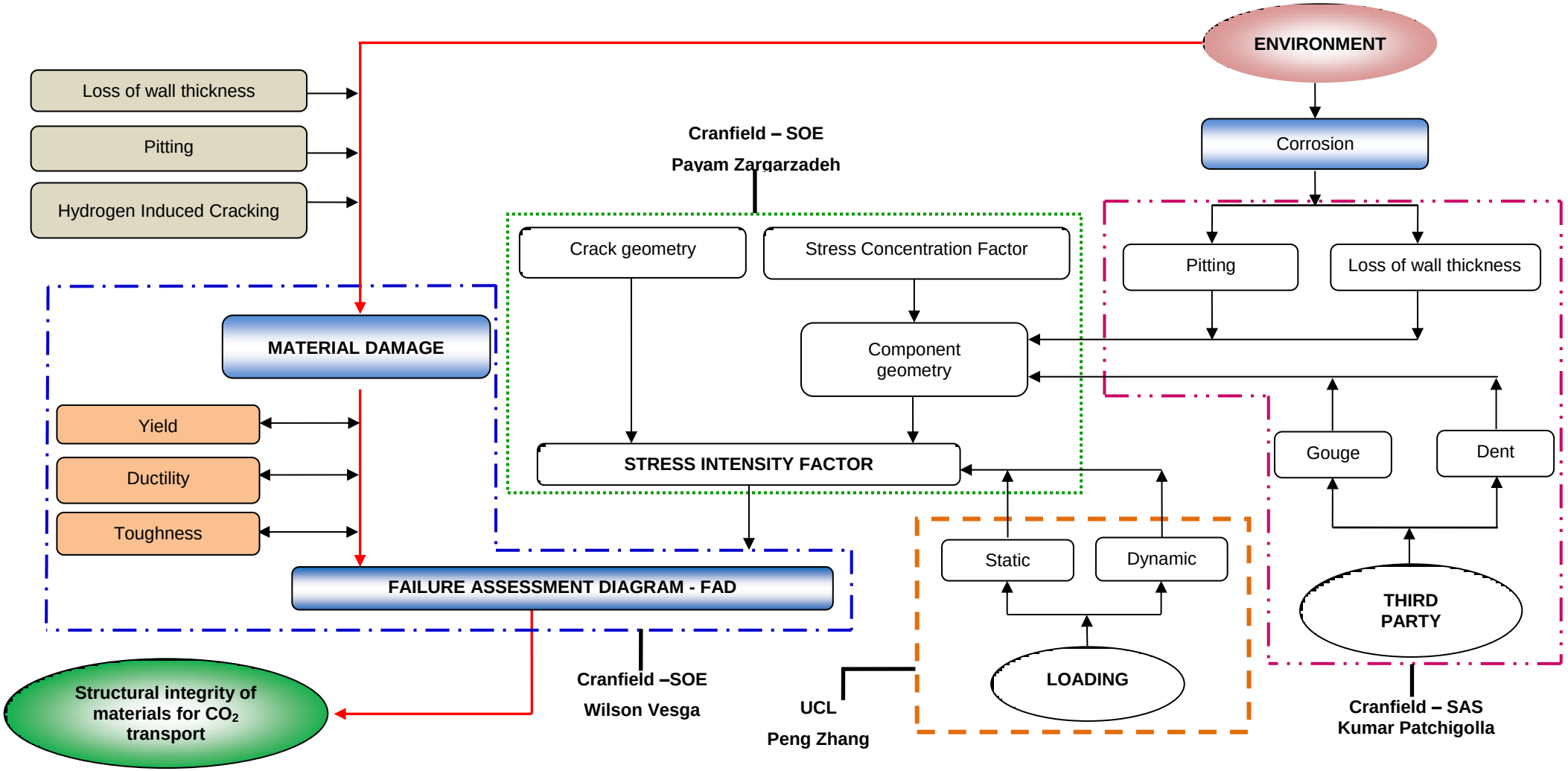

Figure 1-7 General plan of the research proposal identifying contributors

1.4 Thesis overview

The objective of this research is both to assess and develop a novel engineering critical assessment of the integrity of steel used to transport flue-gases.

To achieve this, Chapter 1 presents the background, needs, current approach and problems of CCTS technology. A current state-of-the-art regarding structural integrity of materials involving pipeline material, fracture toughness, environment effects on material, residual stress and the engineering critical assessment by FAD approach is explained in Chapter 2.

Chapter 3 describes in detail the experimental methodology used to evaluate mechanical properties and fracture toughness of the steels used in this investigation as-received and aging condition. Tensile tests are carried out on strip and round bar samples while fracture toughness testing was conducted on pre-cracked Charpy samples.

Round tensile and precracked Charpy samples were exposed to simulated flue-gas containing H_2S and SO_2 impurities. Both virgin and exposed materials were tested from lower temperature to room temperature. Fracture toughness was performed over the range -196°C to 21°C while tensile tests were performed in the range -70°C to 21°C. In addition, cold rolling by combination of different load and width roller, which was performed to induce compressive residual stress on API X100 flat plates, is explained in detail. Both neutron diffraction and blind hole-drilling approaches to determine in-plane compressive-tensile stresses profiles through-thickness are described.

Chapter 4 presents the results obtained from tensile, hardness and Charpy test. Analytical methods such as XRD, scanning electron microscope (SEM), Optical microscope (OM) were used to characterise compounds deposited on the surface of samples as well as fracture surfaces after testing are included here. Fracture toughness analysis is evaluated by a different approaches and discussions are carried out for each topic evaluated.

Chapter 5 addresses residual stress analysis performed in cold rolled samples. Neutron diffraction and Hole-drilling methods are compared in order to establish differences and constraints. Discussion is made taking into account the scope and significance of this approach to measure residual stress analysis and its impact on the integrity of pipes. In addition, this study was incorporated to quantify and better understand the use of compressive stresses as a potential method to be incorporated for crack arrest purposes.

Chapter 6 presents the structural integrity analysis for CO_2 pipelines based on the FAD approach performed by R6 code along with other tools and results obtained in previous chapters in terms of mechanical properties, fracture toughness and residual stress. A leak-before-break approach was conducted taking into account operational pressures, and integrity variation of the materials was evaluated by analysing the FAD locus discrepancy.

Chapter 7 summarised and highlighted the major findings and conclusions obtained from this research, as well as the contribution and discussion of the future work that required to be undertaken in order to advance in the research of this fascinating field of the CCTS technology.

Overall, the thesis presents a comprehensive examination of materials used to transport supercritical CO_2 with impurities and establishes a first-hand methodology to evaluate fracture toughness along with the FAD for assessing the Finest-For-Service of pipelines.

2 LITERATURE REVIEW

2.1 Introduction

This chapter presents a state-of-the-art analysis of materials for CO_2 transportation in terms of environment, material integrity and defect assessment. There is sparse information regarding CO_2 transportation in dense phase via pipelines, these is not a well-established deep-knowledge transporting anthropogenic CO_2. Thus, the baseline is provided from the literature available in the public domain about oil and natural gas field.

2.2 Pipelines steel grades

The early steels were C-Mn steel grades X42 and X52. These steels were microalloyed to improve weldability; however, due to high carbon, poor steel cleanliness and little grain refinement, notch toughness was very poor [60,61]. The development of modern pipeline steel has been performed in an effort to obtain an excellent combination of mechanical properties such as strength, toughness, ductility and weldability thus improving their performance to operate in harsh environments. HSLAs were developed for their potential to be used for high pressure requirements (>15 MPa) without increasing wall thickness but improving economic feasibility in the transportation of gas in arctic regions and in the exploitation of sour oil and gas reserves [62,63].

The latest advances in manufacturing technologies have relied on the integration of metallurgical concepts, such as chemical composition, thermal history, deformation process and microstructure modification, and offer beneficial results by increasing strength, ductility and toughness. However, these complex interactions have been studied by many researchers including Das, Gray, Pickering and Klassem et al. [61,63–66] who have considered all individual operating components required for inclusion to complete multi-parametric analysis; however, gathering all the requirements is often difficult to accomplish as variants in any one of these properties often leads to changes in the others.

Despite this drawback, nowadays, pipelines meet all the requirements for good performance of the material including weldability, strength, toughness, fatigue and collapse resistance, strain tolerance, as well as environment resistance by the use of so-called high strength low alloy (HSLA) steels. The most common HSLA steels in operation are made of API X52, X60, X65, X70, X80 and lately, X100 and X120. Table 2-1 summarises the mechanical requirements for pipelines in accordance with API specification [67].

Table 2-1 Mechanical requirements for PSL2 API pipelines[67]

Grade Steel	$R_{p0.5}$ (MPa)	$R_{p0.2}$ (MPa)	R_m (MPa)	Ratio $R_{p0.5}/R_m$
L415 or X60	415-565	-	520-760	0.93
L450 or X65	450-600	-	535-760	0.93
L485 or X70	485-635	-	570-760	0.93
L555 or X80	555-705	-	625-825	0.93
L625 or X90	-	625-775	695-915	0.95
L690 or X100	-	690-840	760-990	0.97*
L830 or X120	-	830-1050	915-1145	0.99*

*Elongation is calculated by $A_{f=C*}\frac{A_{xc}^{0.2}}{U^{0.9}}$ and lower yield ratio values may be specified by agreement for L690 and L830.

Manufacturing of HSLA grades X65 to X80 usually follows the route of TMCP combined with an accelerated cooling process (ACC) (Figure 2-1) [58]. Even though the combination of TMCP with chemical composition establishes a correct balance between strength, toughness and weldability, precipitation of second phases and solid solution hardening, it can contribute to decrease fracture toughness (Figure 2-2) [64] and modify tensile properties (Figure 2-3) [66].

Application of pipeline API X100 grades is not common and only some trial projects have been undertaken using this steel. Hillenbrand et al. [52,69–72] have been working with this material in order to find the best balance between strength, toughness and weldability.

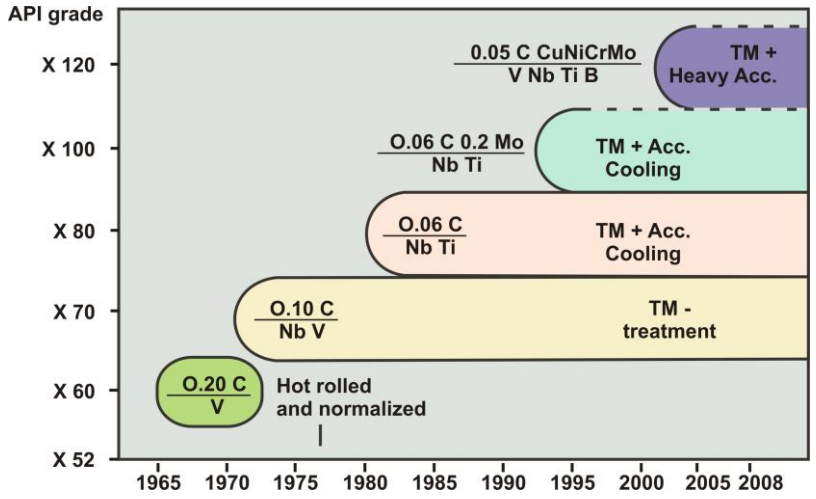

Figure 2-1 Variation of chemical composition of HSLA steels [64]

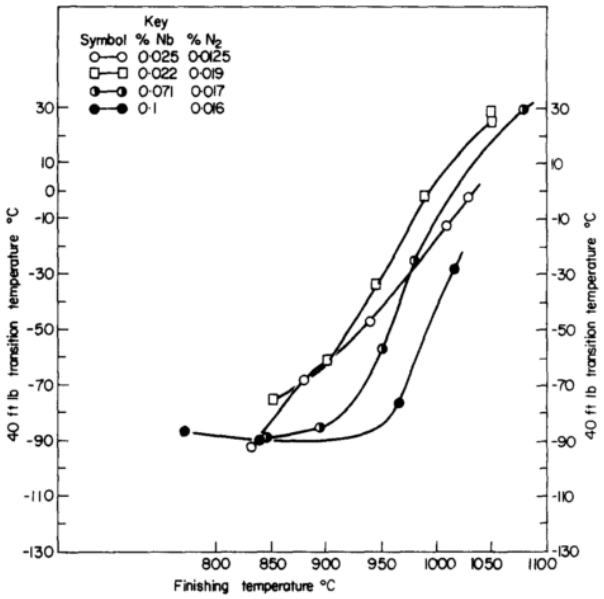

Figure 2-2 Relationship between transition temperature and final temperature of reduction for steels containing less 0.05% of microalloys elements [60]

They have developed a method which is based on selecting the best combination of chemical compositions and rolling conditions, carbon content, cooling rate, cooling stop temperature and carbon equivalent (known as Pcm, CE_{IIW} or CEN). As a result three different approaches can be used; however, approach C (green) is considered to be the best for producing pipeline steels grade X100, as can be seen in Figure 2-4.

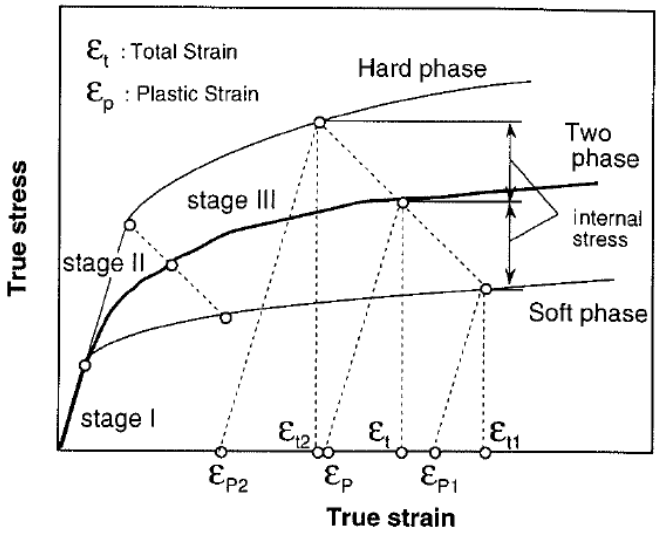

Figure 2-3 Stress-strain curves evaluating the influence of the harder phase on the stress-strain behaviour [68]

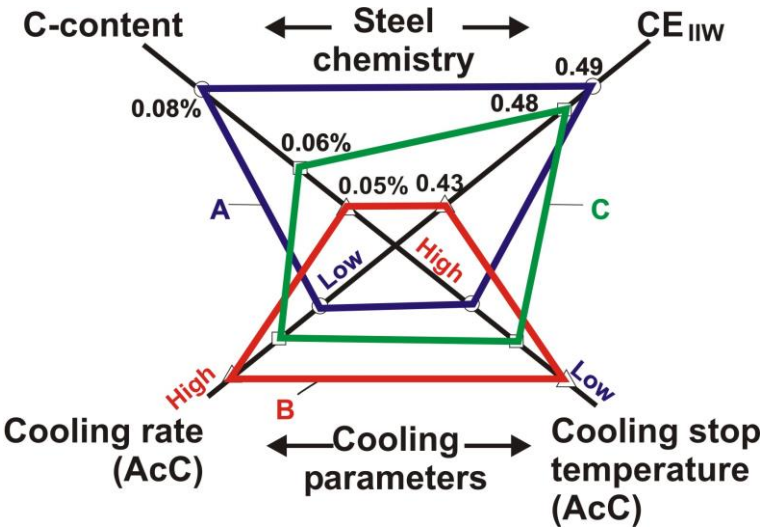

Figure 2-4 Different approaches to develop grade X100 steel [73]

A high temperature process (HTP) approach has been used to produce grades X90 to X120 where Cu and Nb are added. The main advantage of this method is that niobium retards the recrystallization temperature and the material can be rolled at higher temperatures to provide a lower carbon equivalent (Pcm) thus improving toughness [63].

2.2.1 Microstructure and mechanical relations

The appropriate chemical composition, rolling temperature, finish temperature, cooling rate and cooling interrupted temperature are the most significant variables that affect the final microstructure and have been studied extensively [61,74–76]. Figure 2-5 presents the possible variations in microstructure that can be obtained by the TMCP method at different cooling rates.

From the TMCP process, different microstructures can be obtained which are classified into four types: polygonal ferrite (P-F), quasi-polygonal ferrite (Q-F), granular bainite-ferrite (GB-F) and bainite-ferrite (B-F). P-F is transformed at the highest temperatures and slowest cooling rates which nucleate as grain boundary allotriomorphs growing into equiaxed grains.

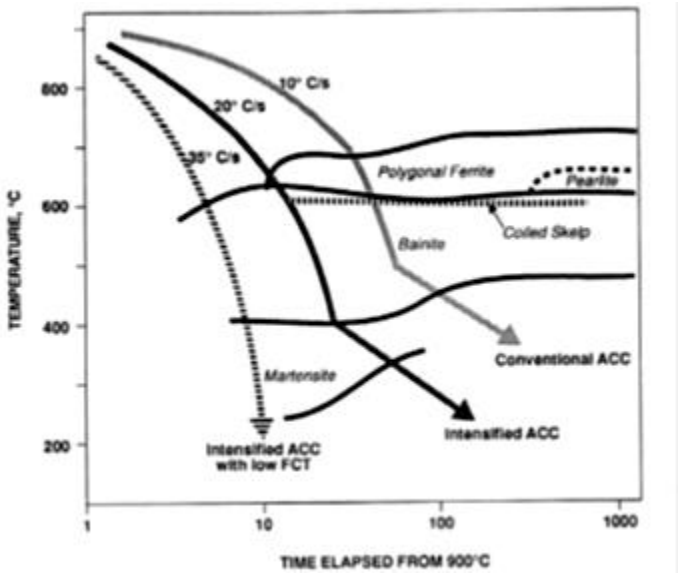

Figure 2-5 Processing methods utilized in TMCP and their characteristics in control of microstructures with reference to a CCT diagram [64]

Q-F and its austenite parent can be transformed together in grains with irregular boundaries containing a high density of dislocations and martensite/austenite (M/A) islands. B-F consists of an elongated ferritic lath with a high density of dislocations and is separated by low angle grain boundaries (LAGBs). G-F is obtained by slower cooling rates containing a high density of dislocations and is separated by LAGBs [76].

The effect of TMCP on the microstructure of HSLA steel was investigated by Zhao et al. [74,75]. They found that the acicular ferrite (A-F) dominated the microstructure and as a result strength and toughness were enhanced. A similar study was made on a commercial API X70 grade P-F microstructure and X90 grade A-F microstructure by Wang et al. [76]. They found that strength and toughness are similarly improved; however, the elongation and Y/T ratio of both steels were not changed by the thermal treatment. A high density of dislocations was observed.

Hillenbrand et al. [73] carried out studies on the impact of microstructures on the mechanical properties of X70, X80 and X100 pipeline steels. Their investigation concluded that strength and toughness were increased by modifying the microstructure from Pearlite-Ferrite (P-F) to Ferrite-Bainite (F-B), leading to the development of the X80 grade. Examples of this microstructure of HSLA steels can be seen in Figure 2-6. The X70 matrix corresponds to F-P, X80 is compound of F-B and X100 by bainite. However characterisation of this structure, mainly X80 and beyond is restricted under optical microscopy.

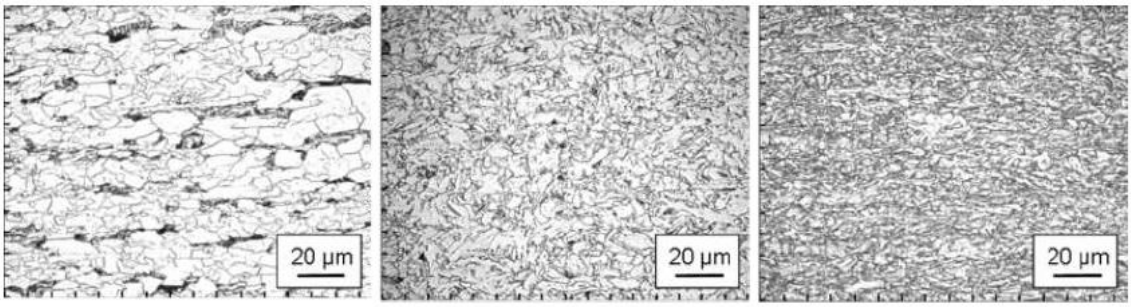

Figure 2-6 Microstructure of HSLA pipeline steels: X70 (left), X80 (centre), X100 (right) [73]

Electron microscopy combined with electron backscatter diffraction (EBSD) has been demonstrated to be powerful. Characterisations of the microtexture, measure of the grain size, type of bainite and crystal orientation allow a more precise identification of the category of steel.

Figure 2-7 presents an inverse pole figure, which is a power tool, to determine boundaries' misorientations, effective grain size, and also high angle and small angle grain boundaries can be measured. These angles are related to constitutive obstacles for dislocation motion, which markedly determine the mechanical properties of the steel [77].

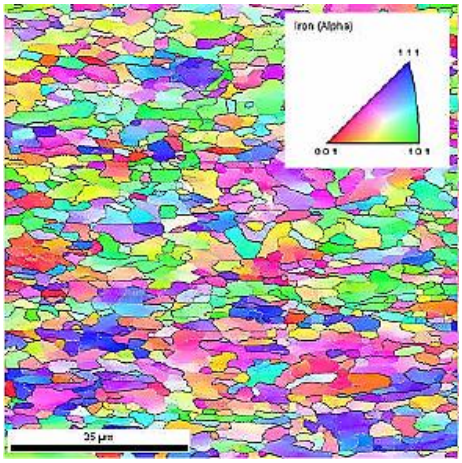

Figure 2-7 Inverse pole chart of HSLA line pipe steel measured by EBSD where each colour determines a preferential crystal orientation [73]

Das et al. [78] investigated the influence of heat treatment on the microstructure and mechanical properties of Cu-strengthened HSLA X100. From the study carried out they found that the coherency of Cu precipitates controlled fatigue crack, susceptibility to ductile fracture and avoids microvoid coalescence. The ageing improves high strength and high toughness. However, some investigations have determined that steel with a microstructure of pearlite-ferrite is considered to be more susceptible to the corrosion process than acicular ferrite and bainite-ferrite [79,80].

The previous discussion about microstructure and processing determining the heterogeneity of the HSLA exists; as a result, mechanical properties can significantly vary both from different manufacturers and heats [81]. This variation in yield strength, ultimate strength and toughness is presented in Figures 2-8 and 2-9 respectively.

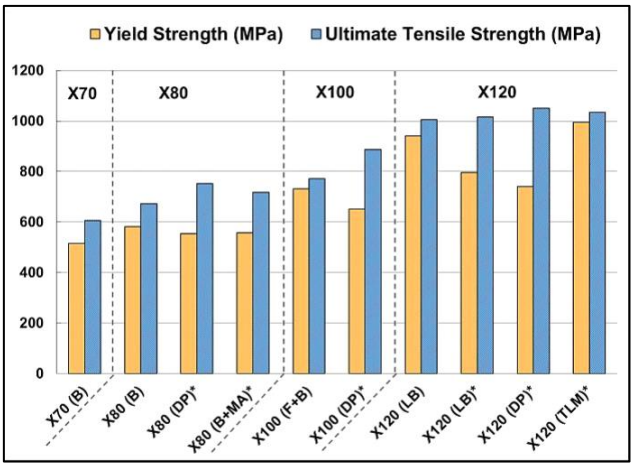

Figure 2-8 Mechanical properties of HSLA steel varying microstructure [81]

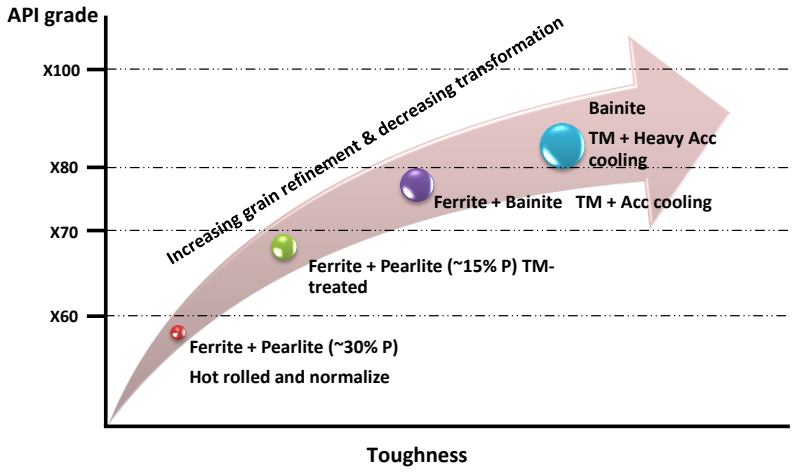

Figure 2-9 Scheme of the microstructure, mechanical and toughness properties evolutions depending on manufacturing process

Aiming at the heterogeneity pipe, there are three directions to be considered: longitudinal, circumferential and through-thickness. The former is linked to the thermal history during the rolling process, while circumferential heterogeneity is associated with the non-axisymmetric cold forming during tube forming.

The latter is related to the effect of cooling rates to modify grain sizes and tension-compression cycles induced during the forming process. Depending on the direction-deformation during the rolling process and tube forming, tensile properties differ for longitudinal and transverse directions during plate and pipe production.

Thus, longitudinal strength properties tend to be lower than transverse strength characteristics as a consequence of anisotropy [82,83]. Also, the strength characteristic that meets steels of the same or closer grade reflecting differences between minimum and maximum yield, or the average of these, could fairly be similar [84], [85].

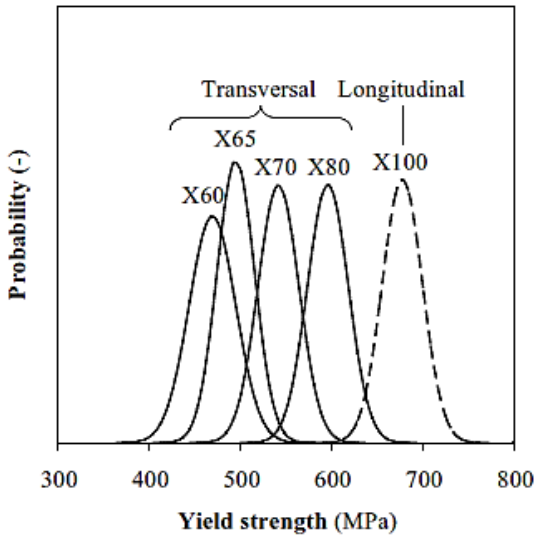

Figure 2-10 Yield strength distribution HSLA steel [81]

This is shown in Figure 2-10 where a probability distribution of the yield strength for steel X60 to X100 reflects the heterogeneity of HSLA steels in both directions. Aspects such as strain hardening, Y/T ratio, and uniform elongation, shown in Figure 2-11, significantly influence the type of steel that is dealt with, and also reflect the scatter on tensile properties of HSLA.

The Y/T ratio is specified in API 5L standard as $R_{t0.5}/R_m$; however, this definition can be redefined as $R_{p0.2}/R_m$ due to $R_{p0.5}$ potentially not taking into account the work hardening applied on steel above X90. Even though $R_{p0.2}$ and $R_{t0.5}$ are closer for most line pipe steel, the significance of the former parameter has gained acceptance over the latter.

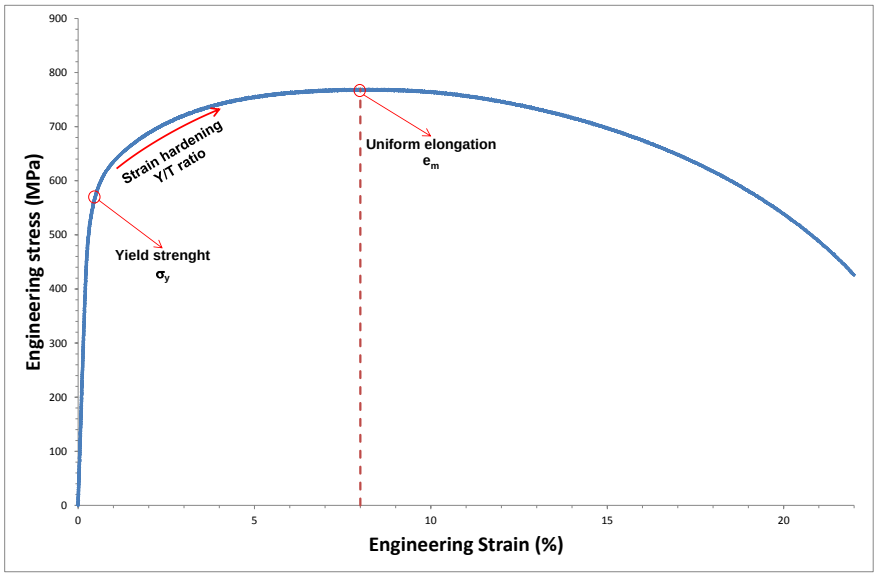

Figure 2-11 Stress-Strain engineering curve

As shown in Figure 2-12, the Y/T ratio has a marked influence on the grade of the steel, indicating that this factor could potentially better describe the physical relevance of this parameter on the onset of plasticity.

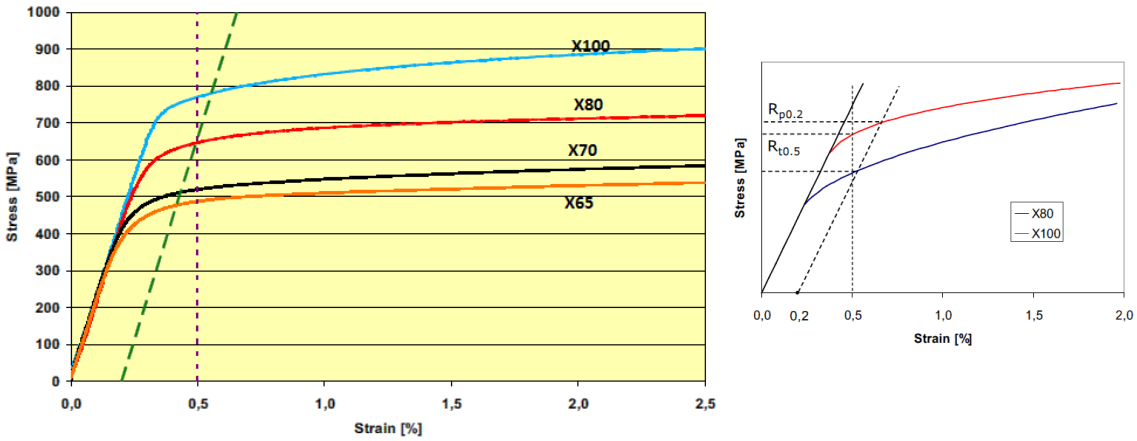

Figure 2-12 Relation between $R_{t0.5}$ and $R_{p0.2}$ for X65 to X100 HSLA steels [52]

To achieve high toughness clean steel, treatment is provided during the casting process. These values are frequently obtained from standard CVN and DWTT tests. Although these methods are currently used as quality control, there are many concerns about the correlation of CVN as a representative measure of fracture toughness. However, as shown Figure 2-13 microstructures have a strong effect on impact toughness [81,86].

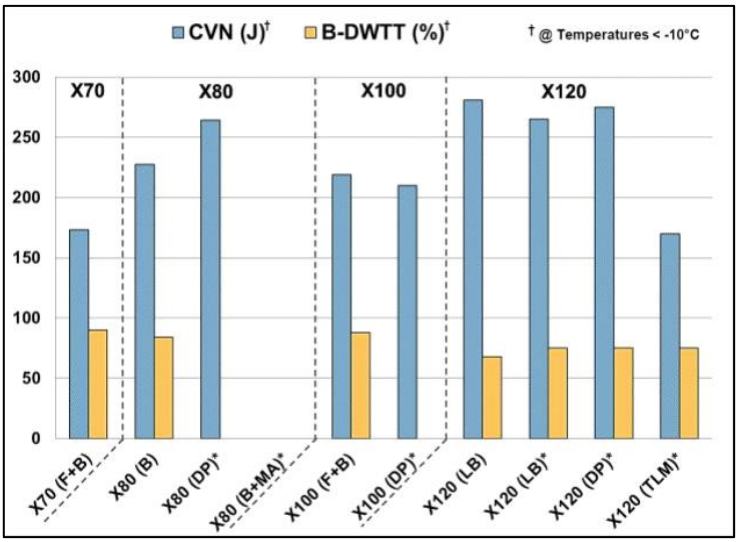

Figure 2-13 CVN and DWTT energies depending of microstructure [81]

2.2.2 Anthropogenic CO_2 environment

The capture of CO_2 from power plants and industrial processes may contain impurities. There are three basic approaches: pre-combustion or integrated gasification combined cycle (IGCC), post-combustion and Oxyfuel. CO_2 produced from these capture technologies might contain more impurities, which may be a drawback for the CCTS system, because realistic compositions are still unknown [8,9,18,25]. A general CCTS scheme is presented in Figure 2-14.

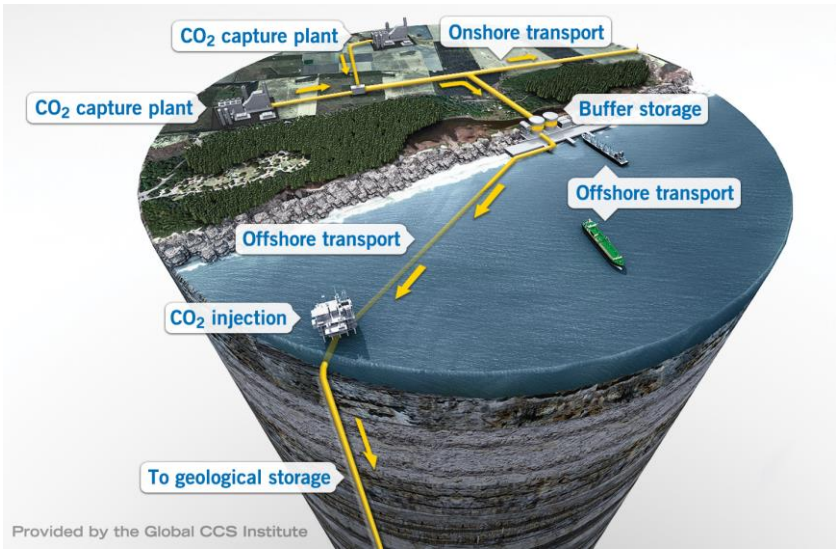

Figure 2-14 Scheme of anthropogenic CO_2 transportation [87]

Although there is a wealth of knowledge on the effects of impurities such as SO_x, NO_x, H_2S, CH_4, H_2 and CO when oil and gas are transported by pipelines, little is known about CO_2 transportation and how impurities affect pipeline mechanical integrity. Moisture is not considered to be an issue but it is clear that the formation of hydrates and acid increases with rising free water [16,17,88,89].

Researchers have shown that some of the identified components could be present in low concentrations in the CCTS system. Thus, the impurities in CO_2 are not concerned with big numbers, even though their effect in the CCTS system should be much higher. For CCTS to become a reality, pipeline integrity will need to be assured.

2.2.2.1 Properties of CO_2

The properties of CO_2 are well known. At standard temperature and pressure, CO_2 exists as a gas. As shown in Figure 2-15, pure CO_2 is characterised by two main points; the triple point (5.18 bar, -56.6 °C) and the critical point (73.77 bar, 31.1 °C). At the first point, CO_2 can exist either as a gas, solid or liquid.

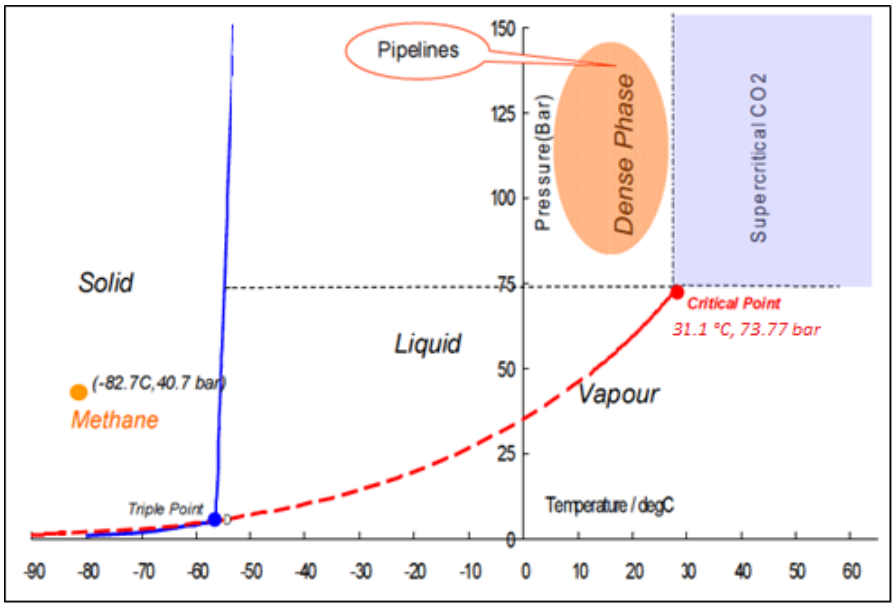

Figure 2-15 Phase diagram for pure CO_2 [2,9].

At the second point, CO_2 exists as a supercritical or dense phase liquid. In this stage, CO_2 becomes identical in the liquid and gaseous phases due to its properties as a pure substance. This condition is considered to be the most efficient for CO_2 transportation over longer distances because the fluid has the density of a liquid and the viscosity and compressibility of a gas.

2.2.2.2 Background on CO_2 Capture

Prior to being transported, CO_2 has to be compressed to a pressure above the critical point; however, as CO_2 is captured from an anthropogenic source these conditions would be changed by the impurity levels present in the flow.

According to Race et al. [9,12,89,90] and Kaufmann [22], the types and concentrations of impurities have a practical impact on the hydraulic parameters of pipelines, such as pressure and temperature drop, and also density and viscosity. As a result, it may be inconvenient to maintain CO_2 as a dense phase due to the formation of two phases of gas-liquid.

Higher H_2S and SO_2 concentrations have negative effects on the health of people regarding toxicity and also sulphur precipitation which can potentially cause equipment blockages. O_2 is interacting with corrosion, causing material damage and pipeline capacity will be reduced by the presence of N_2 [9,12,33,70,90–93].Material embrittlement due to stress corrosion cracking (SCC), sulphide stress cracking (SSC) and hydrogen induced cracking (HIC) are caused by H_2S and H_2. If dewatering is not appropriate, highly corrosive carbonic acid is formed which can lead to CRs rising up to 1-2 mm within two weeks or 10 mm/y [91,94,95].

Reducing the concentration of trace elements and obtaining a high purity CCTS stream is technically viable, but purification leads to additional increments in cost and energy requirements which would be considered economically unfeasible. Despite this, a small amount of impurities may still remain in the system, therefore, it would be much better to transport and store some of these impurities within the CO_2 stream rather than removing them before transportation.

A report was released to the author [96] describing the main aspects of the current state-of-the-art of anthropogenic environments. This document describes the main processes underlying the influence of CO_2 and impurities on the degradation of the material in the CCTS system. From the document different issues were highlighted:

- Change in the composition of the CO_2 stream due to the presence of major or new impurities are inevitable; therefore, it is difficult to predict what the composition will be in the future and the effects upon the transport of CO_2 by pipeline.
- Although pipelines could not normally operate under corrosive conditions, if there is a temperature drop in the gas to below its dewpoint or failure in the dehydration plant, this can lead to the introduction of moisture. Material selection will be critical for CCTS to be successful.

General conclusions were raised from the analysis as follows:

- From the analysed data, it can be seen that the nature of the base alloy and the properties of the environment of CO_2 and their interrelation are important factors that can have a significant impact on CO_2 corrosion and environmental cracking. In spite of the effort made, contradictions exist between the different data available.
- Therefore, as remarked throughout the report, it is not possible to specify the general composition of CO_2 with impurities, mainly due to the complexity of the CO_2 system and the interrelation within the different factors involved. Thus, the composition proposal could be revised and is subject to change by the annotations previously made.
- Although it could be considered that some of the components specified might not even be present in captured CO_2 from power plants, if they are then it is not easy to say without testing how they would behave in a pipeline.

- A realistic specification would be proposed for testing materials used for CO_2 transportation by pipeline based on recommendations from different projects and research, taking into accounts the typical operation range of pipelines, in order to establish a baseline when selecting or testing materials.

Table 2-2 Summary of component mixtures used for testing materials in flue-gas saturated with water

No	Impurity	Level (%)	WHY	Reference
1	NO_2	0.05	Because it might be selected to understand exacting behaviour along with a realistic composition from the Oxyfuel capture process.	[97,98][70]
2	SO_2	0.05	The presence of water could raise corrosion issues causing health and safety issues/challenges From post-combustion capture process.	[70,99–103]
3	H_2S	0.05	Health and safety considerations. Material degradation by HIC. Embrittlement. From pre-combustion capture process.	[70,93,94,104–115]
4	H_2	2	Health and safety issues/challenges. Hydrogen induced cracking. From post-combustion capture process.	
5	O_2	4	Unclear about its effects on anthropogenic CO_2.Issues are being associated with corrosion mechanisms. From Oxyfuel capture process.	[70,116–118]
6	Free H_2O	4	Corrosion issues. Material degradation associated with corrosion mechanisms. From Oxyfuel capture process.	[70,119–122]

In spite of the complexity of CO_2 systems and the lack of clarity on the specification or concentration limits, a gas composition was presented as a final result of the analysis performed. The specification proposed in Table 2-2 is not intended to be a guide or the latest specification, due to the drawbacks of the interaction of the great number of variables involved. However, it is focused to provide some basic input for the evaluation of materials used in transporting CO_2 by pipelines.

2.2.3 Pipeline integrity: Impurities and their effect on material performance

Degradation of pipelines is due mainly to the environment. This may lead to the reduction in the integrity of material and potentially reduce the service life, causing premature degradation or failure. Factors that may contribute or prevent the initiation and attack by the environment are identified; such as pipe coatings, cathodic protection, soil conditions, ambient conditions, temperature, stresses, pipe pressure and cyclic loading. In addition, temperature and metallurgy variations can influence the material degradation.

Mechanical damage and corrosion are classified as two principal causes of the deterioration of pipelines. The former could be caused by the manufacturing process, a third party (welding, dent, gouges, spalling), soil settlement or movement [123–125]. Also, residual stress, external stress and secondary stresses are considered to reduce the service life of materials [37].

In terms of material, the corrosion mechanism activation depends not only on electrolyte conditions but on other factors such as chemical composition and microstructure, which can change the susceptibility of material and influence its corrosion performance [126], as well as impurities, oxides, inclusions, mill scale, orientation of grains, grain boundaries, dislocation, precipitated phases, localized stresses, scratches and nick facilitated localized corrosion [127].

From the corrosion point of view, it reduces a design life due to the rate and severity of corrosion. Corrosion is categorised into eight forms or types which are based on the visual characteristics of the morphology of attack [126]: uniform or general corrosion, crevice corrosion, pitting, intergranular corrosion, selective leaching, erosion corrosion, environment induced cracking and hydrogen damage. Each of the corrosion forms produces characteristics or patterns that determine uniform defects, pitted surfaces, channel and striations [127]. The result is metal loss or stress raisers that could compromise the integrity of the pipeline. The chemical reaction can be given as equation (2-1).

$$H_2O + Fe^{3+} \Leftrightarrow Fe(OH)_3 + 3H^+ \quad \textbf{(2-1)}$$

In oil and gas production systems corrosion under CO_2, H_2S and O_2 are the most prevalent form of materials degradation. CO_2 corrosion also known as sweet corrosion, H_2S corrosion namely as sour corrosion and O_2 corrosion in water injection systems causing the majority of pipelines failures [128–130].

Sweet corrosion is typically characterised by metal dissolution followed by pitting when materials are exposed to carbon dioxide, moisture or similar corrosive agents which form carbonic acid (H_2CO_3) given $FeSO_3$ as the main corrosion product. Deterioration of steel due to interaction with H_2S is reference as sour corrosion. When hydrogen sulphide mixed with moisture a reaction occurred forming FeS corrosion product. If H_2S is presented alone in the system the corrosion rates is lower in the order of 0.5 mm/y or less [131,132].

Figure 2-16 shows a general view of pipeline integrity transporting anthropogenic CO_2. Several authors have discussed the issues of corrosion in anthropogenic environments and the evaluation of materials' compatibility with CO_2 transportation which were derived from material specification guides [133],[134]. Although, there has been considerable effort made to understand the corrosion mechanism and its control in the CO_2 environment, the interaction of CO_2, impurities and material is unknown [110,133,135].

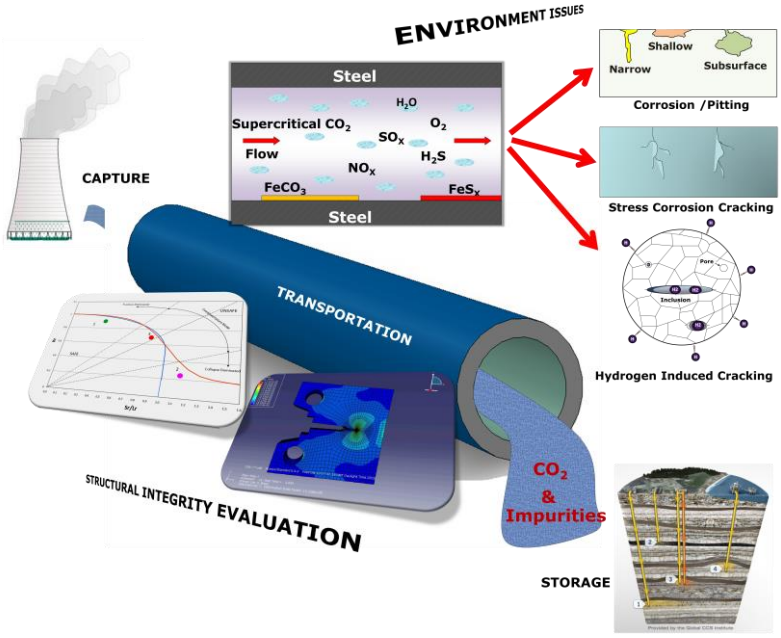

Figure 2-16 Scheme of CCTS technology counting issues that could compromise structural integrity of the system

The CO_2 mechanism can be explained by the chemical reaction in equation (2-2).

$$H_2O + CO_2 \Leftrightarrow HCO_3^- + H^+ \quad \textbf{(2-2)}$$

It is well known that partial pressure and temperature increase the corrosion rate when CO_2 is present; however, the majority of CO_2 studies have conveyed relatively low CO_2 partial pressure characteristics of hydrocarbons production conditions. According to Seiersten [106], the CRs decrease at lower or moderate pressures whilst at high pressure they are higher. The former behaviour can be partly explained by the formation of carbonate films on the surface; while the mechanism for the latter is not well understood. In addition, Seiersten considers that further investigations are required to determine the influence of temperature.

With regard to corrosion prediction models, there is a general consensus that modelling tools are inadequate for use in supercritical CO_2 environments because CRs are much lower than expected and they decrease with increasing pressures above 10 bar [127,136–140].

Although, impurities such as SO_2 and NO_2 are considered to have an important effect on corrosion, water is the impurity which is of greatest concern. Although many operators transporting CO_2 specify 500 ppm as the water limit, a recent research [141] found that the presence of water (~100 ppm) is sufficient for the formation of a second phase and higher CRs reaching 1-2 mm/yr but decreasing significantly when an inhibitor is added (Figure 2-17).

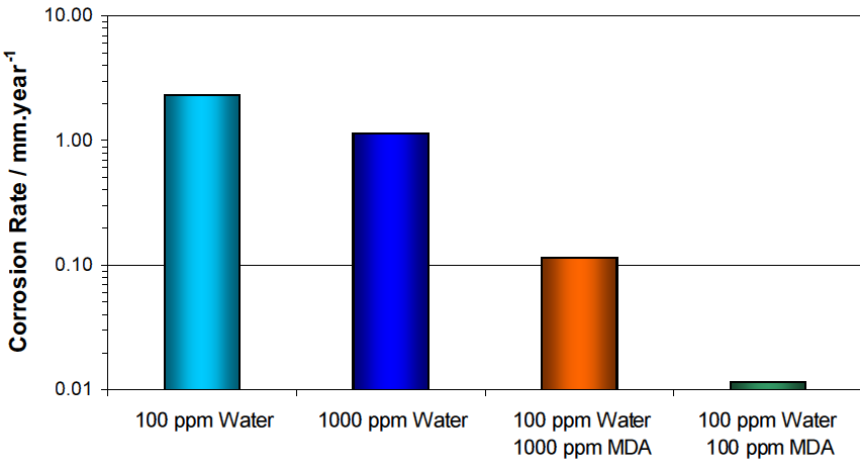

Figure 2-17 Corrosion rate of steel in supercritical environment [141]

Experimental investigation by Electrochemical Impedance Spectroscopy (EIS) of SO_2, NO_2 and O_2 impurities with water in supercritical CO_2 had been conveyed to study their effect on the CRs of carbon steel. It was concluded that the presence of water along with SO_2 and O_2 in supercritical CO_2 causes small increases in corrosion rates, and NO_2 results in CRs in the order of 12 mm/y [141,142]. This behaviour is similar to that reported by Eldevik et al. [143] and Caraballo et al. [32].

Choi and Nešić [144] conducted research by combining experimental work with thermodynamic modelling of a scCO_2-water system to determine the mutual solubilities of CO_2 and water in the two coexisting phases on API X65 steel. They found that the solubility of water in CO_2 and the solubility of CO_2 in water at supercritical conditions increased with increasing pressure; however, the solubility of CO_2 in water was much larger than that of water in CO_2.

Furthermore, a low corrosion rate was obtained in the CO_2 dense phase which is consistent with the literature. Conversely, carbon steel in CO_2 saturated water showed higher values of corrosion but this did not change significantly with a pressure change from 40 to 80 bar. The corrosion products were identified by SEM and EDS and analysis determined that those products corresponds to iron carbonate scales ($FeCO_3$), matching other investigations [94,100,110,125,132,145].

Although, Choi et al. [146] and Dusgtad et al. [110] briefly discussed the corrosion mechanism of carbon steel in supercritical CO_2 containing water, oxygen and sulphur dioxide impurities, reaction mechanisms under the presence of SO_2 in dense phase CO_2 have not yet been discussed in open literature. However, the corrosion behaviour studies of carbon steel exposed to wet air polluted by SO_2 might also be helpful to understand this phenomenon.

For example, the addition of SO_2 in the gas phase can reduce the pH of the system increasing the CRs of the steel when water condenses on the material surface by the formation of sulphurous acid, H_2SO_3. The possible reaction mechanism containing the anodic and cathodic reactions generally accepted is presented in equation 2-3.

$$SO_2 + H_2O \rightarrow H_2SO_3 \qquad \textbf{(2-3)}$$

With regard to material, the influence of microstructure on the CRs was studied by Clover et al. [80] on various grades of carbon steels' ASTM and API. They found that the localized and general corrosion rate varied slightly between different carbon steels. Steels with a banded ferrite/pearlite structure are most susceptible to localized corrosion caused by segregation of the iron carbide phase cementite (Fe_3C). Furthermore, for steels having fine-grained ferrite, ferrite/coarser, and acicular pearlite or tempered martensite microstructures, no significant differences were observed.

From the materials point of view, grain boundaries are at different energy levels which facilitate the localization of corrosion. Local corrosion (pitting) is related to the existence of spot areas on the surface layer of metal that show up as reactive zones compared to the surrounding area; from there cracks could initiate and propagate in the presence of load [147], [148].

Papavinasam et al. [149] conducted research to determine if failure of carbon steel under sour and sweet environments is due to general corrosion, pitting corrosion or localized corrosion. They found that under high temperatures (HTs) the pit density is lower but deeper whilst at lower temperatures the pit density is higher but these are shallower. In contrast, the pit depths decrease with increasing partial pressure of CO_2.

Four types of mechanically and chemically assisted cracking can exist. Fatigue cracking, SCC, SSC and HIC have been recognized as the most frequent mechanism of pipelines failures. In the case of SCC the mechanisms can occur due to a combination of the environment (pH), residual stress (hoop, tensile, axial, fluctuating stress), temperature and material properties (phases, non-metallic inclusions, steel type, surface roughness).

Depending on the condition presented, intergranular or transgranular cracks may occur. The former is determined by high pH, the latter by low pH. The presence of cracks may be as isolated cracks or within colonies [150]. The SSC mechanism can be explained by the chemical reaction given in equation (2-4).

$$H_2 S + Fe = FeS + 2H \quad \textbf{(2-4)}$$

The presence of carbonates in soil is associated with intergranular SCC which has been observed in high transmission gas pipelines; however, transgranular cracks have been detected due to the presence of CO_2 with a pH near to 6.5 [54]. Later work by Parkins [150] concluded that the initiation of transgranular SCC is associated with corrosion pits; in contrast, intergranular cracking depends only on grain boundaries for cracks nuclei.

The pits were associated with non-metallic inclusions and the plasticity localization and localized dissolution were the two major aspects of crack development. Besides, cycling and loading pipelines results in the propagation of both types of SCC but this could be reduced by decreasing temperature and pressure variations and avoiding overprotection from cathodic protection [151].

With regard to hydrogen sulphide gas (H_2S), HIC and SSC embrittlement phenomena can occur when hydrogen diffuses into the material. Regions having high triaxial tensile-stress conditions or defects such as inclusions, precipitates, or dislocations that work as hydrogen trapping sites, cause the embrittlement of steel by the formation of internal cracks known as delamination or blisters [152]. In oil and gas pipeline steels, SSC is one of the main mechanisms of failure. It is now known that increasing the strength of steel results in lower resistance of SSC. Microstructure and chemical composition are two of the variables that affect the steel [80,93,153,154]. The SSC mechanism can be represented in Figure 2-18.

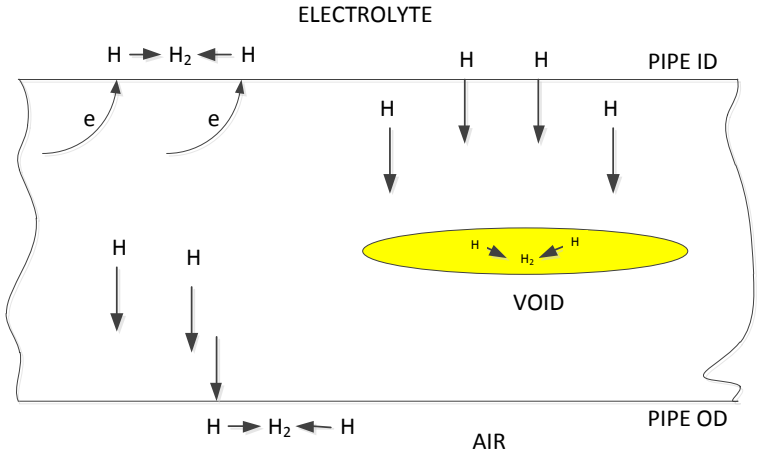

Figure 2-18 Hydrogen Induced Cracking (HIC) mechanisms on steel

Kim et al. [152] evaluated the effect of metallurgical factors on SSC susceptibility for three high strength, low alloys (API X70) under an H_2S environment. They found that Ti-Nb-C-N (~2 μm) constituents act as nucleation sites of cracks perpendicular to the applied stress. Grain boundary networks of F_3C in coarse ferritic-pearlite structures and inter-lath Martensite/Austenite acted as sensitive SSC nucleation.

In addition, non-metallic inclusions favoured the nucleation of blisters parallel to the applied stress. Ferrite-acicular ferrite presented the highest resistance to SSC whilst ferrite-bainite showed the lowest resistance. These results are consistent with later work conducted by Zhao et al. [74], [75] concluding that material component decreases SSC resistance of steel. HIC occurred when atomic hydrogen (H_2) as result of the corrosion reaction between H_2S flux gas and material diffused into the metal and accumulated as gaseous hydrogen at defects, cracks or non-metallic inclusions. The corrosion reaction generally accepted is presented in equations 2-6 to 2-9 [155,156].

Anodic reaction:

$$Fe = Fe^{2+} + 2e^{-} \quad \textbf{(2-5)}$$

Dissociation reactions:

$$H_2 S \rightarrow H^{+} + HS \quad \textbf{(2-6)}$$

$$HS^{-} \rightarrow H^{+} + S^{2-} \quad \textbf{(2-7)}$$

Cathodic reaction:

$$2H^{+} + 2e \rightarrow 2H(atomic-hydrogen) \rightarrow H_2 \uparrow_{(gas)} \quad \textbf{(2-8)}$$

Kim's work discusses the relationship between HIC and SOHIC (stress oriented hydrogen induced cracking). They found that although SOHIC is characterised by the formation of the planar cracks parallel to the rolling direction of steels, the HIC mechanism was uncertain because SOHIC is present in steels with HIC resistance.

It was observed that base metal exhibited a higher susceptibility to SOHIC and the result was similar to the outcomes of Cayard [157] and Koh [158] which have been discussed by Kobayashi [159] who explained the mechanics involved to initiate SOHIC from conventional HIC to a low-strength HIC. It is well known that increasing the strength of steel leads to a decrease in the resistance of material to HIC.

Hardie et al. [160] compared the susceptibility of API X60, X80 and X100 steels to HIC. It was found that the loss of ductility upon hydrogen-charging becomes greater while the strength level of the steel increases. Dong et al. [113] investigated the sulphide SCC of X100 steel in an H_2S environment and found that cracks nucleated at inclusions such as aluminium oxides, titanium oxides and ferric carbides in the steel. Besides, it caused a reduction of plasticity and ductility due to hydrogen charging time.

The minimum amount of H_2S required to inhibit embrittlement is not well established; however, it has been suggested in some studies as 15 ppm or 30 ppm [126],[161]. However low pH with very low H_2S cracking of low carbon alloys is prevalent [133],[162]. Although some diagrams have been published data representing the cracking susceptibility of steel depending on pH vs. H_2S partial pressure, it is not clear which one could cover all the range to evaluate HIC severity [82,163–165].

These conditions may be relevant for CCTS systems where high CO_2 partial pressure and water can lead to low pH, and H_2S may be present as an impurity at a low concentration (<5 ppm) [135], increasing the concern about high strength materials cracking by SSC or SCC.

The presence of O_2 is related to the increase of CRs, especially localized pitting corrosion. Schmitt and Hörstemeier [124] point out that some studies have shown that the corrosion rate in CO_2 is accelerated in the presence of oxygen by 0.5 mm/y per ppm of oxygen; however, Martin [166] finds that in sweet conditions, the presence of O_2 can increase corrosion up to 23 mm/y. If O_2 and H_2S are present in the environment, then $FeSO_4$ can produce further oxidation becoming in FeO(OH) (Ferric Oxyhydroxide). On the other hand, sulphuric acid could appear and react, causing higher CRs with the virgin steel (Eq. 2-9).

$$4FeSO_4 + 6H_2O + O_2 \rightarrow 4FeO(OH) + 4H_2SO_4 \quad \textbf{(2-9)}$$

Figure 2-19 shows the impurity effects on pipelines while Figure 2-20 gives values of the CRs when these are presented in the system. Even though the results were obtained from lab scale on static rate instead of dynamic stream, they quantify the interaction of different components on materials exposed to this environment.

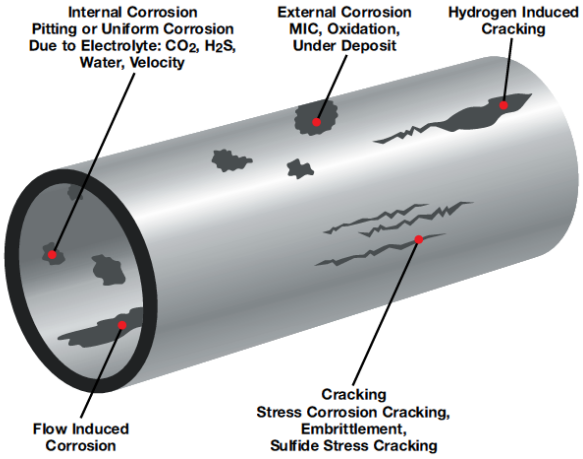

Figure 2-19 Corrosion mechanism in pipeline [167]

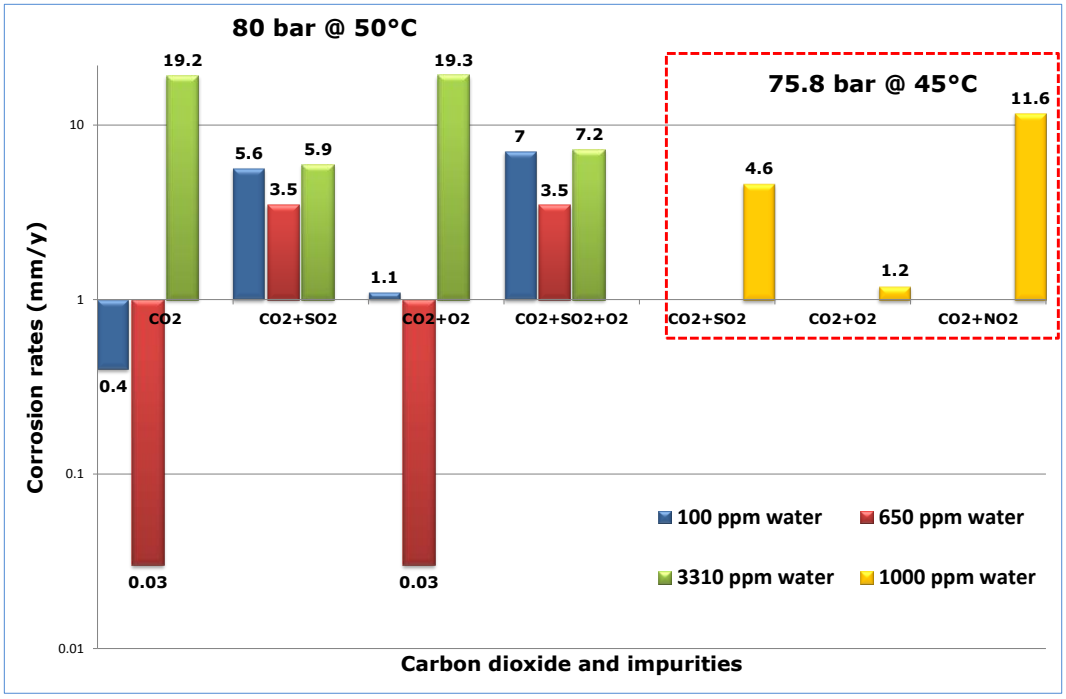

Figure 2-20 CRs of API X65 steel in super critical CO_2 with SO_2 (1%), O_2 (4%) and NO_2 (0.01%) impurities at different amounts of water, pressure and temperature [93,168]

Regarding evaluation of materials properties used to transport supercritical CO_2 little information is available. Recently two works have addressed this issue, one using an outflow model while other carry out an experimental investigation both focused to establish a framework about ductile fracture propagation and fracture toughness.

Mahgerefteh et al [169] using an outflow model, show that the temperature in front of a crack could drastically fall to -70°C in the case of a puncture, which is well below the normal operational conditions of a pipeline. The material used for the calculation was an HSLA steel grade X100 steel and the crack was running along the rolling direction of the pipe. A corrosive environment was considered in this study by taking into account the composition of impurities available in the literature.

Zargarzadeh, P [170] assessed the same kind of steel for leak-before-break (LbB) approach by considering a through-thickness flaw in a cylinder oriented axially. It was found that at -70°C, the critical crack length is 14.8 mm under operating pressure conditions; while at the environment temperature (21°C) the crack length can be extended more than double (~30 mm). However, no evaluation of the material within a simulated flue-gas was performed.

2.3 Fracture mechanics

Fracture mechanics is the area of solid mechanics concerned with the evaluation of crack propagation on materials. It uses methods to calculate the driving force on a crack to determine the materials' resistance to fracture. The route mode a crack extends through the materials is indicative for fracture mechanics which is used to estimate the fracture strength of cracked components under fracture toughness and stress analysis approaches.

Examples of the aforementioned driving force are shear fracture, cleavage fracture, fatigue fracture, crazing and de-adhesion. Thus, the mechanical performance of a structure or components rescinds in the application of elastic and plastic theories on a microscopic scale in order to predict the macroscopic

mechanical failure of bodies. Fracture mechanics is divided into two categories: linear elastic fracture mechanics (LEFM) covering the fundaments of linear elasticity theory and elastic-plastic fracture mechanics (EPFM) considering the plastic behaviour of ductile solids.

2.3.1 Linear elastic fracture mechanics

In 1921 Griffith's crack theory was released, which is based on early Inglis work, in order to explain the failure of brittle materials. Griffith's work was oriented to explain why the potential energy decreased and the surface energy increased when a stressed plate of an elastic material contained a crack. To resolve the energy release concept, it was assumed that both external and internal energy are transferred into surface energy. It was called the Griffith energy balance. The energy release rate ***G*** and the crack resistance force ***R*** are connected by the surface energy of the material which is described by Equations 2-11 to 2-14.

Energy balance;

$$\frac{dU_e}{d_a} - \frac{dU_i}{d_a} = \frac{dU_a}{d_a} \qquad \textbf{(2-10)}$$

Energy release rate;

$$G = \frac{1}{B}\left(\frac{dU_e}{d_a} - \frac{dU_i}{d_a}\right)\left[Jm^{-2}\right] \qquad \textbf{(2-11)}$$

Crack resistance force;

$$R = \frac{1}{B}\left(\frac{dU_a}{d_a}\right) = 2\gamma\left[Jm^{-2}\right] \qquad \textbf{(2-12)}$$

Griffith's crack criterion;

$$G = R = 2\gamma\left[Jm^{-2}\right] \qquad \textbf{(2-13)}$$

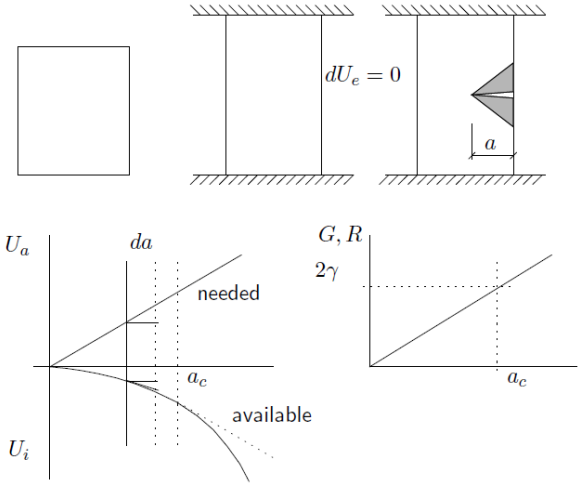

Figure 2-21 Scheme of Griffith's energy balance criterion

Now, considering an infinite plate with a crack length equal to ***2a*** and uniform thickness loaded in mode I, the Griffith stress, σ_{gr}, and the critical crack length, a_c, is calculated.

If $U_i=2\pi a^2 B 1/2[\sigma^2/E)$ and $U_a=4aB\gamma$ [Nm=J]

Griffith's balance ($dU_e=0$)

$$G = \frac{1}{B}\left(\frac{dU_i}{d_a}\right) = \frac{1}{B}\left(\frac{dU_a}{d_a}\right) = R \qquad \textbf{(2-14)}$$

$$2\pi a \frac{\sigma^2}{E} = 4\gamma [Jm^{-2}] \qquad \textbf{(2-15)}$$

Griffith stress;

$$\sigma_{gr} = \sqrt{\frac{2\gamma E}{\pi a}} \qquad \textbf{(2-16)}$$

Critical crack length;

$$a_c = \frac{2\gamma E}{\pi \sigma^2} \qquad \textbf{(2-17)}$$

2.3.2 Elastic-plastic fracture mechanics

Griffith's energy concept is valid for brittle materials but is not suitable for metals where plastic deformation always occurred. Orowan [171] and Irwin [172] concluded independently that plastic deformation is involved in the creation of a new fracture surface resulting in the large amount of additional energy that the small plastic flow generated in the brittle fracture zone.

Based on Westergaard's work [173] on the elastic solution of the stress distribution at a sharp crack, both Irwin and Orowan modified Griffith's elastic surface energy, equation 2-13, by adding a plastic strain work (γ_p) in the fracture process.

$$G = R = 2(\gamma_s + \gamma_p)\left[Jm^{-2}\right] \quad \textbf{(2-18)}$$

$$G = \frac{\pi a \sigma^2}{\mathrm{K}_2} \quad \textbf{(2-19)}$$

Rearranging the equation gives a significant expression in terms of LEFM.

$$\mathrm{K}_I = \sigma\sqrt{\pi a} \quad \textbf{(2-20)}$$

$$\sigma = \sqrt{\frac{G_I \mathrm{E}'}{\pi a}} \quad \textbf{(2-21)}$$

Here, E'**=** E/B. Combining equation 2-18 and 2-21 yields,

For plane stress;

$$G_I = \frac{\mathrm{K}_I^2}{E'} \quad \textbf{(2-22)}$$

For plane strain;

$$G_I = \frac{\mathrm{K}_I^2}{E'}(1-\nu^2) \quad \textbf{(2-23)}$$

From there a parameter K_I is obtained, called the stress intensity factor, which is considered to be the crack driving force (CDF). Also its critical value, K_{Ic}, is a material property known as fracture toughness that determines the resistance force to crack extension. The equations resolved above show a distinctive crack opening mode; however, these can be applied to modes II and III. As shown in Figure 2-22, there are three modes of applying a force to initiate crack propagation, known as Modes I, II and III.

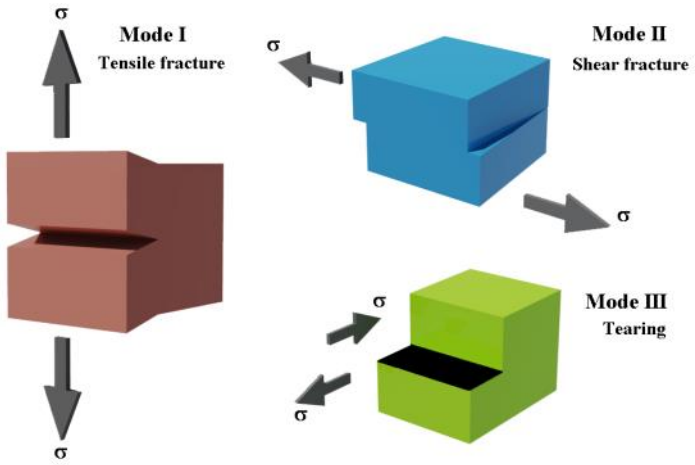

Figure 2-22 Fracture modes to initiate crack extension [174]

Assuming an infinite stress at the crack tip when r=0, that determines a small volume at the crack tip which is slightly bigger than the yield stress, a plastic state is obtained. Dugdale [175] and Irwin [172] established a couple of approximations to estimate the effect; thus, by rearranging equations 2-20 to 2-23, the plastic zone diameter, r_y, is derived by equation 2-25 and sketched in Figure 2-23.

$$\sigma_{ys} = \frac{K_I}{\sqrt{2\pi r_y}} \qquad \textbf{(2-24)}$$

Hence;

$$r_y = \frac{1}{2\pi}\left(\frac{K_I}{\sqrt{\sigma_{ys}}}\right)^2 \qquad \textbf{(2-25)}$$

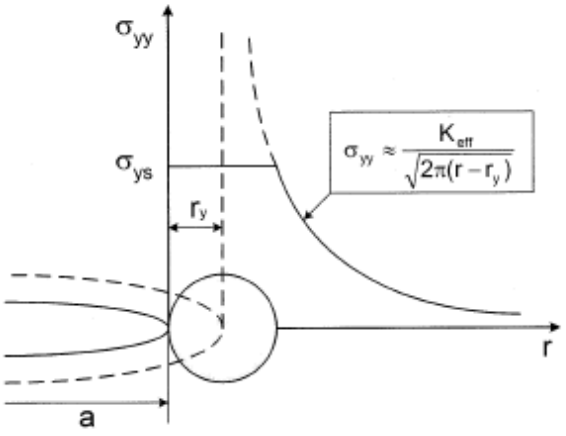

Figure 2-23 Correction of Irwin plastic zone [172]

In thicker samples, conditions of plane strain are retained in the centre of the thickness whereas near to the surfaces plane stress conditions prevail. The plastic zone is much bigger further ahead of the crack near to the outside surfaces than near at the mid-thickness. Thus, if the thickness is less than some critical value that is proportional to $(K_I/\sigma_{ys})^2$ the constraint influence free surfaces, which extends totally through the thickness before the stress intensity reaches K_{Ic}. These conditions can be seen in detail in Figures 2-24.

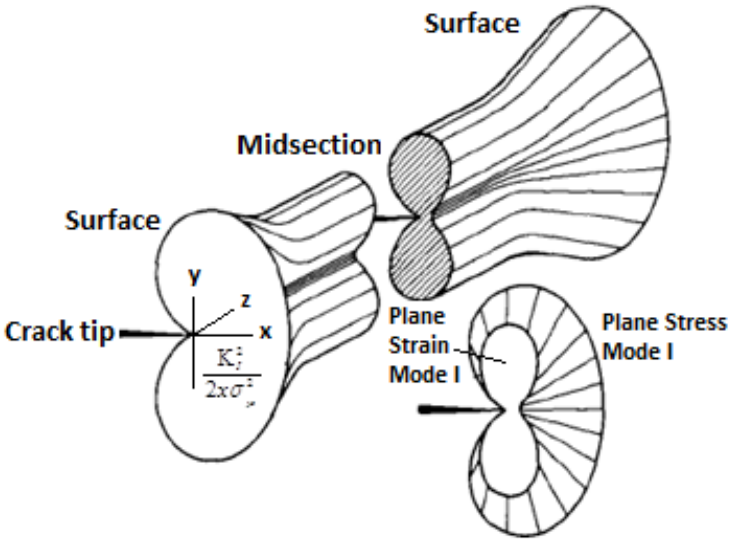

Figure 2-24 Representation of crack tip plastic zone shape showing plane stress and plane strain in a plate specimen (After [176])

2.3.3 Fracture toughness

2.3.3.1 Ductile-Brittle transition temperature (DBTT)

Ductile and brittle fractures are two common mechanics to material failure. Fracture is a process that involves two principal stages: crack initiation and crack propagation. To evaluate the risk of brittle fracture, a DBTT parameter has been chosen as an indication that the material has enough ductility to arrest cleavage initiation, which is a representative indication of material toughness.

DBTT can be accounted for by different methods and geometries which involve static and dynamic approaches [177–180]. The most common dynamic test is known as the Charpy Impact test and determination of DBTT would be accounted for by the curve fitting method [181]; the fracture toughness correlation could be obtained by ASME lower-bound [182], MC [183] or some analytical approaches derived from J resistance curve [59], [184].

In terms of tests, dynamic tests have been performed using non-instrumented and instrumented impact testers with conventional and pre-cracked CVN samples. From there values obtained a curve that can be plotted as a function of energy absorbed vs. temperature to determine DBTT, as depicted in Figure 2-25.

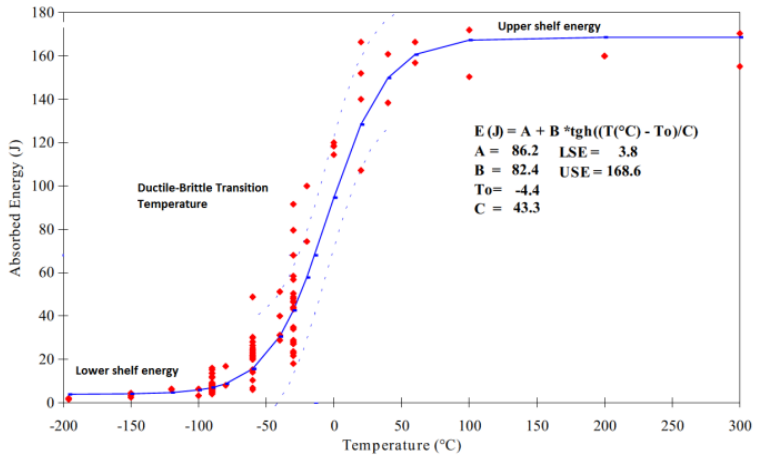

Figure 2-25 Absorbed energy curve for Charpy-V specimen fitted with tanh hyperbolic function [185]

From the Charpy curve, variations of fracture toughness with the temperature, can physically be divided into three regions: brittle (lower shelf), transition (intermediate zone) and ductile (upper shelf). Each region can also be divided into two separates zones. In the brittle zone, lower shelf, size effects are negligible; however, for materials with higher toughness values, the brittle fracture toughness could be affected by a statistical size effect.

The transition region is defined as the region where cleavage and ductile mechanisms are presented during the fracture process. This region is considered to be specimen size, depending on the statistical size effect. Lastly, the upper shelf is characterised as the temperature region where the fracture mechanism is 100% ductile. This region is also size dependent because the statistical size effect and fracture toughness might be affected by specimen constraint.

Depending on the instrument used, fracture toughness could be inferred but there are significant differences. Force-displacement parameters are obtained by instrumented machine (Figure 2-26) while total fracture energy is only available from experimental values with a non-instrumented impact tester.

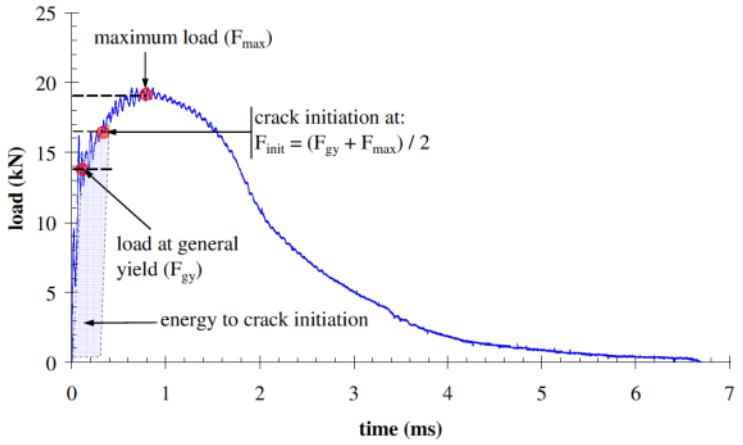

Figure 2-26 Load-time test record of instrumented Charpy showing characteristic points obtained from the graph which are associated with K_{Ic} fracture toughness [185]

From the former, fracture toughness is calculated by analytical approximations whereas from the latter semi or empirical correlations have been developed for this purpose, which can be found in the literature. Charpy energy is neither discretised energy for crack initiation nor for propagation. Thus, its transferability into fracture toughness by the aforementioned correlations appears to be non-unique lumping which therefore effect size, loading rate, crack length-to-width ratio and is also material-dependent. It is well known that a single correlation with derived fracture toughness from Charpy energies is not valid for all materials and conditions.

Extending the notch by introducing a pre-cracked fatigue on the Charpy sample increases the constraint under the root notch. The sharper crack tip increases the level of tensile stress in the blunt crack and also reduces the energy required to initiate crack propagation when the specimen is fractured. Thus, pre-cracking Charpy samples could simulate the conditions when an existing sharp crack extends.

However, comparing energy absorbed by conventional and pre-cracked CVN difference arises due to ligament length. This results in a lowering of the upper shelf energy of the material and shifts the transition temperature upward compared with the notched samples [55,186]. Some of these methods included the calculation of an index temperature, namely T_0, RT_{NDT} and based on fracture mechanics concepts which determine that a stress intensity factor value of 100 $MPam^{0.5}$ prevents crack initiation.

2.3.3.2 Fracture toughness correlations from Charpy energy

In general a conventional CVN test is considered unsuitable for providing toughness information for designing against fractures because of its limited thickness and inapplicability to low- and moderate-toughness materials. However, when correlated with more basic information, the Charpy test is very useful for acceptance and screening purposes.

Although it is well known that a simple correlation between Charpy energy, Cv, and fracture toughness, K_{Ic}, could be obtained, this correlation is not valid for all the materials and conditions. Figure 2-27 plots the type of correlations developed and Tables 2-3 and 2-4 the equations obtained; however, limited data are available, as well as adequate descriptions, and there is considerable scatter of the data to establish the equations.

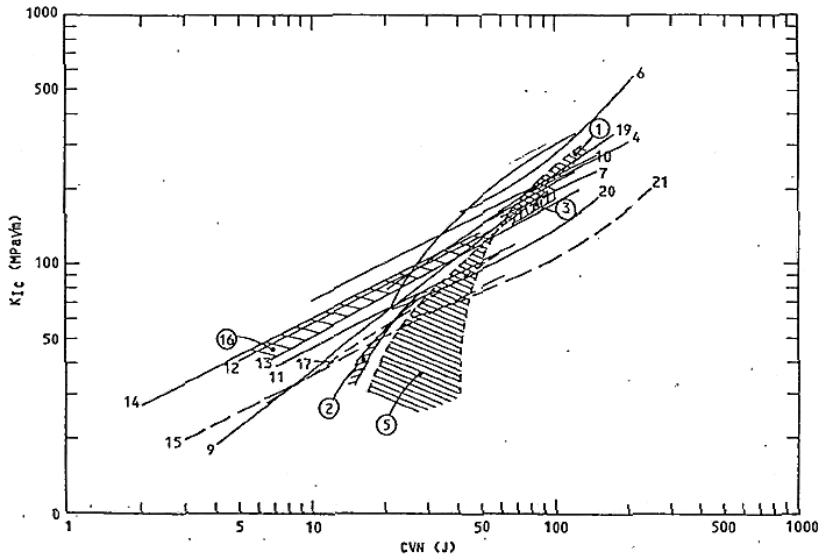

Figure 2-27 Empirical correlations used to associate CVN with K_{Ic} [187]

Regardless of the type of correlation, all correlations have been broadly organised according to the temperature transition curve range of application as follows: lower-shelf, lower-shelf/transition, transition, transition-upper-shelf, upper-shelf and lower shelf/transition/upper-shelf.

Table 2-3 Summary of lower shelf and lower transition correlation

Name	Correlation K_{Ic} (MPa√m)	σ_{UTS} (MPa)	CVN(J) range	Temp (ºC)
Barsom 1	$K_{Ic}{}^2 = 45.1CVN^{1.5}$	270 to 1700	4 to 82	-196 to 27
Barsom 2	$K_{Ic}{}^2 = 105CVN$	270 to 1700	3 to 61	-196 to 0
Sailors	$K_{Ic} = 14.5CVN^{0.5}$	410 to 815	7 to 70	Lower & Transition
Marandet	$K_{Ic} = 19CVN^{0.5}$	274 to 820	5 to 50	-196 to 50
Imai	$(K_{Ic}/\sigma_Y) = 2.5CVN^{0.5}$	Not specified	5 to 215	-196 to -40

Correlations developed by Barsom and Rolfe [49], Marson and Rolfe [188], Sailors and Corten [50] and Marandet and Sanz [189] have received significant consideration; the latter being the only one that considered specimen size independent of the temperature [190]. Therefore Charpy impact energy could meet requirements for certain applications such as quality control during manufacturing, for materials toughness comparison or if there is limited material availability.

Table 2-4 Summary of correlations covering Temperature Shifts

Name	Correlation K_{Ic} (MPa√m)	σ_{UTS} (MPa)	CVN(J)
ASME-PVRC	K_{Ic} = 1.33 exp [0.0261(T-NDTT+89)] + 29	<621	NA
BS PD 6493:1	K_{Ic} = 1.33 exp [0.0261(T-NDTT$_{T40J}$ +89)] + 29	<480	NA
Barsom	$K_{Ic}^{\ 2} = 105CVN$ T=119-0.12*σ_Y (σ_Y < 965 MPa)	270 to 1700	7 to 70
Matsumoto	K_{Ic} = 1.615 exp [0.038(T-ATT+140)] + 31	Not specified	5 to 50
Sanz	$K_{Ic} = 19CVN^{0.5}$ $T_{K100\ MPa\sqrt{m}}$=1.37$T_{CVN\ 28J}$ + 9	274 to 820	5 to 215
Wallin	$T_{K100\ MPa\sqrt{m}}$=T_{K27J} - 18	300 to 1500	NA
Wallin	-	300 to 1500	T= -109 ºC to 20 ºC
Wallin	-	300 to 1500	NA

2.3.4 Mechanics of cleavage fracture

Many different possible mechanisms of cleavage fracture initiation are qualitatively well known. Primarily crack initiation is a critical stress controlled process, where forces acting on the material produce a small failure developing into a propagating and dynamic cleavage crack. Local “initiators” may be precipitates, inclusions or grain boundaries, acting either alone or together [191–193].

Examples of typical cleavage fracture initiation process are presented schematically in Figure 2-28. Cleavage for fracture steps are:

- Microcrack initiation by of a second phase fracturing of a particle or grain boundary.
- Propagation of these microcracks into the surrounding grains.
- Further propagation of extends microcrack into other adjacent grains.

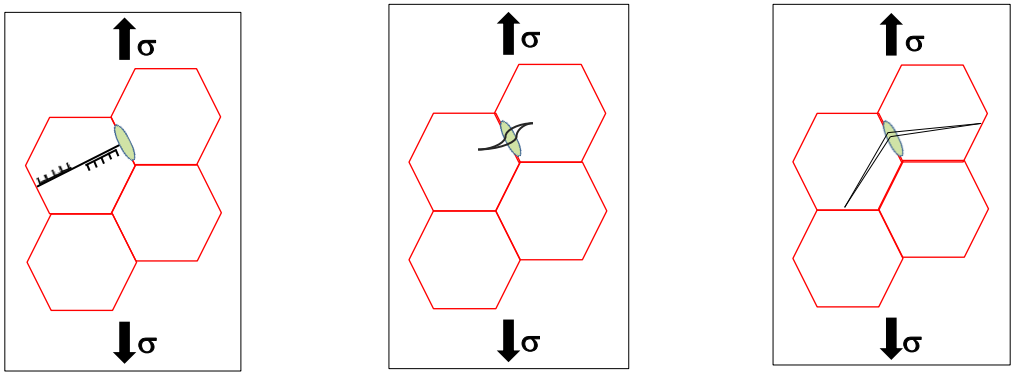

Local stress produces a dislocation pile-up which intrudes on grain boundary carbide.

Cracking of the carbide introduces a microcrack which extended into the matrix.

Advancing microcrack run into the first large angle boundary

Figure 2-28 Schematic of a cleavage fracture initiation mechanics

Depending on temperature, loading rate, loading geometry, and material, different steps are more likely to be most critical. Structural steels at lower shelf temperatures and ceramics show that steps II and III are more difficult to initiate as they tend to control the fracture toughness. At higher temperatures, where gradient stress distribution is smaller, propagation becomes easier in relation to the initiation process. Consequent step I becomes even more dominant for the fracture process. The temperature region where step I dominates is called the transition region.

Specimen with a fatigue cracks fracture surfaces are usually seen as changes in the number of initiation sites visible surfaces, as shown in Figure 2-29. At higher temperatures of the transition region, only a couple of initiation sites are able to be seen contrary at lower shelf temperatures numerous initiation sites are visible. Notched or plain specimens, only have a few initiation sites even on the lower shelf section.

The reason for this is that crack peak stresses are very high almost from the beginning of loading, whereas notched and plain specimens show the peak stresses responses increase gradually during loading episodes.

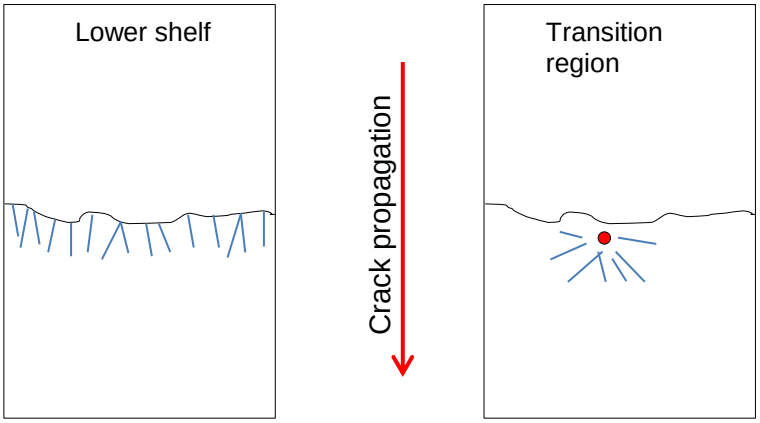

Figure 2-29 Drawing of typical cleavage fracture surfaces for components containing a crack

Because materials are never fully uniform on a microscale level, cleavage fracture initiation is a statistical event, having implications on the macroscopic nature of the brittle fractures. A statistical model is therefore needed to fully describe probability of cleavage fractures [183]. A general statistical model is presented in Fig. 2-30 assuming that the material in front region of the crack contains a distribution of possible cleavage fracture initiation sites, i.e. cleavage initiators.

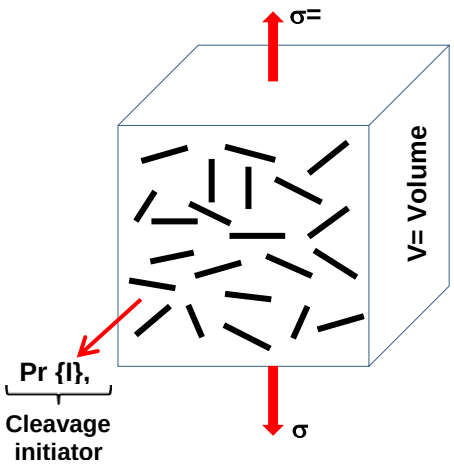

Figure 2-30 Sketch showing assumptions of the statistical model

Cumulative probability distribution for a single initiator is critical and can be expressed as Pr{I} this is a complex function of the initiator size distribution, grain size, temperature, stress and strain rate etc. The source and form of the initiator distribution is not important in the case of a "sharp" crack. But it is necessary to assume that no complete interaction between initiators exists.

Consequently interactions on a local scale are permitted. Groups of cleavage initiations may be required for macroscopic instigation. As long as the cluster is small, it can be interpreted as being a single event. All of these above factors can be structurally grouped into the initiator distribution and they are not important as long as the shape and specific nature of the distribution is not determined from this.

If a particle (or grain boundary) fails, but the broken piece is not capable of replicating a cleavage fracture in the matrix, the particle sized microcrack will blunt and a void will form. Void formation is not considered to be able to initiate a cleavage fracture. Therefore cleavage fracture initiator distribution is affected by void formation, causing a conditional probability for cleavage initiation (Pr{I/O}).

The condition of this is that the cleavage initiator must not have become a void. Cleavage fracture process contains other conditional events such as propagation. Initiated cleavage cracks must be able to permeate through the matrix in order to produce a failure. So, conditional probability is that of propagation after initiation (Pr{P/I}).

Misconceptions originating from the incorrect interpretation of conditions required for plane strain fracture toughness are to assume that only valid K_{IC} results correspond to plane strain. Size requirements given in ASTM E-399, are assumed to be a necessary criterion for plane strain. However in reality requirements are intended to ensure the application of linear-elastic fracture mechanics, meaning that fracture toughness is estimated from load data.

These requirements do not affect limiting conditions for plane strain stress state in front of the crack. Modern finite element analyses have shown that the specimen thickness is able to be reduced by greater than a factor of 10 without losing the plane strain stress state.

Differences between K_{IC} and K_{JC} are that K_{JC} should be estimated via the elastic or plastic parameter ***J*** requiring measurement of load and load-point displacement. As long as the K_{JC} values fulfil the size requirements given in ASTM E1921, they are equally significant as valid K_{IC} values for cleavage fracture. In both instances, fracture toughness is affected by the statistical size effect. Therefore both K_{IC} and K_{JC} values, in the case of cleavage fracture, need to be analysed using the MC method. In 2007, ASTM E1921 uses modern understanding of EPFM, allowing determination of T_o using specimens as small as a pre-cracked CVN, with limits on the preceding deformation fracture being satisfied.

2.3.4.1 Methods to determine fracture initiation

The effects of constraint on cleavage fracture received considerable attention at the end of the last century. In the early 1980s, Landes and Schaffer noticed a statistical “size” effect for specimens failing through transgranular cleavage [194]. They demonstrated that large specimens fail at lower toughness values than small specimens.

In 1984, Wallin and co-workers from the VTT technical research centre in Finland [183] combined the concept of “weakest link” size effect with micro-mechanical models of cleavage fracture proposed by Smith [195], Knott [196], Ritchie [197], and Curry [198], [199]. Later a model developed by Wallin that accounts for the size effects providing a means to calculate statistical confidence bounds on cleavage fracture toughness data was introduced [200]. The combination of these concepts with the observation, first made by Wallin in 1984 and reinforced in 1991 [183], [201] that all ferritic steels exhibit a common variation of cleavage fracture toughness with temperature, gave birth to the notion of a “master” transition curve for all ferritic steels.

The MC concept gave origin to the ASTM E1921 standard which describes the determination of a reference temperature, T_0 in ^oC, which characterises the fracture toughness of ferritic steels that experience the onset of cleavage cracking at elastic, or elastic-plastic K_{Jc} instability, or both. By definition, T_0 is a temperature at which the median of the K_{Jc} distribution from 1T size specimens will be equal to 100 MPa√m.

The three-parameter Weibull model, the cumulative failure probability (63%), the scale parameter K_0 (data-fitting parameter) and the inclusion of K_{min} set as 20 MPa√m, determine the estimated median (50% probability) K_{Jc} of the population tests and is expressed by equations 2-26 for CT and 2-27 for CVN.

$$K_{JC(50\%)} = 30 + 70\exp[(0.019(T - To)]\ MPa\sqrt{m} \quad \textbf{(2-26)}$$

$$K_{JC(50\%)} = 31 + 77\exp[(0.019(T - To)]\ MPa\sqrt{m} \quad \textbf{(2-27)}$$

The reference temperature (T_0), for which K_{Jc} is 100 MPa√m, is calculated from the expression in equation 2-28.

$$T_0 = \mathrm{T} - \frac{1}{0.019}\ \ln\left[\frac{K_{Jc(med)} - 30}{70}\right] \quad \textbf{(2-28)}$$

Correlation between Charpy-V and T_0 can be made by two equations which were developed by Wallin [202] (Eq. 2-29) and Sokolov [203] (Eq. 2-30). The latter is most commonly used in nuclear surveillance programmes.

$$T_0 = T_{28J} - 18\ ^{\circ}\mathrm{C} \quad \textbf{(2-29)}$$

$$T_0 = T_{41J} - 24\ ^{\circ}\mathrm{C} \quad \textbf{(2-30)}$$

T_0 temperature should be relatively independent of the test temperature of the area of interest; hence, data that are distributed over a restricted temperature range, namely $T_0 \pm 50\ ^{\circ}C$, can be used to determine T_0. This temperature range, together with the specimen size requirement, provides a validity window as shown in Figure 2-31.

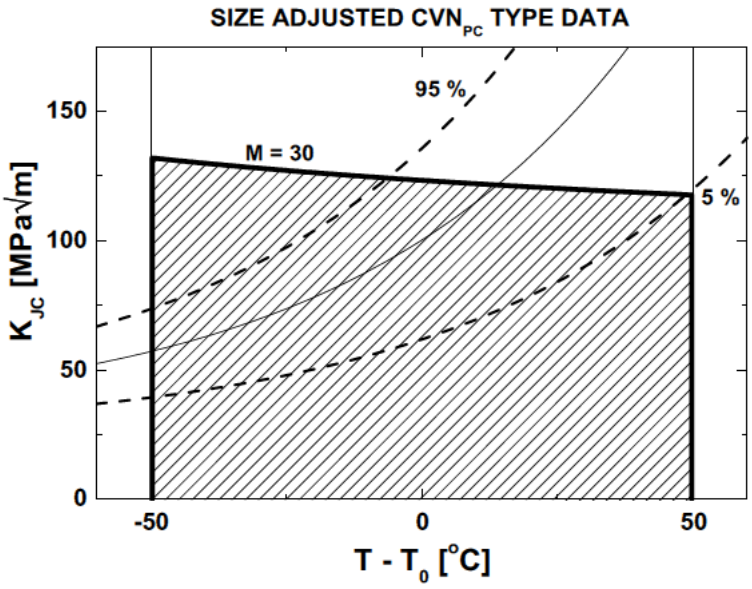

Figure 2-31 Schematic of Master Curve “MC” with validity window of a PCCVN specimen [57]

Comparison between MC and ASME lower bounds have been carried out and it was found the MC described more accurately the cleavage fracture toughness determined for the T_0 index temperature than the calculation by ASME using RT_{NDT}. However, the inherent scatter that affects the DBTT regime fracture toughness steels determination of low cumulative failure probabilities is required for which neither the empirical ASME-reference nor the MC approach is able to deliver a good description for components dealing with lower bound calculations [204].

Pallaspuro et al. [205] found that fracture toughness calculated in high strength steels using the correlation between the Charpy V-impact toughness transition temperature T_{28J} do not follow this and the T_0 temperature estimates could be unconservative, so there is a risk in estimating the brittle fracture toughness based on this parameter.

$$T_0 = 0.8T_{28J} + 14\ ^{\circ}\mathrm{C} \quad \textbf{(2-31)}$$

Schindler [59], [184] has suggested that a physical lower bound exists which depends on the temperature and yield strength and a theoretical model has been proposed to fill the existing gap. The analytical approach developed enables the correlation of K_{Ic} from K_{Jc} for smaller samples. Conversely a thickness-dependent lower bound of K_{Jc} can be obtained which is provided from a lower-bound K_{Ic} obtained by the ASME-code. The considerations and model can be seen in Figure 2-32 and equation 2-32.

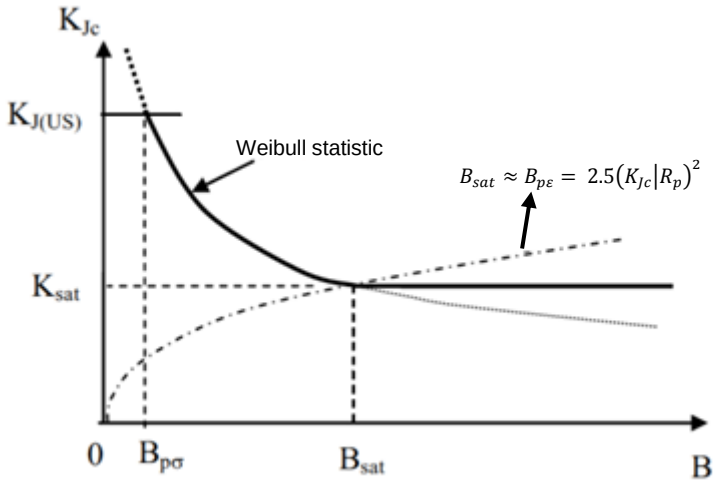

Figure 2-32 Dependence of the lower bound of $\mathbf{K_{Jc}}$ on the thickness B according to the model [184]

$$K_{LB(B)}(T) = \frac{1.257}{B^{0.25} \cdot \sqrt{R_p}} \cdot \{36.5 + 22.8 \cdot \exp[0.036 \cdot (T - T_0 - 19.4°)]\}^{3/2} \quad \text{for } B < 2.5 \cdot \left(\frac{K_{LB(B)}}{R_p}\right)^2 \qquad \textbf{(2-32)}$$

2.3.5 Review of fracture toughness of HSLA steels

Fractures in pipeline steel can be initiated by defects introduced into or developed within the material. There are two main stages of fracture process: crack nucleation and propagation within which two types of fracture or a combination of them can be present: brittle and ductile fracture.

Fracture control involves two main issues: fracture initiation and fracture propagation. The former is controlled by toughness, diameter, wall thickness, grade of pipe, the size of defect and level of stress of the steel.

The latter is controlled by the depressurisation in the pipe, ductile-to-brittle transition temperature of the steel, the backfill conditions and toughness of material [15,143]. The factors that affect the toughness of material are low temperature (i.e. below transition temperature), high strain rate, relationships between strength and ductility, and triaxial state of stress (e.g. notch).

Fracture initiation toughness temperature (FITT) and fracture propagation transition temperature (FTTP) are two parameters usually used to assure that the pipeline has sufficient resistance to the presence of flaws in the pipeline [206,207]. Experimental determination of fracture toughness is considered to be an important and critical aspect in the application of structural integrity assessment of components exposed to a continued load and/or harsh environment.

Also toughness plays an important role in material characterisation, performance evaluation and quality assurance of engineering structures, piping, tanks, vessels, automotive, ship, aircraft and pipelines. The relationship existing between theories and experimentation for fracture toughness analysis based on fracture mechanics concepts are presented schematically in Figure 2-33.

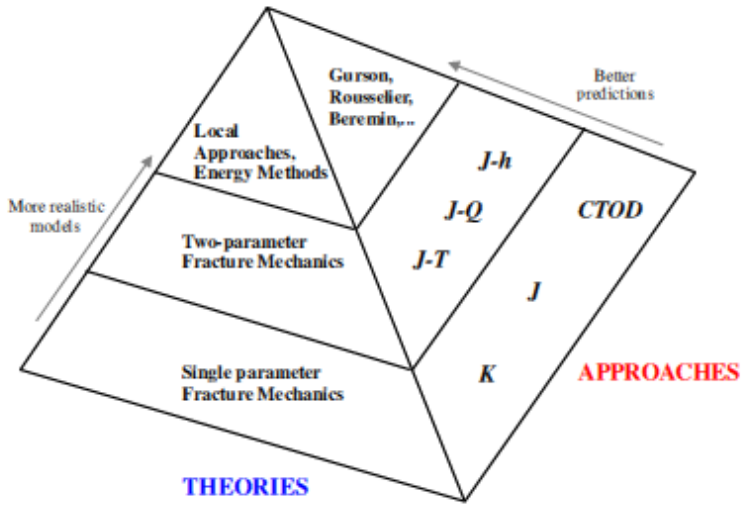

Figure 2-33 Interaction of different theories and approach for fracture mechanic analysis[208]

Evaluation of stress intensity factor, K, or elastic energy release rate G, the J-integral, the crack tip opening displacement (CTOD), and the crack tip opening angle (CTOA), are considered to be the most important parameters to evaluate fracture toughness. Conversely impact toughness is an expression used to define the energy values that can be obtained from CVN and DWTT. J-integral, CTOD, CTOAD and CMOD were developed especially to measure toughness of materials presenting a ductile fracture. Also, stress intensity factors (K) are selected to determine the critical plane strain stress intensity factor (K_{Ic}), but there are some issues in terms of size of specimen, costs and functionality. However, the aforementioned drawbacks could be resolved by DWTT and Charpy V tests [209–211].

The former test ensures the material is not brittle (85% shear area) and the latter is to ensure the steel has sufficient ductility. A minimum toughness is required to prevent brittle fracture which can be achieved if the CVN value is on the upper shelf of the transition curve (Figure 34). According to the specification of API 5L [67] an average of the impact energy is required to be 68 J (minimum 27 J in the L-T notch direction and 41 J in the TL at 0°C) using standard CVN samples for pipelines with 16-20 mm thickness.

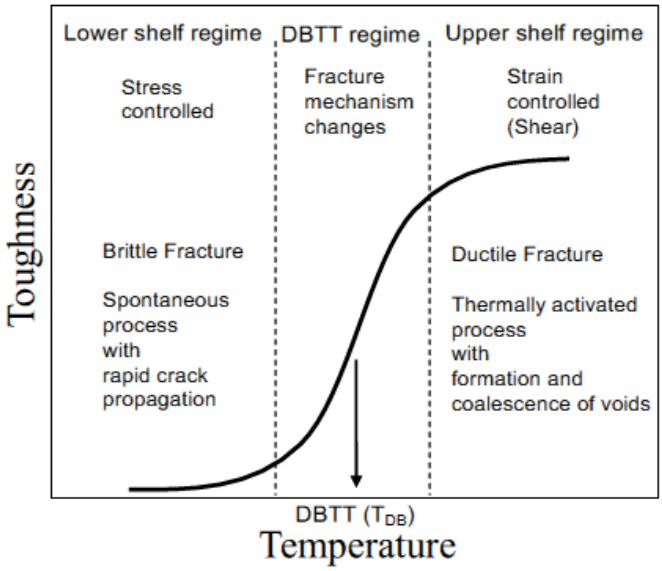

Figure 2-34 Schematic illustration of fracture toughness in terms of Charpy energies and their correspondence regions as function of temperature [212]

However, this value could be different when PCCVN samples are used. If the requirements of DWTT and CVN are met, then brittle fracture can be prevented; however, it does not prevent the cause of a ductile fracture. DWTT and CVN cannot be considered as direct measurements of toughness of material, making both unsuitable for evaluating this parameter on materials. The main reason is due to the small scale specimen that is used, as accuracy and conservative predictions cannot be obtained from them [213]. A large amount of correlation with full scale has been done for relationship behaviour between DWTT and CVN.

Maxey [214] developed an equation which used parameters such as the hoop stress at failure, internal pressure level at failure, flow stress of the material, folias correction, radius of pipe, wall thickness, length of through wall flaw, CVN shelf energy, fracture area of Charpy specimen and Young's modulus to predict fracture initiation. PRC-Battelle, AISI, British Gas, Japan, CSM (Italsider) Mannesmann have developed formulae to predict propagating failure arrest, by CVN energy [75]. Nowadays, one of the concerns with high pressure gas is RDF propagation which is considered to be the fracture mode, instead of CO_2. The Battelle Two Curve Method is the most used methodology for predicting crack initiation prevention [46,71] as can be depicted in Figure 2-35.

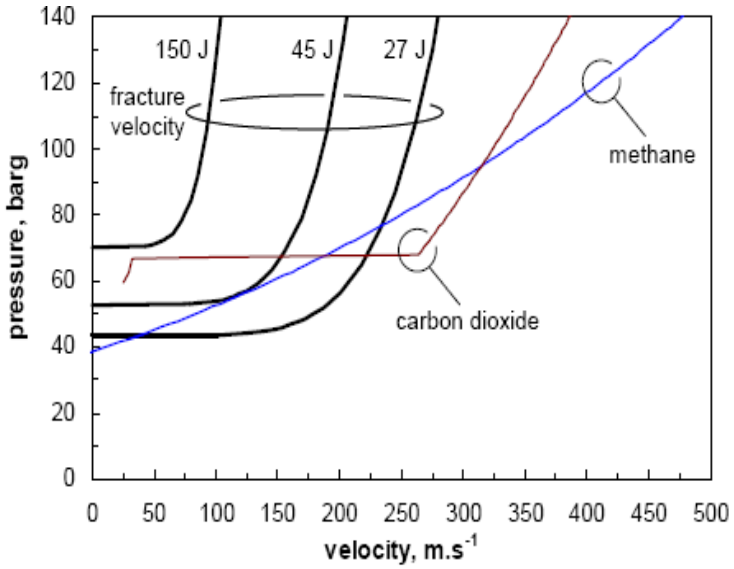

Figure 2-35 Battelle Two Curve Method [15]

Andrews and Batte [215] described how DWTT has been shown to be conservative compared to the full scale pipe burst (West Jefferson) test as shown in Figure 2-36. The results of Charpy, DWTT and West Jefferson demonstrated that the behaviour of HSLA X100 is similar to that of a lower grade pipeline and that the same criteria for brittle fractures resistance can be applied.

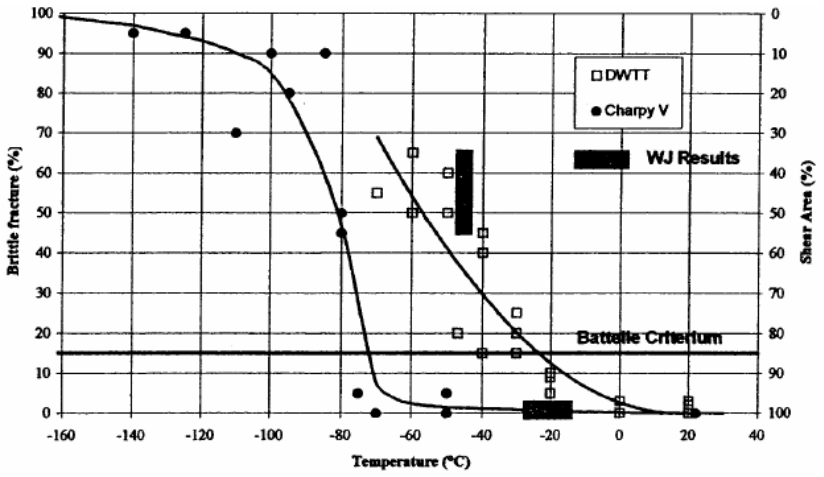

Figure 2-36 DWTT and Charpy transition curves and West Jefferson test results for X100 pipe [215]

However, Demofonti et al. [216] used the value obtained from CVN for arresting ductile fracture propagation with the Battelle simple equation and TCB approach, which is a predictive method for medium high strength steel pipelines. They concluded that this is a highly questionable extrapolation of arrest energy by BTC from lower to higher grades of pipeline, and suggested the application of a correction factor, as is presented in Figure 2-37 and Figure 2-38.

Barsanti et al. [71] conducted an investigation to test high strength pipelines of X80 using the BTC method to predict energy arrest, which is presented in Figure 2-39. It was found that the BTC method is not applicable for this material. Even though the correction factor was introduced for compensating the arrest energy, it was still not easy to determine in X100 HSLA steels.

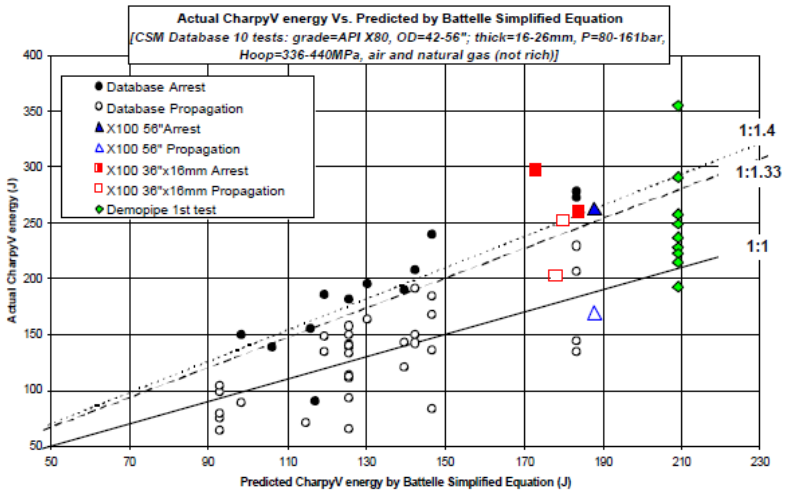

Figure 2-37 Charpy energy vs. Predicted Battelle Simplified Equation [216]

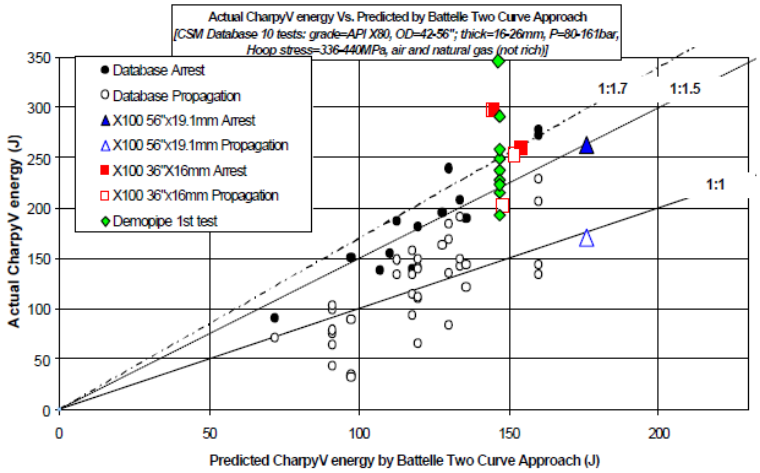

Figure 2-38 Charpy energy vs. Predicted Battelle Two Curve Approach [216]

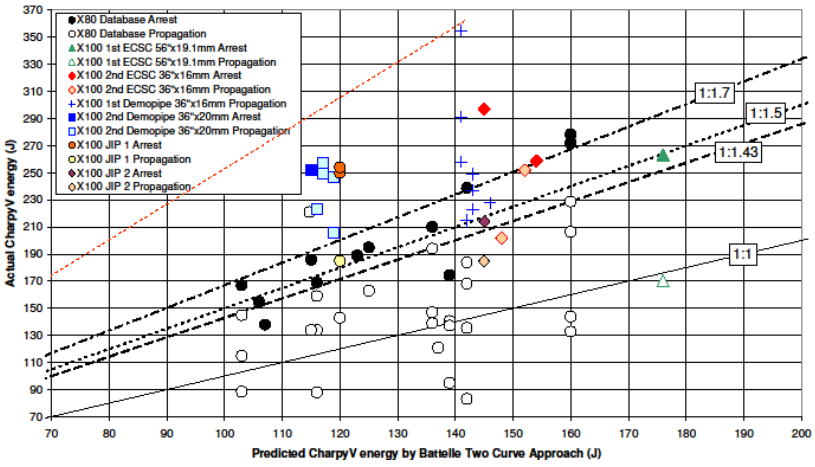

Figure 2-39 Predicted arrest energy on high strength linepipe by BTC [71]

Higuchi et al. [54] proposed a new concept of crack arrestability and developed a new method based on DWTT and Charpy. Although DWTT and Charpy energy are not lineal (Figure 2-40), they proposed converting absorbed energy from CVN to a modified DWTT method. Pre-crack DWTT energy is proposed as the best indicator to express fracture resistance propagation.

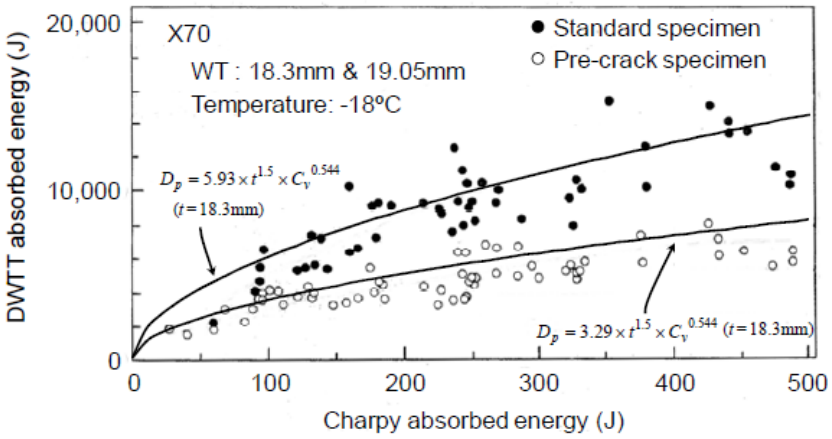

Figure 2-40 Relationship between DWTT and Charpy energy [54]

The model was developed by introducing new parameters in order to compensate for the size effect on fracture velocity. Comparison of the accuracy of the crack velocity prediction on HLS steel by BTC, HLP and Sumitomo methods is presented in Figure 2-41. There is an indication that Sumitomo's model prediction is more reliable than the others; however, this model is only applicable for the transportation of natural gas by pipelines at a higher pressure.

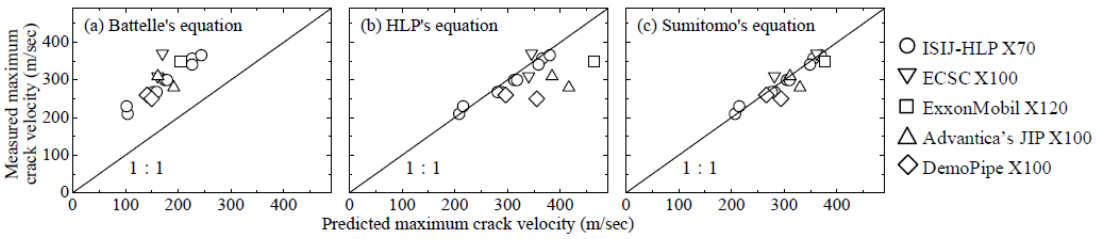

Figure 2-41 Comparison of the accuracy of the crack velocity prediction by each equation [54]

Cosham et al. [15] studied the decompression characteristics of CO_2 and its implications for fracture control when impurities are added. It was found that CO_2 has highly non-linear thermodynamic properties which suggests that in increasing the pressure its behaviour is separated from ideal gas behaviour. Thus, after careful consideration, the trends observed for CO_2 are not the same as those for natural gas. Furthermore, impurities could increase the saturation pressures which require the highest toughness of material, which can be seen in Figure 2-42.

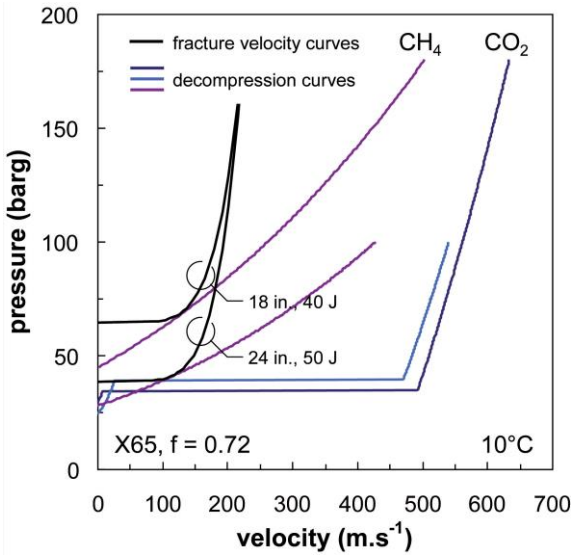

Figure 2-42 Theoretical decompression curves for pure CO_2 and pure CH_4 [46]

Variations in microstructure have an important effect on the fracture toughness of material. Several investigators have reported fluctuations and non-realistic values of K_{Ic} in the case of HSLA steels, C-Mn microalloys steels and C-Mn steel manufactured by HT methods. It was found that when the plane strain fracture toughness is increased the impact toughness decreases which is contrary to the relationship between grain size and toughness [86]. Possible mechanics could be present, such as inter-lath austenite, elimination of twinned martensite plates, changes in the morphology of inclusions, and second phase particles and effects in the notch tip.

A study of the effect of microstructures on fracture toughness in API X70 was conducted by Shin et al. They analysed that the correlation between microstructure and low-temperature toughness has been limited to evaluate DBTT and energy absorber from Charpy values. However, no effects have been studied regarding the microstructure, grain size, and test conditions of DWTT and CVN. In this way, Das et al. [78] found that precipitates and microstructure have an influence on the mechanical properties of the material, and ageing is related to stretch zone width (SZW) and the critical crack extension (Figure 2-43).

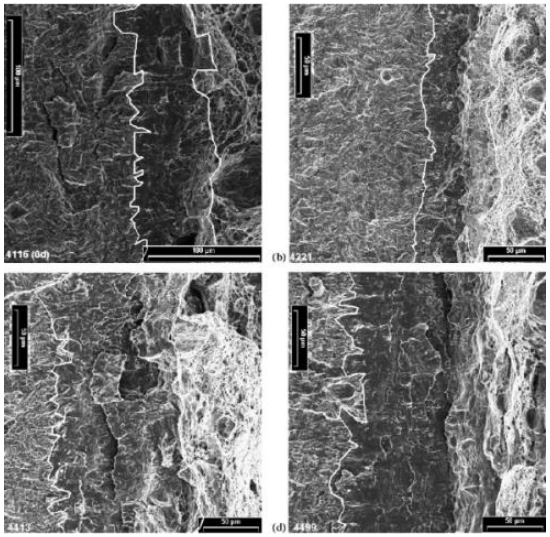

Figure 2-43 Fractography of fracture surface on HSLA steel showing the stretch zone region [78]

Several investigations have been conducted to explain the causes of abnormal fracture appearances (AFAs) in DWTT and CVN where variables such as notch, thickness, crystallographic texture and microstructure were studied [217–222]. The AFAs of DWTT have been classified into three categories according to the causes of cleavage fracture appearance on the fracture surface. Type I can be affected by the rolling supports of the test machine. Type II depends on sharp notch. Five different configurations were investigated: PN (pressed notch), PC (pre-cracked), LC (Lateral compression), Chevron notch (CN) and the so-called “weld notch” (WN) [221,223].

It was concluded that the variety of ductile to brittle transition is significant with the type of notch evaluated. Better results were obtained with LC and WN configurations. Type (III) is affected during crack propagation and it is impossible to avoid or modify. Similarly the phenomenon was analysed by Yang who determined that two types of fracture can be found due to excessive compression deformation and increasing of the thickness locally. The third type is a result of its own material [224]. It can be seen in Figure 2-44.

Figure 2-44 The AFAs in DWTT (a) type I, (b) type II and (c) type III [224]

Shin et al. [218] studied the separation phenomena occurring during the Charpy test of HSLA X80 steel. It was found that bainite elongation was the main cause of this phenomenon, followed by high work hardenability. The length and number of separations depended on fluctuations of temperature. Figure 2-45 shows the surface features determined at lower temperatures.

As discussed before, strength and toughness in the longitudinal direction is much lowers that transversal orientation. For example, Ju et al. [225] found a difference of about 220J when samples of X65 were tested in both longitudinal and transverse directions. Similar steel was studied by Oh et al. [226] but the energy value at the same temperature (-60°C) was 100J.

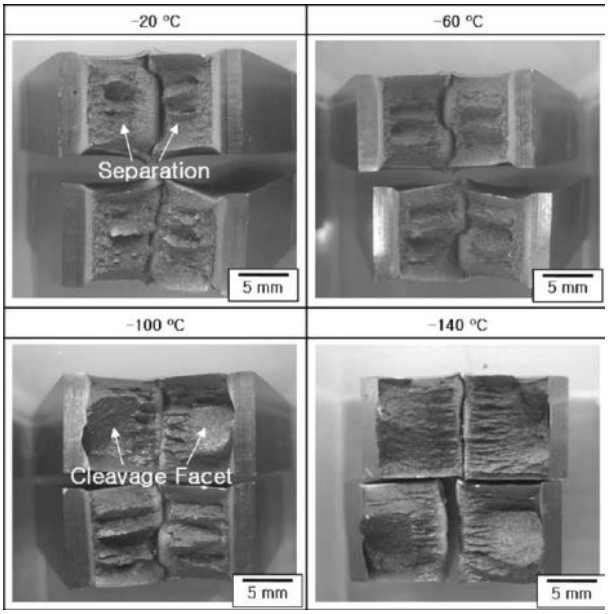

Figure 2-45 Charpy impact specimens fractured at -140°C to -20°C [218]

As known from the literature, fracture toughness is dependent on temperature for many ferritic materials. Parameters such as strain-rate, thickness, microstructure and notch acuity have effects on fracture toughness and shifting CVN transition temperatures (Figure 2-46).

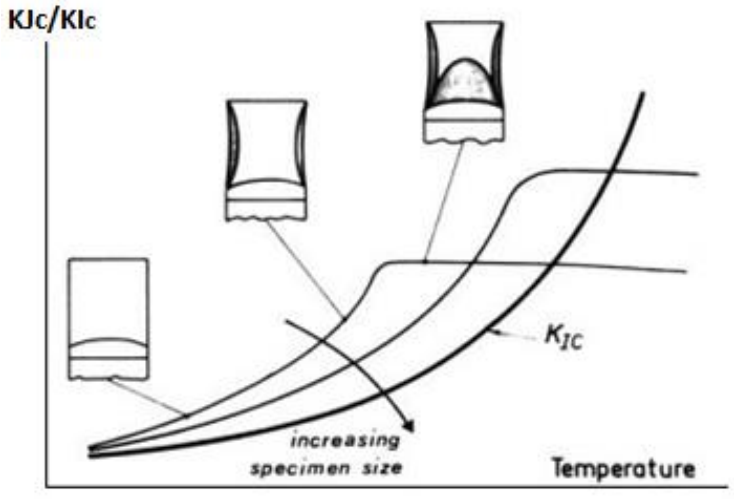

Figure 2-46 Schematic variation of K_{Jc}/K_{Ic} along with temperature for different thickness [227]

In fact, there is a big difference between CVN and valid fracture toughness (K, CTOD and J). The standard Charpy sample is 10x10x55 mm with a blunt notch of 0.25 mm radius while the latter requires a sharp notch introduced by fatigue pre-cracking and large samples to meet plain-strain requirements.

To overcome difficulties associated with the Charpy samples' dimensions and test constraints, some correlations are now in place to associate Charpy energy with fracture toughness from "non-standard" Charpy specimens such as: side-grooved, quasi-static 3PB, sub-size specimens, fatigue pre-cracked specimens, instrumented impact machines and combinations of them. In terms of fatigue pre-cracking, this offered the opportunity to give an alternative solution as this method increases the constraints on root notch when the Charpy specimen is fractured.

The sharper crack tip increases the level of tensile stress at the blunt end and also reduces the energy required to initiate crack propagation. This results in a lowering of the upper shelf energy of the material and shifts its transition temperature upward. Thus, a pre-cracking Charpy test could simulate the conditions through which an existing sharp crack extends. By using an instrumented machine or performing the test under quasi-static loading, the load-time displacement could be obtained and fracture toughness could be calculated by J-integral approximation [227]. However, Robinson and Tetelman [228] carried out an investigation which concluded that the equivalent energy obtained from non-standard pre-cracked specimens produced poor correlations and overestimated K_{Ic} by up to 40%.

Server and Tetelman [186] determined K_{Id} from pre-cracked Charpy samples using an instrumented machine and compared these data with valid static and dynamic fracture toughness on A533B steel from two researches. Their study concluded that by increasing the loading rate, fracture toughness decreases due to strain rate sensitivity of the yield stress. However K_{Id} value shows good agreement with CT data, as presented in Figure 2-47.

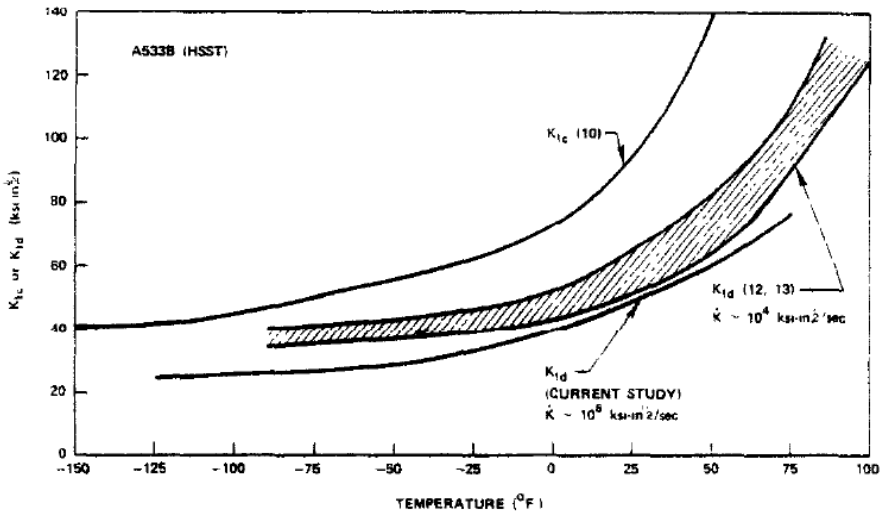

Figure 2-47 Comparison of static and dynamic fracture toughness as a function of temperature by PCCVN specimens [186]

Transferring material toughness values is still a key issue in applications of fracture mechanics to assess the integrity of structural components. For pipelines or structures manufactured using low carbon steels, brittle fracture triggered by transgranular cleavage in the DBTT region represents a potentially catastrophic failure mode. Due to the highly localized character of the failure mechanism, the cleavage fracture toughness exhibits a strong sensitivity to the local stress and deformation fields.

2.4 Residual Stress

Residual stresses (RS) are those which remain in a body under static equilibrium when all external forces (surface tractions and body forces) are removed. These stresses can act alone in a specimen or in addition to applied stresses on the component. In metal structures, residual stress fields can be generated sporadically, by various processes in the manufacturing of materials and joining of components, based on mechanical changes to the microstructure during these processes.

It is shown in Figure 2-50. These include, but are not limited to, hot and cold working, rolling, bending, forging, casting and welding processes. It should also be noted that residual stress fields can also be induced into a metal specimen and can be used to increase the material/ component's resistance to failure/fracture.

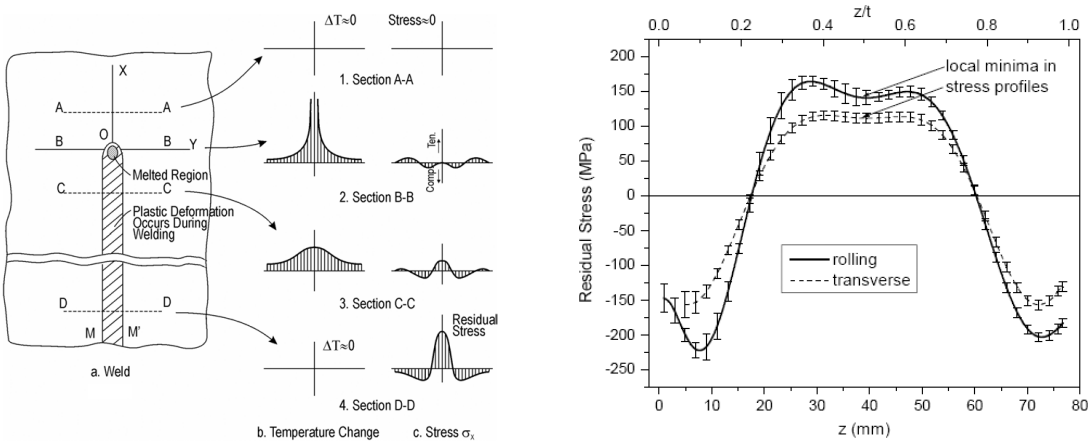

a) Schematic thermal process b) RS from rolling method

Figure 2-48 Residual stresses' origins by thermal and mechanical processes [229]

Depending on the nature of residual stress fields, that nature can be a beneficial or a destructive feature in a component, i.e. residual stresses can be either compressive or tensile in nature. Normally, tensile stress fields are deemed to be destructive and can result in greater likelihood of fatigue failure, whereas compressive stress fields act against tensile loads and reduce the likelihood of fatigue.

2.4.1 Origins of residual Stress

The origins of RS are considered to be the result of size misfits within the material. Such misfits may extend over a long or short distance, describing stresses by their characteristic length, l_0 , which is the length over which the stresses equilibrate [230–232]. Table 2-5 and Figure 2-49 show the classification in terms of length.

Table 2-5 Classification of RS based on the length, l_0

Type stress	Scale	level	length
I	~Structure	Macro	l_{0I}
II	~3 t_0 times of grain size	Micro	l_{0II}
III	< grain size	Atomic	l_{0III}

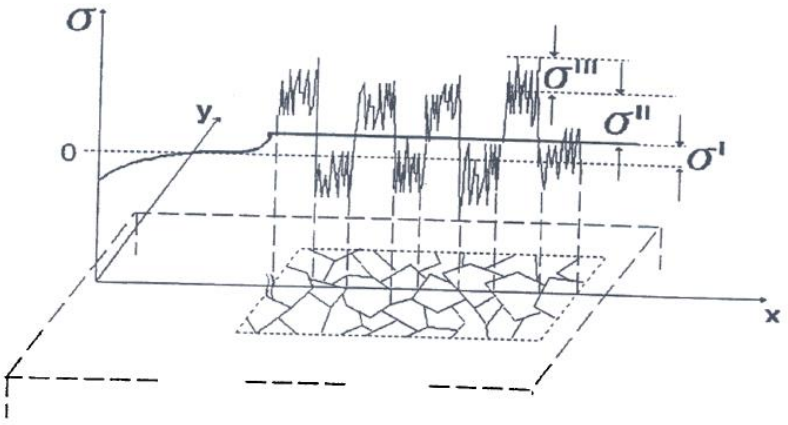

Figure 2-49 Classification of RS based on the length of scales [230]

The misfit that causes or introduces residual stress is induced in various ways. Non-uniform plastic flow, thermal gradients steep and phase transformations are the most common sources of stress, as is presented in Figure 2-50. RS can be defined as either macro or micros stress which should be present in either a structure or component.

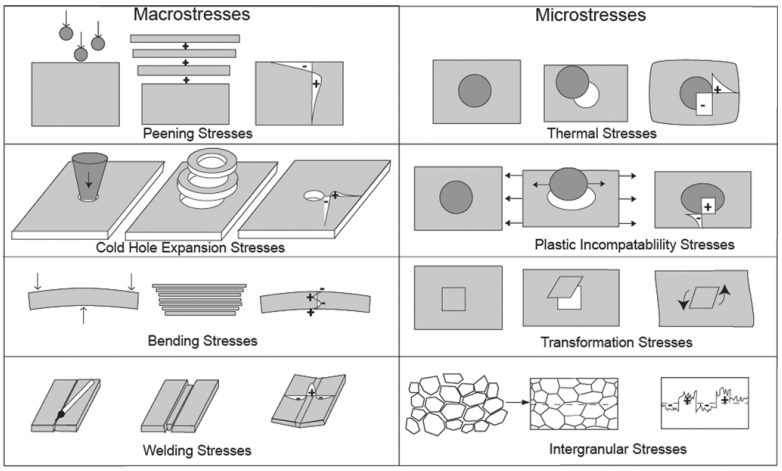

Figure 2-50 Residual stresses' origins and classification depending on the level [230]

Macro stresses defined as Type I RS vary within the bulk of the component in a range further ahead than the grain size. Micro residual stresses are a consequence of microstructure variations and can be classified as Type II or III. Type II is presented at the grain size level, while Type III is generated at the atomic level. Micro RSs can change the sing and/or magnitude over the grain size length. As tensile/compression RSs are both presented (self-equilibrating), their determination is not particularly easy. Quite a wide range of techniques to determine the residual stress area is available, classified as destructive, semi-destructive and non-destructive. Some are applicable on real components or structures while others suit a laboratory scale. As a result, more realistic information becomes available and their combination will be more suitable for structural integrity assessments.

2.4.2 Methods to evaluate residual stress

The effect of residual stresses and the associated consequences are commonly used to explain unexpected engineering failures in components. As a result, the study, measurement and understanding of residual stress fields have become of greater importance in recent years in an attempt to quantify stress fields. Consequently, residual stresses can affect structural behaviour and it is imperative that residual stress fields can be visualized measured and relieved or induced based on the requirements of the engineering application.

Methods developed to measure residual stress are categorized as destructive, semi destructive or non-destructive, as summarised in Table 2-6. Measurement and understanding stress field behaviour will facilitate better design practice against static and dynamic loading and will aid in predicting structural failure and the assessment of structural integrity. Destructive or semi destructive techniques involved removing partially or completely material to determine the relieved residual stress. Non-destructive techniques are usually centred on the diffraction measurement of the lattice parameter that is related to measuring the elastic strain of the specific atomic lattice planes of the stress that is present [233–238].

Table 2-6 Methods to evaluate residual stress

Category	Technique
Destructive	Sectioning technique Contour Methods
Semi-destructive	Hole-drilling technique Ring core method Deep Hole method
Non-destructive	Barkhausen noise X-ray diffraction method Neutron diffraction method Ultrasonic method Magnetic testing method

Differences between the unstressed and deformed lattice are characterised by the (hkl) parameter from their difference residual stresses are determined by Bragg's equation. Except for techniques such as diffraction, which selectively samples "special" grains (i.e. those correctly oriented for diffraction), the sampling gauge volume used is usually significantly larger than the grain size which means that the Type I macrostress is always measured.

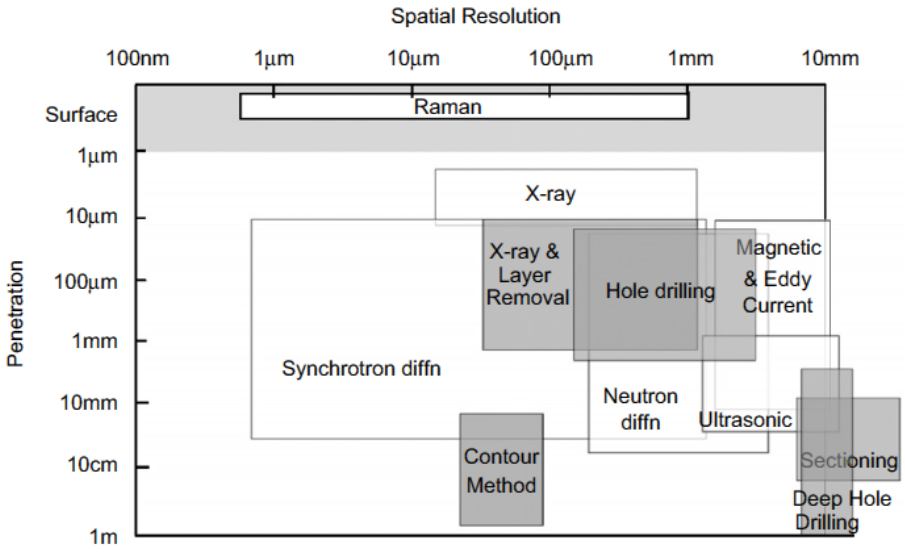

Figure 2-51 Schematic of the current techniques available to measure residual stress in terms of penetration and spatial resolution [238]

Figure 2-51 provides a comparison of the corresponding spatial resolution of destructive and non-destructive methods to measure residual stress fields. Even though there has been immense progress achieved in recent decades to develop methods oriented to determine residual stresses, extensive work is still required to improve efficient and cost-effective methods, analysis and technologies to obtain a more realistic spectrum of material residual stresses redistribution.

2.4.3 Neutron diffraction

Diffraction is perhaps the most important non-destructive resource for determining residual stress fields within crystalline materials and engineering components. The neutron diffraction measurement technique permits an accurate map of the stress fields within a relatively thick component which possesses a crystalline lattice. Despite the high cost and limited accessibility to test equipment (test equipment requires specialist application and is restricted to special testing facilities), the neutron diffraction technique is emerging as the most attractive stress field measurement method.

The strains in a specimen are calculated by the changes within the lattice of the material. This is represented by the relationship between the wavelength of the emitted radiation and the distance between selected lattice planes in the specimen microstructure. The stresses are then calculated through the incorporation of the elastic properties of the material given by Hooke's law. A sample to be examined is placed in a beam of thermal or cold neutrons and the intensity pattern around the sample gives information of the structure of the material.

The diffraction angle and wavelength of the maximum peaks can be expressed, in general, using Bragg's equation (Eq. 2-33):

$$n\lambda = 2d\sin\theta \qquad \textbf{(2-33)}$$

Where ***d*** is the lattice spacing, θ the angle between the wave vector of the incident plane wave, k_o, and the lattice planes, λ its wave length and ***n*** is an integer, the order of the reflection. This equation is the basis of all diffraction measurements of lattice spacing and hence of strain in polycrystalline materials. In an unstressed material the lattice spacing is a constant; however, the lattice spacing can vary according to the applied stress as a result of elastic deformation (Figure 2-52).

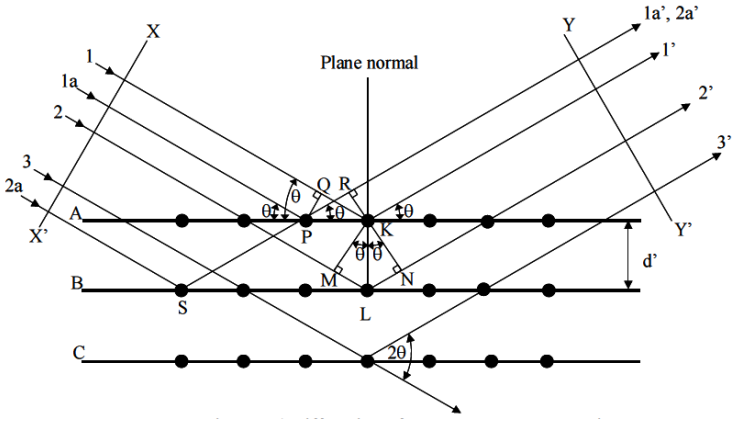

Figure 2-52 Schematic representation of Bragg's diffraction [239]

From Figure 2-52, the interplanar spacing, ***d***, can be determined if the wavelength of the incident beam is known, by measuring the diffraction angle. Thus, the elastic strain change in the material, with the introduction of residual stresses, can be calculated by equation 2-34.

$$\varepsilon_{(x,y,z)} = d_{(x,y,z)} / do \qquad \textbf{(2-34)}$$

The relations between normal strain and normal stress components are expressed by Hooke's law when the material is assumed as elastic, isotropic and homogeneous. The stresses can be expressed in terms of strains. Therefore, the value of strain direction calculated from equation 2-34 is substituted in equations 2-35, 2-36 and 2-37 to solve the system, stress components are given, where $\sigma_{xx}, \sigma_{yy}, \sigma_{zz}$ is the longitudinal, transverse and normal residual stress depending on which direction of stress is to be calculated and the process or method used to introduce residual stress.

For example, in the cold rolling approach, all the directions are utilized as a result of the effects or variations that the process could impose on the material. The values of the constants are E and ν (the material's plane-specific Young's modulus and Poisson ratio, respectively).

$$\sigma_{xx} = \frac{\nu \mathrm{E}}{(1+\nu)(1-2\nu)}(\varepsilon_{xx} + \varepsilon_{yy} + \varepsilon_{zz}) + \frac{\mathrm{E}}{(1+\nu)}(\varepsilon_{xx}) \quad \textbf{(2-35)}$$

$$\sigma_{yy} = \frac{\nu \mathrm{E}}{(1+\nu)(1-2\nu)}(\varepsilon_{xx} + \varepsilon_{yy} + \varepsilon_{zz}) + \frac{\mathrm{E}}{(1+\nu)}(\varepsilon_{yy}) \quad \textbf{(2-36)}$$

$$\sigma_{zz} = \frac{\nu \mathrm{E}}{(1+\nu)(1-2\nu)}(\varepsilon_{xx} + \varepsilon_{yy} + \varepsilon_{zz}) + \frac{\mathrm{E}}{(1+\nu)}(\varepsilon_{zz}) \quad \textbf{(2-37)}$$

2.4.4 Incremental hole-drilling

The incremental hole-drilling (IHD) technique initiated by Mathar in 1933 [240] is classified as a material-removal approach to quantify residual stresses, particularly in structures or components manufactured from metallic materials. This approach is referred to as a semi-destructive method which determines the macro residual stress of a linearly elastic material. It is considered to be a simple, inexpensive, reasonably accurate and reliable technique when it is implemented correctly. Hole-drilling can provide the residual stress distribution across the thickness in magnitude, direction and sense. Once the small hole is drilled the damage caused to the specimen is often tolerable or repairable [241].

Important improvements were introduced during the middle of the last century, for example, the introduction of electrical resistant strain gauges by Soete and Vancrombrugge in 1950 to measure released strains more accurately [242]. As a consequence, hole diameters could be considerably reduced. Soete and Vancrombrugge also realized the necessity of considering the integration field of strain gauges instead of the radial centre line or the centre point.

In order to determine residual stress depth distributions Kelsey [243] developed the incremental evaluation formalism in 1950, assuming that released strains can be assigned to the removed material increment exclusively. The formalism by Kelsey was modified in 1996 by Kockelmann and Schwarz [244], called the differential method. In 1966 Rendler and Vigness introduced the low-speed drilling technique and defined the geometry of the strain gauge rosette making the method easily and methodically reproducible to determine the magnitudes and principal directions of the at the hole position [245] .To prevent the induction of additional stresses as a consequence of machining effects, in 1980 Flaman [246] introduced high speed orbital drilling instead of low speed drilling, results that were confirmed by Yavelak [247].

Figure 2-53 sketch the ICHD principle to evaluate residual stress. Basically, the hole-drilling method involves drilling a small hole of diameter $\boldsymbol{d_0}$ to a depth of up to 1.5 times its diameter at the location of a stressed material. The hole is drilled in steps and for each hole-depth, z direction, residual stresses are released and the corresponding strains on the surface are measured using three strain gauge rosettes which are bonded around the hole on the surface. It is only possible to measure the two in-plane components of the stress field and the stress profile measurement is dependent on the thickness of the sample. Once the drilling is completed and strains recorded, the residual stresses are calculated from equations that use appropriate calibration coefficients obtained by finite elements.

Improvements to eliminate experimental errors measurement was introduced by Bijak-Zochowski [248] using an integral method. Lately Schajer, based on the fundamental work of Bijak, developed an evaluation formula to determine residual stress depth distribution, known as The Integral Method [249,250] which is contained in ASTM E 837 since 2008 [251]. In comparison with the differential method, this formalism can only be carried out on the basis of numerically computed calibration coefficients. However, integral formalism considers strain releases due to changes in stiffness of the hole for material increments which have already been removed in previous steps.

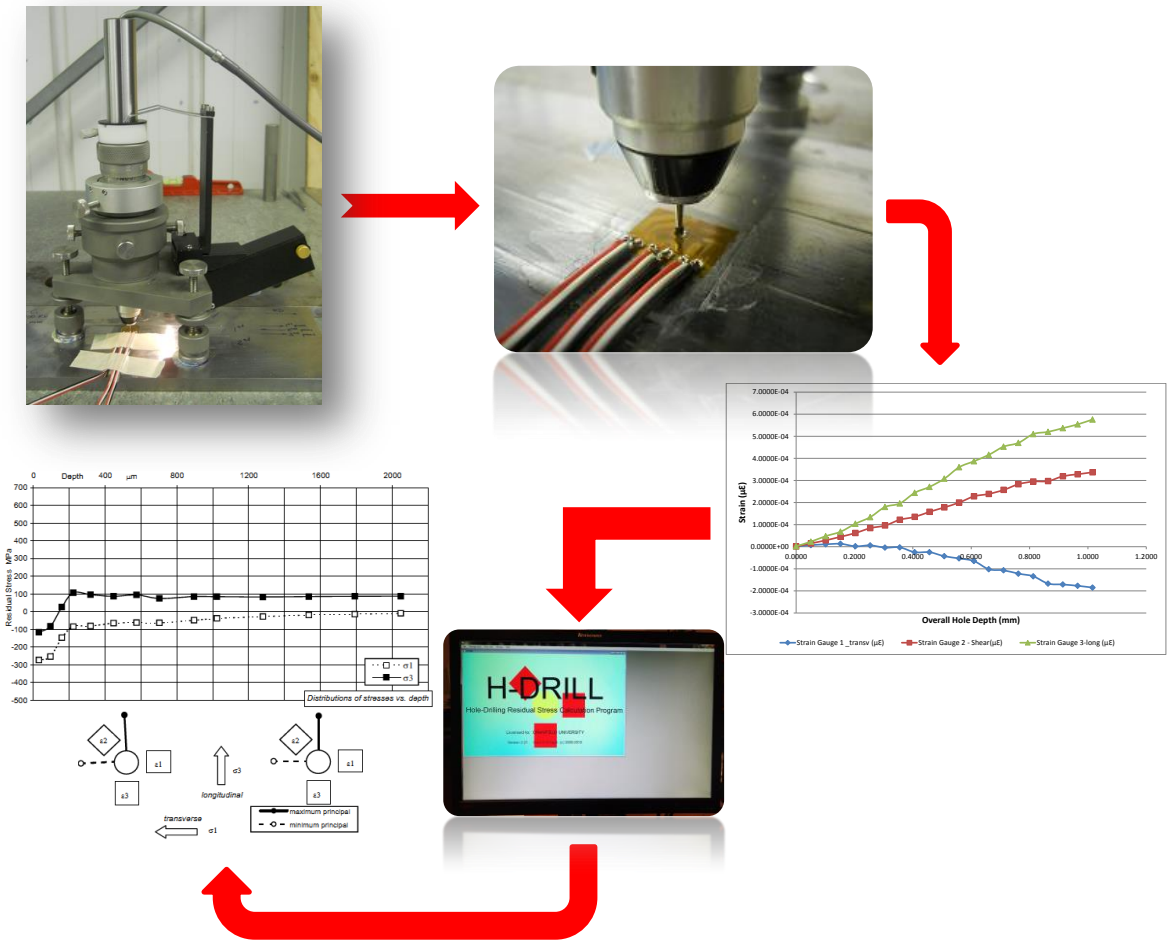

Figure 2-53 ICHD principle to estimate residua stress

Thin specimens are considered to possess a uniform stress profile and the through hole-drilling method is normally employed. For thick specimens with non-uniform stress profiles, the blind hole-drilling method is used, namely Incremental Centre Hole Drilling (ICHD) [241,251,252], as shown in Figure 2-54a and Figure 2-54b, respectively.

The theory of elasticity is usually utilised to correlate the strain relaxation and the residual stresses existing prior to hole-drilling. Thus there is a probability that local yielding presented due to stress concentration in the proximities of the hole should affect calculations of the RS.

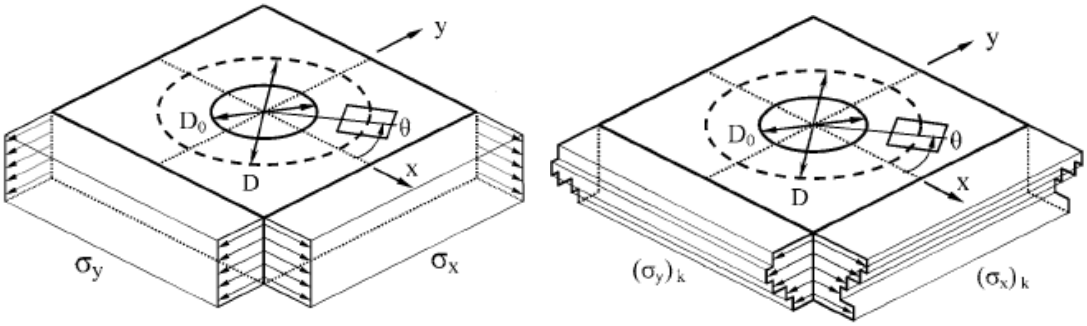

a) Uniform stresses b)Non-uniform stresses

Figure 2-54 Schematic representation of hole geometry and residual stress distribution [251]

If RS reaches a yield strength value circa 60%, the effects become significant [253,254]. According to [245,255–257] residual stresses of 70% yield strength, an error of 15% can be expected in the stress calculation. An overestimation of 20% for residual stresses reaching 90% yield strength is given in [258].

The measurement of in-depth non-uniform residual stresses requires incremental drilling. Currently, four different methods are used to calculate non-uniform residual stresses: the integral method [248,250,259,260], the incremental strain method [243], the power series method [261] and the average stress method [262].

The influence of calculation procedures on residual stress results has been analysed by several authors such as Schajer [261] and Zuccarello [263] using the finite element method. Schajer, for example, concluded that the integral method is a good stress evaluation method when strong stress gradients are present. However, this method implies very precise measurements of relieved strains and depths for each incremental step.

Calculation results are very sensitive to measurement errors because of propagation effects [255,264–269]. Error sensitivity is proportional to the number of hole depth increments (the inverse is true for the power series method) [270,271].

For this reason, the integral method should be used with a few large depth increments. From a comparison of residual calculation procedures and the introduction of new methods, it has been concluded that the differential method and the integral method are the most suitable for the analysis of complex residual stress states[272].

2.4.4.1 Residual stress calculation by the integral method

Methods for measuring through-thickness profiles of residual stress in materials typically involve measuring surface deformations in a sequence of steps as stressed material is incrementally removed. Examples of such techniques are hole-drilling [273], slitting [274] and layer removal [275,276].

Evaluation of the through-thickness stress profile from the measured deformations requires the solution of an inverse equation [277]. Such calculations are well known to be ill-conditioned, causing amplification of modest measurement errors into relatively larger errors in the evaluated stresses.

This error amplification places severe demands on the quality of the measurement technique to ensure that stress evaluation errors remain within an acceptable range. Care must also be taken with the mathematical method used to evaluate the residual stress profile from the measured data. Numerical techniques have been developed to reduce the effects of measurement errors through data averaging [261] and regularization [277].

During the hole-drilling process, removal of material from the first drilling increment results in surface strains (at the gauge) that relate directly to the residual stresses relieved at the hole boundary within that increment. Removal of material from the second increment produces two effects. Firstly, the stiffness of the structure is changed such that there is further relief of stresses within the stratum of material corresponding to the first increment, producing a strain change at the gauge.

Secondly, stresses relieved at the hole boundary of the second increment produce an additional strain change at the gauge. Thus, even if the second increment contains no residual stress, any stress within the first increment will produce a change in strain at the gauge as the second increment is drilled.

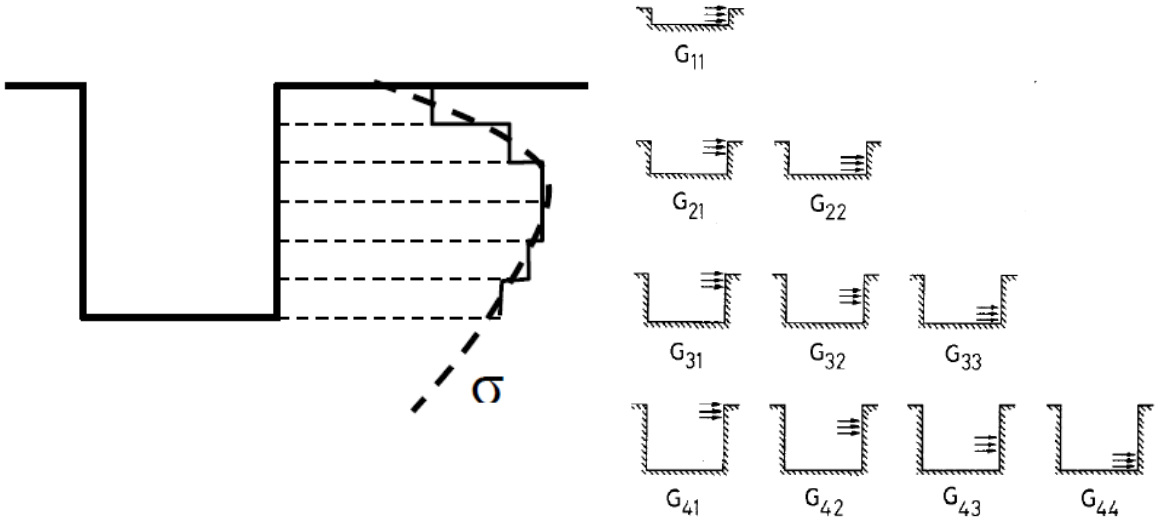

Figure 2-55 Cross section of the hole varying with the depth (left). Physical interpretation of matrix coefficients for the hole-drilling method (right) [235]

Accordingly, different sets of coefficients are required to relate the surface strain changes to residual stresses for each of the stress depth and hole depth combinations shown in Figure 2-55. This example is given for four calculation increments for the $\bar{a}$ coefficients; the $\bar{b}$ coefficients are arranged and calculated in a similar manner. To calculate the residual stresses from the relaxed strains, Schajer [249,250] proposes the following steps:

- The hole should be produced with many small drilling increments so that the resulting strain data can be smoothed or filtered to reduce noise.
- With a smaller number of calculation increments, combination strains p, q and t are calculated from the smoothed strain data.
- Cumulative strain relaxation functions (*A* and *B)* for the measured hole diameter are calculated, by interpolation, from the sets of triangular matrices given in [249] and [251].
- Coefficients $\bar{a}$ and $\bar{b}$ are calculated directly by subtraction of adjacent elements in the cumulative strain function matrices.

- Stresses P, Q and T are calculated for successive increments using the relationships listed below:

$\bar{a}$ P = pE / (1 + ν) **(2-38)**

$\bar{b}$ Q = qE **(2-39)**

$\bar{b}$ T = tE **(2-40)**

The combination of the pressure stress P, Q and T the Cartesian stresses are calculated as, σ_x, σ_y and τ_{xy}. The principal stresses and the direction are computed by equations 2-41 and 2-42.

(σ_{max}), (σ_{min})= P +/- $\sqrt{Q^2 + T^2}$ **(2-41)**

β= ½ arc tan (-T/-Q) **(2-42)**

A positive value of β, for example b = 30°, indicates that σ_{max} lies 30° clockwise of the direction of gauge 1. A negative value of β, say b = –30°, indicates that σ_{max} lies 30° counter-clockwise of the direction of gauge1.

2.5 Structural integrity assessments

The integrity of structures used in the oil, gas and liquids fields is an important issue to prevent failure or catastrophic accidents, especially in pipelines, which are the method widely used for low cost and safe transport of hydrocarbons or products. There are several methodologies and procedures for assessing the significance of defects, which depend on the application [278].

To characterise the remaining strength of pipelines with corrosion defects of both through and part wall, three methods exist. The most popular is ANSI/ASME B31.G and modified ASME B31.G which include an effective area method commonly known as RSTRENG [279,280]. A new assessment was developed by DNV under the denomination of DNV RP F101 [281]. This method is very similar to ASME B31.G and modified ASME B31.G with the difference that flow stress is taken from the ultimate tensile strength and estimation of curve tension-deformation. Nowadays, this method has higher acceptance for corrosion assessment in modern pipeline steels.

The procedure API RP 579 [282] has a specific application for equipment in the petroleum and chemical industries. The methodology addresses flaws from pressure vessels, piping and tanks, and evaluates integrity and the remaining life of components using analytical procedures, material properties and NDE guides [37]. Other methods for assessment purposes are: BS 7910, PDAM, R-6, FITNET-FFS and SINTAP which have been established with the objective of analysing the fracture behaviour of pipelines using FFS assessments [35–37,283–286].

Figure 2-56 show two approaches that have been established. The first uses the concept of a FAD and the second scheme uses a CDF curve. The bases of both approaches are mechanics criteria and plastic limit analysis. The fracture mechanics analysis involves the evaluation of the CDF, the fracture toughness or fracture resistance of the material and the geometry of the component.

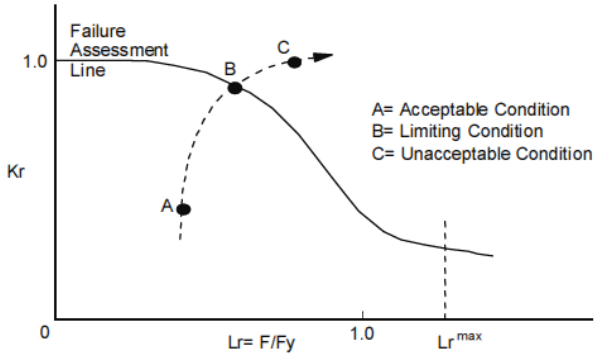

(a) FAD

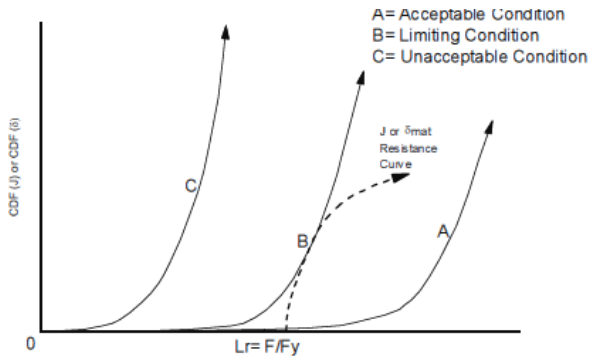

(b) CDF

Figure 2-56 Approaches for the assessment of flaw [39,287]

The crack tip loading is evaluated by elastic-plastic concepts and depends on the structure, crack size and shape, tensile properties and loading. Both approaches are based on elastic-plastic concepts; however, their application is simplified by the use of elastic parameters. The analysis can be made by using either of two methods which obtain identical results; however, the most popular assessment for fitness for purpose is the FAD. For the application of an FFS procedure to either evaluate a defect or optimise a design, the FAD requires the following information:

- Description of mechanism of damage
- Determination of operating conditions, load/stress analysis
- Flaw characterisation (localization, size-NDE)
- Material properties including environmental effects.

2.5.1 R6 Defect assessment approach

Since 1976 the R6 code approach has been constantly developed [288] and is presently at Revision 4. Fractures R6 assess failure of the structure or component by a linear elastic fracture and a fully plastic fracture. The former is controlled by local crack-tip stress-strain fields and the latter by overall plasticity. Previous version of R6 defined a parameter known as S_r to assess proximity to plastic collapse which was demarcated in terms of a limit load based on a flow stress and failure assessment was obtained from a strip-yield model.

Recently version replaced S_r by L_r parameter to define the curve more properly taking into account stronger strain hardening materials such as austenitic steels. To normalised limit load with a cut-off in the failure assessment curve for plastic collapse L_r uses the 0.2 % proof stress allowing that some material hardening beyond yield can be included. However S_r has been retained with specific application in assessing materials particularly relevant to UK nuclear power plant. Other major changes introduced and ongoing area for future improving in the R4 are described in detail in references [283,289,290].

2.5.2 The FAD approach

There are usually assessment modules to be applied in different fields such as fracture, fatigue, creep, corrosion. The FAD method provides three levels of assessment (i.e. 1, 2, 3). The classification is according to the material properties available for FFS assessment. FAD axes are presented as dimensionless parameters known as Stress ratio (Sr), Load ratio (Lr) and Stress Intensity ratio (Kr) [291,292]. These parameters can be calculated using the relations given in the following equations:

$$K_r = \frac{K_I}{K_{mat}} \quad \textbf{(2-43)}$$

$$Lr = P / P_l(\sigma_Y) \quad \textbf{(2-44)}$$

Where K_I is the stress intensity factor at load P, K_{mat} correspond to fracture toughness, P_L is the limit load for a flow stress equal to the material's 0.2% proof stress, σ_y. Stress intensity factor can be obtained by;

$$K_I = (Y\sigma)\ \sqrt{\pi a} \quad \textbf{(2-45)}$$

There are three options to assessment failure of structure within R6 which defines the type of analysis, shape of the FAD curve and material properties requirement. The basic option requires only material properties (tensile and fracture toughness) and simple calculations of K_r and L_r are made.

Stress intensity factors, K, and limit loads, PL, are available for many components in books or may be evaluated by diverse stress analysis approaches, including finite element methods. The option 1 to define $f(L_r)$ is obtained by:

$$\mathrm{f(L_r)} = \left(1 - 0.14L_r^2\right)\left\{0.3 + 0.7\exp(-0.65L_r^6)\right\} \quad \textbf{(2-46)}$$

Where limit is provided by the plastic collapse cut-off and σ_u is the ultimate stress:

$$L_r < L_r^{max} = 1/2\ (1+ \sigma_{u/}\sigma_y) \quad \textbf{(2-47)}$$

Level 1 required basic material information. If a selection of materials detailed stress-strain is choice at option 2 is assumed which is independent of load and geometry. Option 3 curves are characterised to be depended on material, crack size and geometry and required an explicit J-integral analysis.

Increasing type the analysis conservatism is reduced in an assessment but more analysis and data are required which obviously increased the cost to perform this type of analysis. When plain strain conditions are met, K_{Ic} can be expressed as:

$$K_{Ic} = (Y\sigma)\ \sqrt{\pi a} \quad \textbf{(2-48)}$$

However if plain strain is not gathered K_{mat} could be used instead of $K_{Ic;}$ where K_{mat} is the fracture toughness determined either by J-integral or CTOD approach.

$$K_{mat} = \sqrt{\frac{EJ_{mat}}{(1-v^2)}} \quad \textbf{(2-49)}$$

$$K_{mat} = \sqrt{\frac{2\sigma E\delta_{mat}}{(1-v^2)}} \quad \textbf{(2-50)}$$

If primary and secondary stresses are combined in the failure assessment curve, $K_r = f(Lr)$, L_r depends only on the primary stresses not on any secondary load (residual or secondary stresses). Contributions of primary and secondary stress are included in K_r where both primary and secondary stress interaction is covered by means of a factor denoted as ρ (R6 Revision 3) which was modified in revision 4 by introducing the parameter V [290].

V is a multiplication factor used to treat interaction between primary and secondary stresses. Both expressions are as follows where ***p*** and ***s*** superscripts denote primary and secondary stresses:

$$K_r = \frac{K_I^p + K_I^s}{K_{mat}} + \rho \qquad \textbf{(2-51)}$$

$$K_r = \frac{K_I^p + VK_I^s}{K_{mat}} \qquad \textbf{(2-52)}$$

Figure 2-57 represent the assessment points L_r and K_r are plotted on the FAD and compared with the bounding curve defined by $K_r = f(L_r)$ (See).

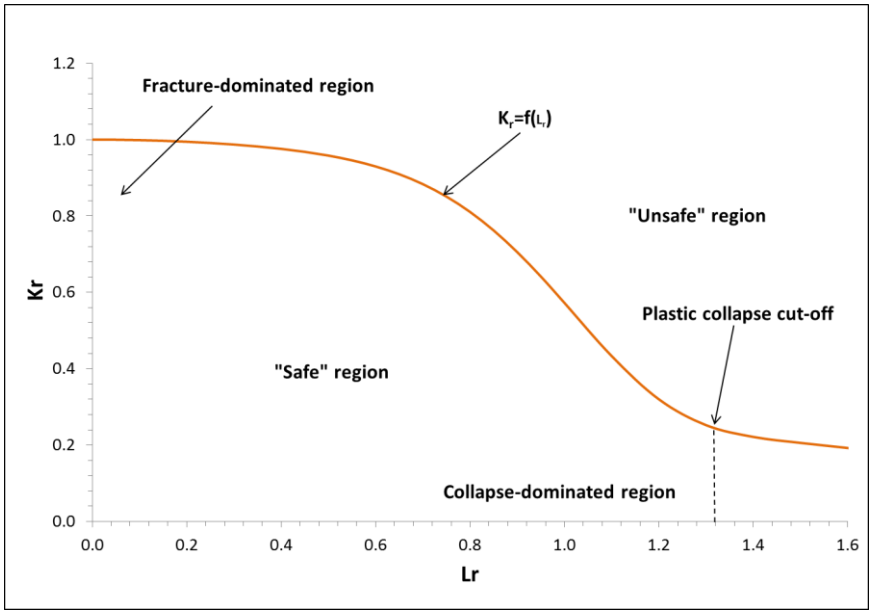

Figure 2-57 The R6 FAD, presenting the level 1 assessment curve. A typical, cut-off L_r is noticeable

If the point lies within the curve the component can be assessed as safe; however, if the point lies outside the curve, the criterion is changed and the point is determined as unsafe. Refined analysis or remedial action should be introduced to assess again the structure and determine its condition.

3 EMPIRICAL PARAMETERS

3.1 Introduction

This chapter is focused to obtain relevant experimental data of three pipeline steels: API X100, X70 and X60. Seven methods were selected as the most relevant within the scope of this project related to assess the integrity of pipeline steels exposed to flue-gas CO_2 environments. Work undertaken is summarised in Figure 3-1. A description of the importance of each approach and its contribution to this investigation is highlighted as follows:

- Material and dimensions (Section 3.2): This section describes the type of materials & dimensions including determination of the rolling direction.
- Metallurgical characterisation (Section 3.3): It is imperative to characterise the metallurgical composition of materials so that chemical reactions and micromechanical mechanism can be properly considered.
- Aging test (Section 3.4): It have been discussed by some authors that exposure of steels in a flue gases atmosphere containing free water, impurities and supercritical CO_2 has a large impact on the mechanical behaviour of the steel [33,90,93,293,294]. Therefore, this aspect has been considered here in order to establish the effect of flue gases and moisture in supercritical CO_2 on mechanical and toughness properties of HSLA steel. In the literature the majority of tests carried out in this area have been performed under static conditions; here a dynamic setting has been used as a first approximation to simulate pipeline flow conditions.
- Mechanical properties evaluation (Section 3.5): The evaluation of the structural integrity by FAD considers two dominant mechanisms. Tensile test data evaluated at low and room temperature was important to evaluate more accurately the plastic collapsed aspect of the FAD curve as L_r is assessed from realistic values covering interaction of primary load stress on fracture.
- Fracture toughness evaluation (Section 3.6): Toughness depends on temperature and material properties. Evaluation of these properties assesses materials from a fracture mechanics perspective allowing

determination of driving force in materials change when different levels of plasticity are introduced due to variation of toughness by temperature and/or other material conditions.

- Residual stress determination (Section 3.7): Residual stress has a big impact on integrity as it can be induced during service or manufacturing processes. These tests allow quantification of these levels and the interaction with primary loads.
- R6 code (Section 3.8): The experimentally derived parameters above and detailed in the following section are considered in Chapter 6 where these are inputs into a R6 FAD approach in order to establish a baseline regarding the integrity of steel used to transport supercritical CO_2 with impurities.

The core test have been structured such that the underlying mechanisms affecting the material, which are currently not well understood, can be examined.

3.2 Material and dimensions

The microalloyed steels used in this study were API 5L [67] specification grade X100, X60 and X70 high strength steel low carbon (HSLA) as-received. Steels X100 and X60 steels were supplied 20 mm and 9 mm thick in the form of flat plate. For API X70 steel, a small pipeline section, 24 mm in thickness, was the material used. Details of plate and pipe dimensions are showed in Appendix A.

Details about the manufacturing method of the steels were not reported; however, it is presumed to be processed by thermo-mechanical controlled rolling (TMCP) and an accelerated cooling process (ACC). As rolling direction was unknown it was initially determined and once identified all the specimens were manufactured following the requirement of ASTM E8 [295], ASTM E23 [180], BS EN ISO 6892-1[296] and BS EN ISO 10002-1[297] standards.

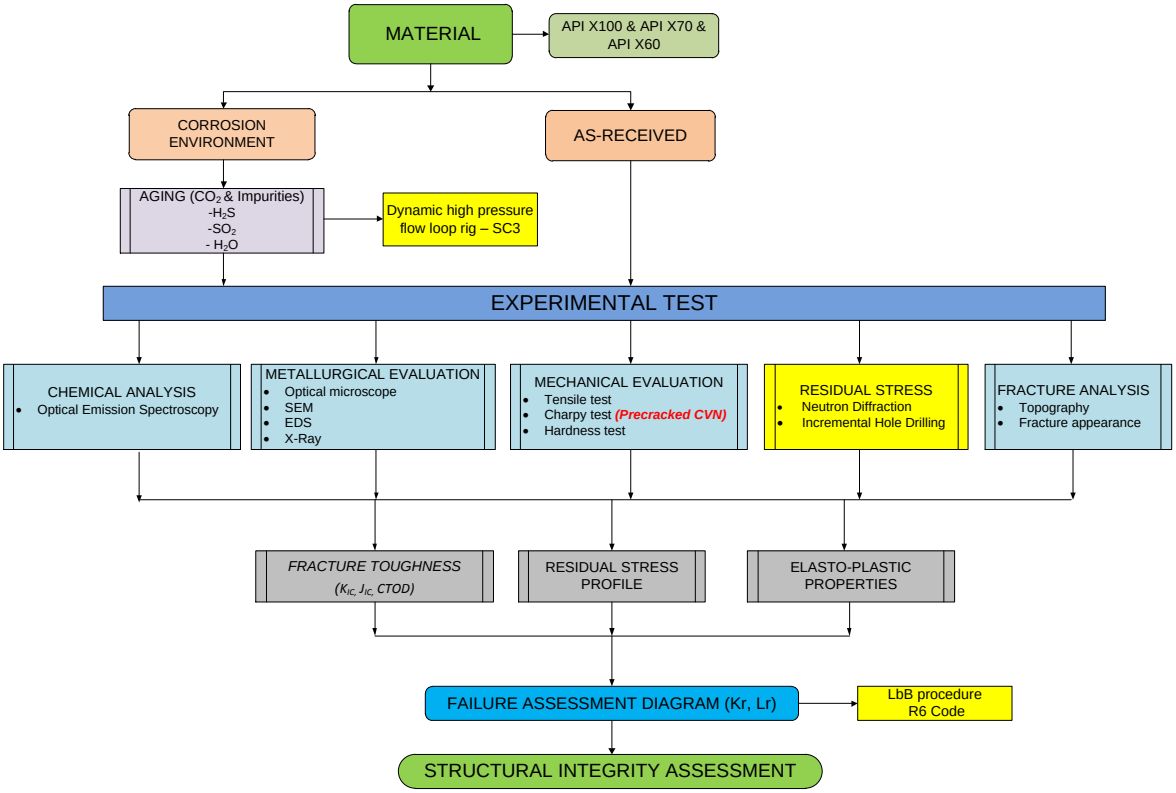

Figure 3-1 Flow chart of experimental work

3.2.1 Rolling direction

There are several methods used to evaluate the rolling direction of steels obtained from TMCP process. One cheaper and straightforward method is the metallographic approach. Basically the method involves metallographic preparation, then using optical microscope deformations of grain boundaries, banding or stretched structural phases, such as inclusions or pearlite blocks, are used as indications of the directional path in the rolling process.

Samples were cut from the edge of each plate and a short pipe section, as shown in Figure 3-2, into 39 mm x 25mm x thickness specimens for metallographic preparation by mechanical method. These were cut in two different directions and identified randomly as longitudinal (L) and transverse (T) along with the central axis of the sample. Following the metallographic preparation steps, which are explained in section 3.3.2, the rolling orientation was determined in all the plates.

Longitudinal orientation was chosen preferentially to manufacturing all the samples, as this in-plane is considered to be critical due to the presence of less tensile and fracture toughness properties and cracks would easily grow in fracture in this orientation.

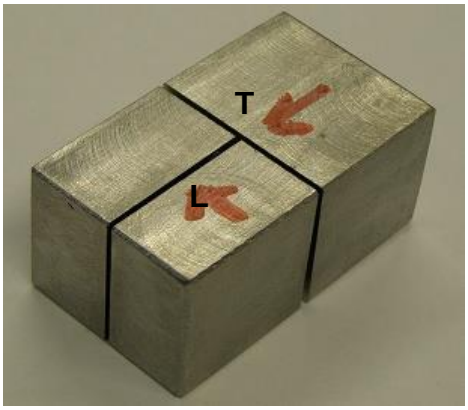

Figure 3-2 Type of specimen used for rolling and metallographic analysis

3.3 Metallurgical characterisation

3.3.1 Chemical composition of HSLA steels

Small samples were sectioned from the plates to determine the chemical composition of all materials in accordance with ASTM A-751 [298]. The chemical composition was undertaken by ESG[2], using the Optical Emission Spectroscopy (OES) approach. Basically, the method determines specific constituents of steel by heating the surface of the sample test until the material emits light which is collected by sensors and then dispersed via a prism. The resultant spectrum shows the presence of specific elements by their wavelength which is a characteristic of each element. located

This wavelength is measured to determine the ratio of the element to the rest of the alloy and calculated as the average percentage of each element present in the alloy tested. The weight measured percentage of each element, such as Carbon, Manganese, Sulphur, Phosphorus, Nickel, Cooper, Vanadium,

[2] Environmental Scientifics Group Ltd (EG) is a company situated in Acrewood Way, St Albans, Hertfordshire, AL4 0JY.

Titanium, Niobium and traces, was made and compared with X100, X70 and X60 specifications in the API 5L standard.

3.3.2 Metallographic characterisation

Metallographic evaluation was made following the ASTM E-3 standard [299]. Longitudinal and transverse sections, of all three steels, were mounted in resin and mechanical grinding was performed using a rotating wheel covered with silicon carbide (SiC) abrasive papers which were ground up to 1200 grit.

Final polishing was made with 6 μm, 3 μm and 1 μm diamond suspension and finished with silica colloidal suspension 0.05 μm. Polished samples were washed in distilled water, swabbing with Isopropyl Alcohol (ISP) and dried with warm air. After that, the samples were analysed without being etched in order to examine the presence of inclusions, oxides or phases that indicated the rolling path by using an optical microscope (OM). Once each sample was studied, it was degreased with acetone and etched for 30 - 60s using Nital solution (98 ml ethanol + 2 ml nitric acid) to reveal the general microstructure. Each specimen was again swabbed with Isopropyl Alcohol (ISP) and dried with warm air.

A Nikon optical microscope and attached camera together with image acquisition software (AcQuis) was used to perform metallography analysis up to 500X magnification both as-polished and etched samples. A scanning electron microscope (SEM) was used to examine the specimens and obtained the representative microstructure of the steels at high magnification. Electron dispersive spectroscopy (EDS) was used to determine the chemical composition of particles and second phases found on the material bulk or the fracture surface area. Figure 3-3 shows the Optical and SEM microscopes used.

Figure 3-3 Left: Optical microscope. Right: Scanning electron microscope (SEM)

3.3.3 Fractography evaluation

Fracture surfaces of tensile and PCCVN specimens were studied under optical inspection with a lower magnification to see fracture morphology differences between steels and conditions of tests in order to establish fracture patterns. An optical stereoscope NIKON model SMZ745T magnification 0.67X to 5X, together with a digital camera AxioCam ERc 5s, were used for this purpose.

Scanning electron examination was performed to determine contamination or particles from the aging test deposited on the fracture surface. EDS analyses were conducted to quantify the composition of elements existing on the layer adhered to the metal surface, and were complemented by the XRD technique. The analytical characterisation was conducted using a FEI S-FEG XL30 SEM complemented by a DX-4EDAX system and an X-Ray diffractometer D5005 Siemens was also used.

3.4 Aging tests of HSLA steels

In spite of the complexity of CO_2 systems and the lack of clarity on the specification or concentration limits, the main objective of this section was focused to integrate the specification proposed in Chapter 2, section 2.2.2 and exposed samples taking into account the real condition that could be present in transporting anthropogenic CO_2. However, each test was performed changing the type of impurity and having constant CO_2 and free amount of water.

3.4.1 Test rig for CO_2 environments

The experimental set up consisted of a pressurised vessel with a circulation pump, high pressure liquid metering pump for delivering liquids (impurities), and gas tanks. In addition, a vacuum pump and cooling/heating system, pressure controller, and capture and data acquisition system were included. The ageing tests are based in standards, however, due to pressure conditions determination of pH was not measured being one of the limitations of this work together with monitoring corrosion by electrochemical methods. Measurement of corrosion rate was performed by weight loss method [300–302].

3.4.1.1 Geometry of the specimen

The Super Critical CO_2 Corrosion Rig (SC^3) includes several coupon geometries such as plates, tubes, bar, precracked Charpy and tensile specimens. The coupons are made from API X60, X70, X100 and non-metallic materials (seals). Table 3-1 presents the dimensions of the samples and Figure 3-4 shows a short arrangement used during the ageing test. Appendices H to J present a sketch containing details of the sample distribution for each reactor.

Table 3-1 Nominal dimensions of samples for the aging test

Parameter	Tube	Round tensile	Plate	PCCVN
Do, mm +/- 0.1	14	4	-	-
Di, mm +/- 0.1	7.98	-	-	-
Width, mm +/- 0.1		-	15	10
t, mm +/-0.1		-	2	10, 7.5
L, mm +/- 0.1	34	28	25	55

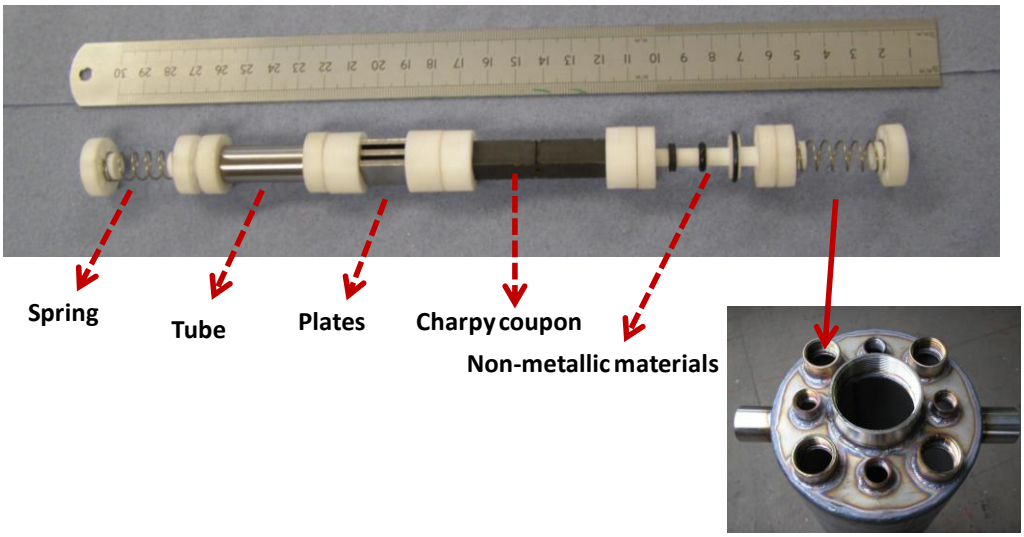

Figure 3-4 Stack of coupons distribution to be mounted on the 1" tubular reactor

3.4.2 Experimental set up

The SC^3 dynamic flow loop consists of the following parts which are shown schematically in Figure 3-5:

- Liquid CO_2 & contaminants supply system.
- Booster pump – up to 700 bar.
- High pressure dynamic flow loop with circulation pump (0-50 g/min).
- 4 reactor, 1m length and 1"OD of the vertical sections connected in series with a different geometry of samples passing directly through the pipe.
- Remote monitoring of the pressure and temperature on the rig through NI Labview application.
- Analytical analyser to monitor impurities composition.
- Drag tube method for H_2S monitoring.

- Protective case to address health and safety issues.

Prior to the aging test, all the samples were polished using finer grades of silicon papers up to 600 grit. The specimens were cleaned in an ultrasonic bath with acetone for 15 minutes and then with Isopropyl Alcohol (IPA). The samples were placed in a desiccator for minimum 24h to remove water and weighted using an electronic balance with a precision of 0.0001 mg.

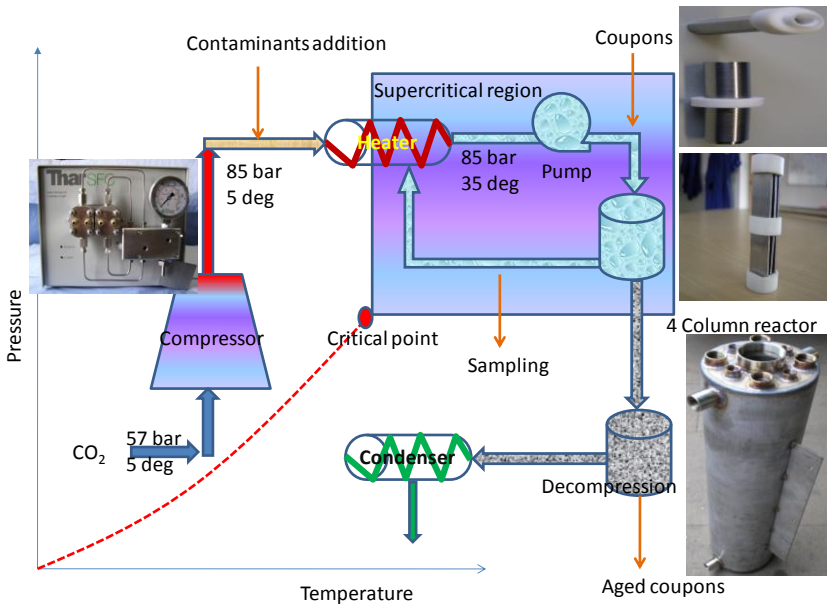

Figure 3-5 Schematic representation of SC^3 dynamic flow loop rig

3.4.3 Operational procedure

The general description of the operating system is described as follows. Once coupons are introduced into the reactor, the CO_2 source is assumed to deliver CO_2 at 5.7 MPa and 5°C. The liquid is saturated with water and is compressed slowly until reaching 9 MPa at the same temperature. When the pressure reaches above the critical pressure, the CO_2 is fed with contaminants either H_2S or SO_2. The mixture is then heated to supercritical condition (45°C) and the recirculation process starts using a pump which keeps the pressure constant.

Pressure and impurities composition are dependent parameters of the process. This means that the pressure and impurities became lower with time due to the consumption of components for the chemical reaction between the materials and the environment.

Following standard procedures established for this work, measurements were made in the morning and from the readings estimated concentrate dosing was added (3% impurity, 97% CO_2). To distribute slug concentration, a standard circulation of the system was made at 50 ml/gr until it reached the target concentration of 500 ppm.

To get the pressure back up, 10% of CO_2 was added to the mixture which was balanced for 15 minutes. If the concentration was close to 500 ppm, the system was restarted but any decaying correction was made. Variation of pressure, impurity concentration and temperature were monitored throughout the test and it was stopped once the exposure time was reached following the plan sketched in Figure 3-6. Then, the system was slowly decompressed and coupons were taken for WLC, surface and corrosion analysis. Appendix K describes all the experimental plans to test steel and non-metallic materials.

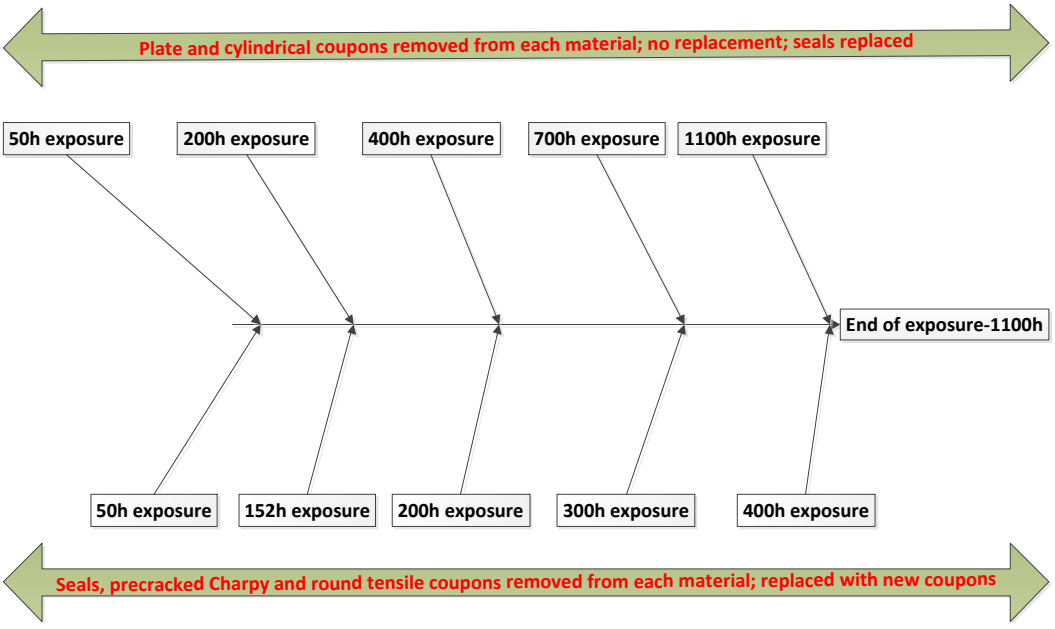

Figure 3-6 Schematic timeline for aging test on SC^3 rig

3.4.4 Evaluation of the material degradation

Conventional methods used to monitor corrosion are based on the conductivity of the medium during the whole period of the test; for example electrochemical methods such as EI and LPR [140]. However, those methods could be inappropriate when applied to a supercritical fluid system due to the high pressure of the system.

The weight loss method (referred to as WLC or coupons) is a common technique used and is easy to implement to evaluate corrosion rates. Coupons of metal in the shape of a strip or disk are normally exposed in the environment (fluids or gas). In this research the coupons used were small pipes and plates to be analysed using this method. WLC unexposed were weighed and after exposure were re-weighed. The difference in weight, time of exposure, exposed surface area and material density were converted to a corrosion rate using equation 3-1 and then plotted. This equation shows the general equation for calculating the corrosion rate.

$$\text{Corrosion rate} = \frac{(\text{Initial weight} - \text{Final weight})}{\text{Area Density exposure time}} \text{Unit factor} \qquad \textbf{(3-1)}$$

The surface composition of the material metallic corroded and seals were examined using SEM and energy dispersive X-ray spectroscopy (EDS) with a scanning voltage of 20 kV. A crystal analysis of the corrosion products was also made using X-ray diffraction (XRD).

Corrosion products were not removed but samples were mounted, using a resin, on a metallographic preparation to be assessed later under a statistical method documented by Encinas-Oropesa, A. [303]. However, although this analysis is beyond the scope of this research, it is currently under review to be carried out.

3.5 Mechanical properties evaluation

The evaluation of mechanical properties in the material was achieved by three mechanical approaches: hardness, tension and Charpy V-Notch (CVN) Test.

3.5.1 Hardness

There are different scales, depending on the material and the load applied. Micro hardness test corresponds to a test performed with loads less than 1 kgf using a square diamond pyramid (Vickers) or elongated diamond pyramid (Knoop). A surface quality of no less than 1 micron is required (metallographic finish) and the precision optical microscope is used with magnifications of around 100X to 400X. All the requirements follow the indications of the international standard ASTM E-384 [304].

3.5.1.1 Experimental set up

Micro hardness tests (HV0.1) were performed on two polished cross sections of each material. Distributed indentations were made on each section using a micro hardness tester Zwick-Rowell, 0.1 kgf to 1000 kgf (Figure 3-7).

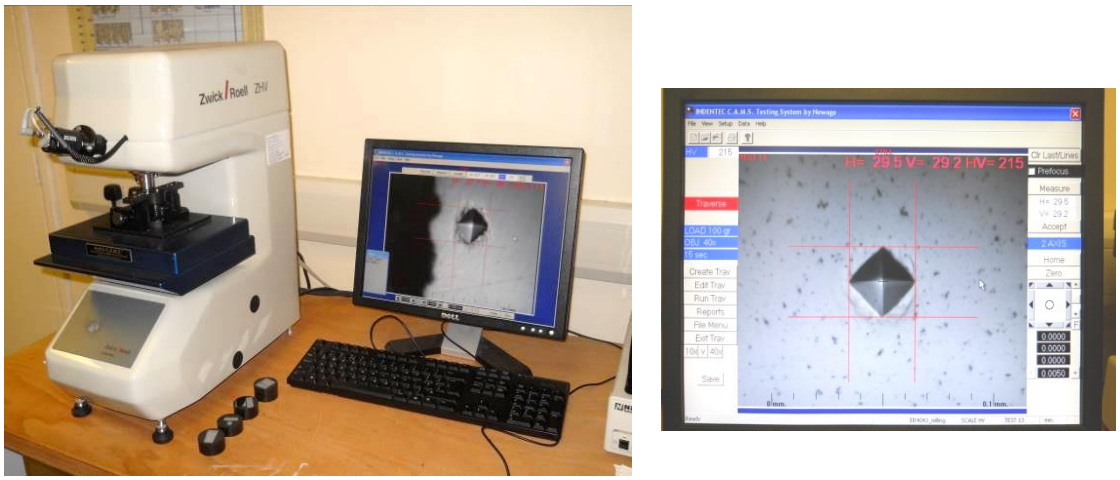

Figure 3-7 Left: Microhardness test set up. Right: Indentation and measurement

Three zones were selected and hardness profiles were performed by making a distributed indentations through-thickness sample (Figure 3-8). Table 3-2 shows the parameters used to perform the hardness tests profiles.

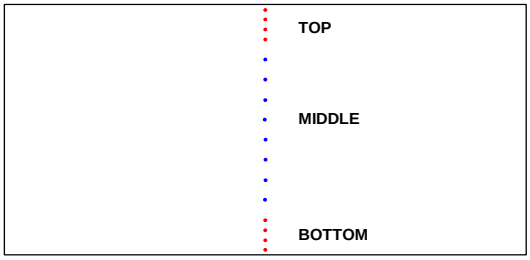

Figure 3-8 A schematic of the hardness test profile performed

Table 3-2 Hardness test parameters

Steel	Load (g)	Time load (s)	Thickness sample (mm)	Depth region (mm)		
				top	middle	bottom
X100	100	15	20	2	16	2
X70	100	15	23	2.4	18	2.4
X60	100	15	9	0.9	7	0.9

3.5.2 Tensile tests

3.5.2.1 Dimensions and geometry of the specimen

Tensile tests were performed in the longitudinal direction in two geometries: pin-load (strip) and round samples following ASTM E8 [295] and BS [296,297] guidance. Pin-loaded tensile samples of API X100 and X60 were fabricated with dimensions of 145 mm x 12.50 mm x 9 mm (Figure 3-9). API X70 strip samples were not machined due to a shortage of material.

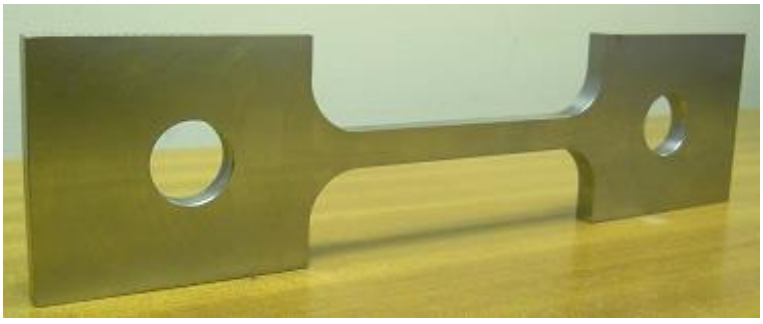

Figure 3-9 Pin-loaded tension test specimen

Figure 3-10 Small-size round tension test specimen

Small-size, round tension specimens 30 mm length and 4 mm diameter were manufactured for all the steels (Figure 3-10). All the samples were machined in alignment with the rolling direction. The dimensions of the specimens are given in Appendix B.

3.5.2.2 Method verification of the alignment of 500 kN and 100 kN servo-hydraulic test machines

Misalignment can be introduced for a number of reasons, such as changing grips, replacement fixtures or fitting new ones. Basically, misalignment has the consequence of applying unwanted stresses which are put on a sample affecting the stress/axial distribution inside the piece.

Two servo-hydraulic Instron machines identified as 8803L1469 (500 KN) and 8801MTL4740 (–100 KN) capacities were used, respectively. Both load cells are 0.5 class and these were calibrated following procedures established by the ISO 7500-1 standard.

The stress distribution was measured, on both the strip and round sample. Following ASTM, BS and ISO procedures, the machine and gripping system was fitted with a strip and round specimen for 500 KN and 100 KN respectively. Both were configured with a set of linear Vishay strain gauges reference CE-06UZL-120 and strain gauges were bonded on the surface of the material using MBOND- 200 compound (modified alkyl cyanoacrylate).

The strip specimen was mounted with two strain gauges, either at the top or at the bottom, while the round sample was bonded with two strain sensors in the middle of the piece mounted on each other at 180°.

The standard suggests the use of four strain gauges for each side, but due to the small width section or diameter of the sample two strain gauges could be used. Once the strain gauges were wired with temperature compensation wire, these were connected to PS3 strain recorded and software was used to record automatically the bending strain which were converted to stress. The strain was measured in the longitudinal direction along with the applied load direction. Figure C-1 presents the set up configuration and strain gauge bounded in detail which was used to verify the system alignment.

3.5.2.3 Tension and environmental test set up

A set of strip (virgin material) and round geometry (parent and aging material) samples were tested by uniaxial load. The tension tests were performed under displacement control at temperatures of –70°C, –40°C, –20°C and 21°C for both strip and round samples of virgin material three samples per datum obtained. Aging samples were only evaluated at –20°C and just one sample was tested due to space constraint in the reactor used to expose the material in simulated flue-gas. An insulated environmental chamber was used with nitrogen as a cooler for the lower temperature test. All specimens were soaked at the test temperature within +/-1°C for a minimum of 60 minutes (strip samples) and 30 minutes (round samples) before the tension test was carried out.

Strip specimens of the parent material were tested using a servo-hydraulic Instron machine of 500 KN capacities while round samples were tested using a servo-hydraulic Instron machine of 100 KN capacities. A calibrated Instron strain gauge extensometer, 50 mm gauge length, +50% –5% maximum strain, and 10 mm gauge length, +1% maximum strain was used to record strain values in the strip and round specimens, respectively.

The former was mounted over the 9 mm thickness and the latter on 4 mm diameter from where strain readings were collected using Wavematrix software together with load and displacement values. All tests were carried out under a constant strain rate equal to about $3.3 \times 10^{-4}\ s^{-1}$.

The yield strength was determined from the strain-stress curve at 0.2% strain offset stress, 0.5% extension-under-load (EUL) and proof strength for X70, X100 and X60 respectively. Figure D-1 presents the set up used for both machines.

3.5.3 Fracture toughness tests

3.5.3.1 Dimensions and geometry of the specimens

Standard CVN samples were cut from the plate in the transverse-longitudinal orientation (T-L) for API X60 and X100, and transverse orientation (L-T) for API X70 steel. The notch end was manufactured using an Electrical Discharge Machine (EDM) and a broaching method which ensures a sharper crack tip. The nominal dimensions, those given in BS EN 10045 [305], BS EN 14556 [179] and ASTM E-23 [180] standards, are presented in Table 3-3.

Table 3-3 Nominal dimensions and tolerances of conventional CVN

Steel	Details on sample, mm			Details on notch, mm		
	H ± 0.075	W ± 0.075	L +0/-2.5	R± 0.025	a ± 0.025	D ± 0.025
X100	10	10	55	0.025	2	8
X70	10	10	55	0.025	2	8
X60	10	7.5	55	0.025	2	8

A sketch of geometry and dimensions is shown in Figure 3-11 showing both conventional and precracked specimens. Two impact test specimen configurations were used. For X100 and X70 a steel Charpy single-beam type A (1T) was machined. For X60, 3/4T a sub-size specimen was selected as the material available does not permit making a standard configuration.

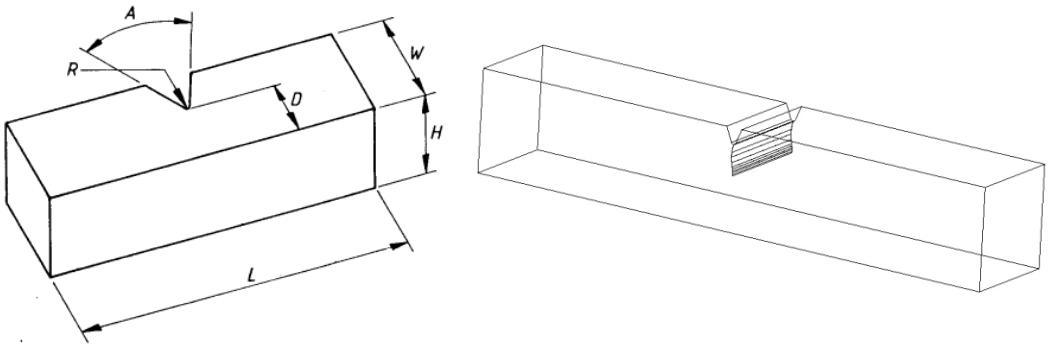

(a) Conventional CVN (b) PCCVN

Figure 3-11 Drawing showing geometry of Charpy V-notch and PCCVN sample

3.5.3.2 Fatigue precracking

Simulating a natural crack by machining a notch starter does not provide plane strain fracture toughness conditions. The significance of precracking is to afford a sharper crack of satisfactory size and straightness which ensures that machining start notch and effects of subsequent crack growth or precracked load history are eliminated [306].

Accomplishing fatigue precracking can be done at room temperature but it is required that the material has to be in the final heat treatment, mechanical work or environmental condition in which it is to be tested. Different approach can be used to conduct fatigue precracking such as: displacement control, load control or K control. Parameters as stress intensity factor (K), K_{max} and ΔK have to be controlled in order to prevent excessive plastic deformation at the crack tip. It is advised that once the advanced crack has reached two-thirds of the final crack length, $0.6K_{max}$ should not be exceeded [180,306,307].

The maximum load to be used can be calculated using an equation given in the ASTM E-23 standard; however, it is related to a three-point bend. For this research a four-point bend specimen's equation (3-2) was used to calculate the maximum load as a stress intensity factor, K, function. Plotted curves can be seen in Figure G-1.

$$P = K_{Ic} BW^2 / 3L\sqrt{a}(1-\mu^2)^{-1/2} f(N/D) \quad \textbf{(3-2)}$$

Where:

P=maximum load

K_{max}=maximum stress intensity= $\sigma*(2*\pi*r_y)^{1/2}$

B=Thickness

W=specimen width

S= Span

f(N/D)= geometrical factor

μ= Poisson's ratio

3.5.3.3 Fatigue precracking procedure

Fatigue precracking was conducted by a four-point bend (4PB) configuration using a servo-hydraulic Instron machine model 8803L1469 500 kN capacity under load control (Figure 3-12). Precracking followed the procedure given in British and ASTM standards [180,306–309].

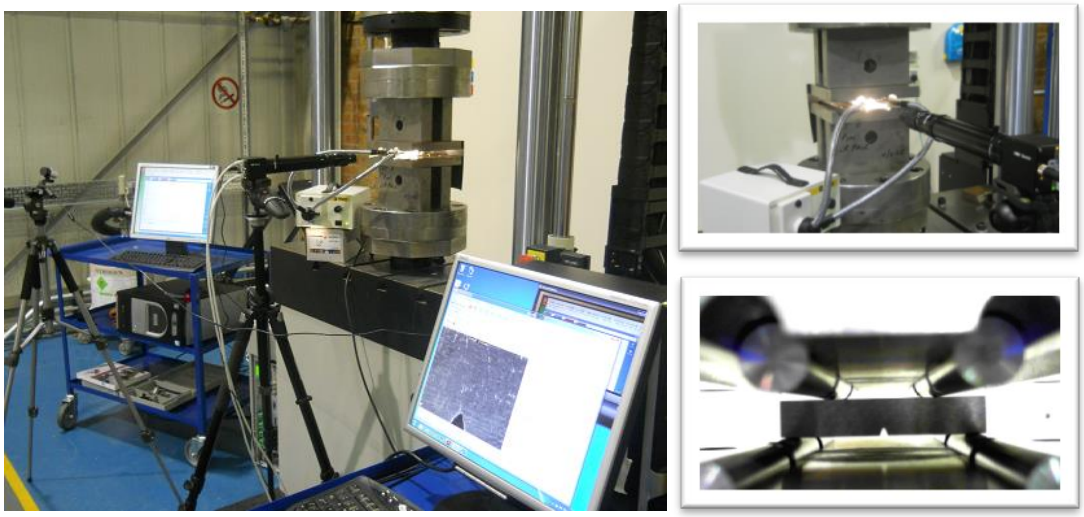

Figure 3-12 Set up for fatigue precracking Charpy V-Notch bar. At the right 4PB bend rig (top) and positioned sample (bottom).

An Instron software "Wavematrix®" was used to create a method where preload, cyclic waveform, load amplitude and frequency parameters were introduced to meet the fatigue precracking criteria described in section 3.5.3.2 and summarised in Table 3-4. A unipolar waveform (90^0) was chosen in order to ensure the load was always under compression from the set point (Figure 3-13).

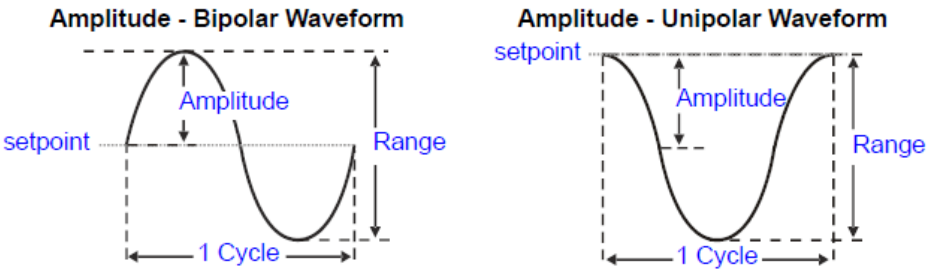

(a) Types of amplitude waveform

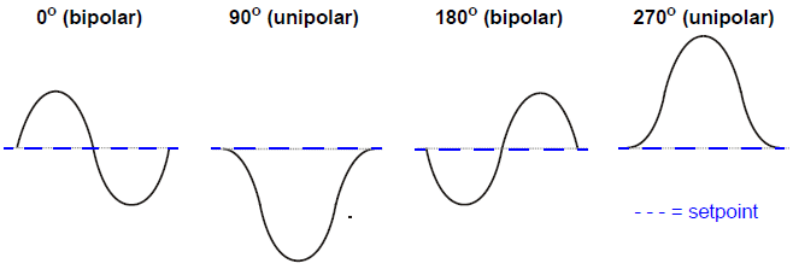

(b) Waveform starting phase

Figure 3-13 Tri-modal waveform

Table 3-4 Fatigue precracking steps

Parameter	Step 1	Step 2	Step 3	Step 4	Step 5
Preload (kN)	-1.8	-1.5	-1.3	-1.1	-1.0
Amplitude (kN)	8	6.5	5.5	5.0	4.2
Frequency	5	5	5	5	5

To prevent any plasticity on the crack tip during fatigue, the 'precracking envelope' method was applied. This established technique is used to increase the load from a specified value (e.g., zero) to the load of interest in a slot of time. The envelope duration was set at 15 seconds, the time that the machine needs to reach the maximum amplitude. The advantage of this method is to achieve a uniform load when both starting and ending the test (Figure 3-14).

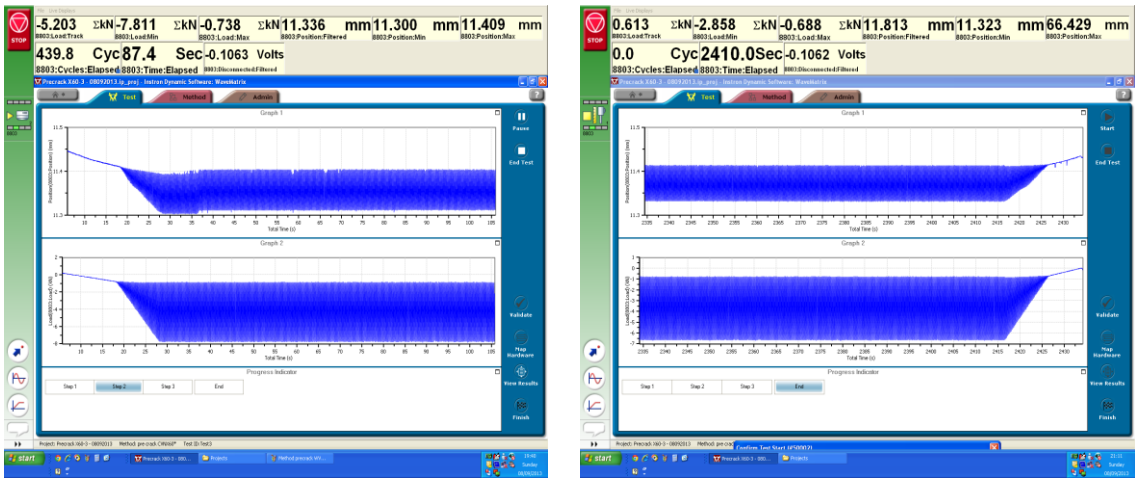

(a) Start envelope (b) End envelope

Figure 3-14 Waveform envelope for fatigue cycling

Five steps were designed to achieve a precracking; length, time, load, position and numbers of cycles were recorded at each step for every sample (Figure 3-15). Precracking was performed, decreasing the maximum stress intensity factor (K_{max}) by using a discrete method.

Figure 3-15 Fatigue precracking method per each step

The stress intensity factor applied during the first stage of the precracking was maintained below 35 MPa√m which was gradually reduced by no greater than 20% at each step (Δa_{sh}) to reach 25 MPa√m which corresponds to the last 0.5 mm (Δa_f) of precracking (Figure 3-16). Fatigue precracking was conducted at R-ratio (P_{min}/P_{max}) equal 0.1.

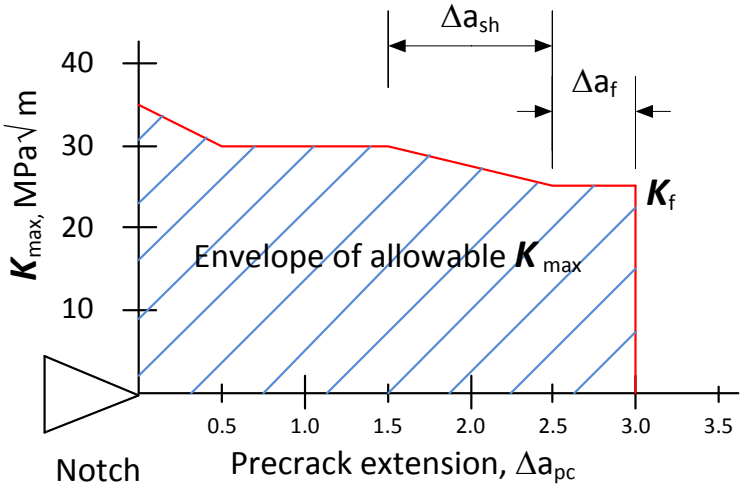

Figure 3-16 K_{max} envelope allowable during precracking

The crack length growth was controlled by using a visual method with a speed camera. Both sides of the sample were polished using emery paper 240 grit, 400 grit and 800 grit to obtain a surface quality on which could be seen the crack initiation and propagation. Fatigue crack length was measured using a Baumer camera fitted with a Navitar lens capable of showing crack extensions of 0.01 mm. A light source was required in order to give plenty of illumination on the surface of the sample to obtain a sufficient resolution on the crack tip.

To record the crack propagation, a software known as StreamPix, was used. A method (script) was set with the purpose of recording five frames per second every minute per each precracking step giving the ability to achieve the crack length resolution advance of 0.01 mm. The crack direction was chosen to be parallel with the rolling direction of the plate.

Monitoring and crack measurements were made on both sides to ensure symmetrical crack information was gathered. If crack propagation was irregular on one side, the samples were rotated to compensate and straighten the crack. Crack length was kept between 2.80 +/- 0.05 mm on the surface from the crack-started notch, achieving a total crack depth of 3 +/- 0.2 mm at the centre of the crack front. An example of the finished fatigue precracking is depicted in Figure 3-17.

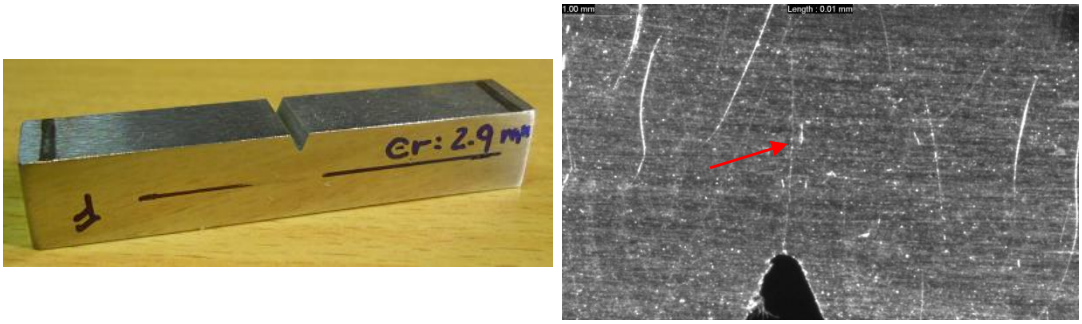

(a) Pre-cracked Charpy sample (b) Fatigue precracking (red arrow)

Figure 3-17 Pre-cracked Charpy V-Notch bar – PCCVN

3.5.3.4 Fracture toughness test using PCCVN

The fracture toughness tests were performed on precracked Charpy specimens (PCCVN) loaded in three point bending in accordance with ASTM, BS EN and ISO standards [177–180,305,307–309]. Specimens were tested at temperatures of –196ºC, –100ºC, –70ºC, –40ºC, –20ºC and 21ºC.

Lower temperature tests were achieved by an environmental cooling chamber covering the temperatures between –20ºC to –70ºC (Figure F1-b1). A polystyrene cooler box was used to keep samples at –100ºC and –196ºC (Figure F1-b2). Samples tested at -100ºC were immersed in a cryogenic bath of nitrogen and anhydrous alcohol liquids and tests carried out at -196ºC were submerged in pure liquid nitrogen. The temperature was controlled by an R-type thermocouple placed on the sample surface and maintained during soaking time and testing within +/-1ºC of the nominal value. Soaking time for all the samples was 30 minutes prior to testing.

The PCCVN specimens were tested using a standard Pendulum Impact Tester 217 Ft-lb (~300J) capacity (see Figure F1- a). A single impact load (high strain rate) of 5 m/s was applied and the total energy absorbed values were obtained from the recorded dial. Total crack length was measured by optical microscope and fracture surfaces analysis was carried out by OM.

To fit the toughness data, transition brittle-ductile behaviour Charpy energy versus temperature data was fitted by hyperbolic tanh function developed by Oldfield which is shown in Figure 3-18 and equation 3-3 [181].

$$Y = A + B\tanh[(T - T_0)/C] \quad \textbf{(3-3)}$$

Where Y is the CVN energy, T is the test temperature, A represents CVN energy at transition temperature T_0, B is the energy jump between brittle-ductile plateaus and C is the temperature range of the Charpy energy transition. Those parameters are adjustable by regression procedures. Based on the regression analysis, two energy values, 28 J and 41 J, were selected and their corresponding temperatures determined.

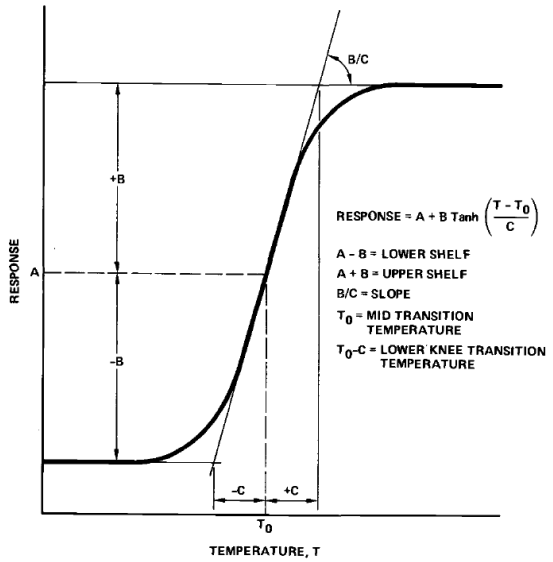

Figure 3-18 Fitting curve for toughness data [181]

3.5.3.5 Post-mortem examination

Crack length measure can be achieved by two approaches known as five-point or area average method [310,311]. The five-point method is characterised bringing acceptable results compared to the area average, as the former being more reliable. In this research, examination of the fracture surfaces was carried out by OM in order to analyse the mechanics of the fracture and/or other features on the fracture zone.

Measurement of the total crack length between the notch root and final crack front were made by optical microscope using a five-point average method [310]. The method follows the ISO 14556 [311], focusing on measurement crack length extension and the values obtained which can be used to establish the variation of toughness under impact loading rates at different temperatures.

The approach is focused on determining the average of five measurements per crack length which are made at five equidistant points. The outer points have to be located 0.01B inward from the references lines. If measurements exceeded 10%, the specimen was discarded (Figure 3-19).

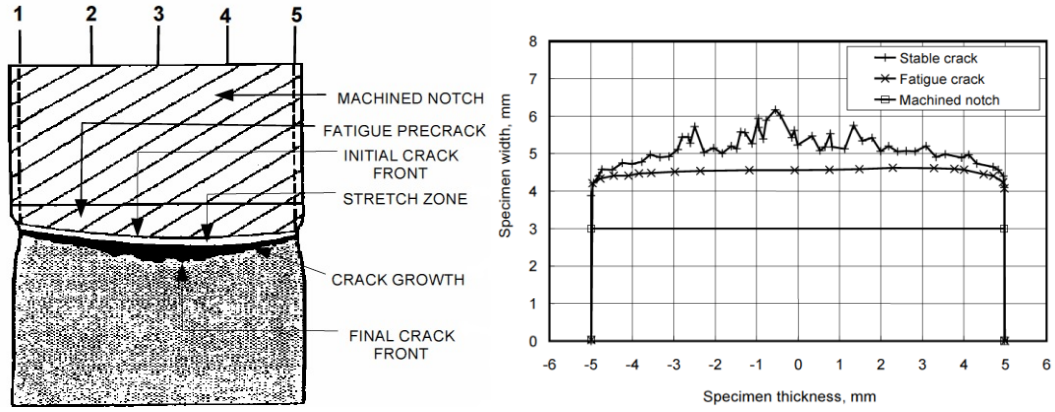

(a) Five-point average (b) Right: Area average

Figure 3-19 Methods to measure crack length on PCCVN specimens [311]

3.5.3.6 Fracture toughness evaluation

Fracture toughness evaluation was performed by using some aspects provided by the master curve and SINTAP approach. Firstly, correlation between Charpy energy absorbed and fracture toughness was performed using equations 3-4 and 3-5 accounted by references [58,190] .

$$K_{mat} = 19CVN^{0.5} MPa\sqrt{m} \quad \textbf{(3-4)}$$

$$K_{mat} = 12CVN^{0.5} MPa\sqrt{m} \quad \textbf{(3-5)}$$

To transfer Charpy energy absorbed to fracture toughness, a different approach can be used such as the Marandet & Sanz correlation, Master Curve (MC), ASME lower-bound approach and SINTAP correlation. Each of them has a different scope and application; however, choosing the correct one or the most suitable is not an easy task. For example, MC becomes a useful alternative method to evaluate the fracture of ferritic steels in the DBTT range which can be treated as a statistical phenomenon.

This phenomenon in turn can be described by a three-parameter Weibull distribution, weakest-link theory and by establishing an index temperature namely, T_0, which is positioned on the temperature axis of the steel of interest in the MC curve, a median fracture toughness values is determined. However, due to the absence of standardisation for the correlation of energy absorbed with fracture toughness obtained from the precracked CVN samples using a non-instrumented machine, an alternative methodology was introduced.

It consisted of establishing an empirical correlation between the superficial energy of conventional and precracked Charpy. A comparison of both energy values obtained were made and a deeper analysis was performed in order to determine tendencies between both geometries.

3.6 Residual stresses determination

The integration of residual stress on this research has as objective to determine compressive-tensile stress distribution induced by cold rolling. The advantage of cold rolling is that it is simple, economical and feasible to be applied and it could be used to introduce compressive stress for crack arrested purpose on pipeline. To evaluate RS two approaches, non-destructive (ND) and semi-destructive (IHD), were chosen to characterise the residual stress fields of cold-rolled specimens manufactured using HSLA steel grade X100.

Neutron diffraction was undertaken using a neutron diffractometer. The ND measurement was used to visualize the stress field pattern and behaviour through the material thickness at various points across the specimen surface. Its points were equally distributed from 0.8 mm to 7.2 mm depth from each other on each side.

Incremental centre hole drilling (ICHD) was performed at the Structural Integrity Laboratory at Cranfield University and Orbiting Incremental hole drilling (O-IHD) was carried out by Stresscraft Ltd. Both ICHD and O-IHD were used to measure the longitudinal and transverse residual stress from surface to 1 mm and 2 mm depth, respectively.

3.6.1 Cold rolling test

3.6.1.1 Geometry and dimensions of the specimens

Rolling tests were carried out on API X100 steel plates which were machined from virgin material at 250mm x 100mm x 10 mm. Then these plates were used to induce residual stress using a rolling rig. The dimensions are summarised in Table 3-5 and a sketch is shown in Figure 3-20.

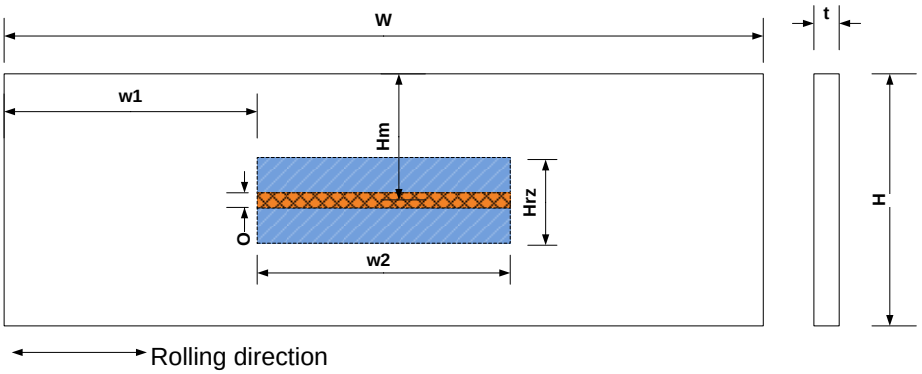

Figure 3-20 Shape and roller area from the samples

Table 3-5 Dimensions of the plates

Parameter	Dimensions in millimetres +/- 0.01 mm			
	A1/A2	B1/B2	C1/C2	D1/D2
H	100.0	100.1	100.1	100.0
Hm	50	50	50	50
Hrz	34	34	34	17
W	251	250	261	250
w1	75	75	80	75
w2	100	100	100	100
O	6	6	6	3
t	10.1	10.2	10.1	9.9

3.6.1.2 Experimental set up and procedures for rolling

Deep rolling was carried out by a machine with a maximum rolling force of 200 KN. The relation between the force applied by the cylinder and the cylinder pressure with repeatability to within +/-2% of the magnitude of the force applied is shown in Figure 3-21.

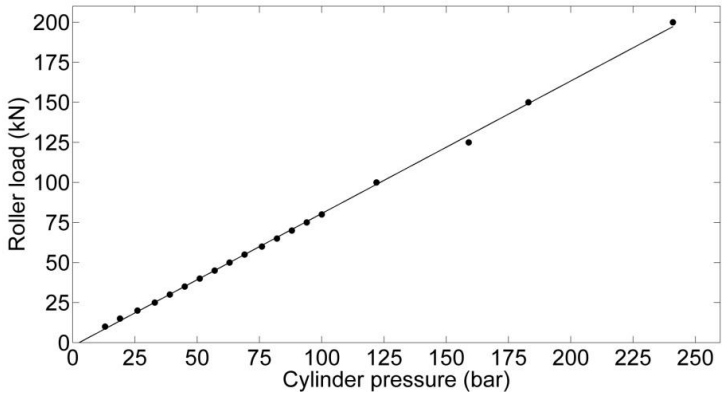

Figure 3-21 Calibration roller load versus cylinder pressure for the rolling machine in constant-force mode [312]

The workpiece was attached to the machine platform base using a clamping system. Plates were aligned along the rolling direction and two paths were produced by axial flat rollers with widths 20 mm and 10 mm, respectively. The load was applied straight to the roller axis by a hydraulic jack mounted vertically and attached to the machine's crossbeam.

The roller speed at which it traversed the plate during rolling was 500 mm/min (8.33 mms^{-1}). The machine and setting are shown in Figure 3-22. The roller area was made as symmetrical as possible about the middle-plane of the plate on both the X and Y axis for both sides of the plate, front and back . To achieve the best stress distribution three passes of rolling were used in all of them [313]. The distance between the edge of the plate and the centre of the roller's contact path was constant and equal to 100 mm for all the samples.

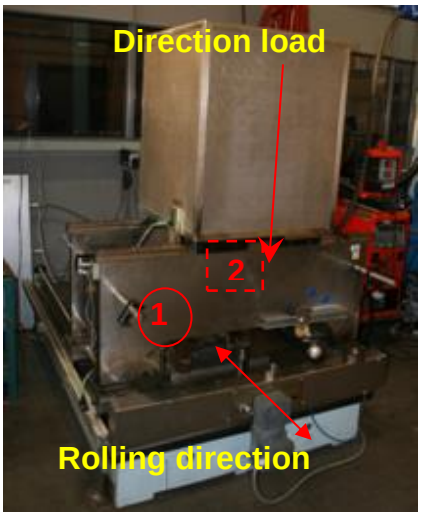

a) **Rolling Machine.** 1. Crossbeam, 2. Hydraulic jack

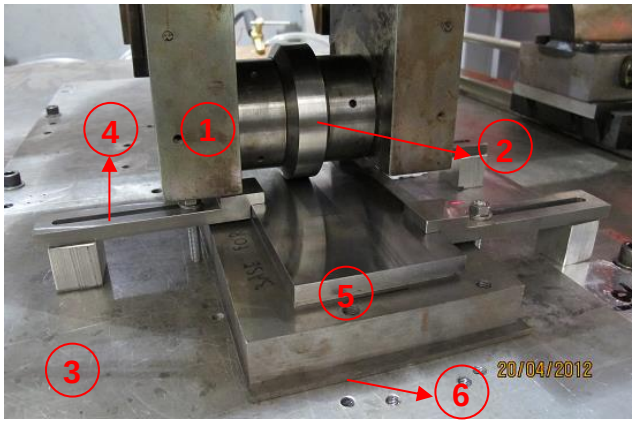

b) **Set up for rolling.** 1. Roller fork, 2. Roller, 3. Platform base, 4. Clamps, 5. Workpiece, 6. Backing plate

Figure 3-22 Experimental setting for cold rolling test

During rolling, each individual plate was held securely with a mechanical clamp as the roller passed over it parallel to the upper edge of the plate. To avoid damage to the clamps, the area of the plate directly underneath the path of the roller was supported by a steel backing plate. Two basic rolling parameters were varied to assess their effect on the specimen: a) the compressive force transmitted through the roller, and b) the roller width (See Table 3-6).

Measurements of the depth through the rolling zone were made in order to establish the depth profile as a result of the load applied. A laser profiler model was used to measure the depth generated by the cold rolling test for both sides of each sample.

Table 3-6 Rolling parameters of API X100 steel

Sample	Sides (Front/Back)	Rolling force (kN)	Roller width (mm)	No. Passed
A	A1/A2	100	20	3
B	B1/B2	150	20	3
C	C1/C2	200	20	3
D	D1/D2	150	10	3

Once the profile was obtained and to ensure that the measurements were being taken into account, the material correction was made in terms of guarantees that the gauge volume was completely immersed in the sample. Figure 3-23 shows the type of profile obtained and Table 3-7 summarised the correction value to introduce during the ND tests.

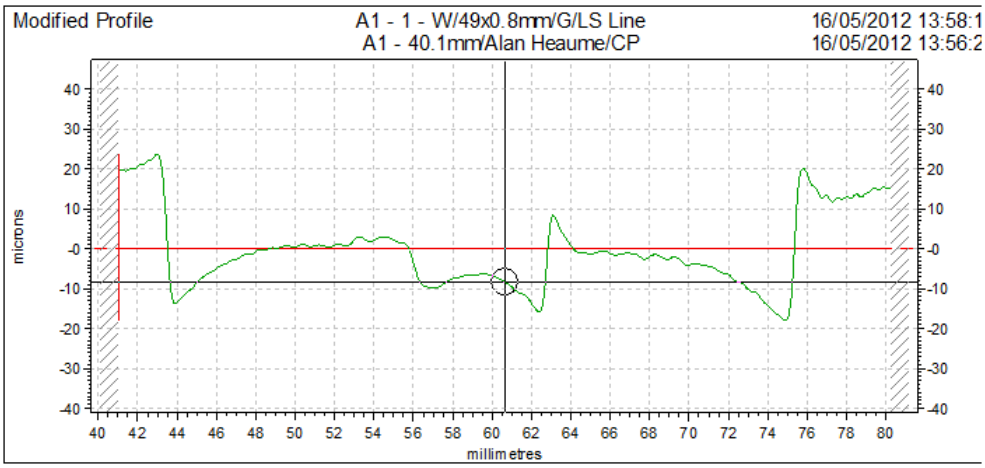

Figure 3-23 Laser profile measured in sample A

Table 3-7 Measurement of depth as result of load applied on plates determined by laser profiler.

Sample	Side	Max. depth, mm
A	A1	0.038
	A2	0.038
B	B1	0.080
	B2	0.080
C	C1	0.125
	C2	0.210
D	D1	0.240
	D2	0.900

3.6.2 Measurement of residual stress

3.6.2.1 Experimental set up and procedures for Neutron Diffraction test

An ND technique was used for measurement of the residual stresses distribution in the specimens rolled previously. The measurement was made using a neutron diffractometer STRESS-SPEC at the FRM II facilities in Munich. The parameters of the instrument are listed in Table 3-8 and the set up can be seen in Figure 3-24.

Table 3-8 Neutron diffraction parameters

Parameter	Value
Wavelength	~1.66 Å
Monochromator	Si (400)
Detector distance	1040 cm
Slit size	Primary Slit, 1 mm x 10 mm
	Secondary Slit: 1 mm
Detector distance	1040 mm
2-Theta	90.8º

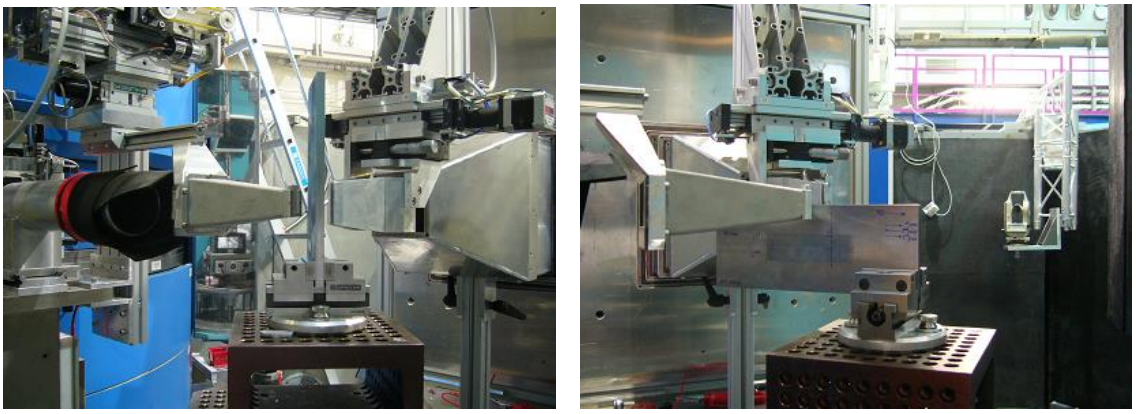

a) Set up for transverse and normal strain measurement

b) Set up for longitudinal strain evaluation

Figure 3-24 Set up at the Stress-Spec instruments at FRM II

To set the thickness of the specimen, the sample was placed and positioned with the help of positioner table and optical positioning system (theodolite) which was set at a nominal angle of 45° to the path of the incident neutron beam.

A point on the surface of the sample was located close to one of the edges of the sample. To determine the exact coordinate where the point is placed, the procedure involved using the diffraction of neutrons across the specimen thickness. The point where the curve changes (inflexion point) corresponds to the exact coordinate in the three directions (X, Y, Z) which is referred to as the reference coordinate. For each point at the surface, seven different points through the wall thickness and length, symmetrical with respect to the mid-plane of each sample, were chosen.

To maximise beam time, only half of the width sample was tested under the assumption that the residual stress distribution is symmetrical and no significant difference can be found. Figure 3-25 presents the beam flux path while Figures 3-26 and 3-27 give the spot location of interest through the thickness and along the surface. Diffraction measurements were accomplished using an instrumental gauge volume (IGV) of 1x1x15 mm^3 for transverse and normal direction, and 1x1x1 mm^3 for longitudinal direction. Table 3-9 shows the estimated time consumed for each gauge volume.

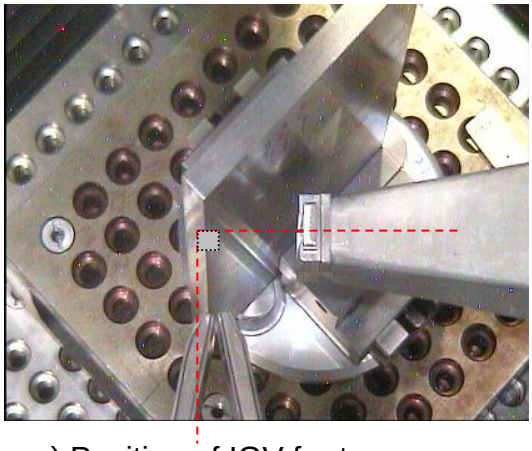

a) Position of IGV for transverse and normal strain measurement

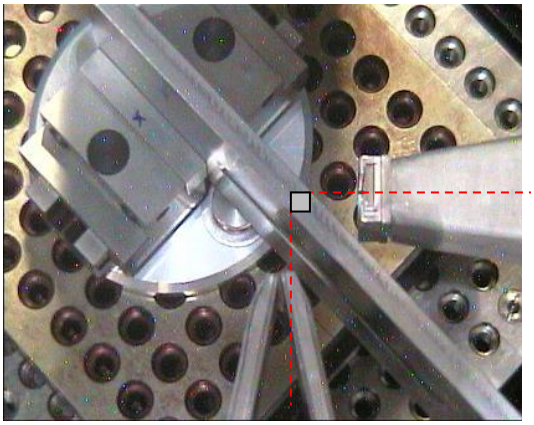

b) Location of IGV for longitudinal strain evaluation

Figure 3-25 Set up at the Stress-Spec instrument.

Table 3-9 Estimated counting time for strain measurement

Description Item	Transverse/Normal	Longitudinal
Gauge volume- Strain scanning, Fe	15x1x1 mm^3	1x1x1 mm^3
Estimated count time per each point	5 min	20 min
Total points per sample	35	35
Total time per sample	175 min	700 min
Total time per 6 samples	700 min	2800 min

Dimensions and points location are summarised in Table 3-10 and a sketch of the rolling zones is shown in Figure 3-26. P1 is located at the overload zone, P2 and P3 at the rolling region and P4 outside rolling track. P5 is positioned outside the rolling areas and considered to be a remote point unaffected by cold rolling process.

Table 3-10 Load applied and location points distance both surface and through-thickness

Parameter	Dimensions in millimetres +/- 0.01 mm			
	A1/A2	B1/B2	C1/C2	D1/D2
Load (kN)	100	150	200	150
Width Roller (WR)	20	20	20	10
Middle-rolled track	17	17	17	8.5
Distance roller area to plate edge	33	33	33	41.5
P1	50	50	50	50
P2	43	43	43	48.5
P3	35	35	35	43.5
P4	31	31	31	39.5
P5	10	10	10	10

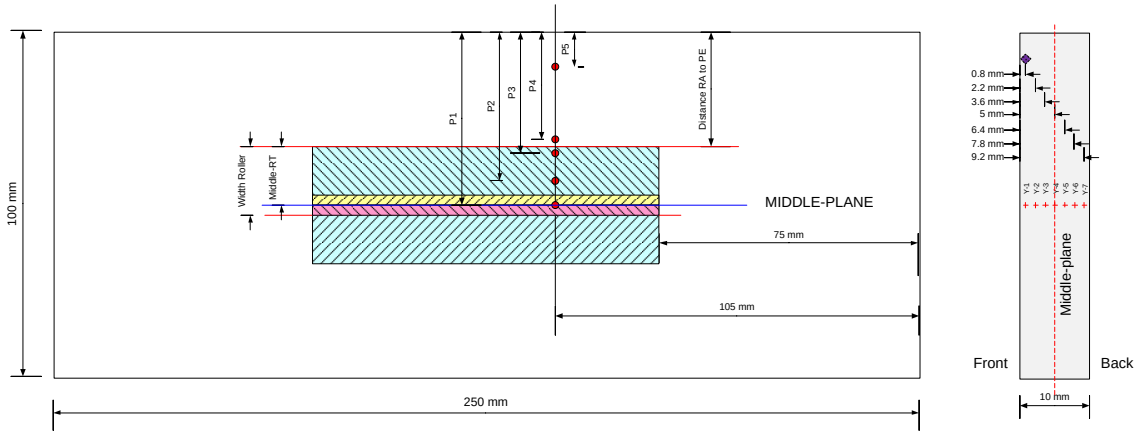

Figure 3-26 Sketch showing points location on both surface through thickness for ND measurement

Reflection at 45.4° was used to measure the in-plane stress components transverse (σ_{yy}) and normal (σ_{zz}) to the surface. As the longitudinal component (σ_{xx}) to the surface is neglected, the specimen was rotated through 90° in the plane, and then strains in the longitudinal direction (σ_{xx}) were evaluated. The coordinate system used to identify the direction is shown in Figure 3-27.

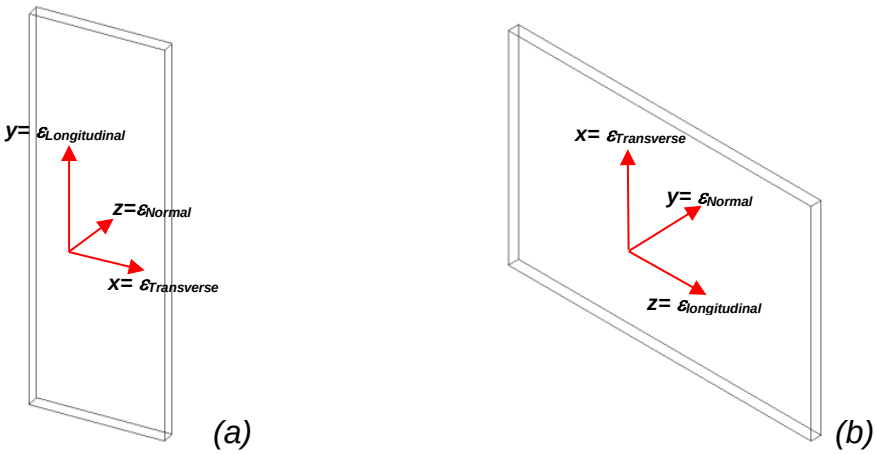

Figure 3-27 Coordinate system using both orientation 1 (a) transverse direction 2 (b) longitudinal direction

Once we had chosen the measurements points and gauge volume for each orientation, the experiment was carried out to determine d-spacing of the stress free ($\boldsymbol{d_o}$) and stressed material ($\boldsymbol{d}$).

Reference measurements were made in the virgin material at a corner of the sample to obtain the reference value (d_o) for the unstressed material. The strain at a point was then measured and $d_{x,y,z}$ were obtained for each direction, which are given in terms of angles.

Using StressTexCalculator® software, the peak position angles obtained from the three normal strain components were used to calculate the strain in direction ε_{xx}, $\varepsilon_{yy,}$ ε_{zz} using equation 3-6. The stress components (σ_{xx}, σ_{yy}, σ_{zz}) were obtained from the three normal strain components using inverse Hooke's law which is represented by equations 3-7 to 3-9.

$$\varepsilon_{(x,y,z)} = (d_{(x,y,z)} - do)/do \quad \textbf{(3-6)}$$

$$\sigma_{xx} = \frac{\nu E}{(1+\nu)(1-2\nu)}(\varepsilon_{xx} + \varepsilon_{yy} + \varepsilon_{zz}) + \frac{E}{(1+\nu)}(\varepsilon_{xx}) \quad \textbf{(3-7)}$$

$$\sigma_{yy} = \frac{\nu E}{(1+\nu)(1-2\nu)}(\varepsilon_{xx} + \varepsilon_{yy} + \varepsilon_{zz}) + \frac{E}{(1+\nu)}(\varepsilon_{yy}) \quad \textbf{(3-8)}$$

$$\sigma_{zz} = \frac{\nu E}{(1+\nu)(1-2\nu)}(\varepsilon_{xx} + \varepsilon_{yy} + \varepsilon_{zz}) + \frac{E}{(1+\nu)}(\varepsilon_{zz}) \quad \textbf{(3-9)}$$

For the rolling approach all the directions are utilized as a result of the effects or variations that the process could impose on the material. Constants E and ν values are the material's plane-specific Young's modulus and Poisson ratio, respectively.

3.6.2.2 Incremental Hole Drilling (IHD)

Spatial resolution of the ND technique is constrained to determine the residual stress profile over distances above 1 mm. As a consequence, a non-destructive measurement is not feasible in the range from 0.0 mm to 1 mm. A powerful method to cover this range is the hole drilling method which was used in this research.

Stresses variation at the sub-surface of the material was determined by incremental hole drilling following the basic procedure described in ASTM, NPL and Measurement Group guidance [241,251,253]. To determine the levels of residual stresses at three points of four steel plates, conventional Incremental Centre Hole Drilling (ICHD) [251] was carried out to 1 mm depth at Cranfield University (SILab). A third party known as Stresscraft Ltd[3], performed a second test to 2 mm deeper using an Orbiting Incremental Hole Drilling (O-IHD) technique on the remote point identified as P5. From both comparisons with the ND method were established. From Figure 3-28 it can be seen that P1 is located at the overload zone. P2 is placed at the rolling zone. P5 (1, 2) is positioned outside the rolling zones and is considered to be a remote point. P5 FAW is a remote point which is not affected by the cold rolling process.

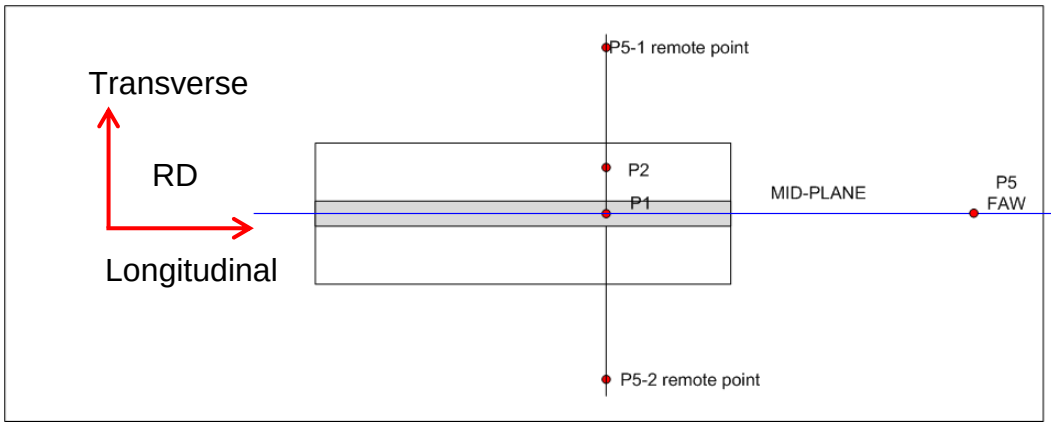

Figure 3-28 A schematic drawing of the points distribution on the sample for the ICHD test

To assess the ICHD, a number of different steps were followed involving surface preparation, strain gauge bonding and drilling a hole. At each point, the plate surface was initially degreased and then ground with emery paper 240 and 320 grit, degreased again and finally neutralised. The target gauges used were Vishay Precision Group type CEA-06-062UL-120 and EA-06-125RE-120 which were installed following the guide established by Vishay Precision Group [314].

[3] Stresscraft Ltd is a company located in St Winefrides Chapel, Pick St, Shepshed, Loughborough LE12 9BB which is dedicated to the provision of stress analysis services.

The steps can be summarised as follows:

1. Degreasing of the surface
2. Conditioning of the surface
3. Neutralising
4. Bonding of the SGR
5. Wiring of the SGR

Each gauge was bonded with element 1 aligned in the transverse direction and element 3 in the longitudinal direction along the rolling direction of the plate. The rosette gauge terminals were wired then connected to a strain indicator for strain readings. The RS 200 milling guide and a miniature PC-controlled 3-axis hole-drilling machine were used for drilling holes 1 mm and 2 mm in depth, respectively.

3.6.2.3 Experimental set up and procedures for Incremental centre-hole drilling

For the ICHD test, each plate was fixed and the RS-200 milling guide was positioned at the centre of the gauge and its pad cemented to the drilling rig to align the instrument with the centre line of the SGR. To ensure the alignment between the centre of the strain gauge and the drill bit (cutter) an adjustable microscope was attached to the equipment and used together with four adjusting screws.

When the system was aligned, the microscope was removed from the guide and the high-speed air turbine was inserted with an inverted cone tungsten carbide (T/C) cutter of 1.6 mm diameter to produce a hole-diameter of ~2.0 mm with a final depth of 1.0 mm achieved by equal increments of 0.05 mm (20 steps). The ICHD setting, plate and strain gauge installations are shown in Figure 3-29.

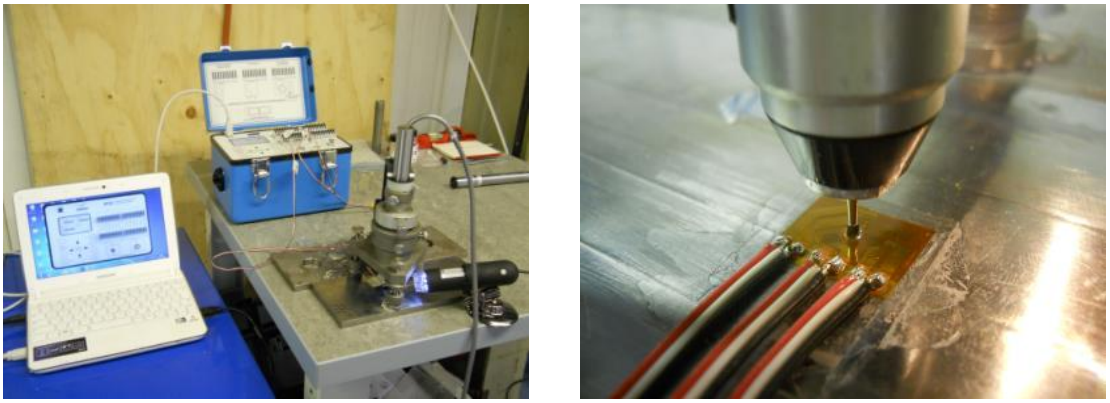

Figure 3-29 Hole drilling set up for 1mm (left) and hole drilling test (right)

Following strain gauge bonding and wiring, the SGR was connected to a strain indicator; the zero (initial) readings were taken at the point of interest and residual stresses released during the drilling were measured. Once the hole was drilled, the diameter was measured using the scale of the microscope and verified by removing the SGR and measuring with an optical microscope. To compute non-uniform residual stress from the raw strain data, an integral method was developed using a Matlab code according to ASTM E837-08 and longitudinal, transverse and shear stress calculations were set into the principal stress and plotted.

3.6.2.4 Experimental set up and procedures for orbiting incremental hole drilling (O-IHD)

A miniature PC-controlled 3-axis hole drilling machine was aligned and each gauge was subjected to orbital drilling at 6 x 32 µm + 6 x 64 µm + 5 x 128 µm + 6 x 256 µm increments respectively. Drilling was carried out using a 2.3 mm diameter inverted cone T/C cutter with a pre-set radial eccentricity to produce a hole-diameter of ~3.9 mm with a final depth of 2.8 mm. A typical set up for drilling is shown in Figure 3-30.

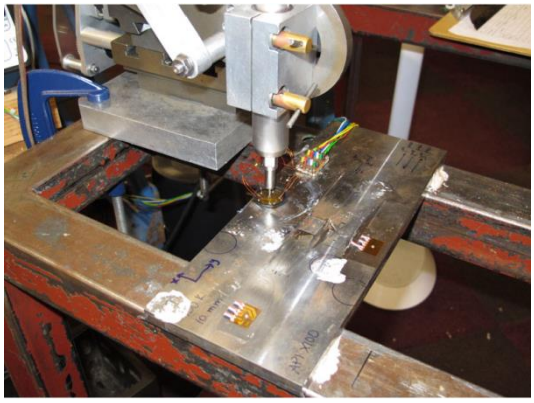

(a) Drilling set up

(b)Strain gauge rosette 125RE bonded

Figure 3-30 Set up for Orbiting Incremental Hole Drilling up to 2 mm

Following completion of the drilling process, the gauge was removed and the hole-diameter measured using an optical head. Relaxed strains measured at the three gauge elements to a depth of 2.0 mm were recorded and analysed using a home-built software by means of the integral method developed by Schajer [249,250]. Within the data reduction program, the strain data were subjected to a variable smoothing (2.0 mm drilled-hole) process and then reduced to direct stress longitudinal, transverse and shear stress components at selected depth increments.

Stresses were further resolved into principal stresses and conventional plots of Cartesian stresses versus depth, and the principal stresses versus the depth were plotted. In Chapter 5 is presented in detail the analyses of the results obtained from ND and incremental hole drilling methods.

3.7 Integrity of materials exposed to simulate flue-gas

All the data obtained for the different tests performed either in the parent or aging material, addressed in the previous sections 3.2 to 3.6 of this chapter, are used to assess the integrity of high strength low carbon steel identified as API X60, X70 and X100, in an simulated flue-gas environment which are carried out in Chapter 6.

However, a short description of the R6 code has been presented below in order to give a better idea of the steps followed to perform the ECA using the FAD approach contained in the R6 software. Numeral 2.5 has described the methodologies available or established with the objective of analysing the fracture behaviour of pipelines using ECA approach. The most popular method is the FAD and the more practical, reliable and economic code used to assess the integrity of structures containing defects is R6 which is utilised in this research [315]. Even though this procedure was developed for use in the nuclear industry, other sectors have found this methodology very useful and it is widely used.

3.7.1 R6 code

The R-code interface is divided in two display panels. The left hand panel is visible at all times, and shows a tree structure of the current project. The right hand panel is used to show different displays, depending on the analysis carried out. The root of the tree is an item showing the current project while at the top level below this are the interviews in the current project. The interview conducts the user through the numerous potential judgment points which are required for the definition of data for Geometry, Materials, Loading, Plastic Collapse, Assessment and Problem definition themes.

Themes are individual sections which are designed by using menus, buttons and defaults making the process effortless. The R6 incorporates a single structure where the user merely identifies at the stage of creating an interview whether an R6 interview is to be created. The program enables more than one project to be open at the same time and switching between projects is achieved by selecting the tabs shown at the bottom of the window. Once the problem is assessed, the R code implements a default process allowing all the available problems to be drawn on a graph on entry to the post-processor.

R6 code is a simple 2-parameter graphical engineering tool for the FAD with a choice of assessment options and analysis types which are dependent on material properties and geometry. The approach considers two parameter, K_r

(Fracture proximity) and L_r (plastic collapse) based on LEFM and LEPM concepts. Two failure modes containing crack-like flaws are classified into three different levels, ranging from option 1 to option 3 [35]. Two criteria can be used: limiting crack size and/or limiting load criteria as is shown in Figure 3-31 and 3-32.

A series of cases are considered where different parameters such as geometry, temperature, gas composition, loading conditions and material characterisations are input in order to perform the engineering critical assessment. Depending of the application different types of defect could be considered for the assessment.

For pressurise system such as vessel or pipeline, part-through thickness flaw and through-thickness flaw oriented axially or circumferentially under leak-before-break concept is now widely applied to assess this type of component. In Figure 3-33 the stage in the description of the LbB concept is sketched, which is explained in detail in BS 7910-13 standard (Annex F).

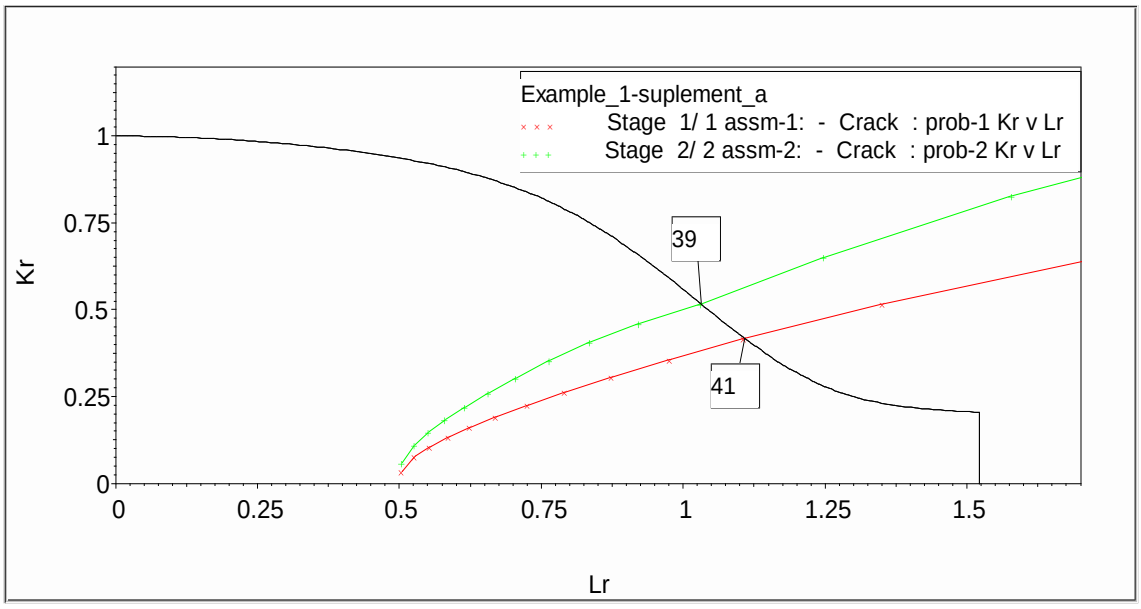

Figure 3-31 Results of the assessment theme under R6 by limiting crack size criteria

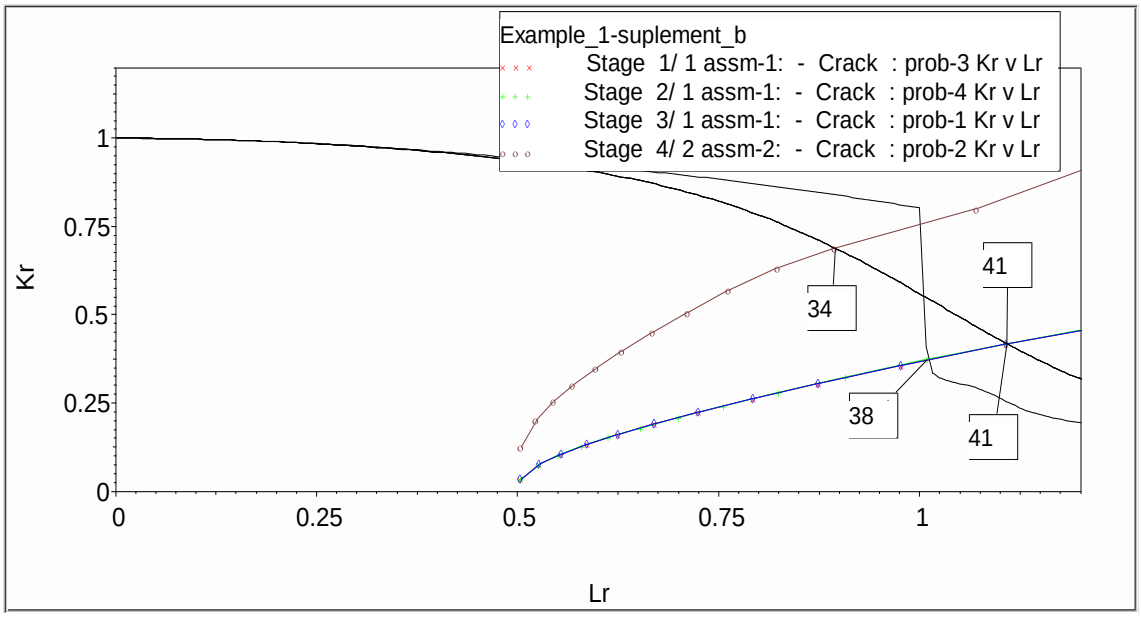

Figure 3-32 Results of the assessment theme under R6 by limiting load criteria

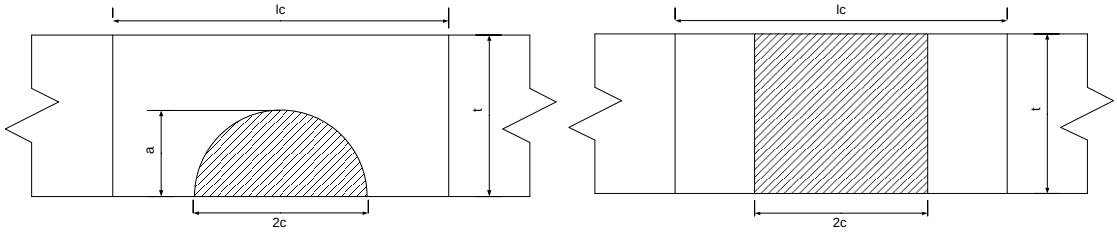

a) Part through-thickness flaw b)Through-thickness flaw

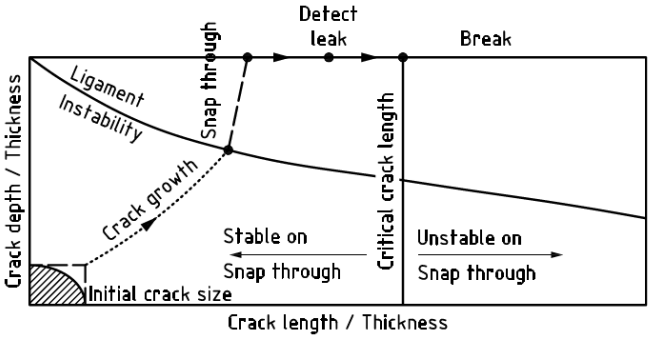

c) LbB diagram

Figure 3-33 Leak-before-Break assessment parts [35]

3.8 Summary

In this Chapter a description of the experimental methodology has been addressed which involved seven different methods. Each section contains the parameters of test, equipment, type of samples, dimensions, experimental set up, as well the environmental conditions under which the tests were carried out in order to meet repeatability and reproducibility of results of measurements. Understanding repeatability as the closeness agreement between independent results obtained with the same method on identical test material, under the same conditions where the absolute difference between two single test results may be expected to lie with a specified probability. In the case of reproducibility, this is similarly measured as the repeatability but under different conditions.

The following chapter covers the mechanical properties evaluation where the influence of temperature, microstructure and environment and their effect on the integrity of the steels studies, it will be discussed.

4 MECHANICAL PROPERTIES & TOUGHNESS OF HSLA STEELS

4.1 Introduction

A good combination of mechanical strength and toughness properties of steels for line pipe applications is required to improve efficiency and performance in the transportation of oil/gas and lately anthropogenic CO_2 over long distances under high pressure. Thus, developing higher grade pipeline steels with excellent cost reduction and operational requirements, and superior metallurgical and mechanical properties, has been found difficult to achieve, particularly for these last two properties [82,85,316–319].

Fracture mechanics is one of the most important tools being used since its development to assess structural components either for new designs or in-service. To undertake fracture assessment, the quantification of material toughness shall be known as K_{Ic}, the crack tip opening displacement (CTOD), fracture toughness of material K_Q and J-integral (J); however, the only one representing lower-bond (plain strain) toughness is K_{Ic}.

One of the most economical, fast and popular methods is the Charpy V-notch test (CVN). From the test values of energy, variants of temperature are obtained and using empirical or semi-empirical correlations fracture toughness is determined. However, it is well-known that CVN evaluates the fracture resistance rather than fracture toughness, which is one of its major disadvantages.

On this investigation fatigue pre-crack specimens has been considered to bring a better estimation of the fracture toughness with the purpose to evaluate the potential of this approach to estimate fracture toughness of HSLA steels. Along with this approach this chapter is focused to determine the mechanical properties and fracture toughness of high strength low carbon alloy grades X60, X70 and X100 in as-received and aging condition.

A general framework of the materials' behaviour in order to establish the evolution of fracture toughness with/without the environment at different temperatures was carried out.

4.2 Experimental procedure

4.2.1 Outline

Strip and round specimens manufactured in the longitudinal direction were obtained from the flat plates and small pipe, and were tested from -70°C to 21°C at a strain rate of 3.3 x 10-3 $^{s-1}$ in accordance with the BS and ASTM standard test method by a servohydraulic Instron machine of 500 kN and 100 kN capacity.

The tensile test was conducted three times for each datum point. The 0.2% off-set flow stress was determined to be the yield strength in the steels showing continuous yielding behaviour, whereas the lower yield point was determined to be the yield strength in the steels showing discontinuous yielding behaviour. Technical details of the metallurgical characterisation, hardness test, tensile test, fracture toughness tests and methods of analysis used are described in detail in Chapter three, numeral 3.2 to 3.5.

4.3 Results and discussion

4.3.1 Chemical composition

The nominal compositions of the steels are given in Table 4-1. Having low carbon content reduced the grain size and carbide formation and increased yielding strength. The existence of manganese increased strength and toughness. The low amount of sulphur and silicon reflects the cleanliness of the steelmaking process and improved toughness due to reduced inclusions formation which could be potential defect initiation sites.

Table 4-1 Nominal composition of the API X60, X70 and X100 steel (wt %)

Element	X60	X70	X100	API 5L
Carbon (C)	0.04	0.05	0.07	0.10-0.12
Silicon (Si)	0.19	0.26	0.30	0.45 -0.55
Manganese (Mn)	1.04	1.89	1.83	1.60-2.10
Sulphur (S)	0.008	0.010	0.009	0.020-0025
Phosphorus (P)	0.013	0.010	0.012	0.010-0.015
Nickel (Ni)	0.03	0.44	0.28	<0.50
Chromium (Cr)	0.03	0.41	0.17	<0.50
Molybdenum (Mo)	<0.01	0.40	0.16	<0.50
Copper (Cu)	0.02	0.45	0.15	<0.50
Vanadium (V)	0.04	0.07	0.01	Their sum must be <0.15
Niobium (Nb)	0.06	0.05	0.04	
Titanium (Ti)	0.01	0.01	0.02	
Aluminium (Al)	0.03	0.01	0.04	-
Cobalt (Co)	<0.01	<0.01	<0.01	-
Boron (B)	-	-	-	<0.004
Iron (Fe)	Balance	Balance	Balance	Balance

*Note: The sum of V + Nb + Ti must be <0.15

Molybdenum content near 0.3% is beneficial as toughness is improved, as well as for chromium, nickel, copper and occasionally boron. Vanadium, titanium and niobium are kept limited to 0.15% for steels with yield strength above X60 due to strengthening by the precipitation of vanadium or niobium carbonitrides which could also harm toughness. The chemical composition determined for the three steels matches the specification of the standard API 5L [67].

4.3.2 Rolling direction

As heat treatment, soak time and cooling rate affect microstructure features, the determination of spherical and elongated non-metallic inclusions are preferred as indicative of rolling orientation. To identify these structural defects as-polished samples are preferred as they give better results than etched surfaces.

Figure 4-1 shows the optical micrographs with a lower magnification (left) indicating the presence of banding. Flattened inclusions of MnS (manganese sulphide) were found at higher magnifications, indicated by the red arrows. The latter feature emerges when steel is fabricated by rolling and inclusions tend to be deformed and elongated in the rolling plane.

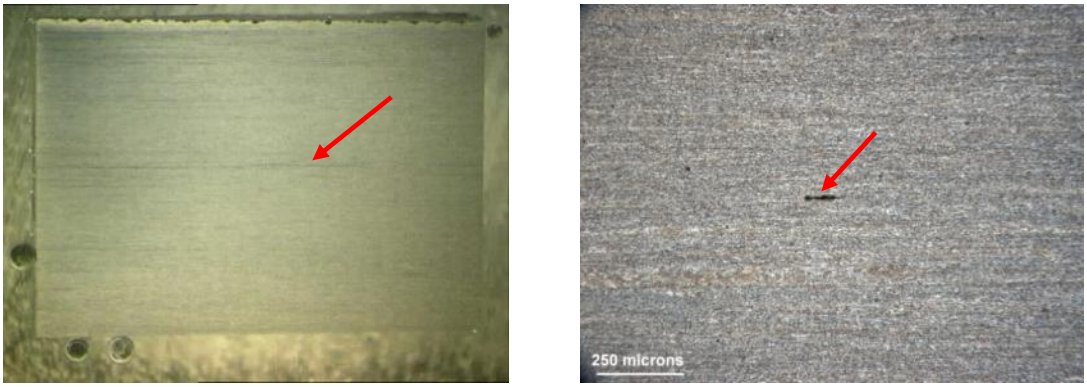

Figure 4-1 Left: Deformation bands direction is indicated by the arrow. Right: arrow indicates the shape of a flattened MnS inclusion presence. Nital 2%.

Thus, if a section contained deformation bands (dark lines along the plane) with non-metallic inclusions, it was selected as a longitudinal axis, as it provided evidence of the direction of the steel rolling mill process. The recrystallization involved the formation of new, strain-free grains, making it difficult to determine grain elongation; however, inclusions, oxides or second-hard particles cannot be regenerated. But cleanliness of the steel could be a drawback in determining the rolling direction.

4.3.3 Hardness test

The Vickers hardness was measured under a 100g load with equal intervals of 0.2 mm near to the top/bottom surface increasing to 1 mm intervals on the middle of the sample thickness, as shown in Figure 4-2 (a, b). The results are plotted in Figure 4-3. From the figure the hardness values of the plates and pipe section are representative of the steel evaluated.

A high content of Manganese (Mn), Nickel (Ni), Copper (Cu) and Molybdenum (Mo) tends to increase the hardness of the material as well as formation of low temperature microstructures, such as martensite, bainite. From Figure 4-3 it can be seen that hardness values for grade X100 and grade X70 are exceeding 248 HV_{100} (~HRC 22) which is the maximum hardness value recommended by NACE for steel in sour environments.

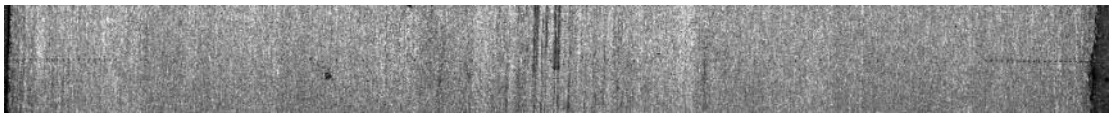

(a) General view

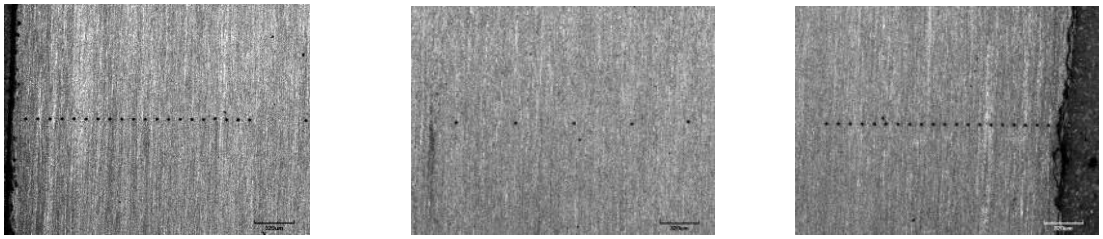

(b) Details of intervals per zone

Figure 4-2 Profile hardness test performed through the thickness, presenting the length covered in each part of the samples' thickness

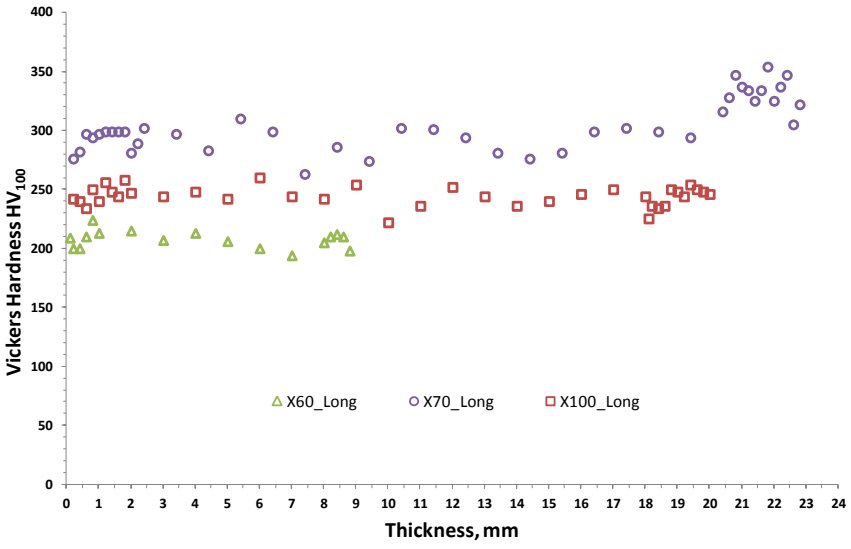

Figure 4-3 Vickers hardness distribution through the thickness for all the steel obtained from longitudinal axis

4.3.4 Metallographic characterisation

Optical micrographs and SEM images of the microstructure of the steels evaluated are shown in Figure 4-4 (a)-(f). Micrographs (a, d) are representative of the microstructure of steel grade X60 which consisted of ferrite (white) with small zones of pearlite (dark). The micrographs do not show significant deformation or banding. Non-banded ferrite/pearlite could emerge as an indication that the microstructure was recovered during the rolling process (hot rolling) which is a typical method used to manufacture steel under 450 MPa yield strength.

Optical micrographs (b, e) and (c, f) corresponding to steel grades X70 and X100 respectively, show a typical tempered structure. From the figures it can be seen that both steels showed a more complex microstructure which can be identified slightly under optical microscopy. The microstructures of both steels are characteristic of rolled and tempered steel owing to TMCP and ACC methods.

The matrix is composed of low carbon lath-like bainite, granular bainite, allotriomorphic and quasi polygonal ferrite (white), and martensite (dark). It is presumed that M/A packets are present, along with bainite lathes. Under high magnification fine precipitates (black dots) dispersed on the matrix could indicate the presence of titanium or niobium carbides. Very small and randomly dispersed stringers of MnS inclusions were observed in the matrix but showed no signs of clustering.

As fine details are not possible to distinguish using optical or SEM, many authors have addressed this study using the EBSD technique; however, this was not performed for this research. A detailed study of the microstructures is beyond the scope of this research; however, their effects on mechanical properties and fracture toughness have been addressed using the literature available on this topic.

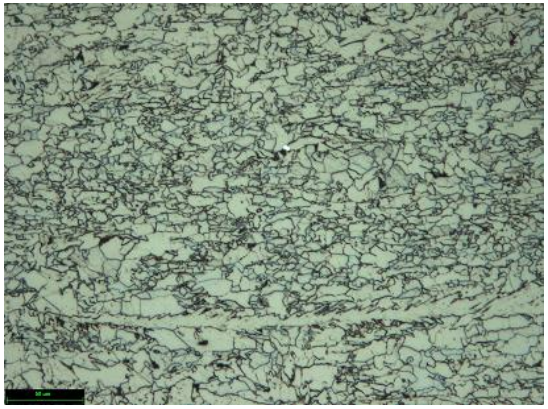

(a) Magnification 500X

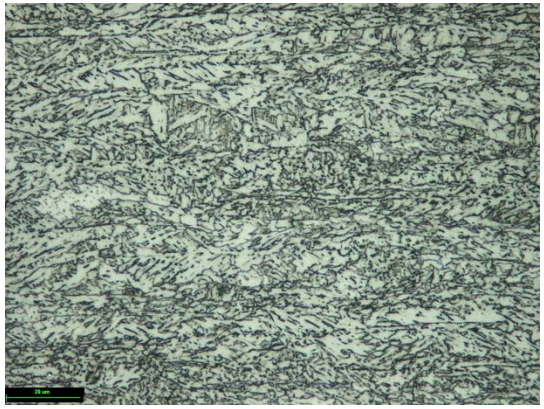

(b) Magnification 500X

(c) Magnification 500X

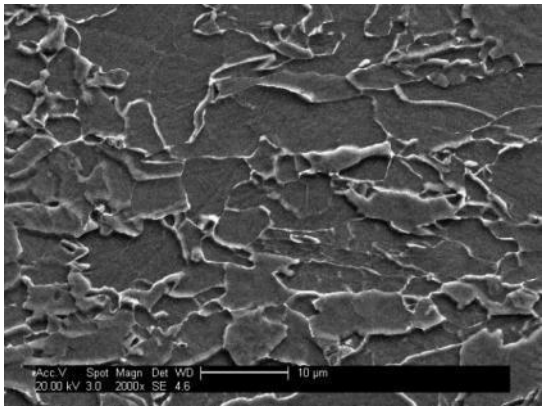

(d) Magnification 2000X

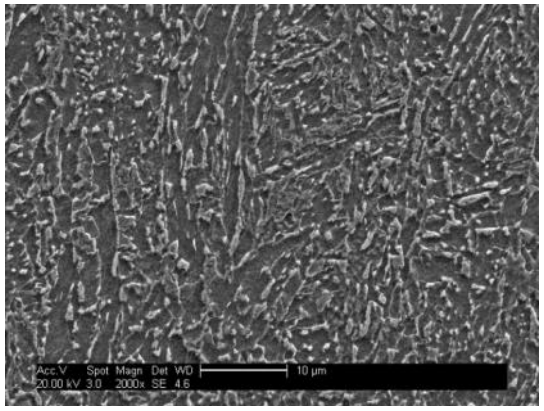

(e) Magnification 2000X

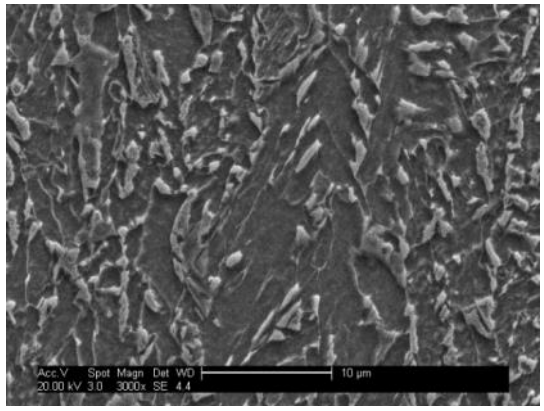

(f) Magnification 3000X

Figure 4-4. Optical and SEM micrographs of microstructure for virgin material on the longitudinal section (a, d) grade X60 (b, e) grade X70 (c, f) grade X100

4.3.5 Tensile tests

The tensile tests have been accomplished on steel grades X60, X70 and X100 over the range 21°C to –70°C temperatures for virgin material while aging samples were performed only at –20°C. Yield strength, tensile strength, yield/tensile ratio and uniformed elongation variation obtained experimentally are presented in detail in Appendices L and M respectively. The former summarises the tensile properties of as-received material while the latter shows mechanical properties of the steels exposed in a simulated flue-gas environment saturated with water.

Pictures of all samples exposed in CO_2, saturated water, SO_2 and H_2S environment at 50h, 150h, 200h, 300h and 400h are presented in Appendix O. A rusty layer is observed on the surface of the samples exposed up to about 200h in SO_2 while a golden colouration can be seen for those introduced in H_2S without layer formation on the surface.

4.3.5.1 Tensile properties of virgin material

It is now accepted that definition of the uniform elongation load, at 0.5%, prejudices the work hardening potential of high strength materials, which is less exploited, compared with the lower yield strength of other steels [73,85] and a 0.2% offset is proposed as a better indication of this. However, the API 5L standard does not explain clearly why a 0.2% offset is a better indication of yield strength instead of the yield point at 0.5% total elongation for grades >L625 (X90).

For this research the calculation of yield stress for steel X100 was made under 0.5% UEL instead of 0.2% offset as it is was determined that the latter parameter underestimated the values. Grade X70 was calculated using the $\sigma_{0.2\%}$ parameter while for grade X60 the process indicated by BS EN 10002-1 standard for proof strength (non-proportional) determination was followed. Figure 4-5a shows typical stress-strain engineering curves for the steels used in this research. A graphical method was applied to obtain yield stress, or proof strength and ultimate strength, as well as uniform elongation.

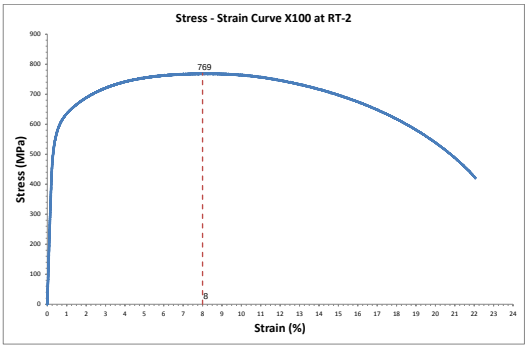

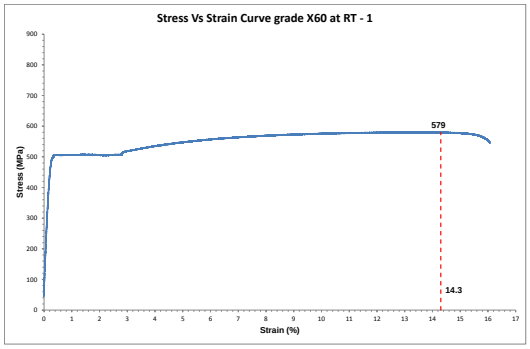

(a) Engineering Stress-Strain Curve

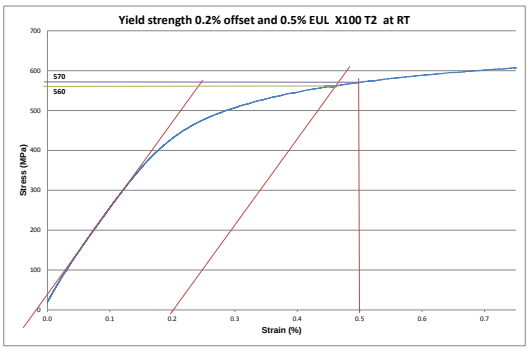

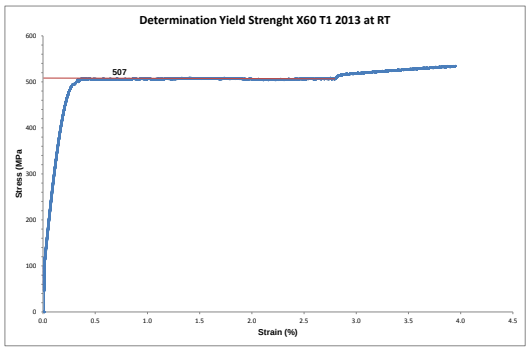

(b) Yield strength at 0.2% offset, 0.5% EUL and proof strength

Figure 4-5 Stress-Strain engineering curve for steel grades X100, X70 and X60

The values obtained are presented in Appendices M and N, but an example is showed in Figure 4-5b. Figure 4-6 shows the variation for yield and ultimate strength of the steels determined under virgin conditions over the range –70°C to 21°C. The mechanical properties of as-rolled plate of grade X100, both strip and round geometry are presented at (a, b). There is a tendency to increase yield and ultimate strength as temperature decreases. This behaviour is more evident for X100 than grades X60 and X70 (See c, d and e).

For API X100, the yield strength reached values in the range of 540 MPa to 640 MPa which is 20% lower than that specified for this steel by API 5L for grades above X90 to 0.5%. The tensile strength was ≥720 MPa which corresponds to the minimum value required from the standard [67].

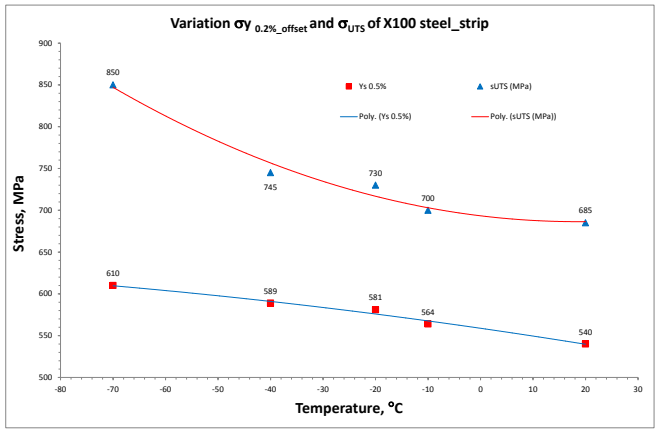

a) Grade X100, strip geometry

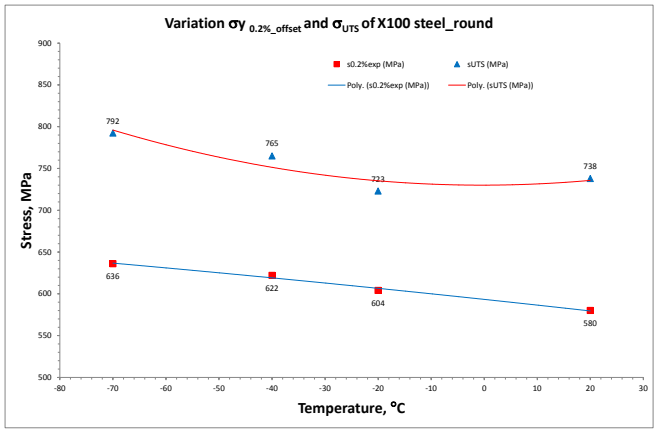

b) Grade X100, round geometry

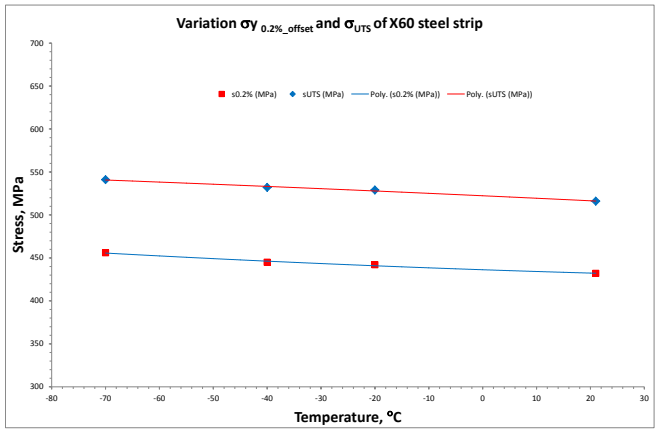

c) Grade X60, strip geometry

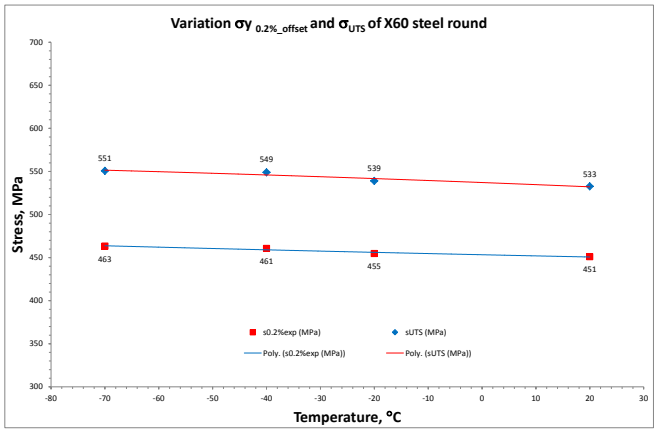

d) Grade X60, round geometry

Figure 4-6 Variation of yield and ultimate yield strength with temperature for steels in as-received condition using strip and round samples

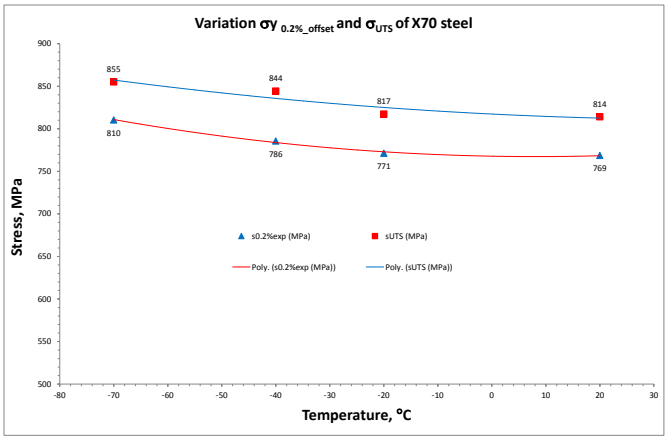

e) Grade X70. Round geometry

Figure 4-7 Variation of yield and ultimate strength vs. temperature for steel in as-received condition

Uniform elongation was at least 6% achieved but yield ratio was clearly lower (maximum 0.84). Since steel grade X60 exhibited yield strength over the range of 431 MPa to 500 MPa and ultimate strength between 520 MPa and 579 MPa, this fulfils the mechanical requirements of the standard for this grade of pipeline steel. However, yield ratio was 10% less than the API specification.

Grade API X70 shows a larger yield and ultimate strength values, at 771 MPa and 814 MPa, respectively. As the specimen was extracted from a pipe section, this could indicate that the material properties have increased due to work hardening induced after the pipe manufacturing process. Yield ratio and uniform elongation was achieved, gathering standard specification.

In general, it can be seen that the stress-strain engineering curves of the X100 and X70 steels do not show the yield phenomenon which was presented for the X60 steel which exhibited a plateau after its yield point then dropped due to the Lüders band formation. The formation of Lüders bands, also named “slip bands” or “stretcher–strain marks”, are presented in metals experiencing tensile stress due to plastic deformation common to low carbon steels and certain Al-Mg alloys.

Even though grades X70 and X100 have low carbon content, the deformation mechanisms on those steels are mainly different as they are affected by the Bauschinger effect. The Bauschinger phenomenon causes loss of strength in TMCP steel when the strain direction is changed during cold worked metal. High strength steels are characterised to be anisotropic which determines that the strength of the material is dependent on the orientation. Microstructure, plastic strain introduces during pipe manufacture, heat treatment and cooling rates can all affect the mechanical properties of those steels [320–322]. Examples of the fracture zone of strip samples of steel grades X100 and X60 are shown in Figure 4-8.

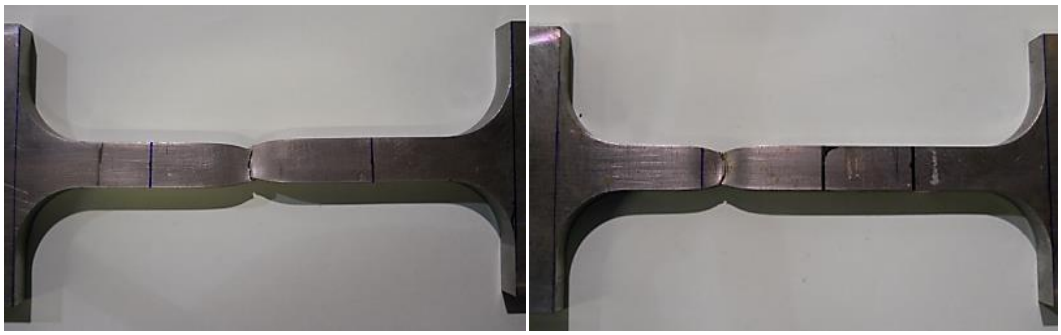

a. Sample 2. RT b. Sample 3 (-70°C)

Figure 4-8 Images showing the fracture zone of the strip tensile samples

It can be seen that one specimen has broken in the middle of the gauge length while the other falls outside/limit of this region but within the parallel length of the sample. In spite of this issue, yield and tensile strength evaluation were assumed as particular material responses, providing a general framework of their mechanical behaviour. It is well-known that the stress-strain curve, flow and fracture properties are strongly dependent on temperature. For body-centred-cubic metals, the yield stress increases rapidly and ductility decreases with decreasing temperature. This behaviour was usual for the samples tested over the range –70°C to 21°C which were presented in Figures 4-6 and 4-7 above.

4.3.5.2 Tensile properties of aging material

The results of the evaluation of mechanical properties of steels exposed in flue-gases are presented in Figures 4-9 to 4-11. The atmosphere is constituted by CO_2 in dense phase, free water (3.3%) plus SO_2 or H_2S impurity, at 500 ppm for each case. Each figure shows the yield and ultimate tensile stress determined for each impurity evaluated. As it was discussed in reference [96] and section 2.2.2 the exactly amounts of impurities on CCTS is unknown, however, 500 ppm was chosen as it value represent the worst scenario for testing materials involving health and safety conditions. Reference [1,23,70,109] are recommended lecture if more details about type and composition levels of impurities is required.

The samples exposed were not strained to failure immediately after exposure as they were stored in a desiccator in order to dry before subsequent weighting. Visual inspections were performed and it was found that samples exposed in the SO_2 atmosphere after 200 h had a layer of rust formed in all of them; these can be seen in the figures in Appendices N and R. The specimens introduced to H_2S had their metallic colour changed to a golden-yellow colouration.

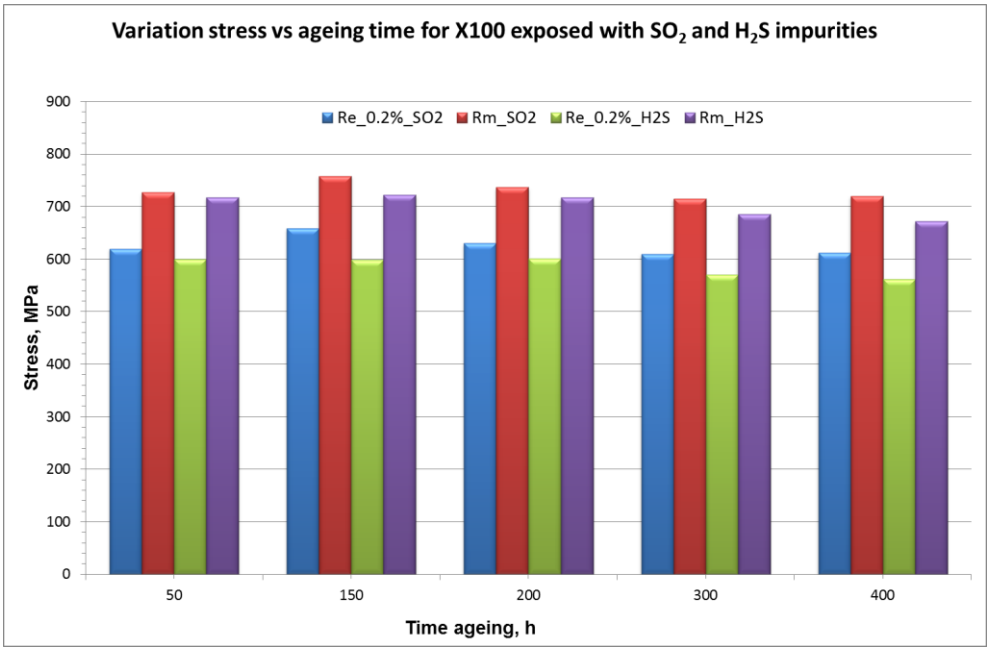

Figure 4-9 Tensile properties of steel X100 exposed in H_2S and SO_2 impurities and tested at –20°C

From the results obtained for grade X100, in the variation of mechanical properties when compared with virgin material at –20°C, there are no significant differences that show any effect on the environment or the mechanical response of the material. A scatter of 20 MPa between virgin and aging samples indicated the variation could be considered normal and within the acceptance level of deviation. Steel X70 presented a similar variation of its tensile properties with a peak of 860 MPa yield strength on SO_2 and 841 MPa for H_2S. Similar tendency were obtained for ultimate tensile strength.

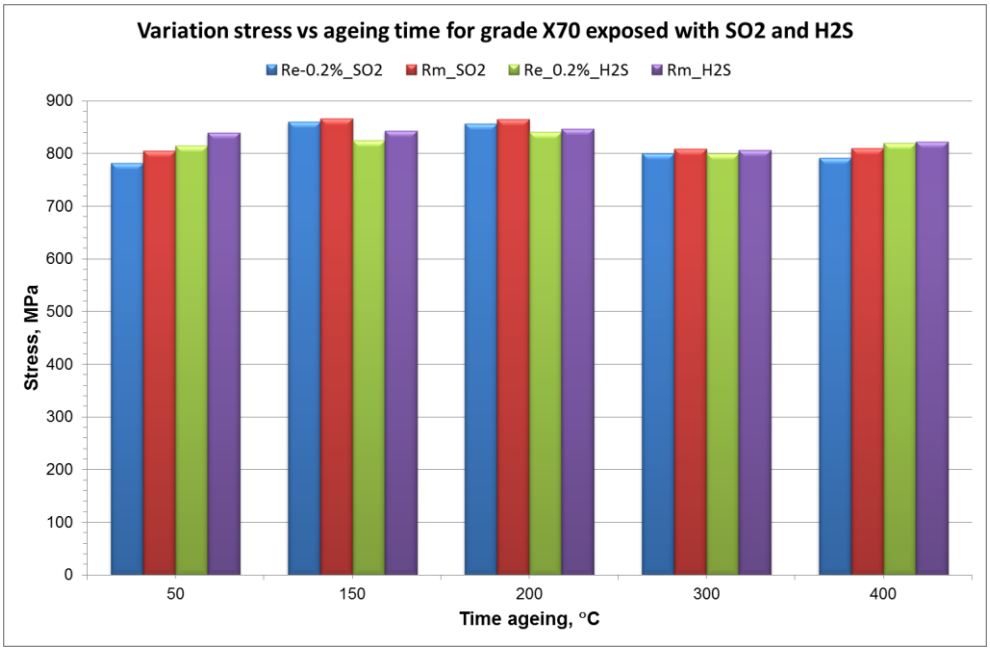

Figure 4-10 Tensile properties of steel X70 exposed in H_2S and SO_2 impurities and tested at –20°C

Embrittlement or corrosion phenomenon reduces yield strength, tensile strength and elongation and a scatter of 80 MPa, compared with virgin value, which could be an indication of material degradation. Even though the material was classified as API X70 this does not guarantee that slight differences could not emerge in the material properties as a consequence of microstructure variation due to the material used to manufacture the samples came from two sections from the same source.

With regard to grade X60, the variation of the properties shown in Figure 4-11 does not present a large discrepancy in the mechanical properties obtained from the material as-received and tested at the same temperature. A scattering of 10% of the results is not a criterion to establish the effects of the environment on the material properties and it could be statistically accepted as an indication of material behaviour rather than material degradation. However, investigations by Al-Mansour et al. [112], Duncan and Wang [318] and Jin et al. [323], indicated that hydrogen embrittlement (HE) has to be included as a potential factor of damage when materials are exposed in a hydrogen environment.

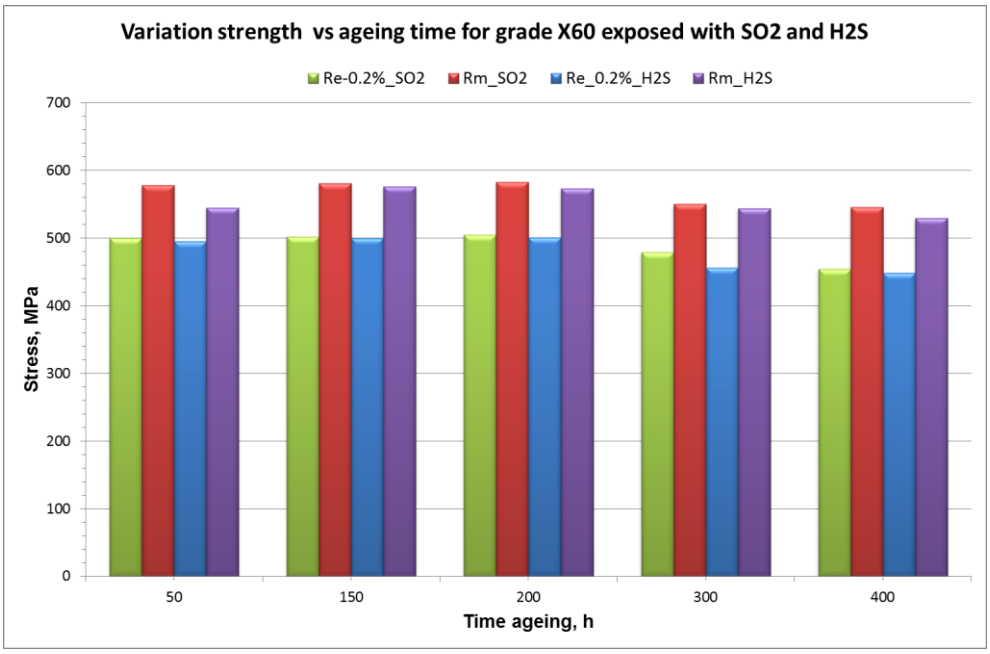

Figure 4-11 Tensile properties of steel X60 exposed in H_2S and SO_2 impurities and tested at -20 °C

4.3.5.3 Fracture surface characterisation of tensile specimens

Fractography analysis of the fracture surface morphology was achieved by OM. The strip samples evaluated are grade X100 and X60. The evaluation was performed in all the samples tested but only samples at 21°C and –70°C are shown in Figure 4-12 (a to d). Photographs (a, b) correspond to steel grade X100 and (c, d) to grade X60. In tension tests after plastic deformation, the cross section started to change due to continued reduction which is imposed as a result of the load action.

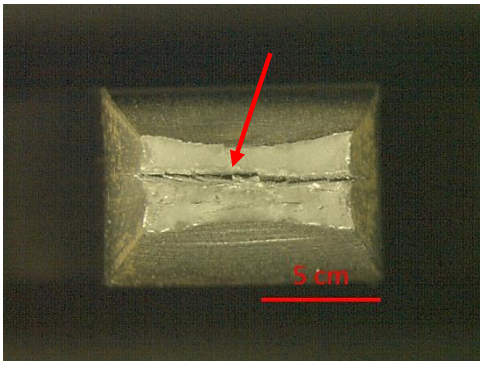

a) X100 at 21°C

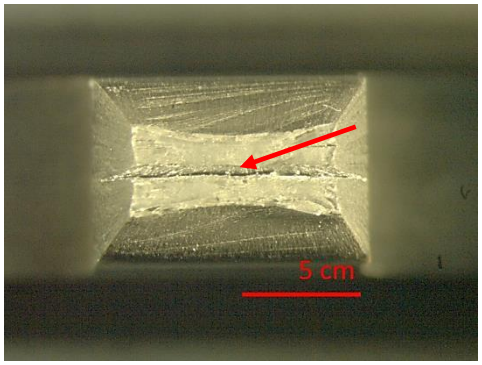

b) X100 at –70°C

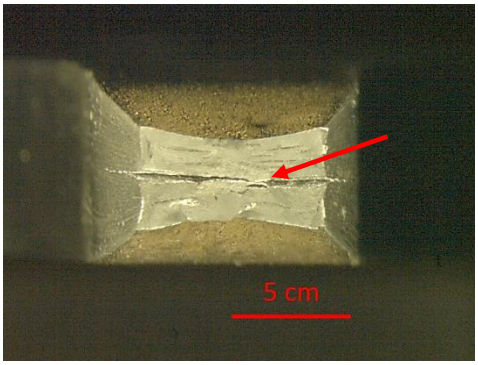

c) X60 at 21°C

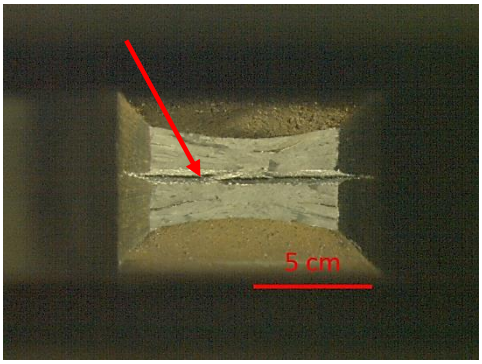

d) X60 at –70°C

Figure 4-12 Fracture surface of strip samples tested at RT and –70°C

For a rectangular specimen, when necking takes place it causes the sides of the minimum section to bend, as shown in figures (a-d). For X100 (a-b) it was observed that after the failure point the load started to decrease but at 30% of the remaining load an abrupt change was determined.

A second load drop was found before the specimen broke. This behaviour was more evident in tests carrying a lower temperature. For X60 a singular jump was not detected in spite of a similar fracture surface being observed. Once the failure process had taken place and the cross section necking started, a crack initiation process at around 10% was also initiated. At this point splitting of the cross section, also named delamination, occurred and the minimum cross section was constituted of two separate strips of the material holding the load up until final failure.

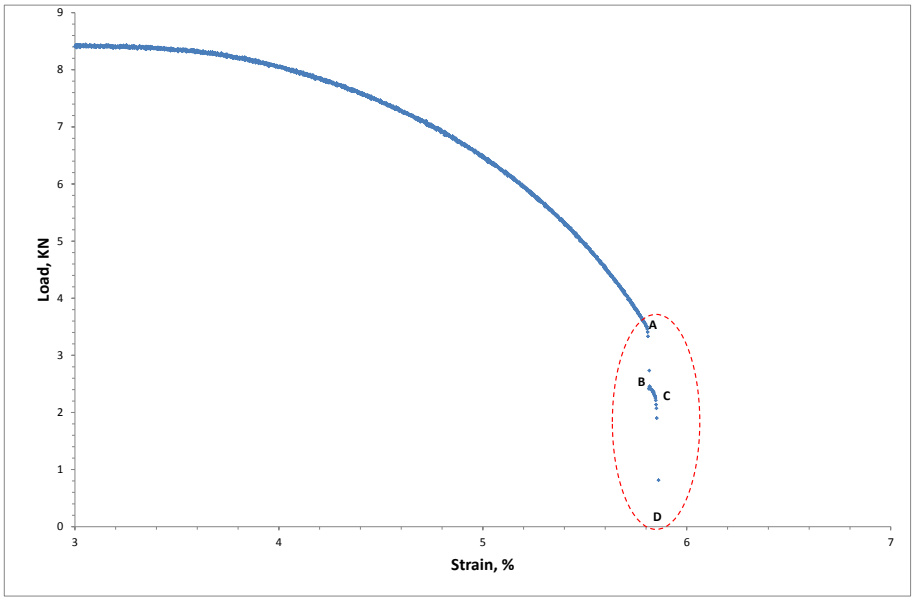

Figure 4-13 Loads vs. elongation at splitting point: A) Failure initiation, B) Starting delamination, C) End of unexpected elongation, D) Final failure

Figure 4-13 presents the splitting phenomenon presence on the stress-strain curve which was detected both in strip and round samples. Figure 4-14 shows fractographs taken at 21°C (a, c, e) and –70°C (b, d, f) of round bars of material as-received which were tested under the same conditions as the strip samples. The fracture surface of X100 at 21°C and –70°C temperature displayed cracks which grew along with the larger axis of the ellipse, referred to as the plane, normal to the minimum cross section and a diametral contraction is observable (ovalisation).

In Figure 4-15 fracture cross sections of steels tested at –20°C for unexposed and exposed in flue-gases are shown. From the figures, crack formation is clearly notorious, and it was found for the three conditions on X100 and X60 while on grade X70 there is clearly defined an environmental contaminant with SO_2 impurity. From all the figures it can be identified that crack propagation in tensile samples is associated with slant and flat fractures. The red arrows identify the slant fracture while the white arrows highlight the flat fracture on the samples.

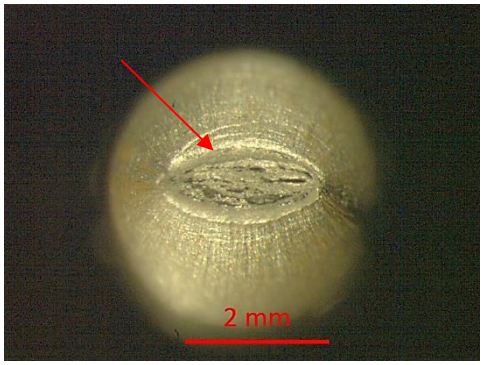

(a) X100 at 21°C

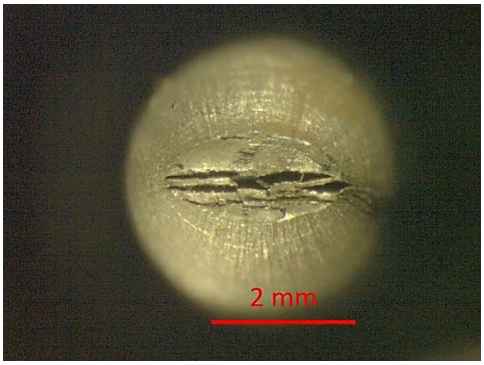

(b) X100 at –70°C

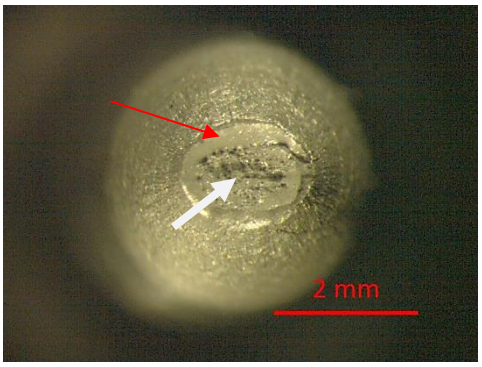

(c) X70 at 21°C

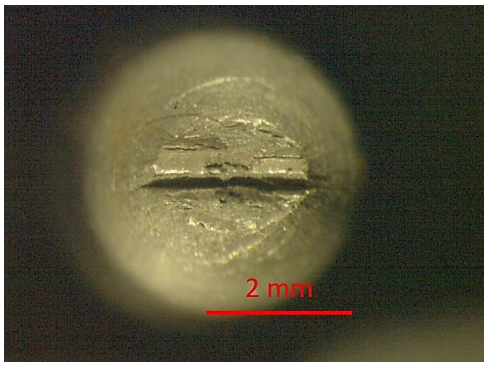

(d) X70 at –70°C

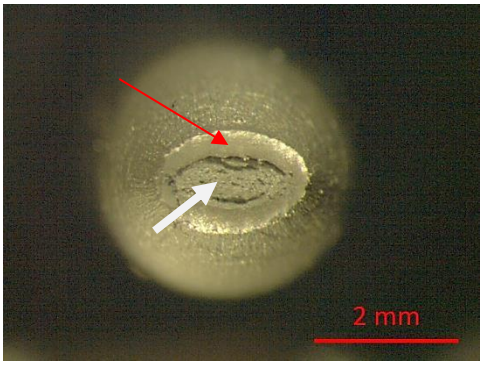

(e) X60 at 21°C

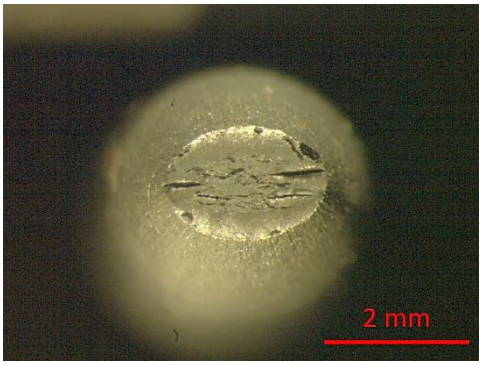

(f) X60 at –70°C

Figure 4-14 Fracture surface of round tensile as-received samples tested at 21°C and –70°C

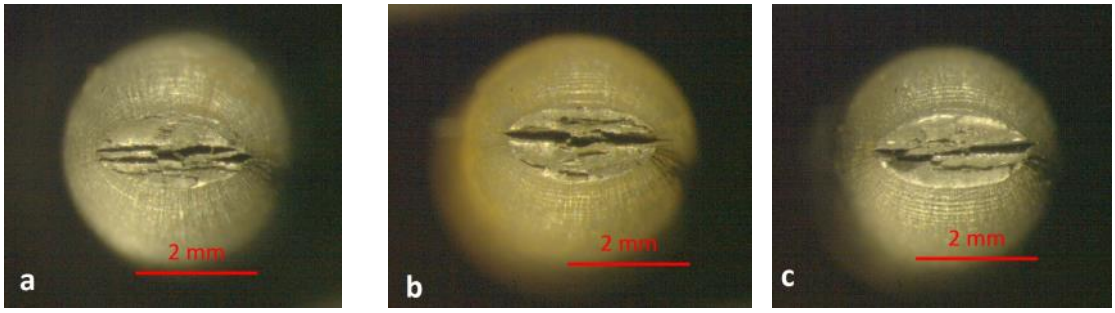

Grade X100 a) Virgin b) SO_2 per 400h c) H_2S per 400h

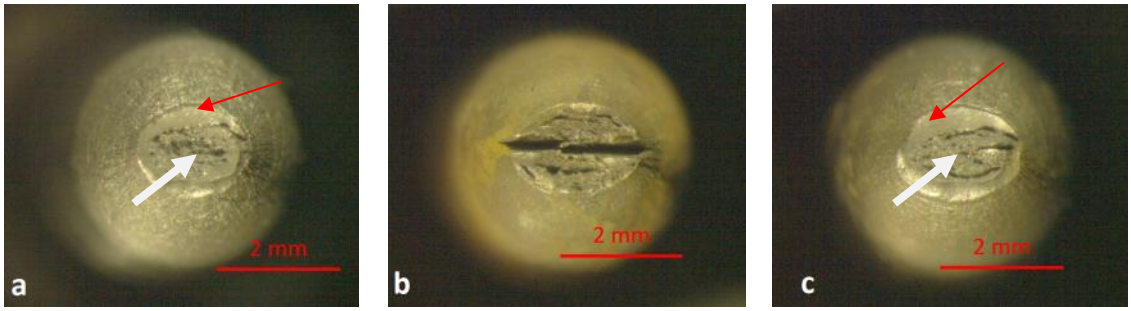

Grade X70 a) As-received (b) SO_2 per 400h c) H_2S per 400h

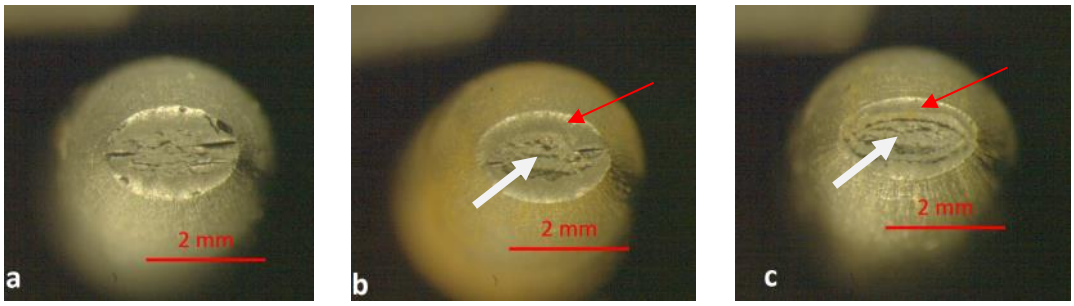

Grade X60 a) As-received (b) SO_2 per 400h c) H_2S per 400h

Figure 4-15 Fracture surface evaluation of round tensile specimen unexposed and exposed in a simulated flue-gas and tested at –20°C

4.3.6 Discussion of microstructure and mechanical properties results

4.3.6.1.1 Hardness

The microhardness profiles of the longitudinal cross sections show, in general, a constant value of the microhardness average through the thickness; these are summarised in Table 4-2. The profile presented in Figure 4-3, illustrated as grade X70, has an increment on the bottom section. This could be the result of the rolling process resulting in the generation of a deformed layer which is reflected in the increment of the hardness. X100 and X60 steel hardness values do not change notably and remain at the same value with no significant difference on the section.

Table 4-2 Vickers hardness values for API X100, X70 and X60 steel HV=100g

Steel	Plane	Section			Section avg.	Total avg.
		Top	Middle	Bottom		
X100	Longitudinal	247	244	244	246	251
	Transverse	256	257	257	256	
X70	Longitudinal	286	285	328	298	302
	Transverse	295	294	333	305	
X60	Longitudinal	209	207	208	207	208
	Transverse	222	201	203	208	

It should be well-known that maximum hardness specified for steels to be exposed to a sweet or sour environment cannot be higher than 248 HV_{200} (HRC ~22). This value cannot be exceeded as this hardness value corresponds to a critical surface–flaw depth of about 0.5 mm for steel to be used in acid environments containing H_2S, as recommended by NACE [164].

However, from the literature, this limit looks unclear. For example, Canadian specification standard CSAZ245.1-2007 still specifies 248 HV as the maximum allowed hardness but CSAZ662-2007 changed the requirements to 250 Vickers. The GOST standard established a limited maximum hardness up to 260 HV. Thus, the permissible range could be between 248 and 260 HV; however, some issues could arise due to the harshness of the environment.

Domizzi and Anteri [293] found that microhardness below 300 HV_{25} has little influence on HIC resistance for steels with a banding F-P microstructure. From Table 4-2 it can be observed that hardness X70 HV > X100 HV > X60 HV which indicates that the former are more susceptible to corrosion degradation or HE.

4.3.6.1.2 Metallurgical characterisation

Chemical composition of high strength steels can differ widely, depending on the mechanical requirements and dimensions of the product. The main function of the alloy elements is to improve strength by mechanical means, such as grain refining, solid solution and precipitation hardening. The interaction between rolling process, cooling rate and chemical composition determines the type and volume of phases to develop, given their particular mechanical toughness properties.

The increase in strength has a direct relation to increasing alloying elements such as Mo, Si and Ni. However, the unknown effects of interactions with other elements result in difficulties in establishing a complete frame of their impact on the material. The combination of V+Mo+Nb produced carbides, nitrides and carbonitrides by secondary hardening while Ni+Mo enhanced hardenability by precipitation hardening which refined the microstructure.

The same effect can be obtained by Ni+B, while Nb+V strengthen properties but a high carbon equivalent could be required. In thicker pipelines, Mo+Nb +Ti is effective to increase strength as well as small ferrite grain size. Favourability on the bainite formation of acicular carbide needles in X70 steels is also mainly attributed to these elements [60,64,324–326]. The final microstructure of TMCP steels are composed of different phases and precipitates, which increases their complexity depending on their chemical composition. Depending on the application, one of the main aspects of steel production is to reduce the low carbon content in order to offer conditions for lower bainite formation [61] but lately the steel industry has started to develop tempered lath martensite and dual phases to produce grade X120.

The steel is in its trial phase, which has been developed for strain-based design application; this implies accomplishing microstructure complexity in order to enhance strength, but compromising toughness, ductility or weldability [84].

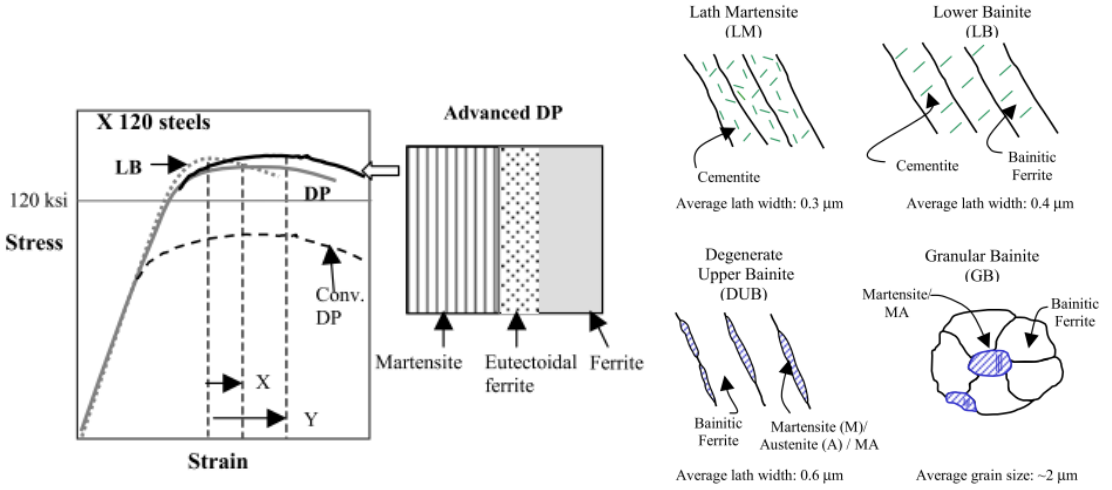

Figure 4-16 Schematic representation of strength improving and microstructure developing for the new generation of HSLA steels [84]

Manufacturing of API X80 and X100 have been focused to produce steel with a bainite structure or dual phase (bainite-ferrite) which enhances mechanical properties to increase deformability for high strain capacity, for example, in Arctic applications [68,82,316,327]. Figure 4-17 shows a novel metallurgical process which improves precipitation hardening by using very fine carbide, formation of MA constituents and recovery of dislocation density.

The effects of the microstructure, grain size, heat treatment, processing method on fracture toughness of micro-alloyed steel have been studied for many researches during recent years [75,328–330]. From those studies it was determined that cleavage fracturing resistance is controlled by grain size and bainitic/martensitic packets. Prior-austenite grain size was assumed to have an effect on cleavage fracture toughness; however, as mentioned by Lee et al. [331], in the event of cleavage fracture on toughness evaluation using pre-cracked specimens, the initiation was a consequence of a second-phase particle.

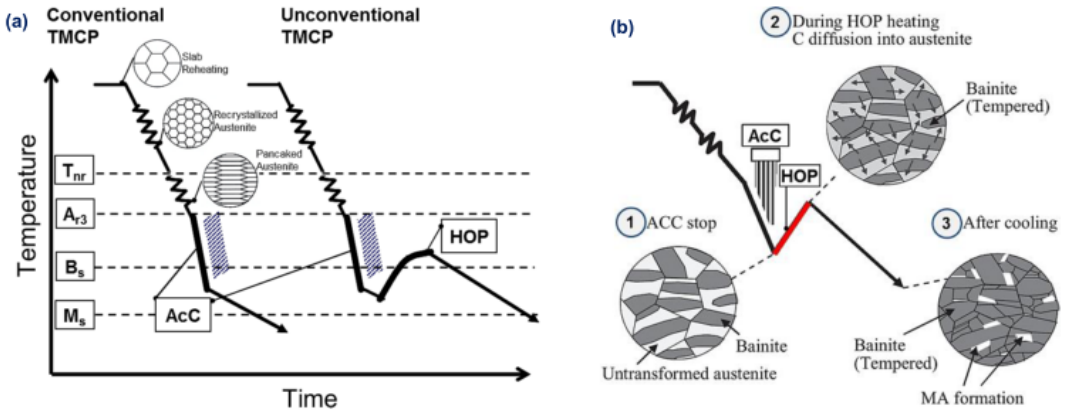

Figure 4-17 Schematic illustration of TMCP processing and microstructural transformation obtained by HOP process [332,333]

Besides, Lee et al. [331] determined that fraction carbides larger than critical size near the crack tip are considered to be the key parameters controlling the cleavage fracture, being more effective than grain size refinement. Parallel studies confirmed the importance of carbide distribution on mechanical and fracture toughness properties. Due to the different controls in terms of temperature process, chemical composition variability, microstructure combination, carbides precipitation and accelerated cooling, conventional and new steels offer a complicated scenario of their mechanical, weld and toughness properties [334,335].

Table 4-3 summarises the different types of microstructure feasible for different processing routes, as well as treatment during steel fabrication extracted from the literature available in the public domain. The scenario of manufacturing HSLA steels offers a multiplicity of options; however, the microstructure options determine a stronger impact on the final mechanical properties and toughness of the steel. From the steel performance point of view, the type of microstructure and chemical composition determine the degradation resistance of the material.

This matter has been recognised and studied for many years, however, even though the stronger investment done there is remaining contradictions which are still in place [61,63,65,84].

Table 4-3 Type of microstructure obtained from TMCP and ACC processes to manufacture HSLA steels [81]

Steel	Manufacturing process	Microstructure
X60	TMCP	• Banding polygonal ferrite-pearlite
X70	TMCP TMCP + QT TMCP + QT+ ACC	• Polygonal ferrite (PF) • Bainite (B) • Bainite (B)+Martensite (M)+Ferrite (F) • Fine*grained bainite
X80	TMCP + ACC	• Lower bainite (LB) • Ferrite (F)+Bainite (B) • Lower bainite (B)+Lath martensite (LM)
X100	TMCP	• Ferrite (F)+Bainite (B)
X120	TMCP + ACC	• Lower bainite (LB) • Ferrite (F)+Martensite (M) • Tempered lath martensite (TLM) • Degenerate bainite (DGB) • Granular bainite (GB)

As observed from Table 4-3 and Figure 4-6, a similar microstructure could be obtained with the same chemical composition only varying ACC and an equivalent mechanical property is achieved. Alloy composition and microstructure have been found to play an important role in the challenges of CO_2 corrosion. Both are particularly critical for the CO_2 corrosion susceptibility of low carbon steels and martensitic stainless steels [124]. In low carbon steels, the martensitic microstructure is more susceptible to localised corrosion than the ferritic-pearlitic microstructure due to less adherent and less crystalline $FeCO_3$ layers forming on the material surfaces [336] (Figure 4-18).

Some elements can help to improve corrosion or embrittlement resistance. Sulphur below 0.01% and additions of calcium or rare earth metals produce globular sulphide inclusions which improve HE resistance.

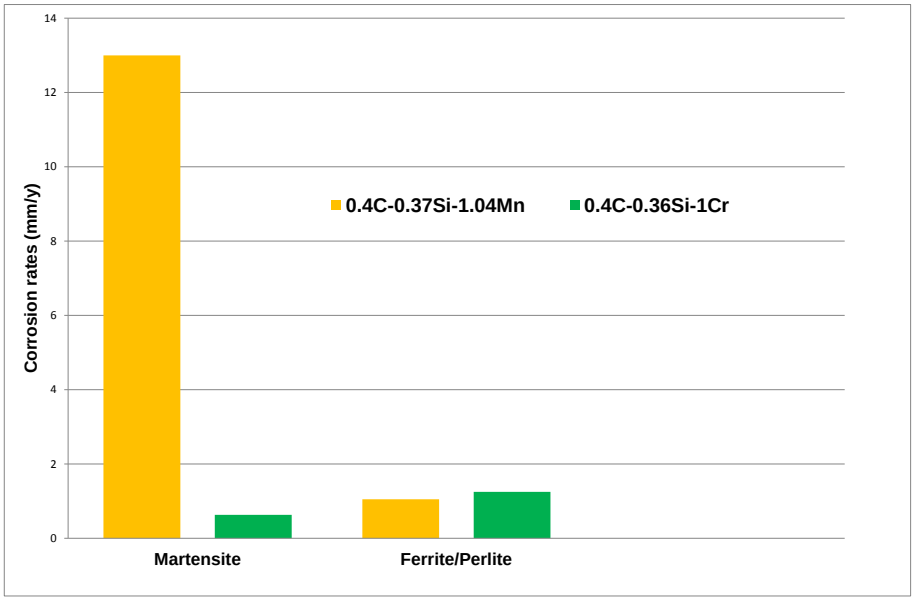

Figure 4-18 Effect of microstructure on CO_2 corrosion of low carbon steel (yellow) and Cr-steel (green) at 60°C, 30 bar CO_2, 5% NaCl, 1 m/s, 720 h

Similarly, segregation effects can be avoided by reducing the amount of carbon, manganese and phosphorus; however, it remains that manganese is beneficial in improving toughness by refining the ferrite grain size. Copper and nickel are also effective in improving resistance to HIC. At pH levels above 5, both form protective films which prevent the diffusion of hydrogen into the steel. Nevertheless, at pH levels below 5 their addition has little advantage due to a protective film not being formed. On the other hand, copper additions of 0.2-0.3% are extremely beneficial in preventing HIC, as determined by the NACE TM 0177-96 standard [302].

A ferrite-pearlite microstructure could be less resistant to corrosion phenomena when steels contain a martensite/bainite structure. López et al., [337] carried out a revision of this issue, finding that banding F-P is more susceptible to the corrosion of steel in CO_2 environments. Its resistance could be improved by adding chromium which was confirmed by Choi and Nešić et al [121,127,338]. Heat treatment is considered to be one of the factors that impact high corrosion rates.

Even though the mechanics of this phenomenon are not well-known yet, formation of $FeCO_3$ layers on the material surface could be protective but depend of the type of microstructure [125,339]. This will be discussed in section 4.3.6.

Hydrogen induced cracking (HIC) is an embrittlement of the steel which occurs when internal cracks are generated due to the recombination of hydrogen gases which are trapped in the lattice of the steel, inclusions or pearlite bands. This phenomenon is internal and does not require any external stress. Kittel et al., [141] studied HIC through immersion testing and hydrogen permeation. They determined that with 1 bar H_2S pressure and pH 4.5, the evolution of HIC is higher but required more than 200h exposures to crack initiation while at 0.1bar cracks were detected after only 96h exposure. The susceptibility of HIC is higher in APIX80 than X100 due to the former being constitutive for bainite lath while the latter, for ferritic/granular bainite, is less[336]. A similar finding was presented by Huang et al., [79] working with steels consisting of granular bainite and M/A (martensite/austenite).

From the microstructure point of view, the steels investigated in this research could be susceptible to corrosion or embrittlement by hydrogen taking into account the environmental conditions when they are exposed in flue-gas.

4.3.6.1.3 Mechanical properties of steel grades X100, X70 and X60

- **Tensile properties of HSLA steel (As-received)**

The results given in Appendix L and plotted in Figure 4-6, indicate that the tensile strength of the X100 plate in the longitudinal direction is lower while X60 and X70 meet the specification of the API 5L standard. From the microstructure analysis and tensile results obtained in this research, it is clear that the X100 plate has a lower yield and tensile strength, 560 MPa and 720 MPa respectively. Even though no SEM or TEM analyses were performed, micrographs obtained at 500X magnifications gave an indication that the higher percentage of white areas on the material bulk correspond to ferrite, resulting in lower materials strength[331,340,341].

Production of plates with yield stress between 620-720 MPa and tensile strength over the range 758-896 MPa to achieve high UEL and low Y/T ratio, can be accomplished by modifying the microstructure. The process implied minimising the contents of phosphorus, sulphur and oxygen with a thorough cleanliness treatment to prevent the presence of inclusion and segregation on the slabs. References [85,342–344] provide an explanation regarding the lower values of the mechanical properties of plates.

During the alloying process after TMCP, a multi-purpose interrupted cooling microstructure, a dual phase structure can be obtained. This dual phase of 10% martensite, 30% bainite and ferrite accomplishes the minimum values required in yield and tensile stress as well as Y/T and UEL. However, it is required that mechanical properties of plates can be maintained at the minimum requirement to achieve the target values during pipe forming and expanding, which increases tensile properties due to work hardening and coating aging [92], [266], [281]. Thus, it could be assumed that the yield ratio will increase after the process.

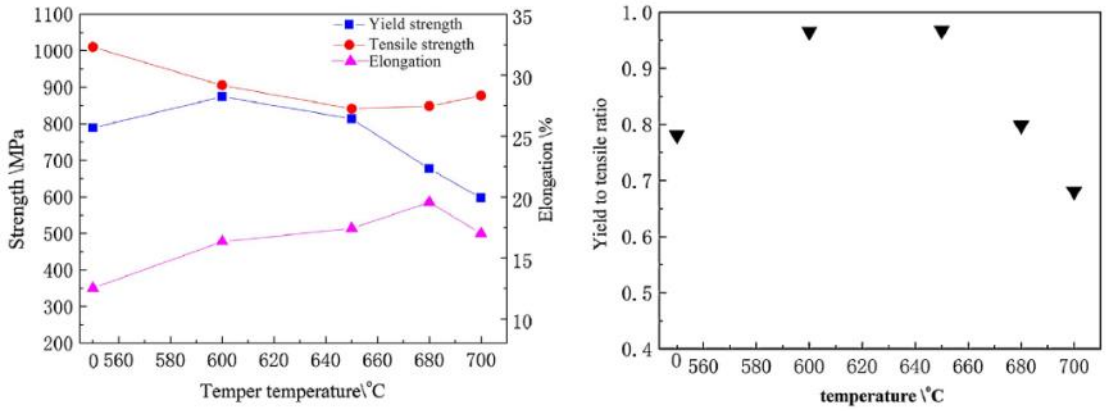

Figure 4-19 Modification of strength and Y/T ratio with temperature [282]

Figure 4-19 shows how the mechanical properties of the high strength steels can be modified with the temperature during the TMCP process. Variations of 50-100°C could increase 100 MPa in strength and 10% in elongation and Y/ratio. The yield strength above 560 MPa and 720 MPa in ultimate strength indicated that the steel could meet API X 100 specifications.

For the X60 and X70 grades there is an indication that the steels are in accordance with the standard values as well as the tensile properties required. Ductile fractures are characterised by three stages: void nucleation, void growing and void coalescence. The void initiation occurs at inclusion and when second-phase particles grow by plastic deformation of the contiguous matrix and coalescence, causing a small crack which is characterised by a zig-zag when the crack goes “slant”, forming the shear lips and finally the specimen breaks into two or more parts.

Ductile fractures are also characterised by cup-cone fractures, and stress triaxiality is a parameter that affects the ductile fracture which is defined as the ratio of hydrostatic stress to the von Mises equivalent stress. The triaxiality value varied with the type of specimen used; for example, for smooth round samples this value is 0.3-0.5, thick/thin plate 0.5-0.8 and cracked samples as CT geometries is 2.0-4.0 [283].

High levels of triaxiality appear when the material is strengthening and the maximum level of voids occurs in the middle of the specimen, resulting in high amounts of dimples. Once the void fraction reaches its critical value, failure is imminent. In reference [283] a polished fracture surface of a notched bar normal to the loading axis was examined revealing a secondary ductile crack orthogonal to the main crack.

This kind of crack is a consequence of delamination mechanics as a result of steel anisotropy which can limit the ductile of high strength steel severely. In addition, growing and coalescence are turning faster and the samples fail in a lower strain if triaxiality increases. Another parameter to consider is the load angle which is associated with a third invariant, the deviatoric stress tensor, affecting the ductile fracture.

A lode angle has some effects on void growth and coalescence. If this parameter decreases, the dimples tend to elongate during growing helping the coalescence process; however, some materials are insensitive while for others its effect is very important for the ductile fracture.

A particular problem arises which is associated with the anisotropy of tensile properties and toughness of the material. Joo et al., [345] in their publication titled “Mechanical anisotropy in steels for pipelines” described in detail the sources and issues derived from the mechanical anisotropy of TMCP steel. This anisotropy affected both tensile response and Charpy values.

The effect of delamination is related to separation on {100} a cleavage plane which decreases the upper shelf regime and irregular contraction (ovalisation) during tensile deformation is then visible. Ovalisation of the fracture surface in a round bar and bend in a rectangular cross section is a characteristic of the anisotropy, particularly on grade X70 and above which can be observed in Figures 4-12 to 4-15 above.

Mirone and Corallo [346] conducted an investigation to determine the mechanism of contraction of the diameter (elliptical shape) to calculate true stress and true strain using an experimental method on API X100 steel. The irregular fracture shape is a consequence of steel anisotropy and failure strain is not sensitive to the lode angle at high triaxiality on smooth samples at the failure point. In X100 steel, delamination has a direct relation with the ellipse morphology of the fracture surface during tensile tests of a smooth round bar.

Initially the shape section exhibited is round but as a result of anisotropic plasticity during material strengthening, an ellipse is formed, giving a ratio between large and small near 2. One of the axes is deformed substantially compared to the other due to necking and the plasticity effect [347]. Thus, a tensile load has a component that tends to open the crack while a high triaxiality factor is developed due to necking towards the internal cracks initiation.

Two kinds of cracks can be formed; however, these cracks are not formed in the same plane of the material. The central crack in a longitudinal direction is created in the L-T plane determining a splitting phenomenon presence. This splitting or delamination happen when two separate strips are formed which are responsible for holding the load until final rupture.

This phenomenon was observed in this investigation during a tension test of strip samples, which is shown in Figure 4-20.

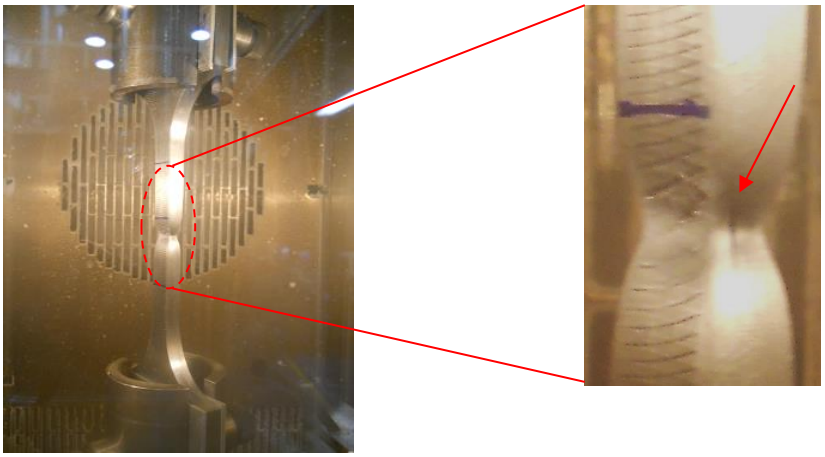

Figure 4-20 Presence of delamination on necking zone of strip sample X100 steel during tensile test which is highlighted by the red arrow

In summary, according to what has been described above, delamination is a particular type of failure on hot rolled plates. An opening force is required and high triaxiality has to be present for failure to occur under these mechanics.

These two driving forces have been reported in different investigations carried out in Charpy, CT and tensile test on steels X70, X80 and X100. Surface analysis has determined that splitting has occurred in the centre of the thick specimens where the triaxiality is high and the necking actuates as the opening force.

- **Tensile properties of steel exposed in simulated flue-gas**

Procedures to determine embrittlement susceptibility of steels in H_2S (hydrogen sulphide) have been covered under NACE TM 0177, MR 0175, TM 0284 and BS EN ISO 15165-2 standards. They complement each other to cover the different mechanisms and type of embrittlement in the presence of H_2S. Hydrogen Induced Cracking (HIC) and Sulphide Stress Cracking (SSC) are two mechanisms that affect pipelines, the difference being that the former does not require any external stress while the latter requires an applied stress.

Presence of SO_2 (sulphur dioxide) is related to the formation of H_2SO_4 (sulphuric acid) or H_2SO_3 (sulphurous acid) in wet environments. As mentioned before, the present research is dealing with samples exposed in supercritical CO_2 with free water adding either SO_2 or H_2S. Therefore it was anticipated that the former atmosphere implied pitting or corrosion damage while the latter involved hydrogen damage by HIC mechanism.

The presence of hydrogen in steel affects the tensile ductility and causes early material failure. The mechanism is unclear but three theories have been accepted to explain the phenomenon: the planar pressure theory, the reduced energy theory and the decohesion theory [283]. HE is characterised by its small plastic deformation and the fracture mode is brittle cleavage or quasi-cleavage. In hydrogen, atmosphere concentrations greater than 10 ppm (0.001%) crack formation could be present without the application of an external force while steels with yield stress above 1000 MPa just 1 ppm is enough to induce crack formation.

Ductility expressed in terms of percentage was determined in one sample due to space constraints for locating more samples on the SC^3 rig. Results are given in Figures 4-21 to 4-23 for steels X100, X70 and X60 respectively. The influence of time of exposure to the atmosphere is minimal and no significant impact on mechanical properties is determined.

Ductility expressed in terms of percentage was determined in one sample due to space constraints for locating more samples on the SC^3 rig. Results are given in Figures 4-21 to 4-23 for steels X100, X70 and X60 respectively. The influence of time of exposure to the atmosphere is minimal and no significant impact on mechanical properties is determined.

It is important to underline that ductility does not change with time or impurity for the steels investigated. It is noted that steel grade X100 ductility is roughly 20%, X70 is 14% and X60 achieves 34%, showing non-sensitivity to HE or corrosion mechanisms during the holding time.

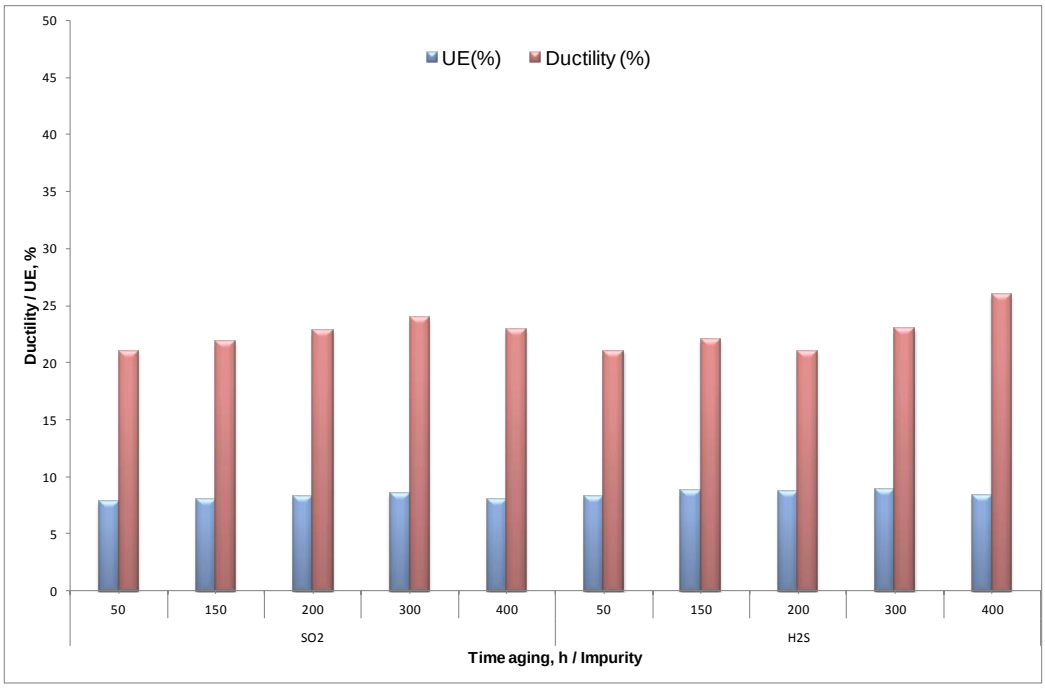

Figure 4-21 Ductility vs. aging time grade X100

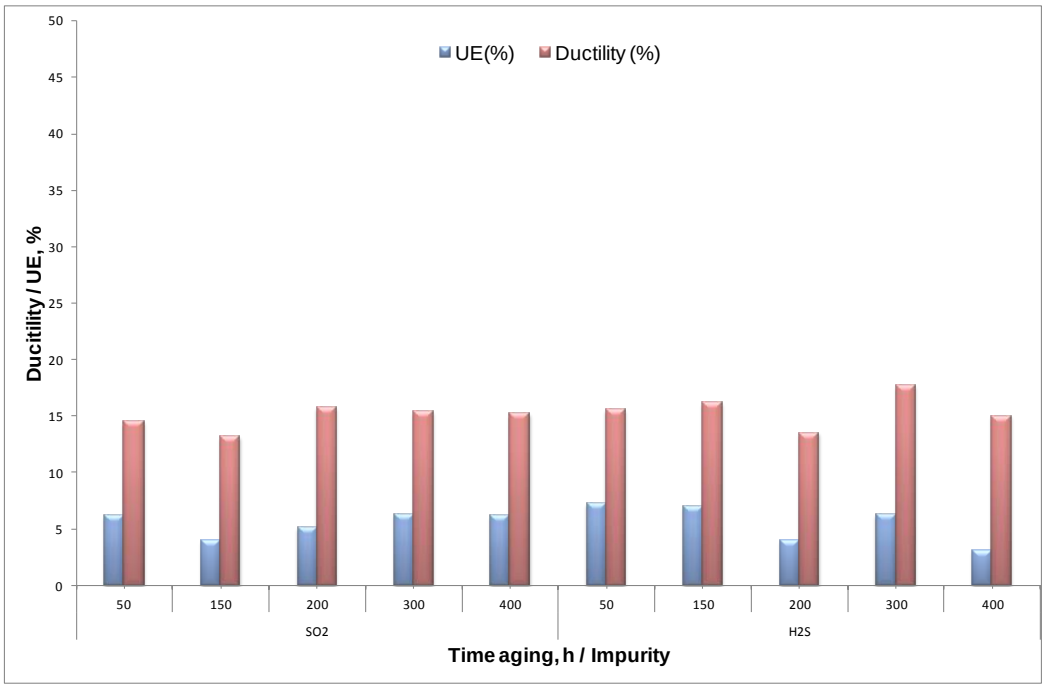

Figure 4-22 Ductility vs. aging time grade X70

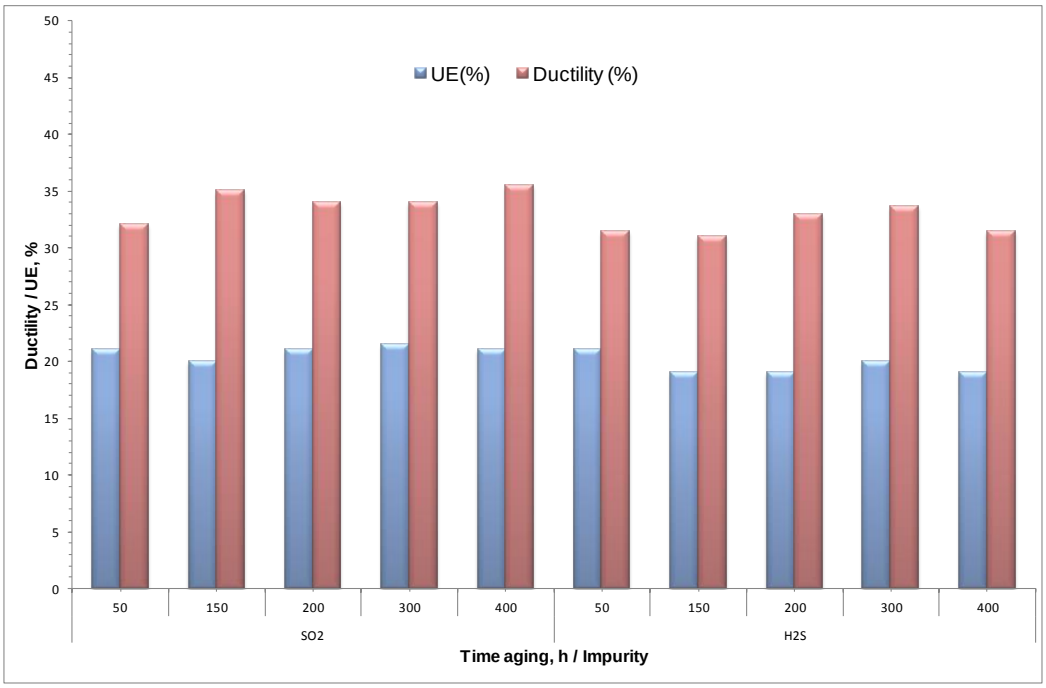

Figure 4-23 Ductility vs. aging time grade X60

The explanation for this is probably done by considering different aspects such as:

- Alloying elements
- Microstructure
- Diffusion of hydrogen into material lattice
- Entrapping hydrogen on interfaces or lattice imperfections
- Hydrogen diffusion environment
- Time of testing after exposure in flue-gas

The effect of the alloying element on HIC is a result of the effects on strength, microstructure and segregation. As mentioned before, Cu reduces the uptake of hydrogen which is increased when CO accompanies Cu. C, Si, Cr, Ni and V have reduced effects on their susceptibility. Forming a film on the surface of the material is promoted by Bi, Pd and Pt; however, their use is very expensive. Ca, Al, Ce and rare earth metals, used during foundry processes, can precipitate or form inclusions which raise hydrogen concentration.

In terms of microstructure such as ferrite/pearlite, upper/lower bainite, martensite (Q&T), these are considered harmful for materials immersed in H_2S atmospheres [79,348,349]. One characteristic of HIC is the formation of a crack or blister in the material occurs due to microstructural heterogeneities in the steel, making these zones stronger areas of hydrogen traps. However, to evaluate the effect of hydrogen, different methods for this purpose have been implemented, such as electrochemical charging which is preferentially used in hydrogen research.

In this investigation, the mechanical degradation due to exposure flue-gas was studied, allowing the hydrogen to diffuse naturally under transport conditions of supercritical CO_2. For hydrogen, one aspect to consider was the impact on mechanical evaluations due to the ingress of H_2 or being trapped in the material. Similar considerations were assumed when SO_2 was present during the test; however, it was also assumed that local or pitting attacks are dealing with loss of strength or ductility.

From the results obtained, in both the tensile test and fractography examination no significant differences have been noticed for the two impurities evaluated. The engineering stress-strain indicated a normal tendency showing, in the case of hydrogen, that it was not present on the material or if it was trapped during the exposure process that it had naturally escaped from the pre-exposed samples.

It is proved for the higher percentage of ductility achieved for specimens exposed either in H_2 or SO_2 atmospheres. Similarly, fracture surfaces showed a high grade of deformation, which is an indication of ductile fracture, and that the presence of brittle areas is restricted to very small zones. Probably cleavage facets or quasi-cleavage could be present but the magnification used does not allow clear identification of this.

An investigation carried out for Chattoraj et al.,[350], probably on grade X60 or lower, established that samples tested immediately after exposure in a hydrogen environment and others on different days after exposure indicated

ductility differences (Figure 4-24a). Restoration of the ductility is presented on samples stored for several days while for those tested after exposure the effects on their ductility was evident.

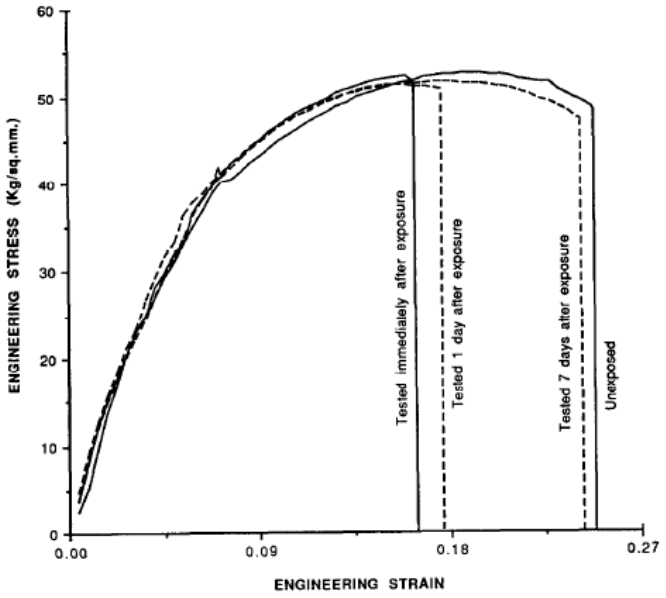

a) Engineering stress-strain curve for specimens tested at different time intervals after exposure in a sour environment

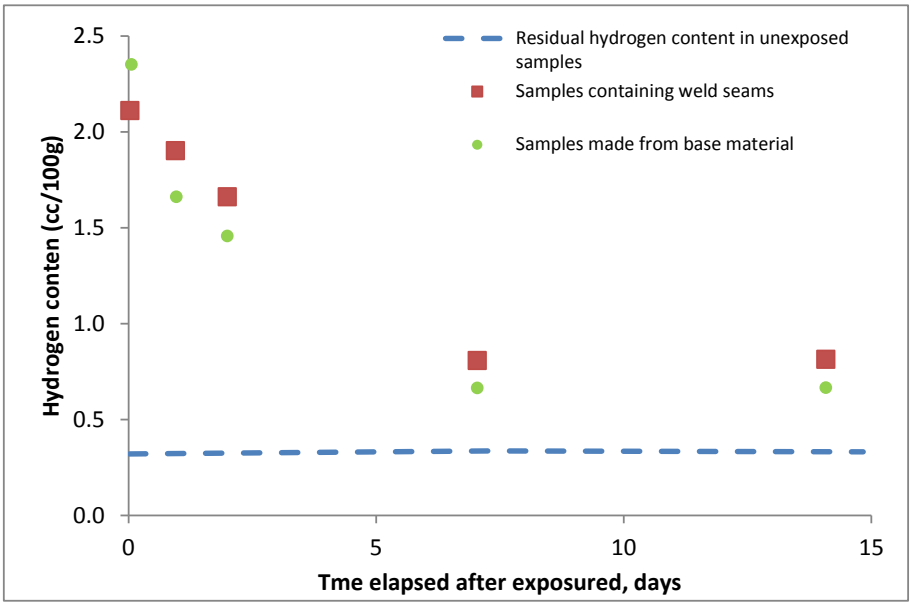

b) Hydrogen content diffusion by natural process

Figure 4-24 Engineering stress-strain curve and natural diffusion of hydrogen content of samples exposed in a sour environment (After [350])

Measurement of the total hydrogen was determined and the concentration values show decreases to values close to the unexposed samples as shown in Figure 4-24b. Zhang et al. [351] studied the correlation between hydrogen-induced stress and HE when using steel API X80, by introducing hydrogen through cathodic charging at different current densities. Using SSRT, test fracture stress and elongation were evaluated and from the results it was found that hydrogen induced both plastic loss and strength loss (Figure 4-25).

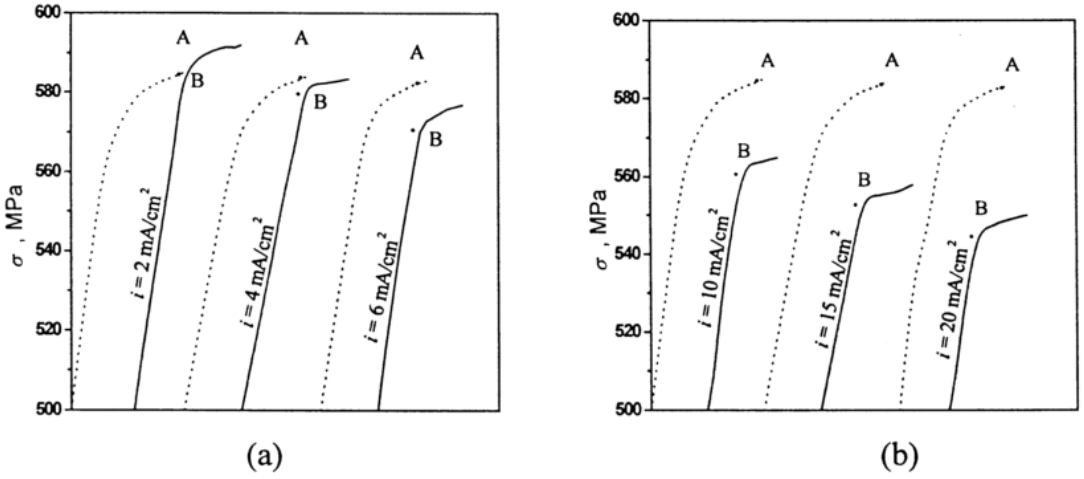

Figure 4-25 Stress-strain curves of six specimens before (dotted lines) and after charging at various current density (solid lines)[351]

Kim et al [352] studied the X70 grade using different test solutions and varied combinations of P_{H2S} and pH value. It was determined that the key parameter affecting HIC is P_{H2S} rather than the pH value of the test solution. An API 5L X100 steel was studied by Jin et al. [260] by means of cathodic polarization to introduce hydrogen.

They found that the concentration of hydrogen in the steel increased with hydrogen-charging current density and that HIC occurs when the critical value is reached. The concentration only was achieved in the steel after 20 h of charging at 30 mA/cm^2. Blister and HIC are presented by crack formation which is associated with Al- and Si-enriched inclusion, rather than MnS inclusion.

4.3.7 Fracture toughness derived from Charpy absorbed energy

Charpy energy data for steel grades X100, X70 and X60 were determined both for as-received and aging material. The temperature range was –196°C up to RT for as-received material while for aging samples it was –20°C. The impact energy absorbed for each material condition and specimen type was fitted with a tanh hyperbolic function to obtain transition temperatures' upper and lower shelf energy represented by the relationship in equation 4-1.

$$Y = A + B\tanh[(T - T_{DBTT})/C] \quad \textbf{(4-1)}$$

Where A, B, C and T_{DBTT} are fittings parameters while T is the test temperature. A represents Charpy energy at transition temperature, T_{DBTT} is the mid transition temperature, B is the energy located in the middle between plateaus and C is the temperature range of the Charpy energy transition. More details are explained in reference [181]. The transition temperature has been determined at half the jump between the brittle and ductile plateaux contained in parameter T_{DBTT}. Table 4-4 summarises the values of the four constants as well as the transition temperature obtained.

Table 4-4 Values of constants of the tanh hyperbolic function for the steels tested

Steel	A	B	C	T_{DBTT} (°C)
X100	49.3	43.67	63.64	-17
X70	46.6	45.9	73.5	-70
X60	14.6	10.1	14	-36

Figures 4-26 to 4-28 present the variations of energy versus temperature for virgin materials, while Figures 4-29 and 4-30 summarise the energy absorbed for steels exposed in anthropogenic CO_2.

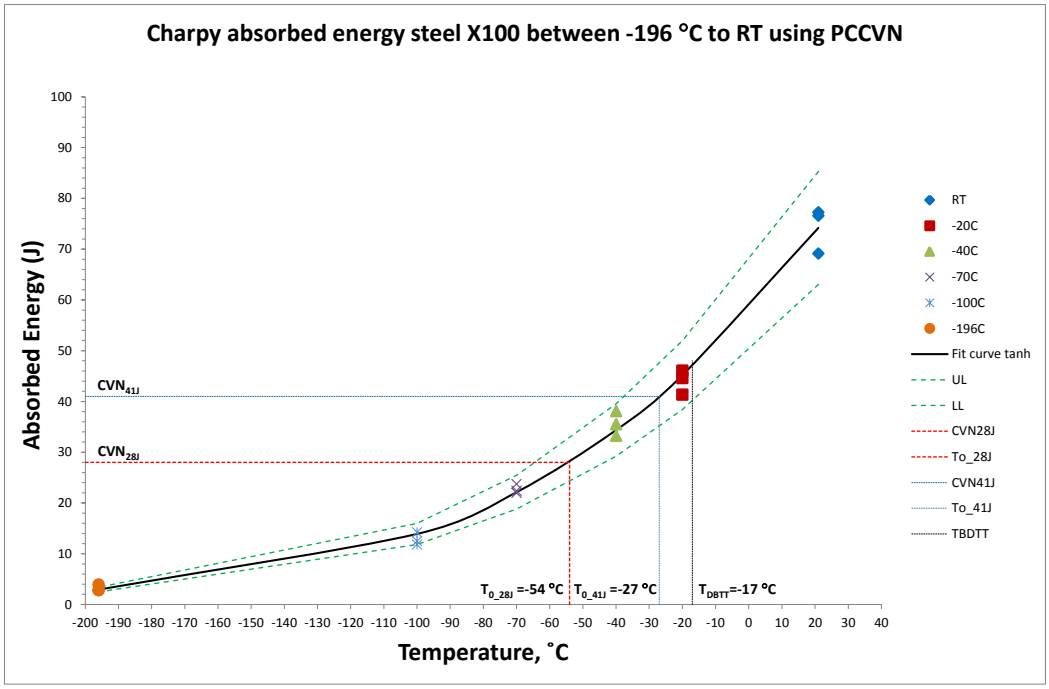

Figure 4-26 Absorbed energy vs. temperature for grade X100. B=1T

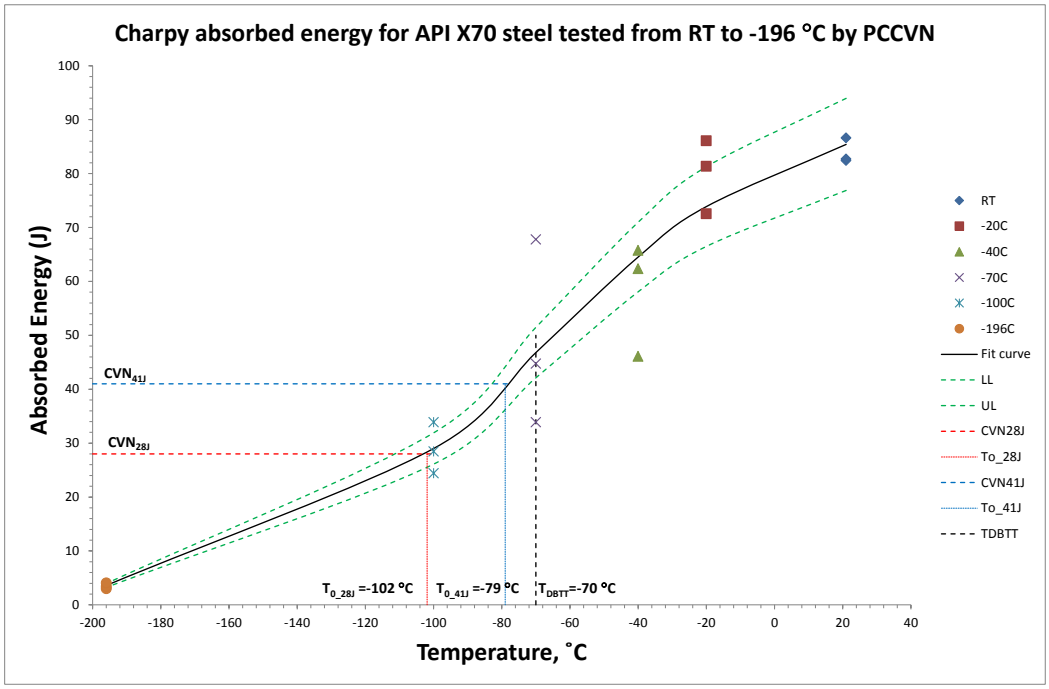

Figure 4-27 Absorbed energy vs. Temperature of grade X70. B= 1T

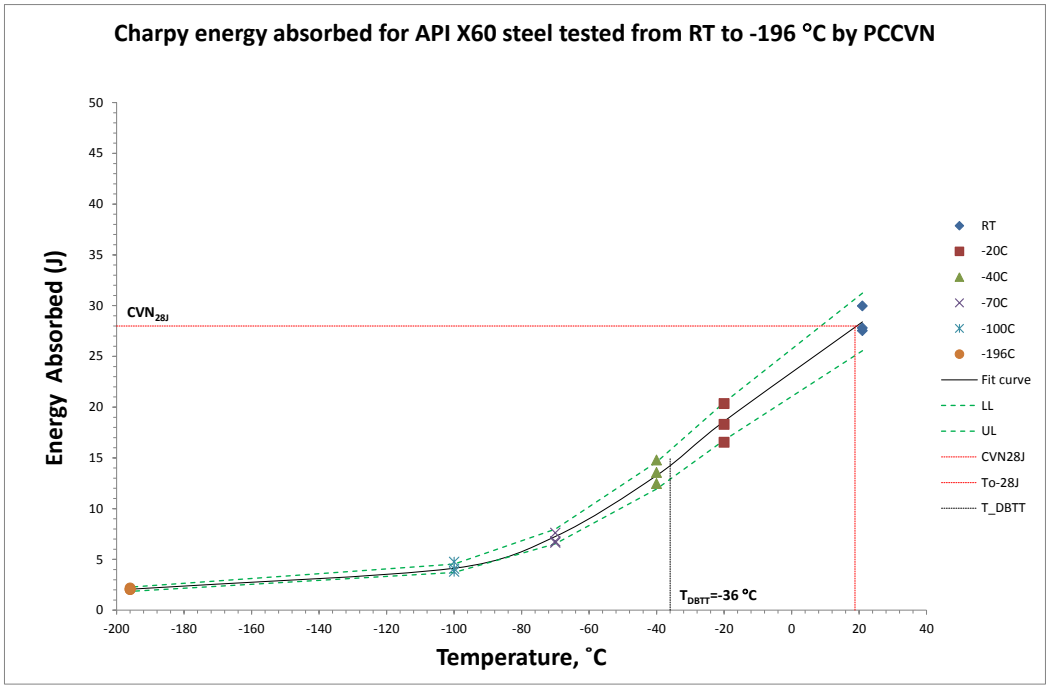

Figure 4-28 Absorbed energy vs. Temperature of grade X60. B= 3/4T

Transition temperatures were determined at conventional levels of 28 joules and 41 joules which are reported in Table 4-5. In addition, a transition temperature T_0 was obtained using the empirical relationship given in equations 4-2 and 4-3 [177], [190].

$$T_{0\_28J} = T_{28J} - 18°C\ (\pm 15°C) \quad \textbf{(4-2)}$$

$$T_{0\_41J} = T_{41J} - 24°C\ (\pm 15°C) \quad \textbf{(4-3)}$$

Table 4-5 Transition temperatures at 27 J and 41 J, °C

Steel	T_{28J}	T_{41J}	T_{0_28J}	T_{0_41J}
X100	-54	-27	-72	-51
X70	-102	-79	-120	--103
X60	19	-	1	-

Figures 4-29 and 4-30 show the variation of the energy absorbed for the steels exposed in SO_2 and H_2S impurities respectively over the range 50 h to 400 h.

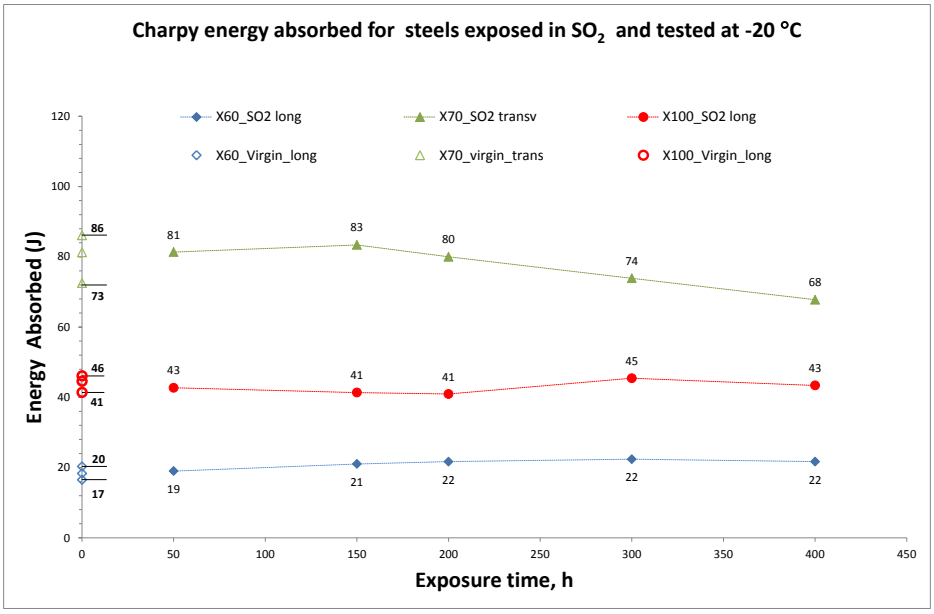

Figure 4-29. Charpy absorbed energy values for API X100, X70 and X60 steel exposed on SO_2 at 90 bar and 45°C.

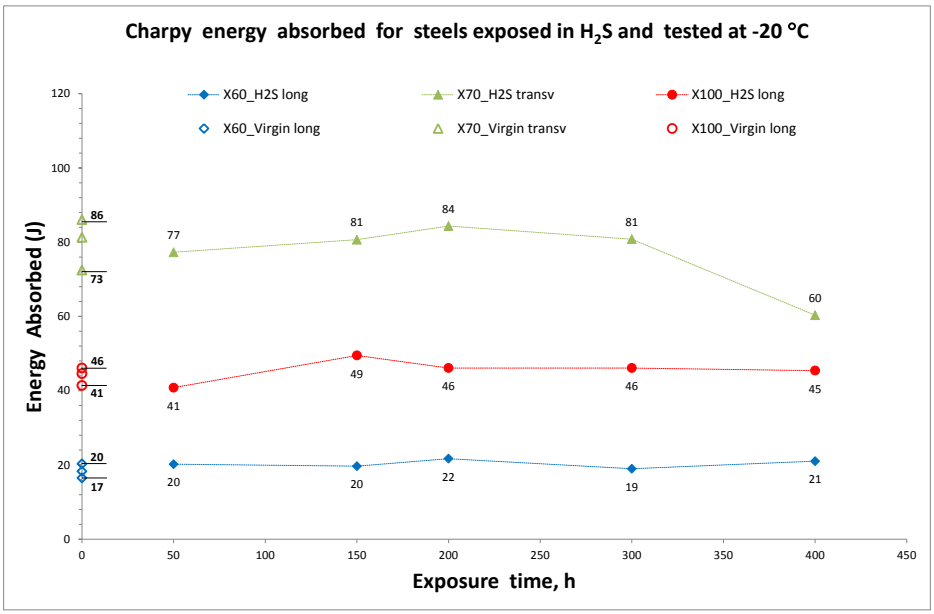

Figure 4-30. Charpy absorbed impact energy values for API X100, X70 and X60 steel exposed in H_2S at 90 bar and 45°C.

A comparison of the energy obtained with virgin material (placed on the Y axis) indicated that no significant variations are present for steel X60 and X100.

However in grade X70 (green triangles) and for both impurities, it was observed that a slight deflection of the energy at 400 h could be an indication that the environment could have some effects on the material. However, to base a conclusion on this finding is not appropriate as only one specimen was tested and maybe it could have been part of the experimental scatter.

Due to the shape of the Charpy transition, there is no unique correlation capable of evaluating for the lower shelf, transition and upper region. There are three correlations commonly used to link energy absorbed with toughness which are part of SINTAP. In this research the energy absorbed with fracture toughness was initially undertaken following references [189,190,353] and represented by equations 4-4 and 4-5.

$$K_{mat} = 19CVN^{0.5} MPa\sqrt{m} \quad \textbf{(4-4)}$$

$$K_{mat} = 12CVN^{0.5} MPa\sqrt{m} \quad \textbf{(4-5)}$$

The toughness values calculated using both correlations are summarised below in Table 4-6 for as-received material and Table 4-7 for aging specimens respectively. It can be seen that the difference between Eq. 4-4 and 4-5 reaches a 37% disparity. This dissimilarity is presented in both sets of data.

From the calculations realised and the literature available in the public domain it was found that the correlations used are only applicable for conventional CVN samples rather than pre-cracked Charpy. It was required to find an empirical correlation to correlate fracture toughness taking into account the Charpy configuration. However, after an exhaustive search it looks as if the correlation does not exist for the test conditions carried out.

Table 4-6 Fracture toughness evaluation of virgin HSLA steels by Marandet & Sanz and SINTAP correlation

Steel	T (°C)	$CVN_{exp\_wv\_avg}$ (J)	$K_{Ic\ exp\ wv\ avg}$ (MPa√m)	
			M & S	SINTAP
X100	21	74.3	164	103
	-20	44.0	126	80
	-40	35.6	113	72
	-70	22.7	90	57
	-100	12.8	68	43
	-196	3.2	34	21
X70	21	84	174	110
	-20	80	170	107
	-40	58	144	91
	-70	49	131	83
	-100	29	102	64
	-196	4	35	22
X60	21	28.4	101	64
	-20	18.4	81	51
	-40	13.6	70	44
	-70	7.0	50	32
	-100	4.2	39	25
	-196	2.1	27	17

Table 4-7 Fracture toughness of aging HSLA steels by Marandet & Sanz and SINTAP correlation

Steel	Impurity	Aging	$CVN_{exp\_wv\_avg}$	$K_{Ic\_exp\_wv\_avg}$ (MPa√m)	
		(h)	(J)	M & S	SINTAP
X100	SO_2	50	43	124	78
		150	41	122	77
		200	41	122	77
		300	45	128	81
		400	43	125	79
	H_2S	50	41	121	77
		150	50	134	84
		200	46	129	81
		300	46	129	81
		400	45	128	81
X70	SO_2	50	81	171	108
		150	83	173	110
		200	81	170	107
		300	74	163	103
		400	68	156	99
	H_2S	50	77	167	105
		150	81	171	108
		200	84	174	110
		300	81	171	108
		400	60	148	93
X60	SO_2	50	19	83	52
		150	21	87	55
		200	22	88	56
		300	22	90	57
		400	22	88	56
	H_2S	50	20	85	54
		150	20	84	53
		200	22	88	56
		300	19	83	52
		400	21	87	55

4.3.7.1 Fracture surface characterisation

Figure 4-31 (a-f) shows the lower magnification fractographs of Charpy impact sample fractures at lower temperatures and RT. At 21°C Figure 4-31 (b, d, f) shows separations that formed in the crack propagation direction for the three steels, and only grade X70 still presented delamination at –70°C. Shear lips are observed in all steels at both edges of the samples impacted upon, decreasing in width as the temperature decreased. Cleavage fractures can be observed on grade X60 at 21°C as well as at –70°C. A mixture of brittle and ductile morphology is observable on the fracture surface of grade X100 while in grade X70 ductile fracture exists at both temperatures.

For steels exposed in SO_2 impurity, the fracture surface of samples X70 and X100 show separation in the middle of the thickness. Even though the shear lips are not visible at the magnification utilised, the separations were observable during the analysis as seen in Figure 4-32(e, d, f). In the impact specimen of X100 steel exposed in H_2S and tested at –20°C showed in Figure 4-33f, there is an indication of delamination in the middle of the thickness at 400 h exposure just for this one.

Investigation carried out for Shin et al. [218] and Yang et al. [354] on API X80 and X100 steel show the effect of microstructure and texture on delamination of these types of steel. Although their work was developed using conventional Charpy samples, the effect of bainite grain orientation, temperature and work hardening due to hammering revealed that all these aspects have a strong effect on the separation mechanism.

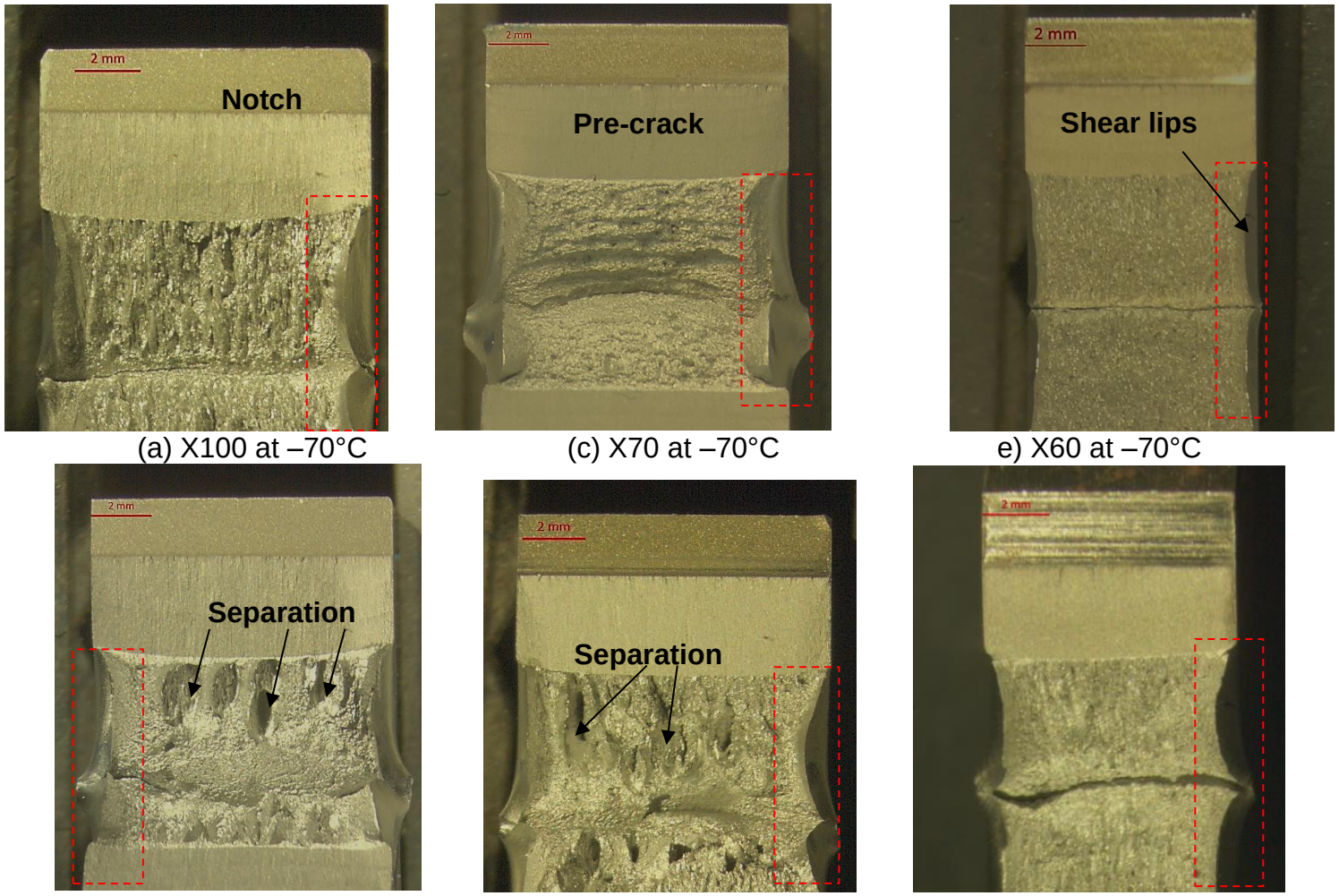

(a) X100 at –70°C (c) X70 at –70°C e) X60 at –70°C

(b) X100 at 21°C (d) X70 at 21°C f) X60 at 21°C

Figure 4-31 Fracture surface of samples obtained at low magnification on virgin PCCVN samples

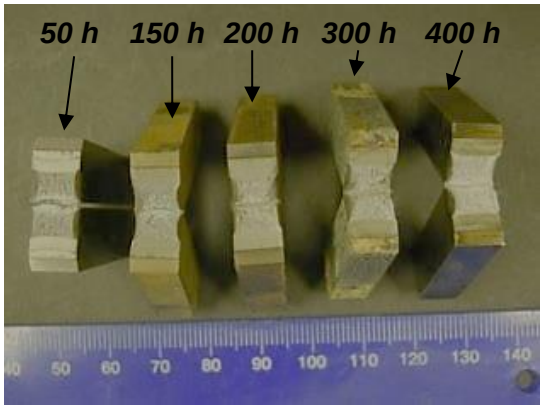

(a) X60 set of samples

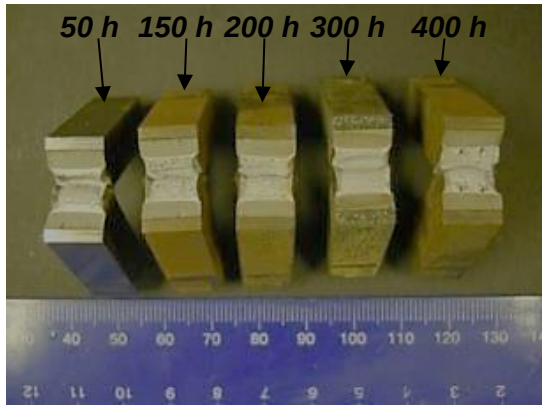

(b) X70 set tested

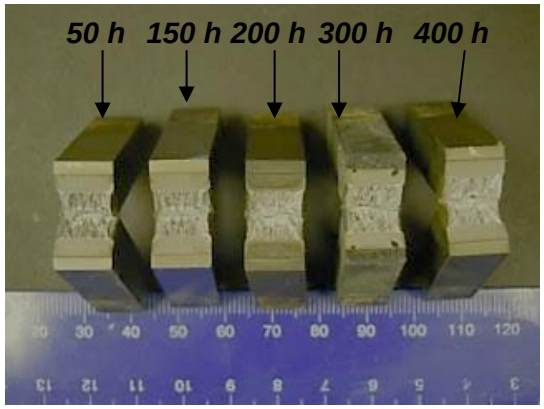

(c) X100 set

(d) X60 at 400h

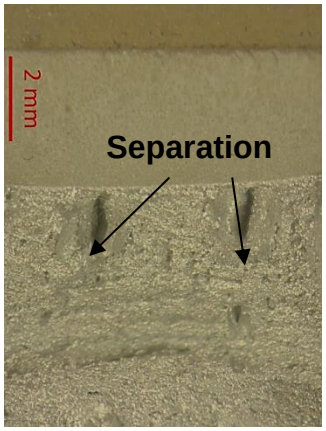

(e) X70 at 400h

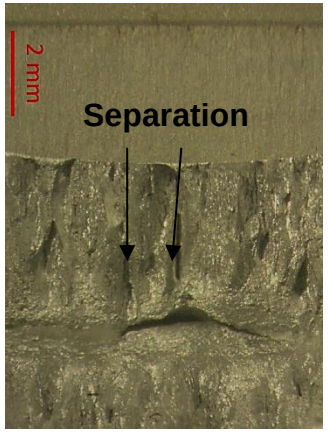

(f) X100 at 400h

Figure 4-32 Fracture surface of pre-cracked Charpy exposed in SO_2 environment and tested at –20ºC

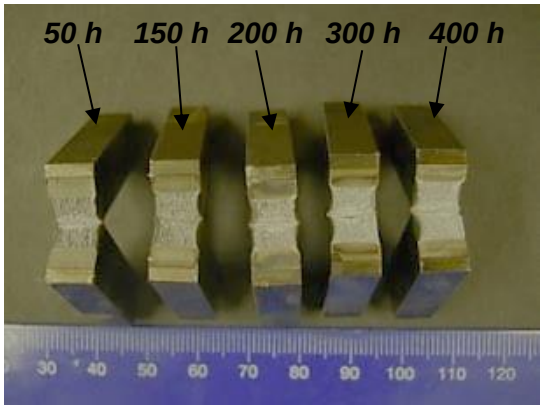

(a) X60 set of samples

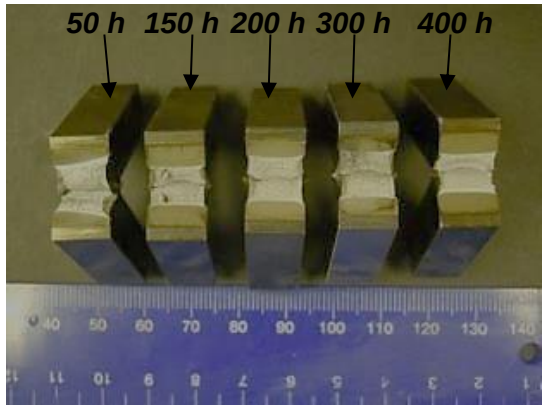

(b) X70 set tested

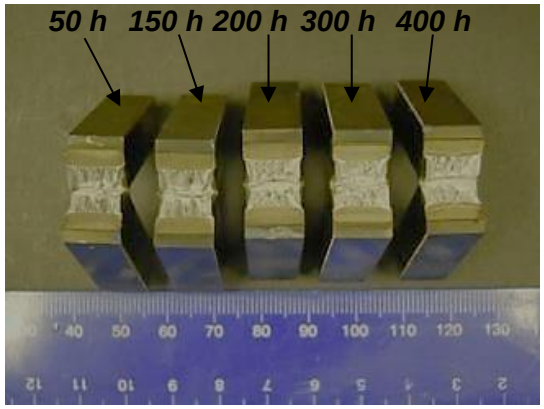

(c) X100 set

(d) X60 at 400h

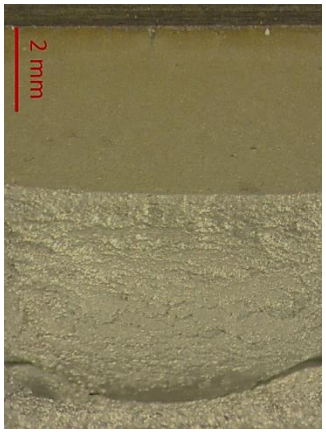

(e) X70 at 400h

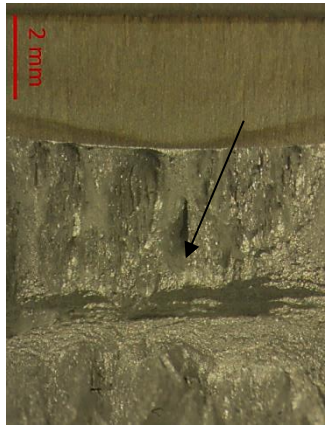

(f) X100 at 400h

Figure 4-33 Fracture surface of pre-cracked Charpy samples exposed in H_2S and tested at –20ºC

4.3.7.2 Discussion results fracture toughness

The data summarised in Tables 4-6 and 4-7 gave an estimation of the fracture toughness as a function of energy absorbed for the material during the test. The equation to correlate Charpy energy with fracture toughness was selected from the equations developed for lower bound and available in the public domain. It determines mainly the minimum fracture toughness value to establish the ductile-brittle transition phenomenon which is the main area of interests when anthropogenic CO_2 is transported by pipeline.

Determination of the T_{DBTT} temperature was analysed by the hyperbolic tanh curve fitting model used to study energy variation with temperature [181]. The model fits very well for X60 and X70 data but was uneven for X100. The reason for this behaviour was due to the insufficient range of data, the asymptote was ill-defined and the parameters are not well determined. This issue was analysed by Urwank [355] who established that this regression algorithm may fail to find the global point in solution space and may only calculate the local best point.

The ASME Code cases N-629 and N-631 approaches have been used for a long time to determine an index temperature which can be correlated with the temperature of transition on the low bound. An alternative method is the Master Curve (MC) [187] that determines an index temperature parameter namely, $T_{o,}$ which is directly associated with a stress intensity factor equal to 100 $MPam^{0.5}$ value. The MC approach relies on the ASTM E 1921 standard which covers all the aspects to determine T_0.

The ASME and MC methodologies, however, need to meet certain conditions to be valid, as follows:

- The impact energy could be obtained from standard or sub-size notched samples.
- If pre-cracked Charpy specimens are used an instrumented impact tester has to be used.
- An instrumented impact test should be performed and K_{Jc} is calculated from the force-displacement value.

- If sufficient tests at appropriate temperatures are not available T_0 cannot be obtained.
- Tensile test results at the test temperature should be available to perform the analysis. Yield strength should be the dynamic yield strength not the static one.
- ASTM E1921-13 requires K_{Jc} value input and not K_{Ic} input.
- Conversion $K_{Jc}=19*CVN^{0.5}$ is very approximate on standard notched samples but no correlation could be applied with pre-cracked Charpy specimens.
- Charpy-V-K_{Ic} correlation is available for standard sized notched specimens based upon cleavage fracture on the 28J (35 J/cm^2).

Sokolov and Nanstand [356], Corwing et al. [48], Lucas et al.[357] and Kumar et al. [358] have been working to develop a correlation of absorbed energy between full-size and sub-size Charpy specimens. The method consists of establishing an empirical ratio between the upper shelves of these two specimens.

Wallin [187,202] developed an empirical correlation which intended to determine Charpy energy values from sub-size specimen to full-size while that of Schindler and Kalkof [59] introduced an analytical approach based on J energy which can estimate fracture toughness in terms of K_{Jc} parameters. All the above-mentioned works have in common that the estimation is applicable to correlate energy from sub-size samples to full-size and the test has to be performed on static conditions or in dynamic circumstances using an instrumented machine.

But no correlation exists nor it is allowed to determine fracture toughness from energy absorbed by testing pre-cracked samples without accomplishing the conditions mentioned before. To overcome the issue and assuming that cross section areas have a correspondence, a procedure is proposed. This method relied on temperature as the parameter, looking to establish a correlation that allows the association of energy with fracture toughness.

The standard Charpy-V test is based on the 28 J (35J/cm^2) impact energy level transition temperatures. 35J/cm^2 is related to the specify energy which is the energy absorbed in Joules (J) divided by the area in cm^2 of the full-size Charpy specimen. Figure 4-34 summarises the phenomenon.

It can be observed that material with a lesser cross section area (A2) offers less resistance to be broken than a sample with a bigger cross section (A1). Based on this concept a correction or normalization factor was introduced taking into account that resistance to breaking materials has the same mechanical properties and fracture toughness, and their areas have an energy correspondence following the assumption in equation 4-6, thus:

$$Resistencia = f(toughness + amount\ of\ material\ present) \quad \textbf{(4-6)}$$

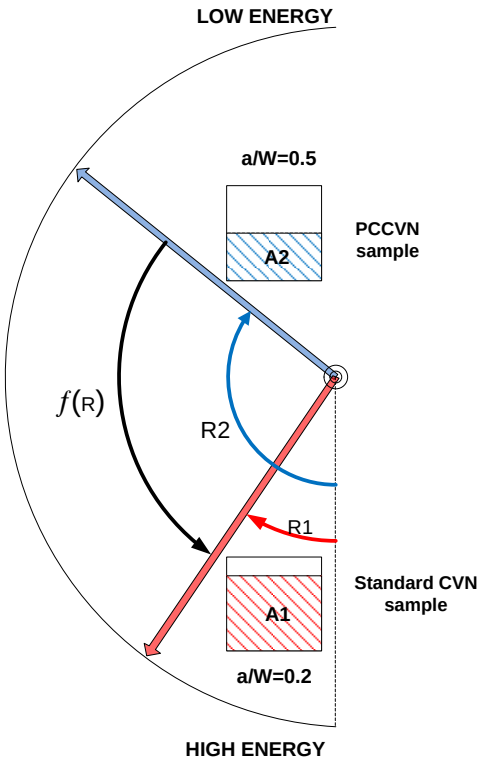

Figure 4-34 Scheme of the final position of the pendulum after breaking a conventional sample (Red) and a PCCVN sample (Blue)

Establishing a correspondence between Charpy conventional and pre-cracked Charpy as a function of the geometrical parameter of the cross section area equation 4-7 is obtained:

$$\frac{Energy_{PCCVN}}{Geometrical\ parameter_{PCCVN}} = \frac{Energy_{CVN}}{Geometrical\ parameter_{CVN}} \quad \textbf{(4-7)}$$

Equation 4-7 can be transformed as:

$$Energy_{CVN} = CF Energy_{PCCVN} \quad \textbf{(4-8)}$$

To solve equation 4-7, the ratio factor of geometrical parameters, from equation 4-8, is calculated which can be used to correct the energy values obtained from PCCVN to CVN. Charpy energy data were scaled and the curve fitting method was applied to determine $\boldsymbol{T_{DBTT}}$ which characterises the ductile-brittle transition temperature.

As a result the absorbed energy and temperature was shifting. However, it is noticeable that if the DBTT temperatures calculated may not be accurate a sophisticated fitting curve approach can be applied or the appearance of the ductile-brittle transition should be used as a parameter to evaluate DBTT in terms of cleavage (50%).

Figures 4-35 to 4-39 show the results obtained from the normalisation accomplished. Table 4-8 summarises the new transition temperatures obtained as a result of the correlation applied.

Table 4-8 Transition temperatures at 27 J and 41 J, °C after scaling energy absorbed

Steel	T_{28J}	T_{41J}	T_{0_28J}	T_{0_41J}	T_{DBTT}
X100	-88	-63	-106	-87	-27
X70	-125	-106	-143	-130	-69
X60	-23	-	-41	-	-24

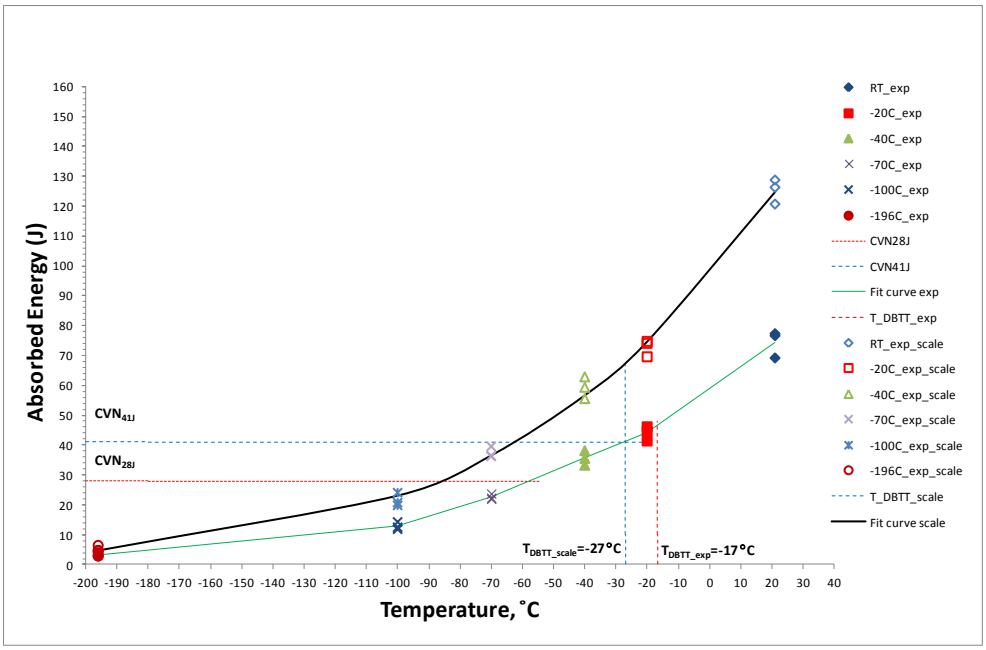

Figure 4-35 Absorbed energy vs. Temperature for grade X100. B=1T

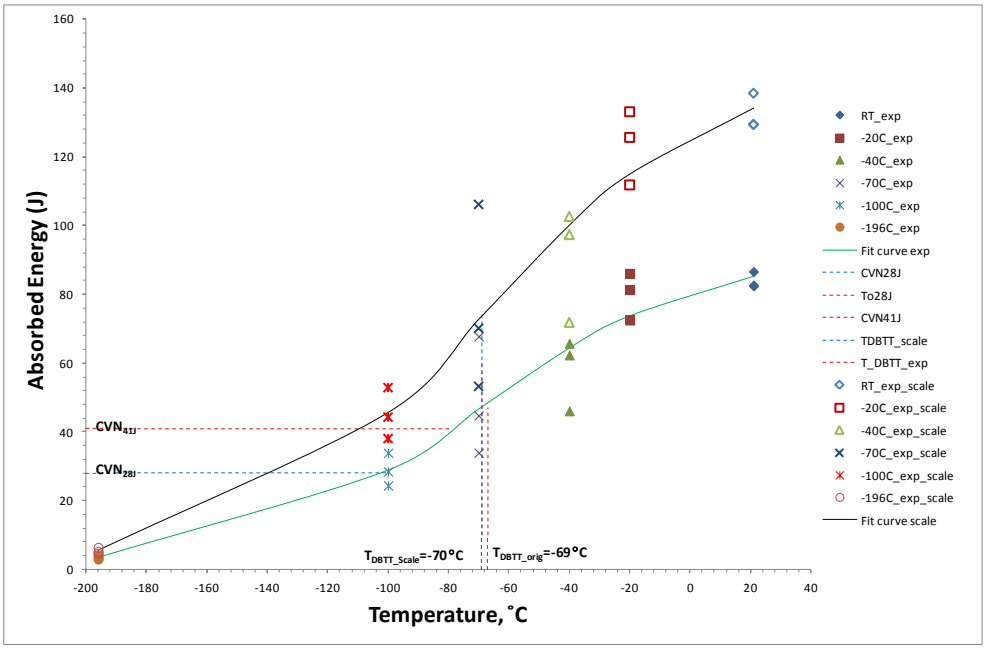

Figure 4-36 Absorbed energy vs. Temperature. Grade X70. B= 1T

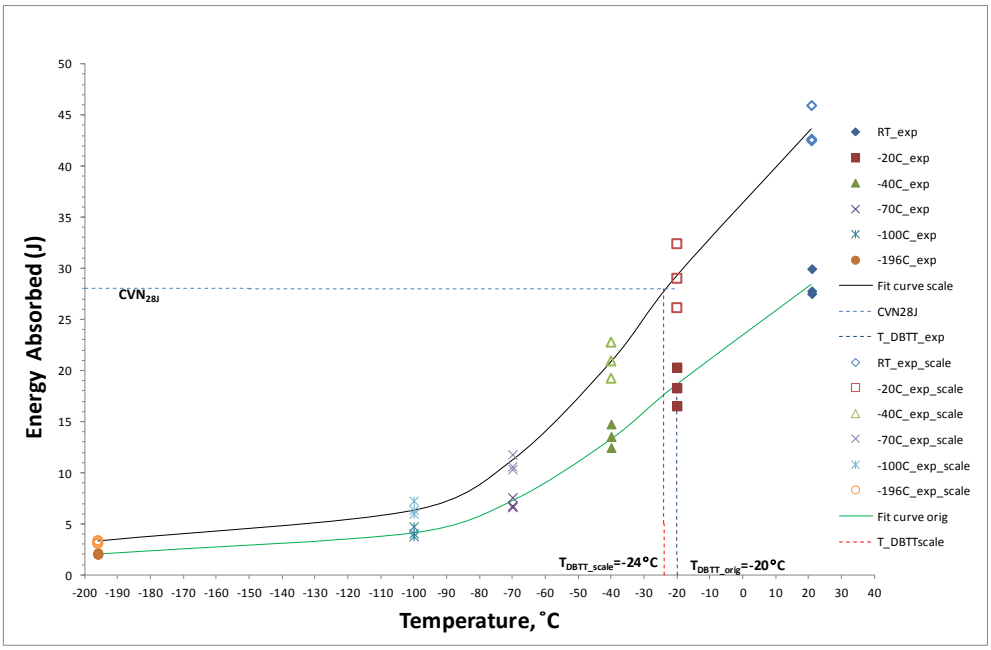

Figure 4-37 Absorbed energy vs. Temperature. Grade X60. B= 3/4T

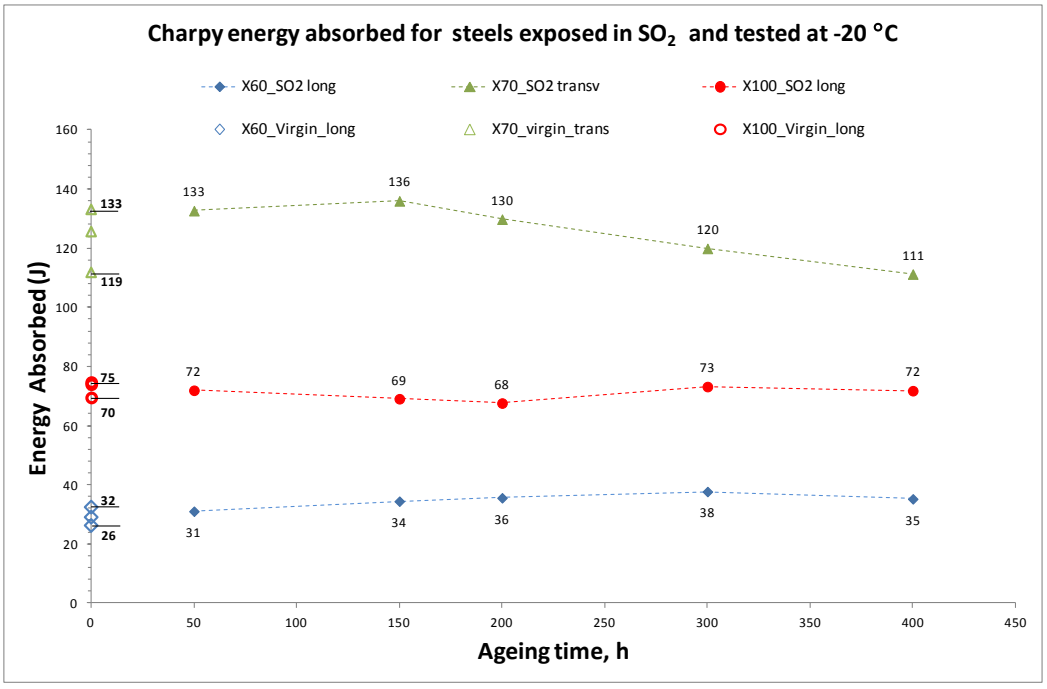

Figure 4-38. Charpy absorbed energy values for HSLA steels exposed in SO_2 at 90 bar and 45°C.

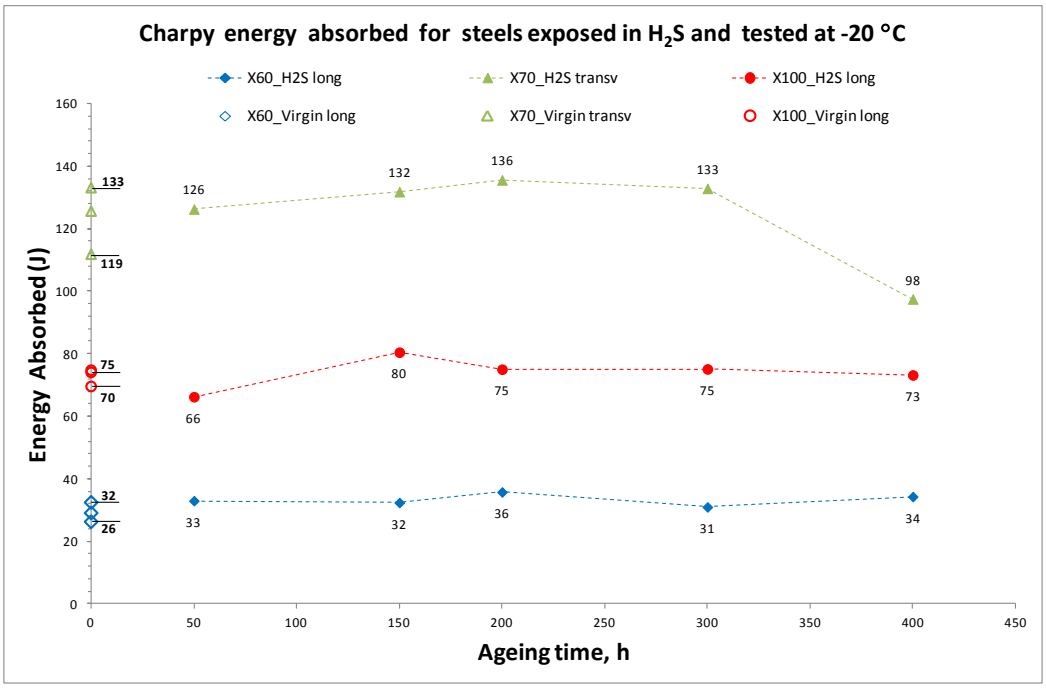

Figure 4-39. Charpy absorbed impact energy values for API X100, X70 and X60 steel exposed on H_2S at 90 bar and 45°C

4.3.7.3 K_{IC} calculations for virgin and aging material

Although it is well known that a single correlation between Charpy test results and fracture toughness could be obtained, this correlation is not valid for all the materials and conditions. According to the specification of API 5L [67] for 16-20 mm thick pipelines, an average of the impact energy is required to be 68 J (minimum 27 J in the L-T notch direction and 41 J in the T-L at 0°C) using standard CVN samples.

However, this value could be different when PCCVN samples are used. It has been found that an impact value in the longitudinal direction is much lower than the transversal orientation. For example, Ju et al. [359] found differences around 220J when samples of X65 were tested both in a longitudinal and transverse direction. Similar steel was studied by Baek et al. [360] but the energy values at the same temperature (-60°C) was 100J for conventional Charpy. Liessem et al. [52,342] evaluated the toughness of the X100 steel using standard CVN samples and found that the impact transition temperature (DBTT) is around –60°C.

It can be seen that the tensile and yield strength could increase and be detrimental to ductility which is not the behaviour presented for the material. In reference [170] the author evaluated the fracture toughness of the API X100 using CT geometries and found the K_Q of the material was 142 $MPam^{0.5}$ at 21°C and the ductile-brittle transition could be below –70°C.

Xue et al. [361] reported that the yield stress increases from 35% to 53% when the material (API X100) is tested at –196°C and –83°C respectively, but no significant differences were found for the elongation. Researches carried out by Fields et al. [362] and Mikalac et al. [363] demonstrated that the difference mentioned above is greatest at the upper shelf where the deformation is totally plastic. At the lower shelf the difference is not large due to the fracture mechanics being cleavage. They conclude that the energy absorption transition temperature range is slight higher for the pre-cracked specimens.

The results obtained and compared with conventional Charpy or CT, indicated that instead of being normalised the energy absorbed by the steels were lower in pre-cracked samples at all temperatures. This result agrees with references [363] and [364] which are shown in Figure 4-40.

From the calculation of fracture toughness and following the revision bibliography [58,177,184,185,190,202,209,220,365,366], it was found that the considerations to determine fracture toughness from PCCVN are not viable. For this reason there is no correspondence between the energy values determined and fracture toughness calculations as it can be seen in Figure 4-41 and Figure 4-42 on API X100 steel. Appendix O, P, Q, S, T and U summarised the raw data obtained from the experimental tests performed on parent and exposed material.

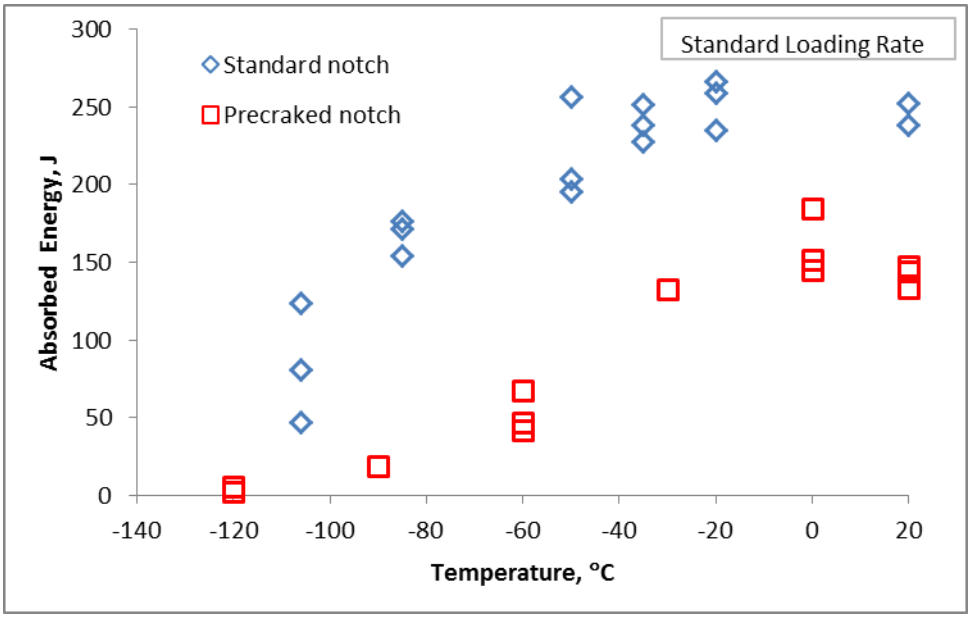

a) Steel API X100 (After [363])

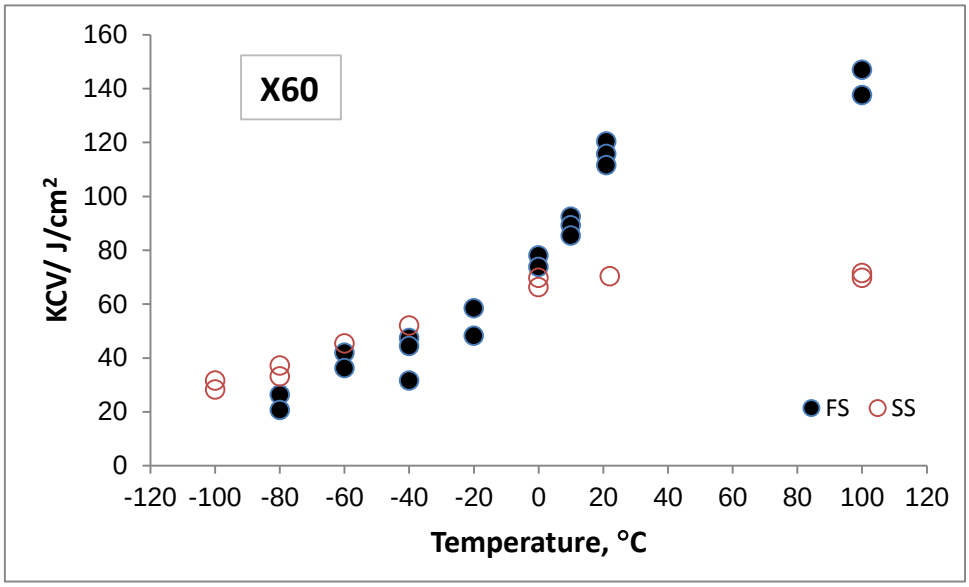

b) Steel API X60. FS: Full size; SS:(Sub-size) (After [364])

Figure 4-40. Variation of the Charpy energy in sub-size and pre-cracked Charpy V-notch samples

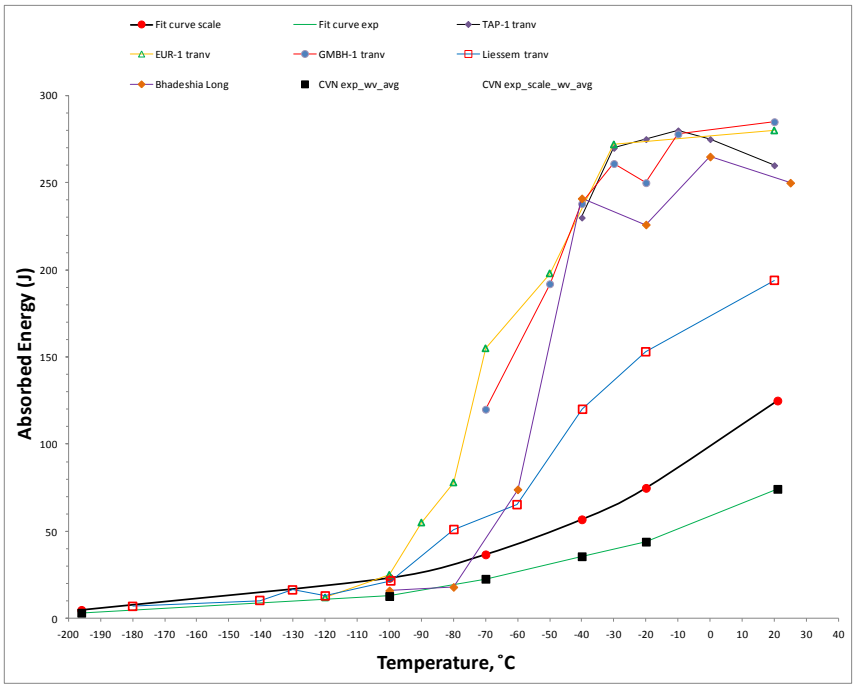

Figure 4-41 Variation of Charpy energy absorbed with temperature for conventional Charpy V-notch (literature) and currently research (PCVN). Steel grade X100.

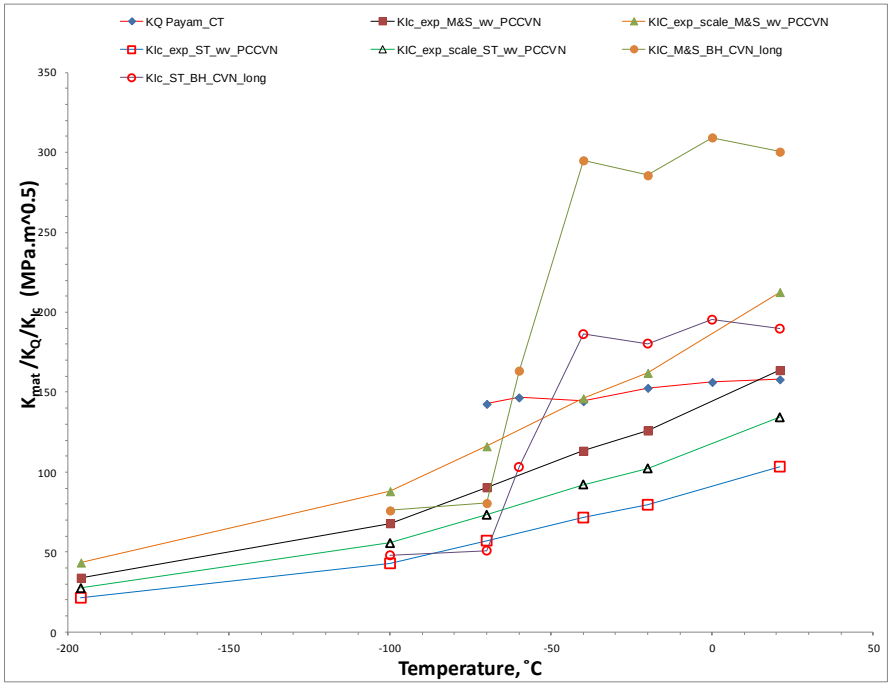

Figure 4-42 Comparison fracture toughness values determined on conventional CVN, CT [297] and PCCVN geometry in the longitudinal direction. API X100

4.3.8 Corrosion and embrittlement of steels in flue-gas saturated with water

In practical and real situations, transporting anthropogenic CO_2 implies that many other species could be present due to the necessity to make CO_2 transportation economically feasible. A combination of CO_2 and H_2S becomes corrosive through the presence of moisture and the corrosiveness is determined solely by the levels of these compounds. With regard to NACE, a fluid is designated as sour when it contains greater than a 0.0035 atmosphere partial pressure of H_2S.

Although pipelines could not normally operate under corrosive conditions, if there is a temperature drop in the gas to below its dewpoint or failure in the dehydration plant, this can lead to the introduction of moisture. Sulphur dioxide, SO_2, enters the atmosphere as a result of both natural phenomena and anthropogenic activities. Coal burning is the single largest man-made source of SO_2, accounting for about 50% of annual global emissions, with oil burning accounting for a further 25 to 30%. SO_2 reacts on the surface of a variety of airborne solid particles, is soluble in water and can be oxidised within airborne water droplets, producing sulphuric acid. This acidic pollution can be transported by wind over many hundreds of kilometres, and is deposited as acid rain.

CO_2 dissolves in the presence of water, forming carbonic acid (H_2CO_3), which is corrosive to low carbon steel. Eq. 4-9 to 4-11 corresponds to the general reactions describing this process.

$$Fe \rightarrow Fe^{2+} + 2e^{-} \quad \textbf{(4-9)}$$

$$2H^{+} + 2e^{-} \rightarrow 2H \quad \textbf{(4-10)}$$

$$CO_2\ (g) + HO_2\ (l) \Leftrightarrow H_2CO_3\ (aq) \quad \textbf{(4-11)}$$

Due to these processes, a layer of iron carbonate, $FeCO_3$, is formed on the steel surface. This film plays an important role in the formation of protective deposits in the first stage of the corrosion mechanism. Moisture and free water is an issue transporting CO_2.

Race et al. [89,367] describe how the acceptable level of water in the pipeline is dependent on the solubility of water in the fluid at the operating temperature and pressure. The solubility limit for water in pure CO_2 at pipeline operating conditions is 2560 ppm. As a result, it is now accepted that corrosion rates in CO_2 pipelines will not occur if the water content is kept at less than 60% of the saturation value (1574 ppm). For industrial applications, the levels of water for pipeline facilities are specified between 288 ppm and 500 ppm.

Figure 4-43 presents SEM images showing corrosion products in a quite regular structure and shaped corrosion products which were piled up in a very regular arrangement. As can be seen from the analysis in this work, the corrosion behaviour of X100, X70 and X60 steels under the present investigation is not mainly due to CO_2 and free water but SO_2 and H_2S also play a very important role. Choi and Nešić briefly discussed the corrosion mechanism of carbon steel in supercritical CO_2 containing SO_2, H_2O and O_2 impurities [121,144,168]. Their results showed that the corroded specimen with 500 ppm SO_2 had a smoother surface in some areas, while other zones had many small protrusions on the corroded surface, and that was probably where the anodic corrosion reactions occurred and match with the results obtained in this investigation (Figure 4-43a).

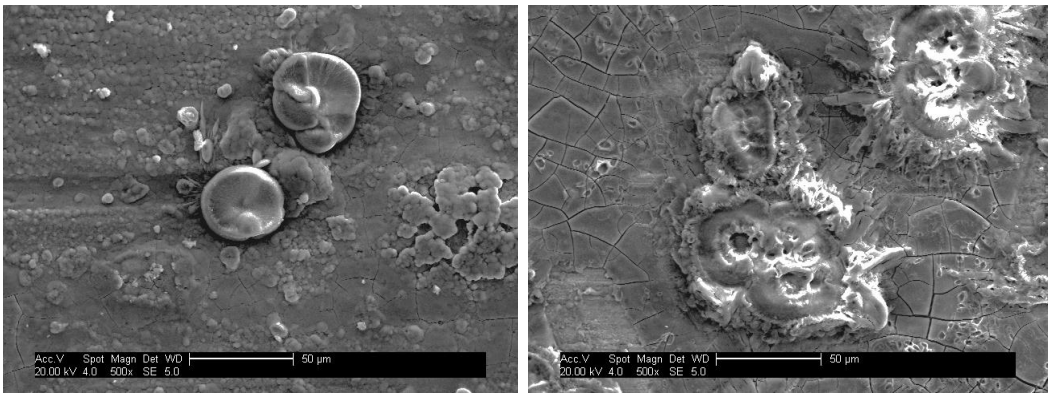

(a) X100 steel. Magn 500X (b) X60 steel. Magn 500X

Figure 4-43 SEM pictures of sample surfaces after being exposed for 400h in flue-gases at a CO_2 partial pressure of 90 bar, 45°C, with 3.3% free water and 500 ppm SO_2

It is characteristic at some points to have many, cellular-shaped corrosion products, which were not visible with lower magnification. In Figure 4-43b, many cracks were observed on the surface of the corrosion products, which are provided by the SEM of X60 steel.

The protectiveness of the surface scale formed in the CO_2 environment depends on the nature of the base alloy (composition, microstructure, heat treatment) and on the properties of the environment, such as temperature, CO_2 partial pressure, pH, flow rate and impurities present [125].

Although this behaviour has been presented at partial pressures relevant for the oil and gas transport (p<10 bar), in the case of transporting CO_2, a partial pressure above 72 bar should give corrosion rates exceeding 10 mm/y. In fact, the corrosion rate will depend on the corrosion layer which has formed on the steel surface [94]. The dissolution of CO_2 at high partial pressures is different from that at low partial pressures due to the non-ideality of the phases.

In low pressure systems, the concentration of dissolved CO_2 is directly proportional to its partial pressure according to Henry's law. However, in high pressure systems this relationship between concentration and pressure is no longer linear and Henry's law cannot therefore be used [337]. The corrosion product film under those experimental conditions looks similar to those obtained by Choi and Nešić [144,146] and Dusgtad et al.'s experiments [110,368].

Results by EDS tests in the region of 10 and 7 (Figure 4-44a); and re-evaluated with XRD (Figure 4-44c), determine that the corrosion product is probably $FeSO_4$. This result reaches good agreement with the results of Dusgtad et al., who determined this product using the same method. Placed in the air, the specimen surface would be a white-grey colour, which was probably related to the efflorescence phenomenon in that the $FeSO_4$ hydrate could be converted to $FeSO_4$ when exposed to the air. This can be seen in Appendix N.

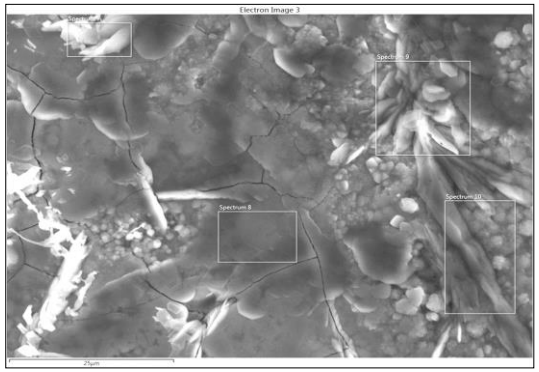

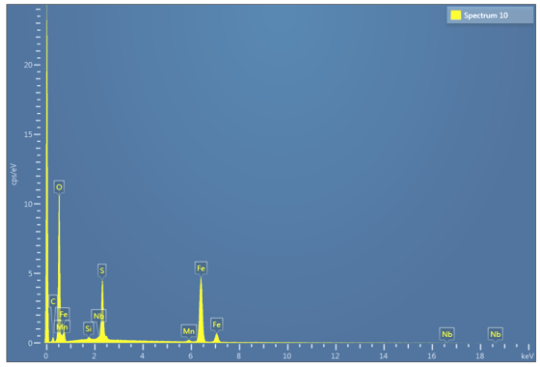

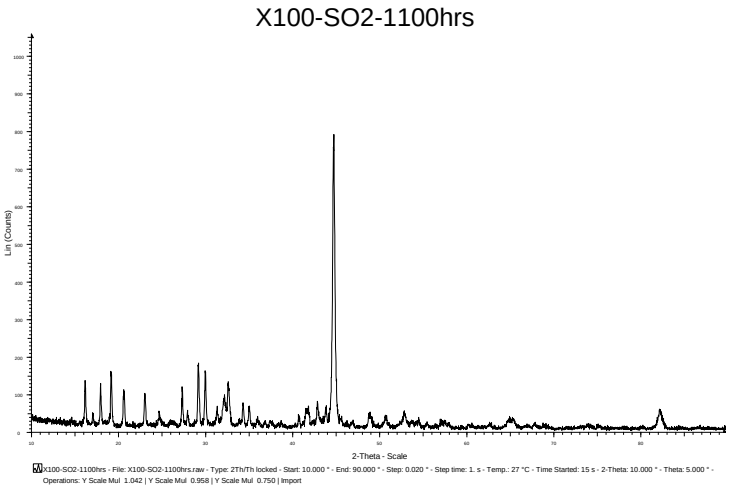

a) Grade X100, exposed 1100h SO_2

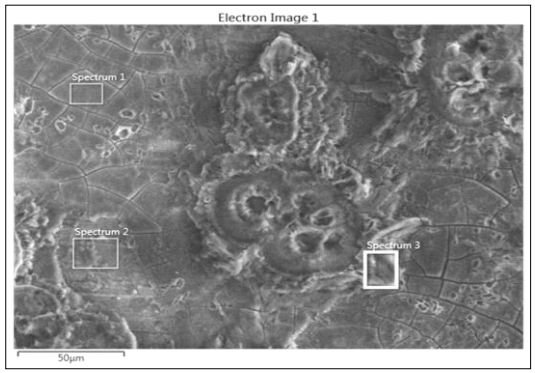

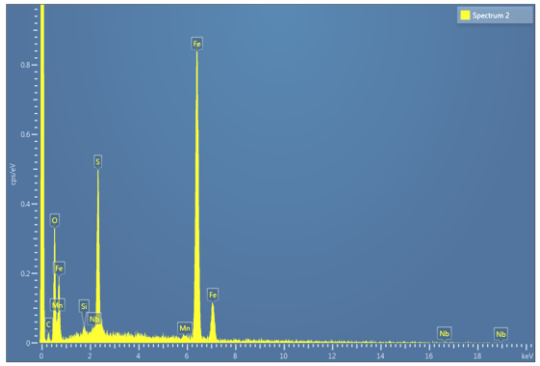

b) Grade X60, exposed 400h SO_2

Figure 4-44 Evaluation layer deposited on the metal surface for samples exposed with SO_2 and analysed by SEM, EDX and X-Ray

For example, the addition of SO_2 in the gas phase can lower the pH of the system, increasing the corrosion rates of the steel when water condenses on the steel surface due to the formation of sulphurous acid, H_2SO_3. The possible reaction mechanisms containing anodic and cathodic reactions generally accepted are presented in equations 4-12 to 4-16.

$$SO_2 + H_2O \rightarrow H_2SO_3 \quad \textbf{(4-12)}$$

$$SO_2 + H_2O \rightarrow SO_3^{2-} + 2H^+ \quad \textbf{(4-13)}$$

$$SO_3^{2-} + H_2O \rightarrow SO_4^{2-} + 2H^+ + 2e^- \quad \textbf{(4-14)}$$

$$Fe^{2+} + SO_4^{2-} \rightarrow FeSO_4 \quad \textbf{(4-15)}$$

$$4FeSO_4 + 6H_2O + O_2 \rightarrow 4FeOOH + 4H_2SO_4 \quad \textbf{(4-16)}$$

The presence of H_2S provides alternative mechanisms for corrosion mitigation since it enables the formation of FeS films on the surface of the material. However, low concentrations of H_2S in CO_2 wet gas systems might result in accelerating corrosion rates, compared with systems without H_2S. The causes of this effect of low concentrations of H_2S in CO_2 are not well understood [124]. Equation 4-17 presents the general corrosion reaction.

$$Fe + H_2S \rightarrow FeS + 2H_{ads} \quad \textbf{(4-17)}$$

The hydrogen is generated by the reduction of the hydrogen ion (H^+), which is produced from the anodic reactions on the material; this can be expressed using equations 4-18 and 4-19 which are widely accepted as the corrosion reactions of steel exposed to a sour environment.

$$H_{ads} + H_{ads} \rightarrow H_2 \quad \textbf{(4-18)}$$

$$H_{ads} \rightarrow H_{abs} \quad \textbf{(4-19)}$$

The dissolution reactions result in the generation of hydrogen ions which would be reduced to hydrogen atoms. These could be absorbed on the surface and combined to form hydrogen gas which is then released into the environment.

If the hydrogen diffuses into regions of high triaxiality tensile stresses or to some microstructural areas that contain defects such as the inclusions (elongated Type II MnS) and segregations zones or bands with lower temperature transformation products (such as bainite and martensite), it becomes entrapped. Moreover, when the material reaches a critical hydrogen concentration value (C_H), it could cause the substantial rearrangement of dislocations and de-cohesion of grain boundaries and the formation of micro crevices at the grain and phase boundaries.

The hydrogen concentration about $C_H \geq 2.1*10^{-6}$ mol/cm^3 can be considered as critical because at this value the steel loses its local strength by 2.5 times in comparison with the test air [369]. This mechanism is known as sulphide stress cracking (SSC) and this phenomenon is observed in stressed components. The formation of surface blisters and/or internal cracks in the absence of applied stress, or under elastic tensile stress developed from the sulphide corrosion process on the steel surface, is called hydrogen induced cracking (HIC) [126,162].

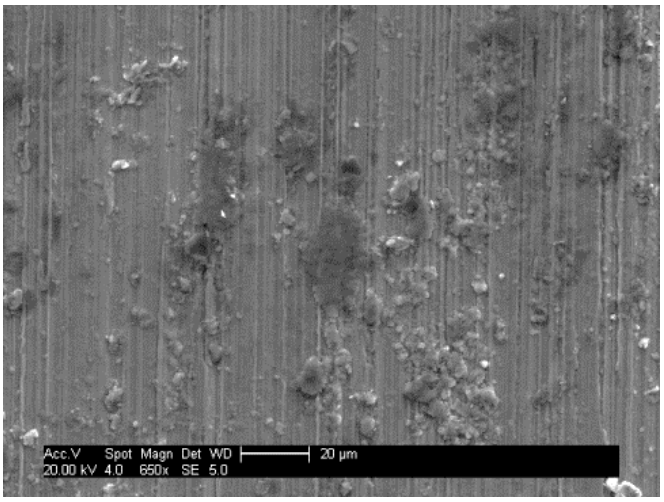

Figure 4-45 SEM image of the surface of the samples after being exposed for 400h in flue-gases , at a CO_2 partial pressure of 90 bar, 45°C, with 3.3% free water and 500 ppm H_2S. Mag 650X.

The effect of the H_2S in the samples exposed in the SC^3 is shown in Figure 4-45 where it can be seen that the layer deposited on the surface of the samples was distributed irregularly.

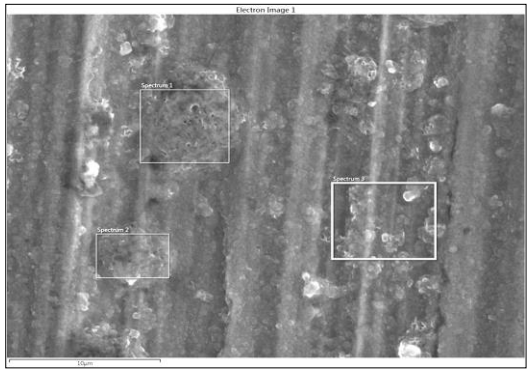

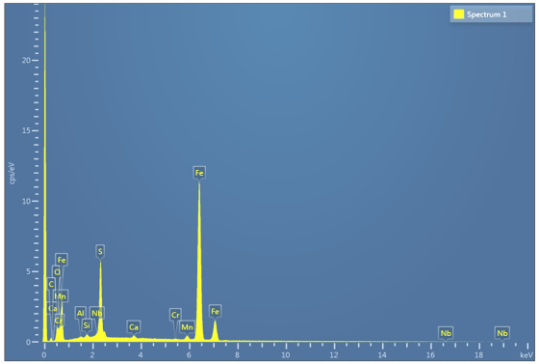

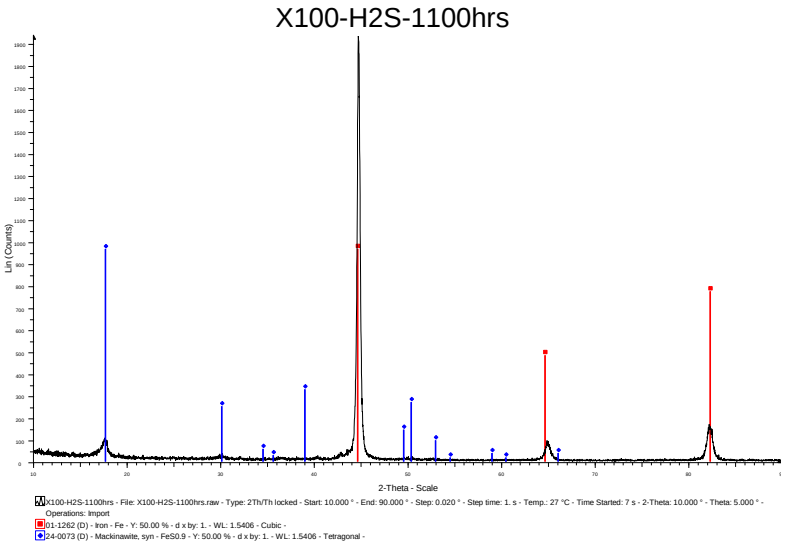

a) Grade X100, exposed1100h with H_2S

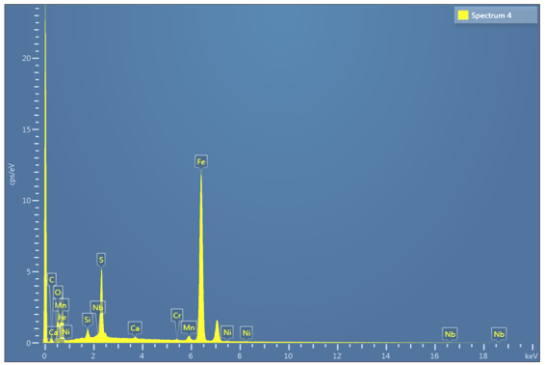

b) Grade X100, exposed 400h with H_2S

Figure 4-46 Evaluation layer deposited on the metal surface for samples exposed on H_2S by SEM, EDX XRD

As few signs of corrosion were observed for all the samples, alternative analysis by EDS and XRD were performed to identify the component. The spectrum of both analyses determined that the compound can be classified as FeSO. Figure 4-46 presents the spectrums and places where tests were made. In addition, as the corrosion was lower, even though free water was in the system, verification was undertaken to quantify the circulating water in the CO_2 rig. The evaluation was made capturing a mass sample of 40 mL from where concentrations were inferred. Water grams were assumed to equal mL @ 90 bar. Table 4-9 presents all the values obtained.

Table 4-9 Measure of water in the SC^3 rig

Test number	H_2O g	g/L	ppmw	ppmv
1	0.034	0.85	1511	850
2	0.065	1.63	2890	1630
ρ_{CO2} at 90 bar, 37 °C = 563 kg/m^3 (By Peacesoftware)				

From the results, it can be inferred that the amount of water in the system was lower than expected for the test run with H_2S and SO_2 giving lower corrosion rates for the steels tested. From the literature a large variance in “saturation” concentrations has been reported, giving solubility for the conditions established in this research at around ~ 0.24 gm/L (426 ppmw, 240 ppmv) which is lower of others investigation that state 3300 ppm for 80 bar, 50°C [109,368,370].

4.4 Summary

Based on the results of the presented investigation on strength and fracture characteristics of the X100, X70 and X60 grade steel, the following major deductions can be made:

- The mechanical properties in three kinds of HSLA steels as-received and aging conditions tested over a range from 196°C to RT has been carried out. The relation between hardness and type of microstructure and their effects on tensile properties along with temperature variation and anisotropy effect is essentially complex due to the possible variations and connections to the obtained similar properties of the material.
- As it was expected the total energy absorbed by the pre-crack Charpy specimens is less than conventional Charpy. The correlations used to determine fracture toughness from the absorbed energy was not reliable as huge differences were observed compared to the literature using conventional CVN.
- Various models were reviewed from the literature and methods used as alternatives to investigate whether or not it might be possible to relate K_{Ic} to Charpy toughness for both pre-cracked and conventional specimens. Following an exhaustive analysis no consistent relationship can be reliably observed. Finally it must be concluded that Charpy toughness cannot be related to fracture toughness.
- The results obtained from the corrosion analysis could encourage using alternative characterisation methods in order to clarify differences between the compounds to establish more precise values. Measurement of pH and corrosion rate on real time by other methods are critical as it could offer more information to understand corrosion mechanics on dynamic systems.
- The repercussion from H_2S and SO_2 on mechanical responses due to embrittlement or corrosion is an issue for steels exposed in anthropogenic CO_2. An attempt to establish or understand the phenomenon, along with microstructure, chemical composition, impurities concentration and their interaction was carried out.

5 RESIDUAL STRESS

5.1 Introduction

Residual stresses can significantly affect the mechanical properties and integrity of components or structures [371], [229]. Those stresses can be produced by the manufacturing process, heat treatment, welding processes and also by service loading. The origin of the residual stress may be a consequence of differential plastic flow, differential cooling rates or phase transformation [230,231].

Depending on the nature of residual stress fields, it can be a beneficial (compressive) or a destructive (tensile) feature in a component. Compressive residual stress can be induced in the subsurface of a material by deforming a layer which varies in depth depending on the method used. Deep rolling, peening processes such as shot peening, laser peening, hammer peening and ultrasonic peening, are some of the techniques utilised for this purpose.

Measurement and understanding of stress field behaviour will facilitate better design practice against static and dynamic loading, and will aid in predicting structural failure and the assessment of structural integrity. Methods of measuring residual stress might be categorized as destructive, semi-destructive or non-destructive. Ring-core, deep-hole and hole-drilling are representative of semi-destructive techniques and magnetic, acoustic or diffraction of Non-destructive approaches [230,233,236,237,372,373].

There are some issues regarding non-destructive technique capabilities such as spatial resolution meaning that the residual stress measure is restricted very near or far from the surface [233,238,275]. Thus, combination of two or more approaches could reduce the constraint. ND and hole-drilling combination are two powerful techniques that working together extended the range to measure RS in thick components [241,245,249,251,259,374,375].

This chapter presents a study carried out by an ND and hole-drilling method to evaluate residual stress variation on cold-rolled specimens. The procedure involved the measurement of the induced stresses and sought to visualize the stress field pattern and behaviour through-thickness across the specimen surface. For the incremental centre hole-drilling (ICHD) and orbiting incremental hole-drilling (OIHD) approaches, residual stress evaluation was performed using an inverse solution known as the integral method. While for the ND calculations the home-software StressTextCalculator® was used.

5.2 Experimental procedure

5.2.1 Outline

API X100 high strength steel as-received and yield strength was obtained from tensile test. The material was used in the form of flat plates to carry out cold rolling, introducing residual stresses (See section 3.6.1). Cold rolling, which was undertaken by a combination of load and axial flat rollers, was carried out in alternative directions to produce two rolling tracks for each side of the plate. As a result, two rolling tracks were obtained, one with three passes and the other with six passes.

Two approaches were used to characterise the residual stress profile in the rolling plates. A set of ND measurements, was performed to size residual stress through-thickness and along the transverse plate section. Details of settings were described previously in section 3.6.2. ND measurements were made using a 1.66 Å constant wavelengths with an IGV of 1x1x1 mm^3 for longitudinal direction, and 15x1x1 mm^3 for transverse and normal direction.

Points measured on the surface and through-thickness is shown in Figure 5-1. Diffraction data obtained from the 211 crystallography plane were used to calculate the elastic strain in-plane which was converted to stresses using the inverse Hooke's law. More detail can be obtained from Chapter 3 section 3.6.2.1.

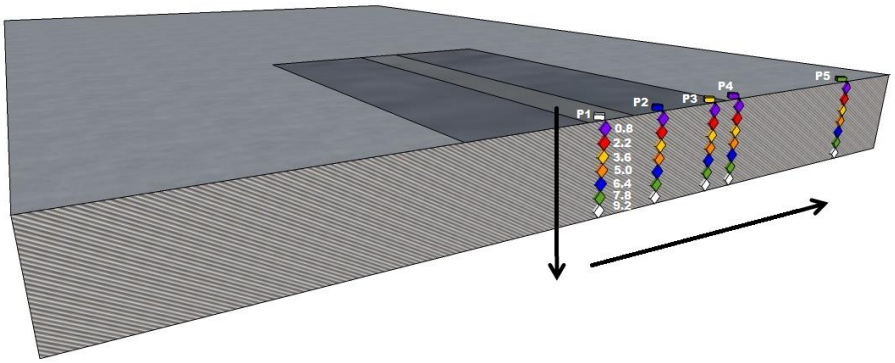

Figure 5-1 A schematic drawing of the selected points for RS analysis on the plate. Arrows indicated the directions abreast the stresses were measured either on the surface or through the thickness.

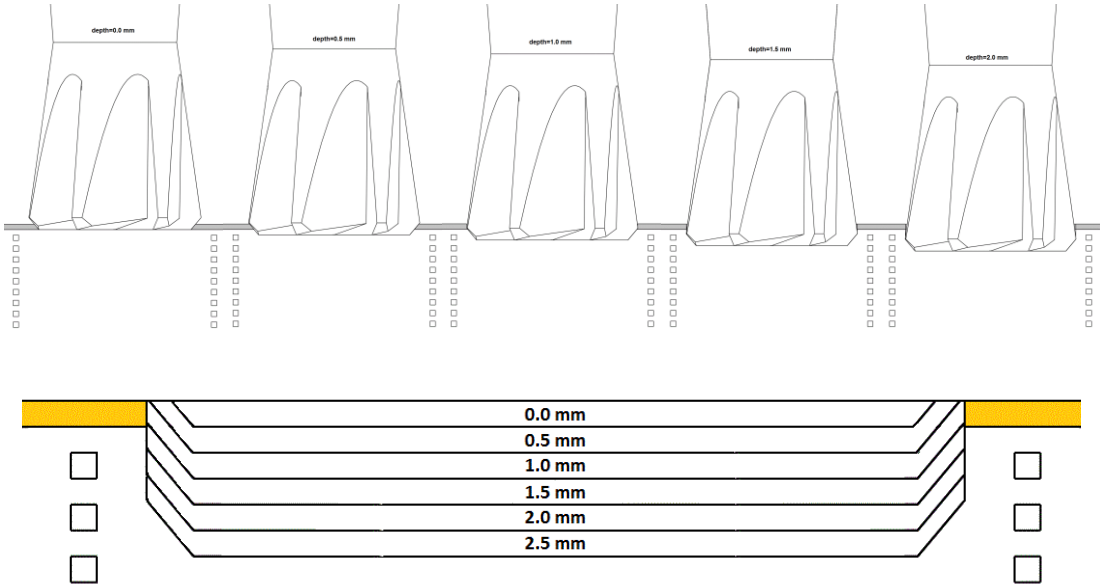

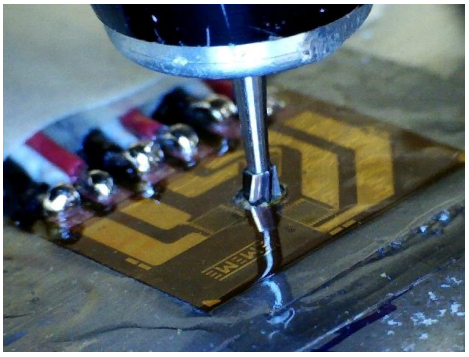

Figure 5-2 A schematic representation drilling a hole performed by ICHD or OIHD from zero to 2 mm depth

Stresses variation at the sub-surface of the material was determined by incremental hole drilling following the basic procedure described in ASTM, NPL and Measurement Group guidance [241,251,253]. ICHD and OIHD were undertaken at the Structural Integrity laboratory at Cranfield University and Stresscraft Ltd[4] respectively, from which comparisons with the ND method were established. A schematic illustration can be seen in Figure 5-2.

Strain releases were recorded using a Vishay strain gauge rosette CEA-06-062 UL-120 and EA-06-125RE-120. Strain data, both ICHD and OIHD, were analysed using the integral method developed by Schajer, allowing the calculation of residual stresses which are invariants with depth. The method was explained in Chapter 2 section 2.4.4.1 and more details can be found in references [249,250,277,374].

5.3 Results

5.3.1 Cold rolling

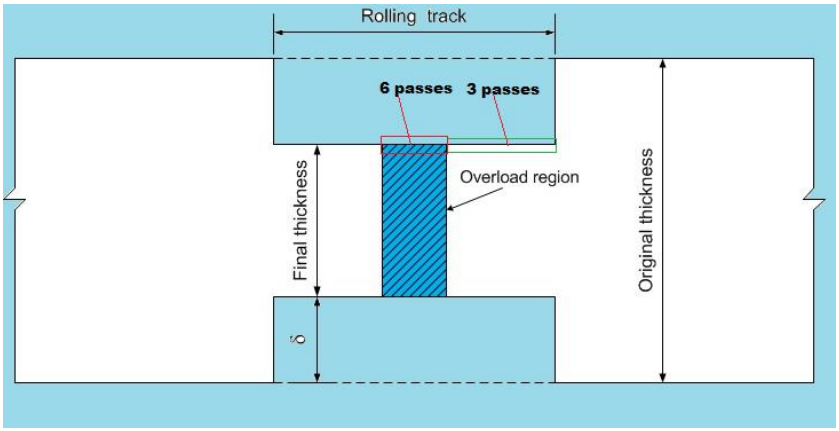

Figure 5-3 A schematic illustration showing transverse depth of indentation (δ) and thickness reduction due to rolling at the centre span of the specimen

Figure 5-3 represents the profile expected to be obtained after the cold rolling process was performed. It was assumed that the rolling track would be shaped with two similar areas with three passes each while an overload area with six passes were expected after the test.

[4] Stresscraft Ltd is a company located in St Winefrides Chapel, Pick St, Shepshed, Loughborough LE12 9BB which is dedicated to the provision of stress analysis services.

Measurements of the depth through the rolling zone were made in order to establish the thickness reduction and deflection outcome of the load applied, as illustrated by Figure 5-4 and summarised in Table 5-1. It can be observed that on samples A and B the depth indentation is similar for both sides.

Table 5-1 Measurement of depth as a result of load applied on the plate by cold rolling

Sample	Side	Thickness plate (mm)	Depth indentation (δ) rolling track (mm)	Thickness reduction (mm)	δ (%) total
A	A1	10	0.038	9.92	0.76
	A2	10	0.038		
B	B1	10	0.080	9.84	1.6
	B2	10	0.080		
C	C1	10	0.125	9.67	3.35
	C2	10	0.210		
D	D1	10	0.240	8.86	11.4
	D2	10	0.900		

In samples C and D the indentation depth is higher for the side where rolling was performed initially while the second side is less. Also the depth value is still similar when applying the same load, even though the width of the roller was decreased from 20 mm to 10 mm.

In order to determine any distortion as a consequence of lateral forces during the deformation process, particularly along with the rolling area, measurements of the sample width were made. Three equally-spaced zones abreast of the indented region were measured indicating dimensional changes as a consequence of the load applied. The maximum peak value was found at the mid-section of the total length of the rolling zone which was chosen as a representative value of the maximum deformation, as shown in Figure 5-4.

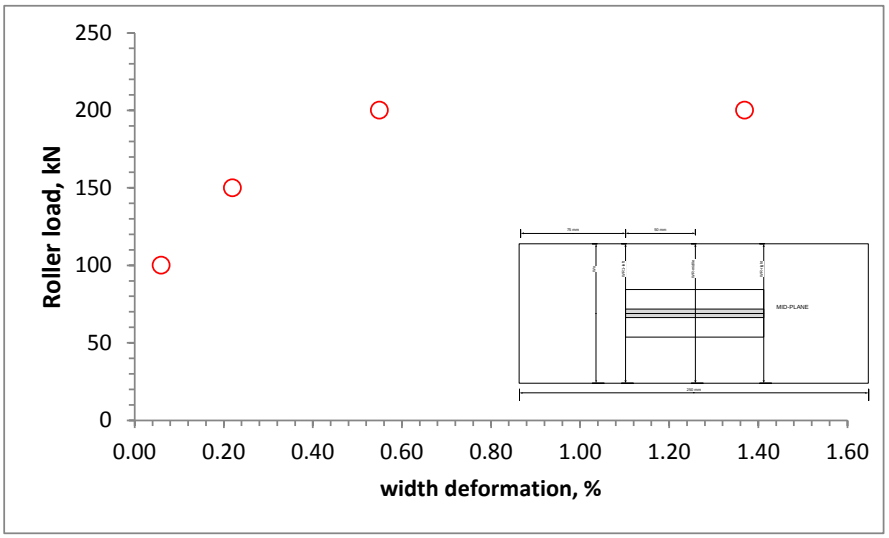

Figure 5-4 Maximum width deformation of the plate applying different load

It is evident from the results that the percentage of deformation is enlarged linearly if the load still increased but it should, however, be noted that by changing the roller width, the deformation increased significantly, by at least 75%. In order to give a clear correspondence with the drawing in Figure 5-3, the profile was divided into three regions which are namely rolled areas 1 and 2 (three passes) and overload area (six passes).

Figure 5-5 shows the profile obtained by laser measurement across the transverse section of the plate. As it can be seen, there were different depths for each part of the rolled areas depending on load applied. Even though there are no significant differences in rolling depth for 100 KN and 150 KN (Figure 5-5a), it can be seen that the rolling track is slightly flat in the centre of the each rolling area (roller areas 1 and 2) but it is slightly deeper over the edge of the same rolling path. Conversely, deformation introduced by applying a 200 kN load (Figure 5-5b) makes the rolling track deeper involving higher compression stresses underneath the surface. In addition, as the plate was rolled without a pair of rollers working at the same time, it is apparent that the indented regions do not match on both sides of the sample. Also, this was found for all specimens and it is likely that a recovery/displacement mechanism is actuating at the roller-plate contact during cold work.

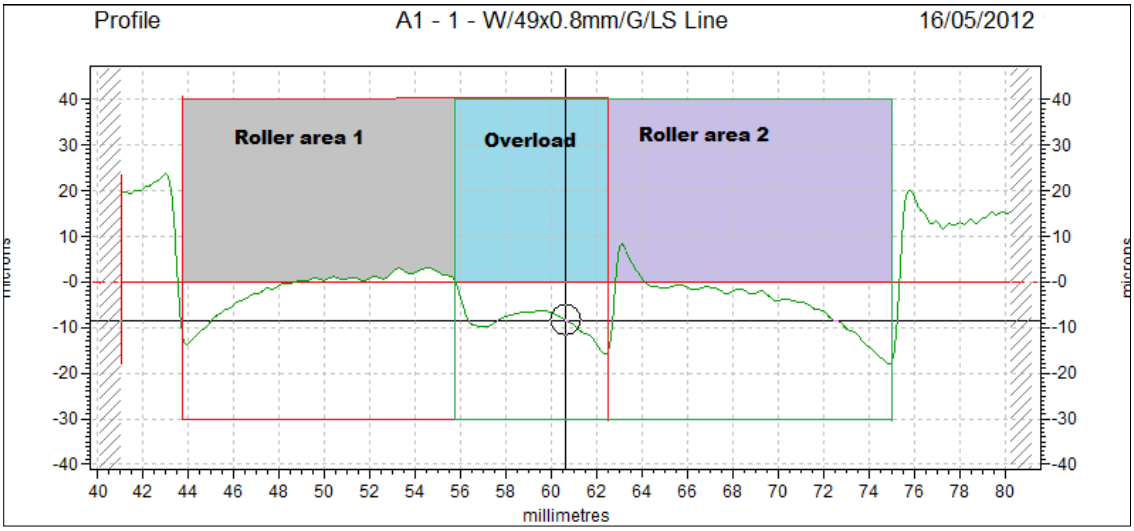

(a). Sample A. 100 kN load, roller width=20 mm

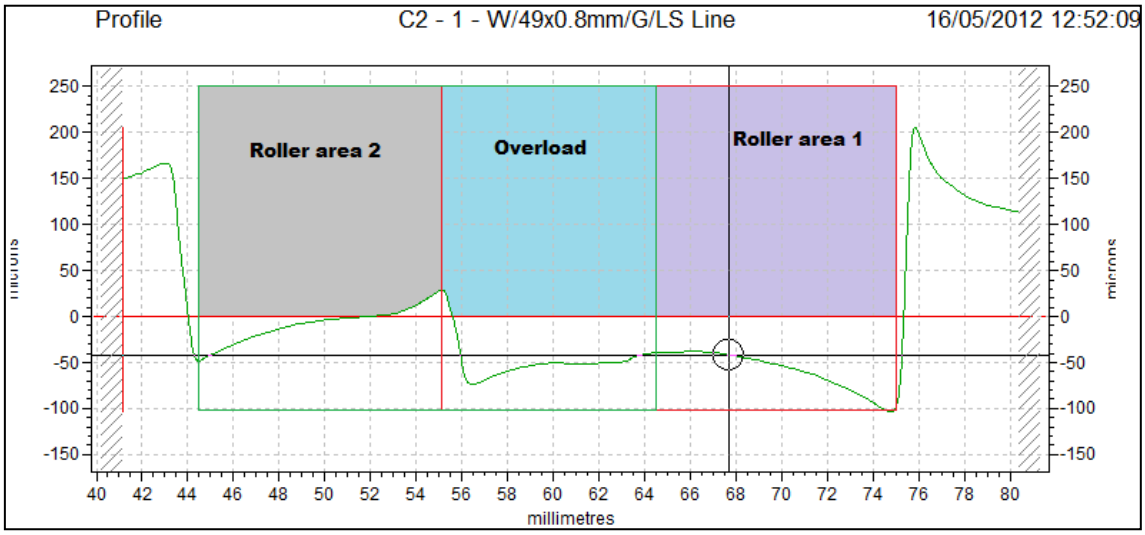

(b) Sample C. 200 kN load, roller width=20 mm

Figure 5-5 A laser profile obtained across the rolling area indicating different depths in track region, namely, roller areas 1 and 2 and overload.

This could imply that a bending moment might be introduced during the rolling process affecting the stressed induced; however, this bending strain was not measured. Likewise, this investigation assumed that stress distribution was equal for both sides of the samples abreast the transverse section; however, comparing Figures 5-3 and 5-5 shows that the zone expected to be found (Roller Area 1, Roller Area 2 and overload) is different. It may, therefore, be inferred that even though the load applied is the same, the roller is not reaching the total depth on both sides and a step is formed.

This could affect load distribution and hence residual stress due to the considerable amount of deformation produced from the previous roller passes. Evidence of this can be found in Figures V-1 and V-2 (Appendix V).

5.3.2 Residual stress measurement

5.3.2.1 Neutron diffraction

It is recognized from the literature that mechanical deformation induces plastic strain distortion on the surface layers of the material induced residual stresses due to the constraining effect of the bulk. However, this plastic deformation and thereby the residual stress decline gradually as one moves into the material as detailed in Figure 5-6. Depending on the method used to generate the deformation layer, it should vary from a few microns to some millimetres in depth. For example, cold rolled should affect the material bulk to 2 mm in depth.

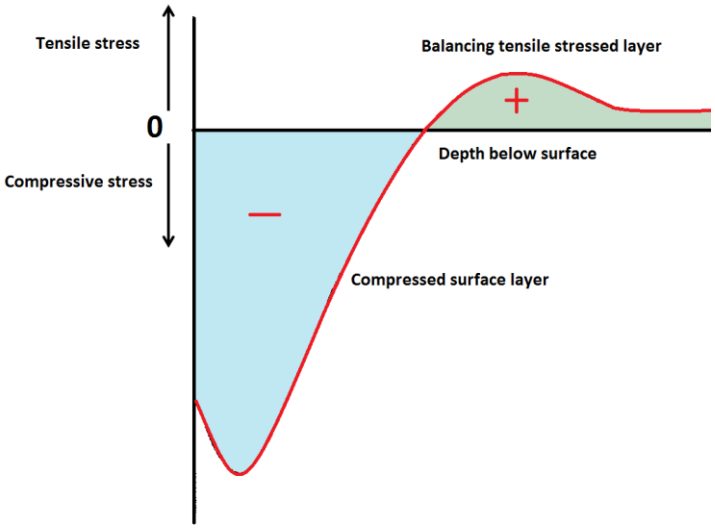

Figure 5-6 A schematic drawing of the stresses variation of the in-plane strain with depth

ND results for sets A, B, C and D are shown in Figure 5-7, separated into plots that give longitudinal stress profiles of through-thickness and along transverse sections of the samples rolled. Transverse and normal distribution profiles can be found in Figure W-1 (Appendix W).

Through-thickness residual stress: The compressive residual stresses developed by cold work on both sides of the specimens are compared in Figure 5-7 (a-d). The magnitude of longitudinal compression stress on a lower load (Sample A) is -140 MPa average, for points 1 to 3 at a nominal depth of 2 mm, from where a slight upward trend rises to nearly 100 MPa tensile stresses at the middle of the material's thickness. This should be a response of the material in order to maintain the equilibrium in the system. Points 4 and 5 are retained in tensile stress across the section up to 200 MPa. An opposite trend was found after increasing the load. Compressive stresses are presented in the few first depths, for points 1 to 4, without significant changes in stresses placed in the middle of the thickness, mainly, for points 4 and 5.

Nevertheless, the residual stress level, at point 3, is reduced to zero when 100 KN and 150 KN loads are applied but is almost identical at points 1 and 2 near the surface. For the latter points, the stress distribution in compression with depth is one magnitude less in sample B compared to sample C – 100 MPa and 200 MPa, respectively. However, in sample D, there is an opposite tendency as the levels of residual compressive surface stress at point 1 (across the section) increased by 100% and increased by 1.5 times more tensile stress than sample C at point 2. Stress levels at point 3 are still the same in both cases.

In the majority of cases, RS distribution at point 5 revealed a considerably tensile uniform tendency across the thickness. However, it can be observed in Figure 5-7 that once the load was increased to 200 KN, there was a noticeable enhancement of 100 MPa tensile stresses in sample C and when the width roller was reduced to 10 mm, specimen D rose to 150 MPa.

Transverse stresses are basically kept in a tensile state varying between 150 MPa to 400 MPa in the middle of the section, decaying to zero near to the surface for samples A and B. The peak stress value is quite high, being 70% of the yield strength of the material. For specimen C, the stresses dropped in sample B, -200 MPa and -50 MPa for points 1, 2 and 3, respectively.

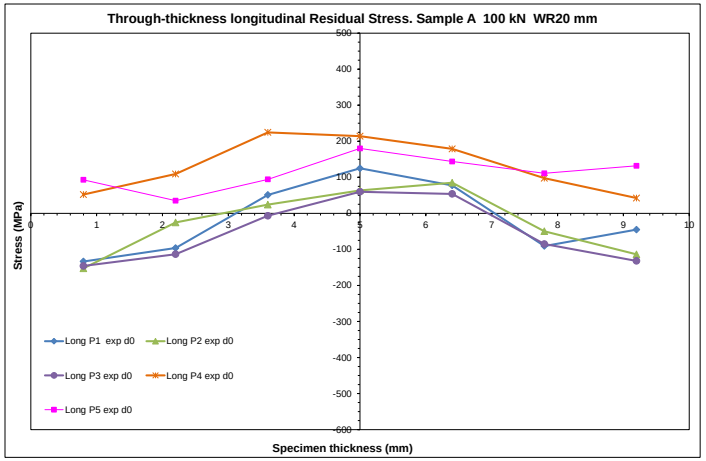

a) Sample A load100 kN

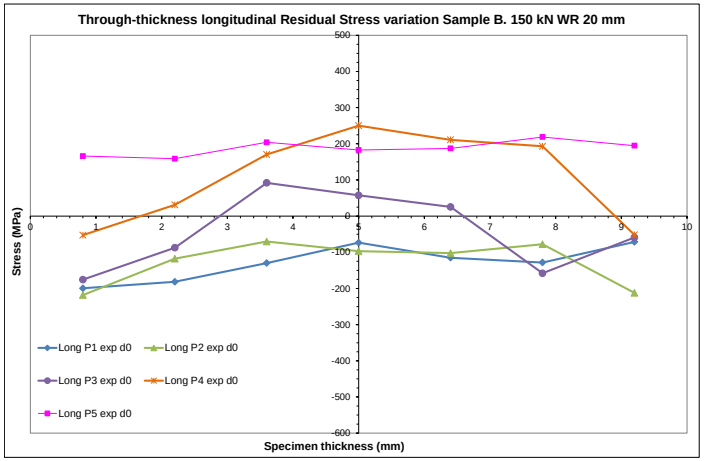

b) Sample B load150 kN

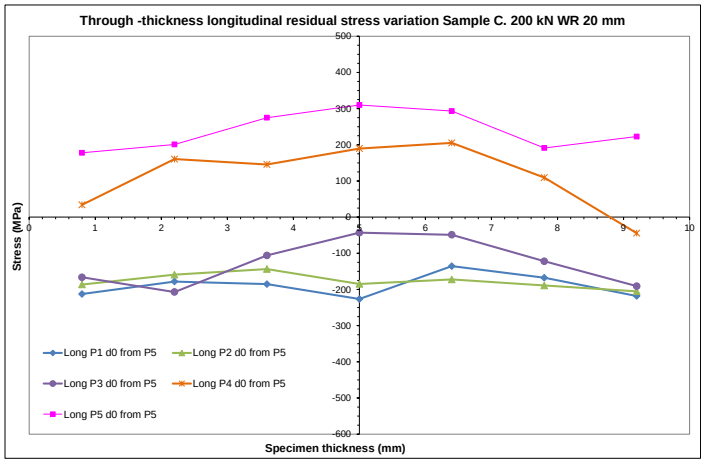

c) Sample A load 200 kN

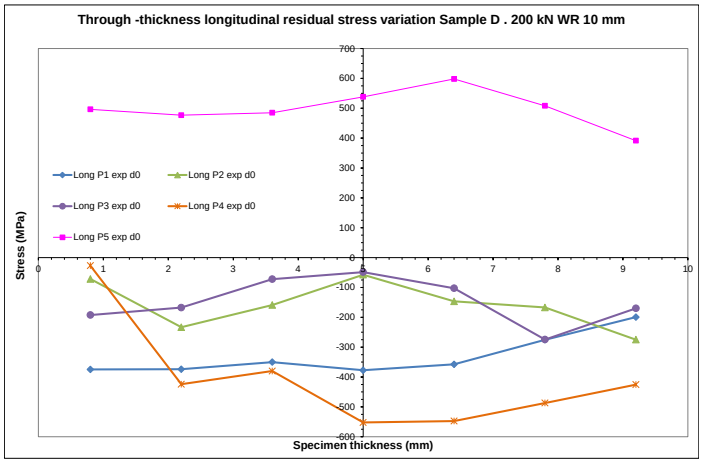

d) Sample B load 200 kN

Figure 5-7 Variation of longitudinal residual stress obtained by ND on samples A, B, C and D through-thickness

There was a substantial increment of 150 MPa at point 5, falling to 200 MPa at point 3. The stress distribution in D revealed a considerably higher variation at the rolling track. The results seem to indicate that the residual stress was dramatically affected by the reduction of the roller width, implying that a considerable plastic deformation is induced during the previous rolling stage.

The overall response of normal stresses indicates a more reasonable distribution along the thickness, even though it was in a tensile mode in the range between 400 MPa to nearly zero for all the points at set A, B, C and D. It is evident that P3 and P4 are varying with the load increment, which is more noticeable in sample D when the stress level falls to nearly zero for P1 and P4. It is observable that near to the wall track their effects are more marked.

Residual stress distribution along with the transverse section: Figure 5-8 compares the residual stress profiles at points 1 to 5 and the depth changing from 0.8 to 9.2 on the rolled steel. Indeed, the graph clearly shows the rolling zone and points' location from the middle to the edge of the plate in accordance with Figure 5-1 above. As mentioned before, the depth stress distribution was clearly affected by load and roller width. In order to consider their effects from the plate centreline to the edge for each point through the thickness, stress distribution was plotted and similar behaviour was observed in all cases, with no unexpected changes from the analysis done previously.

As can be seen from the figures, compression stresses are always presented in one half of the thickness and slightly in tension in the other half of the plate. This could indicate that one of the side's plastic strains was much higher than the other one as rolling was made first on one side and after that the plate was turned and rolled on the other face producing a different deformation layer. Additionally, the longitudinal stresses in point 4 (outside the rolling track) were shifted up in samples A, B and C but dropped dramatically in specimen D with the exception of point 0.8 mm depth. This could suggest that a higher tensile stress is introduced due to the adhesion forces undertaken in the contact side-facing roller-material near to the surface.

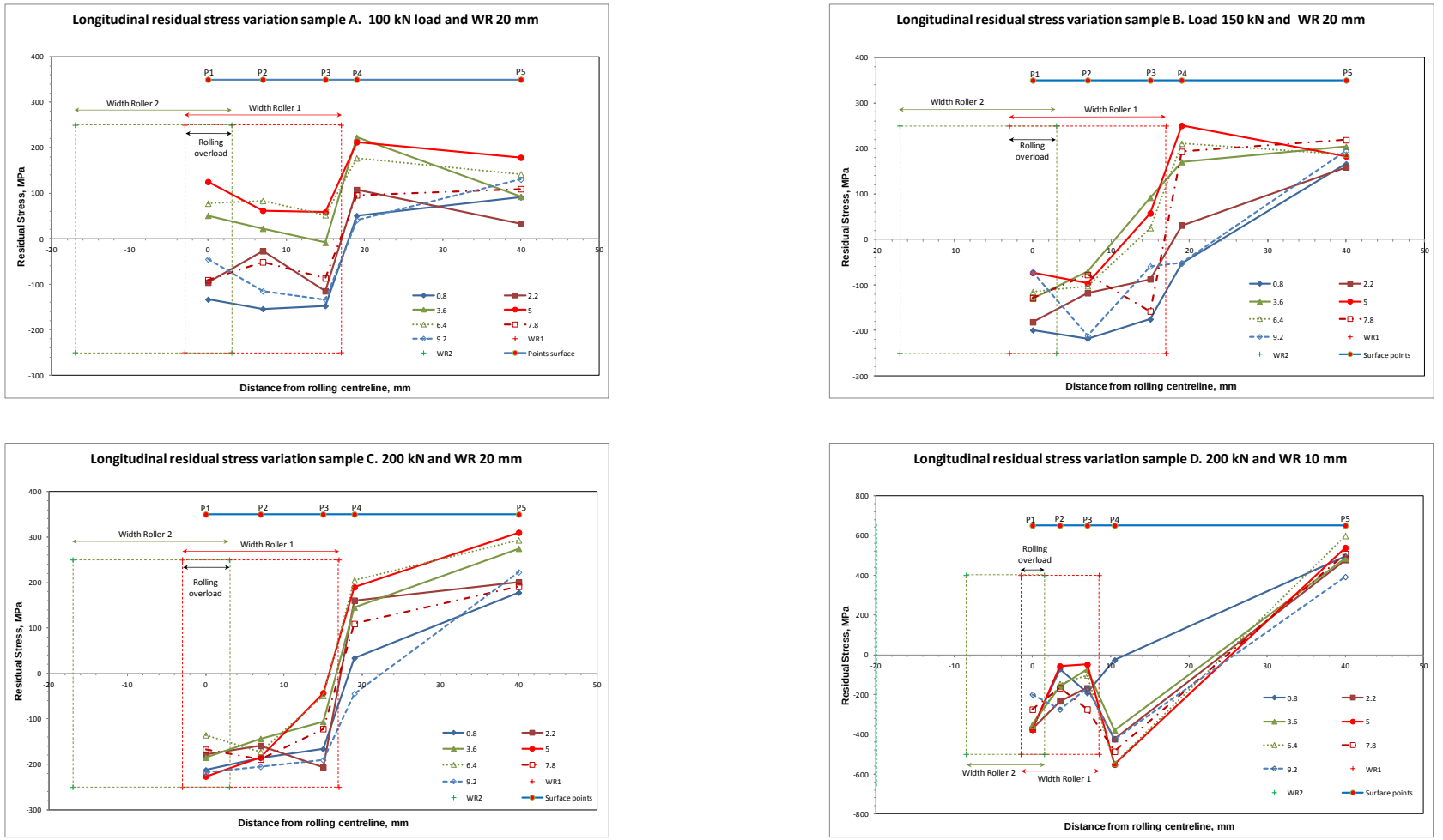

Figure 5-8 Variation of longitudinal stresses in samples A, B, C and D along points on the surface and through-thickness

A contrary effect is produced over 2.2 mm in depth as compression stresses were developed during the rolling. This should be a consequence of the rolling process. However, different views of transverse stresses distribution are presented in Figure X-1 from where the curves indicate that the residual stress in the plate outside, near the edge of the rolling tracks, is affected considerably by roller-material contact. Nevertheless, transverse and normal stress tendency was similar in all the samples indicating that there is reasonable agreement with the analysis undertaken previously.

5.3.3 Incremental hole drilling

The strain relaxations were measured in three directions, longitudinal, transverse and shear, for which three linear equations were used to calculate the residual stresses in the material using the integral method. Details can be found in Chapter 3 section 3.6.5 or in Stefanescu et al., [376] and Schajer [250].

Figure Y-1 (Appendix Y) shows the measurements of the strain released on the rolled samples surface after successive stages varying in depth during the drilling of the hole. Figure 5-9 illustrates the findings of residual stress obtained from 0.0 mm to 1 mm for ICHD and 0.0mm to 2 mm for OIHD with distributed step increments. From the plots a and b, it may be seen that at points 1 and 2 all the surface stresses are in compression, which is in agreement with the theory and expected findings.

For point 5 (plot c), near to the surface the compressive stress was observed in sample A, -24 MPa, and sample B, -113 MPa, respectively. However, for a load of 200 KN, the minimum stress measured was at least 160 MPa (Figure 5-9 c). The same trend was found for the OIHD test in sample A with -116 MPa; however, the tensile stress of 156 MPa was determined in Sample B. Samples C and D preserved tensile conditions at all depths.

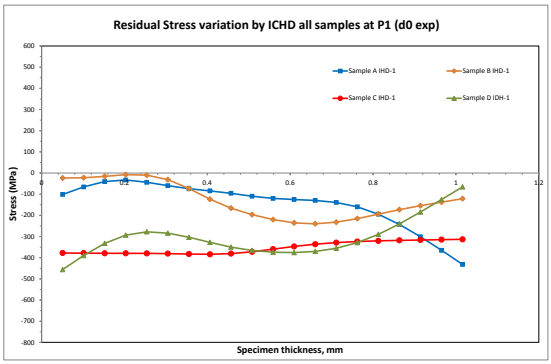

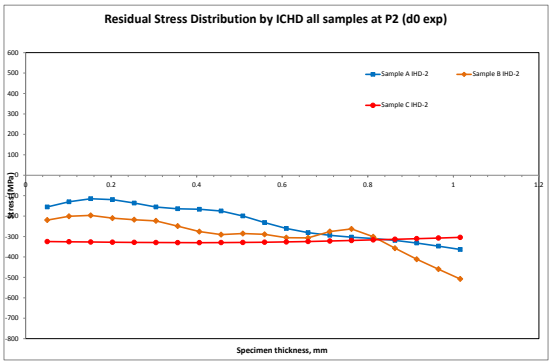

a. Point 1 in the overload zone b. P2 rolling area

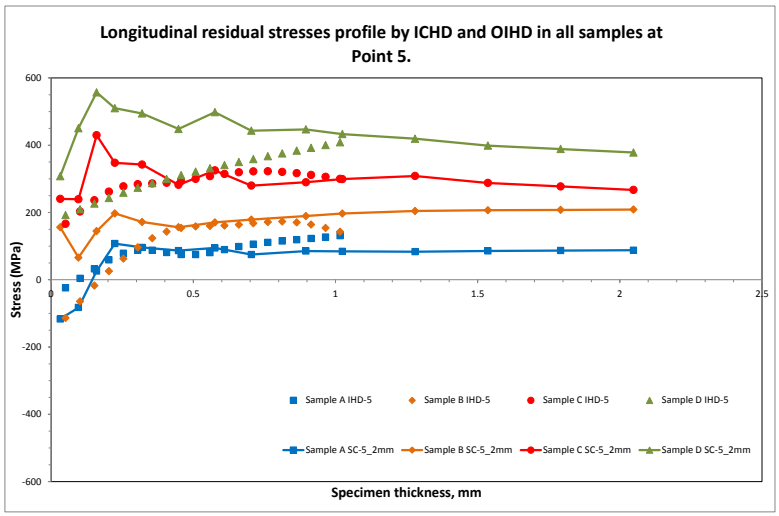

c. P5 far away from the rolling track

Figure 5-9 Comparison of residual stresses distribution obtained in the longitudinal direction by ICHD and OIHD over ranges 1mm and 2 mm, respectively. a. P1 b. P2 c. P 5.

Tables 5-2 to 5-5 summarise the longitudinal, transverse, shear stress and principal stress values obtained which are those averaged over 0.8 mm, 1.0 mm and the total hole depth of 2 mm as stated in ASTM [212] since the steepness of the stress gradients and uncertainties encountered for a non-uniform stress field. The RS data in Table 5-2 indicated that the maximum longitudinal stresses at P1 location at 0.8 mm depth were found to be 73% and 60% of yield stress at 1.0 mm depth in compression in samples D and A, respectively.

Table 5-2 Summary of Residual Stresses in plates A, B, C and D point 1 by ICHD. Six passes.

Plate	Hole depth (mm)	Residual Stresses (MPa)			Principal Stresses (MPa)		Angle
		longitudinal	transverse	shear	maximum	minimum	°
A1	0.8128	-336	-374	-71	-282	-428	53
	1.016	-343	-424	-73	-300	-467	59
B2	0.8128	-194	196	147	245	-244	-19
	1.016	-122	277	166	338	-182	-20
C2	0.8128	-320	28	138	76	-368	-19
	1.016	-313	-180	160	-158	-342	-8
D1	0.8128	-414	-78	-109	-45	-446	17
	1.016	-329	-10	-76	21	-193	23

As listed in Table 5-3, at the P2 location, the amount of residual stress at 0.8 mm becomes 64% of yield strength in compression and 72% compressive stress of yield strength at 1.0 mm deeper in plate B.

Table 5-3 Summary of Residual Stresses in plates A, B, C and D at point 2 by ICHD. Three passes.

Plate	Hole depth (mm)	Residual Stresses (MPa)			Principal Stresses (MPa)		Angle
		longitudinal	transverse	shear	maximum	minimum	°
A1	0.8	-252	-53	28	-49	-256	-8
	1.0	-261	-113	20	-111	-264	-7
B1	0.8	-362	71	86	87	-379	-11
	1.0	-409	50	99	70	-430	-12
C1	0.8	-316	179	162	228	-365	-17
	1.0	-304	242	207	312	-374	-19
D1	0.8	-315	-499	79	-285	-528	65
	1.0	-220	-456	27	-217	-459	52

At point 5 (Table 5-4) the RS amount by the ICHD method at 0.8 mm depth was found to be 89% of yield strength and 94% of yield strength in both tensile condition for sample D. For samples A, B and C the difference was between 56% and 21% of the material yield strength.

Table 5-4 Residual Stresses distribution in plates A, B, C and D at point 5 by ICHD. Zero passes.

Plate	Hole depth (mm)	Residual Stresses (MPa)			Principal Stresses (MPa)		Angle
		longitudinal	transverse	shear	maximum	minimum	°
A2	0.8	125	-17	9	126	-18	-86
	1.0	117	-37	-36	125	-45	77
B1	0.8	173	-277	-5	173	-277	-87
	1.0	143	-496	-12	143	-496	-88
C1	0.8	320	-39	39	408	-42	-85
	1.0	306	-175	-96	307	-40	-85
D1	0.8	506	-75	32	508	-76	82
	1.0	536	-81	29	538	-82	86

Similar tendencies were found by OIHD, varying slightly at 11% less than ICHD at 0.8 mm and reducing to 18% at 1.0 mm depth. At 2.0 mm the difference was 66%, which is higher, taking into account that the depth is twice the distance from the surface.

Table 5-5 Residual Stresses distribution in plates A, B, C and D at point 5 by OIHD. Zero passes

Plate	Hole depth (mm)	Residual Stresses (MPa)			Principal Stresses (MPa)		Angle
		longitudinal	transverse	shear	maximum	minimum	°
A2	0.8	75	-63	-13	76	-64	-5
	1.0	84	-38	-6	85	-38	-3
	2.0	88	-9	-2	88	-9	-1
B1	0.8	179	-108	23	181	-110	5
	1.0	197	-84	25	199	-86	5
	2.0	209	-34	30	212	-37	7
C1	0.8	280	-127	-7	280	-127	-1
	1.0	299	-103	-26	301	-105	-4
	2.0	267	-104	-19	268	-105	-3
D1	0.8	447	-108	11	444	-109	1
	1.0	433	-108	-8	433	-108	-1
	2.0	378	-167	-23	379	-168	-2

The surface stress determined gives an indication of the greater level of compressive residual stress that can be produced by increasing the amount of work hardening as a result of multi-pass rolling. It can also be seen that there is a considerable variation in the residual stress through-thickness. If localised yield should be present during drilling the hole, the results of RS could be overestimated as a result of local yielding. Figures 5-10 display the differences computed for the residual stress values analysed using the integral method for the P1and P2 points by ICHD; while Figure 5-11 shows it for P5 by ICHD and OIHD.

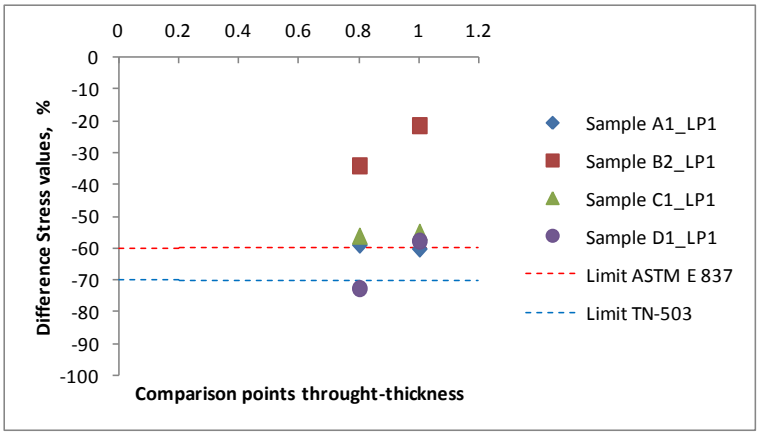

a. Point 1 by ICHD

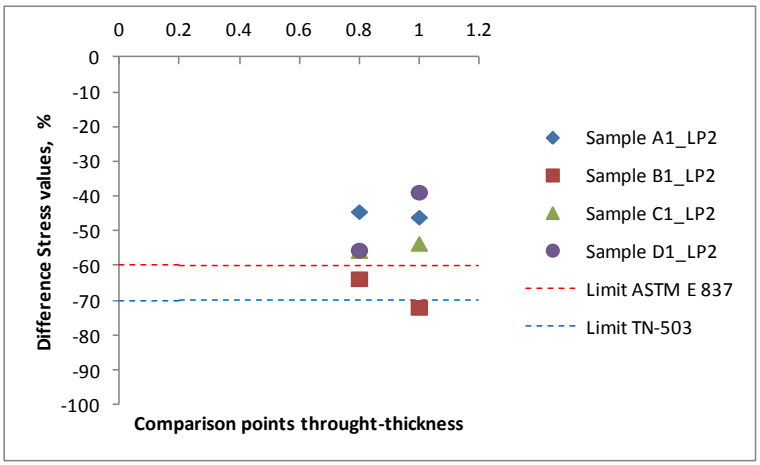

b. Point 2 by ICHD

Figure 5-10 Comparison in percentage of RS obtained by ICHD at P1 and P2 over 1 mm depth. Dotted line indicates limits since RS is valid while negative axis (***y***) indicates compressive stress. L = longitudinal orientation and P = point assessed.

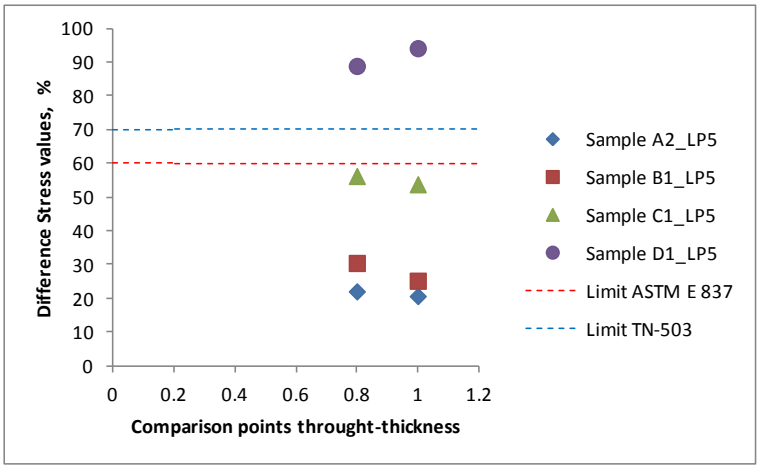

a. Point 5 by ICHD

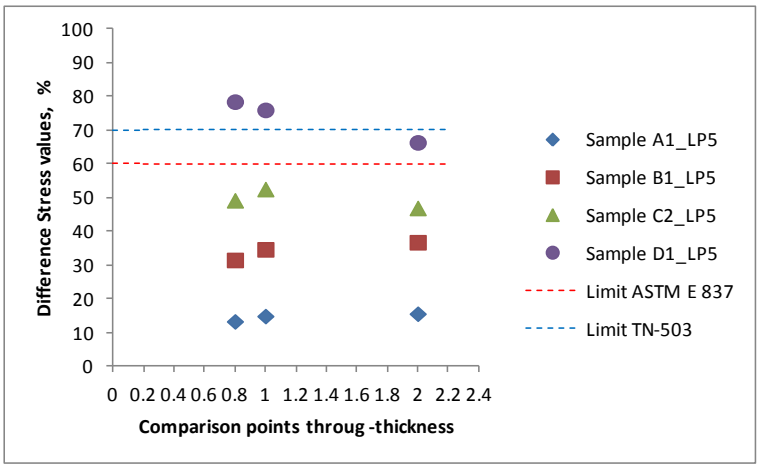

b. Point 5 by OIHD

Figure 5-11 Comparison in percentage of RS obtained by ICHD and OIHD-at P5 over range 1 mm to 2 mm depth. Dotted line indicates the limits up to RS values that are considered valid. Positive axis indicates tensile stress. L= longitudinal orientation and P = point assessed.

However, different investigations have stated and it is consequently accepted that errors can be neglected when computed residual stresses are between 60% and 70% of the material yield stress [251,260]. Thereby, it might be inferred from Figures 5-10 and 5-11 that residual stress measured (compressive/tensile) at less than 343 MPa is valid.

As discussed above, ICHD and OIHD assessments were made for depths of 0.8 mm, 1.0 mm and 2.0 mm which are summarised in Table 5-6. However, as ND is constrained to IGV near to the surface, comparisons for the three methods were performed at 0.8 mm in order to establish differences or tendencies for all of them in line with points 1, 2 and 5. It can be depicted in Table 5-7. Nevertheless, it is important to clarify that only the line point 5 was compared by the three methods used in this investigation. All the results obtained are summarised and discussed in numeral 5.4.

5.4 Discussion of results

5.4.1 Residual stress

As stated in the introduction to this chapter, the combination of IHD and ND complement each other to measure the RS profile induced by any surface modification method. From the results given in section 5.3, which are plotted in Figures 5-12 to 5-14, a discussion of the techniques was required as well as an understanding of the residual stress field pattern obtained. The variation in residual stress between incremental hole-drilling and ND are plotted together in order to estimate the stress profile at points 1, 2 and 5.

From the figures it is noticeable that there is a good match from the data obtained by ND, observable through-thickness; however, there is a particular variation between the two faces of the sample which is common between the stress profiles. Due to the condition of the rolling process, the deformation was made in two steps. When the sample is rolled on one of the sides, compressive stresses are induced causing upward deformation on the plate, generating tensile stress in the middle of the plate and near to the surface. It is presumed that this has an effect on the residual stresses pattern, therefore causing deviation at the different points examined.

Table 5-6 Longitudinal RS obtained by ICHD & OIHD at 1.0 mm and 2.0 mm depths at point 5 in plates A, B, C and D

Plate	Incremental Centre Hole-drilling						Orbiting Incremental Hole-drilling											
	Residual stresses at depth 1.0 mm						Residual stresses at depth 1.0 mm						Residual stresses at depth 2.0 mm					
	Residual Stresses (MPa)			Principal Stresses (MPa)		Angle	Residual Stresses (MPa)			Principal Stresses (MPa)		Angle	Residual Stresses (MPa)			Principal Stresses (MPa)		Angle
	σ_{xx}	σ_{yy}	τ_{xy}	σ_1	σ_2	°	σ_{xx}	σ_{yy}	τ_{xy}	σ_1	σ_2	°	σ_{xx}	σ_{yy}	τ_{xy}	σ_1	σ_2	°
A	117	-37	-36	125	-45	77	84	-38	-6	85	-38	-3	88	-9	-2	88	-9	-1
B	143	-96	-12	143	-196	-88	197	-84	25	199	-86	5	209	-34	30	212	-37	7
C	306	-175	-96	307	-40	-8	299	-103	-26	301	-105	-4	267	-104	-19	268	-105	-3
D	536	-81	29	538	-82	86	433	-108	-8	433	-108	-3	378	-167	-23	379	-168	-2

Table 5-7 Comparison longitudinal RS measured by ICHD, OIHD and ND at 0.8 mm depth in samples A, B, C and D. Units in MPa.

Plate	Point 5 (0 passes)			Point 2 (3 passes)		Point 1 (6 passes)	
	OIHD	ICHD	ND	ICHD	ND	IHD	ND
A	85	125	91 +/- 49	-252	-245 +/- 40	-336	-263 +/- 39
B	189	173	166 +/- 36	-362	-384 +/- 43	-194	-199 +/- 52
C	290	320	177 +/- 42	-316	-363 +/- 42	-320	-320 +/- 42
D	447	506	496 +/- 75	-315	-275 +/- 67	-414	-374 +/- 26

Reversing the sample and rolled with the same load, part of the compressive stress induced is used to reduce tensile stresses developed in the previous part. It can also be found that residual stresses were slightly tensile for all the points. Due to misalignment or mis-positioning it might be expected to see a disparity in the readings as a result of the bend introduced.

Chahardehi et al. [377] investigated the residual stresses effect in fatigue by laser peening and found that the compressive stresses were reduced due to the introduction of new tensile stresses when the sample treated both faces at different times. Similarly, Coules et al. [312]and Cozzolino [378], reported the same effect in their investigation using a low carbon steel in a pre-welding process.

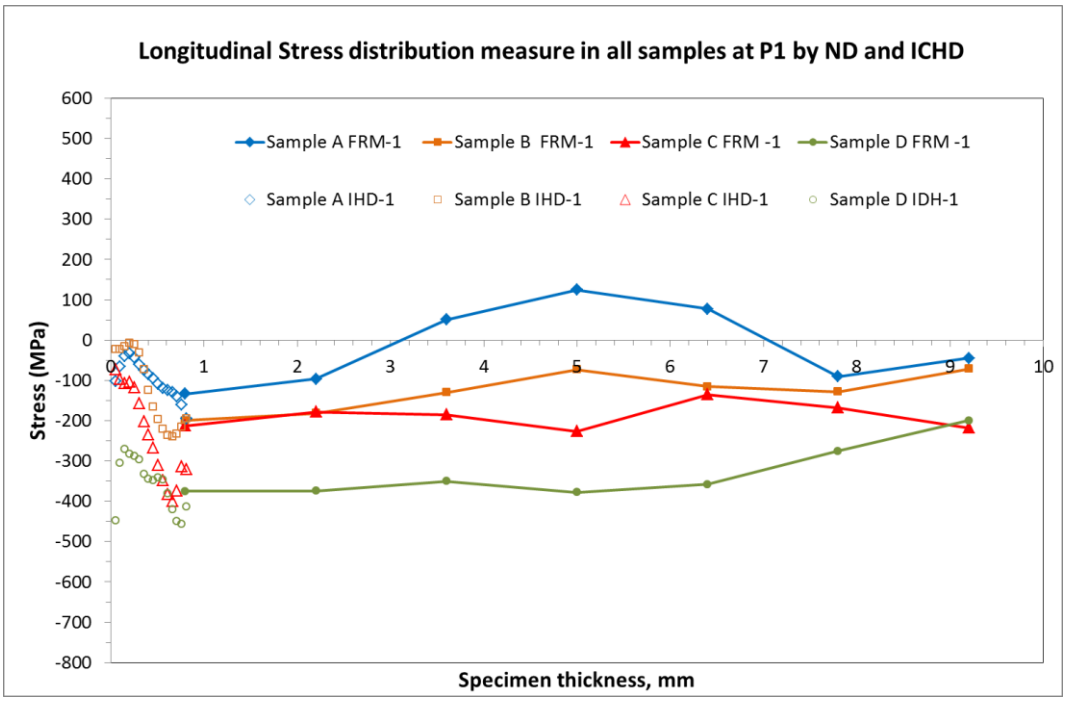

Figure 5-12 Comparison longitudinal residual stresses distribution obtained by ICHD and ND at point 1 at 0.8 mm depth.

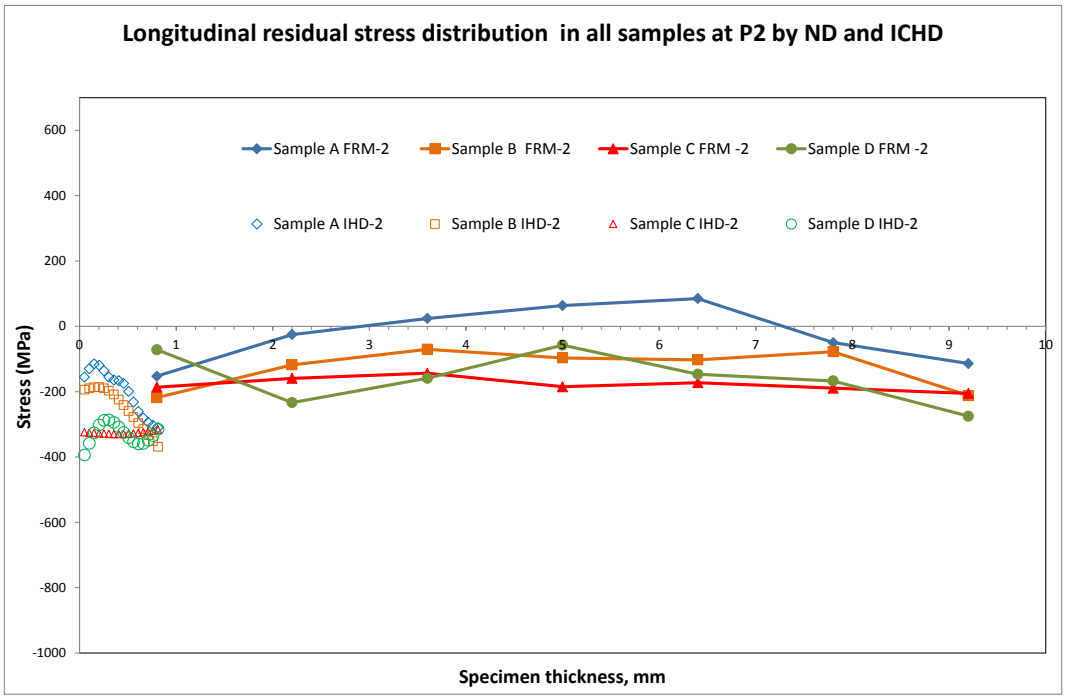

Figure 5-13 Comparison residual stresses distribution obtained by ICHD and ND at point 2 at 0.8 mm depth in a longitudinal direction

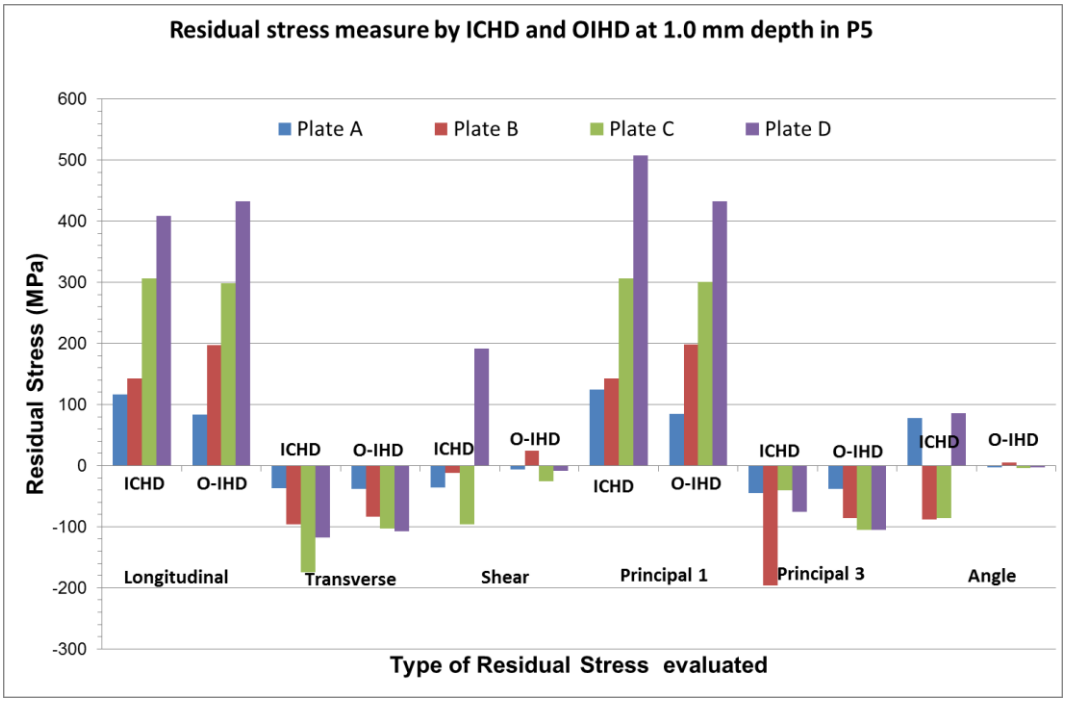

Figure 5-14 Comparison residual stress variation in longitudinal, transverse and normal directions at 1.024 mm depth by ICHD and OIHD methods in P5

This should explain the tendency for one of the sides of the samples to be less compressive or more tensile when the RS was measured. Figure 5-14 shows the results of the residual stress measurement using the three methods used in this investigation. Reasonable results were obtained for the points of interest in common. The results are quantitatively similar and the three methods have good reproducibility but they may have considerable inaccuracies, particularly the incremental hole-drilling.

The residual stress evaluated by incremental hole-drilling, ICHD and OIHD, shows good agreement with the expected tendency for cold rolling. Figure 5-15 presents a comparison of residual stress measurements using ICHD and OIHD for P5. In the majority of the cases, the results indicate that the stress in the longitudinal and transverse directions were similar for all the samples with a slight difference for sample C in the transverse orientation for both methods.

Sample C reached almost 100 MPa more using ICHD or OIHD than ND. Although this behaviour it is not clear compare with the tendency in the other samples, it could be assumed that there is remarkable influence of the scatter of the amount of compressive strains measured by ND technique for this particular sample. Table 5-8 summarises the residual stress determined by OIHD and ND which are compared at a 2.0 mm depth at point 5. It can also be seen that values at 2 mm for both ND and OIHD seem consistent as good agreement exists between the RS measurement as a result of the load applied.

There are other factors which account for the differences in the measured residual stress profiles for the conventional and orbiting methods. These factors can be broadly classified into two main categories: firstly differences caused by the technique and secondly, variations which originate due to the material properties. Thus a number of factors need to be analysed for the stresses values measured for the two measurement techniques.

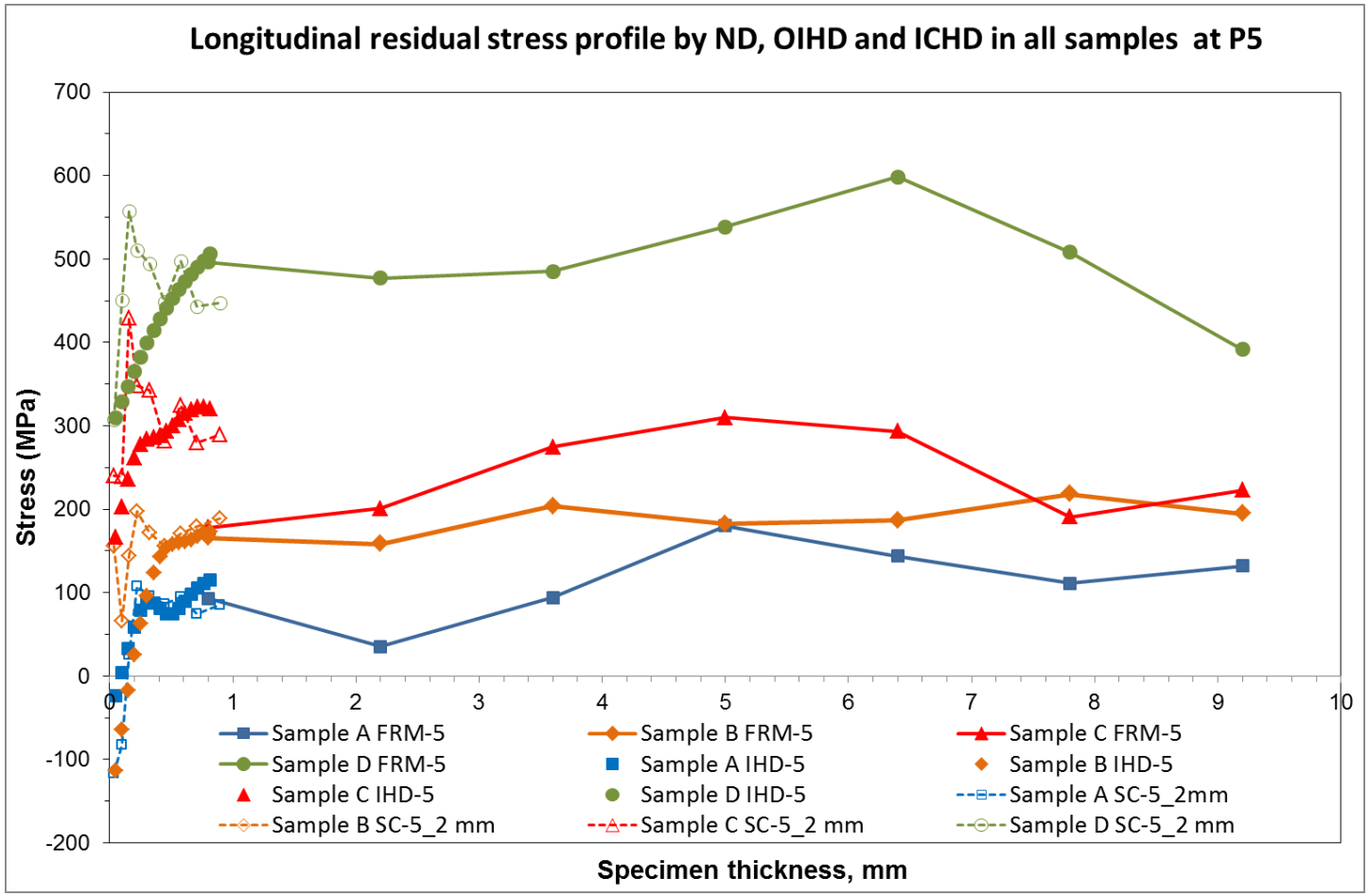

Figure 5-15 In-depth longitudinal residual stresses comparison by ND, ICHD and OIHD over the range to 0.8 mm at P5

Table 5-8 Results of residual stresses obtained by ND and OIHD on plates A, B, C and D at point 5 at 2.0 mm depth

Plate	Residual Stresses (MPa))	
	OIHD	ND
A	88	111 +/- 74
B	208	159 +/- 55
C	267	201 +/- 57
D	378	477 +/- 102

From the computed stresses, it was found that there was a significant difference existing on the stresses and the calculated angle. It has been pointed out by some researchers, such as Scafidi et al. [271,379], Render and Vigness [245], Schajer [272], Nau et al. [256,270] and Nobre et al. [380] that variations in the RS are part of the experimental uncertainty which undoubtedly affects the final value. In reference [263] it is emphasized that hole-drilling is highly sensitive to small errors in strain measurement as it can cause large errors in the computing stresses.

Casavola et al. [381] investigated the integral and power series stress calculation methods using two commercial systems. They found that different responses are obtained depending on how the strain measurement error was evaluated. The error in Restan software was 400% higher than H-Drill at 20 depths as the latter has implemented Tikhonov regularisation. In addition the errors increasing in the strain measurements at a higher drilling step, due to conventional strain gauges, are less sensitive at a higher depth.

By reducing the number of steps, the error level on the calculation is reduced. It could be that one of the causes regarding the lower stress values obtained in this investigation, and taking into account the integral method used to evaluate the data in this research, was developed without the regularisation mentioned by Casavola et al.

Results from ICHD, calculated by integral method, exhibited considerable uncertainties in the first step up to 0.3 mm approximately, reducing of measure with the depth. This behaviour has been reported in other investigations [230,382–384] and it has been found that the residual stresses were always lower in magnitude. Nau and Scholtes [256] investigated the effect of bit geometry and drilling techniques. They used the RS-200 Milling Guide, standard strain gauge rosette, six-blade bit, two-blade bit and diamond bits. This study found that the geometry and positioning depth have a significant influence on the strain measurements.

The RS measurements by orbital drilling (OIHD) with six-blade bits for the first increments are uncertain as sometimes they can be compressive and sometimes tensile. Also another consequence of the inaccuracy of the measurement is due to chamfers that affect the depth settings. In order to explain this, Nau and Scholtes simulate the effect of different deviations from the ideal depth position (see Figure 5-16). The results show that deviation from the ideal position, ***t*** +/- 0.005 mm, means the error involved is at least +/-15 MPa and at ***t*** +/-0.015 mm the error is +/-35 MPa.

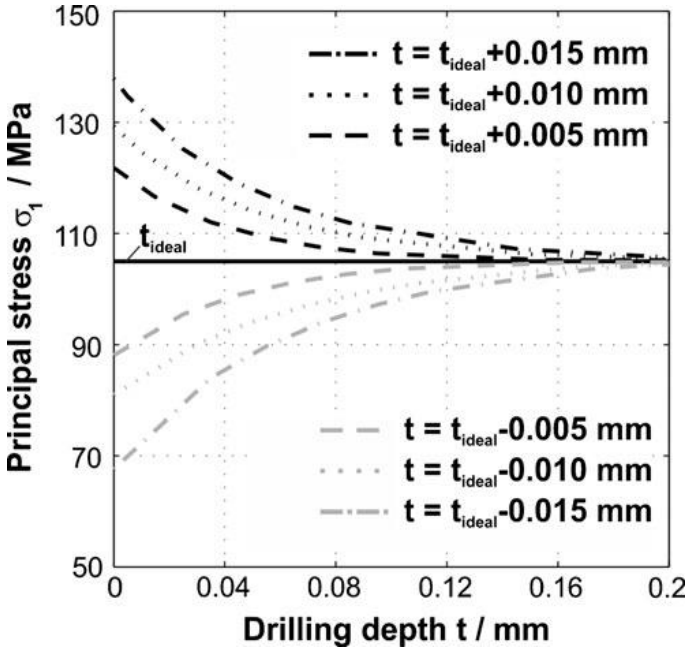

Figure 5-16 Relationship between initial depth setting and hole diameter inaccuracy by FE [320]. Stress reference is 105 MPa.

From this simulation it could be concluded that the determination of residual stress between 0.0 mm to 0.2 mm depth and error of +/-33% is always present which increased RS uncertainties near to the surface and explains clearly the findings reported by others researches although it was not explained at the time [374,382]. In addition, simulation of the release strains by conventional drilling with six-blades is approximately 60% less than the ideal one for the three directions evaluated.

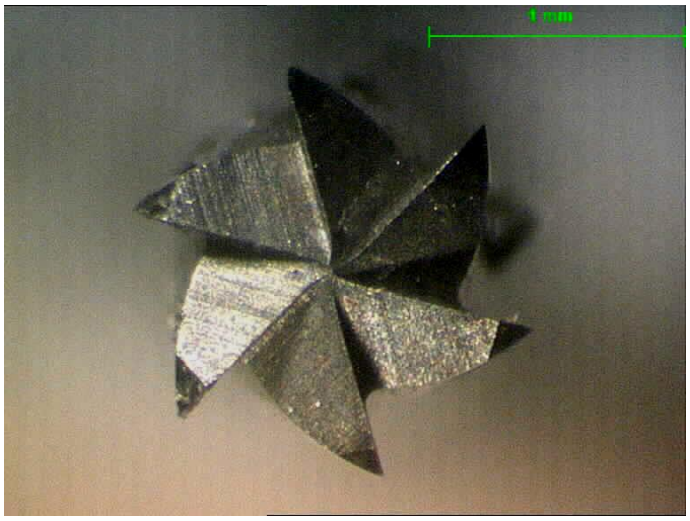

a. Cutter profile by OM

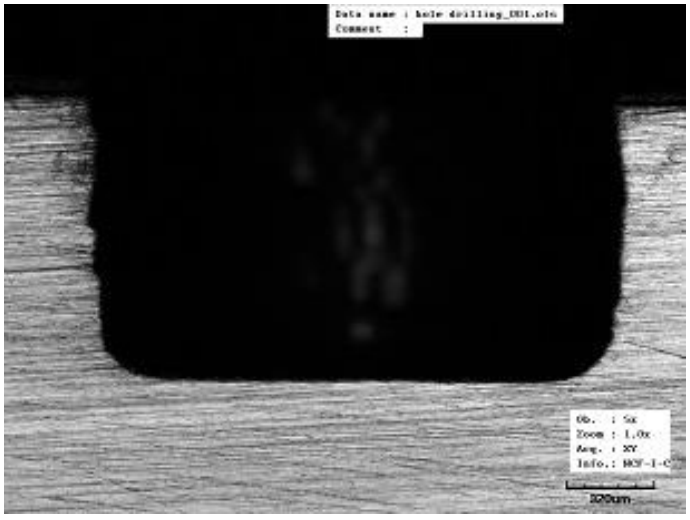

b. Hole-drilling profile after test

Figure 5-17 Typical configuration of bits used to drill a hole (a) Six-blade bit (b) ICHD hole profile obtained by optical microscope

In order to verify the type of cutter utilised and the hole-profile obtained, a sample was prepared after the hole was drilled. A precision cutter was used to obtain a half-section of the hole. Figure 5-17 shows the geometry of the bit and the hole-drilling profile. It can be seen that the cutter has a chamfer which is 0.05 mm length at an angle of 42°.

It is noticeable that the hole shape differs from the ideal cylindrical hole with a flat bottom and sharp edges assumed from the calculation using the integral method. To understand the issues with the depth setting, a drawing was made which is presented in Figure 5-18. The total diameter of the bit is about 1.6 mm; however, only a small part of the hole has been chosen (rectangular red) to give a detail of the remaining material consequences of the chamfer found on the bit.

The scheme clearly presented that the final hole diameter cannot be completely drilled during the first steps, due to the chamfer's dimensions, or to achieve the total hole depth with any accuracy. This verification matches the work in references [256,257,380,382]. In summary, it can be concluded that the experimental parameters have a considerable influence on the reliability of residual stress determination by the hole drilling method. It is clear that each method has important advantages and drawbacks, too.

For ND the method is very accurate but requires special facilities and extreme care for a high accuracy result, which made it very expensive. Hole drilling has the advantage of being semi-destructive and can be used for large structures and it is portable and less expensive. Here it is important to clarify that hole drilling is considered "semi-destructive" because the hole would raise the local stresses at the surface and make crack initiation more likely.

Inaccuracy and the necessity for surface preparation could be one of its major disadvantages. However, from this research it could be highlighted that in spite of the error implicated in each technique, the results obtained, summarised in Figure 5-19, show that one important feature of all the figures is the similarity of the trends and magnitudes of the RS evaluates.

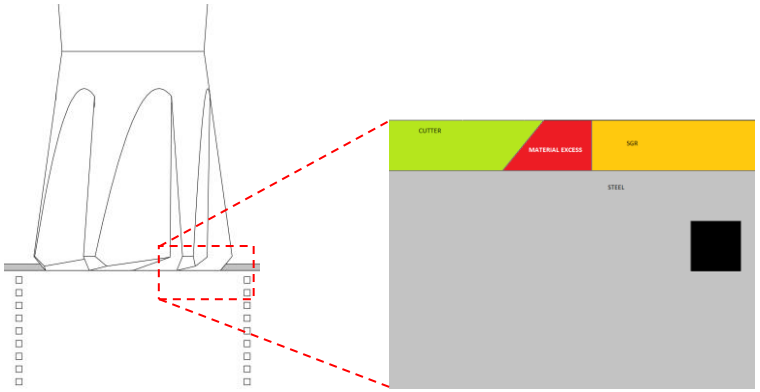

a. Non-zero

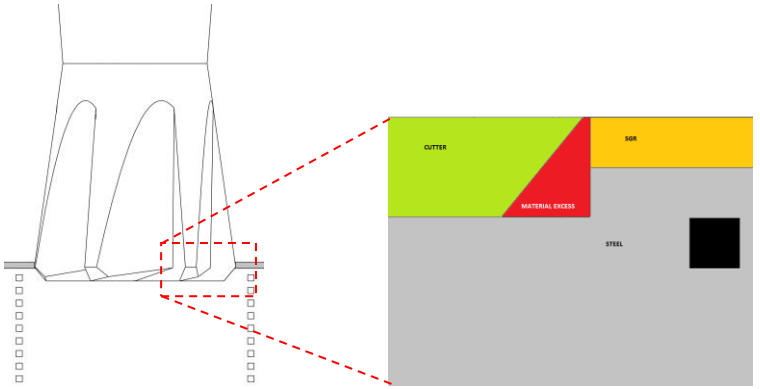

b.-0.05 mm

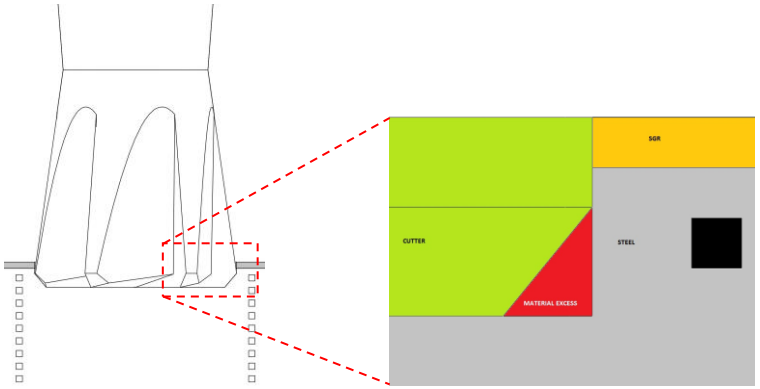

c. -0.15 mm

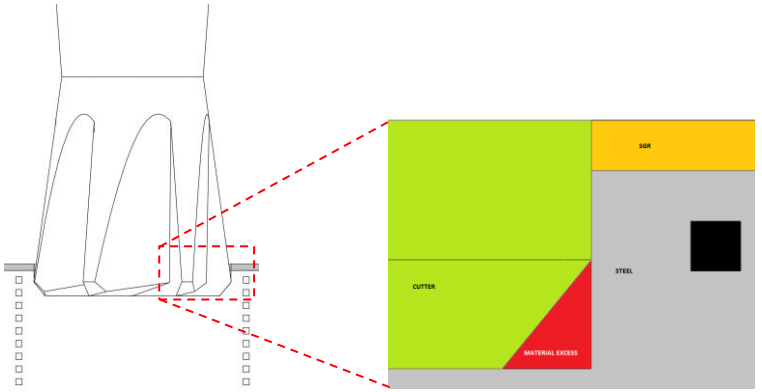

d.-0.20 mm

Figure 5-18 A schematic drawing of the incremental hole-drilling process up to 0.20 mm depth

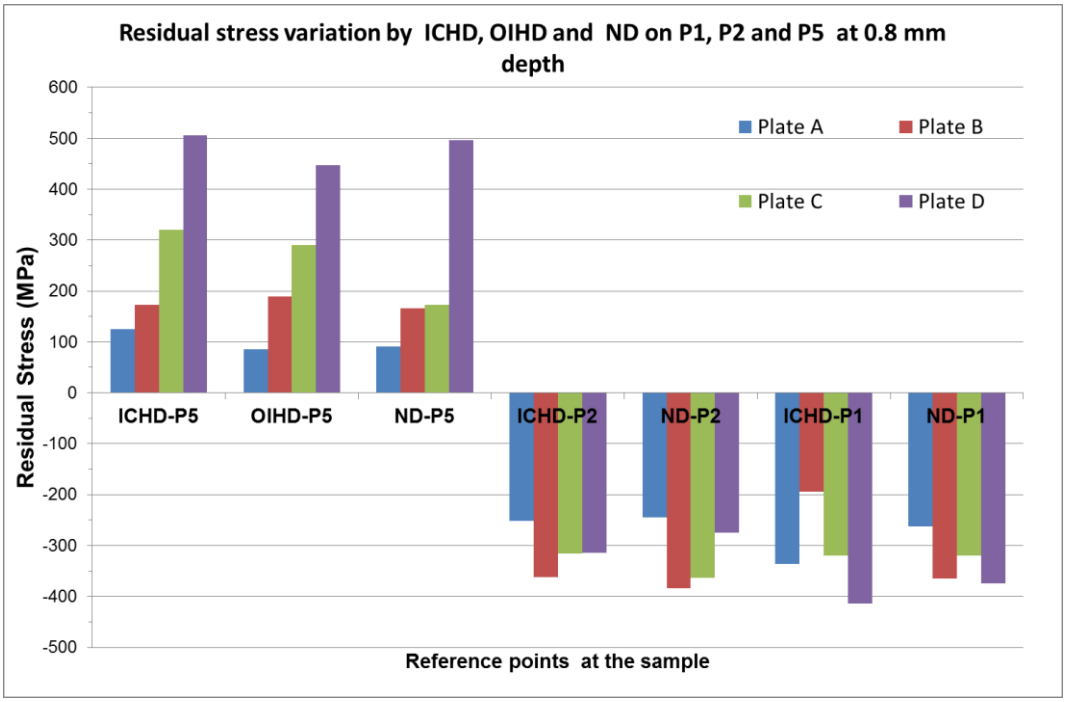

Figure 5-19 Comparison residual stress distribution by ICHD, OIHD and ND at 0.8 mm depth in a longitudinal direction

5.4.2 Elastic-plastic stress

Classical Hertz theory established the elastic solution for the contact stress of two surfaces, either a cylinder-cylinder or cylinder-flat plane. From this theory the pressure distribution and stress in the contact region to introduce deformation on the surface have been explained in detail by many authors such as Hamilton [385], Ollerton [386], Merwin and Johnson [387].

The influence that the residual stress state induces beneath the contact surface of rolling near the surface is marked by the presence of two stresses: one oriented in the longitudinal direction (σ_{xx}) and the other in the transverse direction (σ_{yy}). The normal stress (σ_{zz}) can usually be ignored as it is particularly small [388]. Residual stresses induced by plastic deformation during repeated loading have been investigated and a good match between theoretical assumptions and experimental measurements have been reported in the literature available [389–392].

From the literature it has been pointed out that the minimum Hertz stress necessary to produce residual stresses depends on the material strength and the order of stresses; magnitude is always reached in the first cycle of loading [393]. However, the maximum number of passes to induce plastic deformation, carrying compressive stresses, is conditioned at the historical cycle loading and determined by a point of steady state beyond which its slightly plastic deformation could be introduced but once a limit point is reach distortion will not be contained for the elastic material.

Investigations carried out by Knight et al. [313,394], and Chahardehi et al. [377] analysed the significance of surface modification and its effect to improve fatigue life and corrosion resistance of components by introducing beneficial residual stress. Wang and Mote [395] investigated the effect of localised rolling in bandsaw steel strips, and found that compressive RS grew asymptotically as the rolling load increases.

Reference [394] investigated the influence of compressive residual stress controlling the cold rolling process. They found that after three roller passes a greater amount of compressive residual stresses are introduced as a result of deformation arising. Figure 5-20 illustrates the results obtained for both works where it was found the number of rolling passes to obtain an effective RS distribution is dependent on load applied.

In reference [378] a simulation of cold rolling was made on a low carbon steel. Figures 5-21 and 5-22 show comparisons of the variation of the predicted longitudinal plastic strain in the upper and lower surfaces across the plate width, between the frictionless and friction models, after rolling at 55 mm from the edge, with 50, and 200 KN loads, respectively, and unclamping.

The stretching of the material, along with the rolling direction (longitudinal), was indicated for a positive value of the plastic strain. As the rolling action was only near the surface, an asymmetrical plastic strain through the thickness was caused. Furthermore, a limitation of the longitudinal plastic strain to the rolling path was caused by rolling with a low load of 50 KN.

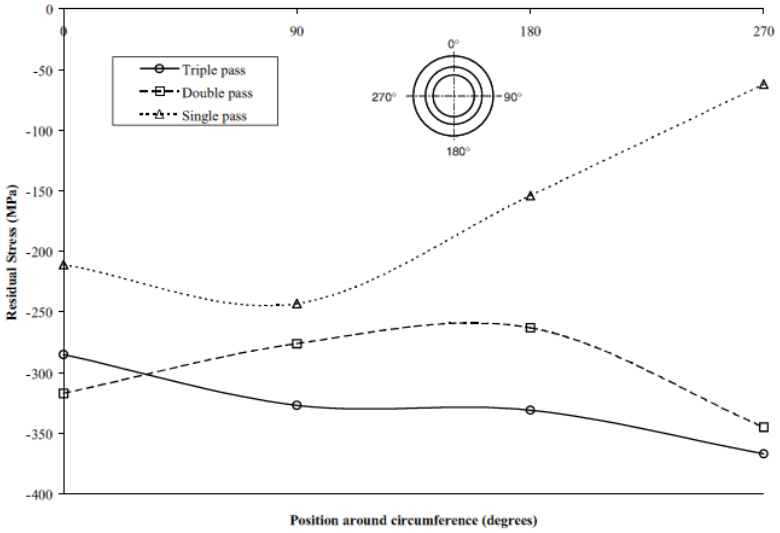

a. Drillstring thread [394]

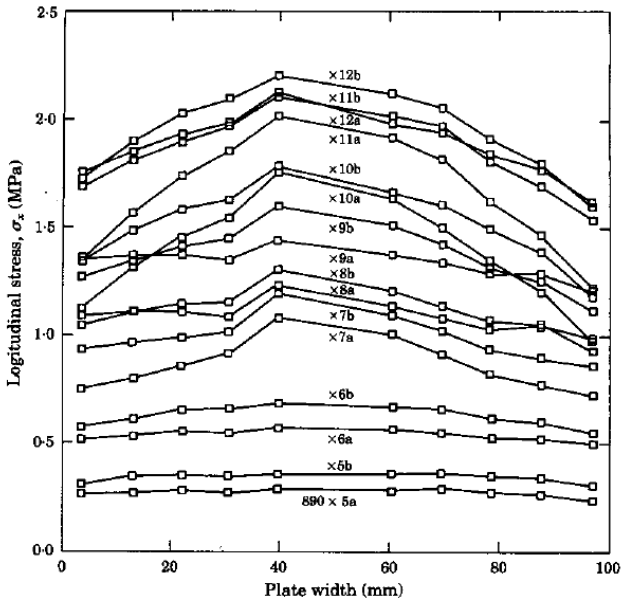

b. Bandsaw plates [395]

Figure 5-20 Variation of RS as a consequence of the number of passes

It was observed that a direct relationship between rolling load and longitudinal plastic strain was found. Increasing rolling load plastic strain is magnified in magnitude with a wider deformed plastic region. The high plastic deformation peak was observed with the highest load, 200 KN, and 10 mm wide roller.

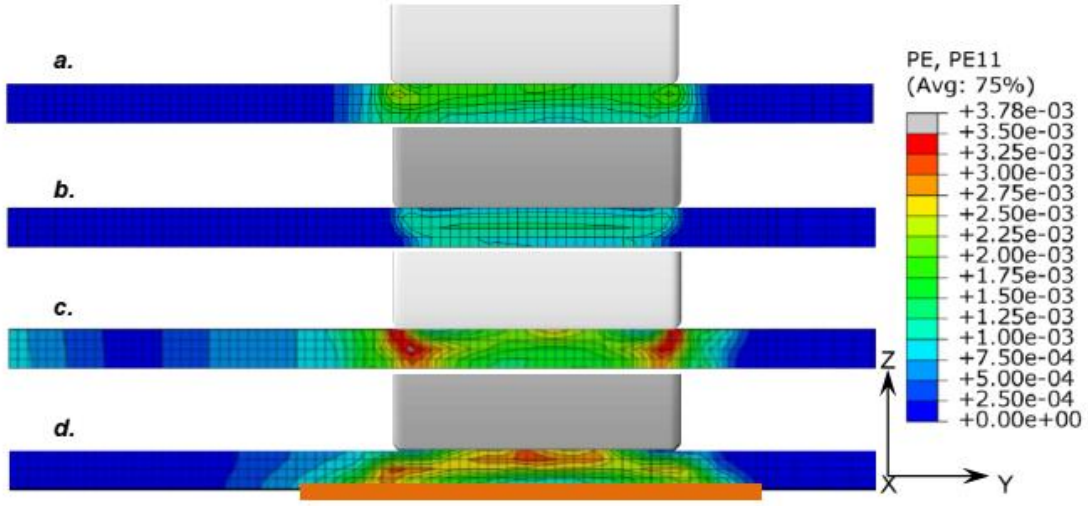

Figure 5-21 Contour plot of longitudinal plastic strain after rolling with 50 KN load *a.* frictionless, *b.* with friction; and 200 KN *c.* frictionless, *d.* with friction [378]

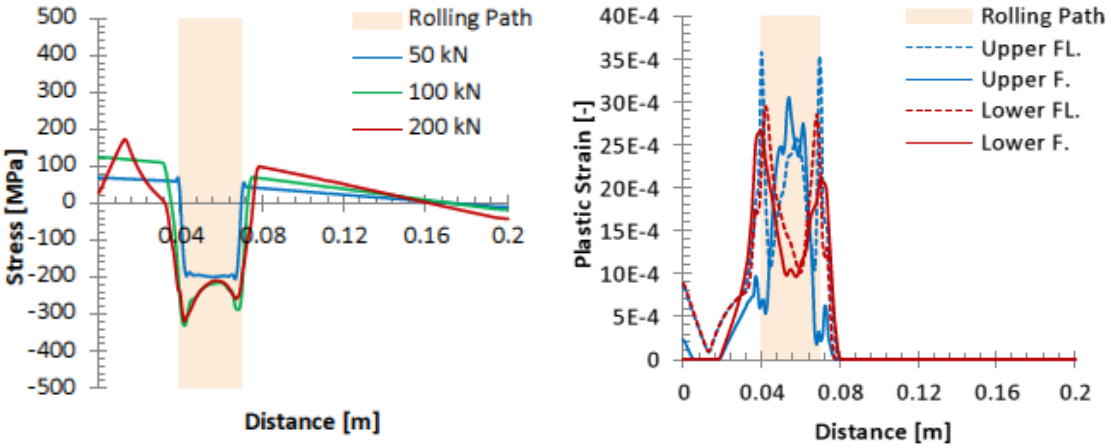

Figure 5-22 Variation of RS and plastic strain as a consequence of the number of passes[378]

Figure 5-23 represents the transverse cross section of the samples where cold rolling was performed. As mentioned above, two section areas were established, two with three passes each and one with six passes. From the plot, the features of the rolling track can be observed. At lower loads the contact area is elastic; however, by increasing the load the stress field will reach the material yield point.

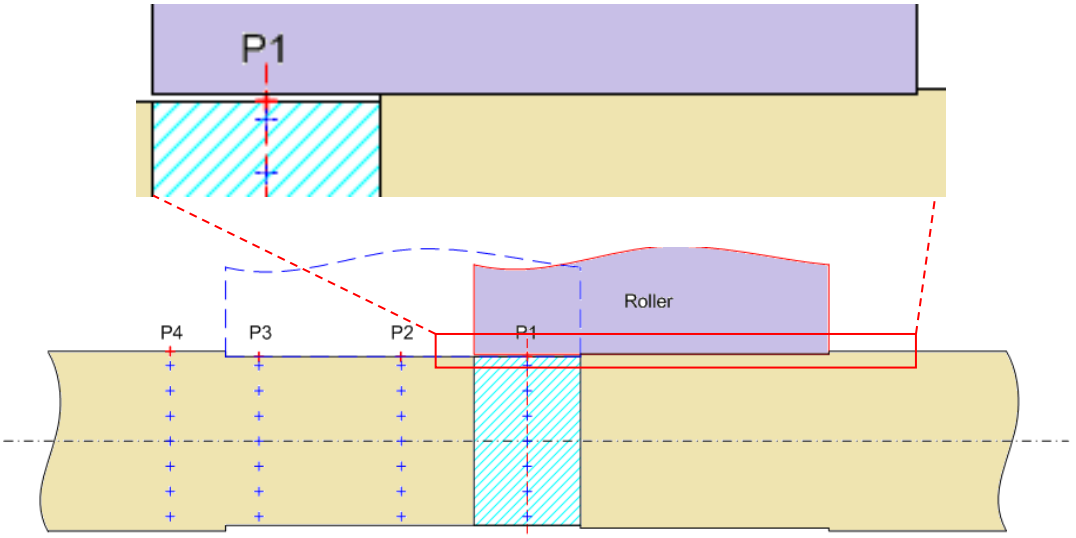

Figure 5-23 A schematic drawing of the transverse section of the plate on the rolling track showing deformation depth differences on both sides of the plate during the rolling process

At higher loads some plastic flow is present leaving residual stress under the rolling track after the roller has passed. If subsequent passes of the load are applied the material is exposed to a combination of residual and contact stresses. Hence, for loads not greatly in excess of the elastic limit, plastic deformation will be contained by the elastic material and the order of the elastic and plastic strains will be the same. However, once the yield point is passed a plastic deformation is formed and the shakedown limit is exceeded. Local plastic deformation is in place in a layer at a depth of approximately ***0.7a*** according to Hertz's theory. During this deformation the surface is compressed only slightly below its original level and residual elastic compressive stress is acting parallel to the surface.

The analysis presented above is orientated to give an explanation about the rolling process. The samples used in this investigation were rolled following the process detailed in Chapter 3. Therefore, it could be inferred that the number of passes applied to each zone has enough energy to induce compressive stresses beneath the rolling track area. However, it was found that the step produced during the process could affect the stresses.

During rolling, increasing rolling loads caused deep penetration of the roller in the material which produces the build-up of material in front of the roller, as shown in Figure 5-24 (a-c), causing local work hardening in the portion of material in front of the roller. As a result of the work-hardening, the roller is not able to cause similar plastic deformation since the load applied was constant, as can be seen schematically in Figure 5-24a.

Once the material reached the point where no more work-hardening can be inferred further, Figure 5-24a, the roller jumped and then it underway rolling material again with the difference that the new material has not been deformed to the same scale, as shown in Figure 5-24 b and c. As a result ripple marks might be formed in the surface of the material after rolling due to the huge rolling loads.

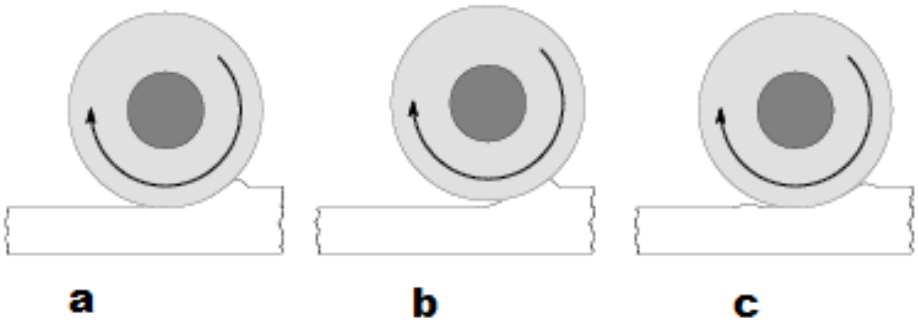

Figure 5-24 A schematic drawing showing normal plastic deformation during cold rolling [378]

Furthermore, numerical simulations conducted by Cozzolino [378], have shown that local rolling carried out with constant rolling penetration (instead of the rolling load), caused variations in the vertical rolling force causing the ripple marks on the material surface.

It could be inferred that the asymmetric distribution of stresses could be introduced due to the rolling process that was made by steps on one side. If this assumption is correct, it is expected that the amount of the compressive stress on point 1 will be greater than that on point 2 as the number of passes was double.

However, the values listed in Table 5-7 show that the values do not follow the pattern that was expected and random values were found. This indicated that the preliminary deformation was affecting the second step or that the roller was not in flat contact with the material surface.

5.5 Summary

- Beneficial longitudinal and transverse residual stress induced through thickness increasing along the load is enlarged mainly in points 1 to 3, averaging at point 4 and marginally affecting point 5 which remains tensile. Normal stresses were always tensile (150 MPa) inferring, perhaps, that the remaining stresses are present from the manufacturing process.
- Cold rolling, depending on the load applied, generates transverse, lateral and longitudinal deformations in the rolling track and on the outside of it. The lateral plastic deformation widens the plate where the peak is located in the middle of the rolling area.
- The longitudinal plastic deformation induces residual longitudinal compression in the rolling track and longitudinal tension in the plate outside the rolling track. Residual stress in the rolling track is highly compressive and is proportional to the magnitude of the average longitudinal plastic strain.
- The compressive RS induced by rolling in the rolling path is equilibrated by tensile RS beside the rolling path. Asymmetrical distribution is the effect of the load applied.
- The stress values obtained for ICHD were lower compared with ND; however, a reasonable correlation was found and a good agreement between stresses measured by OIHD was determined.
- The reproducibility of the three methods shown a reasonable agreement between the stresses determined at the depth of the cross-over point of 0.8 mm, 1.0 mm and 2.0 mm.
- The results obtained by ICHD, OIHD and ND may be different as the stress values average over different layers. Combinations of these give a good

agreement and offer the most suitable of the stress profiles on the surface as well as across the depth of the specimen.

Next Chapter failure assessment diagram have been performed by R6 code. The analyses are carried out by integrating all the mechanical properties evaluated in previous Chapter. Operational pressures where supercritical conditions of CO_2 are met contributed to enhance the understanding about the integrity of pipelines exposed a flue-gases and tested over range -70°C to 21 °C by a Leak-before-break approach.

6 ENGINEERING CRITICALITY ASSESSMENT

6.1 Introduction

The main concern in transporting flue-gas by pipeline is determined by operating conditions (high pressure and temperature), flaw-crack presence for material-environment interaction, material defects and installation damage. When a flaw is present, the probability of failure increases in the system.

For CCTS to become a reality, pipeline integrity will need to be assured. Implementation of integrity managed programmes could minimise risk and prevent likely failures by addressing properly the integrity threats based on structural integrity assessment. Structural integrity assessment involves many aspects, such as engineering critical assessment and fitness-for-purpose services (FFS), where methodologies and procedures are well-known for assessing the significance of defects in components, depending on the application [37,284,396–398].

R6 is one of these procedures and the failure assessment diagram (FAD) is the most popular for flaw assessment. Zerbst et al. [284,292] and Ainsworth et al. [288,289,397] present an overview of the major methods currently in use where FAD is the common assessment route for analytical assessment. FAD is a plot of the failure envelope of the crack, demarcated in terms of K_r, L_r and flow stress parameters that define the failure assessment diagram for each condition tested.

In accordance with the scope of this research, to assess the integrity of the steels used in this research, either in virgin condition or exposed simulated flue-gas, all the data obtained over the previous sections such as tensile properties, fracture toughness and residual stress values were collected along with other input such as physical properties which were obtained from the literature to complement the information required to perform the analysis.

The aim is to establish an engineering framework for HSLA steels working at a lower temperature plus in a harsh atmosphere which are assessed under FAD option 2 of the LbB procedure within the BS 7910-13 guide [35].

6.2 Leak-before-Break (LbB) procedure

A leak-before-break (LbB) assessment has been applied previously in the nuclear sector; however, it is now common practice in engineering to design or assess pressure vessels and pipelines. There are two LbB procedures to be considered. The first is called the “detectable leakage” procedure considered to be a through-wall flaw, which cannot be a part-penetrating flaw. The procedure starts under the assumption that fluid leakage can be detected before a flaw reaches the limiting length.

The second is known as the “Full leak-before-break” procedure and it can be applied when flaws are detected or felt likely to occur. Both procedures involve the following steps:

- Characterising the type of defect or assuming one
- Determination of the limiting length, $2c_c$,of through-thickness flaw
- Calculation or estimation of flaw length, $2c_L$ or $2c_b$, of a through-wall flaw that leaks at the minimum detectable rate under normal conditions of operation
- Calculation of crack opening area
- Calculation of leak rate from flaw
- Estimation time to detect leak from flaw
- Calculation time of flaw to grow to limiting length
- Assess results.

These LbB procedures are basically applied when gases or liquids are involved; however, transportation of anthropogenic CO_2 implicates other aspects which could be critical, and therefore have to be included to assess the system or a pipeline. The data referenced here has been taken from the EGIG [399] report released in 2011 and related to European gas transmission systems:

- Pressure of operation of the current pipelines is undertaken at 65 bar (6.5 MPa), however the tendency is to operate above 75 bar. The most popular grade of steel used is X52, X60; however, notably applications of X65 and X70 have been increasing in the last 10 years. Grade X80 above have started to be used with some restrictions. The most frequently used wall thicknesses are 5 to 10 mm which are increasing to 15 to 20 mm; however, there is no reported thickness beyond 25 mm.
- To transport supercritical CO_2 the optimal pressure is 150 bar (15 MPa); however, the presence of impurities such as H_2S, SO_2 or CH_4 have effects such as the sudden expansion of depressurisation due to a sudden drop in temperature which could reach the DBTT, causing catastrophic failure through brittle-collapse mechanism.
- Damage mechanisms derived from the interaction of material-environment could induce crack or pitting which can trigger a driving force on the crack tip for crack propagation. In the case of leakage or gas decompression, the presence of residual stresses could add extra stress, contributing as driving forces to initiate the crack propagation phenomenon [400,401].
- In the case of an oil or gas leak, the current technology is well developed [402–405]; however, for anthropogenic CO_2 the scenario is critical. CO_2 is heavier than air and might accumulate in depressions. A release of CO_2 would have a negative impact on human life, animals, plants and environment above concentrations of 10% and would be lethal over 25%. Higher H_2S and SO_2 concentrations also have negative effects on health related to toxicity [406–408]. This clearly indicates that sensitivity sensors and methods for fast responses are required [409].

The general overview presented here has indicated that an assessment within the analysis of LbB procedures could be applied as it is considered to be the best approach to determine critical crack length towards avoiding catastrophic failures of pipelines transporting anthropogenic CO_2 in a supercritical phase.

6.3 Failure assessment approach

Basically there are three FAD assessment levels namely options 1, 2 and 3 which, in this order, provide decreasingly conservative procedures. However, in turn, these require an increased knowledge of the mechanical properties, quality of data and obviously there will be an increase in cost.

Linear elastic stress analysis was used to determine toughness ratio K_r and the load ratio, L_r. For a given flaw and load, K_r and L_r are plotted on an FAD. In the diagram, the horizontal axis represents the stress ratio and the vertical axis denotes the stress intensity ratio. The solid curve indicates the threshold for failure that encloses the regions of safety. The FAD curve is defined according to the accuracy required of the analysis indicated by the equations presented within the diagram of Figure 6-1 and represented by the FAD locus in Figure 6-2.

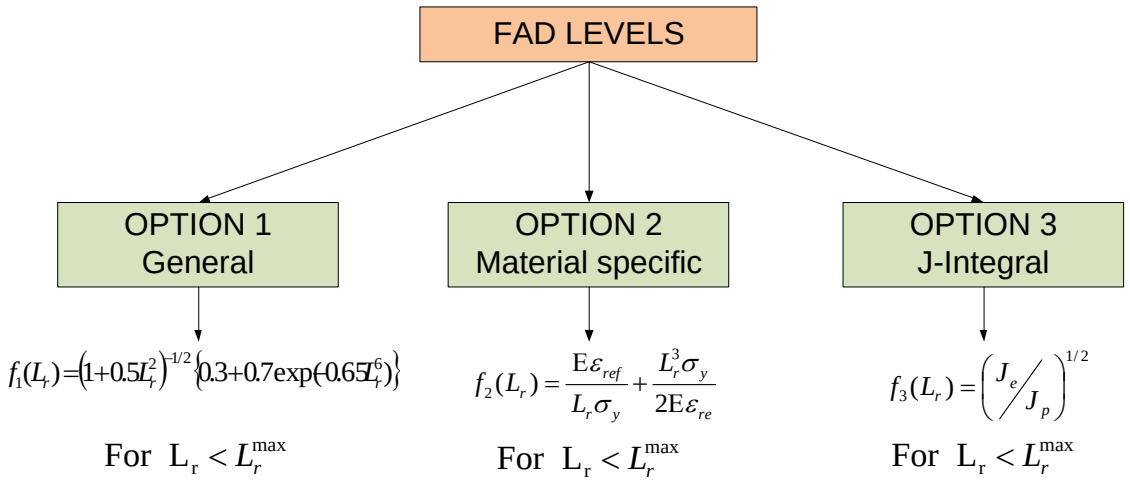

Figure 6-1 Options existing for FAD assessment

Figure 6-3 summarises the type of considerations taken into account to assess pipes or cylinders which would be similar in terms of analysis to be performed. However, the major difference that is addressed is regarding the orientation of the crack on the component, which is indicated by the axial or circumferential direction.

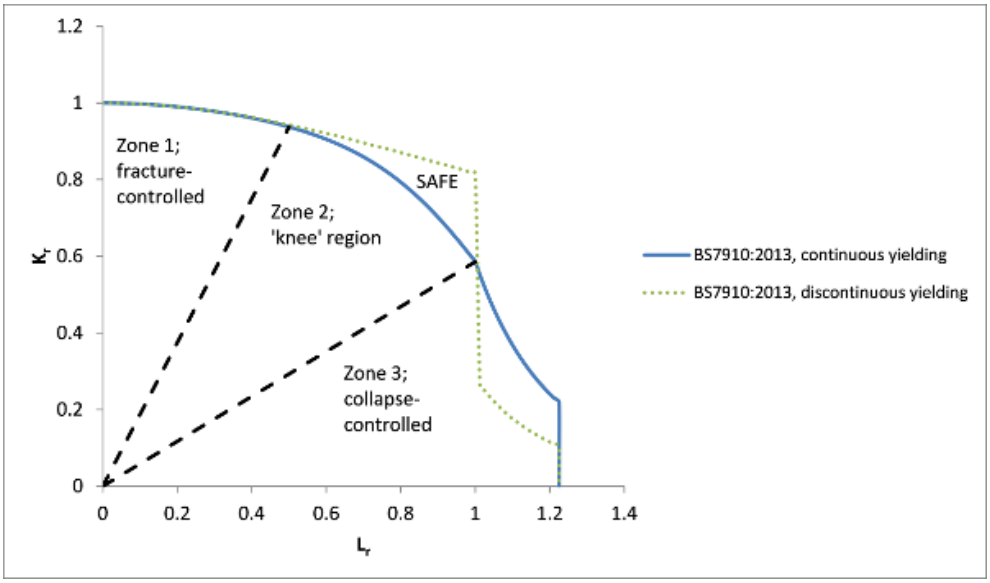

Figure 6-2 FAD yielding curve at option 1 defined by BS 7910 [410]

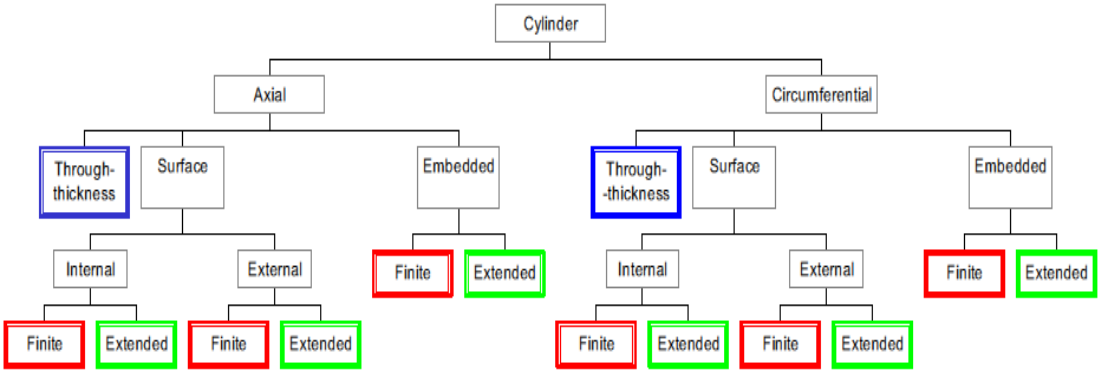

Figure 6-3 Cylindrical geometries considered for pipes and cylinders [411]

Following the previous considerations, the FAD selected to assess the material in this investigation was material-specific (BS 7910-13 option 2) which requires that a stress-strain engineering curve has to be available to obtain more accurate results compared with a standard FAD.

The type of defect considered is an axial through-wall flaw in a cylinder oriented axially, as shown in Figure 6-4, [IV.3.4.9] [278] or [A.28] [35]. Parameters to assess the operational conditions and material properties have been summarised in section 6.4.

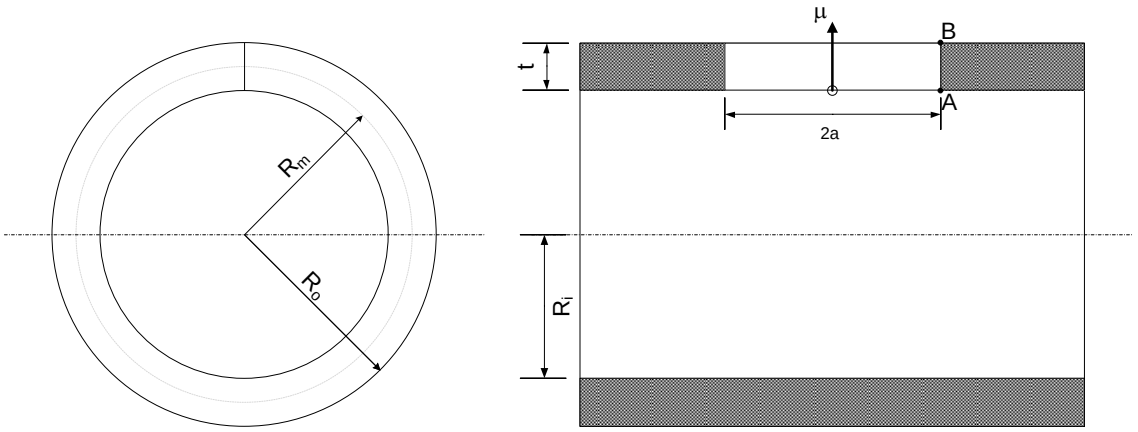

Figure 6-4 Through–wall flaw in a cylinder oriented axially [35,278]

As explained in Chapter two numeral 2.5, the requirements for performing assessment option 2 considering a through-thickness flaw, include the following considerations which are taken from BS 7910-13 annex M:

$$K_r = \frac{K_I}{K_{mat}}; K_I = (Y\sigma)\sqrt{\pi a} \quad \textbf{(6-1)}$$

$$(Y\sigma) = (Y\sigma)_p + (Y\sigma)_s \quad \textbf{(6-2)}$$

$(Y\sigma)_p$ and $(Y\sigma)_s$ correspond to primary and secondary stress which are calculated as follows:

$$(Y\sigma)_p = Mf_w[k_{tm}M_{km}M_mP_m + k_{tb}M_{km}M_m\{P_b + (k_m - 1)P_m\}] \quad \textbf{(6-3)}$$

$$(Y\sigma)_s = M_mQ_m + M_bQ_b \quad \textbf{(6-4)}$$

M_{km} and M_{kb} are equal to 1 as the flaw or crack is located in a region of local stress concentration, so equation 6-3 can be simplified as:

$$(Y\sigma)_p = M_mP_m + M_mP_b \quad \textbf{(6-5)}$$

P_m and P_b correspond to primary membrane stress and primary bending stress respectively. The stress intensity magnification factor can be calculated by equation 6-6.

$$M_m = M_1 + M_2 \quad \text{at the outside surface}$$
$$M_m = M_1 - M_2 \quad \text{at the inside surface}$$
$$M_b = M_3 + M_4 \quad \text{at the outside surface}$$
$$M_b = M_3 - M_4 \quad \text{at the inside surface} \qquad \textbf{(6-6)}$$

M_1 to M_4 are given in BS 7910-2013, Annex M, Table M.1(a-d) in terms of λ both membrane and through wall bending loading. The parameters Q_m and Q_b, in equation 6-4, are the secondary membrane and bending stresses respectively. In addition, the stress magnification factor should be applied if angular or axial misalignment, or both, can cause variation in the stress at the welded join when it is loaded.

If there is a misalignment k_t, k_{tm}, k_{tb} and k_m parameters have to be determined and, therefore, the bending stress (σ_s) might be determined from Annex D in the BS 7910-13. For axial through-thickness flaws in pipes under internal pressure, the stress intensity factor is calculated from Eq. 6-7;

$$K_I = K_I^{membrane} + K_I^{bending} \qquad \textbf{(6-7)}$$

As no bending stresses are assumed, only the membrane stress is dominant. There is a consideration that the general bulging factor M=fw should be taken as 1 which is covered by parameter λ defined by equation 6-8.

$$\lambda = \{12(1-\nu^2)\}^{0.25}\left(a \Big/ \sqrt{r_m B}\right) \qquad \textbf{(6-8)}$$

Where ν is Poisson's ratio, ***a*** is half of the flaw and B is the thickness of the pipe.

The solution in equation 6-6 is only valid for long cylinders or pressure vessels with closed ends. The range of the application for λ is determined for Eqs. 6-9 and 6-10.

$$0 \le \lambda \le 12.211 \quad \textbf{(6-9)}$$

$$5 \le r_m / B \le 100 \quad \textbf{(6-10)}$$

fw = 1 if the actual flaw area is not greater than 10% of the load bearing cross section area.

The primary and secondary stress interaction is covered in Annex R BS 7910-13 where major changes were introduced in the current version, expressed by Eq. 6-11. The term ***V*** determines a multiplying factor that compensates for plasticity derived from the work-hardening process.

$$K_r = \frac{K_I^p + VK_I^s}{K_{mat}} \quad \textbf{(6-11)}$$

In the new edition of BS 7910 the contradiction between K/J-based and CTOD-based calculations was resolved by calculating the resistance of the material in terms of K_{mat}, which is derived directly from K_{Ic} by K_J (J test) or K_{CTOD} (CTOD values). K_J is calculated by equation 6-12 and K_{CTOD} by equation 6-13.

$$K_J = \sqrt{\frac{EJ_{mat}}{(1-\nu^2)}} \quad \textbf{(6-12)}$$

$$K_{CTOD} = \sqrt{\frac{m\sigma_y E\delta_{mat}}{(1-\nu^2)}} \quad \textbf{(6-13)}$$

Values of stress intensity factors or fracture toughness (K_{Ic}, K_{Jc}, K_δ) can be expressed in terms of MN/m$^{3/2}$, N/mm$^{3/2}$ or MPa*m$^{1/2}$ units. However, note that the conversion factor could be applied as follows:

1.0 MN/m$^{3/2}$ = 1.0 MPa*m$^{1/2}$ = 31.625 N/mm$^{3/2}$ (that is (N/mm$^{3/2}$)*10$^{3/2}$)

The coefficient *m* is related to the tensile properties of the material at the same temperature of the fracture toughness test which is derived from the SINTAP and FITNET procedures as follows:

$$m = 1.517(\sigma_y / \sigma_U)^{-0.3188} \quad \textbf{(6-14)}$$

Thus the equation is applicable to the range;

$$0.3 \le (\sigma_y / \sigma_U) \le 0.98 \quad \textbf{(6-15)}$$

Equation 6-14 is basically oriented to be used with CTOD data. If equation 6-14 cannot be used *m* could be equal to 1.5 which covers high-strength pipeline steels. By determining K_I and K_{mat} the coordinate K_r can be determined. To calculate the parameter L_r, equation 6-16 is used. Annex P in BS 7910-13 gives the equation 6-17 to calculate the reference stress as follows:

$$L_r = \frac{\sigma_{ref}}{\sigma_y} \quad \textbf{(6-16)}$$

$$\sigma_{ref} = 1.2 M_T P_m + \frac{2P_b}{3(1 - \frac{2a}{W})} \quad \textbf{(6-17)}$$

Where;

$$M_T = \{1 + 1.6(\frac{a^2}{r_i B})\}^{0.5} \quad \textbf{(6-18)}$$

The hoop stress is identified by P_m and the bending stress transverse to the flaw is P_b. R-code determines L_r using the following loads:

- Secondary stress distribution obtained from elastic analysis
- Secondary stress distribution by an elastic-plastic analysis
- Stress distribution from the strains

The stress component actuating perpendicular to the crack plane, referenced as a hoop component, can be calculated using equation 6-19.

$$\sigma_{yy} = \frac{\mathrm{E}}{(1+\nu)(1-2\nu)}(1-\nu)\varepsilon_{yy} + \nu(\varepsilon_{xx} + \varepsilon_{zz}) \quad \textbf{(6-19)}$$

The loading factor is used as a sensitivity variable which is applied in critical crack analysis to all the variable loads (primary and secondary). Stress can be expressed as Pa, MPa or GPa[5].

6.4 Input parameters for assessment

To assess the integrity of the steels selected for this study, guides from LbB procedures in BS 7910-2013 [35] and content in the R6 code [278] were followed. In order to evaluate the limits of the LbB criteria, the through-thickness axial crack has been considered. The geometrical definition, shown in Figure 6-4, as well as fluid and mechanical properties summarised in section 6.4.1 were used to assess the steels in the longitudinal direction by the FAD approach, option 2.

Loading considerations are as follows: the pipe is subjected to internal pressure which implies that two types of crack could be developed; part through and through-thickness crack size. In the former case, the maximum part through-crack size could turn into through-thickness and unstable fracture. In the latter, the maximum through-wall crack size determines the bursting of the tube.

Determination of the critical crack length in both cases is necessary to verify the LbB criteria; however, for the purpose of this investigation only through-thickness crack size is evaluated by the R6 code. The critical size and limited load have been assessed for internal pressures of 7.5, 9 and 15 MPa at 37°C, taking into account that these forces meet both supercritical conditions and operational pressure when transporting anthropogenic $CO_{2.}$

[5] 1 Pa = N/m^2;
1 MPa = N/mm^2= $(N/m^2)10^6$;
1 GPa = KN/mm^2=$(N/m^2)10^9$

6.4.1 Parameters to assess the integrity of steels

Table 6-1 Technical input data of the materials [67]

Parameter	Steel grade API X100, X70 & X60
Geometry	Cylinder
Length (m)	500
Outside diameter (mm)	610
Mean radius (mm)	300
Wall thickness (mm)	10
R/t ratio ≥ 5	30
Fluid transporting	CO_2
Operating pressure (MPa)	7.5, 9, 15
Leaking pressure (MPa)	0.1
SIF ((MPa*$m^{1/2}$)	1.1
Type of flaw	Through-thickness

Table 6-2 CO_2 physical properties [412,413]

Property	Value		
Pressure (MPa)	7.5	9	15
Temperature (°C)	37	37	37
Density (kg/m^3)	253.4	563	802.5
Viscosity (Pa*sec)	0.00001	0.000023	0.00007

Conversion factor: 1 centipoise = 0.001 Pascal*second

Table 6-3 Tensile properties of X100 steels

T_{test} (°C)	$\sigma_{0.5\%exp}$ (MPa)	σ_{UTS} (MPa)	($\sigma_{0.5\%}$ + σ_{UTS})/2	UE(%)
20	570	769	669	8.8
-20	604	723	664	7.9
-40	622	765	694	7.7
-70	636	792	714	7.4

Table 6-4 Tensile properties of X70 steels

T_{test} (°C)	$\sigma_{0.2\%exp}$ (MPa)	σ_{UTS} (MPa)	$\sigma_{0.2\%} + \sigma_{UTS}/2$	UE(%)
20	769	814	791	7.9
-20	771	817	794	7.6
-40	786	844	815	8.0
-70	810	855	833	7.6

Table 6-5 Tensile properties of X60 steels

T_{test} (°C)	$\sigma_{0.5\%exp}$ (MPa)	σ_{UTS} (MPa)	$\sigma_{0.5\%} + \sigma_{UTS}/2$	UE(%)
20	451	533	492	17.5
-20	455	539	497	19.7
-40	461	549	505	17.7
-70	463	551	507	13.8

Table 6-6 Fracture toughness values for HSLA steels from $K_{Ic}/K_Q/K_{Jc}$ ($MPa*m^{1/2}$)

Steel	Temperature, °C				Reference
	RT	-20	-40	-70	
X100	147	138	130	114	[170]
X70	190	140	120	98.5	[414]
X60	250	200	150	110	[415]

Table 6-7 Residual stress distribution through-thickness on steel API X100

Depth (mm)	Residual stress at Point 2 (MPa)		
	Sample A	Sample B	Sample C
0.2	-119	-210	-327
0.5	-199	-285	--329
0.8	-153	-218	-186
2.2	-25	-117	-159
3.6	24	-70	-144
5	64	-97	-185
6.4	85	-102	-172
7.8	-50	-78	-189
9.2	-114	-212	-205
9.5	-105	-206	-296
9.8	-83	-196	-304

6.5 Results, analysis and discussion

The results of the assessments performed in this investigation are summarised in sections 6.5.1 and 6.5.2. The former is based on limiting load (LL) and the latter on limiting crack size (LCS) analysis. The applied force assumed was only internal pressure as this is the main force on the pipeline and the load factor was established to be 1.2 in order to keep similar conditions to hydrostatic testing. The data collected is presented in figures and tables which contained the main values obtained and extracted from the analysis carried out by the R6 code.

6.5.1 Limited crack size

6.5.1.1 API X100 steel

Figures 6-5 to 6-13 are FAD-option 2 for flaws in the base metal with axial stress and longitudinal crack growth through-thickness. Tensile properties over range -70°C to 21°C temperature and fracture toughness were applied at the middle thickness of the material, which is parallel to the crack direction, and those were evaluated at 7.5MPa, 9MPa and 15MPa operational pressure.

The failure assessment plotted in Figure 6-5 to 6-7 indicated that for a constant flaw of 5 mm the loci is moving towards L_r when the pressure applied increases. This tendency is similar to the flaws assessed at 10 mm and 20 mm, as represented in Figures 6-8 to 6-13 respectively. Besides it was observed that the crack length decreased as the temperature of the material reduced. In Tables 6-8 to 6-10 the length of the crack versus pressure is summarised where it is observable that at 15 MPa pressure the crack length was not affected for the flow stress evaluated a different temperature.

Even though its value was the lower one with values around 13 mm length, keeping the pressure constant and varying the crack length, the Kr/Lr ratio was stable at 7.5MPa and 9MPa but decreased slightly at 15MPa. Once the crack length reached the critical length, it started to initiate and fell into the failure region of the FAD loci. The FAD indicates that the material is more susceptible to elastic failure when the pressure increases.

Table 6-8 Steel X100_RT_to_-70C_LCS_Crack length 5 mm_LF=1.2. Crack initiation analysis

Temperature °C	Pressure MPa	Crack length, mm	Res. Tough ($MPam^{1/2}$)	Total SIF ($MPam^{1/2}$)	Kr-R6	Lr-R6
21	7.5	64	147	134.0	0.912	0.596
	9	49	147	130.2	0.886	0.666
	15	13	147	96.4	0.655	0.994
-20	7.5	60	138	127.7	0.925	0.552
	9	46	138	124.7	0.904	0.621
	15	14	138	98.8	0.716	0.939
-40	7.5	56	130	121.3	0.933	0.527
	9	43	130	118.6	0.912	0.596
	15	13	130	96.6	0.743	0.911
-70	7.5	48	114	107.2	0.941	0.496
	9	36	114	105.0	0.921	0.567
	15	11	114	87.0	0.763	0.888

Table 6-9 Steel X100_RT_to_-70C_LCS_Crack length 10 mm_LF=1.2. Crack initiation analysis

Temperature °C	Pressure MPa	Crack length, mm	Res. Tough ($MPam^{1/2}$)	Total SIF ($MPam^{1/2}$)	Kr-R6	Lr-R6
21	7.5	64	147	134.0	0.912	0.595
	9	49	147	130.2	0.886	0.666
	15	13	147	96.3	0.655	0.994
-20	7.5	60	138	127.7	0.925	0.552
	9	46	138	124.7	0.904	0.621
	15	14	138	98.8	0.716	0.939
-40	7.5	56	130	121.2	0.933	0.527
	9	43	130	118.6	0.913	0.596
	15	13	130	96.6	0.743	0.911
-70	7.5	48	114	107.2	0.941	0.496
	9	36	114	105.0	0.921	0.567
	15	11	114	87.0	0.763	0.888

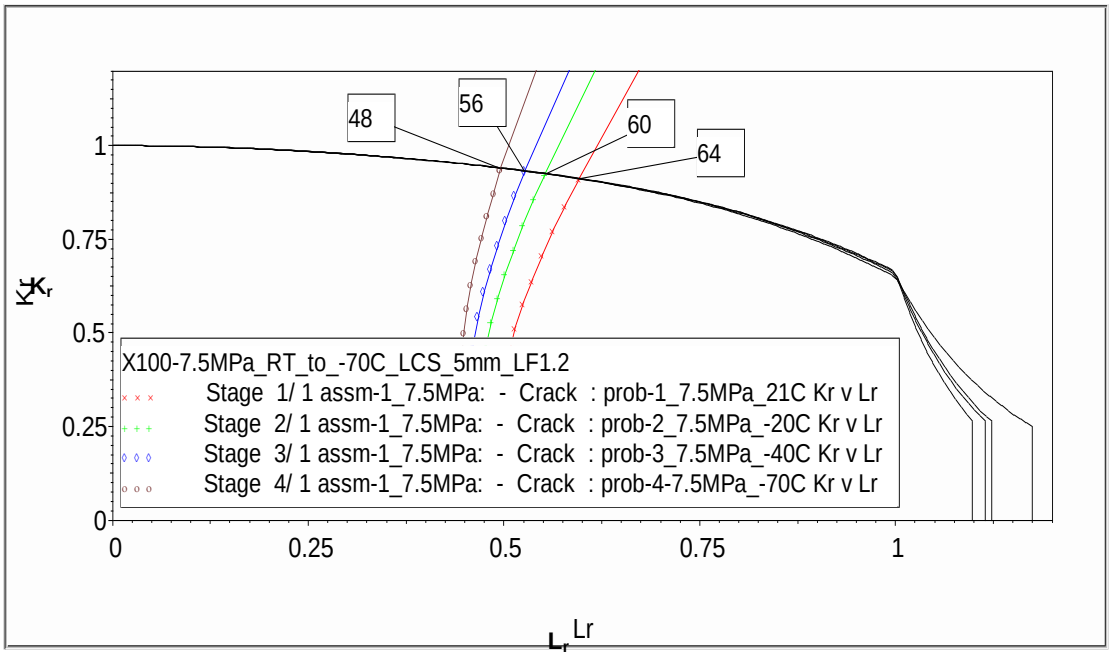

Figure 6-5 FAD assessment by limited crack size at 7.5 pressure with 5mm crack length and load factor=1.2 over -70°C to 21°C

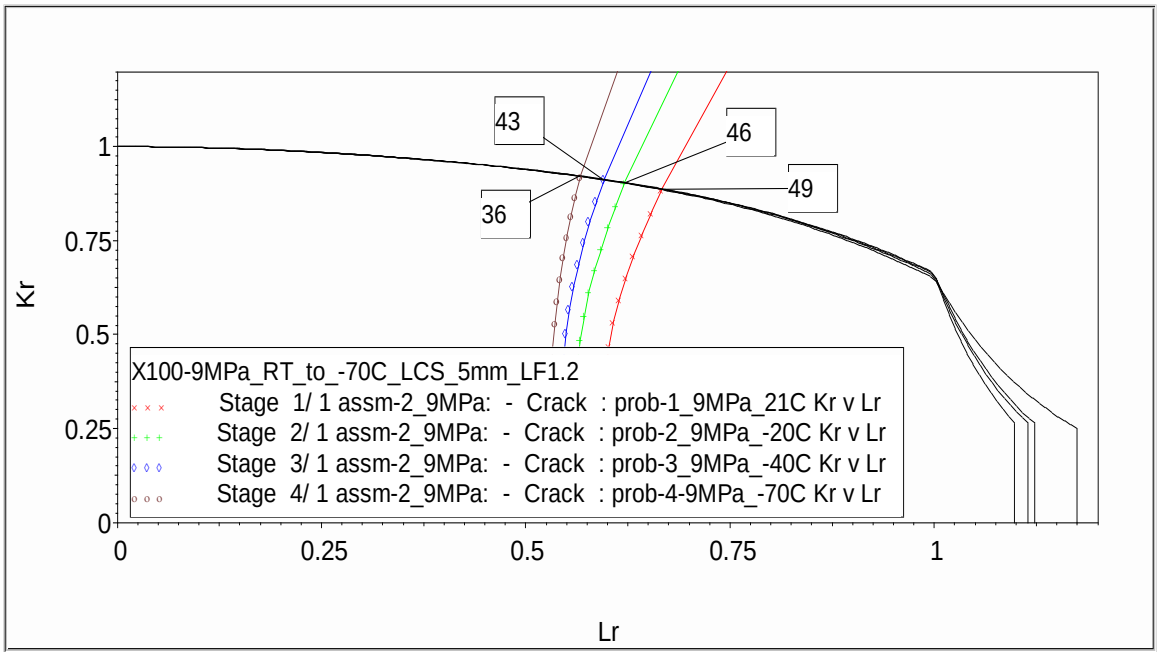

Figure 6-6 FAD curve by limited crack size analysis at 9 MPa operational pressure with 5mm crack length and load factor=1.2 over -70°C to 21°C

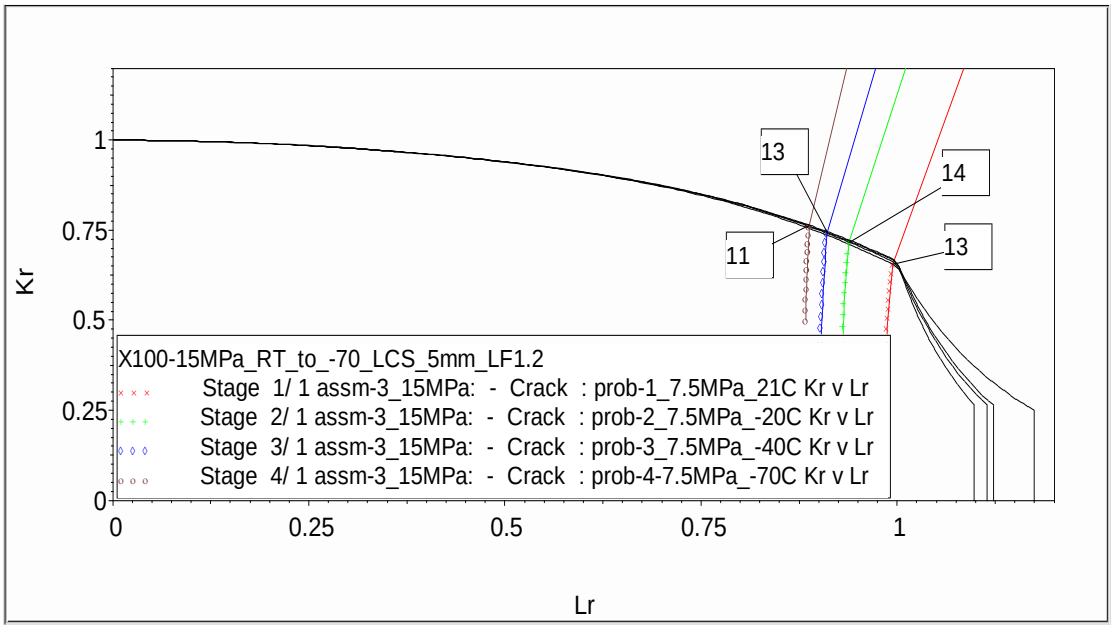

Figure 6-7 FAD locus by limited crack size at 15MPa internal pressure with 5 mm crack length and load factor=1.2 over -70°C to 21°C.

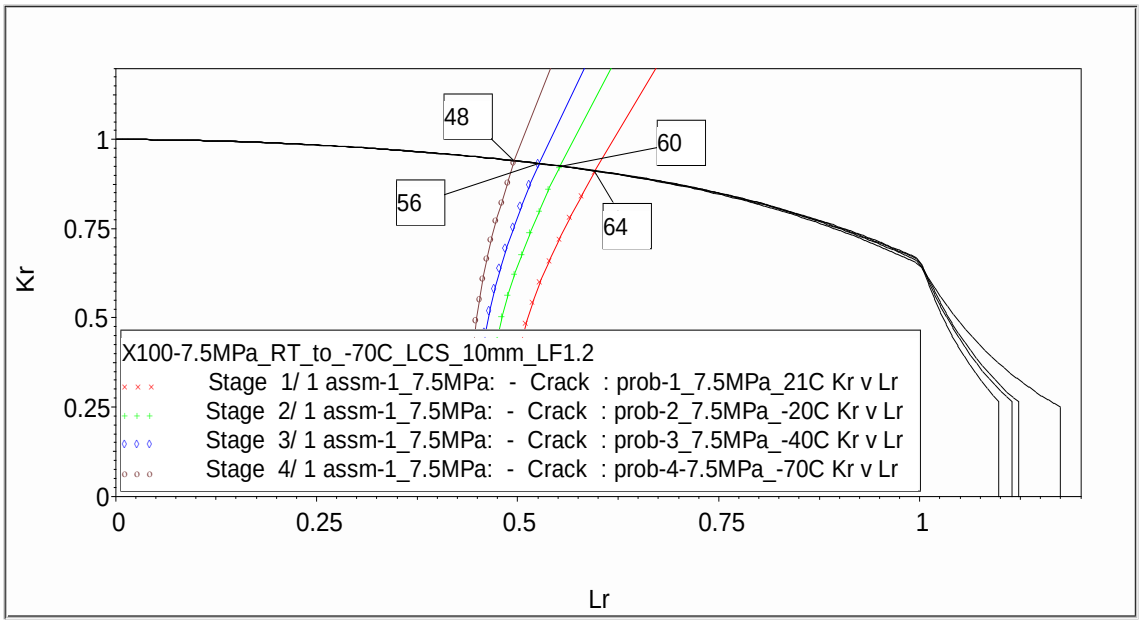

Figure 6-8 FAD assessment by limited crack size at 7.5 pressure with 10mm crack length and load factor=1.2 over -70°C to 21°C

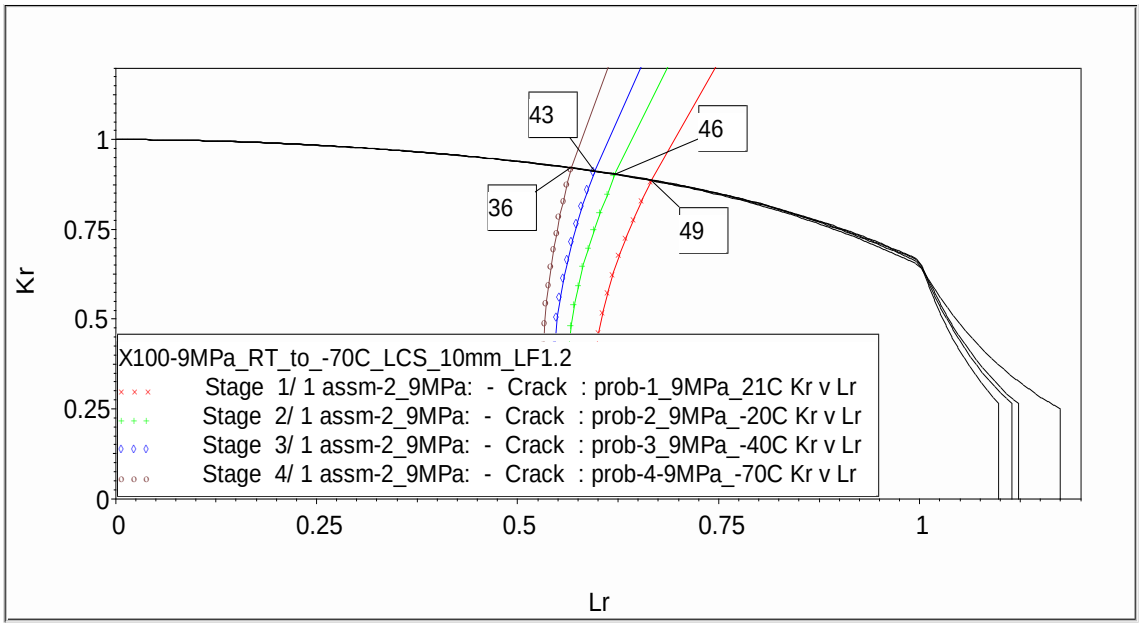

Figure 6-9 FAD curve by limited crack size analysis at 9 MPa operational pressure with 10mm crack length and load factor=1.2 over -70°C to 21°C

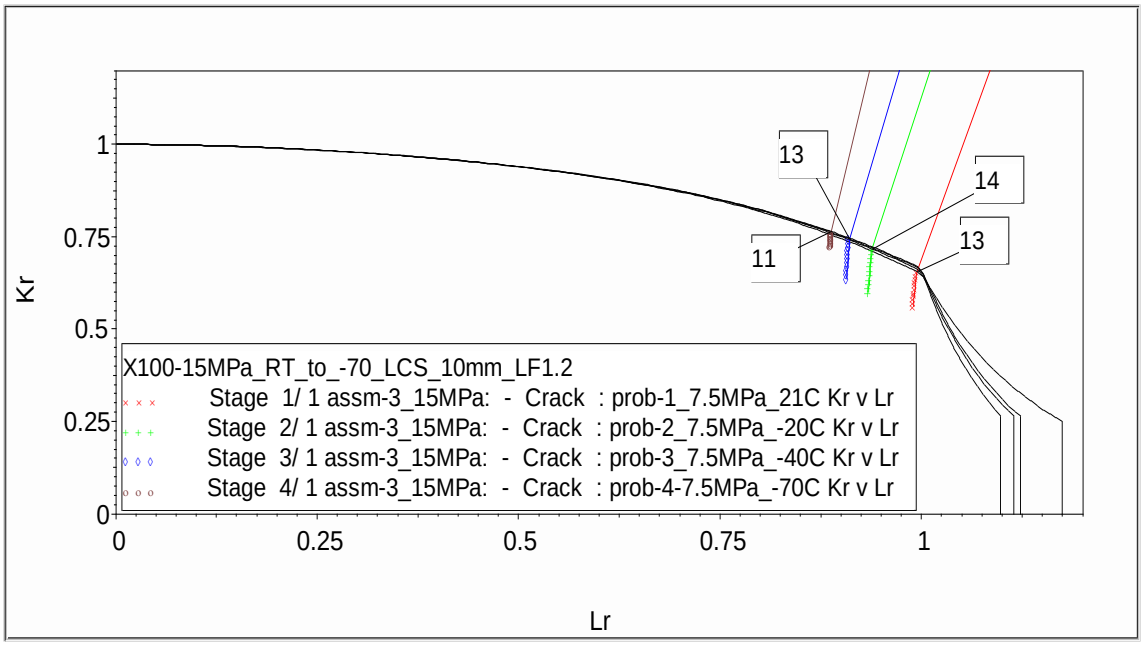

Figure 6-10 FAD locus by limited crack size at 15MPa internal pressure with 10mm crack length and load factor=1.2 over -70°C to 21°C

Table 6-10 Steel X100_RT_to_-70C_LCS_Crack length 20 mm_LF=1.2. Crack initiation analysis

Temperature °C	Pressure MPa	Crack length, mm	Res. Tough ($MPam^{1/2}$)	Total SIF ($MPam^{1/2}$)	Kr-R6	Lr-R6
21	7.5	64	147	134	0.912	0.596
	9	49	147	134	0.886	0.666
	15	20	147	122.1	0.83	1.007
-20	7.5	60	138	127.7	0.925	0.552
	9	46	138	127.7	0.904	0.621
	15	20	138	122.1	0.884	0.95
-40	7.5	56	130	121.2	0.933	0.527
	9	43	130	118.6	0.912	0.596
	15	20	130	122.1	0.939	0.922
-70	7.5	48	114	107.2	0.941	0.496
	9	36	114	107.2	0.921	0.567
	15	20	114	122.1	1.071	0.902

Focusing on the lower temperature, the results indicate that at lower pressure the material is more resistant as crack length can increase to around 64 mm in length. Since the level 2 FAD includes tensile properties, fracture toughness and residual stress, the main difference or changes of the FAD curve were at the collapse region. The cut-off line is moved from 1.175 to 1.1, with the temperature order as follows from right to left: 21°C >-70°C >-40°C >-20°C.

Zargarzadeh [297] found that with the steel grade X100 at -70°C, if a crack reaches 9.9 mm in length then crack initiation is inevitable. The author used for the assessment mechanical properties extracted from the API standard; however, compared with the crack length obtained in this research under the same conditions (except for the fracture toughness which is higher) the difference is 10% (~1.2 mm). When experimental values are applied to assess any structure it becomes less conservative if values are used from other source.

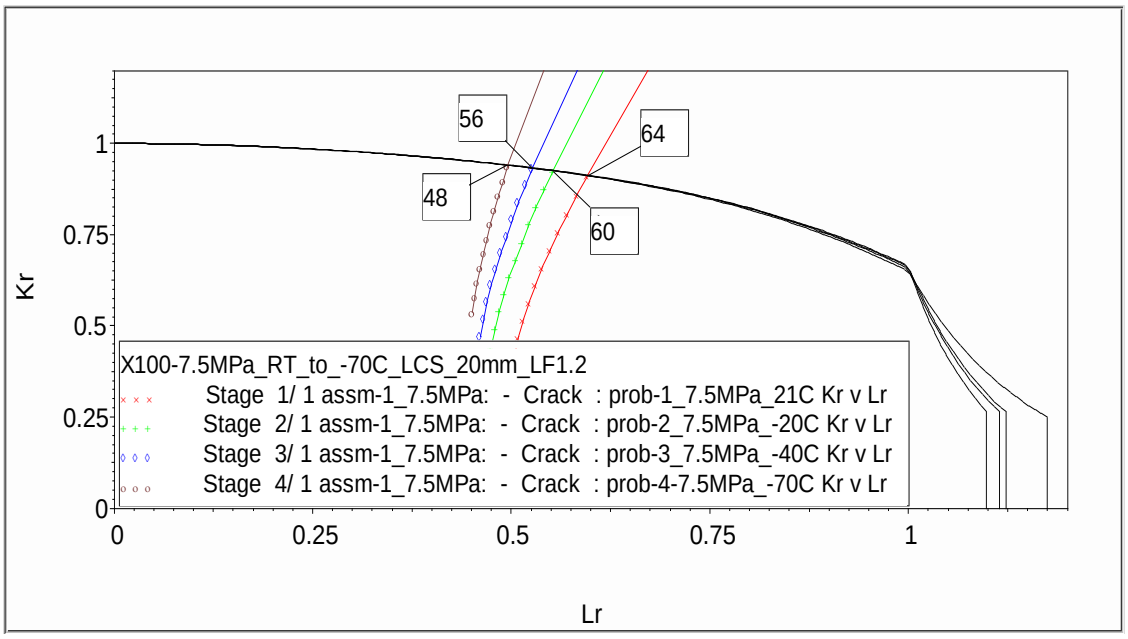

Figure 6-11 FAD assessment by limited crack size at 7.5 pressure with 20mm crack length and load factor=1.2 over -70°C to 21°C

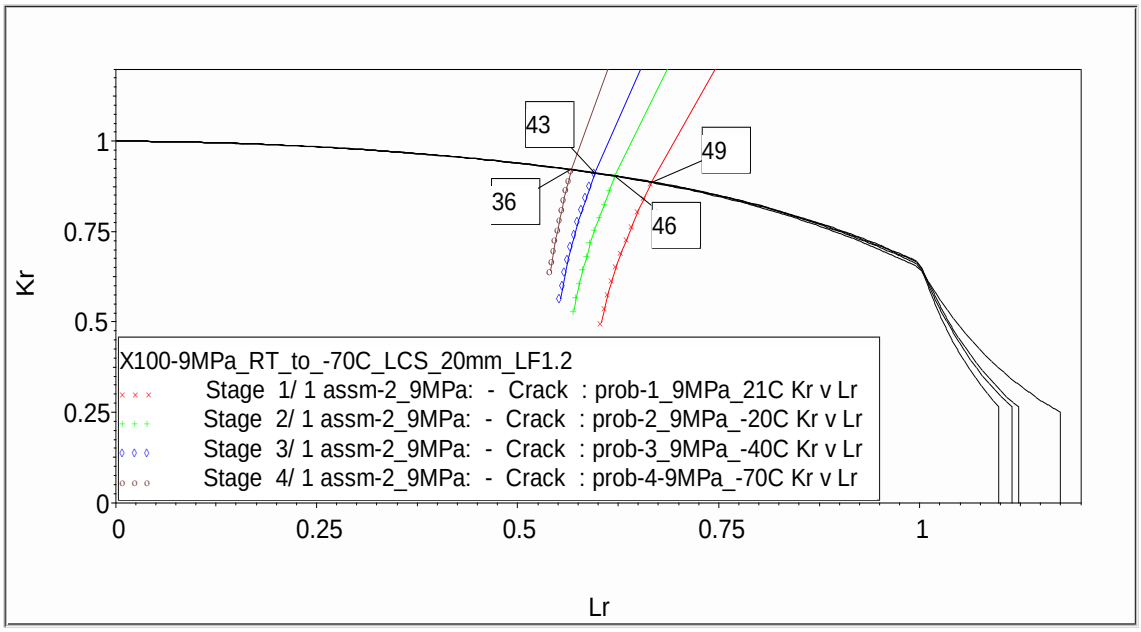

Figure 6-12 FAD curve by limited crack size analysis at 9 MPa operational pressure with 20mm crack length and load factor=1.2 over -70°C to 21°C

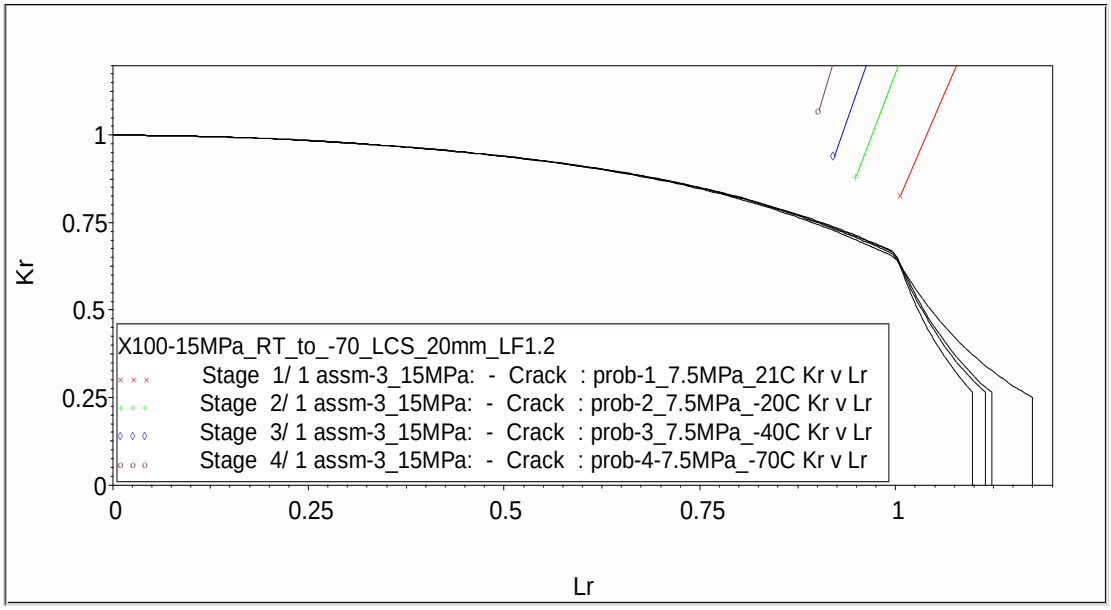

Figure 6-13 FAD locus by limited crack size at 15MPa internal pressure with 20mm crack length and load factor=1.2 over -70°C to 21°C

From the analysis performed, it could be concluded that for a crack-like flaw for pressure up to 9 MPa, a crack length of 20 mm is acceptable for the established conditions for X100 pipeline steel. However, with pressure at about 15 MPa the crack length could be around 11 mm from the analysis performed at option 2

level. It can be seen from the FAD analysis that crack assessment at room temperature is located in a combined zone and more susceptible to plastic collapse than for the lower temperature where the behaviour is the opposite. The effect of the residual stress on the stress intensity factor is related to K_r which could be higher if no residual stresses are present.

6.5.1.2 API X70 steel

Similar analyses were performed on steels grade X70 and X60 but only at 15 MPa operational pressures. For X70 steel the results are shown in Figures 6-14 to 6-16 which correspond to 15 MPa pressure and crack lengths of 5, 10 and 20 mm.

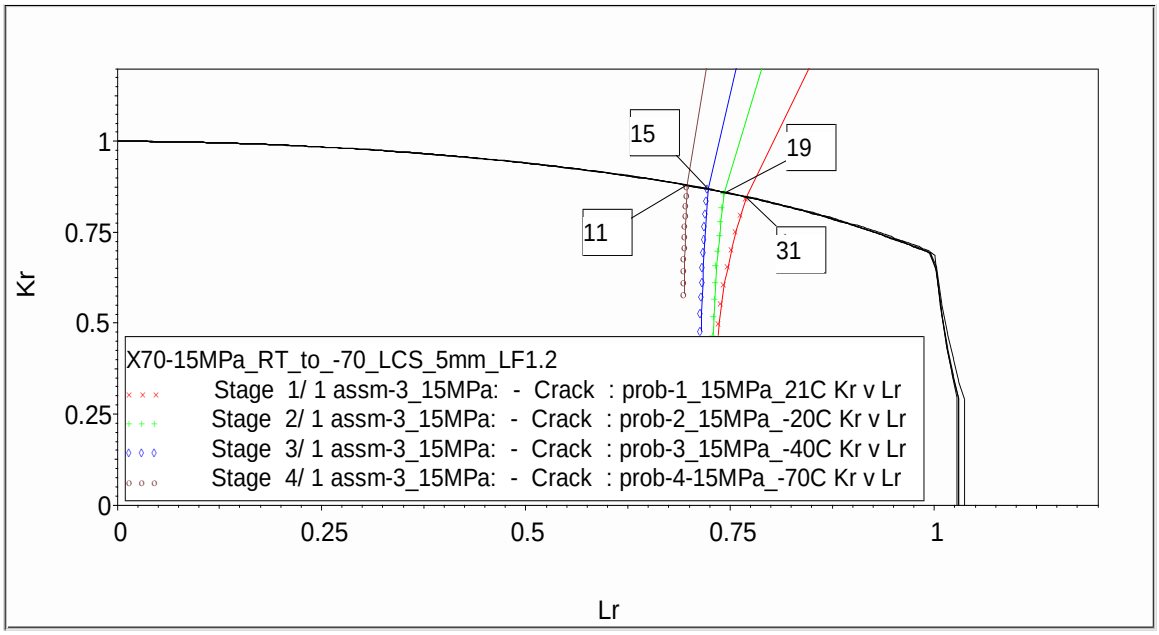

Figure 6-14 FAD locus by limited crack size analysis at 15 MPa operational pressure with 5 mm crack length

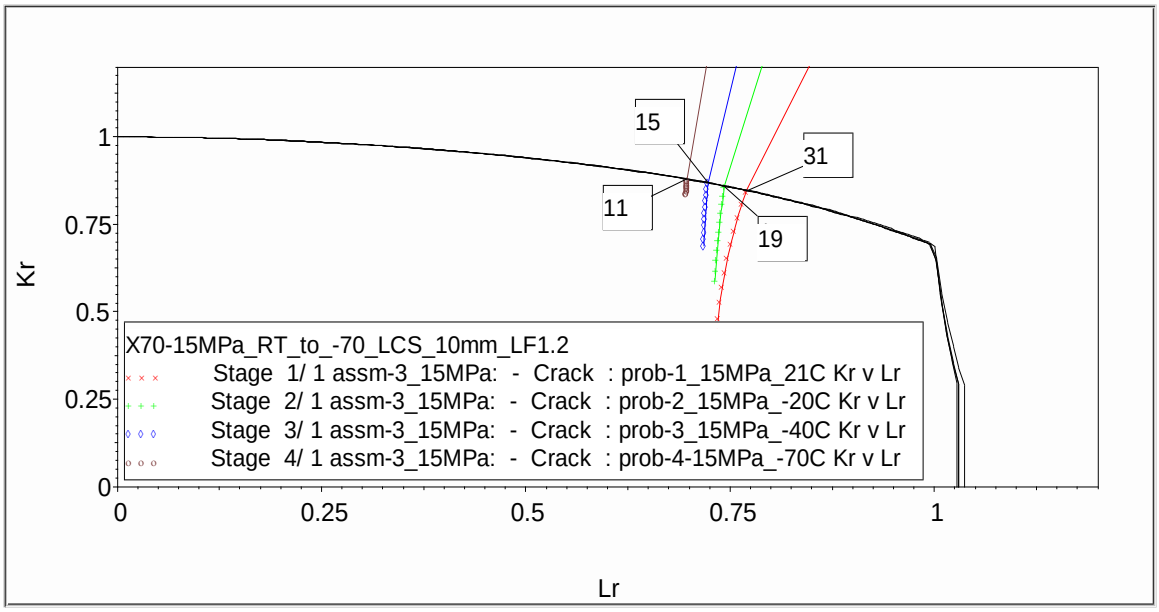

Figure 6-15 FAD locus by limited crack size analysis at 15 MPa operational pressure with 10 mm crack length

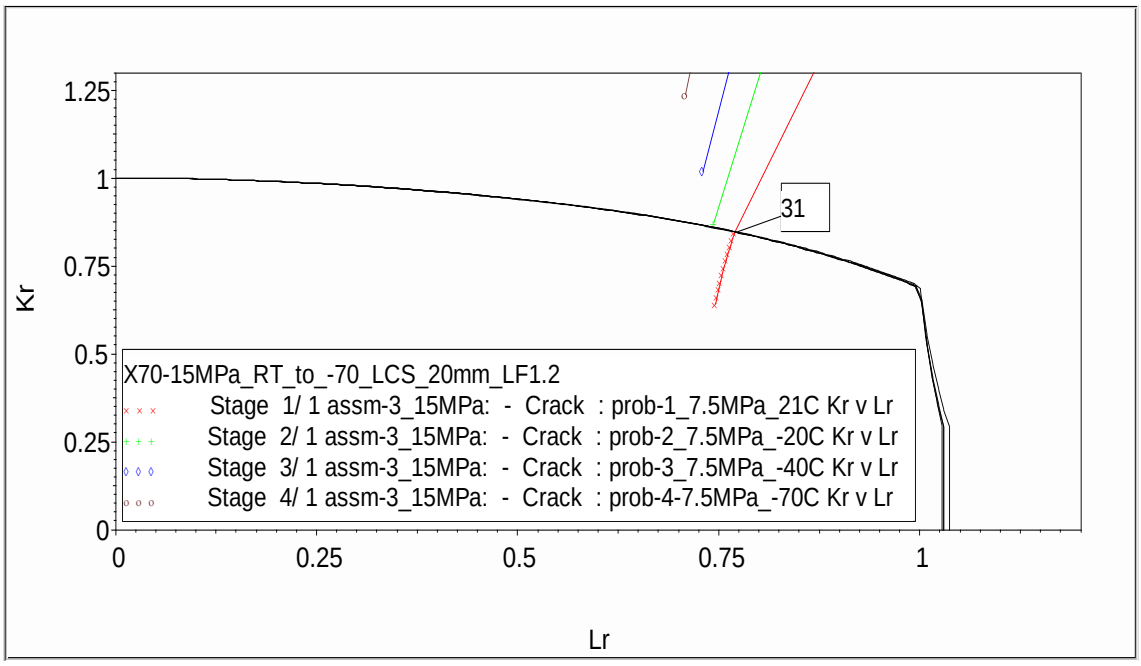

Figure 6-16 FAD locus by limited crack size analysis at 15 MPa operational pressure with 20 mm crack length

Table 6-11 Steel X70_RT_to_-70C_LCS_Crack length 5, 10, 20 mm_LF=1.2. Crack initiation analysis

Flaw Length, mm	Temperature °C	Crack length, mm	Res. Tough ($MPam^{1/2}$)	Total SIF ($MPam^{1/2}$)	Kr-R6	Lr-R6
5	21	31.5	190	160.8	0.846	0.77
	-20	19.5	140	120.2	0.859	0.743
	-40	15.2	120	104.2	0.868	0.723
	-70	10.9	98.5	86.6	0.879	0.697
10	21	31.5	190	160.8	0.846	0.77
	-20	19.5	140	120.3	0.859	0.743
	-40	15.2	120	104.2	0.868	0.723
	-70	10.9	98.5	86.6	0.879	0.697
20	21	31.5	190	160.8	0.846	0.77
	-20	20	140	122.1	0.872	0.744
	-40	20	120	122.1	1.017	0.73
	-70	20	98.5	122.1	1.239	0.708

The tendency is similar to the X100 behaviour where the mechanisms involved are mixed brittle-collapse mechanics, as can be observed on the assessment curve. No residual stresses were applied; therefore, only membrane stresses from the internal pressure are involved.

From the data in Table 6-11, it is clear that if the crack extended to 20 mm the system becomes unstable when the material reaches -20°C, falling into the unsafe zone. At 5 and 10 mm flaw length, the system is stable; however, the assessment points (K_r, L_r) move closer to the failure assessment curve as the temperature decreases

6.5.1.3 API X60 steel

Figures 6-17 to 6-19 show the assessment for steel X60 which was carried out using 9 MPa instead of 15 MPa as at the latter pressure value the component failure before any crack length is extended. From Table 6-12 the results show that the crack length is reduced as the temperature decreases due to the material turning more brittle and K_r is the dominant mechanism of failure.

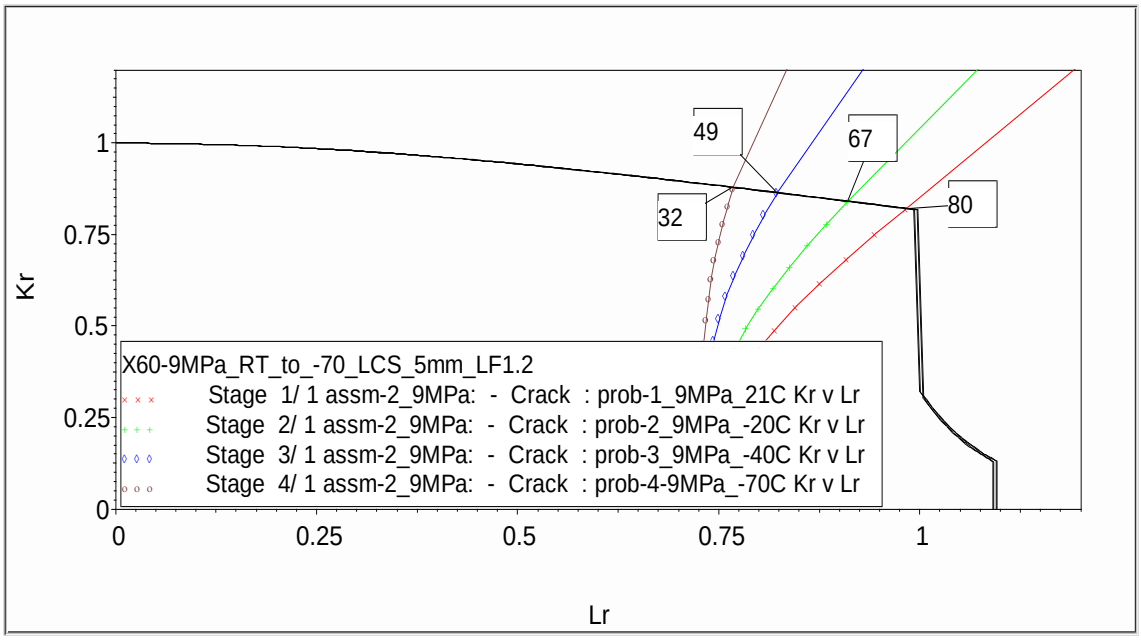

Figure 6-17 FAD locus by limited crack sized analysis at 9MPa operational pressure with 5 mm crack length

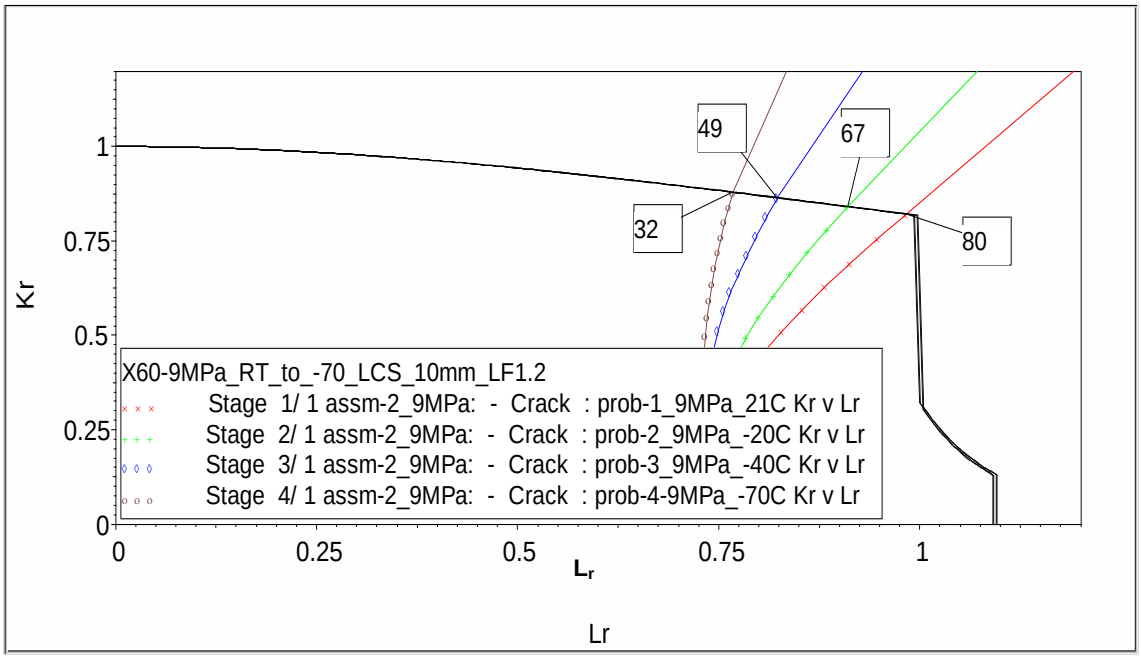

Figure 6-18 FAD locus by limited crack size analysis at 9MPa operational pressure with 10 mm crack length

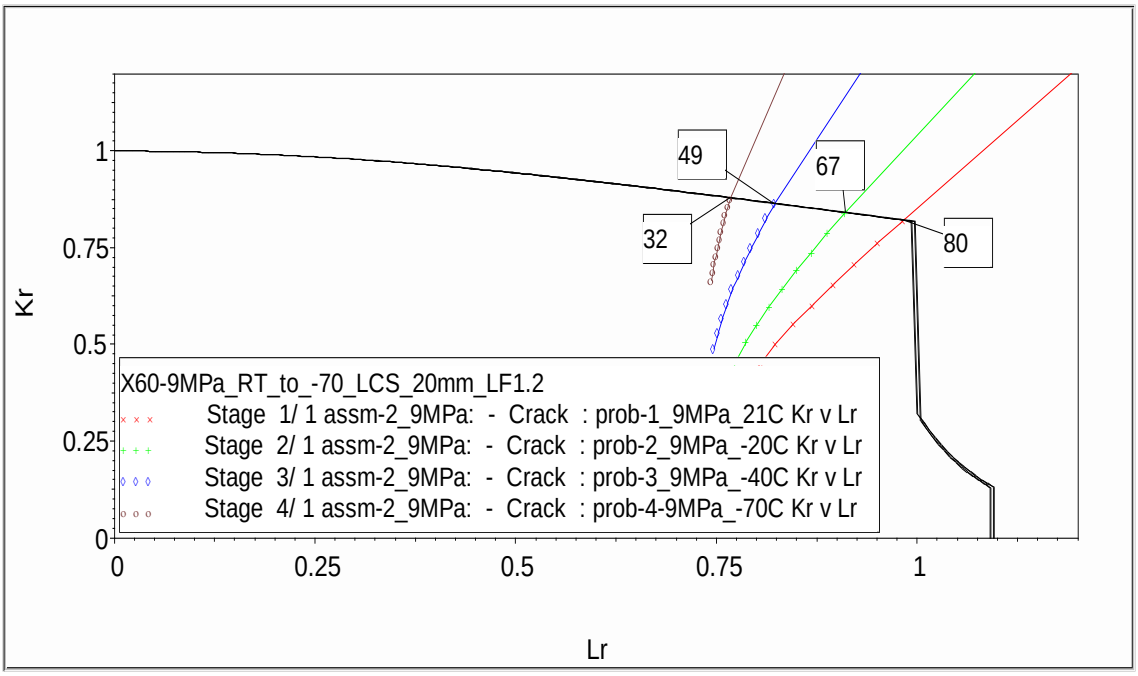

Figure 6-19 FAD locus by limited crack size analysis at 9MPa operational pressure with 20 mm crack length

Table 6-12 Steel X60_RT_to_-70C_LCS_Crack length 5, 10, 20 mm_LF=1.2. Crack initiation analysis

Flaw Length, mm	Temperature °C	Crack length, mm	Res. Tough (MPam$^{1/2}$)	Total SIF (MPam$^{1/2}$)	Kr-R6	Lr-R6
5	21	80.3	240	197	0.821	0.983
	-20	67.2	200	168.2	0.841	0.91
	-40	48.5	150	129.7	0.864	0.822
	-70	31.6	110	96.7	0.879	0.767
10	21	80.3	240	197	0.821	0.983
	-20	67.2	200	168.2	0.841	0.91
	-40	48.5	150	129.7	0.864	0.822
	-70	31.6	110	96.7	0.879	0.767
20	21	80.3	240	197	0.821	0.983
	-20	67.2	200	168.2	0.841	0.91
	-40	48.5	150	129.7	0.864	0.822
	-70	31.6	110	96.7	0.879	0.767

However, the flow stress affects the component too and has an important influence as the assessment points are located in the region where both mechanics are present. Comparing the results obtained with those performed

on X100 and X70 steel, the difference in the pressure assessed clearly determines the lower integrity of the X60 which is determined by the mechanical properties of the material. However, the tendencies for fracture toughness, temperature and flaw length all follow the same pattern.

6.5.2 Limited load

6.5.2.1 API X100 steel

Limited load analyses were performed in order to determine where the load of design could be affected by the operational pressure and crack length. Tables 6-13 to 6-15 are organised to show the main values when the system is unstable, denoting a failure of the component. For fracture initiation, the load factor limiting condition for a single primary load is determined by the intersection with the failure assessment curve of the locus of assessment points for different values of load.

Table 6-13 Steel X100_RT_to_-70C_LL_Crack length 5 mm_LF=1.2. Failed criteria

Temperature	Pressure	Res. Tough	Total SIF	Kr-R6	Lr-R6	Load factor
°C	MPa	(MPa*m$^{1/2}$)	(MPa*m$^{1/2}$)			
21	7.5	147	65.7	0.447	1.131	2.75
	9		67.6	0.46	1.164	2.36
	15		65.7	0.447	1.131	1.38
-20	7.5	138	67.0	0.485	1.089	2.81
	9		68.9	0.499	1.12	2.41
	15		67.0	0.485	1.089	1.4
-40	7.5	130	68.5	0.527	1.08	2.87
	9		70.4	0.541	1.11	2.46
	15		68.5	0.527	1.08	1.43
-70	7.5	114	68.9	0.604	1.063	2.89
	9		70.8	0.621	1.092	2.47
	15		68.9	0.604	1.063	1.44

For the analysis performed using pressure 7.5 MP to 9 MPa and crack length constant equal to 5 mm, the load factor determined could indicate that the component at lower temperatures failed, at 2.89, 2.47 and 1.44. As the design pressure is set at 1.2 times the operation pressure, the load factor obtained could indicate that once the crack length extends to 5 mm the component is able to carry out a greater load than the design pressure. It could be assumed as the maximum load value to be reached.

Figure 6-20 shows the intersection of the points for the different loads assessed. Table 6-14 shows that the values obtained for the different temperatures which follow the same tendency but with less value. Figures 6-21 and 6-22 show the locus points are moving toward K_r. For pressure at 15 MPa and crack length extended to 20 mm, it can easily be seen from Table 6-15 that the crack assessment results in a load factor of 1.17 for room temperature decreasing to 1.07 at -70°C. It indicates that once the crack length reaches 20 mm, a crack is initiated and falls into the unsafe zone of the FAD curve.

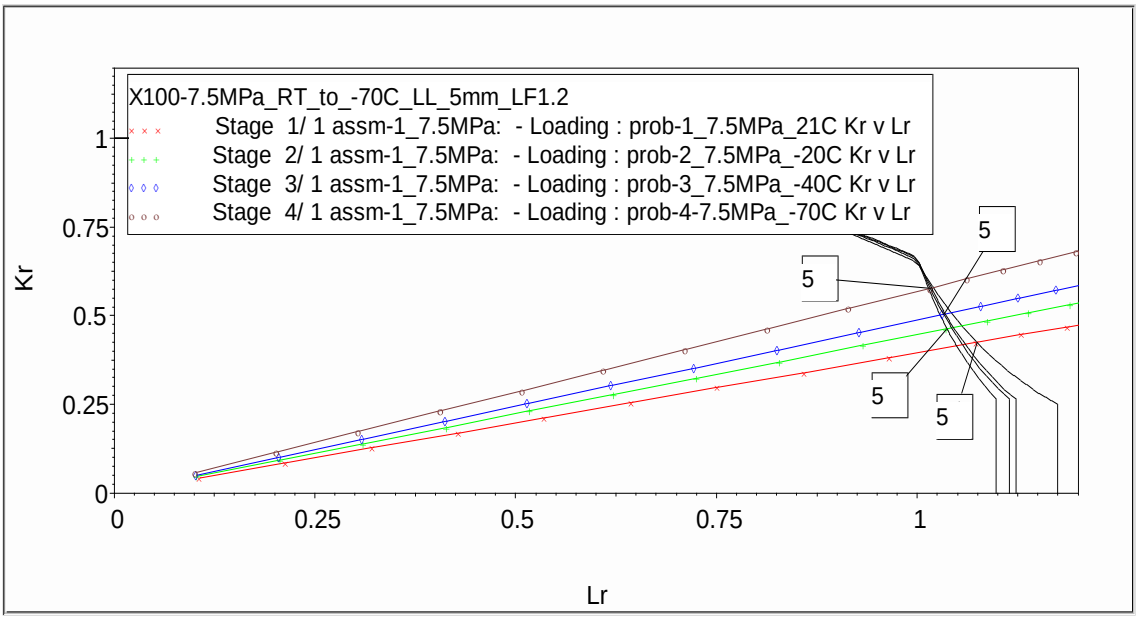

Figure 6-20 FAD locus by limited load analysis at 7.5 MPa operational pressure with 5 mm crack length

Table 6-14 Steel X100_RT_to_-70C_LL_Crack length 10 mm_LF=1.2. Failure criteria

Temperature	Pressure	Res. Tough	Total SIF	Kr-R6	Lr-R6	Load factor
°C	MPa	(MPa*m$^{1/2}$)	(MPa*m$^{1/2}$)			
21	7.5	147	90.5	0.615	1.082	2.62
	9		93.2	0.634	1.115	2.25
	15		90.5	0.615	1.082	1.31
-20	7.5	138	93.7	0.679	1.058	2.72
	9		96.4	0.699	1.089	2.33
	15		93.7	0.679	1.058	1.36
-40	7.5	130	93.9	0.722	1.03	2.72
	9		96.7	0.744	1.06	2.34
	15		93.9	0.722	1.03	1.36
-70	7.5	114	90.3	0.792	0.968	2.62
	9		93.0	0.816	0.997	2.25
	15		90.3	0.792	0.968	1.31

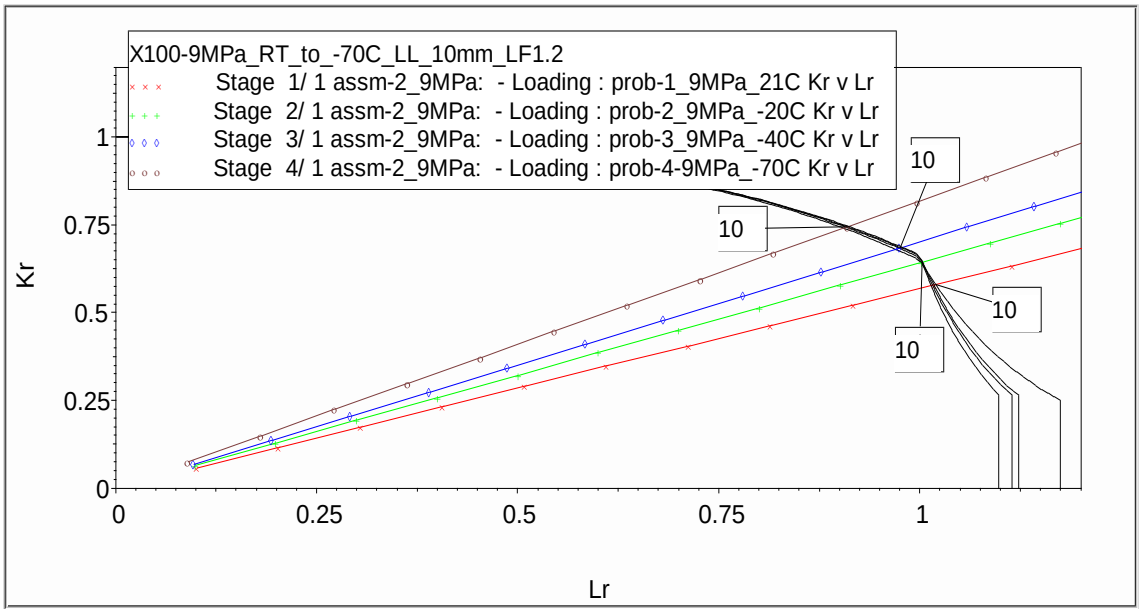

Figure 6-21 FAD locus by limited load analysis at 9 MPa operational pressure with 10 mm crack length

Table 6-15 Steel X100_RT_to_-70C_LL_Crack length 20 mm_LF=1.2. Failure criteria

Temperature	Pressure	Res. Tough	Total SIF	Kr-R6	Lr-R6	Load factor
°C	MPa	(MPa*m$^{1/2}$)	(MPa*m$^{1/2}$)			
21	7.5	147	118.7	0.807	0.979	2.33
	9		122.8	0.835	1.013	2.01
	15		118.7	0.807	0.979	1.17
-20	7.5	138	118.4	0.858	0.921	2.33
	9		122.4	0.887	0.953	2.01
	15		118.4	0.858	0.921	1.16
-40	7.5	130	116.2	0.894	0.878	2.28
	9		120.2	0.925	0.909	1.97
	15		116.2	0.894	0.878	1.14
-70	7.5	114	108.8	0.954	0.804	2.14
	9		112.8	0.99	0.834	1.85
	15		108.8	0.954	0.804	1.07

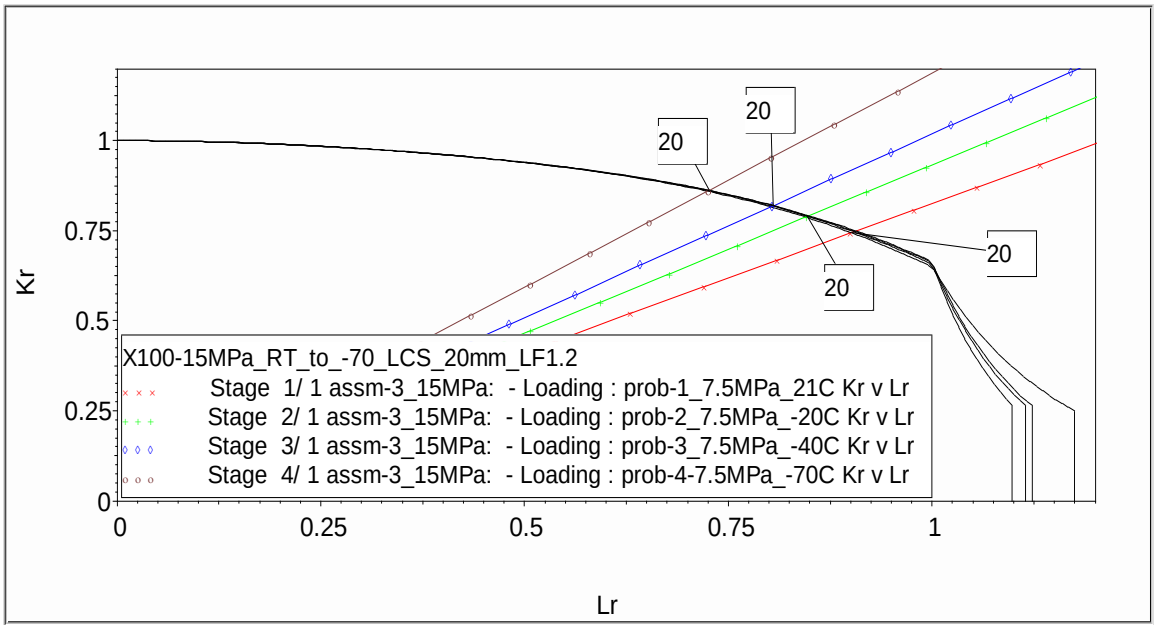

Figure 6-22 FAD locus by limited load analysis at 15 MPa operational pressure with 20 mm crack length

6.5.2.2 API X70 steel

Figures 6-23 to 6-25 show the behaviour of the locus assessed due to temperature and pressure of the operation. As can clearly be seen, the load factor decreased as the pressure increased. The correspondence between fracture toughness and Lr is inversely proportional while with K_r it is directly proportional.

As was observed from the analysis of the steel X100, the same tendency has been followed on the variation on the load factor and L_r being opposite for K_r. From Table 6-16 it can be seen that the load factor decreases with the temperature and gives a clear indication that the material could meet the requirements or integrity totally for all temperatures below 9 MPa. However, a 15 MPa and temperature above -20°C could be used as the material has enough capacity to carry the load conditions. The integrity requirements of the material decay when temperature falls to -20°C.

Table 6-16 Steel X70_RT_to_-70C_LL_Crack length 5, 10 and 20 mm_LF=1.2. Failure criteria.

Temperature	Pressure	Res. Tough	Total SIF	Kr-R6	Lr-R6	Load factor
°C	MPa	(MPa*m$^{1/2}$)	(MPa*m$^{1/2}$)			
21	7.5	190	81.2	0.428	1.037	3.41
	9		118.5	0.624	1.051	2.86
	15		152.2	0.801	0.931	1.5
-20	7.5	140	80.7	0.577	1.028	3.38
	9		110.9	0.792	0.981	2.68
	15		129	0.921	0.787	1.27
-40	7.5	120	81.7	0.681	1.02	3.42
	9		103.8	0.865	0.901	2.51
	15		117.4	0.978	0.702	1.15
-70	7.5	98.5	77.2	0.784	0.936	3.24
	9		93.7	0.951	0.789	2.26
	15		103	1.045	0.598	1.01

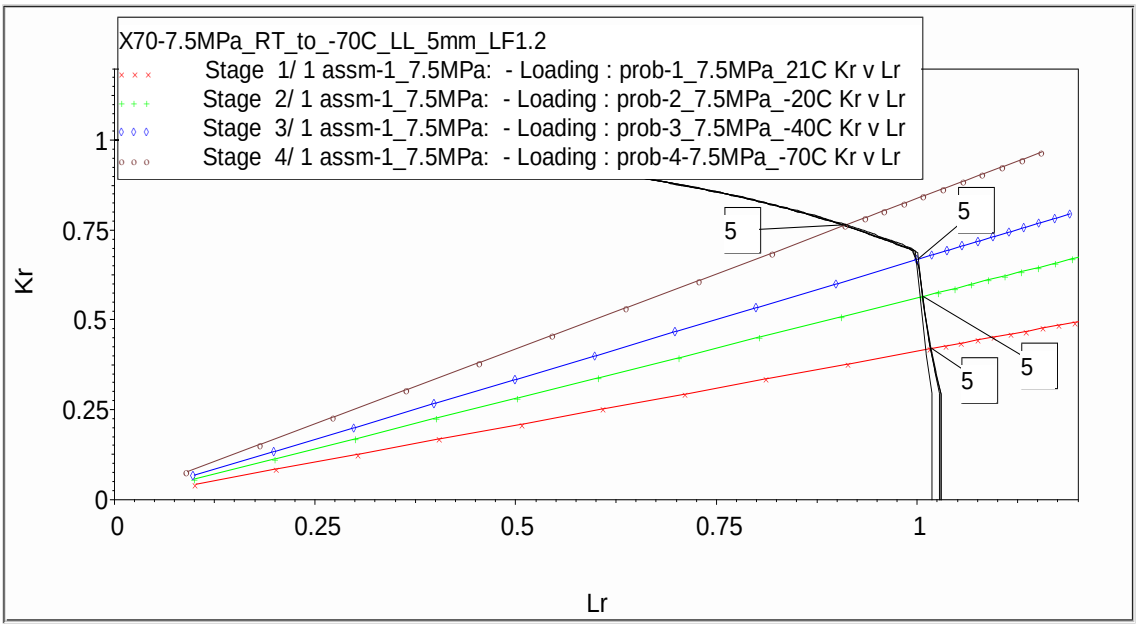

Figure 6-23 FAD locus by limited load analysis at 7.5 MPa operational pressure with 5 mm crack length

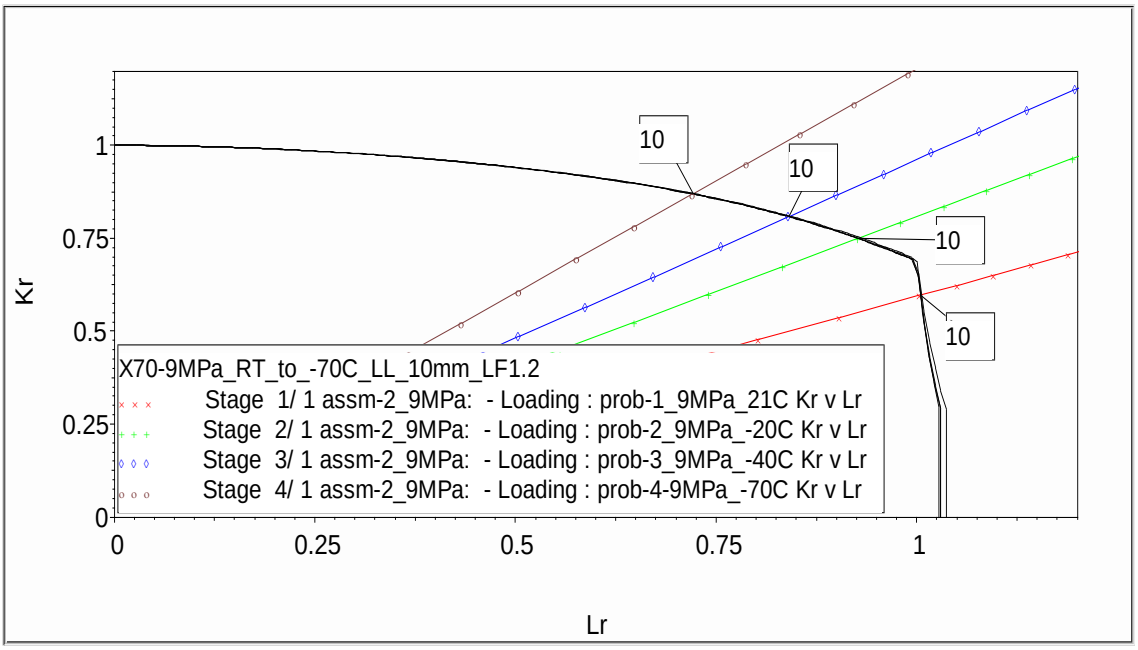

Figure 6-24 FAD locus by limited load analysis at 9 MPa operational pressure with 10 mm crack length

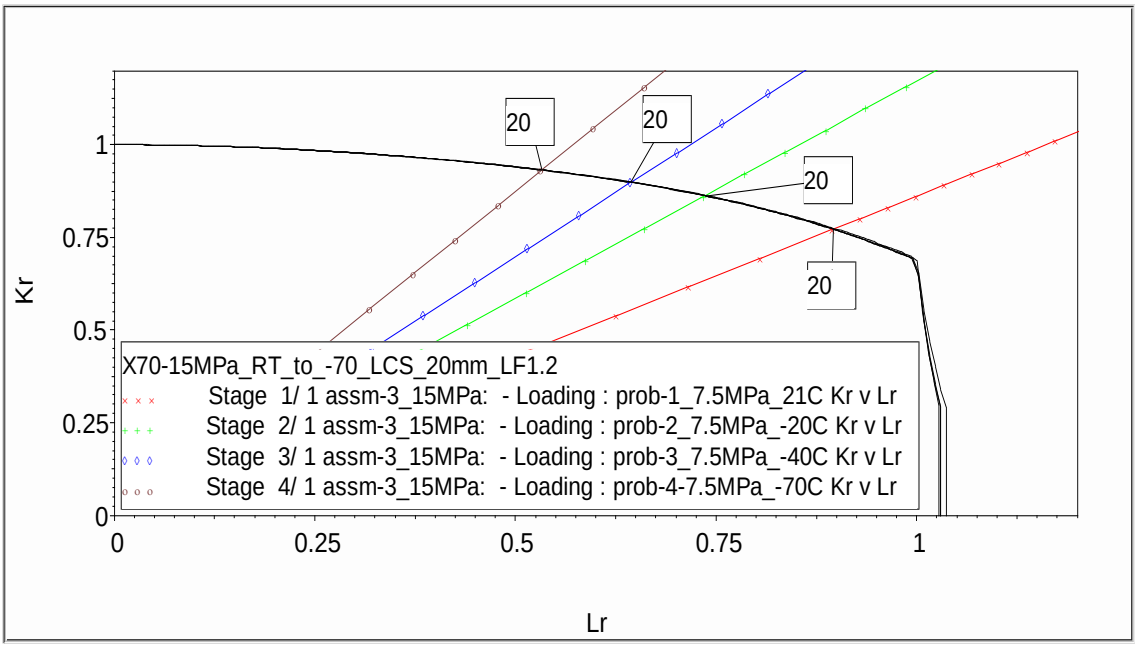

Figure 6-25 FAD locus by limited load analysis at 15 MPa operational pressure with 20 mm crack length

6.5.2.3 API X60 steel

For the analysis performed on the steel X60, Table 6-17 shows that the integrity of the material is compromised when the pressure of the operation is beyond 7.5 MPa and the flaw length is longer than 5 mm. In this case, in particular, even though the tendency looks similar to X100 and X70 steel, it shows that the material at 7.5 MPa with a crack length of not more than 5 mm is able to carry out the loading conditions without any compromise.

Beyond these limits, crack and pressures values have a stronger impact on the material where the material or component cannot be used to work in these conditions. The mechanics of the fracture show that collapse at the lower temperature, -70°C, is the most critical parameter for all the cases. Figures 6-26 to 6-28 show the assessment performed.

Table 6-17 Steel X60_RT_to_-70C_LL_Crack length 5, 10 and 20 mm_LF=1.2. Failure criteria.

Temperature	Pressure	Res. Tough	Total SIF	Kr-R6	Lr-R6	Load factor
°C	MPa	(MPa*m$^{1/2}$)	(MPa*m$^{1/2}$)			
21	7.5	240	52.8	0.22	1.148	2.21
	9		74.02	0.308	1.119	1.07
	15		106.7	0.445	1.112	1.05
-20	7.5	200	52.5	0.262	1.132	2.2
	9		73.8	0.369	1.107	1.07
	15		107.5	0.537	1.11	1.06
-40	7.5	150	51.9	0.346	1.105	2.18
	9		74.6	0.498	1.104	1.08
	15		108.6	0.724	1.107	1.07
-70	7.5	110	52	0.473	1.102	2.18
	9		74.9	0.681	1.103	1.09
	15		103	0.936	1.046	1.01

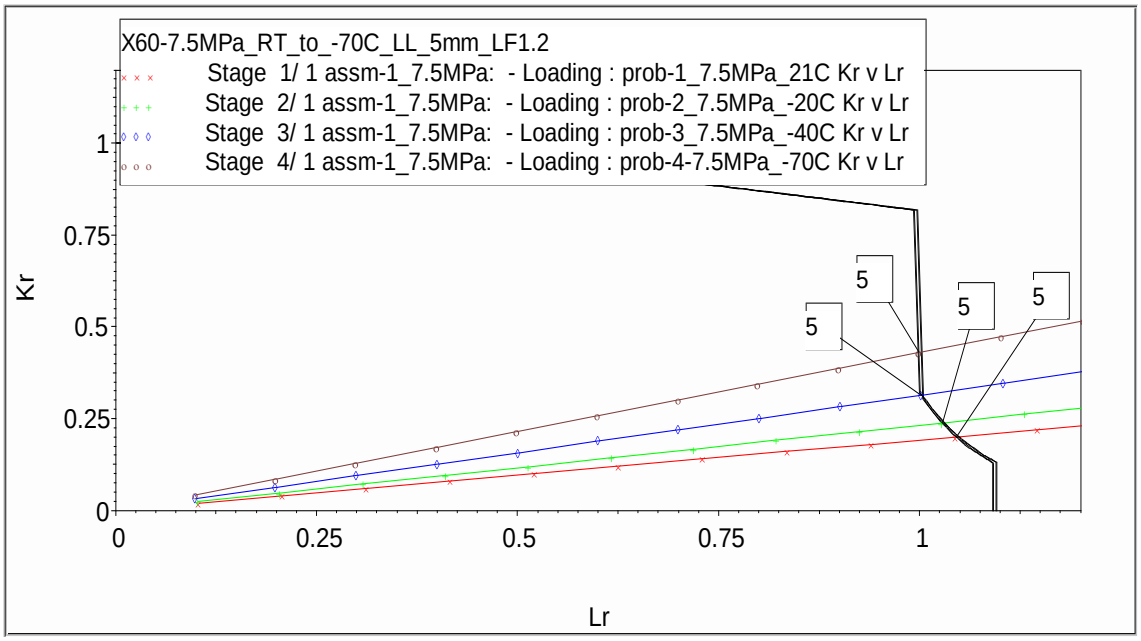

Figure 6-26 FAD locus by limited load analysis at 7.5 MPa operational pressure with 5 mm crack length

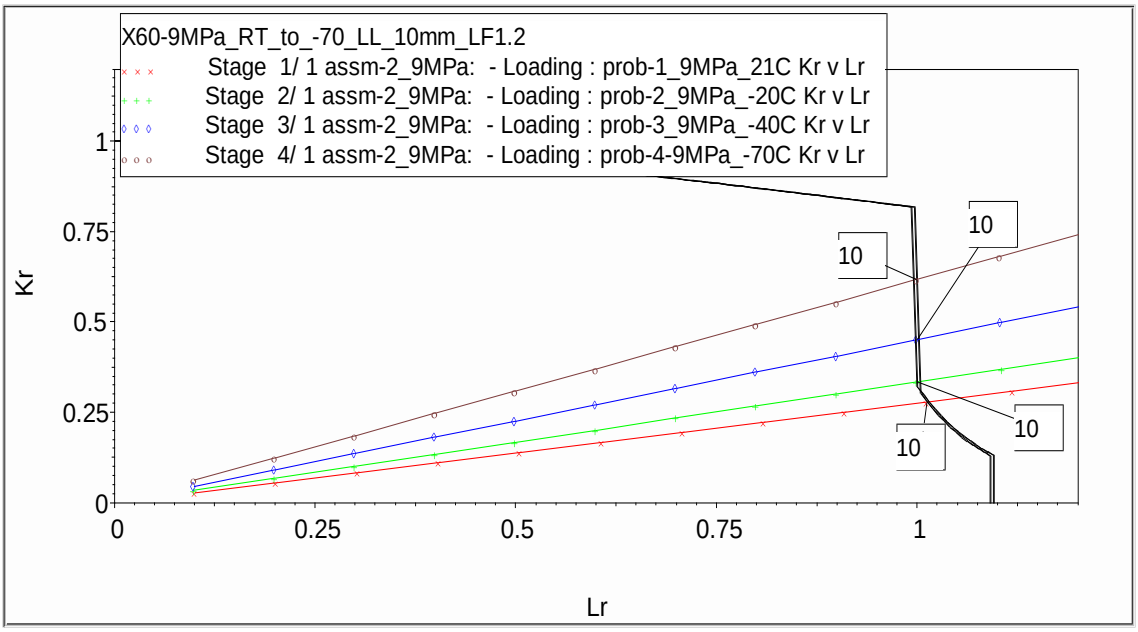

Figure 6-27 FAD locus by limited load analysis at 9MPa operational pressure with 10 mm crack length

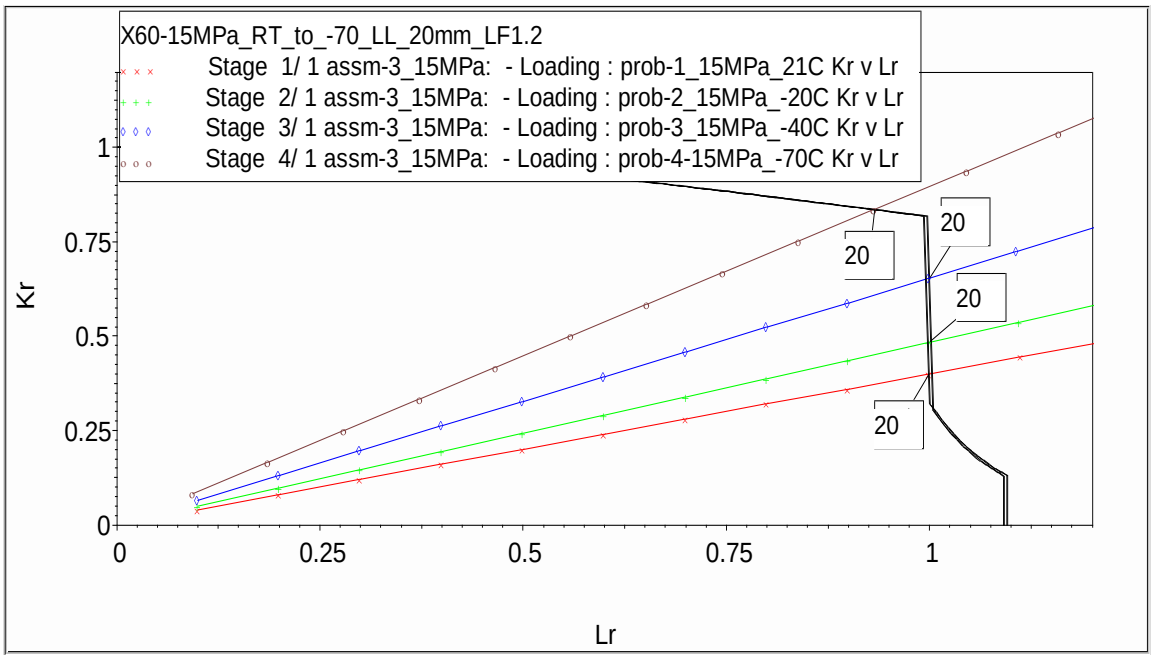

Figure 6-28 FAD locus by limited load analysis at 15 MPa operational pressure with 20 mm crack length

6.6 Summary

From the above considerations the analyses performed in this chapter focused on determining the effect or influence of material properties on the FAD. A first approximation could indicate that if a crack is located at point 1 (Figure 6-29) and kept constant, if the fracture toughness of the material decreases then the curve could be seen as moving towards point 1. Conversely, if the toughness were to increase, the curve would move away from point 1. However, if tensile residual stresses are present, then point 1 will move towards the right, while compressive residual stress would cause point 1 to move to the left.

On the other hand, at point 2, plastic collapse is affected by ductility which could indicate that collapse is more likely at lower temperatures. The two lines plotted from the origin through the K_r/L_r ratio of 1.1 and 0.4 divide the diagram into three regions indicated by two blue arrows. From the 1.1 ratio line to the $K_r/\sqrt{\delta_r}$ axis a potential benefit is achieved if residual stresses are alleviated. Conversely little advantage is seen for improving tensile properties.

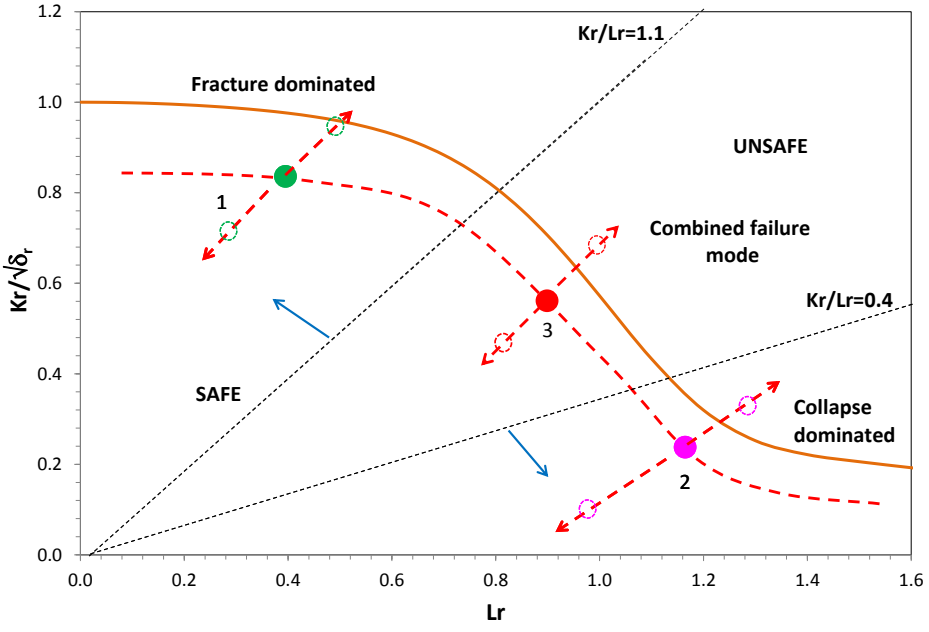

Figure 6-29 FAD representing the possible variations of the locus as a result of the effect of material properties on K_r and L_r

Similarly, from the 0.4 ratio line towards the L_r axis, advantage is obtained by enhancing tensile properties and a slight benefit if toughness is improved. Point 3 corresponds to the zone delimited by the 1.1 and 0.4 ratio lines, where the interaction between tensile properties, stress intensity factor, fracture toughness, temperature, residual stress or any secondary loads effect the failure mechanism and likely to be a mixed mode.

However, the assumptions made above differ from the analysis carried out by limiting both load and crack size on API X100steel, where the only part modified was the cut-off limiting L_r for all the cases evaluated. No extension of the assessment curve on the fracture dominated region was observed while the FADs' assessments show that acceptable crack lengths were located inside the failure assessment line. Details were shown in sections 6.5.1.1 and 6.5.2.1.

Likewise, the results for each assessment performed, including and excluding residual stresses in the calculations, show that the residual stress has no significant effect on the FAD (Figure 6-30). It could be a consequence of the high plasticity induced, indicating that the plastic collapse load is independent of any initial residual stress [290].

In addition, it was observed that the critical point for limiting crack analysis was a crack 20 mm in length at 15 MPa pressure at -70°C. The equivalent case at room temperature was assessed as "safe". For limiting load analysis at the same pressure and crack length, the data show that failure occurs before the design pressure ($1.2\sigma_H$) is reached.

For steel grades X70 and X60, the assessments were performed in the same manner as for steel grade X100. However, the mechanical response in the functional hardening region of the stress-strain engineering curve is different for both the two steel options used. For example, X60 is characterised by a plateau on the stress-strain curve; therefore all the analyses were performed using the FAD for discontinuous yielding, whilst for X70 steel this phenomenon was not observed and the analysis was accomplished by continuous yielding.

Lower temperature, i.e. -70°C, and higher pressure are critical factors as the combination of both of these affects the integrity of the physical parameters of the steel.

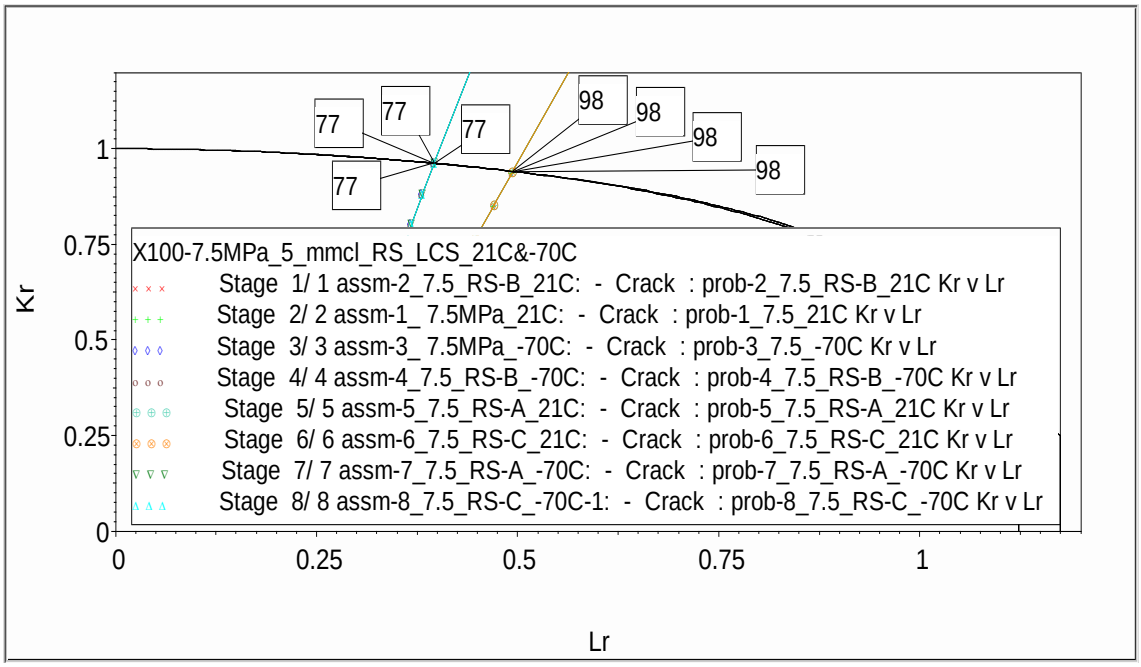

Figure 6-30 FAD curve representing slight effect of residual stress on fracture

7 SUMMARY, CONCLUDING REMARKS AND OUTLOOK

7.1 Summary

This thesis has been structured through the development of experimental and analytical methods for investigating the integrity of materials used for manufacturing pipelines and their interaction with simulated flue-gas. The background and main activities to develop the objectives of this research are presented in Chapter 1. In Chapter 2 a detailed review is introduced to establish the state-of-the-art on Capture, Transport and Storage of CO_2 along with fracture mechanics. The integrity issues of pipelines and structural integrity assessment concepts are also covered.

Chapter 3 describes in detail the methodology used to complete and achieve metallurgical characterisation, mechanical properties, fracture toughness, aging tests, residual stress and engineering critical assessment of pipeline steel. Chapter 4 describes the mechanical properties and fracture toughness of material on virgin and aging conditions, while residual stress evaluation is accomplished by neutron diffraction and Hole drilling tests which are presented in Chapter 5.

Finally Engineering Critical Assessment based on the FAD approach is presented in Chapter 6 to evaluate the integrity of pipelines transporting supercritical CO_2 with impurities using a “leak-before-break” approach.

7.2 Concluding remarks

The context of the present investigation, which was presented in Figure 1-7, underlined the core parts undertaken in this research as well as main contributors. Aspects as mechanical behaviour of material, residual stress and the effect impurities on the integrity of steels exposed in simulated flue-gas was undertaken and explained.

As a result of the current experimental work, the results and analysis performed determine the integrity of HSLA steels. The foremost conclusions are summarised as follows:

1. Tensile properties of API X100, X70 and X60 steels tested over range -70°C to 21°C in the longitudinal direction show lower values compared with the transverse orientation data obtained from the literature and API 5L standard. Features of the fracture surface indicated the influence of the anisotropy with remarkable effect on API X100. Variation of the tensile properties along with temperature was noticed which followed the behaviour expected. Vickers hardness values determined susceptibility of X100 and X70 steel in sour environments.

2. Comparison between tensile tests performed on virgin and aged samples indicated that the samples tested did not show significant variation on the mechanical properties. Ductility was not affected both as-received and exposed to a SO_2/H_2S environment which indicates an influence of the alloying element or dissipation of hydrogen before testing.

3. Specimen exposed to SO_2 and H_2S and analysed by XRD and EDS analytical methods determined that the layer deposited on the surface was hydrated $FeSO_4$ and FeSO. The corrosion products from SO_2 impurities were regularly distributed while the layer formed within a H_2S atmosphere was distributed irregularly. The layer formed could be considered to be protective as no signs of corrosion were noticed. Another aspect was the lower amount of free water on the system which prevents corrosion process.

4. Metallurgical characterisation defines that the steels have a combination of microstructure as a consequence of the manufacturing as well as cooling processing routes which differed according to chemical composition. Steel grades API X100 and X70 were composed of martensite, granular bainite and polygonal ferrite with fine precipitates distributed in the matrix. For API X60 steel small amounts of pearlite

distributed on the ferrite matrix where no deformation or banding were determined.

5. Fracture toughness evaluation by precracked Charpy tests determined that energy variation with temperature is lower when a fatigue crack is introduced. Toughness data obtained by using precracked samples tested in a conventional impact tester was found not to be viable as no consistency was found with the data available in the public domain. A Master curve and lower bound correlations can be used but the tests have to be performed on an instrumented pendulum machine or quasit-static test.

6. The compressive-tensile residual stress profile obtained from ND and ICHD measurement showed good agreement between the approaches used; however, unavoidable inaccuracies from the method have influenced stress level determination. It was found that the compressive stress distribution through the thickness increased according to the load on the rolling track.

7. A leak-before-break running FAD assessment, analysed by limiting crack size and limiting load under three operational pressures showed that the tensile stress, residual stresses and fracture toughness influenced the integrity of material under the existence of different flaw length. In API X100 steel with properties evaluated at -70°C and pressure about 15 MPa, crack initiation is inevitable at crack length above 10 mm. API X70 exhibit similar tendency but at crack length below 10 mm at -70°C and 15 MPa pressure. API X60 showed that at 15 MPa the component fails before any crack length is reached.

Following the conclusions highlighted previously a general comments could be presented in order to clarify the importance or impact of these results obtained in the CCTS framework.

- Pipelines are considered to be the most suitable solution to safely and efficiently transport at minimal expense supercritical CO_2 over long distances. Depending on fuel type, energy conversion process and capture process, there are large variations in the composition of CCTS, due to the inclusion of other CO_2 sources. Stronger implications not only for the construction of new pipelines, but also for the reuse of old pipelines are of paramount interest.

- Manufacturing companies and regulating bodies are presently developing concise guidelines or standards to establish a combination of an appropriate chemical composition and proper processing of manufacturing to guarantee final mechanical properties which would meet the technical requirements to transport fluids above 7.5 MPa. However, such guidelines are currently only being considered for transporting oil and gas, not supercritical CO_2 with impurities.

- The selection of appropriate steel for CCTS application requires a clear understanding of the loading applications and environmental challenges that the pipeline faces. Despite efforts to accomplish the required technical specifications, issues remain due to uncertainties between interactions of impurities with material at pressures above 15 MPa where fracture toughness is a weak factor due to manufacturing constraints, despite material strength.

- Structural integrity of materials or components infers their capacity to withstand a design service of any type of load resistance to breaking before the intended life of the designated structure. Loss of integrity implies that the structure or component is no longer able to be load-carrying as a consequence of excessive forces and strain due to loads or deterioration from external conditions either directly or indirectly associated with mechanical, physical and chemical properties. Engineering criticality assessment is of critical importance in order to evaluate the integrity of components within the framework of realistic data.

- Unless efforts are made to reduce the gap between compositional specifications for CO_2 mixtures, lack of CCTS operational knowledge and the uncertain long-term financial environment, then regulatory constraints and the acceptability of CCTS as a potential promoter for both reduction in GHGs and achievement of the 2020 targets agreed by the European Union in June 2009 will be jeopardised.

7.3 Contributions of this PhD

This research has developed specific material performance criteria for supercritical CO_2 transport by pipeline as a first step towards creating requirements for the safe design or reuse of steels in this environment. Improvement of knowledge of failure mechanisms gives the experimental data collected concerning HSLA steels exposed to flue-gasses as one of the most relevant technical topics in this investigation.

Furthermore, the information and data on the damage tolerance of steel has been collected and used to evaluate its structural integrity by the development of a defect assessment approach. The data generation and elaboration of the FAD based on experimental evidence are considered novel, as they could provide a possible explanation of issues related to materials transporting supercritical CO_2 with impurities, to be used on fracture arrest predictions or fracture control models or methods.

The current investigation has three main objectives. Firstly, to apply experimental data to the determination of modes of fracture within HSLA steel; secondly to measure impurities and establish their role on fracture toughness and material damage; thirdly to provide FAD assessment results on the integration of all material properties of virgin and aging samples.

- A general framework for material properties, integrity and assessment methodologies has been established. This included clear definitions of aspects such as variation of chemical composition, microstructure and

mechanical properties in relation to pipeline integrity, and methods to evaluate the structural integrity of systems transporting supercritical CO_2.

- The establishment a new methodology to expose materials in simulated flue-gases using an unique dynamic loop system to provide a baseline for aging tests, it is considered as one of the most important contributions of this investigation.

- Practical procedures to perform each test are described based on a systematic methodology which combines guidance from the standardisation and proprietary developmental work. Collected data can be used as a reference point for future work or for developing models on pipeline transportation of flue-gas.

- Determination of the constraints for fracture toughness using standard and non-standard samples is presented, indicating both the advantages and disadvantages.

- A FAD-based engineering critical assessment for CO_2 has been presented showing the effect of different pressure values and material properties by limited crack size and limiting loading analyses by Leak-before-break methodology is considered other important contribution of this research.

7.4 Limitations of the research

The limitations of this research are outlined in Chapters 4 and 5. A deeper analysis including more precise identification of embrittlement deterioration by hydrogen, such as the presence of crack or blister formation and its interactions with microstructure, was not carried out. Performing such an analysis would determine important information to understand how HIC mechanics operate.

Regarding the aging processes, constraints on space have limited the number of samples to meet the minimum standard requirements which have increased uncertainties about the variation of tensile and toughness properties. In addition, determination of H_2 concentration, determination of corrosion rates

using electrochemical techniques as well as pH which were not carried out due to the limitation of monitoring samples or adequate instrumentation inside the chamber need to be undertaken.

With regard to the cold rolling process to induce compressive residual stress, the utilisation of one roller could be the cause of the final distribution of residual stress, which was enhanced more on one side than the other. Performing the test by using two pairs of rollers would guarantee a better compressive stress distribution throughout the material thickness.

7.5 Further Work

As the studies carried out in this research are a new area of investigation, this work does not give a complete explanation of all parameters involved in both fracture mechanics and an aging environment. Additional work may be needed, including:

- The presence of hydrogen on steels can cause reduction of fracture toughness. Therefore conducting investigation to evaluate J_{ISCC}/K_{ISCC} on pipeline steel, for example API X100, could provide an estimate of toughness in flue-gas environments based on fracture mechanics criteria in order to establish an alternative methodology to evaluate the structural integrity of linepipe in terms of FAD.

- To study corrosion phenomena under stress by including conventional and precracked samples (standard/non-standard geometries) to investigate the effect of free water and flue-gas and their impact on structural integrity of linepipe at pressure above 7.5 MPa, 35 °C with pH varying between 3.0 to 5.5.

- Determination of compressive residual stress by cold rolling tests at different distances between each track to understand RS distribution and its effect in the in-plane directions. Additionally, to include laser peening as an alternative to compare the RS profile with cold rolling methods.

- Investigate residual stress profiles by X-Ray to determine the distribution near the surface and complement values obtained from ICHD and ND. In so doing, establish correlations to develop a model to predict residual stress on steel with 625 MPa yield strength and above.

REFERENCES

1. Intergovernmental Panel on Climate Change (IPCC). Special report on carbon dioxide capture and storage. 2005. Available at: http://www.ipcc.ch/publications_and_data/publications_and_data_reports.shtml#2
2. International Energy Agency-Greenhouse Gas Programme. Safety in carbon dioxide capture, transport and storage. 2009.
3. GWArt. Carbon dioxide gallery. Carbon dioxide gallery. 2014. p. 3.
4. Blunt M. Carbon dioxide storage. Grantham Institute for climate change. 2010.
5. Davison J., Thambimuthu K. Technologies for capture of carbon dioxide. In: Rubin ES, Keith DW, Gilboy CF, Wilson M, Morris T, Gale J, et al. (eds.) Greenhouse Gas Control Technologies 7. Oxford: Elsevier Science Ltd; 2005. pp. 3–13. Available at: DOI:DOI: 10.1016/B978-008044704-9/50002-1
6. GHG IEA. Potential for improvements in gasification combined cycle power generation with CO2 capture . IEA Greenhouse Gas R&D programme; 2003.
7. Michael K., Golab a., Shulakova V., Ennis-King J., Allinson G., Sharma S., et al. Geological storage of CO2 in saline aquifers—A review of the experience from existing storage operations. International Journal of Greenhouse Gas Control. Elsevier Ltd; July 2010; 4(4): 659–667. Available at: DOI:10.1016/j.ijggc.2009.12.011 (Accessed: 22 March 2014)
8. Oosterkamp A., Ramsen J. State-of-the-art Overview of CO2 pipeline transport with relevance to offshore pipelines. Polytec, Norway. . Norway; 2008.
9. Seevam PN., Downie MJ., Race JM. Transport of CO2 for Carbon Capture and Storage in the UK. Society of Petroleum Engineers International. Aberdeen, Scotland, U.K.: OnePetro; 2007. pp. 1–8. Available at: DOI:10.2118/109060-MS
10. Z.X. Zhang, G.X. Wang, P. Massarotto VR. Optimization of pipeline transport for CO2 sequestration. Kidlington, ROYAUME-UNI: Elsevier; 2006. p. 14.

11. Gale J., Davison J. Transmission of CO2—safety and economic considerations. 6th International Conference on Greenhouse Gas Control Technologies. 2004; 29(9–10): 1319–1328. Available at: DOI:10.1016/j.energy.2004.03.090

12. Seevam PN., Race JM., Downie MJ., Hopkins P. Transporting the Next Generation of CO2 for Carbon, Capture and Storage: The Impact of Impurities on Supercritical CO2 Pipelines. ASME Conference Proceedings. ASME; 2008; 2008(48579): 39–51. Available at: http://link.aip.org/link/abstract/ASMECP/v2008/i48579/p39/s1

13. Cooper R., Barnett J. Pipelines for transporting CO2 in the UK. Energy Procedia. 2014; 63: 2412–2431. Available at: DOI:10.1016/j.egypro.2014.11.264

14. Steeneveldt R., Berger B., Torp TA. CO2 Capture and Storage: Closing the Knowing–Doing Gap. Carbon Capture and Storage. 2006; 84(9): 739–763. Available at: DOI:DOI: 10.1205/cherd05049

15. Cosham A., Eiber RJ. Fracture propagation of CO2 pipelines. Energy. 2003; (049): 115–124.

16. Anheden M., Andersson A., Bernstone C., Eriksson S., Yan J., Liljemark S., et al. CO2 quality requirement for a system with CO2 capture, transport and storage. In: Rubin ES, Keith DW, Gilboy CF, Wilson M, Morris T, Gale J, et al. (eds.) Greenhouse Gas Control Technologies 7. Oxford: Elsevier Science Ltd; 2005. pp. 2559–2564. Available at: DOI:DOI: 10.1016/B978-008044704-9/50373-6

17. Buit L., Ahmad M., Mallon W., Hage F. CO2 EuroPipe study of the occurrence of free water in dense phase CO2 transport. 10th International Conference on Greenhouse Gas Control Technologies. 2011; 4: 3056–3062. Available at: DOI:DOI: 10.1016/j.egypro.2011.02.217

18. de Visser E., Hendriks C., Barrio M., Mølnvik MJ., de Koeijer G., Liljemark S., et al. Dynamis CO2 quality recommendations. TCCS-4: The 4th Trondheim Conference on CO2 Capture, Transport and Storage. 2008; 2(4): 478–484. Available at: DOI:DOI: 10.1016/j.ijggc.2008.04.006

19. GHG IEA. Impact of Impurities on CO2 Capture, Transport and Storage. IEAGHG; 2004.

20. Koornneef J., Ramirez A., van Harmelen T., van Horssen A., Turkenburg W., Faaij A. The impact of CO2 capture in the power and heat sector on the emission of SO2, NOx, particulate matter, volatile organic compounds and NH3 in the European Union. Atmospheric Environment. 2010; 44(11): 1369–1385. Available at: DOI:DOI: 10.1016/j.atmosenv.2010.01.022

21. Franco A., Diaz AR. The future challenges for 'clean coal technologies': Joining efficiency increase and pollutant emission control. Energy. March 2009; 34(3): 348–354. Available at: DOI:10.1016/j.energy.2008.09.012 (Accessed: 8 April 2014)

22. Kaufmann KD. CO2 Pipelines - Conclusion: Impurity types, concentration influence hydraulic design. Oil & Gas Journal. 2010; : 1–6.

23. de Koeijer G., Borch JH., Drescher M., Li H., Wilhelmsen Ø., Jakobsen J. CO2 transport–Depressurization, heat transfer and impurities. Energy Procedia. Elsevier; January 2011; 4: 3008–3015. Available at: DOI:10.1016/j.egypro.2011.02.211 (Accessed: 11 April 2014)

24. Miller BG. CO2 Capture and Storage. Clean Coal Engineering Technology. Boston: Butterworth-Heinemann; 2011. pp. 483–511. Available at: DOI:DOI: 10.1016/B978-1-85617-710-8.00010-8

25. Olajire AA. CO2 capture and separation technologies for end-of-pipe applications – A review. 7th International Conference on Sustainable Energy Technologies, 7th International Conference on Sustainable Energy Technologies. 2010; 35(6): 2610–2628. Available at: DOI:DOI: 10.1016/j.energy.2010.02.030

26. Sass B., Monzyk B., Ricci S., Gupta A., Hindin B., Gupta N. Impact of SOx and NOx in Flue Gas on CO2 Separation, Compression, and Pipeline Transmission. Carbon Dioxide Capture for Storage in Deep Geologic Formations. Amsterdam: Elsevier Science; 2005. pp. 955–981. Available at: DOI:DOI: 10.1016/B978-008044570-0/50144-6

27. Pipitone G., Bolland O. Power generation with CO2 capture: Technology for CO2 purification. International Journal of

Greenhouse Gas Control. 2009; 3(5): 528–534. Available at: DOI:DOI: 10.1016/j.ijggc.2009.03.001

28. Myhrvold T., Helle K., Johnsen K., Hussain A. Development of a guideline for the qualification of CO2 capture technology. Proceedings of the 9th International Conference on Greenhouse Gas Control Technologies (GHGT-9), 16–20 Nov. 2008, Washington, DC, USA. 2009; 1(1): 1527–1534. Available at: DOI:DOI: 10.1016/j.egypro.2009.01.200

29. Maldal T., Tappel IM. CO2 underground storage for Snøhvit gas field development. 6th International Conference on Greenhouse Gas Control Technologies. 2004; 29(9-10): 1403–1411. Available at: DOI:DOI: 10.1016/j.energy.2004.03.074

30. Cole IS., Corrigan P., Sim S., Birbilis N. Corrosion of pipelines used for CO2 transport in CCS: Is it a real problem? International Journal of Greenhouse Gas Control. 2011; 5(4): 749–756. Available at: DOI:10.1016/j.ijggc.2011.05.010

31. Xu M. Status of trace element emission in a coal combustion process: a review. Fuel Processing Technology. 15 February 2004; 85(2-3): 215–237. Available at: DOI:10.1016/S0378-3820(03)00174-7 (Accessed: 11 April 2014)

32. Caraballo A., Rabindran P., Chahardehi A., Winning IG., Brennan FP. Fracture Control Strategy for the Conversion of Oil and Gas Pipelines to Transport CO2. In: Conference TPT (ed.) 6th Pipeline Technology Conference. Germany: The Pipeline Technology Conference-PTC; 2011.

33. Seevam P., Race J., Downie M., Barnett J., Cooper R. Capturing Carbon Dioxide: The feasibility of re-using existing pipeline infrastructure to Transport Anthropogenic CO2. In: IPC2010 (ed.) ASME Conference Proceedings. Calgary, Alberta, Canada: ASME; 2010. pp. 129–142. Available at: http://link.aip.org/link/abstract/ASMECP/v2010/i44212/p129/s1

34. American Petroleum Institute. API 579 - Fitness-For-Service. API SPEC 5L. Washington, D.C.: American Petroleum Institute; 2007.

35. BS 7910:2013. Guide to methods for assessing the acceptability of flaws in metallic structures. London; 2013.

36. BS PD 6493:1991. Guidance on methods for assessing the

acceptability of flaws in fusion welded structures. 1991.

37. Milne I., Ainsworth RA., Dowling AR., Stewart AT. Assessment of the integrity of structures containing defect. International Journal of Pressure Vessels and Piping. 1988; 32: 3–104.

38. Cosham A., Hopkins P. The effect of dents in pipelines—guidance in the pipeline defect assessment manual. The 10th International Conference on Pressure Vessel Technology (ICPVT-10). 2004; 81(2): 127–139. Available at: DOI:DOI: 10.1016/j.ijpvp.2003.11.004

39. Webster, S., Bannister A. Structural integrity assessment procedure for Europe – of the SINTAP programme overview. Engineering Fracture Mechanics. January 2000; 67(6): 481–514. Available at: DOI:10.1016/S0013-7944(00)00070-9

40. Gutiérrez-Solana F., Cicero S. FITNET FFS procedure: A unified European procedure for structural integrity assessment. Papers presented at the 24th meeting of the Spanish Fracture Group (Burgos, Spain, March 2007. 2009; 16(2): 559–577. Available at: DOI:DOI: 10.1016/j.engfailanal.2008.02.007

41. Horsley DJ. Background to the use of CTOA for prediction of dynamic ductile fracture arrest in pipelines. Engineering Fracture Mechanics. February 2003; 70(3–4): 547–552. Available at: DOI:http://dx.doi.org/10.1016/S0013-7944(02)00136-4

42. de Luna S., Fernández-Sáez J., Pérez-Castellanos JL., Navarro C. An analysis of the static and dynamic fracture behaviour of a pipeline steel. International Journal of Pressure Vessels and Piping. January 2000; 77(11): 691–696. Available at: DOI:DOI: 10.1016/S0308-0161(00)00058-2

43. Gorrochategui I., González-Posada MA., Gutiérrez-Solana F. On the structural integrity assessment of elastic–plastic redundant cracked structures. Engineering Fracture Mechanics. 2006; 73(17): 2710–2722. Available at: DOI:10.1016/j.engfracmech.2006.03.003

44. Haušild P., Berdin C., Bompard P. Prediction of cleavage fracture for a low-alloy steel in the ductile-to-brittle transition temperature range. Materials Science and Engineering: A. 2005; 391(1–2): 188–197. Available at: DOI:10.1016/j.msea.2004.08.067

45. He M., Li F. Modified transformation formulae between fracture toughness and CTOD of ductile metals considering pre-deformation effects. Engineering Fracture Mechanics. 2010; 77(14): 2763–2771. Available at: DOI:http://dx.doi.org/10.1016/j.engfracmech.2010.06.021

46. Cosham A., Jones GB., Eiber RJ., Hopkins P. Don't drop drop-weight tear test. The Journal of Pipeline Engineering. 2010; 9(2): 69–84.

47. Fearnehough GD. Fracture propagation control in gas pipelines: A survey of relevant studies. International Journal of Pressure Vessels and Piping. 1974; 2(4): 257–282. Available at: DOI:10.1016/0308-0161(74)90007-6

48. Corwin WR., Hougland AM. Effect of Specimen Size and Material Condition on the Charpy Impact Properties of 9Cr-1Mo-V-Nb Steel. In: W. R. Corwin and G. E. Lucas (ed.) The use of small-scale Specimens for testing irradiated material, ASTM STP 888. Philadelphia, USA: American Society for Testing and Materials; 1986. pp. 325–338.

49. Rolfe JM., Barsom ST. Correlations between KIc and charpy V-Notch test results in the transition-temperature range. Impact testing of metals, ASTM STP 466. 1970; 1: 281–302.

50. Sailors HT., Corten RH. Relationship between material fracture toughness using fracture mechanics and transition temperature tests. In: ASTM (ed.) National Symposium on fracture mechnanics, ASTM STP 514. 1972. pp. 164–191.

51. Buzzichelli G. Designing against ductile fracture propagation in very high strength steel gas pipelines: A review. M. Fuentes A.Martín-Meizoso and J.M.Martínez-Esnaola ME (ed.) European Structural Integrity Society. Elsevier; 2000; Volume 26: 235–252. Available at: DOI:DOI: 10.1016/S1566-1369(00)80052-7

52. Liessem A., Hillenbrand HG. Challenges in linepipe manufacturing for high strenght pipelines. In: Pipeline Research Council International. (ed.) 16th Biennal Pipeline Research Joint Technical Meeting. Canberra, Australia: Pipeline Research Council International, Inc.; 2007. pp. 1–12.

53. Heerens J., Ainsworth RA., Moskovic R., Wallin K. Fracture toughness characterisation in the ductile-to-brittle transition and

upper shelf regimes using pre-cracked Charpy single-edge bend specimens. International Journal of Pressure Vessels and Piping. 2005; 82(8): 649–667. Available at: DOI:10.1016/j.ijpvp.2004.11.005

54. Higuchi R., Makino H., Takeuchi I. New concept and test method on running ductile fracture arrest for high pressure gas pipeline. The Korean Gas Union. 2011. pp. 1–8. Available at: http://www.kgu.or.kr/download.php?tb=bbs_017&fn=wgcFinal00210.pdf&rn=wgcFinal00210.pdf.

55. Wallin K., Nevasmaa P., Planman T., Valo M. Evolution of the Charpy-V test from a quality control test to a materials evaluation tool for structural integrity assessment. In: Pineau DF and A (ed.) European Structural Integrity Society. Elsevier; 2002. pp. 57–68. Available at: DOI:DOI: 10.1016/S1566-1369(02)80006-1

56. Wallin K. Fracture Toughness Transition Curve Shape for Ferritic Structural Steels. Fracture of Engineering Materials and Structures. Springer Netherlands; 1991. pp. 83–88. Available at: DOI:10.1007/978-94-011-3650-1_10

57. Wallin K., Nevasmaa P., Laukkanen A., Planman T. Master Curve analysis of inhomogeneous ferritic steels. Engineering Fracture Mechanics. November 2004; 71(16–17): 2329–2346. Available at: DOI:http://dx.doi.org/10.1016/j.engfracmech.2004.01.010

58. Wallin K. Structural integrity assessment aspects of the Master Curve methodology. Engineering Fracture Mechanics. January 2010; 77(2): 285–292. Available at: DOI:http://dx.doi.org/10.1016/j.engfracmech.2009.02.010

59. Schindler H., Kalkhof D. Lower bounds and saturation effects of dynamic fracture toughness in the brittle-to-ductile transition regime of ferritic steels. Transactions, SMiRT-22. San Francisco, California, USA; 2013. pp. 1–10.

60. Gray JM., Siciliano F. High Strength Microalloyed Linepipe : Half a Century of Evolution. In: Division. UCCM (ed.) Proceedings of an international symposium on high-strength, low-alloy steels. Washington, D.C., U.S.A.: Microalloying 75, Distributed by American Society for Metals.; 1975. pp. 1–26.

61. Gray JM. Technology of microalloyed steel for large diameter

pipe. International Journal of Pressure Vessels and Piping. 1974; (2): 95–122. Available at: DOI:10.1016/0308-0161(74)90019-2

62. Rothwell AB. Fracture Propagation Control for Gas Pipelines -- Past, Present and Future. Proceedings of the Third International Pipeline Technology Conference. Brugge, Belgium: Elsevier Scientific; 2000. pp. 387–405.

63. Das AK. The Present and the Future of Line Pipe Steels for Petroleum Industry. Materials and Manufacturing Processes. 22 March 2010; 25(1-3): 14–19. Available at: DOI:10.1080/10426910903202427 (Accessed: 31 July 2014)

64. Gray JM. An Independent View of Linepipe and Linepipe Steel for High Strength Pipelines: How to get Pipe that's Right for the Job at the Right Price". In: Limited MTPt (ed.) API X-80 Pipeline Cost Workshop. Hobart, Australia.: APIA; 2002. pp. 1–19.

65. Pickering FB. High-Strength, Low-Alloy Steels - A Decade of Progress. In: 75 M (ed.) Proceedings of an international symposium on high-strength, low-alloy steels. USA: Union Carbide Corporation; 1975. pp. 1–9.

66. Klassen RJ., Bassim MN., Bayoumi MR., Wilsdorf HGF. Characterization of the effect of alloying elements on the fracture toughness of high strength, low alloy steels. Materials Science and Engineering. June 1986; 80(1): 25–35. Available at: DOI:10.1016/0025-5416(86)90299-5 (Accessed: 31 July 2014)

67. ANSI/API 5L-44th. Specification for Line Pipe - ANSI/API 5L. 2007. Available at: http://api1.net/s/specification-for-line-pipe-w3504.pdf (Accessed: 13 March 2014)

68. Huper T., Endo S., Ishikawa N., Osawa K. Effect of volume fraction of constituent phases on the stress-strain relationship of dual phase steels. ISIJ International. 1999; 39(3): 288–294. Available at: DOI:10.2355/isijinternational.39.288

69. Hillenbrand HG., Liessem A., Bierman K., Heckman CJ., Schwinn V. Development of high strength material and pipe production technology for grade X120 line pipe. In: ASME (ed.) 2004 International Pipeline Conference. Calgary, Alberta, Canada; 2004. pp. 1743–1749. Available at:

http://proceedings.asmedigitalcollection.asme.org/proceeding.aspx?articleid=1646414

70. Oosterkamp A., Ramsen J. State-of-the-Art Overview of CO2 Pipeline Transport with relevance to offshore pipelines. Report to the Research Council of Norway. Report number POL-O-2007-138-A. 2008.

71. Barsanti L., Mannucci G., Hillenbrand HG., Demofonti G., Harris D. Possible Use of New Materials for High Pressure Linepipe Construction: An Opening on X100 Grade Steel. ASME Conference Proceedings. ASME; 2002; (36207): 287–298. Available at: http://link.aip.org/link/abstract/ASMECP/v2002/i36207/p287/s1

72. Demofonti G., Mannucci G., Roovers P. Existing methods for the evaluation of material fracture resistance for high grade steel pipelines. 3R International. 2008; : 1–14.

73. Hillenbrand HG., Liessem A., Kalwa C., Erdelen-Peppler M., Stallybrass C. Technological solutions for high strength gas pipelines. Berpipe. 2008. pp. 1–16. Available at: http://www.bergpipe.com/files/ep_tp_80_08en.pdf (Accessed: 1 January 2011)

74. Zhao M-C., Yang K., Shan Y-Y. Comparison on strength and toughness behaviors of microalloyed pipeline steels with acicular ferrite and ultrafine ferrite. Materials Letters. 2003; 57(9-10): 1496–1500. Available at: DOI:DOI: 10.1016/S0167-577X(02)01013-3

75. Zhao MC., Yang K., Shan Y. The effects of thermo-mechanical control process on microstructures and mechanical properties of a commercial pipeline steel. Materials Science and Engineering: A. September 2002; 335(1-2): 14–20. Available at: DOI:10.1016/S0921-5093(01)01904-9 (Accessed: 6 August 2014)

76. Wang W., Yan W., Zhu L., Hu P., Shan Y., Yang K. Relation among rolling parameters, microstructures and mechanical properties in an acicular ferrite pipeline steel. Materials & Design. October 2009; 30(9): 3436–3443. Available at: DOI:10.1016/j.matdes.2009.03.026 (Accessed: 6 August 2014)

77. Zajac KH., Schwinn S., Tacke V. Characterisation and quantification of complex bainitic microstructures in high and

ultra-high strength linepipe steels. Materials Science Forum. 2005; 50: 387–394.

78. Das SK., Sivaprasad S., Das S., Chatterjee S., Tarafder S. The effect of variation of microstructure on fracture mechanics parameters of HSLA-100 steel. Materials Science and Engineering: A. 2006; 431(1-2): 68–79. Available at: DOI:DOI: 10.1016/j.msea.2006.05.093

79. Huang F., Liu J., Deng ZJ., Cheng JH., Lu ZH., Li XG. Effect of microstructure and inclusions on hydrogen induced cracking susceptibility and hydrogen trapping efficiency of X120 pipeline steel. Materials Science and Engineering: A. October 2010; 527(26): 6997–7001. Available at: DOI:10.1016/j.msea.2010.07.022 (Accessed: 30 September 2014)

80. Clover D., Kinsella B., Pejcic B., De Marco R. The influence of microstructure on the corrosion rate of various carbon steels. Journal of applied electrochemistry. 2005; 35: 139–149. Available at: DOI:10.1007/s10800-004-6207-7

81. Rosado DB., Waele WD., Vanderschueren D. Latest developments in mechanical properties and metallurgycal of high strenght line pipes. Sustainable Construction and Design. 2013; 4(1): 1–10.

82. Schwinn V., Fluess P., Liessem A., Schroeder J. Concepts of grade X100 for high toughness and strain based design application. Proceedings of the Eighteenth (2008) International Offshore and Polar Engineering Conference. Vancouver, BC, Canada,: The International Society of Offshore and Polar Engineers; 2008. pp. 1–6. Available at: http://www.onepetro.org/mslib/app/Preview.do?paperNumber=ISOPE-I-08-295&societyCode=ISOPE

83. Nagai K., Shinohara Y., Sakamoto S., Tsuru E., Asahi H., Hara T. Anisotropic Strain Aging Behavior of High Strength UOE Linepipes. Anisotropy of the stress-strain curves for line pipe steels. Calgary, Alberta, Canada: ASME; 2010. pp. 59–65. Available at: http://www.onepetro.org/mslib/app/Preview.do?paperNumber=ISOPE-I-09-444&societyCode=ISOPE

84. Koo JY., Luton MJ., Bangaru N V., Petkovic RA., Fairchild DP.,

Petersen CW., et al. Metallurgical design of ultra high-strength steels for gas pipelines. 13th Internationla Offshore and Polar Engineering Conference. Honolulu, Hawai: The International Society of Offshore and Polar Engineers; 2004. pp. 10–18. Available at: http://e-book.lib.sjtu.edu.cn/isope2003/pdffiles/volume4/4002p010.pdf

85. Hillenbrand HG., Liessem A., Biermann K., Heckmann CJ., Schwinn V. Development and production of linepipe steels in grade X100 and X120. Seminar of X120 grade high performance pipe steels. Beijing, China.: EUROPIPE; 2005. pp. 1–11. Available at: http://scholar.google.co.uk/scholar?hl=en&q=Development+and+production+of+linepipe+steels+in+grade+X100+and+X120&btnG=&as_sdt=1,5&as_sdtp=#1

86. Kumar AS., Kumar BR., Datta GL., Ranganath VR. Effect of microstructure and grain size on the fracture toughness of a micro-alloyed steel. Materials Science and Engineering: A. 2010; 527(4–5): 954–960. Available at: DOI:10.1016/j.msea.2009.09.027

87. Institute Global CCS. Understanding CCS. http://www.globalccsinstitute.com/content/what-ccs. 2014. pp. 1–5.

88. Watt J. Carbon dioxide transport infrastructure: key learning and critical issues. Journal of pipeline engineering. 2010; 9(4): 213–222.

89. Race J., Seevam P., Downie MJ. Challenges for Offshore Transport of Anthropogenic Carbon Dioxide. In: ASME (ed.) 26th International Conference on Offshore Mechanics and Arctic . San Diego, California, USA: ASME; 2007. pp. 589–602. Available at: http://link.aip.org/link/abstract/ASMECP/v2007/i4269X/p589/s1

90. Seevam PN., Race JM., Downie MJ. Carbon dioxide pipelines for sequestration in the UK: An engineering gap analysis. Journal of pipeline engineering. 2007; 6(3): 140–141.

91. Zhao Q., Li YX. The influence of impurities on the transportation safety of an anthropogenic CO2 pipeline. Process Safety and Environmental Protection. Institution of Chemical Engineers; January 2014; 92(1): 80–92. Available at:

DOI:10.1016/j.psep.2013.10.007

92. Wang J., Ryan D., Anthony EJ., Wildgust N., Aiken T. Effects of impurities on CO2 transport, injection and storage. Energy Procedia. Elsevier; January 2011; 4: 3071–3078. Available at: DOI:10.1016/j.egypro.2011.02.219 (Accessed: 22 March 2014)

93. Ayello F., Evans K., Thodla R., Sridhar N. Effect of impurities on corrosion of steel in supercritical CO2. NACE. 2010; 2(10193): 1–16.

94. Hesjevik SM., Olsen S., Seiersten M. Corrosion at high CO2 pressure. Corrosion. San Diego Ca: NACE International; January 2003; (03345): 1–12. Available at: http://www.onepetro.org/mslib/app/Preview.do?paperNumber=NACE-03345&societyCode=NACE

95. McGrail BP., Schaef HT., Glezakou V-A., Dang LX., Owen AT. Water reactivity in the liquid and supercritical CO2 phase: Has half the story been neglected? Energy Procedia. Elsevier; February 2009; 1(1): 3415–3419. Available at: DOI:10.1016/j.egypro.2009.02.131

96. Vesga Rivera W., Brennan FP. Supercritical CO2 environments and their effects on material performance. Cranfield; 2012.

97. Jung W., Nicot JP. Impurities in CO2-Rich Mixtures Impact CO2 Pipeline Design: Implications for Calculating CO2 Transport Capacity. SPE International Conference on CO2 Capture, Storage, and Utilization. 2010. Available at: DOI:10.2118/139712-MS

98. Kaufmann KD. Impurity types , concentration influence hydraulic design. Oil & Gas Journal. 2010; 108(14): 60–63.

99. Seiersten M. Material selection for CO2 transportation Our project Corrosion of carbon steel – Increase design confidence by establishing. 2003.

100. Xiang Y., Wang Z., Xu C., Zhou C., Li Z., Ni W. Impact of SO2 concentration on the corrosion rate of X70 steel and iron in water-saturated supercritical CO2 mixed with SO2. The Journal of Supercritical Fluids. Elsevier B.V.; September 2011; 58(2): 286–294. Available at: DOI:10.1016/j.supflu.2011.06.007

101. Koornneef J., Ramirez A., van Harmelen T., van Horssen A., Turkenburg W., Faaij A. The impact of CO2 capture in the

power and heat sector on the emission of SO2, NOx, particulate matter, volatile organic compounds and NH3 in the European Union. Atmospheric Environment. Elsevier Ltd; April 2010; 44(11): 1369–1385. Available at: DOI:10.1016/j.atmosenv.2010.01.022 (Accessed: 11 April 2014)

102. Wang J., Ryan D., Anthony EJ., Wildgust N., Aiken T. Effects of impurities on CO2 transport, injection and storage. Energy Procedia. January 2011; 4: 3071–3078. Available at: DOI:10.1016/j.egypro.2011.02.219 (Accessed: 22 March 2014)
103. Billingham MA., Lee CH., Haines M., Smith L. Corrosion and materials selection issues in c arbon capture plants. NACE Corrosion. 2012; C2012(01371): 1–13.
104. Conder RJ., Felton P., Place C., Dent P. Hydrogen embrittlement testing of high dtrenght low carbon martensitic steels. NACE. 2010; 10(10290): 1–14.
105. Michler T., Yukhimchuk A a., Naumann J. Hydrogen environment embrittlement testing at low temperatures and high pressures. Corrosion Science. December 2008; 50(12): 3519–3526. Available at: DOI:10.1016/j.corsci.2008.09.025 (Accessed: 11 April 2014)
106. Seiersten M. Material selection for separation, transportation and disposal of CO2. Corrosion. 2001; (1042): 1–10.
107. Scully JR., Dogan H., Li D., Gangloff RP. Controlling hydrogen embrittlement in ultra-high strength steels. Corrosion. 2004; (04563): 1–20.
108. Thodla, R., Francois, A., Sridhar N. Materials performance in supercritical CO2 environments. NACE. 2009; (09255): 1–14.
109. de Visser E., Hendriks C., Barrio M., Mølnvik MJ., de Koeijer G., Liljemark S., et al. Dynamis CO2 quality recommendations. International Journal of Greenhouse Gas Control. October 2008; 2(4): 478–484. Available at: DOI:10.1016/j.ijggc.2008.04.006 (Accessed: 25 March 2014)
110. Dugstad A., Clausen S., Morland B. Transport of dense phase CO2 in C-steel pipelines – when is corrosion an issue? NACE. 2011; (11070): 1–15.
111. W.K.Kim KYK., T.W.Yun., B.Y.Yang. The effect of metallurgical

factors on SSC of high strength pipeline steel. NACE. 2008; (08496): 1–9.

112. Al-Mansour M., Alfantazi AM., El-boujdaini M. Sulfide stress cracking resistance of API-X100 high strength low alloy steel. Materials & Design. 2009; 30(10): 4088–4094. Available at: DOI:DOI: 10.1016/j.matdes.2009.05.025

113. Dong CF., Liu ZY., Li XG., Cheng YF. Effects of hydrogen-charging on the susceptibility of X100 pipeline steel to hydrogen-induced cracking. International Journal of Hydrogen Energy. Elsevier Ltd; December 2009; 34(24): 9879–9884. Available at: DOI:10.1016/j.ijhydene.2009.09.090 (Accessed: 11 April 2014)

114. López Turconi G., Fukui T., Ono T., Pérez T. Alternatives for High Strength Materials in sour environments. SPE International. 2005; (SPE 97582): 1–6.

115. Ikeda A., Kaneko T., Ando Y. On the evaluation method of sulfide stress cracking susceptibility of carbon and low alloy steels. Corrosion Science. 1987; 27(10-11): 1099–1115. Available at: DOI:DOI: 10.1016/0010-938X(87)90101-6

116. Buhre BJP., Elliott LK., Sheng CD., Gupta RP., Wall TF. Oxy-fuel combustion technology for coal-fired power generation. Progress in Energy and Combustion Science. January 2005; 31(4): 283–307. Available at: DOI:10.1016/j.pecs.2005.07.001 (Accessed: 21 March 2014)

117. Wall T., Liu Y., Spero C., Elliott L., Khare S., Rathnam R., et al. An overview on oxyfuel coal combustion—State of the art research and technology development. Chemical Engineering Research and Design. August 2009; 87(8): 1003–1016. Available at: DOI:10.1016/j.cherd.2009.02.005 (Accessed: 21 March 2014)

118. Toftegaard MB., Brix J., Jensen P a., Glarborg P., Jensen AD. Oxy-fuel combustion of solid fuels. Progress in Energy and Combustion Science. Elsevier Ltd; October 2010; 36(5): 581–625. Available at: DOI:10.1016/j.pecs.2010.02.001 (Accessed: 21 March 2014)

119. Buit L., Ahmad M., Mallon W., Hage F. CO2 EuroPipe study of the occurrence of free water in dense phase CO2 transport. Energy Procedia. January 2011; 4: 3056–3062. Available at:

DOI:10.1016/j.egypro.2011.02.217 (Accessed: 11 April 2014)

120. Dugstad A., Morland B., Clausen S. Corrosion of transport pipelines for CO2–Effect of water ingress. Energy Procedia. Elsevier; January 2011; 4: 3063–3070. Available at: DOI:10.1016/j.egypro.2011.02.218 (Accessed: 11 April 2014)
121. Choi YS., Nešić S. Corrosion behaviour of carbon steel in supercritical CO2 - water environments. NACE. 2009; (09256): 1–20.
122. Zhanga, Y., Gao, K., Schmittb G. Water effect on steel under supercritical CO2 condition. NACE Corrosion. 2011; (11378): 1–15.
123. Llongueras JG., Mendoza-Flores J., Duran-Romero R., Muñoz A., Hernandez J. Mechanism of FeCO3 Formation on API X70 Pipeline Steel in Brine Solutions Containing CO2. Corrosion 2005. Houston, Tx: NACE International; 2005. pp. 1–7. Available at: http://www.onepetro.org/mslib/app/Preview.do?paperNumber=NACE-05297&societyCode=NACE
124. Schmitt G., Horstemeier M. Fundamental Aspects of CO2 Metal Loss Corrosion - Part II: Influence of Different Parameters on CO2 Corrosion Mechanisms. Corrosion. San Diego Ca: NACE International; January 2006; (6112): 1–26. Available at: http://www.onepetro.org/mslib/app/Preview.do?paperNumber=NACE-06112&societyCode=NACE
125. Dugstad A. Fundamental Aspects of CO2 Metal Loss Corrosion Part I: Mechanism. Corrosion. 2006; (06111): 1–18.
126. Brown B., Lee K-L., Nešić S. Corrosion in Multiphase Flow Containing Small Amounts of H2S. Corrosion. San Diego Ca: NACE International; 2003. pp. 1–8. Available at: http://www.onepetro.org/mslib/app/Preview.do?paperNumber=NACE-03341&societyCode=NACE
127. Nešić S. Key issues related to modelling of internal corrosion of oil and gas pipelines – A review. Corrosion Science. December 2007; 49(12): 4308–4338. Available at: DOI:10.1016/j.corsci.2007.06.006 (Accessed: 11 July 2014)
128. Kermani B., Martin J., Esaklul K. Materials design

strategy:Effects of H2S/CO2 corrosion on materials selection. CORROSION. 2006; (06121): 1–18.

129. Pargeter RJ. Susceptibility to SOHIC for Linepipe and pressure vessel- Review of current knowledge. NACE Corrosion. 2007; (07115): 1–27.

130. Kermani B., Daguerre F. Materials optimization for CO2 transportation in CO2 capture and storage. NACE -Corrosion. 2010; (10334): 1–14.

131. Smith L., Craig B. Corrosion mechanisms and material performance in environments containing hydrogen sulfide and elemental sulfur. SACNUC Workshop. 2008. pp. 1–21.

132. Olsen S. Corrosion Control by Inhibition, Environmental Aspects, and pH Control: Part II: Corrosion Control by pH Stabilization. NACE International;

133. Cassagne T., Moulié G., Duret C. Limits of use of low alloy and stainless steels in upstream sour environments. CORROSION. Atlanta, GA: NACE International; 2009. Available at: http://www.onepetro.org/mslib/app/Preview.do?paperNumber=NACE-09079&societyCode=NACE

134. The British Standard Institution. Petroleum and natural gas industries. Materials for use in H2S-containing environments in oil and gas production. Cracking-resistant carbon and low-alloy steels, and the use of cast irons. BS EN ISO 15156. 30/11/2009: BSOL; 2009.

135. Chambers B., Kane RD., Yunovich M. Corrosion and Selection of Alloys for CCS (Carbon Capture and Storage) Systems: Current Challenges. SPE International Conference on CO2 Capture, Storage, and Utilization. New Orleans, Louisiana, USA; 2010. pp. 1–11. Available at: http://www.onepetro.org/mslib/app/Preview.do?paperNumber=SPE-139521-MS&societyCode=SPE

136. Choi YS., Nešić S. Determining the corrosive potential of CO2 transport pipeline in high pCO2–water environments. International Journal of Greenhouse Gas Control. 2011; In Press,. Available at: DOI:DOI: 10.1016/j.ijggc.2010.11.008

137. Choi YS., Nešić S. Effect of Impurities on the Corrosion Behavior of Carbon Steel in Supercritical CO2 ? Water

Environments. NACE. 2010; (10196): 1–15.

138. Fosbøl PL., Thomsen K., Stenby EH. Improving Mechanistic CO2 Corrosion Models. Corrosion. NACE International; 2009; (09561): 1–23.

139. López-Rendón R., Alejandre J. Molecular Dynamics Simulations of the Solubility of H 2 S and CO 2 in Water. Journal of the Mexican Chemical Society. 2008; 52(1): 88–92.

140. Vitse F., Nešić S., Gunaltun Y., de Torreben DL., Duchet-Suchaux P. Mechanistic Model for the Prediction of Top-of-the-Line Corrosion Risk. Corrosion. NACE International; 1 December 2003; 59(12): 1075–1084. Available at: DOI:10.5006/1.3277527

141. Kittel J., Smanio V., Fregonese M., Garnier L., Lefebvre X. Hydrogen induced cracking (HIC) testing of low alloy steel in sour environment: Impact of time of exposure on the extent of damage. Corrosion Science. 2010; 52(4): 1386–1392. Available at: DOI:DOI: 10.1016/j.corsci.2009.11.044

142. Kittel J., Martin JW., Cassagne T., Bosch C. Hydrogen induced cracking (HIC) - Laboratory testing assessment of low alloy steel linepipe. Corrosion. New Orleans LA: NACE International; 2008. pp. 1–8. Available at: http://www.onepetro.org/mslib/app/Preview.do?paperNumber=NACE-08110&societyCode=NACE

143. Eldevik F., Graver B., Torbergsen LE., Saugerud OT. Development of a Guideline for Safe, Reliable and Cost Efficient Transmission of CO2 in Pipelines. Greenhouse Gas Control Technologies 9 Proceedings of the 9th International Conference on Greenhouse Gas Control Technologies (GHGT-9), 16–20 November 2008, Washington DC, USA. 2009; 1(1): 1579–1585. Available at: DOI:10.1016/j.egypro.2009.01.207

144. Choi YS., Nešić S. Effect of Water Content on the Corrosion Behavior of Carbon Steel in Supercritical CO2 Phase with Impurities. NACE. 2011; (11377): 1–15.

145. Dugstad A. Mechanism of Protective Film Formation During CO2 Corrosion of Carbon Steel. NACE Corrosion. San Diego, California, USA: NACE International; 1998. pp. 1–6.

146. Choi YS., Nešić S. Effect of impurities on the corrosion

behavior of carbon steel in supercritical CO2 - Water environments. Corrosion. San Antonio, TX: NACE International; January 2010; Available at: http://www.onepetro.org/mslib/app/Preview.do?paperNumber=NACE-10196&societyCode=NACE

147. Wu Y., Dai J., Zhang J., Liu W., Fan X., Lu M. Comparison of Corrosion Behavior of X65 Pipeline Steel In CO2-H2S And CO2 Environment At Different Flow Velocities. NACE Corrosion. Salt Lake City, Utah: NACE International; 2012. pp. 1–12.

148. Mansor NII., Abdullah S., Ariffin AK., Syarif J. A review of the fatigue failure mechanism of metallic materials under a corroded environment. Engineering Failure Analysis. July 2014; 42: 353–365. Available at: DOI:http://dx.doi.org/10.1016/j.engfailanal.2014.04.016

149. Papavinasam S., Doiron A., Jian L., Park D., Pei L. Sour and sweet corrosion of carbon steel: general or pitting or localized or all of the above? NACE. 2010; (10332): 1–23.

150. Parkins RN. A review of stress corrosion cracking of high pressure gas pipelines. Corrosion. 2000; (00363): 1–23.

151. Elboujdaini M., Wang YZ., Revie RW., Parkins RN., Shehata MT. Stress Corrosion Crack Initiation Processes: Pitting and Microcrack Coalescence. CORROSION. Orlando, Fl: NACE International; 2000. pp. 1–31. Available at: http://www.onepetro.org/mslib/app/Preview.do?paperNumber=NACE-00379&societyCode=NACE

152. Kim WK., Kim KY., Yun TW., Yang BY. The effect of metallurgical factors on SSC of high strength pipeline steel. NACE CorrosionCorrosion. New Orleans LA: NACE International; 2008. pp. 1–9. Available at: http://www.onepetro.org/mslib/app/Preview.do?paperNumber=NACE-08496&societyCode=NACE

153. Maier HJ., Popp W., Kaesche H. A method to evaluate the critical hydrogen concentration for hydrogen-induced crack propagation. Acta Metallurgica. 1987; 35(4): 875–880. Available at: DOI:DOI: 10.1016/0001-6160(87)90164-7

154. Lunarska E., Ososkov Y., Jagodzinsky Y. Correlation between critical hydrogen concentration and hydrogen damage of

pipeline steel. Proceedings of the Selected Papers of the First International Conference on Hydrogen Treatment of Materials. 1997; 22(2-3): 279–284. Available at: DOI:DOI: 10.1016/S0360-3199(96)00178-4

155. Cramer SD., Covino, B. S. J. ASM Handbook, Volume 13C - Corrosion: Environments and Industries. First. ASM International. Materials Park, Ohio, USA: ASM International; 2006. Available at: http://app.knovel.com/web/toc.v/cid:kpASMHVCC1/viewerType:toc/root_slug:asm-handbook-volume-13c/url_slug:asm-handbook-volume-13c

156. Winston R. Uhlig's Corrosion Handbook. Third. Uhlig's Corrosion Handbook. John Wiley & Sons, Inc.; 2011. 1-1253 p. Available at: DOI:10.1002/9780470872864.ch87

157. Cayard MS., Kane RD., Cooke DL. An Exploratory Examination Of The Effect Of SOHIC Damage On The Fracture Resistance Of Carbon Steels. Corrosion. NACE International; 1997; (525): 1–16.

158. Koh SU., Kim JS., Yang BY., Kim KY. Effect of Line Pipe Steel Microstructure on Susceptibility to Sulfide Stress Cracking. Corrosion Science. 2004; (March): 244–253.

159. Kobayashi K., Dent P., Fowler CM. Effects of Stress Conditions and Microstructure on SOHIC Susceptibility. Corrosion. 2014; (3883): 1–15.

160. Hardie D., Charles EA., Lopez AH. Hydrogen embrittlement of high strength pipeline steels. Corrosion Science. 2006; 48(12): 4378–4385. Available at: DOI:DOI: 10.1016/j.corsci.2006.02.011

161. Brown B., Nešić S., Parakala S. CO2 Corrosion in the Presence of Trace Amounts of H2S. Corrosion. New Orleans, La: NACE International; 2004. pp. 1–9. Available at: http://www.onepetro.org/mslib/app/Preview.do?paperNumber=NACE-04736&societyCode=NACE

162. Pundt A., Kirchheim R. Hydrogen in metals: Microstructural aspects. Annual Review of Materials Research. Inst Mat Phys, D-37077 Gottingen, Germany.; Pundt, A, Inst Mat Phys, D-37077 Gottingen, Germany.; apundt@ump.gwdg.de rkirch@ump.gwdg.de: ANNUAL REVIEWS; 2006; 36: 555–

608. Available at: DOI:10.1146/annurev.matsci.36.090804.094451

163. Schröder J., Schwinn V., Liessem A. Recent developments of sour service line pipe steels Data on Production Pipe. In: TMS (ed.) International Symposium Microalloyed Steels for the Oil and Gas Industry, to be published by TMS. 2006.

164. NACE MR0175/ ISO 15156-1. Petroleum and natural gas industries. Materials for use in H 2S-containing Environments in oil and gas production. 2001.

165. Bai Y., Knauf G., Hillenbrand HG. Materials and design of high strength pipelines. The Tenth International Offshore and Polar Engineering Conference. Seattle, USA: The International Society of Offshore and Polar Engineers; 2000. pp. 1–9. Available at: http://www.onepetro.org/mslib/app/Preview.do?paperNumber=ISOPE-I-00-147&societyCode=ISOPE

166. Martin RL. Corrosion Consequences of Oxygen Entry Into Sweet Oilfield Fluids. SPE Permian Basin Oil and Gas Recovery Conference. Midland, Texas: Society of Petroleum Engineers; 2001. Available at: DOI:10.2118/70029-MS

167. Karami M. Review of Corrosion role in gas pipeline and some methods for preventing it. Journal of Pressure Vessel Technology. ASME; 6 September 2012; 134(5): 54501. Available at: http://dx.doi.org/10.1115/1.4006124

168. Choi YS., Nešić S. Dermining the corrosive potential of CO2 transport pipeline in high pCO2 – water environments. International Journal of Greenhouse Gas Control. 2011; 5: 788–797. Available at: DOI:10.1016/j.ijggc.2010.11.008

169. Mahgerefteh H., Brown S., Denton G. Modelling the impact of stream impurities on ductile fractures in CO2 pipelines. Chemical Engineering Science. 28 May 2012; 74(0): 200–210. Available at: DOI:http://dx.doi.org/10.1016/j.ces.2012.02.037

170. Zargarzadeh P. Structural integrity of CO2 transportation infrastructures. PhD thesis. Cranfield University; 2013.

171. Orowan E. Fracture and strength of solids. Rep. Prog. Phys. 1949; 12: 185–232.

172. Irwin GR. Analysis of stresses and strains near the end of a

crack traversing a plate. J. Appl. Mech. 1957; 24: 361–364. Available at: citeulike-article-id:810675

173. Westergaard HM. Bearing pressures and cracks. Journal of Applied Mechanics. 1939; 49(A): 49–53.

174. Rocha-Rangel E. Fracture toughness determinations by means of indentation fracture. Nanocomposites with Unique Properties and Applications in Medicine and Industry. 2011. pp. 21–38.

175. Dugdale DS. Yielding of steel sheets containing slits. Journal of the Mechanics and Physics of Solids. May 1960; 8(2): 100–104. Available at: DOI:http://dx.doi.org/10.1016/0022-5096(60)90013-2

176. Srawley JE. Linear elastic fracture mechanics: A review of principles and methods. In: Dobson MO (ed.) Symposium on fracture toughness concepts for weldable structural steels. Risley, UK: United Kingdom Atomic Energy Autorithy; 1969. pp. A1–A13.

177. ASTM E 1921:2010. Standard test method for determination of reference temperature , To , for ferritic steels in the transition range. 2010. Available at: DOI:10.1520/E1921-10

178. BS EN ISO 12737:2010. Metallic materials — Determination of plane- strain fracture toughness. 2010.

179. BS EN ISO 14556:2000. Steel — Charpy V-notch pendulum impact test — Instrumented test method. 2006.

180. ASTM E 23:2007. Standard test methods for notched bar impact testing of metallic materials. 2008.

181. Oldfield W. Fitting Curves to toughness data. Journal of testing and evaluation. 1979; 7(6): 326–333.

182. Marston TU. Flaw Evaluation Procedures: Background and Application of ASME Section XI Appendix A, EPRI NP-7 19-SR. Palo Alto, Calif.; 1978.

183. Wallin K., Saario T., Törrönen K. Statistical model for carbide induced brittle fracture in steel. Metal Science. Maney; 1 January 1984; 18(1): 13–16. Available at: DOI:10.1179/030634584790420384

184. Schindler HJ., Kalkhof D., Viehrig HW. Variability and Lower Bound of Fracture Toughness of Welds in the Ductile to Brittle

Transition Regime. Procedia Materials Science. 2014; 3(0): 732–737. Available at: DOI:http://dx.doi.org/10.1016/j.mspro.2014.06.120

185. Chaouadia R., Puzzolante JL. Procedure to Estimate the Crack Resistance Curve from the Instrumented Charpy V–Notched Impact Test. ICF12, Ottawa 2009. 2012. pp. 1–10.
186. Server, W. L. and Tetelman AS. The use of precracked Charpy specimens to determine fracture toughness. Engineering Fracture Mechanics. 1972; 4: 367–375.
187. Wallin K. Guidelines for deriving fracture toughness estimates from normal and miniature size Charpy-V specimen data. Rakenteiden Mekaniikka. 1992; 25(3): 24–40.
188. Marson JM., Rolfe ST. Fracture and Fatigue Control in Structures Applications of Fracture Mechanics. Philadelphia: ASTM; 1938.
189. Marandet B., Sanz G. Evaluation of the toughness of thick medium strenght steels by LEFM and correlations between KIc and CVN. ASTM STP631 Flaw Growth and Fracture. 1977. pp. 72–95.
190. Pisarski HG., Wallin K. The SINTAP fracture toughness estimation procedure. Engineering Fracture Mechanics. January 2000; 67(6): 613–624. Available at: DOI:http://dx.doi.org/10.1016/S0013-7944(00)00076-X
191. Pineau a. Development of the Local Approach to Fracture over the Past 25 years: Theory and Applications. International Journal of Fracture. 2006; 138(1-4): 139–166. Available at: DOI:10.1007/s10704-006-0035-1
192. Kroon M. Micromechanics of cleavage fracture initiation in ferritic steels by carbide cracking. Journal of the Mechanics and Physics of Solids. 2005; 53(1): 171–196. Available at: DOI:10.1016/j.jmps.2004.05.008
193. Mcmahon CJ., Cohen M. Initiation of cleavage in polycrytalline iron. Acta Metallurgica. 1965; 13: 591–604.
194. Landes JD., Shaffer DH. Statistical characterization of f racture in the transition re.gion. Fracture Mechanics, 12th Conference, ASTM STP 700. 1980. pp. 368–382.

195. Smith E. Cleavage fracture in mild steel. International Journal of Fracture Mechanics. Kluwer Academic Publishers; 1968; 4(2): 131–145. Available at: DOI:10.1007/BF00188940

196. Knott JF. Micro-mechanisms of fracture and the fracture toughness of engineering alloys. In: Taplin DMR (ed.) Advances in Research on the Strength and Fracture of Materials. Pergamon; 1978. pp. 61–92. Available at: DOI:http://dx.doi.org/10.1016/B978-0-08-022136-6.50016-0

197. Ritchie RO., Knott JF., Rice JR. On the relationship between critical tensile stress and fracture toughness in mild steel. Journal of the Mechanics and Physics of Solids. November 1973; 21(6): 395–410. Available at: DOI:http://dx.doi.org/10.1016/0022-5096(73)90008-2

198. Curry DA., Knott JF. Effects of Microstructure on cleavage fracture stress in steel. Metal Science. 1978; 12: 511–514.

199. Curry DA., Knott JF. Effect of microstructure on cleavage fracture toughness of quenched and tempered steels. Metal Science. 1979; 13: 341–345.

200. Wallin K. The scatter in KIc results. Engineering Fracture Mechanics. 1984; 19: 1085–1093.

201. Wallin K. Irradiation damage effects on the fracture toughness transition curve shape for reactor pressure vessel steels. International Journal of Pressure Vessels and Piping. 1993; 55(1): 61–79. Available at: DOI:http://dx.doi.org/10.1016/0308-0161(93)90047-W

202. Wallin K. A simple theoretical Charpy-V – KIC correlation for irradiation embrittlement. ASME Pressure Vessels and Piping Conference, Innovative Approaches to Irradiation Damage and Fracture Analysis-PVP-Vol 170. 1989. pp. 1–6.

203. Sokolov M., Nanstad RK. Comparison of irradiation-induced shifts of KJC and Charpy impact toughness for reactor pressure vessel steels. Small Specimen Test Techniques, ASTM STP 1329. 1998. pp. 238–252.

204. Heerens J., Pfuff M., Hellmann D., Zerbst U. The lower bound toughness procedure applied to the Euro fracture toughness dataset. Engineering Fracture Mechanics. March 2002; 69(4): 483–495. Available at: DOI:10.1016/S0013-7944(01)00069-8

205. Pallaspuro S., Limnell T., Suikkanen P., Porter D. C. Procedia Materials Science. 2014; 3(0): 1032–1037. Available at: DOI:http://dx.doi.org/10.1016/j.mspro.2014.06.168

206. Knott JF. The Science and Engineering of Fracture. In: V.V. Panasyuk A2M.C. Pandey A2O.Ye. Andreykiv A2J.F. Knott A2P. Rama Rao A2R. O. Ritchie and D.M.R. TaplinA2 V.V. Panasyuk O.Ye. Andreykiv, J.F. Knott, P. Rama Rao,R.O.Ritchie MCP, Taplin DMR (eds.) Advances in fracture resistance and structural integrity. Oxford: Pergamon; 1994. pp. 13–49. Available at: DOI:http://dx.doi.org/10.1016/B978-0-08-042256-5.50011-1

207. Balart MJ., Knott JF. Effects of geometry and flow properties on the fracture toughness of a C–Mn reactor pressure vessel steel in the lower shelf region. International Journal of Pressure Vessels and Piping. 2006; 83(3): 205–215. Available at: DOI:http://dx.doi.org/10.1016/j.ijpvp.2005.12.001

208. Cicero S., Ainsworth RA., Gutiérrez-Solana F. Engineering approaches for the assessment of low constraint fracture conditions: A critical review. Engineering Fracture Mechanics. May 2010; 77(8): 1360–1374. Available at: DOI:http://dx.doi.org/10.1016/j.engfracmech.2010.02.026

209. Zhu XK., Joyce JA. Review of fracture toughness (G, K, J, CTOD, CTOA) testing and standardization. Engineering Fracture Mechanics. 2012; 85: 1–46. Available at: DOI:10.1016/j.engfracmech.2012.02.001

210. Putatunda SK. A comparison of various fracture toughness testing methods. Engineering Fracture Mechanics. 1986; 25(4): 429–439. Available at: DOI:10.1016/0013-7944(86)90257-2

211. Holmes B., Priest AH., Walker EF. Prediction of linepipe fracture behaviour from laboratory tests. International Journal of Pressure Vessels and Piping. 1983; 12(1): 1–27. Available at: DOI:DOI: 10.1016/0308-0161(83)90005-4

212. Kameda J. A kinetic model for ductile-brittle fracture mode transition behavior. Acta Metallurgica. December 1986; 34(12): 2391–2398. Available at: DOI:10.1016/0001-6160(86)90142-2

213. Wallin. K. The size effect in Klc results wallin. Engineering Fracture Mechanics. 1985; 22: 149–163.

214. Maxey WA. Fracture initiation, propagation and arrest. 5th Symposium on Line Pipe Research. 2005. pp. 1–6.

215. Andrews RM., Batte AD. Developments in fracture control technology for gas pipelines utilising high strength steels. The Korean Gas Union. 2011. pp. 1–11. Available at: http://www.kgu.or.kr/download.php?tb=bbs_017&fn=10127_1045835094_14215_1.pdf&rn=10127_1045835094_14215_1.pdf. (Accessed: 18 January 2012)

216. Demofonti G., Mannucci G., Hillenbrand HG., Harris D. Suitability evaluation of X100 steel pipes for high pressure gas transportation pipelines by full scale tests. In: International Petroleum Technology Institute (ed.) 2004 International Pipeline Conference. Calgary, Alberta, Canada: ASME; 2004. pp. 1685–1692.

217. Liu Y., Feng Y., Ma Q., Song X. Dynamic fracture toughness of X70 pipeline steel and its relationship with arrest toughness and CVN. Materials & Design. 2002; 23(8): 693–699. Available at: DOI:10.1016/S0261-3069(02)00077-8

218. Shin SY., Hong S., Bae JH., Kim K., Lee S. Separation phenomenon occurring during the Charpy Impact test of API X80 pipeline steels. Metallurgical and Materials Transactions A. Springer US; 2009; 40(10): 2333–2349. Available at: DOI:10.1007/s11661-009-9943-9

219. Sung HK., Sohn SS., Shin SY., Lee S., Kim NJ., Chon SH., et al. Effects of finish rolling temperature on inverse fracture occurring during drop weight tear test of API X80 pipeline steels. Materials Science and Engineering: A. 2012; 541: 181–189. Available at: DOI:http://dx.doi.org/10.1016/j.msea.2012.02.019

220. Shin SY., Hwang B., Kim S., Lee S. Fracture toughness analysis in transition temperature region of API X70 pipeline steels. Materials Science and Engineering: A. 2006; 429(1-2): 196–204. Available at: DOI:DOI: 10.1016/j.msea.2006.05.086

221. Hong S., Shin SY., Lee S., Kim NJ. Effects of specimen thickness and notch shape on fracture modes in the Drop Weight Tear Test of API X70 and X80 linepipe steels. Metallurgical and Materials Transactions A. 23 April 2011; 42(9): 2619–2632. Available at: DOI:10.1007/s11661-011-

0697-9 (Accessed: 8 August 2014)

222. Haskel H., Pauletti E., Martins JP., Carvalho ALM. Evaluation of delamination mechanisms from Charpy impact test in API-X70 steel. In: http://www.icf13.org/ (ed.) 13th International Conference on Fracture. Beijing, China: http://www.gruppofrattura.it; 2013. pp. 1–10.

223. Ishihara T., Kondo J., Kitada T., Akiyama T. Drop weight tear test of linepipe materials by using laterally compressed specimens. Transactions ISIJ, Vol. 27, 1987 (219). 1987; 27(219): 218–221.

224. Yang Z. The fracture during Drop-Weight Tear Test of high performance pipeline steel and its abnormal fracture appearance. Procedia Materials Science. 2014; 3: 1591–1598. Available at: DOI:10.1016/j.mspro.2014.06.257 (Accessed: 31 July 2014)

225. Ju JB., Lee JS., Jang JI. Fracture toughness anisotropy in a API steel line-pipe. Materials Letters. 2007; 61(29): 5178–5180. Available at: DOI:DOI: 10.1016/j.matlet.2007.04.007

226. Oh CK., Kim YJ., Baek JH., Kim YP., Kim WS. Ductile failure analysis of API X65 pipes with notch-type defects using a local fracture criterion. International Journal of Pressure Vessels and Piping. 2007; 84(8): 512–525. Available at: DOI:DOI: 10.1016/j.ijpvp.2007.03.002

227. Rod P., Marandet B., Phelippeau G., Rousselier G. Effect of specimen dimensions on critical J-value at the onset of crack Extension. Fracture mechanics: Fifteeen symposium, ASTM STP 833. 1984. pp. 606–621.

228. Robinson JN., Tetelman AS. Comparison of various methods of measuring KIc on small precracked bend specimens that fracture after general yield. Engineering Fracture Mechanics. 1976; 8(2): 301–313.

229. Withers PJ. Residual stress and its role in failure. Reports on Progress in Physics. 1 December 2007; 70(12): 2211–2264. Available at: DOI:10.1088/0034-4885/70/12/R04 (Accessed: 18 July 2014)

230. Withers PJ., Bhadeshia H. Residual stress. Part 1–measurement techniques. Materials Science and Technology.

2001; 17(April): 355–365. Available at: http://www.maneyonline.com/doi/abs/10.1179/026708301101509980 (Accessed: 15 February 2014)

231. Withers PJ., Bhadeshia HKDH. Residual stress. Part 2 – Nature and origins. Materials Science and Technology. April 2001; 17(4): 366–375. Available at: DOI:10.1179/026708301101510087

232. Bouchard PJ., Withers PJ. The appropriateness of residual stress length scales in structural integrity. Journal of Neutron Research. 1 January 2004; 12(1): 81–91. Available at: DOI:10.1080/10238160410001734504

233. Ruud CO. A review of selected non-destructive methods for residual stress measurement. NDT International. 1982; 15(1): 15–23. Available at: DOI:10.1016/0308-9126(82)90083-9

234. Withers PJ. Mapping residual and internal stress in materials by neutron diffraction. Comptes Rendus Physique. September 2007; 8(7-8): 806–820. Available at: DOI:10.1016/j.crhy.2007.09.015 (Accessed: 21 January 2014)

235. Holden TM. Macroscopic residual stress measurements by neutron diffraction. 2010. pp. 1–33.

236. Rossini NS., Dassisti M., Benyounis KY., Olabi a. G. Methods of measuring residual stresses in components. Materials & Design. Elsevier Ltd; March 2012; 35(August): 572–588. Available at: DOI:10.1016/j.matdes.2011.08.022 (Accessed: 21 January 2014)

237. Webster GA., Wimpory RC. Non-destructive measurement of residual stress by neutron diffraction. Journal of Materials Processing Technology. November 2001; 117(3): 395–399. Available at: DOI:10.1016/S0924-0136(01)00802-0

238. Withers PJ., Turski M., Edwards L., Bouchard PJ., Buttle DJ. Recent advances in residual stress measurement. International Journal of Pressure Vessels and Piping. March 2008; 85(3): 118–127. Available at: DOI:10.1016/j.ijpvp.2007.10.007 (Accessed: 28 January 2014)

239. Fitzpatrick, M.E., Fry, A. T., Holdway, P, Kandil, F. A., Shackleton, J., adn Suominen L. Determination of Residual Stresses by X-ray Diffraction - Issue 2. A National

Measurement Good Practice Guide. 2005.

240. Mathar J. Determination of initial stresses by measuring the deformation around drilled holes. Trans ASME. 1934; 56(4): 249–254.

241. Grant P V., Lord JD., Whitehead PS. Measurement Good Practice Guide No . 53 - Issue 2. The Measurement of Residual Stresses by the Incremental Hole Drilling Technique. Teddington, Middlesex. UK; 2006.

242. Soete W., Vancrombrugge R. An industrial method for the determination of residual stresses. Proc. Society for Experimental Stress Analysis (SESA)Society for Experimental Stress Analysis (SESA). 1950; 8(1): 17–28.

243. Kelsey RA. Measuring Nonuniform Residual Stresses by the Hole Drilling Method. Proc. Society for Experimental Stress Analysis (SESA). 1956; 14(1): 181–184.

244. Sobolevski EG. Residual Stress Analysis of Components with Real Geometries Using the Incremental Hole-Drilling and a Differential Evaluation Method. Kassel University; 2007.

245. Rendler NJ., Vigness I. Hole-drilling strain-gage method of measuring residual stresses. Experimental Mechanics. 1966; 6(12): 577–586. Available at: http://link.springer.com/article/10.1007/BF02326825 (Accessed: 8 December 2014)

246. Flaman MT. Brief investigation of induced drilling stresses in the center-hole method of residual-stress measurement. Experimental Mechanics. Kluwer Academic Publishers; 1982; 22(1): 26–30. Available at: DOI:10.1007/BF02325700

247. Yavelak JJ. Bulk-Zero Stress Standard-AISI 1018 Carbon-Steel Specimens. Experimental Techniques. Blackwell Publishing Ltd; 1 April 1985; 9(4): 38–41. Available at: DOI:10.1111/j.1747-1567.1985.tb02014.x

248. Bijak-Zochowski M. A semidestrucitve method of measuring residual Stress. VDI-Berichte. 1978; (313): 469–476.

249. Schajer GS. Measurement of Non-Uniform Residual Stresses Using the Hole-Drilling Method. Part I—Stress Calculation Procedures. Journal of Engineering Materials and Technology. 1 October 1988; 110(4): 338–343. Available at:

DOI:10.1115/1.3226059

250. Schajer GS. Measurement of Non-Uniform Residual Stresses Using the Hole-Drilling Method. Part II—Practical application of The Integral Method. Journal of Engineering Materials and Technology. 1988; 110(4): 344–349.

251. ASTM E 837:2008. Standard Test Method for Determining Residual Stresses by the Hole-Drilling Strain-Gages. 2008. Available at: DOI:10.1520/E0837-08E01.practice

252. Whitehead PS. Practical experiences in hole drilling measurements of residual stress. In: Society of Experimental Mechanics (ed.) Proceedings of the SEM annual conference. Indianapolis, Indiana USA; 2010. pp. 209–219. Available at: DOI:10.1007/978-1-4419-9792-0 (Accessed: 3 February 2014)

253. Vishay Precision Group. TN-503-6. Measurement of Residual Stresses by the Hole-Drilling Strain Gage Method. 2005.

254. Ajovalasit A., Scafidi M., Zuccarello B., Beghini M., Bertini L. AIAS TR-01:2010. The hole-drilling strain gauge method for the measurement of uniform or non-uniform residual stresses. 2010.

255. Ajovalasit A. Measurement of residual stresses by the hole-drilling method: Influence of hole eccentricity. The Journal of Strain Analysis for Engineering Design. 1 October 1979; 14(4): 171–178. Available at: DOI:10.1243/03093247V144171 (Accessed: 15 February 2014)

256. Nau A., Scholtes B. Evaluation of the High-Speed Drilling Technique for the Incremental Hole-Drilling Method. Experimental Mechanics. Springer US; 2013; 53(4): 531–542. Available at: DOI:10.1007/s11340-012-9641-1

257. Nobre JP., Kornmeier M., Dias AM., Scholtes B. Use of the hole-drilling method for measuring residual stresses in highly stressed shot-peened surfaces. Experimental Mechanics. Kluwer Academic Publishers; 2000; 40(3): 289–297. Available at: DOI:10.1007/BF02327502

258. Beghini M., Bertini L., Santus C. A procedure for evaluating high residual stresses using the blind hole drilling method, including the effect of plasticity. The Journal of Strain Analysis for Engineering Design. 1 July 2010; 45(4): 301–318. Available

at: DOI:10.1243/03093247JSA579 (Accessed: 15 February 2014)

259. Niku-Lari A., Lu J., Flavenot JFF. Measurement of residual-stress distribution by the incremental hole-drilling method. Journal of Mechanical Working Technology. Kluwer Academic Publishers; May 1985; 11(2): 167–188. Available at: DOI:10.1016/0378-3804(85)90023-3

260. Flaman MT., Manning BH. Determination of residual-stress variation with depth by the hole-drilling method. Experimental Mechanics. Kluwer Academic Publishers; 1985; 25(3): 205–207. Available at: DOI:10.1007/BF02325088

261. Schajer GS. Application of Finite Element Calculations to Residual Stress Measurements. Journal of Engineering Materials and Technology. American Society of Mechanical Engineers; 1 April 1981; 103(2): 157. Available at: DOI:10.1115/1.3224988 (Accessed: 15 February 2014)

262. Nickola WE. Practical subsurface residual stress evaluation by the Hole Drilling Method. Proceedings of the SEM Spring Conference on Experimental Mechanics. New Orleans, Louisiana, USA; 1986. pp. 47–58.

263. Zuccarello B. Optimal Calculation Steps for the Evaluation of Residual Stress by the Incremental Hole-drilling Method. Experimental Mechanics. 1998; 39(2): 117–124.

264. Barsanescu P., Carlescu P. Correction of errors introduced by hole eccentricity in residual stress measurement by the hole-drilling strain-gage method. Measurement. April 2009; 42(3): 474–477. Available at: DOI:10.1016/j.measurement.2008.09.002 (Accessed: 15 April 2014)

265. Kabiri M. Measurement of residual stresses by the hole-drilling method: Influences of trasnverse sensitivity of the gages and relived-strain coefficients. Experimental Mechanics. 1984; 24(3): 252–256.

266. Kim C., Yang WH., Heo SP. Influence of inclined holes in measurement of residual stress by the hole drilling method. KSME International Journal. Korean Society of Mechanical Engineers; 2001; 15(12): 1647–1654. Available at: DOI:10.1007/BF03185119

267. Oettel R. The Determination of Uncertainties in Residual Stress Measurement (Using the hole drilling technique). 2000.

268. Sicot O., Gong XL., Cherouat A., Lu J. Influence of experimental parameters on determination of residual stress using the incremental hole-drilling method. Composites Science and Technology. February 2004; 64(2): 171–180. Available at: DOI:10.1016/S0266-3538(03)00278-1 (Accessed: 15 February 2014)

269. Beghini M., Santus C., Valentini E., Benincasa A. Experimental verification of the hole drilling plasticity effect correction. Materials Science Forum. 2011; 681: 151–158.

270. Nau A., Mirbach D., Scholtes B. Improved Calibration Coefficients for the Hole-Drilling Method Considering the Influence of the Poisson Ratio. Experimental Mechanics. Springer US; 2013; 53(8): 1371–1381. Available at: DOI:10.1007/s11340-013-9740-7

271. Scafidi M., Valentini E., Zuccarello B. Error and Uncertainty Analysis of the Residual Stresses Computed by Using the Hole Drilling Method. Strain. 28 August 2011; 47(4): 301–312. Available at: DOI:10.1111/j.1475-1305.2009.00688.x (Accessed: 15 February 2014)

272. Schajer GS., Altus E. Stress Calculation Error Analysis for Incremental Hole-Drilling Residual Stress Measurements. Journal of Engineering Materials and Technology. 1 January 1996; 118(1): 120–126. Available at: http://dx.doi.org/10.1115/1.2805924

273. Schajer GS. Hole-Drilling Residual Stress Measurements at 75 : Origins , Advances , Opportunities. In: Society for Experimental Mechanics (ed.) SEM Annual Conference. 2009. pp. 1–4.

274. Hill MR. The Slitting Method. Practical Residual Stress Measurement Methods. John Wiley & Sons, Ltd; 2013. pp. 89–108. Available at: DOI:10.1002/9781118402832.ch4

275. Bendek E., Lira I., François M., Vial C. Uncertainty of residual stresses measurement by layer removal. International Journal of Mechanical Sciences. December 2006; 48: 1429–1438. Available at: DOI:10.1016/j.ijmecsci.2006.07.002 (Accessed: 15 February 2014)

276. Feja K., Hauk V., Krug WK. Residual Stress Evaluation of a Cold-rolled Steel Strip Using X-rays and a Layer Removal Technique *. Material Science and Enginerring. 1987; 92: 13–21.

277. Schajer GS., Prime MB. Use of Inverse Solutions for Residual Stress Measurements. Journal of Engineering Materials and Technology. 2006; (3): 37–382.

278. Milne I., Ainsworth RA., Dowling AR., Stewart AT. R6: Assessment of the integrity of structures containing defects. Revision 4. Bristol UK; 2009.

279. Valenta F., Sochor M., Španiel M., Michalec J. Remaining load carrying capacity of gas pipelines damaged by surface corrosion. International Journal of Pressure Vessels and Piping. January 1994; 59(1-3): 217–226. Available at: DOI:10.1016/0308-0161(94)90156-2

280. ASME B31G:2012. Manual for determining the remaining strength of corroded pipelines. 2012.

281. Det Norske Veritas-DNV. DNV RP-F101:2010. Corroded pipelines. Høvik, Norway; 2010.

282. API 579. Fitness-For-Service. 2007.

283. Sharples, J K. Ainsworth, R A., Budden, P J., and Dowling AR. Developments in UK defect assessment procedure R6 revision 4 and BS 7910. Proceeding of the 3rd international conference SDSMS’03. Klaipeda; 2003. pp. 280–296.

284. Zerbst U., Hamann R., Wohlschlegel A. Application of the European flaw assessment procedure SINTAP to pipes. International Journal of Pressure Vessels and Piping. January 2000; 77(11): 697–702. Available at: DOI:10.1016/S0308-0161(00)00059-4

285. Cosham A., Hopkins P., Macdonald KA. Best practice for the assessment of defects in pipelines – Corrosion. Engineering Failure Analysis. 2007; 14(7): 1245–1265. Available at: DOI:DOI: 10.1016/j.engfailanal.2006.11.035

286. U. Zerbst, M. Schödel, S. Webster RAA. Fitness for service fracture assessment of structures containing cracks. International Journal of Fatigue. 2010; 32(8): 1397–1398. Available at: DOI:10.1016/j.ijfatigue.2010.02.009

287. SINTAP. Assessment of the integrity of structures containing flaws. 1999.

288. Milne I., Ainsworth RA., Dowling AR., Stewart AT. Background to and validation of CEGB Report R/H/R6- Revision 3. International Journal of Pressure Vessels and Piping. 1988; 32: 105–196.

289. Ainsworth RA., Hooton DG. R6 and R5 procedures: The way forward. International Journal of Pressure Vessels and Piping. March 2008; 85(3): 175–182. Available at: DOI:10.1016/j.ijpvp.2007.10.003 (Accessed: 3 December 2014)

290. Ainsworth RA., Sharples JK., Smith SD. Effects of residual stresses on fracture behaviour—experimental results and assessment methods. The Journal of Strain Analysis for Engineering Design. 1 January 2000; 35(4): 307–316. Available at: DOI:10.1243/0309324001514431

291. Budden PJ., Sharples JK., Dowling AR. The R6 procedure : recent developments and comparison with alternative approaches. nternational Journal of Pressure Vessels and Piping. 2001; 77: 895–903.

292. Zerbst U., Schwalbe KH., Ainsworth RA. An Overview of failure assessment methods in codes and standards. In: Milne I, Ritchie RO, Karihaloo B (eds.) Comprehensive Structural Integrity. Oxford: Pergamon; 2003. pp. 1–48. Available at: DOI:DOI: 10.1016/B0-08-043749-4/07053-1

293. Domizzi G., Anteri G., Ovejero-García J. Influence of sulphur content and inclusion distribution on the hydrogen induced blister cracking in pressure vessel and pipeline steels. Corrosion Science. 2001; 43: 325–339.

294. Capelle J., Gilgert J., Dmytrakh I., Pluvinage G. The effect of hydrogen concentration on fracture of pipeline steels in presence of a notch. Engineering Fracture Mechanics. Elsevier Ltd; 2011; 78(2): 364–373. Available at: DOI:10.1016/j.engfracmech.2010.10.007

295. ASTM E8/E8M: 2009. Standard Test Methods for Tension Testing of Metallic Materials 1. 2010. Available at: DOI:10.1520/E0008

296. BS EN ISO 6892-1:2009. Metallic materials — Tensile testing- Part 1: Method of test at ambient temperature. 2009.

297. BS EN 10002-1:2001. Metallic materials — Tensile testing — Part 1: Method of test at ambient temperature. 2001.

298. ASTM A751 -14. Standard Test Methods, Practices, and Terminology for Chemical Analysis of Steel Products. 2014.

299. ASTM E3:2011. Standard Guide for preparation of metallographic specimens. 2013. Available at: DOI:10.1520/E0003-11.2

300. ASTM G1:2003 (Reap 2001). Standard practice for preparing , cleaning , and evaluating corrosion test. 2012. Available at: DOI:10.1520/G0001-03R11.2

301. NACE TMO 169:2000. Standard Test Method Laboratory Corrosion Testing of Metals. 2000.

302. NACE TMO 177:1996. Standard test method laboratory testing of metals for resistance to sulfide stress cracking and stress corrosion cracking in H2S environments. 1997.

303. Encinas-Oropesa A. A study of hot corrosion of single crystal superalloys and platinum-aluminide coatings. Cranfield University; 2005.

304. ASTM E384:2011. Standard Test Method for Knoop and Vickers Hardness of Materials. 2011.

305. BS EN 10045-1:1990. Charpy impact test on metallic materials — Part 1: Test method (V and U nocthes). 1990.

306. ASTM E 647-2008. Standard Test Method for Measurement of Fatigue Crack Growth Rates. 2010. Available at: DOI:10.1520/E0647-08E01.2

307. ASTM E 399:2009. Standard test method for linear-elastic plane-strain fracture toughness KIc of metallic materials. 2010. Available at: DOI:10.1520/E0399-09E01.2

308. ASTM E 1820:2006. Standard test method for measurement of fracture toughnes. 2007.

309. BS 7448-1:1991. Fracture mechanics toughness tests. Method for determination of KIc, critical CTOD and critical J values of metallic materials. 1991.

310. Scibetta M., Lucon E., Van Walle E., Valo M. Towards a uniform precracking procedure for fracture toughness testing. International Journal of Fracture. Kluwer Academic Publishers; 2002; 117(3): 287–296. Available at: DOI:10.1023/A:1022072320277

311. ISO 14556:2000. Metallic materials. Charpy V-notch pendulum impact test- Instrumented test method. 2000.

312. Coules HE., Cozzolino LD., Colegrove P., Wen S. The Effect of Pre-Weld Rolling on Distortion and Residual Stress in Fusion Welded Steel Plate. Materials Science Forum. 2011; 681: 486–491.

313. Knight MJ., Brennan FP., Dover WD. Fatigue life improvement of threaded connections by cold rolling. The Journal of Strain Analysis for Engineering Design. 1 January 2005; 40(2): 83–93. Available at: http://sdj.sagepub.com/content/40/2/83.abstract

314. Vishay measurements group. TN-505-4 Strain Gage Selection : Criteria , Procedures , Recommendations. 2010.

315. Nevasmaa P., Wallin K. Structural integrity assessment procedures for European industry. SINTAP. Task 3 status: Review report : Reliability based methods. REPORT VAL A:: SINTAP VTT / 4. Espoo; 1997.

316. Marchenko VN., Zin'ko BF. Current trends in the development and production of steels and pipes for gas and oil pipelines: An international scientific-technical conference. Metallurgist. 22 August 2008; 52(3-4): 167–174. Available at: DOI:10.1007/s11015-008-9027-x

317. Corbett KT., Bowen RR., Petersen CW. High-strength steel pipeline economics. In: PolarEngineers TIS of O and (ed.) International Offshore and Polar Engineering Conference. Honolulu, Hawai; 2004. pp. 1–8. Available at: http://e-book.lib.sjtu.edu.cn/isope2003/pdffiles/volume4/4014p105.pdf (Accessed: 31 July 2014)

318. Duncan IJ., Wang H. Estimating the likelihood of pipeline failure in CO2 transmission pipelines: New insights on risks of carbon capture and storage. International Journal of Greenhouse Gas Control. February 2014; 21: 49–60. Available at: DOI:10.1016/j.ijggc.2013.11.005 (Accessed: 15 July 2014)

319. Yoo JY., Ahn SS., Seo DH., Song WH., Kang KB. New Development of High Grade X80 to X120 Pipeline Steels. Materials and Manufacturing Processes. Taylor & Francis; 11 February 2011; 26(1): 154–160. Available at: DOI:10.1080/10426910903202534

320. Luo H., Dong H. Development of X80-X120 high grade linepipe steels and their applications. China Metallurgy. 2006; 04: 1–9. Available at: http://en.cnki.com.cn/Article_en/CJFDTOTAL-ZGYE200604001.htm (Accessed: 31 July 2014)

321. Joo MS., Suh DW., Bae JH., Sanchez Mouriño N., Petrov R., Kestens LAI., et al. Experiments to separate the effect of texture on anisotropy of pipeline steel. Materials Science and Engineering: A. 30 October 2012; 556(0): 601–606. Available at: DOI:http://dx.doi.org/10.1016/j.msea.2012.07.033

322. Joo MS., Suh DW., Bae JH., Bhadeshia HKDH. Role of delamination and crystallography on anisotropy of Charpy toughness in API-X80 steel. Materials Science and Engineering A. 2012; 546: 314–322. Available at: DOI:10.1016/j.msea.2012.03.079

323. Jin TY., Liu ZY., Cheng YF. Effect of non-metallic inclusions on hydrogen-induced cracking of API5L X100 steel. The 10th Chinese Hydrogen Energy Conference. 2010; 35(15): 8014–8021. Available at: DOI:DOI: 10.1016/j.ijhydene.2010.05.089

324. Matrosov MY., Éfron LI., Il'inskii VI., Severinets IY., Lipunov YI., Éismondt KY. Use of accelerated cooling to improve the mechanical and processing properties of rolled plates used to make large-diameter gas-line pipe. Metallurgist. 2005; 49(5-6): 220–229.

325. Kneissl AC., Baldinger P. Structure and properties of TM processed HSLA steels. Le Journal de Physique IV. November 1993; 03(C7): C7–C77 – C7–C82. Available at: DOI:10.1051/jp4:1993708

326. Charleux M., Poole WJ., Militzer M., Deschamps A. Precipitation Behavior and Its Effect on Strengthening of an HSLA-Nb / Ti Steel. Metallurgical and Materials Transactions A. 2001; 32A: 1635–1647.

327. Schütz W., Kirsch HJ. Extended property combinations in thermomechanically control processed steel plates by

application of advanced rolling and cooling technology. Ironmaking & Steelmaking. 2001; 28(2): 180–184. Available at: http://www.maneyonline.com/doi/abs/10.1179/030192301677939 (Accessed: 31 July 2014)

328. Wang W., Yan W., Zhu L., Hu P., Shan Y., Yang K. Relation among rolling parameters, microstructures and mechanical properties in an acicular ferrite pipeline steel. Materials & Design. 2009; 30(9): 3436–3443. Available at: DOI:DOI: 10.1016/j.matdes.2009.03.026

329. Zong C., Zhu G., Mao W. Effect of Crystallographic Texture on Anisotropy of Yield Strength in X100 Pipeline Steel. Journal of Iron and Steel Research, International. August 2013; 20(8): 66–71. Available at: DOI:http://dx.doi.org/10.1016/S1006-706X(13)60143-0

330. Shibanuma K., Aihara S., Matsubara M., Shirahata H., Handa T. Prediction Model of Cleavage Fracture Toughness of Ferrite Steel. 13th International Conference on Fracture. Beijing, China; 2013. pp. 1–10.

331. Lee KH., Kim MC., Won-Jon Y., Lee BS. Evaluation of microstructural parameters controlling cleavage fracture toughness in Mn–Mo–Ni low alloy steels. Materials Science and Engineering: A. 10 March 2013; 565(0): 158–164. Available at: DOI:http://dx.doi.org/10.1016/j.msea.2012.12.024

332. Shikanai N., Mitao S., Endo S. Recent Development in Microstructural Control Technologies through the Thermo-Mechanical Control Process (TMCP) with JFE Steel's High-Performance Plates. JFE Technical Report. 2008; (11): 1–6.

333. Shigeru E., Naoki N. Development of Thermo-Mechanical Control Process (TMCP) and High Performance Steel in JFE Steel. JFE Technical Report. 2015; (11): 1–7.

334. Cao R., Li G., Fang XY., Song J., Chen JH. Investigation on the effects of microstructure on the impact and fracture toughness of a C–Mn steel with various microstructures. Materials Science and Engineering: A. March 2013; 564: 509–524. Available at: DOI:10.1016/j.msea.2012.11.120 (Accessed: 30 September 2014)

335. Lee S., Kim S., Hwang B., Lee BS., Lee CG. Effect of carbide distribution on the fracture toughness in the transition

temperature region of an SA 508 steel. Acta Materialia. November 2002; 50(19): 4755–4762. Available at: DOI:10.1016/S1359-6454(02)00313-0 (Accessed: 30 September 2014)

336. Ueda M., Ikeda A. Effect of Microstructure and Cr Content in Steel on CO2 Corrosion. Corrosion. Denver, Co: NACE International; 1996. pp. 1–9. Available at: http://www.onepetro.org/mslib/app/Preview.do?paperNumber=NACE-96013&societyCode=NACE

337. López DA., Pérez T., Simison SN. The influence of microstructure and chemical composition of carbon and low alloy steels in CO2 corrosion. A state-of-the-art appraisal. Materials & Design. 2003; 24(8): 561–575. Available at: DOI:DOI: 10.1016/S0261-3069(03)00158-4

338. Nešić S., Lee KLJ., Ruzic V. A Mechanistic Model of Iron Carbonate Film Growth and the Effect on CO2 Corrosion of Mild Steel. Corrosion. Denver, Co: NACE International; 2002. pp. 1–9. Available at: http://www.onepetro.org/mslib/app/Preview.do?paperNumber=NACE-02237&societyCode=NACE

339. Dugstad A., Halseid M. Internal Corrosion In Dense Phase CO2 Transport Pipelines - State of the Art And the Need For Further R&D. Corrosion. NACE International; 2012. pp. 1–8. Available at: http://www.onepetro.org/mslib/app/Preview.do?paperNumber=NACE-2012-1452&societyCode=NACE

340. Wang W., Shan Y., Yang K. Study of high strength pipeline steels with different microstructures. Materials Science and Engineering: A. 2009; 502(1-2): 38–44. Available at: DOI:DOI: 10.1016/j.msea.2008.10.042

341. Wang X., Zhao H., Shang C., He X. The microstructure and properties of high performance steels with low yield-to-tensile ratio. Journal of Alloys and Compounds. 2013; 577(S1): S678–S683. Available at: DOI:10.1016/j.jallcom.2012.05.129

342. Liessem A., Knauf G., Zimmermann S. Strain Based Design—What the Contribution of a Pipe Manufacturer Can Be. The Seventeenth (2007) International Offshore and Polar Engineering Conference. Lisbon, Portugal: The International

Society of Offshore and Polar Engineers; 2007. pp. 3156–3163. Available at: http://www.onepetro.org/mslib/app/Preview.do?paperNumber=ISOPE-I-07-500&societyCode=ISOPE

343. Morozov YD., Matrosov MY., Nastich SY., Arabei a. B. New generation of high-strength tube steels with a ferrite-bainite structure. Metallurgist. 21 November 2008; 52(7-8): 450–456. Available at: DOI:10.1007/s11015-008-9080-5

344. Benzerga AA., Leblond JB. Ductile fracture by void growth to coalescence. Advances in Applied Mechanics. Elsevier; 2010. pp. 169–305. Available at: DOI:http://dx.doi.org/10.1016/S0065-2156(10)44003-X

345. Joo MS., Suh DW., Bhadeshia DH. Anisotropy of Charpy Properties in Linepipe Steels. Cambridge University; 2013.

346. Mirone G., Corallo D. Stress–strain and ductile fracture characterization of an X100 anisotropic steel: Experiments and modelling. Engineering Fracture Mechanics. 2013; 102(0): 118–145. Available at: DOI:http://dx.doi.org/10.1016/j.engfracmech.2013.02.027

347. Ghajar R., Mirone G., Keshavarz A. Ductile failure of X100 pipeline steel – Experiments and fractography. Materials & Design. 2013; 43(0): 513–525. Available at: DOI:10.1016/j.matdes.2012.07.032

348. Michler T., Naumann J. Microstructural aspects upon hydrogen environment embrittlement of various bcc steels. International Journal of Hydrogen Energy. 2010; 35(2): 821–832. Available at: DOI:DOI: 10.1016/j.ijhydene.2009.10.092

349. Beidokhti B., Dolati A., Koukabi AH. Effects of alloying elements and microstructure on the susceptibility of the welded HSLA steel to hydrogen-induced cracking and sulfide stress cracking. Materials Science and Engineering: A. 2009; 507(1-2): 167–173. Available at: DOI:DOI: 10.1016/j.msea.2008.11.064

350. Chattoraj I., Tiwari SB., Ray AK., Mitra A., Das SK. Investigation on the mechanical degradation of a steel line pipe due to hydrogen ingress during exposure to a simulated sour environment. Corrosion Science. 1995; 37(6): 885–896. Available at: DOI:DOI: 10.1016/0010-938X(95)00001-Z

351. Zhang T., Chu WY., Gao KW., Qiao LJ. Study of correlation between hydrogen-induced stress and hydrogen embrittlement. Materials Science and Engineering A. 2003; 347(1-2): 291–299. Available at: DOI:DOI: 10.1016/S0921-5093(02)00600-7

352. Kim WK., Koh SU., Yang BY., Kim KY. Effect of environmental and metallurgical factors on hydrogen induced cracking of HSLA steels. Corrosion Science. Elsevier Ltd; December 2008; 50(12): 3336–3342. Available at: DOI:10.1016/j.corsci.2008.09.030 (Accessed: 3 October 2014)

353. Bannister AC. Structural integrity assessment procedures for European industry. SINTAP. Sub-Task 3.3 report : Final issue. Determination of fracture toughness from Charpy impact energy : procedure and validation. Rotherham, UK; 1998.

354. Yang XL., Xu YB., Tan XD., Wu D. Influences of crystallography and delamination on anisotropy of Charpy impact toughness in API X100 pipeline steel. Materials Science and Engineering: A. June 2014; 607: 53–62. Available at: DOI:10.1016/j.msea.2014.03.121 (Accessed: 8 September 2014)

355. Urwank P. Unambiguous curve fitting and error estimation for charpy impact test data of reactor pressure vessel steel. Journal of nuclear Materials. 1989; 161: 24–29.

356. Sokolov M., Nanstand R. On impact testing of subsize Charpy V-notch type specimens. 2008.

357. Lucas WRC and GE. (ed.) Subsized Bend and Charpy V-Notch Specimens for Irradiated Testing. The use of small-scale specimens for testing irradiated materials, ASTM STP 888. Philadelphia, USA: American Society for Testing and Materials; 1986. pp. 304–324.

358. Kumar AS., Louden BS., Garner FA., Hamilton ML. Recent Improvements in Size Effects Correlations for DBTT and Upper Shelf Energy of Ferritic Steels. In: Corwin WR, F. M. Haggag and WLS (eds.) Small Specimen Test Techniques Applied to Nuclear Reactor Vessel Thermal Annealing and Plant Life extension, ASTM STP 1204. Philadelphia, USA: American Society for Testing and Materials; 1993. pp. 47–61.

359. Lee JS., Ju JB., Jang JI., Kim WS., Kwon D. Weld crack assessments in API X65 pipeline: failure assessment diagrams

with variations in representative mechanical properties. Materials Science and Engineering A. 2004; 373(1-2): 122–130. Available at: DOI:DOI: 10.1016/j.msea.2003.12.039

360. Baek JH., Kim YP., Kim CM., Kim WS., Seok CS. Effects of pre-strain on the mechanical properties of API 5L X65 pipe. Materials Science and Engineering: A. 2010; 527(6): 1473–1479. Available at: DOI:DOI: 10.1016/j.msea.2009.10.017

361. Xue Q., Benson D., Meyers MA., Nesterenko VF., Olevsky EA. Constitutive response of welded HSLA 100 steel. Materials Science and Engineering: A. 2003; 354(1–2): 166–179. Available at: DOI:10.1016/S0921-5093(03)00007-8

362. Fields BA., Low III SR., Early JG. The Effect of Fatigue Pre-Cracking Versus V-Notching on Impact Testing of Charpy Specimens. In: ASTM (ed.) STP 1072 Charpy Impact Test: Factors and Variables. Holt, J. M. Philadelphia, USA: American Society for Testing and Materials; 1990. pp. 120–133.

363. Mikalac S., Vassilaros MG., Rogers HC. Precracking and Strain Rate Effects on HSLA-100 Steel Charpy Specimens. Holt JM (ed.) Charpy Impact Test: Factors and Variables. Philadelphia, USA: American Society for Testing and Materials; 1990; STP 1072: 134–147.

364. Strnadel B., Matocha K. Testing samples size effect on notch toughness of structural steel. Metalurgija. 2009; 48(4): 253–256.

365. Wallin K. Distribution free statistical assessment of scatter and size effects in the Euro fracture toughness data set. Engineering Fracture Mechanics. May 2013; 103(0): 69–78. Available at: DOI:http://dx.doi.org/10.1016/j.engfracmech.2012.05.018

366. Joyce JA., Tregoning RL. Development of the T0 reference temperature from precracked Charpy specimens. Engineering Fracture Mechanics. May 2001; 68(7): 861–894. Available at: DOI:10.1016/S0013-7944(00)00135-1

367. Sandana D., Dale M., Charles EA., Race J. Transport of Gaseous and Dense Carbon Dioxide in Pipelines: Is There an Internal Stress Corrosion Cracking Risk? NACE Corrosion. Orlando, Fl: NACE International; 2013. pp. 1–15. Available at: http://www.onepetro.org/mslib/app/Preview.do?paperNumber=

NACE-2013-2516&societyCode=NACE

368. Dugstad A., Halseid M., Morland B., Sivertsen AO. Dense phase CO2 corrosion and the impact of depressurization and accumulation of impurities. Corrosion. NACE International; 2013. pp. 1–6. Available at: http://www.onepetro.org/mslib/app/Preview.do?paperNumber=NACE-2013-2785&societyCode=NACE

369. Pluvinage G. Defect Assessment on Pipe Transporting a Mixture of Natural Gas and Hydrogen. Damage and Fracture mechanics: Failure analysis of engineering materrials and structures. 2009. pp. 19–32.

370. Haghbakhsh R., Hayer H., Saidi M., Keshtkari S., Esmaeilzadeh F. Density estimation of pure carbon dioxide at supercritical region and estimation solubility of solid compounds in supercritical carbon dioxide: Correlation approach based on sensitivity analysis. Fluid Phase Equilibria. 25 March 2013; 342(0): 31–41. Available at: DOI:http://dx.doi.org/10.1016/j.fluid.2012.12.029

371. Kandil F. A., Lord JD., Fry AT., Grant P V. A Review of Residual Stress Measurement Methods- A guide to technique selection. Teddington, Middlesex; 2001. Available at: www.npl.co.uk

372. De Giorgi M. Residual stress evolution in cold-rolled steels. International Journal of Fatigue. Elsevier Ltd; March 2011; 33(3): 507–512. Available at: DOI:10.1016/j.ijfatigue.2010.10.006 (Accessed: 28 January 2014)

373. Webster GA., Wimpory RC. Non-destructive measurement of residual stress by neutron diffraction. The International conference on Processing and manufacturing of Advanced Materials. 2001. pp. 395–399. Available at: DOI:10.1016/S0924-0136(01)00802-0

374. Schajer GS., Rickert TJ. Incremental computation technique for residual stress calculations using the integral method. Proceding of the SEM annual conference. Indianapolis, Indiana USA; 2011. pp. 185–191. Available at: DOI:10.1007/978-1-4419-9792-0

375. Birley, S. S. and Owens A. Blind hole drilling technique for

residual stress measurement: application in ndt. NDT International. February 1980; 13(1): 3–9. Available at: DOI:10.1016/0308-9126(80)90118-2

376. Stefanescu D., Truman CE., Smith DJ., Whitehead PS. Improvements in Residual Stress Measurement by the Incremental Centre Hole Drilling Technique. Experimental Mechanics. 1 May 2006; 46(4): 417–427. Available at: DOI:10.1007/s11340-006-7686-8 (Accessed: 30 January 2014)

377. Chahardehi A., Brennan FP., Steuwer A. The effect of residual stresses arising from laser shock peening on fatigue crack growth. Engineering Fracture Mechanics. Elsevier Ltd; July 2010; 77(11): 2033–2039. Available at: DOI:10.1016/j.engfracmech.2010.03.033 (Accessed: 15 February 2014)

378. Cozzolino LD. Finite element analysis of localised rolling to reduce residual stress and distortion. PhD thesis. Cranfield University; 2014.

379. Scafidi M., Valentini E., Zuccarello B. Effect of the hole-bottom fillet radius on the residual stress analysis by the hole drilling method. JCPDS-International Centre for Diffraction Data. 2009; : 263–270.

380. Nobre JP., Batista AC., Nau A., Paepegem W V., Scholtes B. Using the incremental hole-drilling technique for measuring residual stresses in fibre-reinforced. In: European Conference on Composites Materials (ed.) ECCM 15th. Venice-Italy; 2012. pp. 24–28.

381. Casavola C., Pappalettera G., Pappalettere C., Tursi F. Effects of Strain's Error on Residual Stresses Calculated by HDM. In: Ventura CE, Crone WC, Furlong C (eds.) Experimental and Applied Mechanics, Volume 4 SE - 47. Springer New York; 2013. pp. 395–402. Available at: DOI:10.1007/978-1-4614-4226-4_47

382. Faghidian S., Goudar D., Farrahi G., Smith DJ. Measurement, analysis and reconstruction of residual stresses. The Journal of Strain Analysis for Engineering Design. 2012. pp. 254–264. Available at: DOI:10.1177/0309324712441146

383. Sasaki T., Takahashi S., Kanematsu Y., Satoh Y., Iwafuchi K., Ishida M., et al. Measurement of residual stresses in rails by

neutron diffraction. Wear. October 2008; 265(9-10): 1402–1407. Available at: DOI:10.1016/j.wear.2008.04.047 (Accessed: 22 April 2014)

384. Niku-Lari A., Lu J., Flavenot JF. Measurement of residual-stress distribution by the incremental hole-drilling method. Experimental Mechanics. Kluwer Academic Publishers; 1985; 25(2): 175–185. Available at: DOI:10.1007/BF02328809

385. Hamilton GM. Plastic Flow in Rollers Loaded above the Yield Point. Proceedings of the Institution of Mechanical Engineers. 1 June 1963; 177(1): 667–675. Available at: http://pme.sagepub.com/content/177/1/667.abstract

386. Ollerton E. Stresses in the Contact Zone. Proceedings of the Institution of Mechanical Engineers, Conference Proceedings. 1 June 1963; 178(5): 161–171. Available at: DOI:10.1243/PIME_CONF_1963_178_157_02

387. Merwin JE., Johnson KL. An Analysis of Plastic Deformation in Rolling Contact. Proceedings of the Institution of Mechanical Engineers. 1 June 1963; 177(1): 676–690. Available at: DOI:10.1243/PIME_PROC_1963_177_052_02

388. Pomeroy RJ. Measurement of residual stresses in rolling contact. Wear. December 1970; 16(6): 393–412. Available at: DOI:http://dx.doi.org/10.1016/0043-1648(70)90167-5

389. Bahadur A., Mitra A., Ravi Kumar B., Palit Sagar S. Evaluation and Correlation of Residual Stress Measurement in Steel. Journal of Nondestructive Evaluation. Springer US; 2007; 26(2-4): 47–55. Available at: DOI:10.1007/s10921-007-0019-8

390. Johnson KL. A review of the theory of rolling contact stresses. Wear. January 1966; 9(1): 4–19. Available at: DOI:10.1016/0043-1648(66)90010-X (Accessed: 16 April 2014)

391. Berthe L., Sainsot P., Lubrecht AA., Baietto MC. Plastic deformation of rough rolling contact: An experimental and numerical investigation. Wear. April 2014; 312(1-2): 51–57. Available at: DOI:10.1016/j.wear.2014.01.017 (Accessed: 22 April 2014)

392. Jiang Y., Sehitoglu H. Rolling contact stress analysis with the application of a new plasticity model. Wear. January 1996; 191(1-2): 35–44. Available at: DOI:10.1016/0043-

1648(95)06663-2 (Accessed: 22 April 2014)

393. Haines DJ., Ollerton E. Contact Stress Distributions on Elliptical Contact Surfaces Subjected to Radial and Tangential Forces. Proceedings of the Institution of Mechanical Engineers. 1 June 1963; 177(1): 95–114. Available at: DOI:10.1243/PIME_PROC_1963_177_014_02

394. Knight MJ., Brennan FP., Dover WD. Controlled failure design of drillstring threaded connections. Fatigue Fracture of Engineering Materials and Structures. November 2003; 26(11): 1081–1090. Available at: DOI:10.1046/j.1460-2695.2003.00697.x

395. Wang J., Mote CD. Analysis Of Roller-induced Residual Stresses In Bandsaw Plates. Journal of Sound and Vibration. August 1994; 175(5): 647–659. Available at: DOI:10.1006/jsvi.1994.1351 (Accessed: 15 April 2014)

396. Zerbst U., Ainsworth RA., Schwalbe K. Basic principles of analytical flaw assessment methods. International Journal of Pressure Vessels and Piping. 2001; 77: 855–867.

397. Ainsworth RA., Bannister AC., Zerbst U. An overview of the European flaw assessment procedure SINTAP and its validation. International Journal of Pressure Vessels and Piping. 2000; 77: 869–876.

398. Zerbst U., Hamann R., Beeck F., Scheider I., Brocks W. Engineering failure assessment methods applied to pressurised components. Nuclear Engineering and Design. 1 September 2000; 200(3): 371–382. Available at: DOI:http://dx.doi.org/10.1016/S0029-5493(00)00252-1

399. EGIG. 8th Report of teh European Gas Pipeline Incident Data Group. 2011.

400. Leis BN., Eiber RJ., Carlson L., Gilroy-Scott A. Relationship between apparent (total) Charpy V-notch toughness and the corresponding dynamic crack-propagation resistance. Proceedings of the International Pipeline Conference, IPC. 1998. pp. 723–731. Available at: http://www.scopus.com/inward/record.url?eid=2-s2.0-0031627675&partnerID=40&md5=d12312deed991549527304ac7625734b

401. Takeuchi I., Makino H., Okaguchi S. Crack arrestability of high-pressure gas pipelines by X100 or X120. 23rd World Gas …. 2006; Available at: http://www.igu.org/html/wgc2006/pdf/paper/add10389.pdf (Accessed: 31 July 2014)

402. Murvay PS., Silea I. A survey on gas leak detection and localization techniques. Journal of Loss Prevention in the Process Industries. Elsevier Ltd; November 2012; 25(6): 966–973. Available at: DOI:10.1016/j.jlp.2012.05.010 (Accessed: 14 October 2014)

403. Billmann L., Isermann R. Leak detection methods for pipelines. Automatica. 1987; 23(3): 381–385.

404. Meng L., Yuxing L., Wuchang W., Juntao F. Experimental study on leak detection and location for gas pipeline based on acoustic method. Journal of Loss Prevention in the Process Industries. Elsevier Ltd; January 2012; 25(1): 90–102. Available at: DOI:10.1016/j.jlp.2011.07.001 (Accessed: 14 October 2014)

405. Safitri A., Gao X., Mannan MS. Dispersion modeling approach for quantification of methane emission rates from natural gas fugitive leaks detected by infrared imaging technique. Journal of Loss Prevention in the Process Industries. March 2011; 24(2): 138–145. Available at: DOI:10.1016/j.jlp.2010.11.007 (Accessed: 30 October 2014)

406. Det Norske Veritas-DNV. Mapping of potential HSE issues related to large-scale capture, transport and storage of CO2. Høvik, Norway; 2008. Available at: www.dnv.com

407. McGillivray A., Wilday J. Comparison of risks from carbon dioxide and natural gas pipelines. RR749. Harpur Hill, Buxton. UK.; 2009. Available at: http://www.hse.gov.uk/research/rrpdf/rr749.pdf

408. Wilday J., Wardman M., Johnson M., Haines M. Hazards from carbon dioxide capture, transport and storage. Process Safety and Environmental Protection. Institution of Chemical Engineers; November 2011; 89(6): 482–491. Available at: DOI:10.1016/j.psep.2011.09.002 (Accessed: 25 July 2014)

409. van Leeuwen C., Hensen A., Meijer HAJ. Leak detection of CO2 pipelines with simple atmospheric CO2 sensors for

carbon capture and storage. International Journal of Greenhouse Gas Control. Elsevier Ltd; November 2013; 19: 420–431. Available at: DOI:10.1016/j.ijggc.2013.09.018 (Accessed: 30 October 2014)

410. Hadley I., Pisarski H. Overview of BS 7910:2013. In: ESIA (ed.) 12th International Conference on Engineering Structural Integrity Assessment. Manchester, UK: ESIA; 2013. pp. 1–12.

411. Hadley I., Goldthorpe M., Wei L. Compilation of K-solutions for fitness-for-service procedures. Cambridge, UK; 2006.

412. Span R., Wagner W. New equation of state for carbon dioxide covering the fluid region from the triple point temperature to 1100 K at pressures up to 800 MPa. The Journal of Physical Chemistry. 1996; 25(6): 1–88.

413. Ouyang LB. New Correlations for Predicting the Density and Viscosity of Supercritical Carbon Dioxide Under Conditions Expected in Carbon Capture and Sequestration Operations. The Open Petroleum Engineering Journal. 18 November 2011; 5(1): 13–21. Available at: DOI:10.2174/1874834101104010013

414. Shin SY., Hwang B., Lee S., Kim NJ., Ahn SS. Correlation of microstructure and charpy impact properties in API X70 and X80 line-pipe steels. Materials Science and Engineering: A. 2007; 458(1-2): 281–289. Available at: DOI:DOI: 10.1016/j.msea.2006.12.097

415. Kang M., Kim H., Lee S., Shin SY. Correlation of microstructure with tensile and crack tip opening displacement properties at low temperatures in API linepipe steels. Metals and Materials International. 2015; 21(4): 628–638. Available at: DOI:10.1007/s12540-015-4607-3

APPENDICES CHAPTER THREE

Appendix A Dimensions of plates

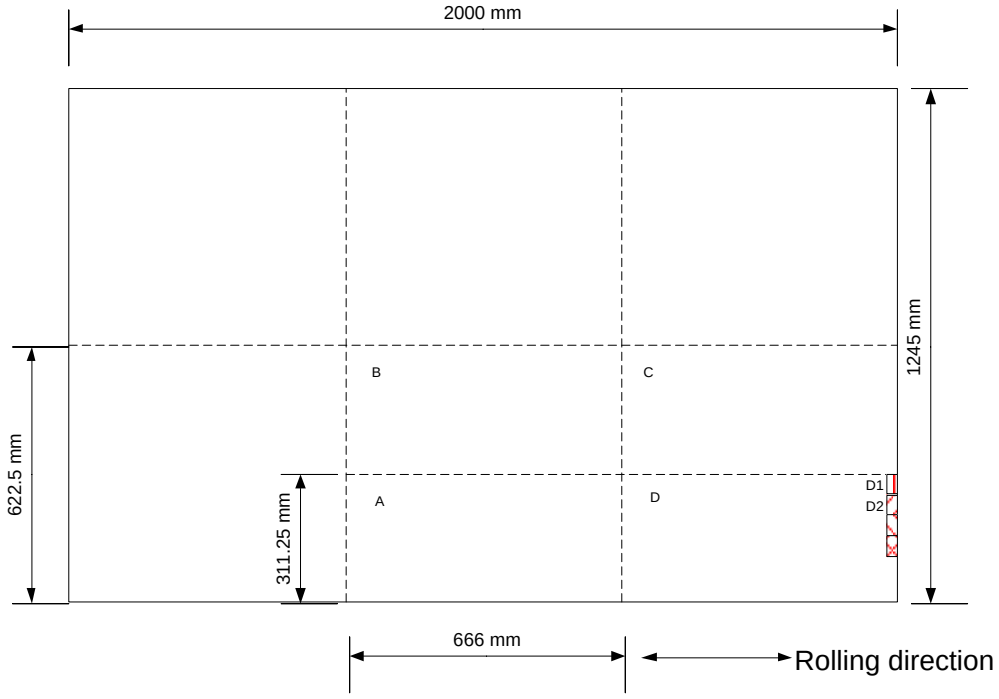

Figure A-1 Schematic illustration of the cutting of plates and samples of API X100 steel for chemical composition and metallographic analysis

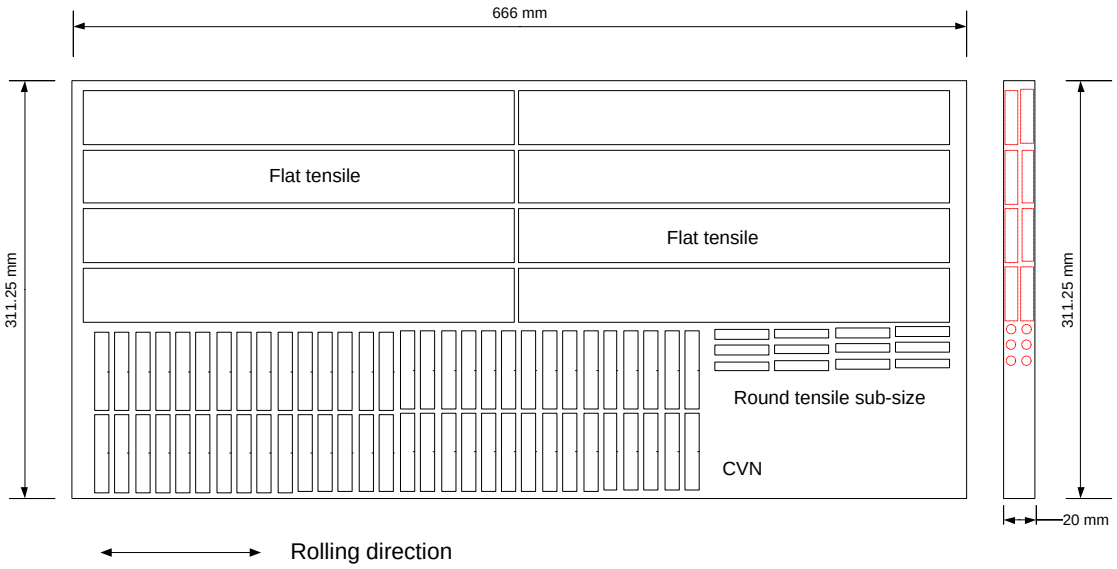

Figure A-2 Schematic illustration of the cutting of plates and samples of API X100 steel

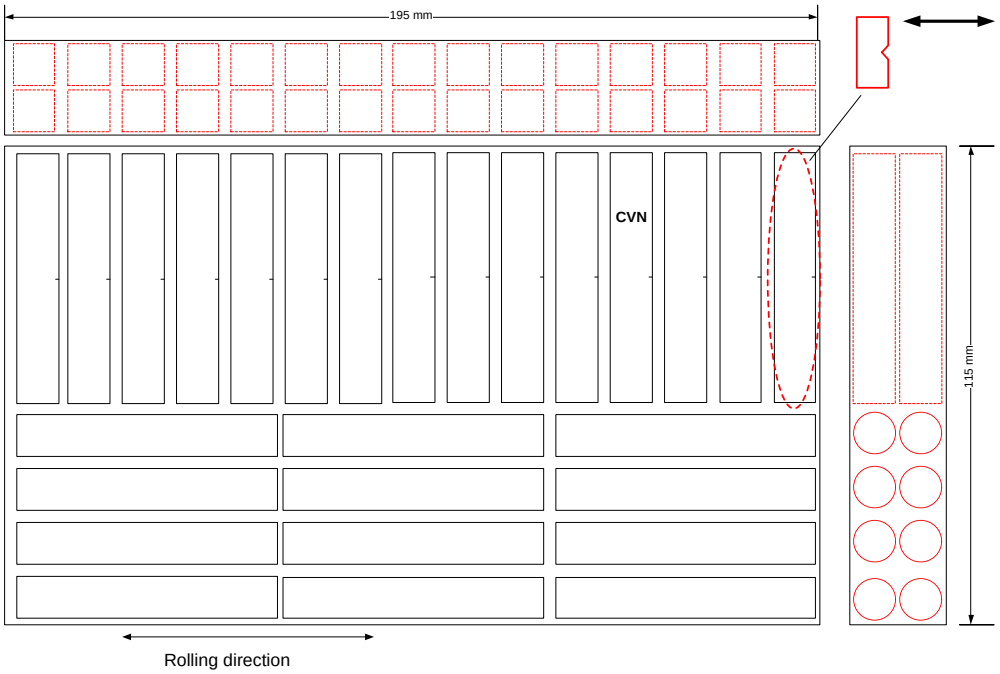

Figure A-3 Schematic illustration of the cutting of plates and samples of API X70 steel

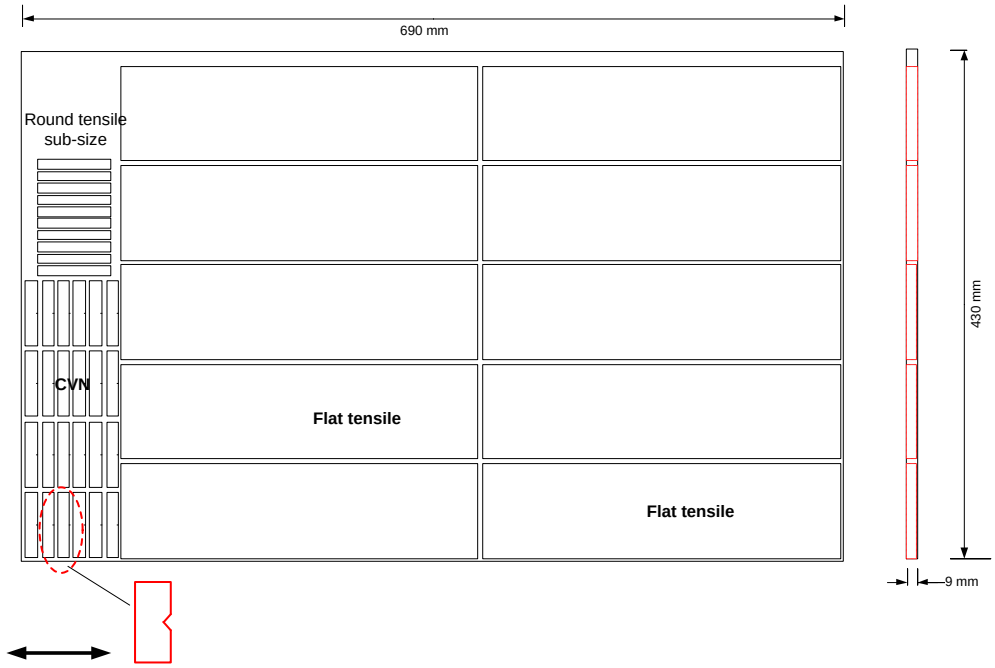

Figure A-4 Schematic illustration of the cutting of plates and samples of API X60 steel

Appendix B Schematic illustration of tensile specimens used for tensile test with typical dimensions

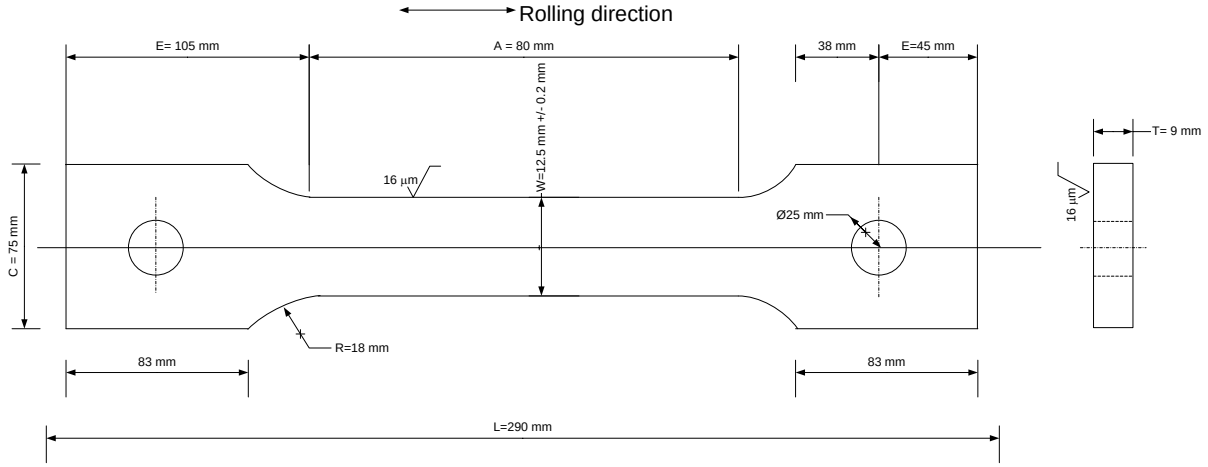

(a) Pin-loaded specimen for tension test with 50 mm gauge length. Units in mm.

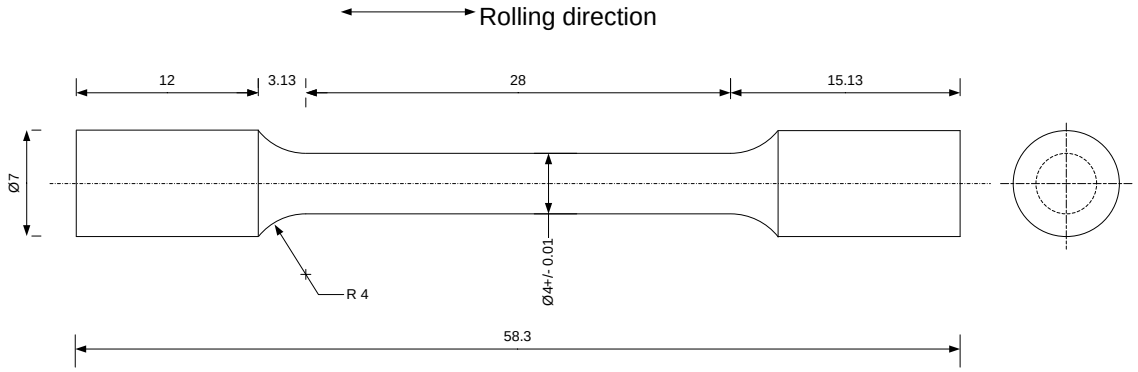

(b) Small-size round specimen proportional to standard specimen for tension test.

Figure B-1 Shape and dimensions of specimen for tension test with 50 mm and 10 mm gauge. Units in mm.

Appendix C System alignment

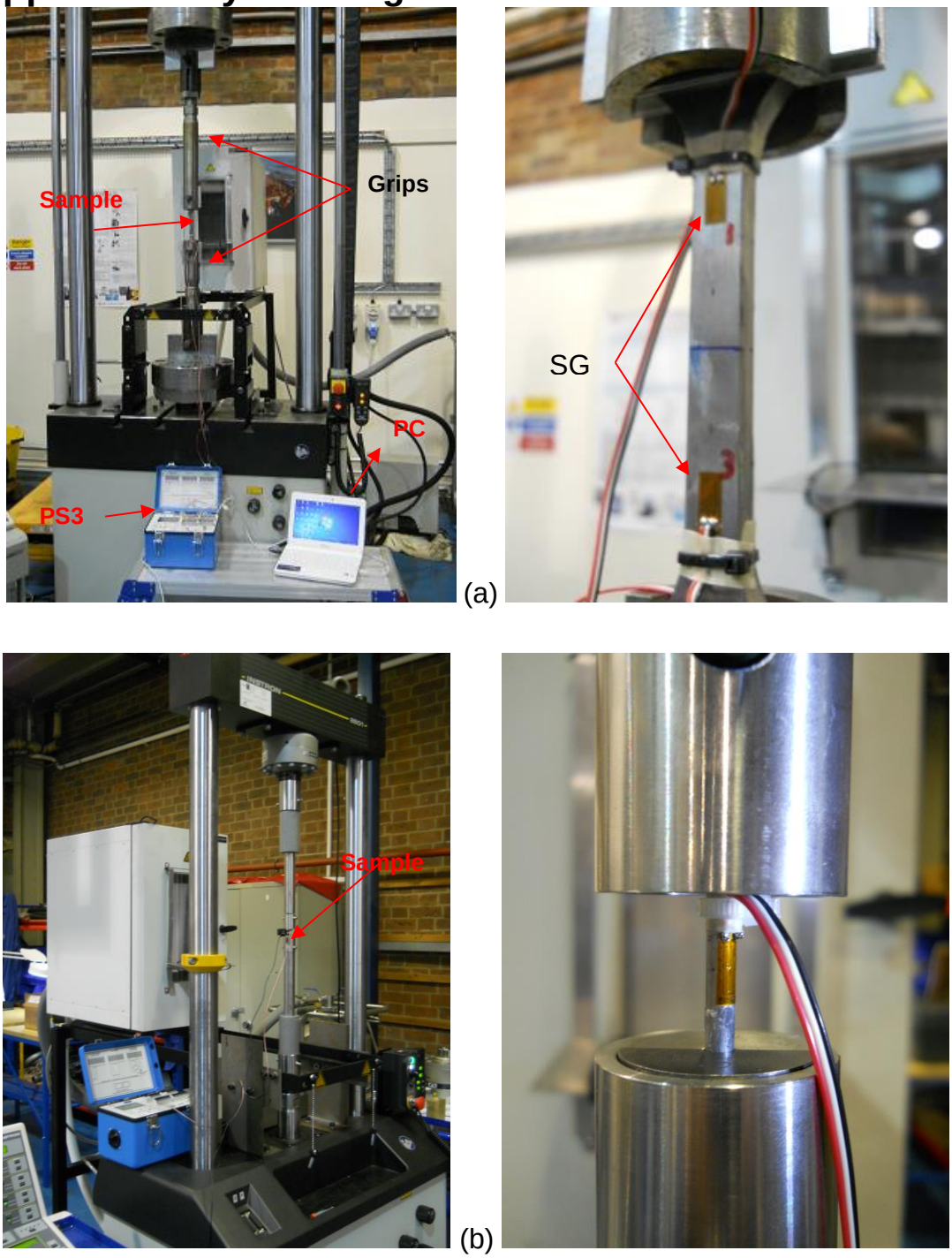

Figure C-1 Configuration to verify alignment (a) 500 kN, strip sample and (b) 100 kN round sample. Both are using linear strain gauge. Left: Set up. Right: Strain gauge (SG).

Appendix D Set up tensile test

(a) 500 kN machine

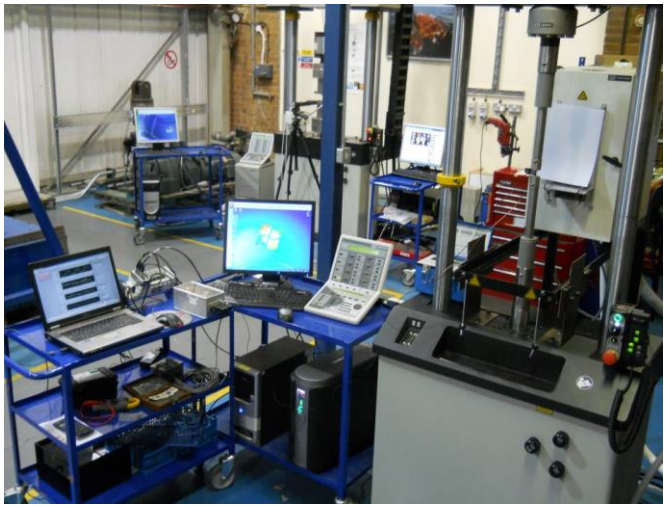

(b) 100 kN machine using round sample

Figure D-1 Experimental set up for tensile test of flat and small round specimens

Appendix E Nominal dimensions and tolerances Charpy V-Notch (CVN)

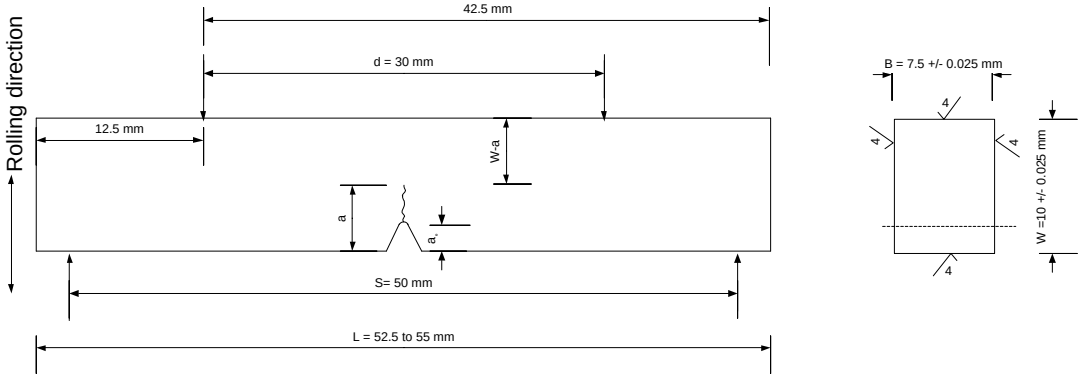

(a) API X60. B= 3/4T

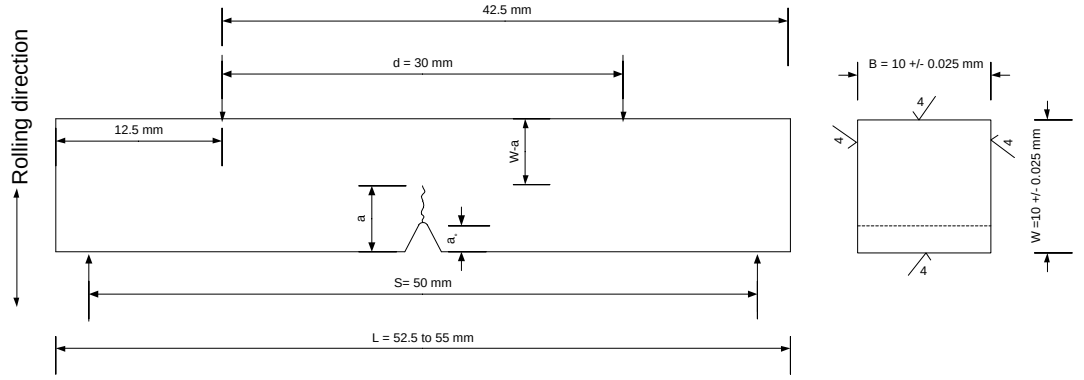

(b) API X100 and X70. B= 1T

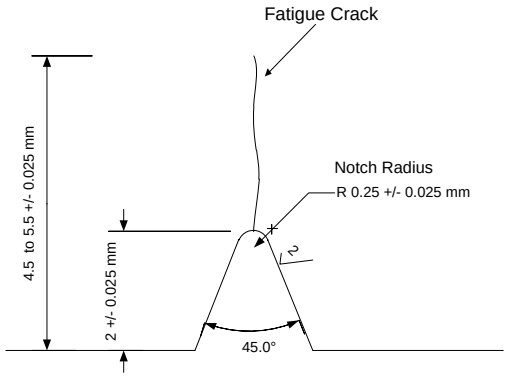

(c) Notch dimensions

Figure E-1 Charpy V-Notch a, b) General dimensions (b) Notch dimensions

Appendix F Charpy V-Notch Set up

(a) Pendulum Impact tester 217 Ft-lb (~300 J) capacity

1) From –70ºC to –20ºC

2) Test at –196ºC and –100ºC

(b) Set up to PCCVN test a lower temperature.

Figure F-1Pendulum impact testing machine and environmental chamber, datalogger, laptop and Nitrogen tank used to test a lower temperature

Appendix G Precracking curves for API X100, X70 and X60

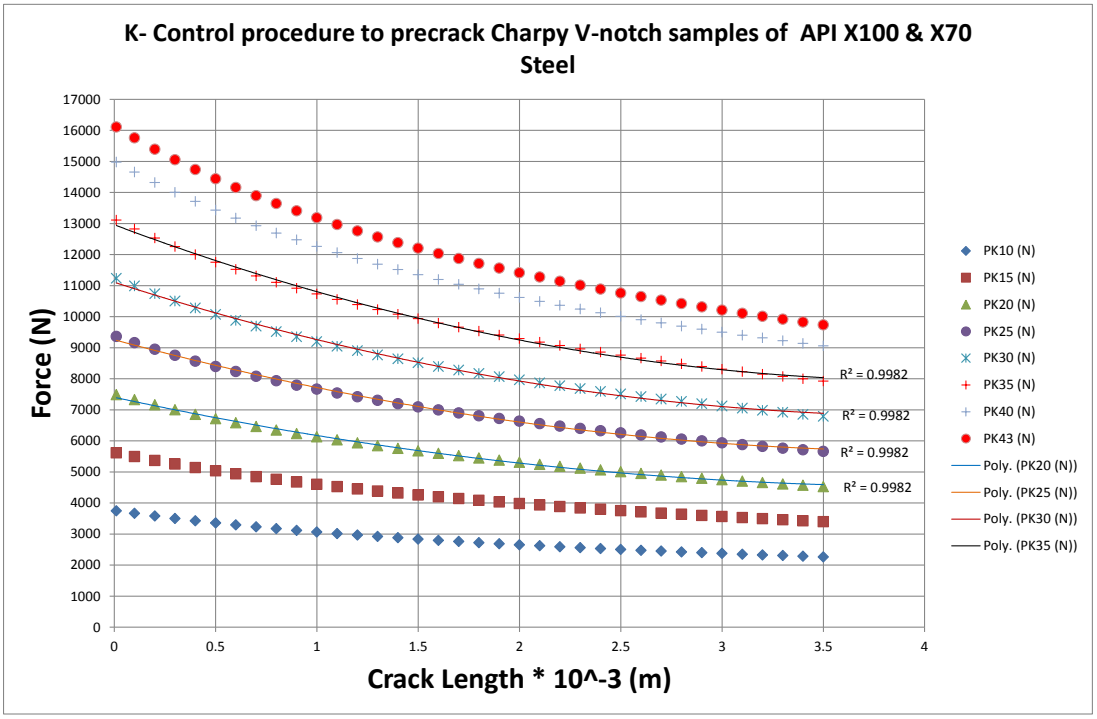

Figure G-1 Curve for API X100 and API X70 Steel

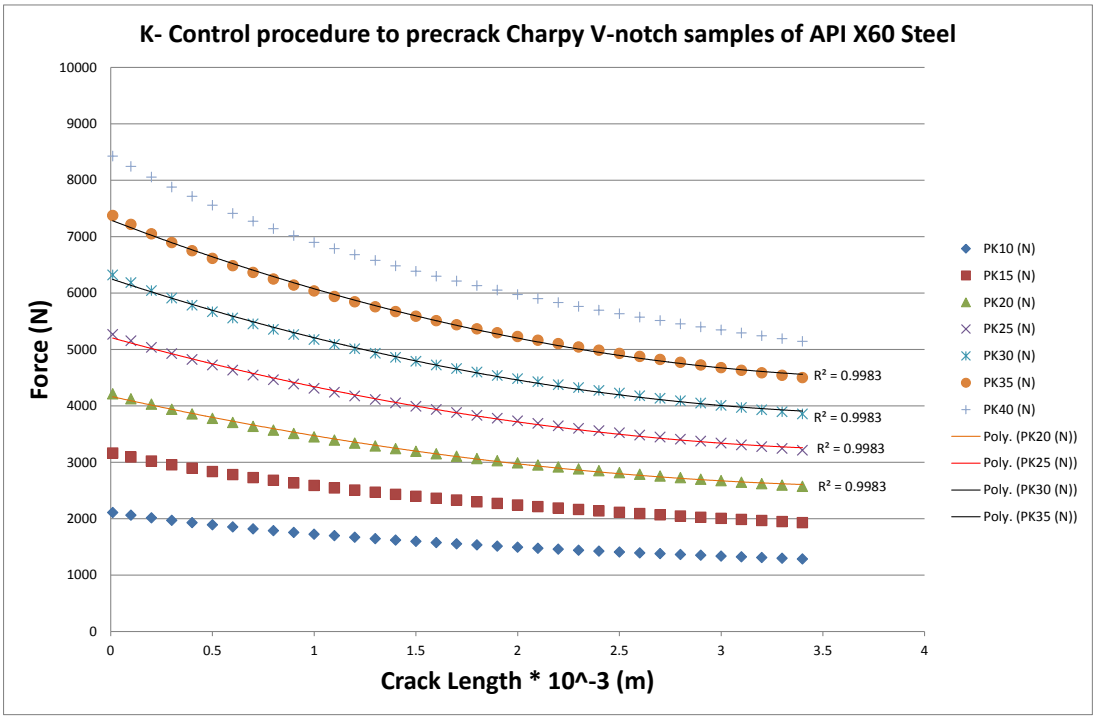

Figure G-2 Curve for API X60

Appendix H Distribution samples aging test- API X60

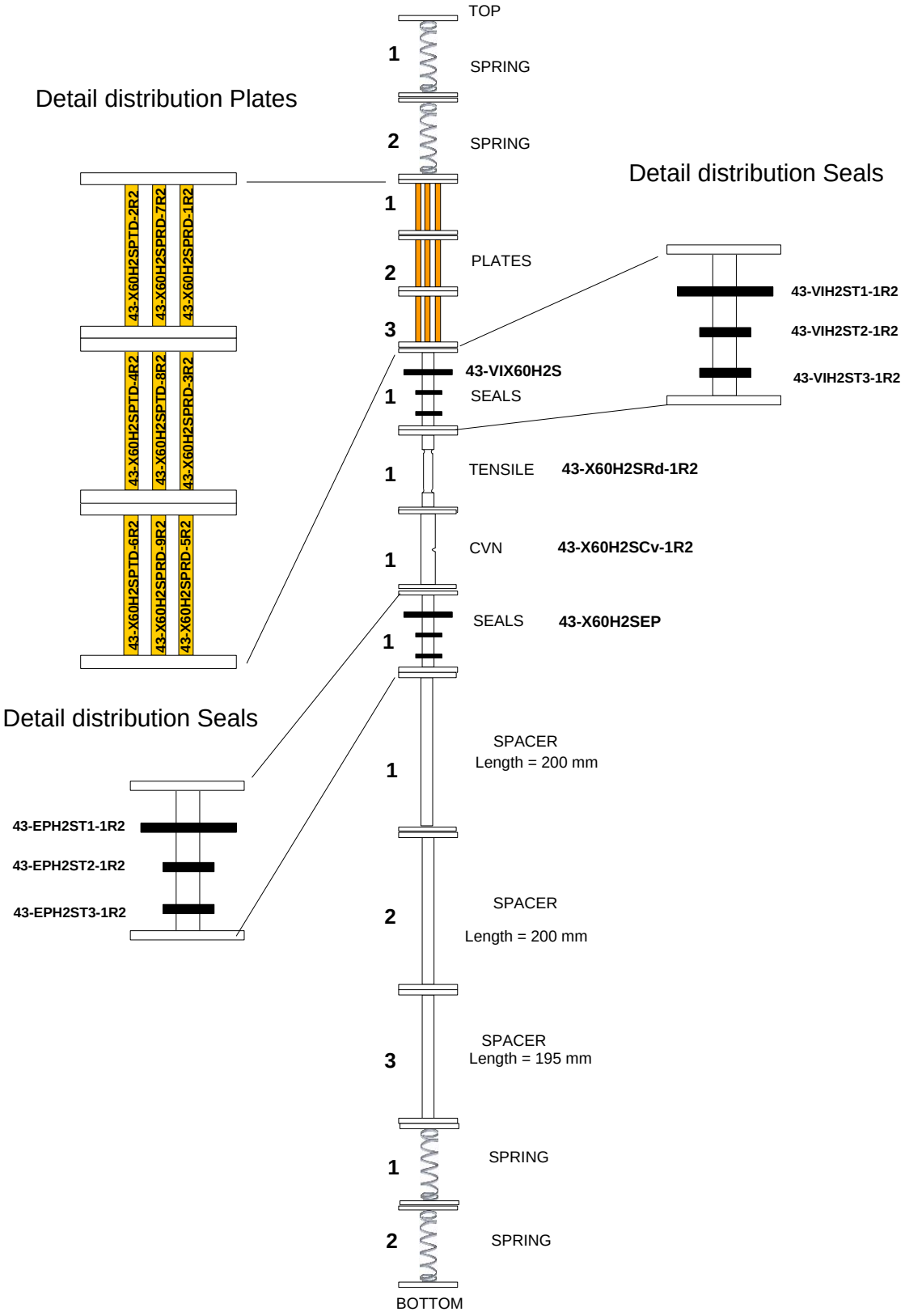

Appendix I Distribution samples aging test- API X70

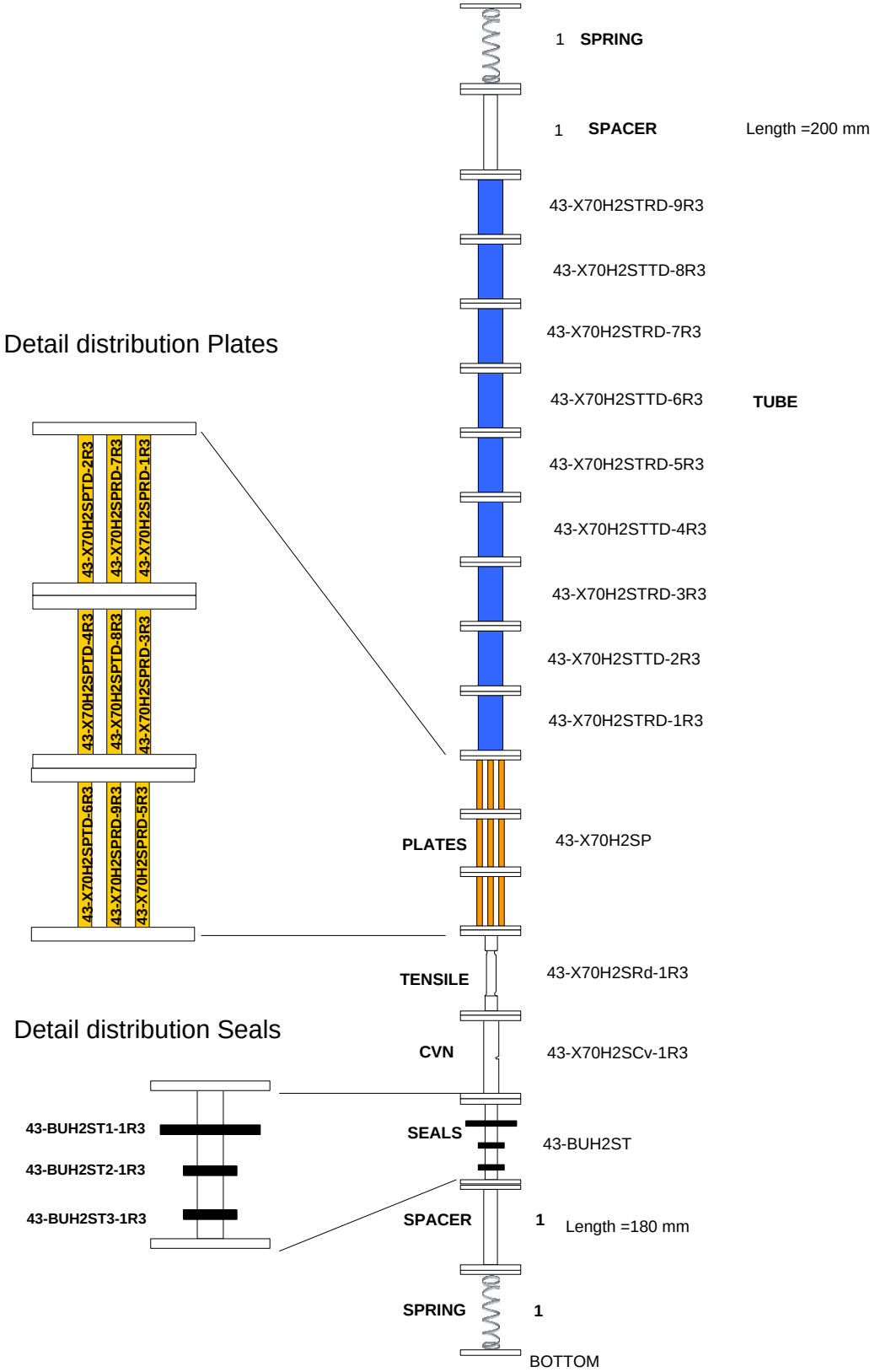

Appendix J Distribution samples aging test- API X100

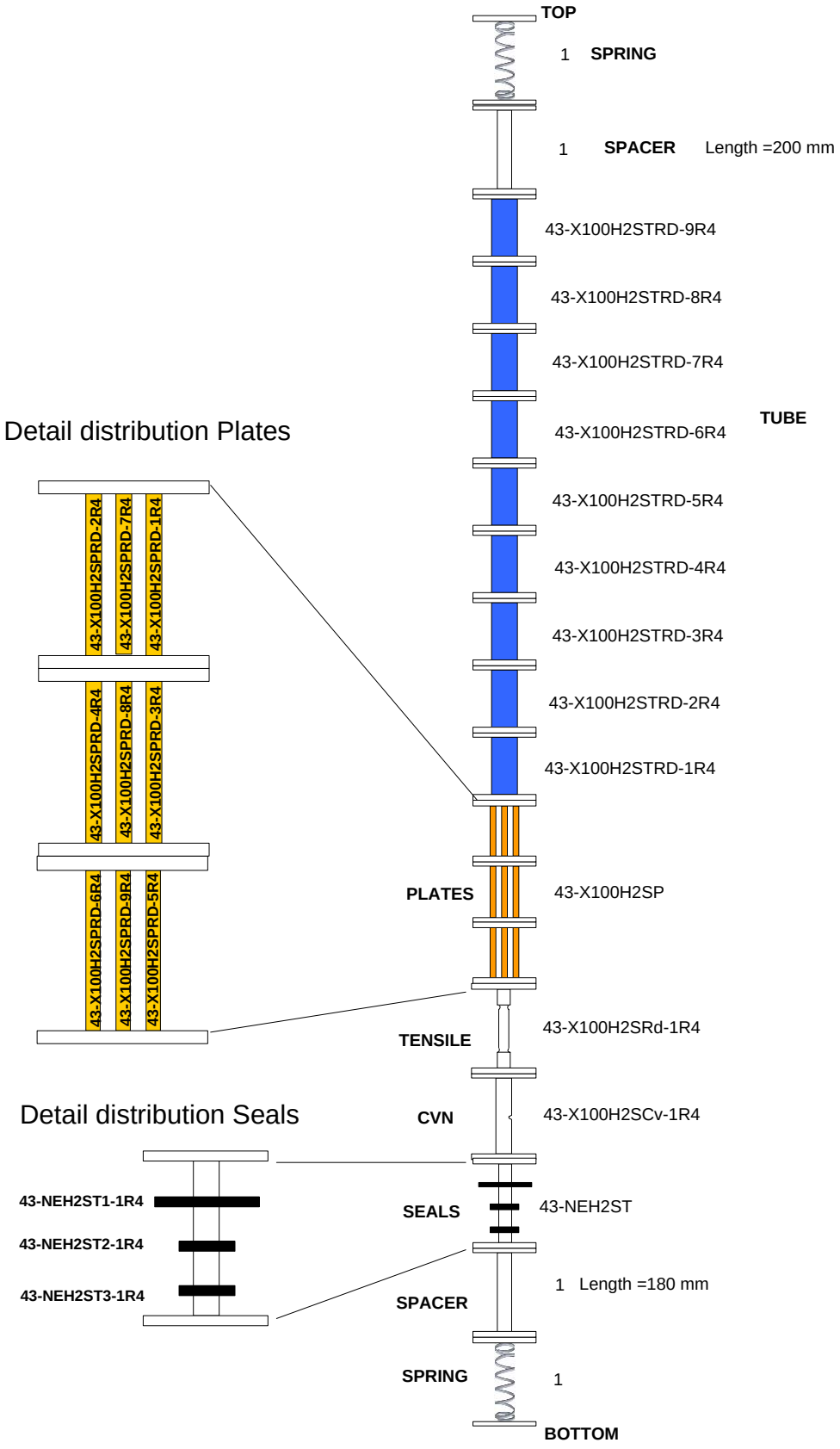

Appendix K Aging parameters

Phase	Environment saturated with water	Material	*In test*	*Post test*
1	Pure CO_2 + 0.5 mol% SO_2	Tubes Plates	Flow rate Temperature	Weight loss pH of fluid collected
2	Pure CO_2 + 0.5 mol % H_2S	Round tensile PC-CVN	Pressure Gas composition	Optical Microscope Scan Electron Microscope
3	Pure CO_2	O-Ring		

Material	Temperature, °C	Pressure, bar	Immersion time, h	H_2O, g	Initial SO2,ppm	Initial H_2S,ppm	Initial CO_2,ppm	Mass flow Rate, g/min
API X60	45	95	50,150,200,400 700 and 1100	1.23	500	500	10000	50
API X70	45	95	50,150,200,400 700 and 1100	1.23	500	500	10000	50
API X100	45	95	50,150,200,400 700 and 1100	1.23	500	500	10000	50
Seals	45	95	50,150,200,400 700 and 1100	1.23	500	500	10000	50

APPENDICES CHAPTER FOUR

Appendix L Mechanical properties of virgin steels tested over range RT to –70°C temperatures

Steel	*Shape*	T_{test} *(°C)*	$\sigma_{0.2\%}$ *(MPa)*	*Std dev (MPa)*	σ_{UTS} *(MPa)*	*Std dev (MPa)*	$\sigma_{0.2\%}/\sigma_{UTS}$	$(\sigma_{0.2\%}+\sigma_{UTS})/2$	*UE (%)*
X100	Strip	21	540	16	688	31	0.79	613	6.2
	Round	21	580	9	738	17	0.79	659	8.7
	Strip	-20	581	8	730	9	0.8	632	7.2
	Round	-20	604	7	723	14	0.84	664	7.9
	Strip	-40	589	13	745	19	0.79	656	6.2
	Round	-40	622	9	765	7	0.81	694	7.7
	Strip	-70	610	22	850	38	0.72	730	6.9
	Round	-70	636	9	792	3	0.80	714	7.4
X60	Strip	21	432	7	516	8	0.84	474	14.3
	Round	21	472	9	536	3	0.88	504	17.5
	Strip	-20	442	7	529	4	0.84	486	18
	Round	-20	452	8	540	2	0.84	496	19.7
	Strip	-40	445	9	532	10	0.84	489	18.5
	Round	-40	451	2	538	2	0.84	495	17.7
	Strip	-70	456	12	541	9	0.84	499	11.3
	Round	-70	462	13	552	8	0.84	507	13.8
X70	Round	21	769	3	814	10	0.94	791	7.9
	Round	-20	771	4	817	8	0.94	794	7.6
	Round	-40	786	6	844	14	0.93	815	8.0
	Round	-70	810	5	855	8	0.95	833	7.6

Appendix M Tensile properties of aging steels for different hours and tested at –20°C

Steel	*Impurity*	*$Time_{test}$ (h)*	*$\sigma_{0.2\%}$ (MPa)*	*σ_{UTS} (MPa)*	$\sigma_{0.2\%}/\sigma_{UTS}$	$(\sigma_{0.2\%} + \sigma_{UTS})/2$	*UE(%)*
X100	SO2	50	620	727	0.85	674	7.8
		150	658	758	0.87	708	8
		200	630	737	0.85	684	8.2
		300	610	715	0.85	663	8.5
		400	612	720	0.85	666	8
	H2S	50	600	718	0.83	659	8.2
		150	598	722	0.83	660	8.8
		200	601	717	0.88	659	8.7
		300	570	685	0.83	628	8.9
		400	562	672	0.84	617	8.3
X70	SO2	50	782	805	0.97	794	6.1
		150	860	867	0.99	864	4
		200	857	865	0.99	861	5.1
		300	800	809	0.99	805	6.2
		400	792	810	0.98	801	6.1
	H2S	50	815	840	0.97	828	7.3
		150	825	843	0.98	834	7
		200	841	847	0.99	844	4
		300	800	807	0.99	804	6.21
		400	820	822	1.00	821	3
X60	SO2	50	500	578	0.87	539	21
		150	502	581	0.86	542	20
		200	505	583	0.87	544	21
		300	479	550	0.87	515	21.5
		400	454	546	0.83	500	21
	H2S	50	495	545	0.91	520	21
		150	500	576	0.87	538	19
		200	501	573	0.87	537	19
		300	456	544	0.84	500	20
		400	448	529	0.85	489	19

Appendix N Set of samples exposed for different hours in simulated flue-gas

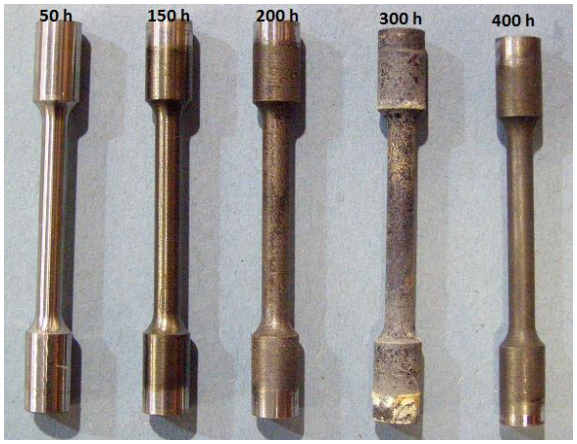

a. Grade X60, impurity SO_2

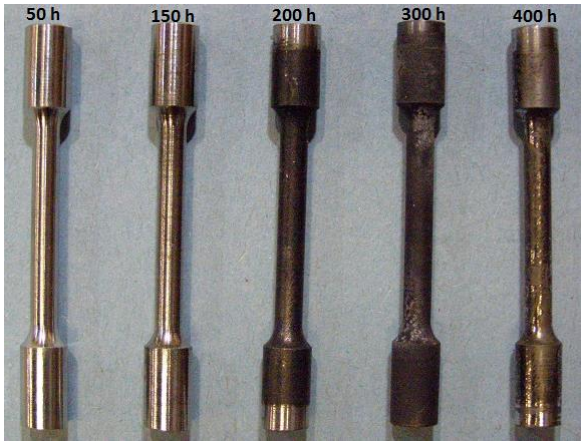

(b) Grade X70, impurity SO_2

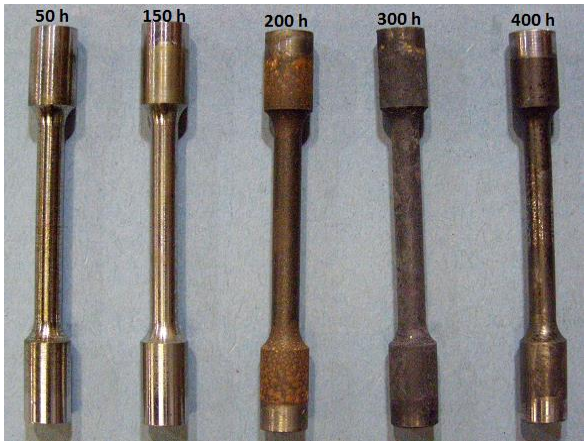

(c) Grade X100, impurity SO_2

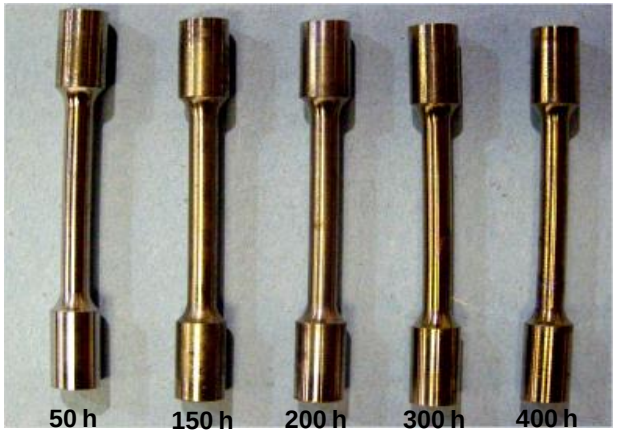

d) Grade X60, impurity H_2S

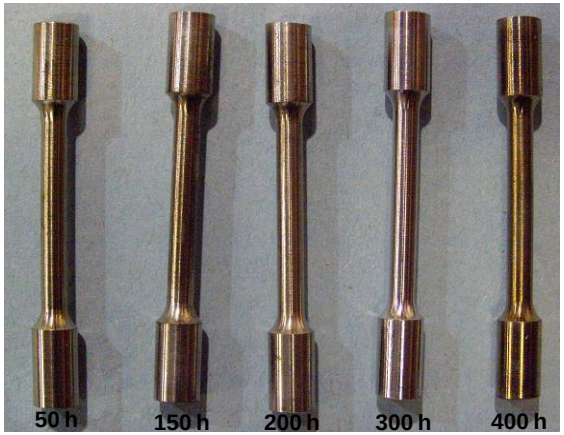

(e) Grade X70, impurity H_2S

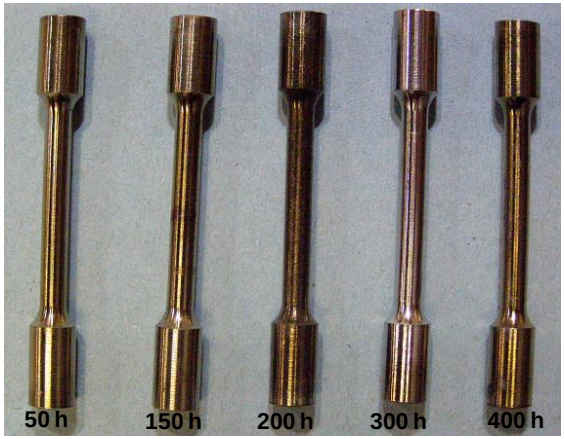

(f) Grade X100, impurity H_2S

Appendix O Charpy absorbed energy grade X100 as-received over range -196°C to RT temperature tested in non-instrumented machine 300 J by PCCVN. B= 1T

T (°C)	a_1 (mm)	b_1 (w-a) (mm)	Ratio (a/w)	CVN_{exp_wv} *(J)*	$CVN_{exp\_scale\_wv}$ *(J)*
21	2.81	4.85	0.51	76.6	126.3
21	3.05	4.58	0.54	69.1	120.7
21	2.86	4.80	0.52	77.3	128.7
-20	2.74	4.94	0.51	46.1	74.7
-20	2.90	4.76	0.52	41.4	69.5
-20	2.84	4.82	0.52	44.6	74
-40	2.81	4.85	0.51	38.1	62.8
-40	2.87	4.79	0.52	33.2	55.5
-40	2.87	4.79	0.52	35.5	59.3
-70	2.73	4.94	0.51	22.4	36.2
-70	2.86	4.80	0.52	23.7	39.5
-70	2.84	4.82	0.52	22.0	36.4
-100	2.84	4.82	0.52	12.5	20.7
-100	2.89	4.77	0.52	11.8	19.8
-100	2.92	4.74	0.53	14.2	24.1
-196	2.75	4.92	0.51	2.8	4.6
-196	2.76	4.91	0.51	3.9	6.4
-196	2.86	4.80	0.52	2.8	4.7

Appendix P Charpy absorbed energy grade X70 as-received over range -196°C to RT temperature tested in non-instrumented machine 300 J by CVN_{PC}.B= 1T

T (°C)	a_1 (mm)	b_1 (w-a) (mm)	Ratio (a/w)	CVN_{exp_wv} *(J)*	$CVN_{exp\_scale\_wv}$ *(J)*
21	3.00	5.01	0.50	86.6	138.5
21	2.91	5.10	0.49	82.4	129.4
21	2.89	5.12	0.49	82.7	129.4
-20	2.83	5.18	0.48	86.1	133.1
-20	2.82	5.18	0.48	81.3	125.6
-20	2.81	5.19	0.48	72.5	111.8
-40	2.88	5.13	0.49	62.4	97.4
-40	2.88	5.13	0.49	65.8	102.6
-40	2.87	5.14	0.49	46.1	71.8
-70	2.89	5.11	0.49	67.8	106.1
-70	2.90	5.11	0.49	44.7	70.1
-70	2.91	5.10	0.49	33.9	53.2
-100	2.86	5.15	0.49	28.5	44.3
-100	2.87	5.13	0.49	33.9	52.9
-100	2.87	5.14	0.49	24.4	38
-196	2.90	5.11	0.49	3.0	4.7
-196	2.82	5.19	0.48	3.4	5.2
-196	2.91	5.09	0.49	4.1	6.4

Appendix Q Charpy absorbed energy grade X60 as-received over range -196°C to RT temperature tested in non-instrumented machine 300 J by CVN_{PC}.B= ¾ T

T (°C)	a_1 (mm)	b_1 (w-a) (mm)	Ratio (a/w)	CVN_{exp_wv} (J)	$CVN_{exp\_scale\_wv}$ (J)
21	2.84	5.17	0.48	27.5	42.6
21	2.78	5.22	0.48	30.0	45.9
21	2.77	5.24	0.48	27.8	42.3
-20	2.98	5.02	0.50	20.3	32.4
-20	2.94	5.06	0.49	16.5	26.2
-20	2.96	5.05	0.50	18.3	29
-40	2.81	5.19	0.48	14.8	22.8
-40	2.82	5.19	0.48	12.5	19.2
-40	2.82	5.18	0.48	13.6	20.9
-70	2.86	5.15	0.49	7.6	11.8
-70	2.87	5.14	0.49	6.6	10.4
-70	2.90	5.11	0.49	6.8	10.6
-100	2.89	5.12	0.49	4.1	6.4
-100	2.77	5.24	0.48	4.7	7.3
-100	2.94	5.07	0.49	3.8	6.0
-196	2.80	5.20	0.48	2.0	3.1
-196	2.84	5.17	0.48	2.2	3.4
-196	2.76	5.25	0.48	2.0	3.1

Appendix R PCCVN set of samples exposed at different hours in flue-gas

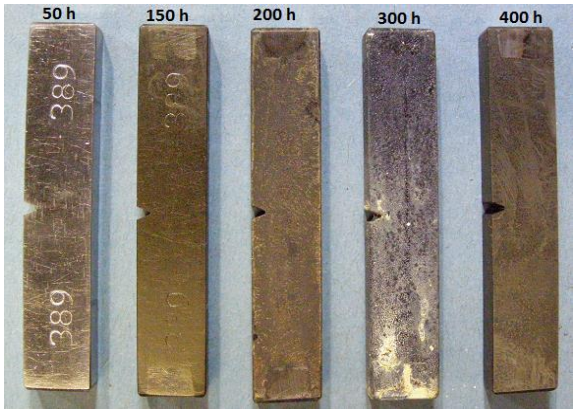

(a) Grade X60, impurity SO_2

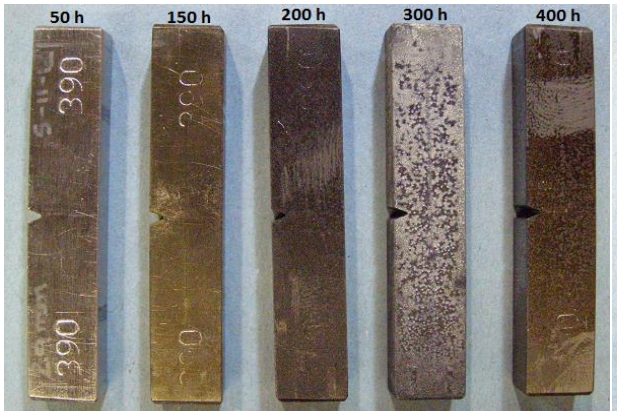

(b)Grade X70, impurity SO_2

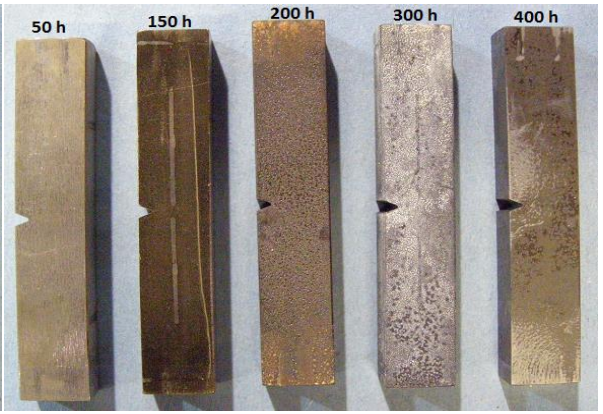

(c) Grade X100, impurity SO_2

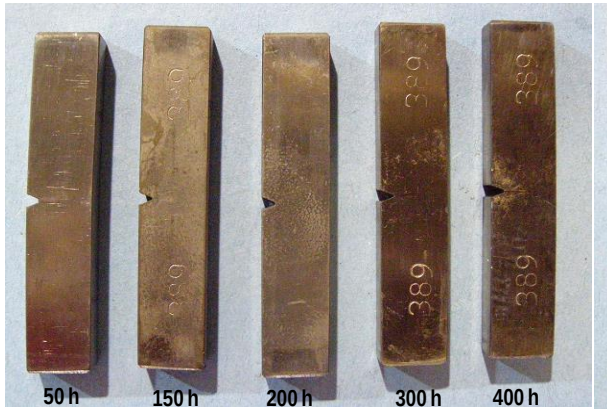

d) Grade X60, impurity H_2S

(e) Grade X70, impurity H_2S

(f) Grade X100, impurity H_2S

Appendix S Energy absorbed of steels exposed in flue-gas over range 50h to 400h tested at -20°C using a non-instrumented machine 300J capacity

Steel	Gas Impurity	$Aging_{temp}$ (°C)	a_1 (mm)	b_1 (w-a) mm	Ratio (a/W)	CVN_{exp_wv} (J)	$CVN_{exp\_scale\_wv}$ (J)
X100	SO_2	50	3.25	4.75	0.53	42.7	126
		150	3.21	4.79	0.52	41.4	132
		200	3.16	4.85	0.52	40.9	136
		300	3.04	4.97	0.50	45.4	133
		400	3.17	4.84	0.52	43.4	98
	H_2S	50	3.07	4.93	0.51	40.8	72
		150	3.08	4.92	0.51	49.5	69
		200	3.09	4.92	0.51	46.1	68
		300	3.09	4.91	0.51	46.1	73
		400	3.04	4.97	0.50	45.4	72
X70	SO_2	50	3.10	4.91	0.51	81.3	133
		150	3.10	4.91	0.51	83.4	136
		200	3.07	4.93	0.51	80.0	130
		300	3.07	4.93	0.51	73.9	120
		400	3.13	4.88	0.51	67.8	111
	H_2S	50	3.11	4.90	0.51	77.3	126
		150	3.11	4.90	0.51	80.7	132
		200	3.03	4.98	0.50	84.3	136
		300	3.14	4.87	0.51	80.8	133
		400	3.05	4.95	0.51	60.3	98
X60	SO_2	50	3.11	4.90	0.51	19.0	31
		150	3.12	4.89	0.51	21.0	34
		200	3.12	4.88	0.51	21.7	36
		300	3.25	4.75	0.53	22.4	38
		400	3.07	4.93	0.51	21.7	35
	H_2S	50	3.10	4.91	0.51	20.2	33
		150	3.14	4.86	0.51	19.7	32
		200	3.15	4.86	0.51	21.7	36
		300	3.10	4.91	0.51	19.0	31
		400	3.10	4.91	0.51	21.0	34

Appendix T Fracture toughness of steels exposed in simulate flue-gas tested at -20°C and determine by Marandet & Sanz correlation

Steel	Impurity	Aging temp	$K_{Ic\_exp\_wv\_M\&S}$	$K_{Ic\_exp\text{-}scale\_wv\_M\&S}$
		(h)	$(MPa.m^{0.5})$	$(MPa.m^{0.5})$
X60	SO_2	50	83	106
		150	87	111
		200	88	113
		300	90	117
		400	88	113
	H_2S	50	85	109
		150	84	108
		200	88	114
		300	83	106
		400	87	111
X70	SO_2	50	171	219
		150	173	222
		200	170	216
		300	163	208
		400	156	200
	H_2S	50	167	214
		150	171	218
		200	174	221
		300	171	219
		400	148	188
X100	SO_2	50	124	161
		150	122	158
		200	122	156
		300	128	163
		400	125	161
	H_2S	50	121	155
		150	134	170
		200	129	165
		300	129	165
		400	128	163

Appendix U Fracture toughness of steels exposed in simulated flue-gas tested at -20°C and determine by SINTAP correlation

Steel	Impurity	Aging temp (h)	$K_{Id\_exp\_wv\_ST}$ $(MPa.m^{0.5})$	$K_{Id\_exp\text{-}scale\_wv\_ST}$ $(MPa.m^{0.5})$
X60	SO_2	50	83	106
		150	87	111
		200	88	113
		300	90	117
		400	88	113
	H_2S	50	85	109
		150	84	108
		200	88	114
		300	83	106
		400	87	111
X70	SO_2	50	171	219
		150	173	222
		200	170	216
		300	163	208
		400	156	200
	H_2S	50	167	214
		150	171	218
		200	174	221
		300	171	219
		400	148	188
X100	SO_2	50	124	161
		150	122	158
		200	122	156
		300	128	163
		400	125	161
	H_2S	50	121	155
		150	134	170
		200	129	165
		300	129	165
		400	128	163

APPENDICES CHAPTER FIVE

Appendix V Laser profile for rolled samples

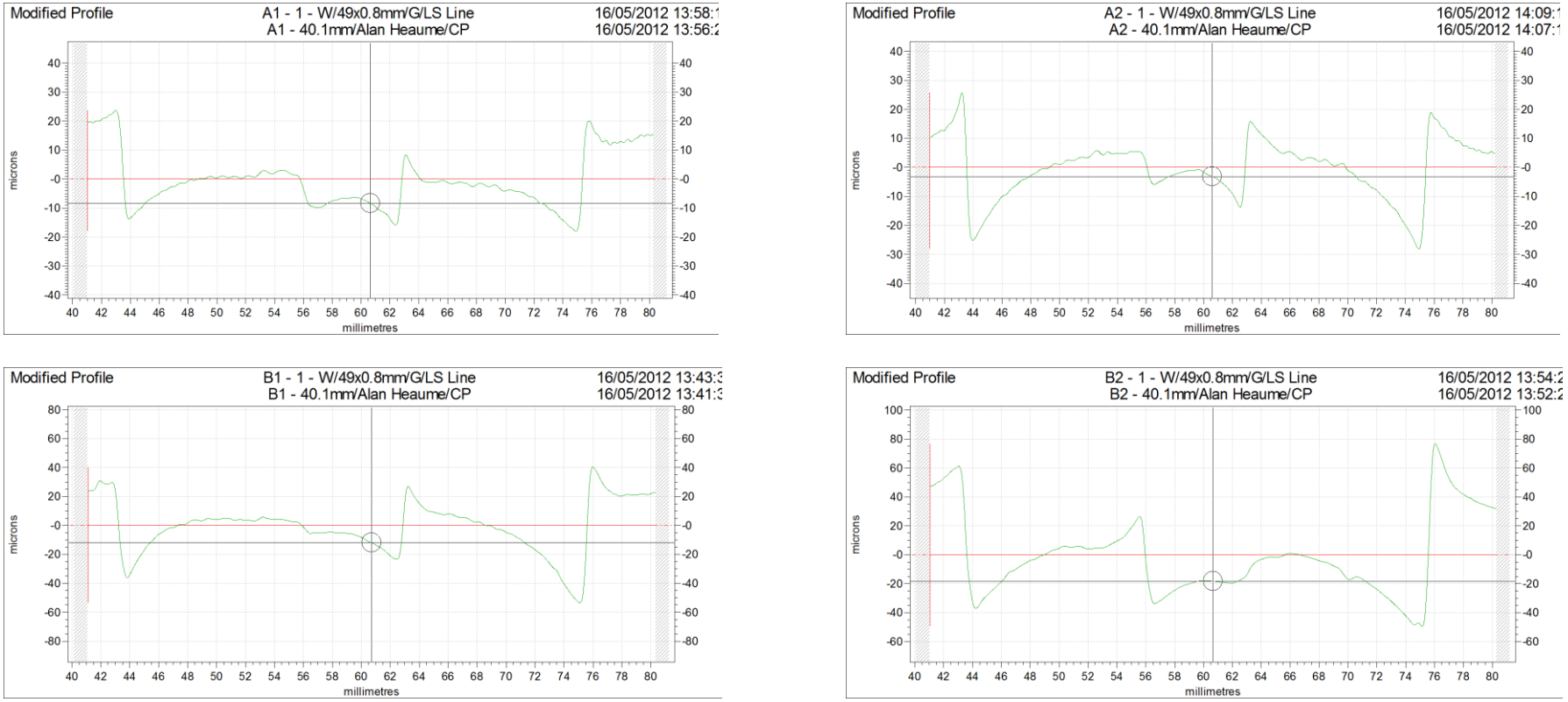

Figure V-1 Profile rolling track determined using a laser profiler for samples A and B

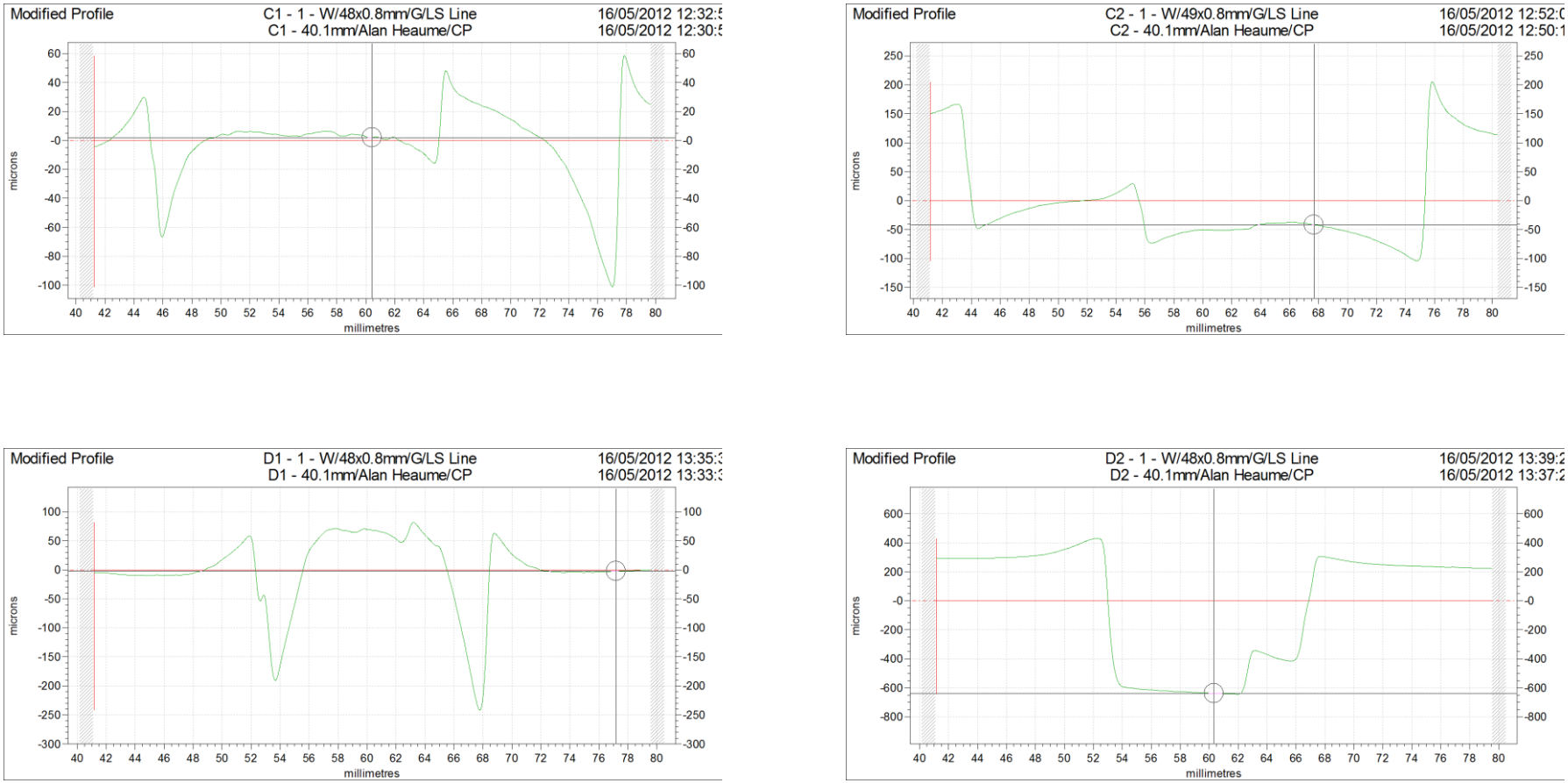

Figure V-2 Profile rolling track determined using a laser profiler for samples A and B

Appendix W Transverse and Normal residual stresses

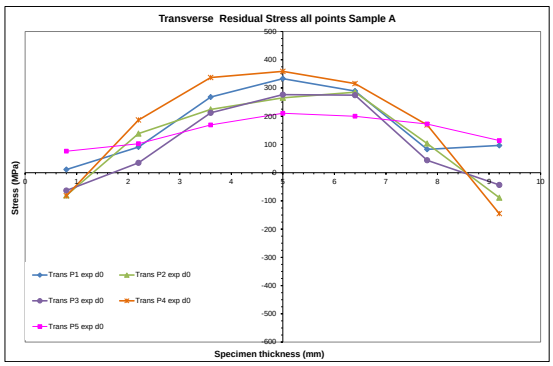

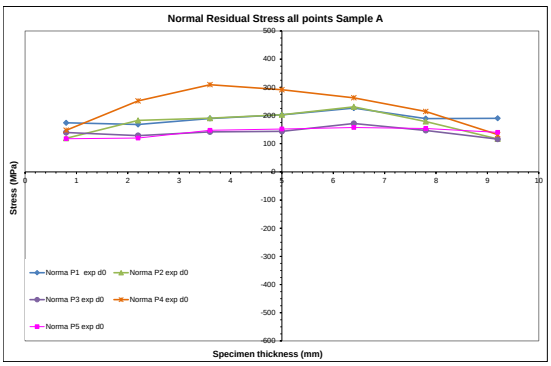

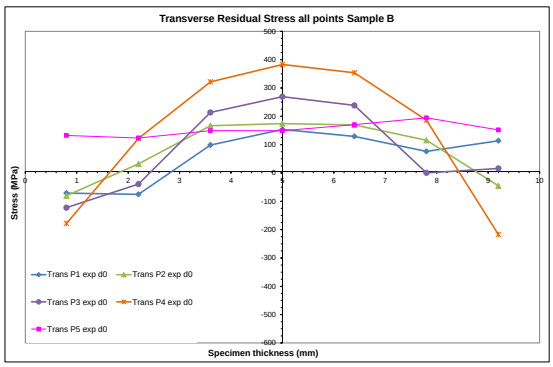

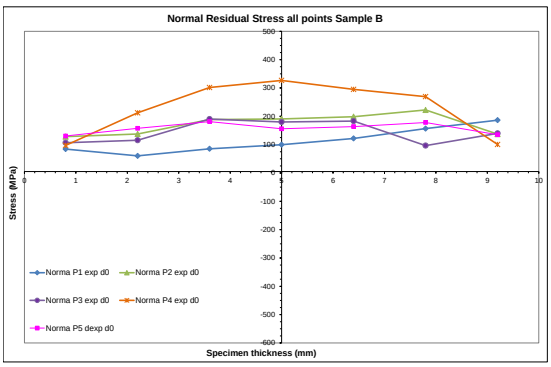

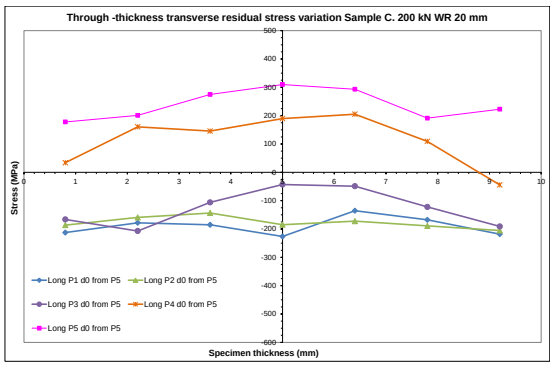

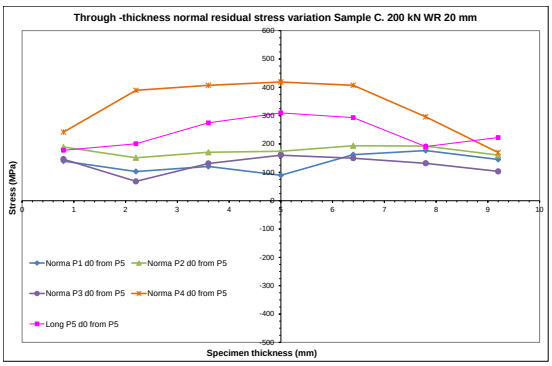

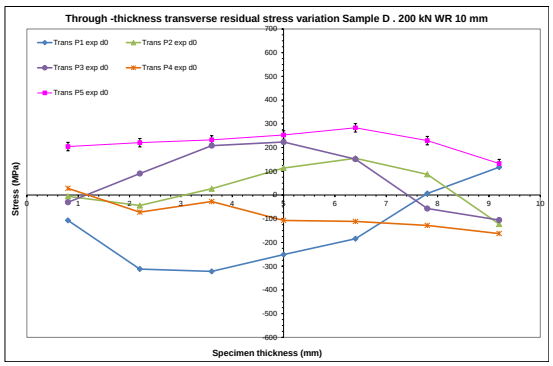

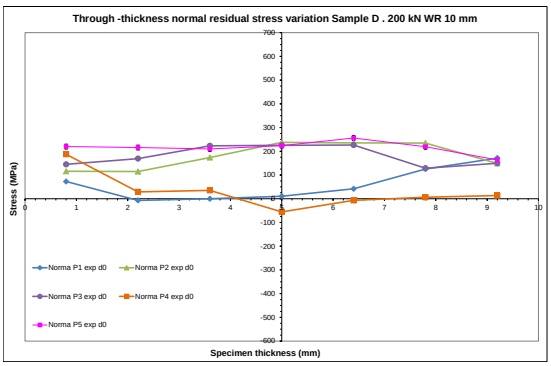

Figure W-1 Residual stress variation on samples A, B, C and D from ND test through-thickness

Appendix X Transverse and Normal residual stresses

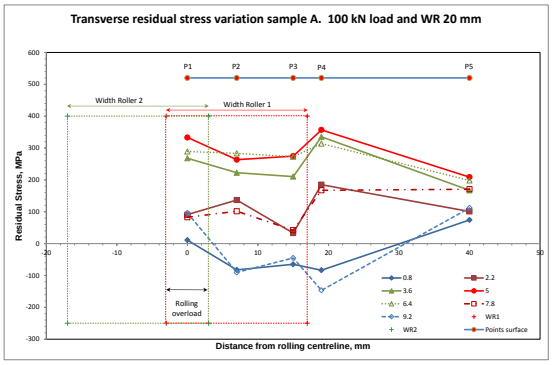

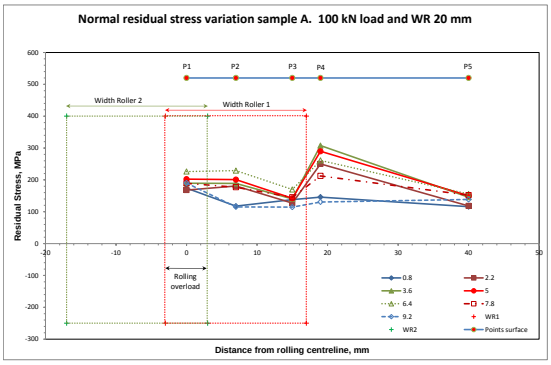

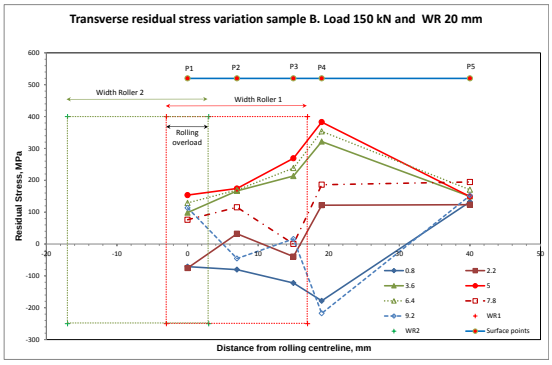

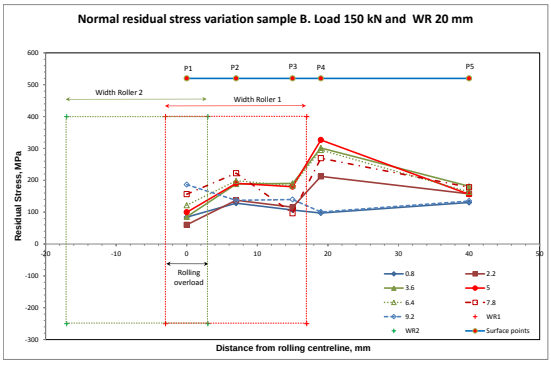

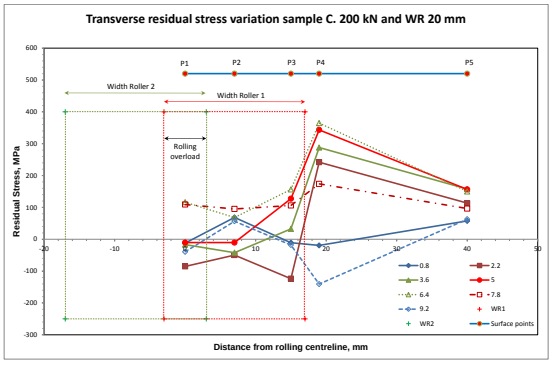

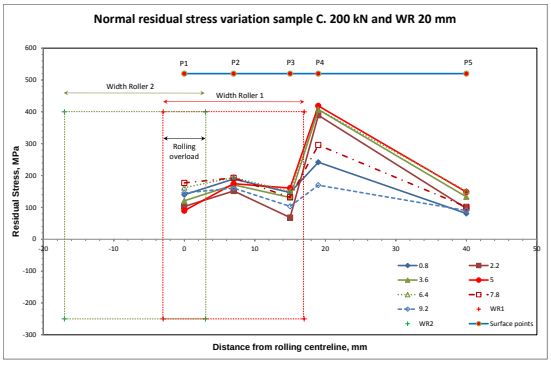

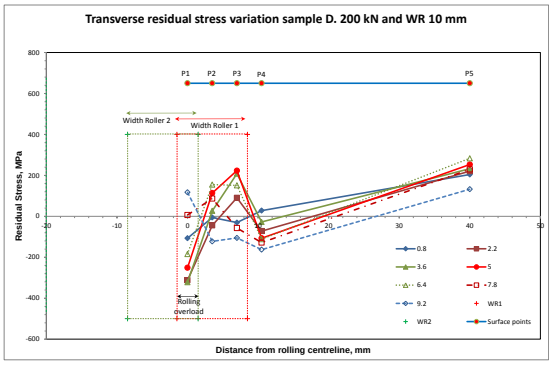

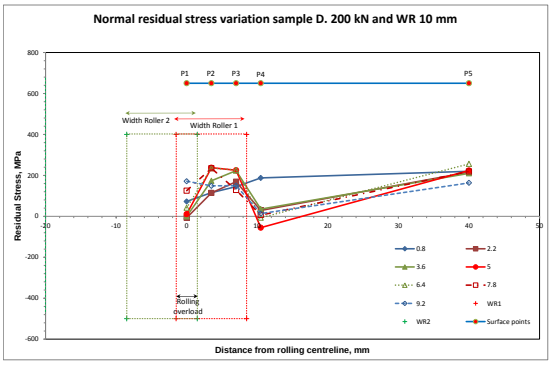

Figure X-1 Residual stress samples A, B, C and D from ND test along transverse section

Appendix Y Strain data variation with depth obtained by ICHD

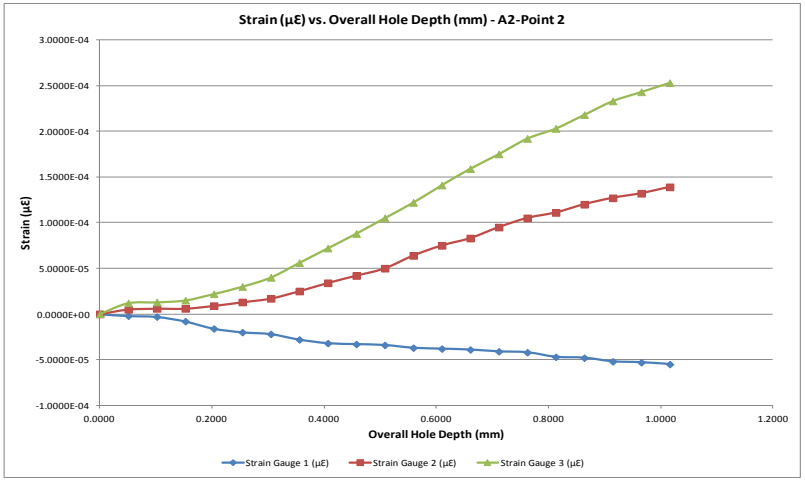

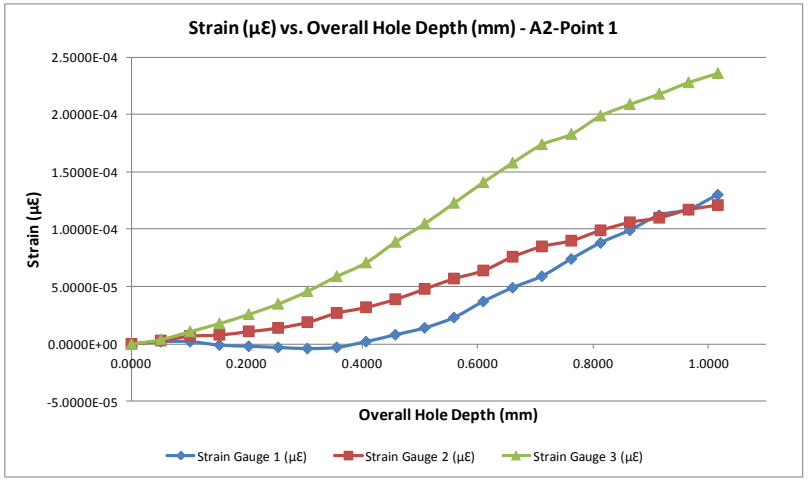

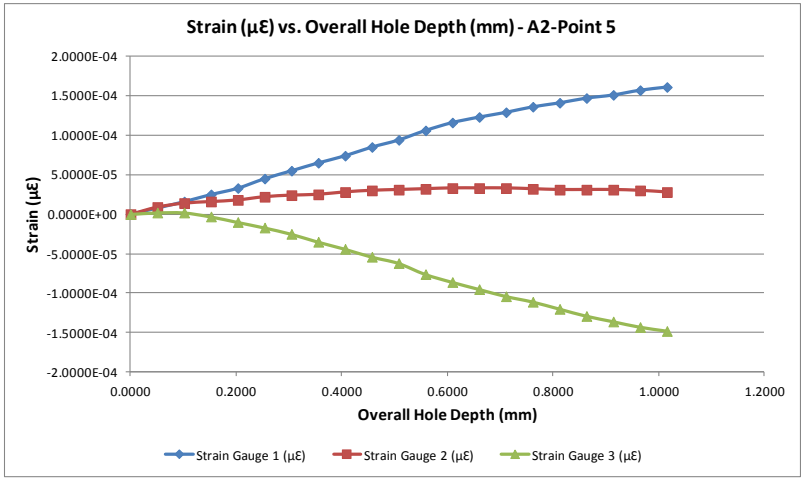

Figure Y-1 Typical curves for strains measurements. Sample A

Appendix Z Transverse RS by ICHD and OIHD

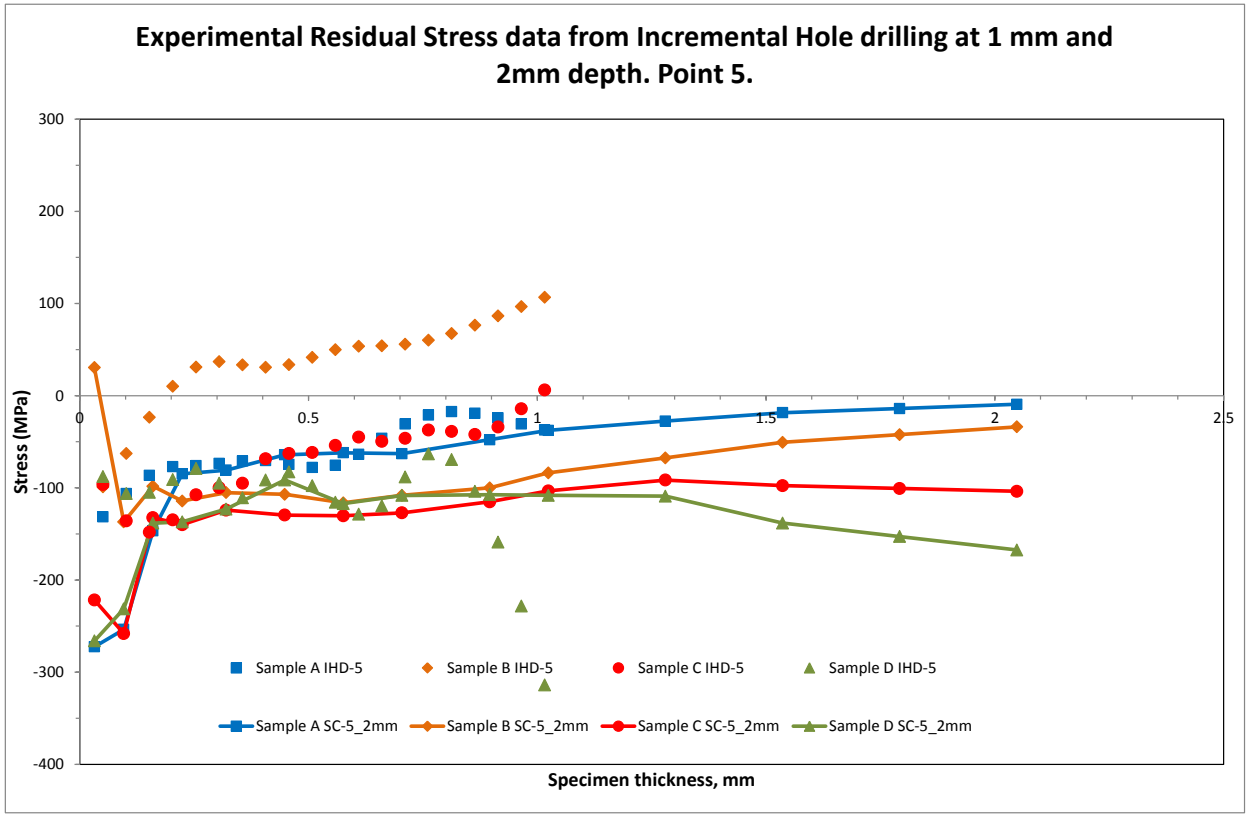

Figure Z-1 Comparison transverse RS by ICHD

Appendix AA Transverse RS by ND and ICHD

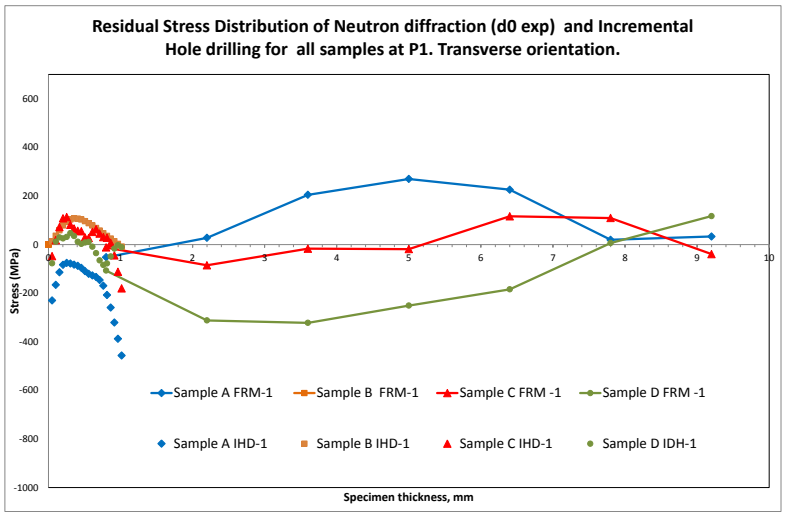

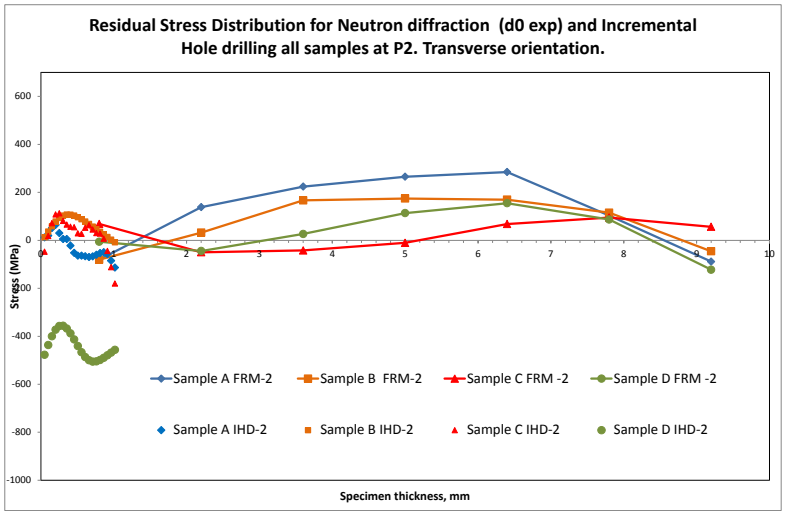

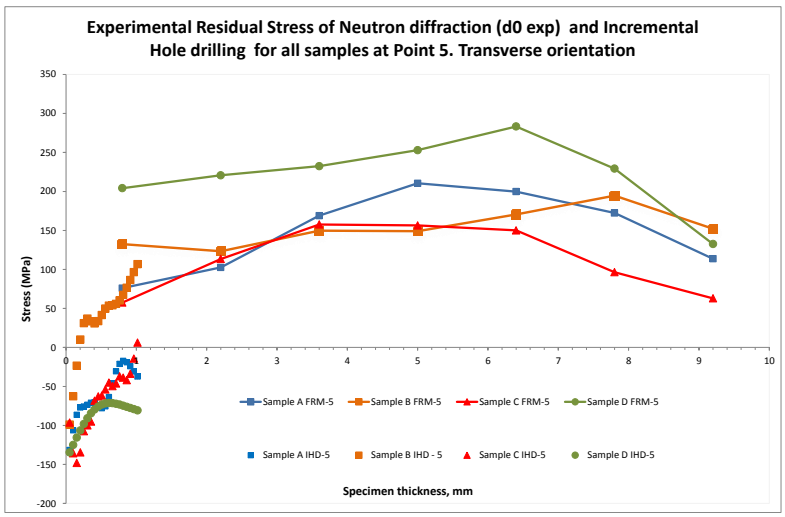

Figure AA-1 Comparison transverse stresses in samples A, B, C and D through-thickness at points 1, 2 and 5.